Indira Gandhi Centre for Atomic Research

Annual Report - 2015

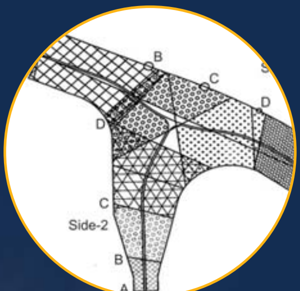

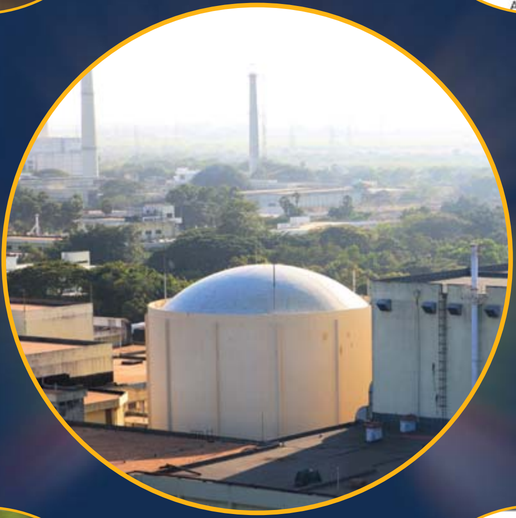

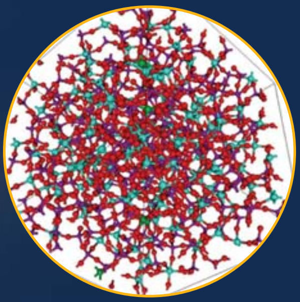

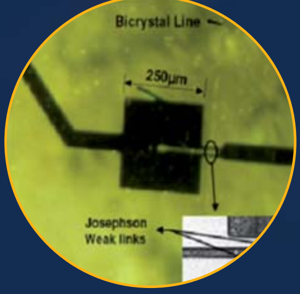

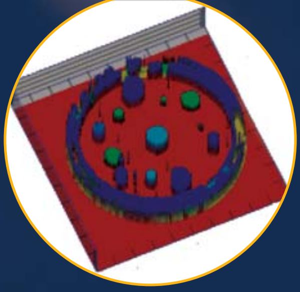

Government of India
Department of Atomic Energy
Indira Gandhi Centre for Atomic Research
Kalpakkam - 603 102

IGCAR

INDIRA GANDHI CENTRE FOR ATOMIC RESEARCH

Annual Report - 2015

सत्यमेव जयते

Government of India
Department of Atomic Energy
Indira Gandhi Centre for Atomic Research
Kalpakkam 603 102

“Actions today mould our tomorrows”

- Indira Gandhi

"…. The relative role of indigenous science & technology and foreign collaboration
can be highlighted through an analogy.
Indigenous science and technology plays the part of an engine in an aircraft,
while foreign collaboration can play the part of a booster.
A booster in the form of foreign collaboration can give a plane an assisted take-off,
but it will be incapable of independent flight unless it is powered by engines of its own.
If Indian industry is to take-off and be capable of independent flight,
it must be powered by science & technology based in the country ..."

- Homi Jehangir Bhabha

"…..There is a totality about modernisation, and in order to gain confidence,
we must experiment with our resources even at the risk of failure.
There is a need for a constant interplay between basic sciences, technology,
industrial practice and management, if economic progress is to result
from the activity undertaken"

- Vikram Sarabhai

Address for Correspondence
Dr. M. Sai Baba
Chairman, Apex Editorial Committee
Associate Director, Resources Management Group
Indira Gandhi Centre for Atomic Research
Kalpakkam - 603 102
Phone : +91-44-27480115
Fax : +91-44-27480060
Email : msb@igcar.gov.in
Website : www.igcar.gov.in

CONTENTS

Back Cover

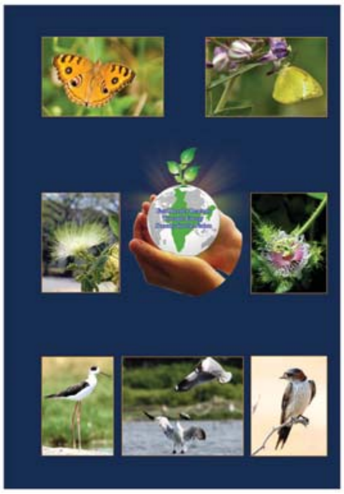

Front Cover

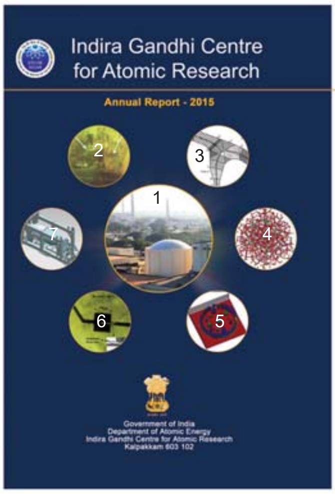

Front Cover

1. Fast Breeder Test Reactor
2. A view of dimensional measurement-cum-laser dismantling machine in hot cell 1
3. Radiographic testing shooting sketch showing regions covered in each stage
4. Structure of iron phosphate glass with 4 % Fe^{2+} concentration
5. Wavelet processed three dimensional image of defects in coarse grained austenitic stainless steel by ultrasonic testing
6. High temperature superconducting quantum interference device fabricated on bicrystal substrate
7. Cask handling at Prototype Fast Breeder Reactor

Back Cover
Flora and Fauna at Kalpakkam

Published by
Scientific Information Resource Division, Resources Management Group
Indira Gandhi Centre for Atomic Research, Kalpakkam - 603 102

Foreword

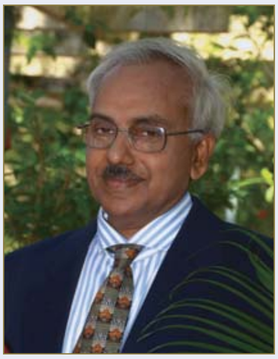

I am happy to share with you the Annual Report from IGCAR for 2015. Our Centre continues to tread the path of excellence in the domain of R&D in the Fast Reactor and associated fuel cycle technologies.

Fast Breeder Test Reactor is presently in the 24th irradiation campaign, after replacing the control rods and their outer sheaths, with an increased number of thoria blanket subassemblies undergoing irradiation. It gives us lot of confidence that all the short and medium term recommendations of SARCOP including post-Fukushima and seismic retrofits have been implemented. Periodic safety review of KAMINI for seeking five-year extension of licensing is in progress. Prototype Fast Breeder Reactor is in final stages of commissioning. We are working closely with BHAVINI towards early criticality of PFBR. R&D towards improvements for FBR 1 and 2 is in progress.

A position paper on the need and rationale for metal fuel test reactor has been submitted to DAE for consideration. A conceptual core design for 100 MWt Metal Fuel Test Reactor and that of two more oxide fuelled Commercial Breeder Reactors of 600 MWe is being evolved, with improved economy and enhanced safety features. A number of experimental facilities have been established or commissioned during the year, notable amongst them being the 100 tonne multi axis shake table, first of its kind in our country, RISHI (Research facility for Irradiation studies in Sodium at High temperature), an innovative out of pile test loop, with passive systems under DAE-CEA collaboration on JHR (Jules Horowitz Reactor) and a multiple fuel pin test facility, RABITS (Rupture And Ballooning In TubeS) for testing the ballooning behaviour of clad tubes.

It is heartening that reprocessing programme has matured very well and we are able to conduct about multiple campaigns every year at the CORAL. The operating experience with CORAL has given good insights into the design and commissioning of Demonstration Fast Reactor Fuel Reprocessing Plant (DFRP). Using advanced alkoxyacetamide reagents, synthesized in house, partitioning of actinides from high active waste has been demonstrated. In addition, the organo-functionalized inorganic and magnetic materials have been developed and demonstrated for magnetic assisted mutual separation of lanthanides and actinides. Concurrently, progress in R&D of pyro chemical reprocessing and setting up of High Temperature Electro refining setup is going on in full swing.

Fast Reactor Fuel Cycle Facility (FRFCF), an important project for the success of Fast Reactor programme in the Country, being constructed with inputs from BARC and NFC. Construction of Training Centre, Administration Building, Central Surveillance, Safety & Health Physics building and other service buildings are progressing very well. All the required actions have been initiated for the construction of various plants of FRFCF in a planned manner and procurement of long delivery items.

We have made considerable progress in the domains of Electronics and Instrumentation. The international acclaim for our efforts in the area of Wireless Sensor Networks (technology transferred to ECIL for broader reach), successful monitoring of plutonium in air, a state-of-the-art 400 nodes, 9600 cores supercomputing cluster system with performance rating of 200 teraflops and progress in R&D for instrumentation of future FBRs, stand a testimony to our abilities. Successful demonstration of the Online Nuclear Emergency Response Decision Support system (ONERS) along with weather prediction system and environmental research in the areas such as bioremediation for uranium recovery (fresh and sea water) are some more feathers in the crown.

It gives me immense happiness that our Centre is in the forefront in development of newer materials development, preparation, characterization, simulation, newer techniques for synthesis and methodologies for analysis in aiding the various aspects of mission programmes of the Centre.

We are happy to share the summary of a few of the achievements in the previous year in this report. We have formulated a vision document to identify short-term and long-term goals for the Centre. We look forward to achieving them and taking even greater strides in the coming year with your continued support and guidance.

I would like to compliment the editorial team steered by Dr. M. Sai Baba for bringing out this document with an invigorating modern design even while keeping up the traditional flavor. I would also like to appreciate colleagues from Resources Management Group, Shri G. Pentaiah and Shri K. Varathan in particular for their contributions and efforts in bringing out this report.

(Dr. S.A.V. Satya Murty)
Director, IGCAR

Mission of IGCAR

« *To conduct a broad based multidisciplinary programme of scientific research and advanced engineering development, directed towards the establishment of the technology of Sodium cooled Fast Breeder Reactors (FBR) and associated fuel cycle facilities in the Country*

« *The development and applications of new and improved materials, techniques, equipment and systems for FBRs and*

« *To pursue basic research to achieve breakthroughs in fast reactor technology*

Vision

To be a Global Leader in Sodium cooled Fast Breeder Reactor
and associated Fuel Cycle Technologies by 2020

Editorial

I have great pleasure in presenting the Annual Report of Indira Gandhi Centre for Atomic Research for the year 2015 as the Chairman of the Editorial Committee. Annual report of the Centre highlights the significant activities we have undertaken in the last one year. Even while bringing out the challenges in R&D programmes, it nevertheless reveals the variety and profundity of the programmes. It has been a dedicated effort involving collection of relevant articles and articulating to the benefit of a technical reader. I am supported by a team of able editorial committee members, whose pain staking effort has gone into bringing the report in the present form, after multiple iterations of editing.

Keeping in line with the mission and vision of the Centre, the articles have been distributed in chapters to highlight the achievements in each of the aspects, (viz.) FBTR, PFBR, R&D of FBRs, Fuel Cycle, Basic Research and Infrastructure Facilities.

The flagship of the Centre, FBTR, has continued to operate successfully reaching newer milestones in efficiency. Loading of additional thoria blanket subassemblies, fabrication of U-Zr fuel slugs for irradiation, safety review of KAMINI as a part of retrofitting and testing of newer devices like fission chambers are described in various articles in the chapter on FBTR. The commissioning of PFBR is at an advanced stage of completion. While our Centre has provided the R&D required, miscellaneous activities including simulation and testing of devices in sodium, design of shielded cask for fuel transport and functional testing of systems towards enhancing safety carried out are described in Chapter II. In Chapter III, the progress in R&D towards design and development of core and components of future breeder reactors including metal fuelled fast reactors with emphasis on improved economics and safety, is described in various articles. Fast Reactor Fuel Cycle Facility, holds a great promise in facilitating closing of the fuel cycle. Articles on the progress of construction of this facility and the progress of supporting R&D towards closing of the fuel cycle by the aqueous and pyroprocessing route are described in Chapter IV. Despite being a mission oriented Centre, exciting research in basic sciences and engineering are carried out towards achieving breakthroughs and benchmarks in technology. Chapter V lists some significant articles towards the development of newer materials, processes, property measurements and simulation studies being undertaken in the Centre. Articles in Chapter VI, highlights the major infrastructural and system developments in 2015. Chapter VII provides a diary of significant events including seminars, workshops and eminent and popular lectures/colloquia and also showcases our achievements in the form of awards and honours. The Editorial Committee sincerely thanks the authors who have contributed interesting articles highlighting the achievements.

The Editorial Committee is indebted to Dr. S. A. V. Satya Murty, Director, IGCAR for his outstanding leadership, continuous guidance and emphasis on adherence to time schedules, which have been effective in bringing out this report in time and with quality. The committee is particularly thankful to Shri G. Pentaiah and Shri K. Varathan of Resources Management Group, for their contributions towards expediting the publication.

M. Saibaba

(M Sai Baba)
Chairman, Editorial Committee &
Associate Director,
Resources Management Group

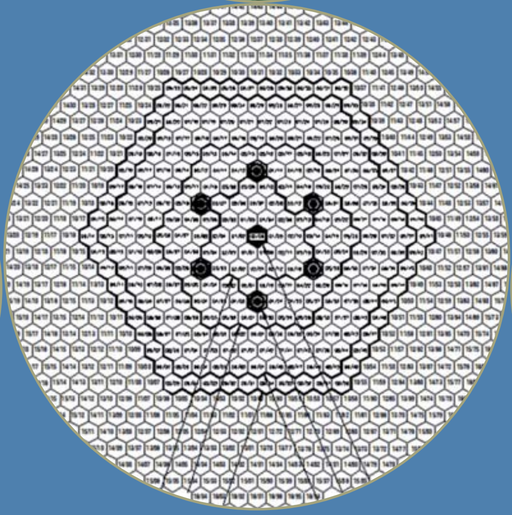

CHAPTER I

Fast Breeder Test Reactor

I.1 Loading of Thoria Blanket Subassemblies in FBTR

FBTR core consists of 745 closely packed locations, with fuel at the centre, surrounded by nickel reflectors, thoria blankets and steel reflectors. The original full core of FBTR (65 subassemblies of MOX) envisaged loading of 342 thoria subassemblies in the 9th through 14th rings. Currently, only the 9th ring of the core has been loaded with thoria blankets. It is proposed to progressively load thoria blankets in the 10th, 11th, 12th, 13th & 14th rings. They will remain in place till the end of life of the reactor, as originally envisaged.

Prior to starting 24th irradiation campaign, it is proposed to load 126 thoria subassemblies in 10th and 11th rings. 72 subassembly are proposed to be loaded at the end of 24th irradiation campaign.

Each thoria subassembly consists of seven blanket pins covered by a hexagonal sheath (Figure 1). Each pin contains a stack of fifty four sintered thorium oxide pellets. They are placed inside a clad tube made of austenitic stainless steel AISI 316 L. All the seven pins are identical. The pins are free to expand axially towards the top. The details of the pin are:

Total length & diameter: 1153.0 & 16.0 mm
Pellet length & diameter: 20.0 & 15.35 mm

Nuclear Fuel Complex, Hyderabad has fabricated all the thoria subassemblies required for the 9th through 14th rings as per the original requirement. In addition to the fifty four subassemblies loaded in the 9th ring in 1999, which are undergoing irradiation, 15 numbers of thoria subassemblies were loaded temporarily in the 15th and 16th ring locations before the start of the 23rd campaign (with SARCOP permission), for eventual transfer to inner locations, pending a decision on the final destination of the thoria subassembly. The remaining fresh thoria subassemblies continue to be stored in fresh fuel area.

The residual life of FBTR is dictated by the dpa on grid plate. Based on the operating history, it is estimated that the current residual life of FBTR is 5.6 effective full power years. It is estimated that after 5.6 years of irradiation in the core in the present core configuration, the linear heat rating in the thoria subassemblies in the 9th, 10th, 11th and 12th rings (Figure 2), would be 21.2, 8.9, 6.36 and 5.1 W/cm respectively. It may be noted that for the 9th ring the linear heat rating is more as these subassemblies have been in the reactor since 1999. The linear heat rating values are less than the allowed limit of 54 W/cm. The total power generated by the 252 subassemblies in the 9th through 12th rings is estimated to be 818 kWt at the end of 5.6 effective full power years .

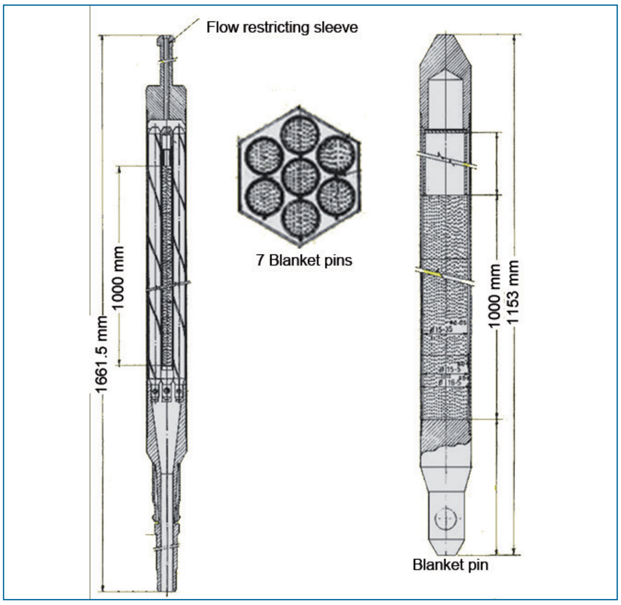

Fig. 1 *Thoria blanket subassembly*

The thoria subassemblies loaded in FBTR will remain in the reactor till the end of life of FBTR and will be removed and sent for reprocessing during unloading of entire core of FBTR.

The dose on the maximum rated blanket subassembly at the end of life in the reactor and after two years cooling is 2130 R/h compared to 5170 R/h for a MK-I fuel subassembly, which has seen a burn-up of 155 GWd/t and after two years cooling. This includes the activity build-up due to ^{232}U.

Based on the above information safety authorities gave approval for loading thoria subassemblies in 9th and 10th rings prior to starting of 24th irradiation campaign. The loading of thoria in these rings has been completed.

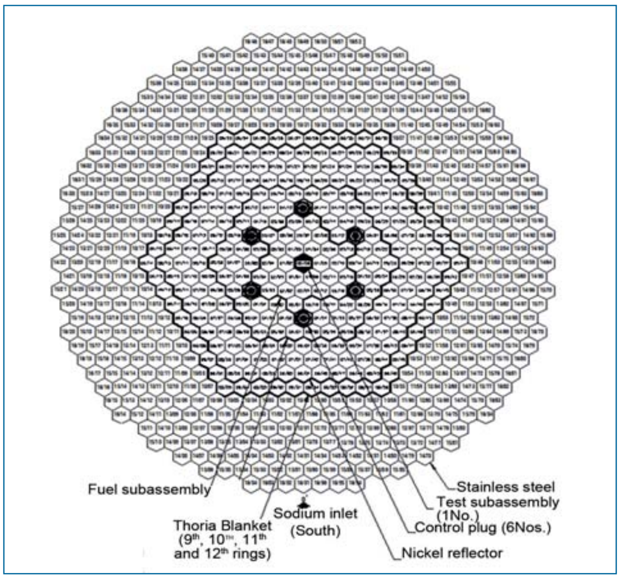

Fig. 2 *FBTR core*

I.2 Dimensional Changes in FBTR Fuel Pins as a Function of Position within the Core

Austenitic stainless steel components in the core of a fast reactor undergo significant dimensional changes and distortions due to irradiation induced swelling and creep, limiting useful life of a fuel subassembly in the reactor. While dilation of fuel pins can lead to coolant flow reduction and local temperature increase, the dilation and bow of hexcan can result in fuel handling difficulties. Dimensional changes induced by swelling and creep are a strong function of the displacement damage (dpa) and the temperature of irradiation. The typical clad-midwall temperature in FBTR ranges from ~410 °C at core bottom to ~570 °C at the core top, while the displacement damage is 85 dpa at core center and axially drops down to about 52 dpa at either end. Valuable insights on dimensional stability of 20% CW AISI 316 SS clad of FBTR have been obtained as a function of its position within the core through extensive post-irradiation measurements.

The dilation strains (in cladding derived from profilometry data has been compared with swelling strains calculated from immersion density measurements to assess the relative contributions of swelling and creep. It is seen that the swelling strains constitute almost 90% of the total diametral strains in the 1st ring fuel pins, while for the 3rd ring pins, the contribution of void swelling to the total diametral strain is relatively less and the contribution of creep induced strains is significantly higher (Figure 1).

Higher creep strain in the 3rd ring pins is attributed to severe fuel clad mechanical interaction on the account of higher swelling of the carbide fuel operating at relatively lower linear heat rate (linear heat rating ~250 W/cm) as compared to the heat rate of 400 W/cm in the 1st ring. The higher fuel clad mechanical interactions in the 3rd ring pins is also seen to result in higher length increase in the fuel pins. It is well known that the fuel pin length increase is primarily caused by the void swelling of cladding integrated over its length. However, under severe fuel clad mechanical interaction conditions, the axial swelling of fuel enhances axial strains on the clad over and above the axial strain due to void swelling. This is evident from Figure 2 which reveals higher increase in the pin length corresponding to higher fuel stack length increase in the data sets of 1st and 3rd ring fuel pins with similar displacement damage. The number of fuel pins within the fuel subassembly, having pin length increase (ΔL) exceeding 5 mm (over a length of 531.5 mm) progressively increases from 1st ring

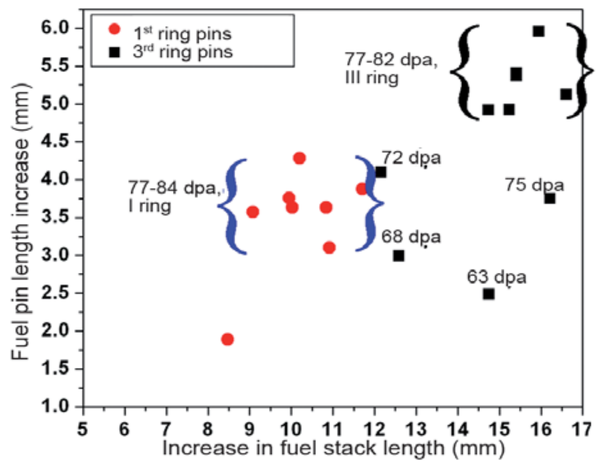

Fig. 2 Comparison of the fuel stack length increase with fuel pin length increase

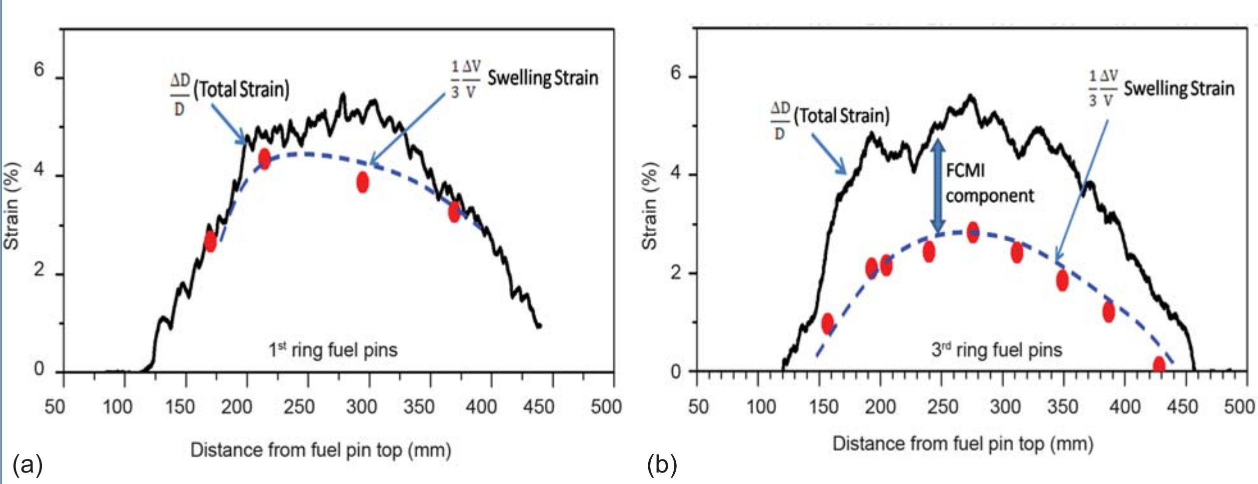

Fig. 1 Swelling and creep components of diametral strain of fuel pins in (a) 1st and (b) 3rd ring fuel pins of similar burn-up and displacement damage

towards the 3rd ring positions (Figure 3). This validates the increasing influence of fuel clad mechanical interaction to overall pin length increase as we move towards the outer rings.

Besides increase in the diameter and length, localized bending and ovalisation were also noticed in the fuel pins of 3rd ring possibly caused by the restraining forces of spacer wire on axial cladding strains as well as the restraint and interaction with adjacent pins.

In summary, (i) though the diametral strains in 1st and 3rd rings pins are more or less comparable, the relative contributions of swelling and creep strains vary as a function of core position and (ii) the increase in overall fuel pin length as well as localized distortions are higher in 3rd ring pins as compared to fuel pins of central location or 1st ring. These effects are primarily due to the swelling of carbide fuel.

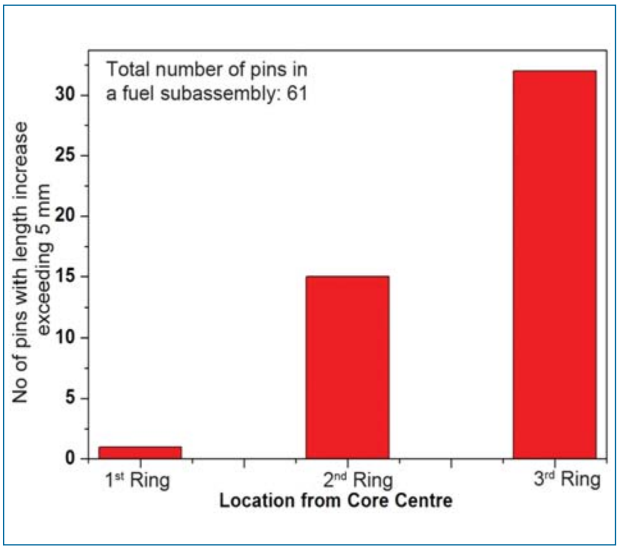

Fig. 3 *Number of pins with length increase greater than 5 mm as a function of position in core*

I.3 Constitutive Description of Flow Behaviour of Post-irradiated 316 Austenitic Stainless Steel at Low dpa

Grid plate, which supports the entire core subassemblies in FBTR was made up of Type 316 SS operates at 623 K and experiences a cumulative dose of a few displacements per atom (dpa). In order to assess the irradiation induced degradation of grid plate, tensile properties of Type 316 SS were evaluated at 300 and 623 K for irradiation doses up to 2.57 dpa. At both temperatures, systematic increase in the yield and ultimate tensile strengths, and decrease in the ductility with increasing dose were noticed. In austenitic stainless steels, irradiation induced degradation in the mechanical properties results from the evolution of defects such as Frank loops and network dislocations, cavities and precipitation of new phases. However, the dominance of these individual defects depends largely on the irradiation temperature and dose. From numerous literature data, it is evident that the evolution of Frank loops and their variation with dose play an important role in controlling degradation in the grid plate irradiated at 623 K. In this context, it becomes necessary to identify the role of Frank loops and their interaction with network dislocations during post-irradiated deformation in type 316 SS. In order to obtain better insight into the physical phenomena controlling the deformation behaviour, detailed work hardening analysis in the framework of internal-variable approach has been performed. The description of work hardening also becomes essential for determining the stress-strain field distribution for the assessment of useful remaining life of reactor structural components using finite element analysis.

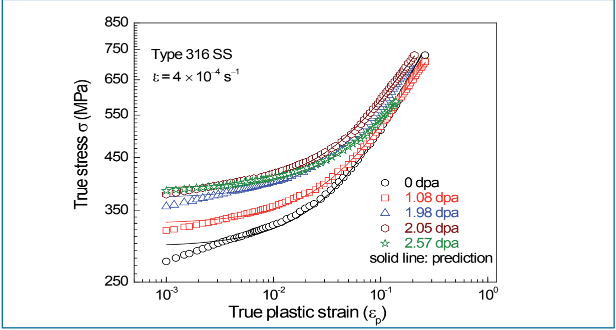

Fig. 1 *True stress-true plastic strain obeying internal-variable approach at 623 K for different dose levels*

The description of flow behaviour of the steel is interrelated to the network dislocation density (ρ_N) and irradiation induced defect (Frank loops) density (ρ_{lp}) based on dispersed barrier hardening model. In the internal-variable model, the first-order differential equations for the evolution of network dislocation density (ρ_N) and irradiation induced defect (Frank loops) density (ρ_{lp}) are coupled with the evolution of flow stress with plastic strain in order to predict the macroscopic deformation behaviour of the steel at 300 and 623 K. The differential equations were numerically integrated and unknown constants in the equations were optimized by interior-point algorithm. The model appropriately describes the post-irradiated type 316 SS flow behaviour at all the conditions. As an example, the variations in true stress-true plastic strain data at 623 K as well as the predicted data for different irradiated conditions are presented in Figure 1. Based on optimization, the observed irradiation induced defect annihilation parameter (ψ) at 300 K exhibits insignificantly low values which indicates the dominance of network annihilation on strain softening rather than annihilation of Frank loops by network dislocations (unfaulting mechanism). Significant increase in ψ found at 623 K suggested that unfaulting mechanism during deformation is thermally activated. Further, marginal increase in ψ value at 623 K with increasing irradiation dose indicates that the strain softening due to annihilation of Frank loops also depends on the initial irradiation induced defect density. These observations clearly suggested that the increase in unfaulting of loops with dose dominates at 623 K. This is also discernible in the variations of predicted irradiation induced defect density (ρ_{lp}) with plastic strain at 300 and 623 K for different irradiation doses (Figure 2). It can be seen that the defect density remains constant at 300 K, whereas there is a rapid decrease in defect density with plastic strain at 623 K. This investigation also suggested that the possibility of localised deformation due to annihilation of Frank loops results in dislocation channeling at 623 K against homogeneous deformation at 300 K in irradiated type 316 SS.

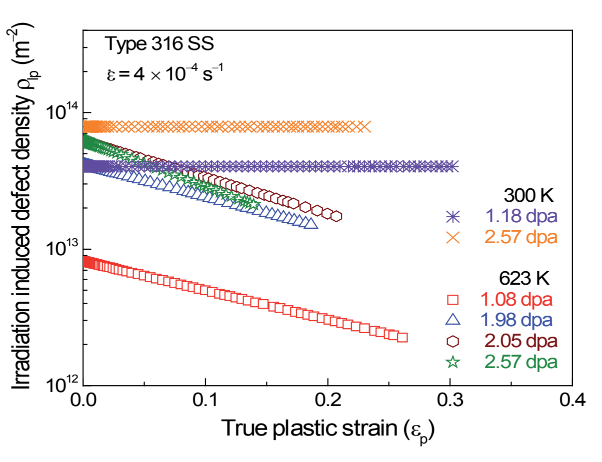

Fig. 2 *Evolution of predicted irradiation induced defect density with plastic strain at 300 and 623 K for different irradiated conditions*

I.4 Evolution of Dismantling Machines for Irradiated Fuel Subassemblies: from FBTR to PFBR

Remote dismantling of irradiated fuel and experimental subassemblies and extraction of fuel bundle and pins are critical operations in Radiometallurgy Laboratory hot cells for facilitating post-irradiation examination (PIE) as well as dispatch of fuel pins to CORAL for reprocessing. The design and development of customized hot cell equipment for dimensional measurements and dismantling of fuel subassemblies have undergone considerable evolution and improvements over the years.

The first generation system was a 4-axis computerized numerical control (CNC) milling machine developed in the 80's (Figure 1). The machine had a remotely changeable touch trigger sensor module for dimensional measurements and solid carbide slitting saw modules for longitudinal

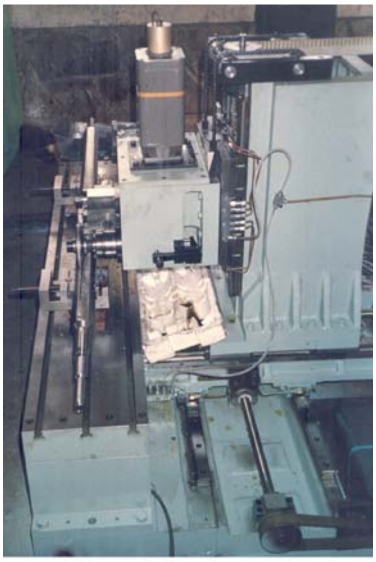

Fig. 1 *First CNC machine in hot cell 2*

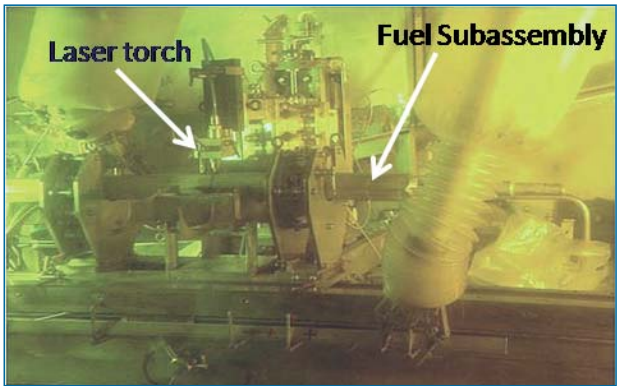

Fig. 2 A view of dimensional measurement-cum-laser dismantling machine in hot cell 1

and transverse cutting of hexagonal sheaths of fuel subassemblies (FSA). It had an end mill cutter module for preparation of tensile specimens from the hexagonal sheaths of dismantled FSAs. AC servo motors with optical encoders were used in the X, Y, Z stages and tool spindle of the machine. Dimensional measurements of FSA could be carried out with an accuracy of ± 25 μm. Metrology is essential to quantify the distortions of FSAs due to irradiation swelling and creep.

The machine has served admirably for the PIE campaigns over 15 years. However, the machine was quite large, heavy, and despite being designed for minor remote repairs/ replacements, it had no provision for replacement of large components like X, Y and Z stages. Remote repairs of the machine became increasingly difficult due to failure of optical encoders, obsolescence of electronic components of motion control system, and mechanical problems like failures of Z-stage drive bellow coupling, lubrication system, etc., necessitating replacement with a new machine.

A highly compact and remotely operated 5-axis CNC dimensional measurement-cum-laser dismantling machine (DMLD) was subsequently developed and commissioned in the operating hot cells for carrying out profilometry and dismantling of subassemblies (Figure 2). Nd-YAG laser was adopted for cutting the hexagonal sheath considering the advantages like non-contact and coolant-free operation, absence of cutting forces, reduction in kerf-width and absence of chips.

Redundancy was provided for cutting operation by incorporating a motorized diamond wheel cutting module in the machine. By adopting laser and diamond wheel cutting techniques which require nil or negligible cutting forces, the foot print and weight of the machine could be reduced significantly from 1.7 x 1.2 metre and 1500 kgf to 2 x 0.2 metre and 400 kgf respectively. A special holder with top-open design which facilitates innovative vertical loading and rotation of subassembly during cutting was designed and it has functioned well. Eddy current based radiation resistant linear scales were used for position sensing. Redundancy was provided by using stepper motors for X, Y and Z stages, as it provides an alternate position sensing input. Hexagonal cross sections and overall profile of the FSA could be reconstructed with an accuracy of ±16 μm. The machine is intended to operate in environments with radiation dose levels of the order of 10^4 Gy/hour.

Introduction of the new machine into the operating

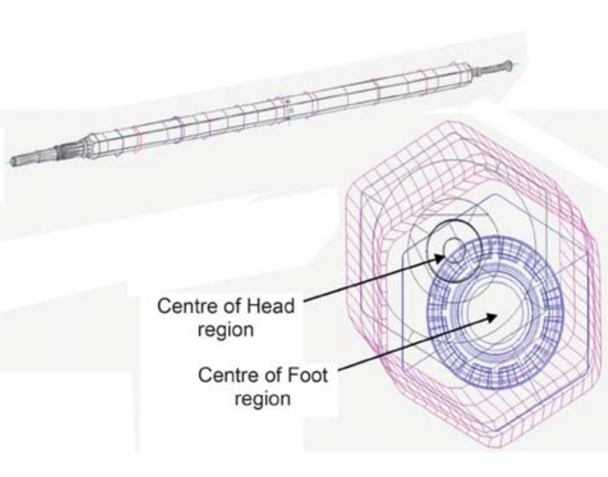

Fig. 3 Reconstructed 3-D views of FSA, illustrating typical hexagonal cross sections as well as head-to-foot misalignment

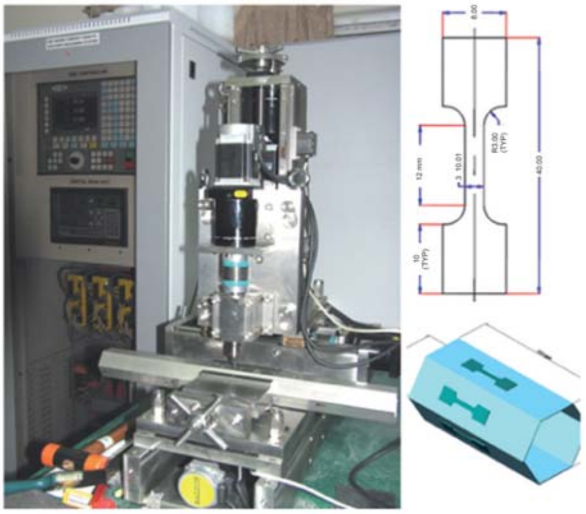

Fig. 4 Remote tensile specimen machining system

hot cell was done through the roof-plug-opening after detailed preparatory works, mock-up trials and safety clearances. The machine was interfaced with the laser system, power and control systems installed in the operating area using cables laid through leak-tight wall-penetrations. The DMLD system has been in use for visual examination, profilometry and dismantling of several experimental and high burn-up FSAs since 2007. Figure 3 shows the reconstructed 3-D view of an FSA.

For machining sub-size tensile specimens from the hexagonal sheath, a modular compact high precision CNC 4-axis tensile specimen machining system was developed. This system is routinely being used to machine sub size tensile specimens (overall length: 40 mm, gauge length: 12 mm and gauge width: 3 mm) with an accuracy of ±10 µm (Figure 4).

The evolved design philosophy has been adopted in the design of an FSA dismantling machine for head end facility (HEF). This is comparatively a large CNC 6 axis machine, with a work table 4.5 metre long and 0.66 metre wide, designed for profilometry and dismantling of FBTR and PFBR FSAs with hexagonal sheath thickness up to 3.2 mm, using laser cutting torch as well as motorized slitting. The machine has two X-carriages to support 4.5 metre long PFBR FSA weighing 250 kgf, during dismantling (Figure 5). This machine is under construction and its commissioning and use for dismantling of PFBR fuel assemblies will serve as a milestone in the evolutionary growth of customized hot cell equipment.

In general, these remotely operated hot cell machines are designed in compliance with ASTM C1533-02 “Standard Guide for General Design Considerations for Hot Cell Equipment components”. They are of stainless steel construction with modular features. Components are given higher factor of safety to ensure structural stability of the equipment during hostile hot cell operating situations like accidental falls, hits, etc. The sizes and weights of the modules are finalized considering the capacities of in-cell material handling devices and the hot cell material transfer ports. The design anticipates that each component needs at least one repair in the life time of the equipment. The modules are incorporated with features like inter-changeability of components, self- alignment, lifting bails, etc., for the ease of remote replacements and repairs.

The design concepts for hot cell equipment have evolved over the years and improvements have been progressively implemented, with respect to the increased radiation tolerances of components, compactness, modularity, and provisions for introduction into an operating hot cell, faster repair and recovery as well as decommissioning of the machine at the end of life.

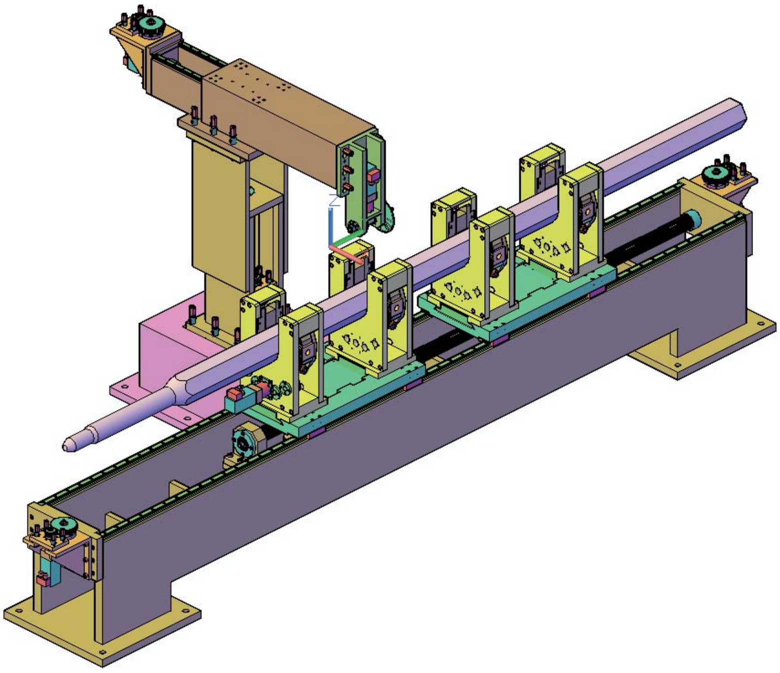

Fig. 5 Fuel subassembly dismantling machine for head end facility

I.5 Design, Development and In-Situ Testing of Electronics for Subassembly Flow Meter of FBTR

In Fast Breeder Test Reactor coolant flow rate through the individual fuel subassemblies is measured using eddy current flow meter (ECFM) as part of periodic surveillance before every start-up. These flow measurements are being carried out to confirm that fuel subassemblies are getting required flow. The standalone electronics for ECFM was designed and developed for this purpose.

Eddy current flow sensor is an electromagnetic device consisting of three coils wound on a soft iron bobbin. The primary coil is in the middle and is excited with a constant current source of 200 mA (±1 mA) at a constant frequency of 400 Hz (±1 Hz). The two secondary coils are wound symmetrically on either side of the primary coil on the same core. When the sensor is positioned on the top of the subassembly it produces an output which is proportional to the velocity of the sodium entering the subassembly. The magnetic flux generated by the primary coil interacts with the moving sodium and produces eddy currents which distort the primary field, resulting in unequal coupling of the two secondary coils. The coupling in the up-stream coil is more than down-stream coil. The difference between the two secondary coil (VS1-VS2) voltages is proportional to the sodium flow. Further, the ratio (VS1 – VS2) / (VS1 + VS2) is computed in order to eliminate the effect of temperature on the induced signal and flow is calculated using the formula Q = K * ((VS1 – VS2) / (VS1 + VS2)) m^3/hr, where K = 0.497 (specific to the present sensor).

The instrument electronics consists of 5 major modules (Figure 1) viz., waveform generator module which generates a stable sinusoidal voltage signal, Power amplifier module which converts the sinusoidal voltage signal to current to excite the primary coil of the sensor, Pre-amplifier module amplifies, isolates and filters the signals from secondary coils and feeds to signal processor module. The signal processor module digitizes and computes the average value of the voltage of the secondary coils and flow display module computes the flow based on the average values obtained from signal processor module.

A single 3U module holder houses the instrument electronics. Modular design approach was adopted to ensure adequate cooling and ease of maintainability.

The instrument was tested in FBTR before commencement of irradiation campaign number 24. The flows of seven numbers of subassemblies were measured using a personal computer based data acquisition system, which requires an elaborate configuration and setup. The developed instrument was also connected in parallel and flow readings were measured. The readings were taken three times for each subassembly to ensure repeatability. The flow measured using the developed instrument was compared with the personal computer based system. It was observed that the flow values matched within ±0.1 m^3/hr. Also it was observed that the variation in flow among the various subassemblies was within ±4%.

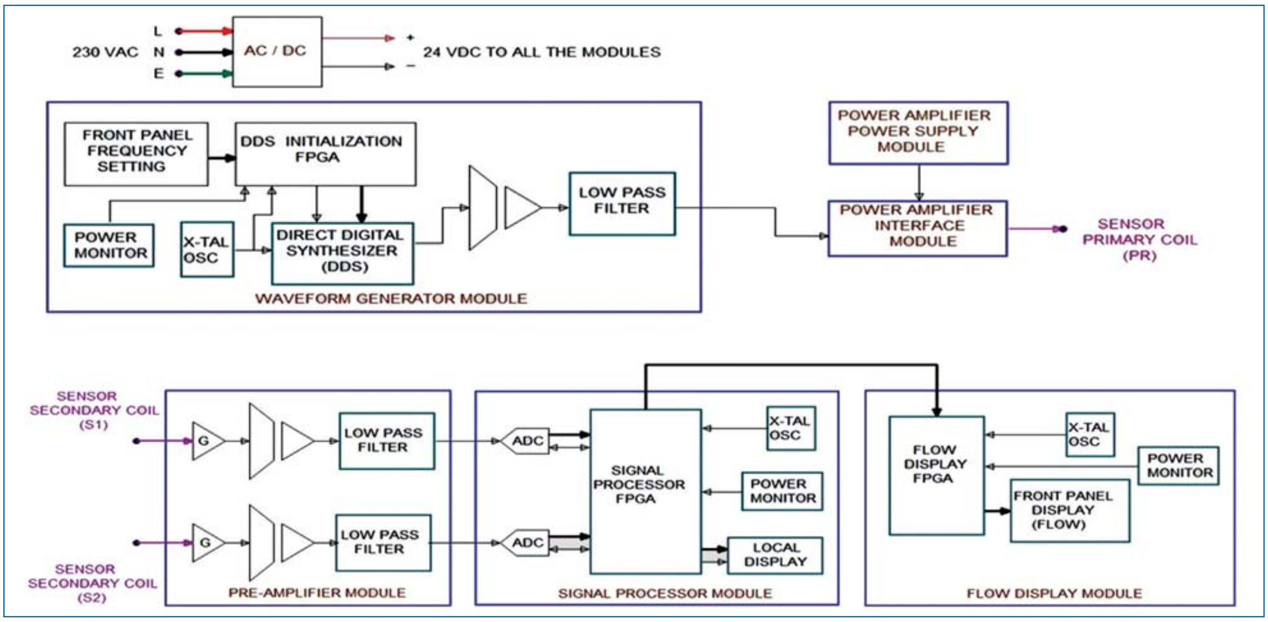

Fig. 1 Block diagram

I.6 Data and Information Storage using NAS in CDPS of FBTR

Central Data Processing System (CDPS) in FBTR, consists of two subsystems namely SS-I and SS-II, connected in fault tolerant configuration. Each subsystem consists of three ED20 based embedded systems namely Safety critical System (SCS), Safety Related System (SRS) and Non-Safety System (NSS). About 600 plant parameters are supervised and controlled continuously by these subsystems for the safe and reliable operation of reactor. Since the subsystems are limited by their storage and display capabilities, they are interfaced with personal computer based data server and message server to overcome the limitations.

Three-tier architecture of CDPS shown in Figure 1, consists of embedded systems at the bottom layer, data server and message server at the middle layer. GUI and display station located in control room will be top most layer and accessible to plant operator.

Embedded system at the bottom layer interfaces with field sensors. They are mainly to scan, do supervision and send the values to Data Server periodically. Data Server will receive and store the data in local database so that it can be served based on request made by operator in GUI. Data server is capable of storing signal values for one day duration.

Similarly, these subsystems, based on processing, will generate messages. These messages are in coded format and sent to message server. Message server will decode and construct original message so that it can be stored in local database and sent to display station for display and also to printer for hardcopy. Message Server is featured to store the last two thousand messages.

Apart from these subsystems, CDPS consists of some personal computer based data acquisition systems like fast data logger systems (FDLS), event sequence recorder system (ESR-I & II) and radiation and air activity monitoring systems (RAAMS) etc. FDLS is used to scan some important parameters at 100 ms interval and automatically store their values at 2 minutes before and 2 minutes after any power or reactivity transient. ESR-I & II are used to scan the digital input contacts at 20 ms interval. Whenever SCRAM takes place, the system will generate a history file for incident analysis which will contain messages generated before SCRAM and after SCRAM. RAAMS system is used to log the signals from various radiation monitors. Also, it calculates activity discharge. All the values are stored at every shift interval.

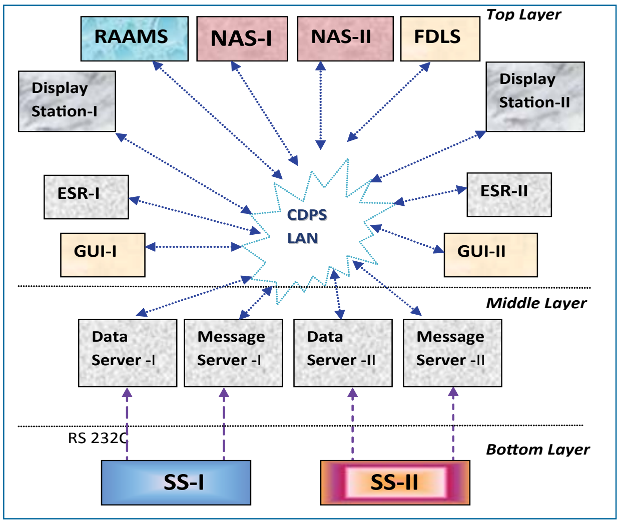

Fig. 1 Three tier architecture -CDPS

Though the systems are featured to have storage and create history file during incident, the files are confined to the individual systems. To have continuous and centralized storage for all data and information generated by CDPS systems, a network attached storage (NAS) unit is procured and commissioned in CDPS.

Data storage

The systems named NASSERVER-1 & 2 are used to fetch the data from respective data servers at every one hour interval. The application program was developed using Visual Studio2010. The application program sends query periodically to retrieve data from database. At the end of the day, a file is created with system name, date and time of file creation as filename and retrieved data will be written in the file.

The file will be copied into NAS-I & NAS-II units. The status of NASSERVER-I & II application program will be displayed in their respective Display Station located in control room. Apart from this, the data from RAAMS is also stored in NAS units at the end of every shift.

Information storage

Display Stations receive messages from both Message Server and ESR. Display Station is programmed to count the messages received and dump the messages in a file on reaching a count value that is set in the program. The file is then copied into NAS-I & NAS-II.

Storage units

Two numbers of NAS units are procured and connected to CDPS LAN. The data and messages generated by CDPS systems are stored in these units continuously. The stored data will be available for period of one year. One year stored data will be copied into DVD media and reposted for future reference.

I.7 Fabrication of U-6wt.% Zr Fuel Slugs for Test Irradiation in FBTR

Sodium bonded metallic fuel pins containing U-19wt.%Pu-6wt.%Zr ternary alloy as fuel slug and U-6wt.% Zr as blanket slug in T91 clad are being developed for future fast breeder reactors in India. Towards this a demonstration facility for metallic fuel fabrication is being established. Both the fuel and blanket slugs would be fabricated by injection casting method. This method is being developed for the fabrication of plutonium bearing fuel slugs for the first time in our department. In view of the complexities involved in the design of the process as well as process equipment, it is envisaged that a few iterations would be necessary before finalizing the design of the process equipment for fabricating plutonium based metallic fuels. Hence, a mock-up facility was established to initially fabricate U-6Zr slugs by injection casting method, gain experience and fine-tune the design of the process and equipment based on the operating experience of the mock-up facility. Preliminary experiments were carried out to fabricate U-6Zr slugs.

An engineering scale injection casting equipment of 10 kg (U-19%Pu-6%Zr ternary alloy) capacity was designed, fabricated and installed inside a glove box filled with high-purity argon (Figure 1). Argon gas is circulated through high efficiency particulate air filters and purification systems in order to maintain the purity of the glove box atmosphere. The injection casting equipment consists of a process chamber, quartz mould cassette with pre-heaters, systems to move the mould cassette vertically up and down to the required extent using a piston – cylinder arrangement driven pneumatically by pressurized inert gas, an induction furnace and associated vacuum system and pressurizing system with controls.

The process chamber has two sections, separated by movable thermal (radiation) shields: lower section houses a high-density graphite crucible for alloy melting with movable thermal shields and the upper section houses mould cassette with pre-heaters to pre-heat the mould cassette to required temperature. These two sections are separable and the upper section is horizontally movable to facilitate loading of alloying materials inside the melting chamber. The process chamber is suitable for melting metals or alloys under a dynamic vacuum of 10^{-5} mbar with provision for isolating the chamber and pressurizing with argon upto 2 kg/cm^2 (gauge). Lower section is welded to the base of the containment box. Temperatures of various parts of the furnace are measured and continuously monitored by both thermocouples (Type K in the upper section and copper coils and Type B or S in the melting chamber) and a pyrometer, which views directly inside the graphite crucible. Dedicated furnace power supply and control and cooling water circulation systems are provided outside the containment box.

Fig. 1 *Injection casting equipment*

The crucible used for melting cum injection casting process is made of high-density graphite. The inner surface of the crucible is coated with yttria to prevent carbon contamination of the charge. The crucible is heated by an induction heater. Required quantities of uranium and zirconium metal ingots were loaded into the graphite crucible. The loading was done inside an inert atmosphere glove box commissioned for this purpose. The graphite crucible along with the charge was then double sealed in a polythene cover and transferred to injection casting process chamber. After evacuation, inerting and degassing, enough super heat was provided to take care of cooling during injection casting step. A cassette of quartz moulds pre-heated to 873 K was then lowered into the melt so that the lower ends of the quartz tubes are sufficiently dipped inside the alloy melt for injecting the molten alloy into the quartz tubes. Melting chamber was then rapidly pressurized to allow the melt

Fig. 2 *U-6Zr slugs*

Fig. 3 *X-radiograph of U-6Zr slugs*

to rise to pre-determined height into the quartz moulds. As the quartz moulds and argon gas are relatively cold, the alloy rapidly cools in it. The process conditions are such that the alloy freezes only in the moulds and the residual melt in the melt chamber is still liquid. Quartz moulds were then withdrawn from the melt to facilitate removal of fuel slugs along with quartz moulds.

In order to explore and understand various injection casting variables such as casting temperature, injection pressure, pressurizing rate, mould pre-heating temperature, yttria coating on the inner surface of the graphite crucible etc., experiments were carried out to fabricate copper slugs by injection casting method. The X-radiogrpahy of the as-cast copper slugs obtained from the initial few runs showed several internal pores in the upper region of the slugs. The defects were overcome by optimizing the casting parameters and improving the process conditions. Defect-free acceptable copper slugs were subsequently fabricated.

After successful fabrication of defect-free copper slugs, experiments were carried out to fabricate U-6Zr fuel slugs (Figure 2). Uranium metal in the form of ingots (12 mm diameter and 10 mm length – supplied by Atomic Fuels Division, BARC) and zirconium in the form of sponge (supplied by Nuclear Fuel Complex, Hyderabad) were the starting materials for the fabrication of the slugs. After melting the alloy components the temperature of the melt was raised to 1723 K before injection casting. In each experimental run slugs of 320 mm length and 4.9 mm diameters were fabricated. The as-cast U-6Zr slugs were subjected to chemical, metallurgical and physical characterization. The engineering-scale injection casting runs with U-6Zr alloy were repeated a few times. The quality of the fuel slugs was acceptable and a reasonable yield of 75% could be achieved. The dimensions of the slugs were measured using a metrology bench comprising of a laser micrometer for diameter measurement, a laser height gauge for length measurement and an eddy current coil for measuring internal defects. The internal defects such as cracks and pores were also measured by neutron radiography (Figure 3). The chemical composition of the slugs was measured both by conventional chemical methods as well as by gamma spectrometry. The metallic impurities in the slugs were analysed by ICP-AES. The distribution of U and Zr in the slugs was ascertained by energy dispersive X-ray analysis. X-ray diffraction studies were carried out to identify the phases presented in the slug. In addition, optical microscopic studies were carried out in order to understand the microstructural characteristics of the slug. After successful validation, defect-free fuel grade U-6Zr slugs were fabricated.

I.8 Periodic Safety Review of KAMINI Reactor for Relicensing

KAMINI Reactor is a ^{233}U fuelled, light water moderated/cooled and beryllium Oxide reflected low power research reactor designed to operate at a nominal power of 30 kW and is located in the basement of the hot cell of Radio Metallurgy Laboratories, IGCAR, Kalpakkam (Figure 1). The reactor functions as a neutron source with a flux of 10^{12}n/cm^2/s at core centre and facilities carrying out neutron radiography of radioactive and non-radioactive objects and neutron activation analysis of variety of samples. Experimental facilities consist of three beam tubes with a flux of 10^8n/cm^2/s, one of them equipped with special setup for radiography of

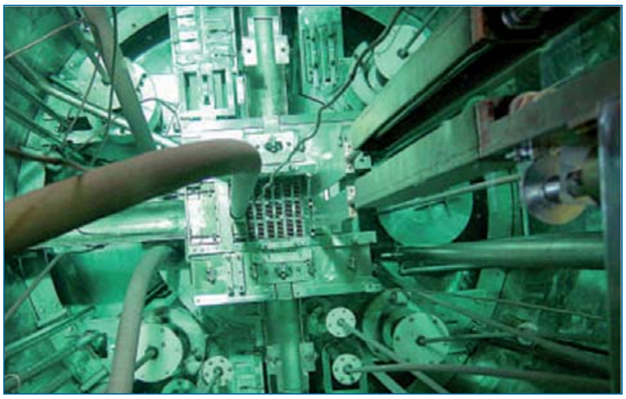

Fig. 1 *KAMINI reactor top view*

irradiated elements. There are two locations outside the reflector in the reactor tank for irradiation of larger samples at a flux level of 10^{10}n/cm^{2}/s and one location at the reactor core periphery for short irradiation at a flux level of 10^{11}n/cm^{2}/s using pneumatic sample transfer system.

Commissioning of the reactor was started after obtaining clearances at various stages from safety authorities in 1995. After obtaining the clearance from safety authorities for operation up to 100 W, fuel loading was done. First criticality was made on October 29, 1996. Operation of reactor at 0.5 W for physics experiments viz., Void coefficient of reactivity measurement, absolute power calibration using uranium wires and absorber rod worth measurement were completed. Subsequently reactor power was raised to 5 kWt after obtaining clearance from safety authorities and satisfactory operation of systems at high power was demonstrated. After completing the shielding augmentation, reactor power was raised to nominal power of 30 kWt on September 17, 1997. With the installation and commissioning of secondary circuit, the commissioning activities were completed and license for regular operation of the reactor at nominal power was obtained from AERB w.e.f 1st July 1998. Based on the feedback from commissioning experience, the technical specification document for reactor operation was rectified and got approved. SARCOP visited the reactor on August 21, 1998 and took over the safety review of the reactor from PDSC (K).

This reactor is used for neutron radiography of irradiated FBTR fuel, Activation analysis and Radiation Physics Research. KAMINI has also been utilized for neutron radiography of pyro devices, meant for space applications and testing of neutron detectors. Presently this is the only operating reactor with this fuel and therefore it serves as a facility to study the physics characteristics of ^{233}U fuelled reactor systems. Neutron radiography of irradiated fuel pins of Fast Breeder Test Reactor (FBTR) up to 1,55,000 MWd/t burn-up and failed fuel was carried out.

In recent years, there has been a pressing demand from ECIL and BARC for testing and calibration of the various types of neutron detectors developed and manufactured by BARC in KAMINI reactor due to the non availability of APSARA Reactor for testing. These detectors have to be tested in the neutron flux of 10^{4} to 10^{10}nv. Two vertical dry tubes of diameter 74 mm and 103 mm and 3750 mm length with removable shield plugs were installed permanently inside the reactor tank at 35 and 90 cm horizontally from the centre of the reactor core. High temperature fission chambers (HTFC) developed for PFBR is tested in KAMINI up to a neutron flux of 5×10^{9} nv & gamma field of 5×10^{5} R/hr at a temperature of 570 °C. For testing the HTFC detectors in KAMINI reactor, a test assembly made up of inconel tube capable of maintaining the detector temperature at 570 °C using electrical heaters is installed on the east side of the reactor in the pool above spent fuel storage stand.

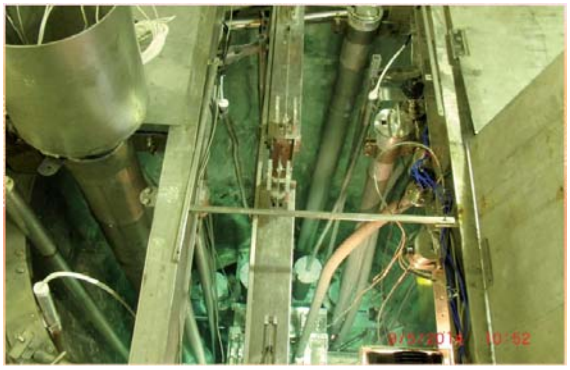

Fig. 2 *Location of dry tubes and high temperature test set up*

Renewal of license of KAMINI reactor

For renewal of authorization for operating the KAMINI reactor, comprehensive safety review of plants was carried out, considering the cumulative effects of plant ageing and irradiation damage, system modifications, operational feedback, status and performance of safety systems and safety support systems, technical developments, manpower training, radiological protection practices, plant management structure etc. These comprehensive safety reviews termed as Periodic Safety Review (PSR) is intended to further enhance plant safety throughout the service life of the plant. PSR is prepared by taking into account improvements in safety standards and operating practices, cumulative effects of plant ageing, modifications, feedback from operating experience, and development in science and technology.

Based on SARCOP recommendation, this document was submitted to OPSD, AERB. Further, PSR was reviewed by the working group constituted by AERB. Based on the preliminary review of PSR carried out by AERB and from the review outcome, it was observed that the performance of KAMINI has been satisfactory. Several modifications / replacements have been carried out in order to improve performance and reliability of the systems and enhancement of safety.

I.9 Testing & Qualification of High Temperature Fission Chambers

High Temperature Fission Chambers (HTFC) are used for in-vessel neutron flux monitoring over a wide-range – start-up, intermediate and power for reliable detection of neutrons produced during nuclear fission in the PFBR core. In addition, HTFCs are also used for delayed neutron monitoring for detection of wet rupture in the fuel clad. These detectors, developed by BARC and fabricated by ECIL were tested for their functional performance evaluation in order to qualify for neutron flux monitoring in PFBR. Prototype detectors were earlier tested in FBTR up to neutron flux of ~$2x10^9$ n/cm^2-s and up to a temperature of 450 ºC in experimental canal. As part of the qualification, it was decided to test these Fission Chambers in KAMINI reactor with suitable detector housing with external heating arrangements so as to get the same operating conditions for detector viz. temperature 570 ºC, neutron flux up to 2×10^9 nv and gamma field up to 5×10^5 R/hour as in PFBR.

For this, a special detector housing assembly was designed, fabricated and installed in KAMINI reactor. The assembly comprises the following:

1. Electrical heaters
2. Thermal insulation
3. Detector housing arrangement
4. Shielding blocks
5. Temperature controller

Following design issues were addressed in order to establish a reliable test facility for testing the detectors:

- Optimized size of the assembly to minimize the buoyancy effect during installation
- Material selection for high temperature (570 ºC) operation and minimum irradiation activation
- Ensuring safe temperature rise inside the assembly
- Radiation resistant soft-cables for heater terminations
- Ensuring reliable heating using electrical heaters
- Providing adequate temperature sensors for measuring temperature at various locations inside the assembly
- Arranging shielding for neutron and gamma streaming radiation.

Meeting all the above requirements, a special assembly was fabricated using Inconel-600. Rock-wool was used as thermal insulator for preventing heat loss to outside environment i.e. KAMINI water pool. Ferroboron

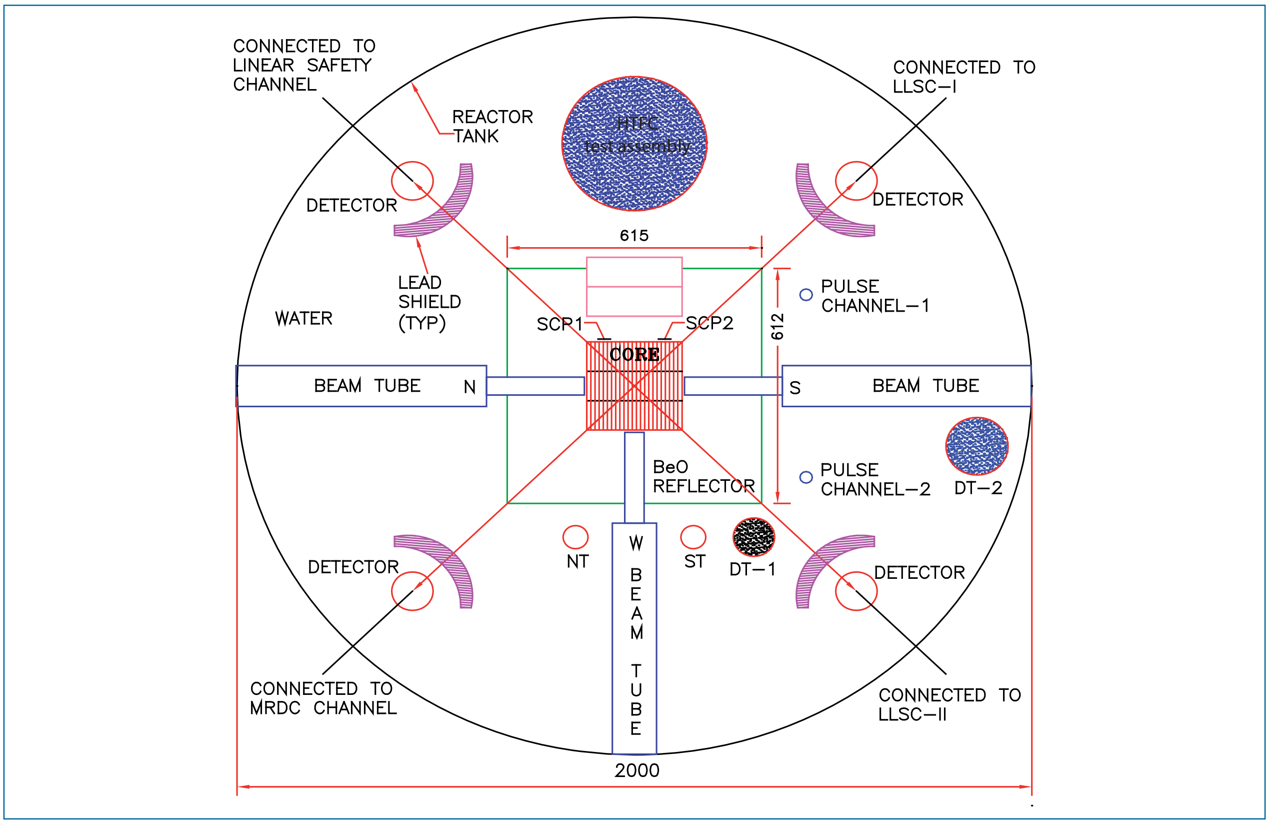

Fig. 1 *Assembly installation location in KAMINI (plan view)*

filled shield plugs were used for neutron and gamma shielding along with supplementary shield blocks.

The size of the assembly was chosen as 3700 x 200 mm OD (cylindrical tube) housing concentrically placed Inconel-600 inner tube (3625 x 73 mm OD) wrapped with two MI cable type heaters on its outer surface, and annular space between the tubes filled with approximately 10 kilogram of rock-wool. Total seven thermocouples were provided for temperature monitoring and control and distributed inside the assembly (on the outer surface of inner tube) up to 2500 mm from bottom. Two surface heaters, each 1.6 kW, have been wrapped around the inner tube in parallel, with uniform pitch length targeted to provide equal heating per unit length. Two shield plugs – inner plug and outer plug – were also provided on the top (400 mm deep) of the assembly for capping inner tube and annular gap between inner and outer tubes, respectively. Shielding blocks were provided with ferroboron granules filled bricks to prevent neutron and gamma streaming from the reactor during operation. The shielding was further enhanced by providing supplementary shielding in the form of ferroboron filled SS bricks stacked upto 400 mm over the assembly in a cylindrical trough. Figure 1 shows a plan view of test assembly in KAMINI.

A temperature monitoring and control unit has been used for temperature control inside the test assembly. The controller can monitor 10 thermocouples with an overall scan cycle of 10 seconds. The temperature control scheme uses redundant thermocouples, provided on outer surface of inner tube and on the detector and mineral insulated cables, for heater feed back control. Thus, overall a reliable temperature control scheme was envisaged for monitoring and control of the temperature inside the assembly.

The performance of the thermal insulator (rock-wool) was tested in a mock-up test facility on 1:13 scale-down model of KAMINI water pool. After 8 hours of continuous heating, the average temperature rise observed was 8 ºC which corresponds to only 0.6 ºC temperature rise in KAMINI. The mock-up test results showed good thermal performance of the chamber and heat transfer was conservative with theoretically arrived value of 2 ºC.

During mock-up, time required to raise the temperature from room temperature to 570 ºC was also measured and found to be approximately 150 minutes with 90% controller output. This corresponds to ~3.5 ºC average temperature rise per minute and ascertained the adequate heating capacity of heaters to meet the various heating rates required. Subsequently, the setup was successfully installed in KAMINI reactor.

HTFC detectors (6 numbers) of control plug were tested at room temperature and at 570 °C from 10 W to 30 kW power with 1 °C /min. of heating rate. Similarly, testing of DND detectors for IHX location (3 numbers) was also carried out at room temperature and at 550°C from 10 W to 1 kW power.

Detector response, both in pulse and mean square voltage (MSV) mode, was measured with respect to reactor power. Parameters such as insulation resistance (IR), neutron sensitivity, saturation voltage (HV) and γ-field discrimination (DB) plateaus were recorded during each test at both temperatures and at various power levels. Also, linearity in response of detector and pulse characteristics were obtained during the testing. A typical HV and DB plateau of the detector tested is shown in Figures 2a and 2b. Figure 2c is linearity in response at 570 ºC. It is observed that detectors showed satisfactory performance with an average sensitivity of 0.25 ± 0.03 cps/nv at room temperature and 570 ºC, and IR values of the order of 10^{10} Ω at room temperature and 10^{8} Ω at 570 ºC. The linearity in the response, for both pulse and Campbell, was found to be within ± 10 % with an effective overlap of more than 1.5 decades at room temperature and 570 ºC. The neutron pulse rise time is noted to be in the range of 15-25 ns with typical pulse width of 80-100 ns at room temperature and 570 ºC. The marginal change observed in the neutron sensitivity and in pulse characteristics at high temperature (570 ºC) in comparison to room temperature was found to be within acceptable limit.

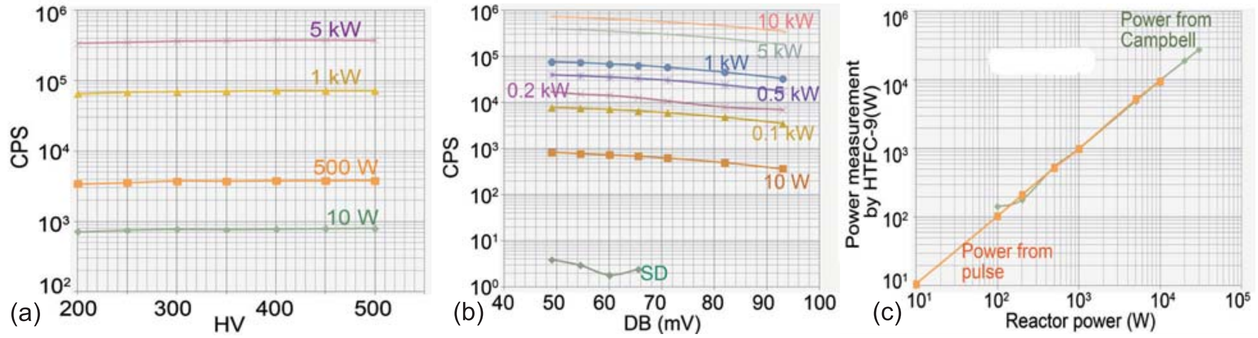

Fig. 2 (a) HV, (b) γ-field discrimination plateau of the detector tested and (c) linearity in response observed at 570 ºC

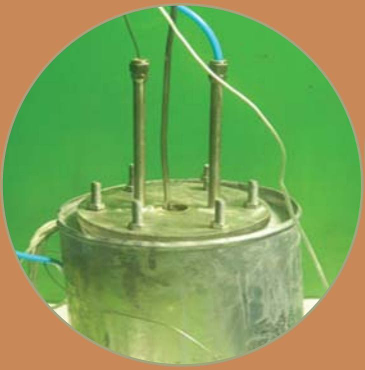

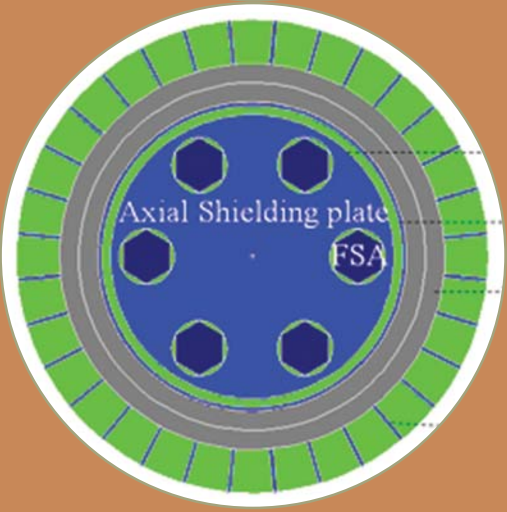

CHAPTER II

Prototype Fast Breeder Reactor

II.1 Construction Status of PFBR

Reactor assembly

Primary Sodium Pump has been integrated with the coupling for manual rotation to gain confidence before coupling the pump with the motor. Towards commissioning of two primary sodium pumps in their respective locations in the reactor, no-load test on motor with variable frequency drive was done and the functional performance in air has been completed by demonstrating free rotation of the pumps.Top view of reactor assembly is shown in Figure 1.

Activities related to the core temperature monitoring were completed and the total system has been validated physically. The thermo-well tips inside the reactor vessel were exposed to hot air jets one by one and simultaneously respective temperature readings in main control room were monitored. In order to meet the regulatory requirements and to ensure proper functions of core monitoring thermocouples, a dedicated mock up test facility was commissioned to measure the response time of thermocouples in hot air jet, water bath and finally sodium at simulated temperatures.

In the reactor assembly, the instrumentation cable layout has been rerouted, particularly cables on the control plug to demonstrate the removal / assembly operations for the shutdown systems in case of maintenance. Further the cables have been dressed to eliminate any possibility of electromagnetic induction effects. The trailing cable system along with robust support structures housing eighteen numbers of cables to transmit the signals from various sensors incorporated in the components mounted on the rotatable plugs has been commissioned.

For the reactor assembly and primary circuits, the major activity completed is the erection, commissioning and functional tests of periscope in main vessel. Baseline data for inner vessel to assess the deformations under seismic loadings has been collected. All preparatory activities for the pressure hold test of the reactor vessel and connected primary sodium circuits has been completed.

As a pre-requisite for main vessel preheating, insertion of nitrogen purging tool in central canal location, modification of preheating circuit spool pieces for interspace region, installation of dummy flanges in in-vessel transfer port & sodium sampling point with inlet / outlet pipes were carried out.

Sodium systems

The major steps towards commissioning of primary and secondary sodium systems, viz. cleaning of internal surfaces of components and piping with flushing of instrument air and preheating before sodium filling have been completed by adopting optimized and logical sequences.

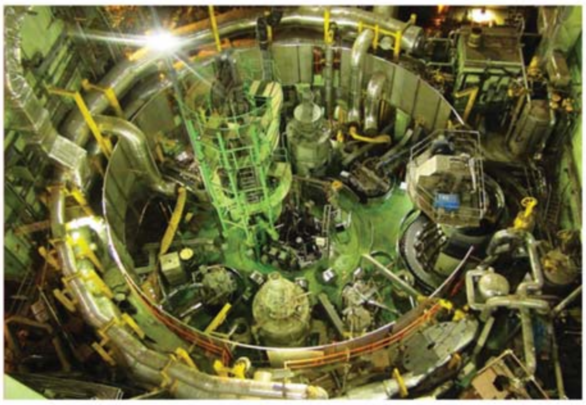

Fig. 1 *Top view of reactor assembly*

Recently, melting of large quantity sodium (230 tonnes) in the tanks has been completed and steady & stable flow of sodium with full control has been established in the purification loop and sodium has been ultra-purified (<1ppm of Oxygen). An integrated pre-heating exercise of secondary sodium loop-2 comprising main circuit along with associated purification circuits have been commenced.

Fuel handling system

Installation and commissioning of all necessary instrumentation for the fresh fuel handling scheme starting from transfer cask to placing into the ex-vessel transport port have been completed. As a part of technical demonstration, a full-scale mock-up drill has been carried out.

The components and systems lying in the spent fuel subassembly transport path have been commissioned. All the 9 Control Rod Safety Drive Mechanisms (CSRDM) has been operated from main control room and the drop time, torque, force and displacements were measured. The results clearly demonstrated the perfect alignments achieved with all possible manufacturing and erection tolerances, thus raising confidence on the operation of control rod drive mechanism.

Smooth operations of inclined fuel transfer machine have been exercised by transferring the dummy subassemblies between the in-vessel and ex-vessel transfer ports at room temperature in air. Under this task, operation of transfer arm motor from variable frequency drive has also been completed.

A full scale mock-up drill has been demonstrated to the Specialist Group of AERB with the transfer of randomly selected sub-assembly from the reactor to spent fuel washing facility and vice-versa. During this task, operation of Transfer Arm, Large & Small Rotatable Plug from Handling Control Room and Inclined Fuel Transfer Machine, Cell Transfer Machine through

***Fig. 2** Transfer pot movement*

variable frequency drive has been perfected (Figure 2). The baseline data for monitoring the horizontality of core support structure as well as large & small rotatable plugs have been generated through Transfer Arm operations. The same have been confirmed through optical measurement techniques.

Power conversion system

In Turbine Generator system, the hydrotest of operation grade decay heat removal pipes were completed. Generator air leak tightness test for 72 hours have been completed successfully. Motor driven Boiler Feed Pump load operation was done with 60% scoop position and full load operation was carried out for about 12 hours. Motor Driven Boiler Feed Pump, booster pump and Hydraulic coupling have been commissioned through Distributed Control System. Complete Turbine, Generator & Exciter assembly has been put on barring gear again.

Leak tightness of isolation valves for all the eight Steam Generators have been checked with pneumatic operation and closed loop flushing is in progress before preheating of Steam generator tubes with DM water.

Tertiary systems

Sea water intake offshore concrete works is nearing completion and Bell mouth concrete of sea water intake structure has been completed (Figure 3). Temporary coffer-dam in the caisson have been dismantled which enables drawl of sea water. Grouting of horizontal tunnel has been completed and anti-bio fouling painting has been completed.

Auxiliary Sea Water Pump has been commissioned along with Steam Water System components by circulating sea water from the off-shore in take structure to cool the raw water, thereby to maintain the temperature of high power motor (10.2 MW) driving the boiler feed pump. With this, the commissioning of steam generators has been taken up. Regarding steam water system commissioning, the temporary stop log gates have been removed from sea water intake structure to draw sea water into condensate cooling system.. Condenser tube side water fill test has been completed.

Inspection system

The movement of In-Service Inspection (ISI) vehicle for main vessel bimetallic joint (DISHA) has been successfully demonstrated in the mock up facility. On gaining adequate confidence in mock up facility, DISHA vehicle was moved in reactor assembly and the Roof Slab bimetallic joint was visually recorded towards accumulating the base line data. In this process, the vehicle insertability, retrieval and visual inspection of the weld joints on the upper portion of the main vessel were established.

All the construction activities have been completed and commissioning of sodium systems is in advanced stage. AERB granted permission to carry out the pre-requisite activities before filling the sodium in secondary sodium circuit-1 (east loop). BHAVINI has successfully commissioned the activities meeting all the stipulations without having any safety problems, particularly without any sodium leak.

The project has achieved an overall physical progress of 97.64% at the end of January-2016 and is marching towards attaining its first criticality.

***Fig. 3** Sea water intake structure*

II.2 Experimental Simulation of the Behavior of SGDHR System of PFBR during SCRAM and Station Black Out

Safety Grade Decay Heat Removal (SGDHR) system of PFBR is designed to pick up the decay heat from the hot pool of the reactor through decay heat exchanger (DHX), transport it to the sodium to air heat exchanger (AHX) through the piping system and then reject it to the atmospheric air through air heat exchanger. The chimney provided in the SGDHR system drives air flow through the shell side of air heat exchanger by natural convection.

Reactor transients will lead to temperature variations in the hot pool sodium and the magnitude and rate of temperature variation in the hot pool sodium will have influence on the heat transport characteristics of the SGDHR system. Experiments were conducted in SADHANA facility to study the response of the heat transport system to the design basis reactor transients. The rate of reduction of hot pool sodium temperature is found to be maximum during reactor SCRAM among all the design basis events based on plant dynamics studies. The analysis revealed that hot pool sodium temperature falls by 96°C in the first 600 seconds and further 49°C in the next 600 seconds from the initiation of spurious SCRAM. The rate of rise of hot pool sodium temperature is found to be maximum during the station black out (SBO) with one SGDHR circuit unavailable and operation of other circuits are initiated after a delay of half an hour. With this condition, the plant dynamics studies have indicated that the hot pool lower part sodium temperature falls from 547°C by 39°C in first 420 seconds and hot pool upper part temperature rises from 520°C by 68°C in 11250 seconds. The temperature variations predicted for those two transients were simulated in the test vessel of SADHANA facility and the effect of these plant transients on the heat transport behavior of SGDHR system was studied.

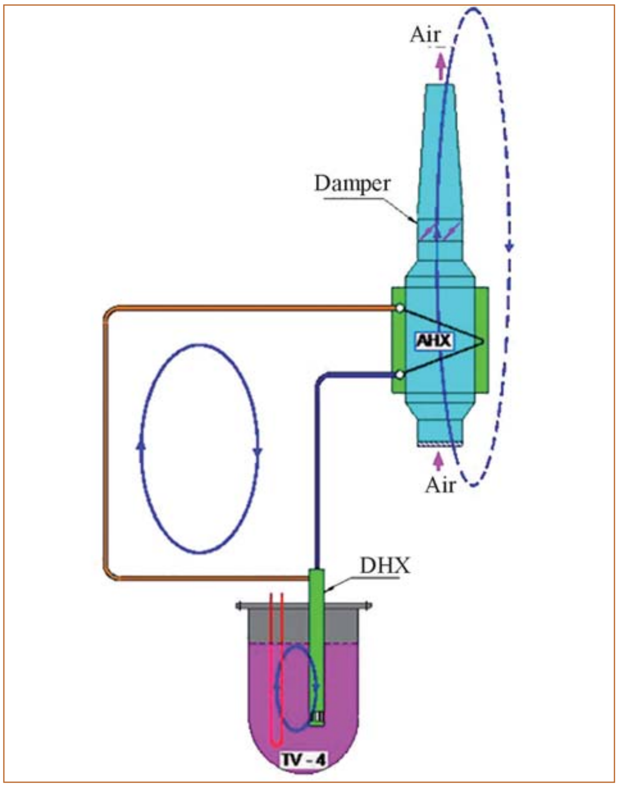

***Fig. 1** Schematic of SADHANA facility*

SADHANA experimental facility is scaled down in power compared to the SGDHR system of PFBR. The schematic of the SADHANA facility is shown in Figure 1. The nominal heat removal capacity of the facility is 355 kW. The elevation difference between the thermal centers of the secondary sodium system of SADHANA is 19.5 metre. A vertical test vessel of 1000 mm OD and 3000 mm height simulates the hot sodium pool of the PFBR. It houses the model decay heat exchanger, 22 numbers of electrical heaters with capacity of 20 kW each and sodium level probes. Decay heat exchanger and air heat exchanger in SADHANA are similar to the decay heat exchanger Type - A and air heat exchanger Type - A in SGDHR of PFBR respectively. A chimney with 700 mm external diameter and 23 metres height at the AHX outlet will induce the natural draft required for the flow of air across the air heat exchanger tubes. The required rate and magnitude of cooling sodium in the test vessel is achieved by injecting cold sodium at a temperature of 310°C. The rate of heating required to simulate the station black out is achieved by electric heaters.

The rate of reduction in hot pool sodium temperature during spurious SCRAM is higher than the rate of reduction in temperature of sodium in hot leg of SGDHR circuit. Since the hot pool temperature is lesser than the temperature of hot leg, the sodium in the SGDHR circuit loses the heat through decay heat exchanger also. This scenario was experimentally demonstrated during the experiments.

The pool temperature inside the test vessel was reduced by injecting cold sodium. The dampers were opened and the full air flow corresponding to pool temperature was generated within a minute. The secondary sodium flow started to increase and reached the maximum

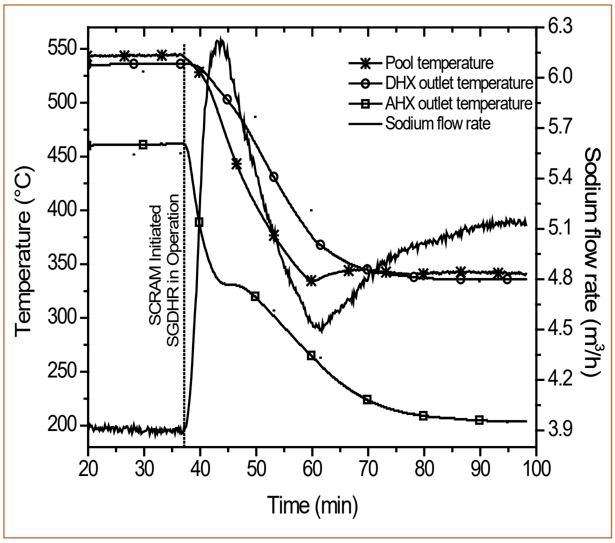

Fig. 2 *Results of spurious SCRAM with immediate damper open*

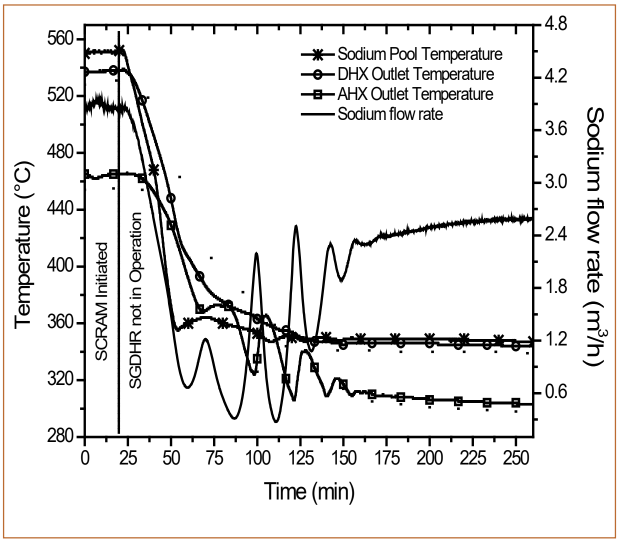

Fig. 3 *Results of spurious SCRAM - air damper fails to open*

flow corresponding to the pool temperature within 9 minutes. The sodium flow reduced as sodium pool temperature began to fall. During this transient the pool temperature was lesser than the temperature of sodium in secondary circuit. When the rate of drop in hot pool temperature reduced, the heat loss of secondary circuit through decay heat exchanger was also reduced. Further decay heat exchanger started to pick up heat from hot pool and the secondary sodium flow increased and followed the pool temperature. The response of temperatures at decay heat exchanger outlet, air heat exchanger outlet and sodium flow in secondary circuit are shown in Figure 2. During a spurious SCRAM incident if the dampers in the SGDHR system fails to open, the sodium flow in the SGDHR circuit will be low compared to the damper opened case and the fluctuations in the sodium flow and sodium temperature at heat exchanger outlets will be more severe. This scenario is experimentally studied and observed that when sodium in hot leg experiences less temperature than cold leg sodium, the secondary sodium flow reduces and again rises when the temperature of hot leg sodium is higher than cold leg sodium. Evolution of temperature and sodium flow are given in Figure 3. The flow direction of sodium in the secondary circuit during SCRAM was maintained same as initial without any flow reversal.

For reproducing the temperature profile as in the reactor transients during station black out, the sodium pool temperature was reduced by injecting cold sodium and the required rate of heating was achieved by immersed heaters.

The dampers were in crack open position. The cold sodium was injected to reduce the pool temperature from 550 to 510°C within 10 minutes and pool temperature was raised to 570°C by electrical heaters. The sodium flow in secondary circuit was reduced initially as sodium pool temperature was falling and started to increase along with increase in pool temperature. After half an hour of initiation of transient, the dampers were opened. The air flow reached maximum in a minute and the sodium flow reached maximum corresponding to the pool temperature within 9 minutes after opening of damper. The temperature evolution and sodium flow are shown in Figure 4.

The behavior of the SGDHR system during design basis plant transients was experimentally studied in SADHANA facility. It has been observed that the heat transport capability of the system follows the hot pool sodium temperature for most of the cases. The direction of flow in secondary system of SGDHR remained unchanged during all the design basis plant transients without any flow reversal.

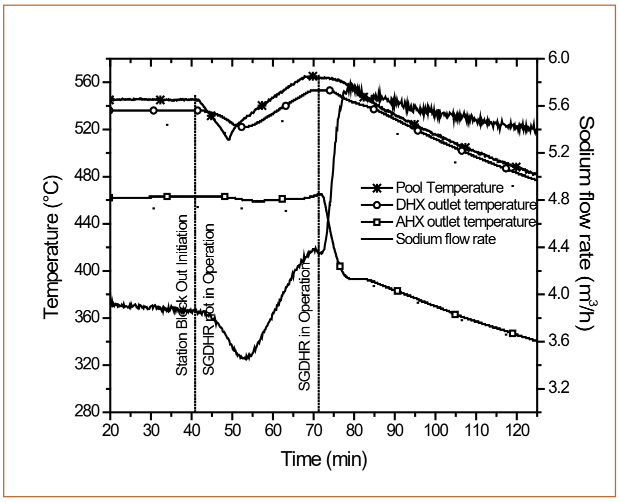

Fig. 4 *Results of station block out with half hour delay in damper open*

II.3 Performance Testing of PFBR Sonar Device

Vibration measurement of PFBR fuel subassemblies during commissioning is a safety requisite. It is planned to measure subassembly vibrations in PFBR during its isothermal operation at 200 °C with dummy subassemblies in the core. Since conventional contact type sensors such as acceleroemeters, strain gauges etc. cannot be used for high temperature under sodium measurements, sonar device employing ultrasonic technique was developed.

Sonar device is equipped with three ultrasonic sensors at the bottom of the spinner tube (Figure 1). Sensors S1 and S2 are mounted at an angle of 30° with the horizontal and the sensor S3 is at an elevation of 680 mm above S1 and S2. S1 and S2 are used to focus on to the subassembly crown region for vibration measurement. S3 is focussed to the central canal shroud tube in the control plug, which is the stationary reference used for the measurement.

The developed sonar device was assembled and tested for its performance. A vessel with subassembly heads positioned inside was used for performance testing. Figure 2 shows the test setup. During the preliminary testing, focusing trials on single subassembly head and multiple subassembly heads were carried out. Ultrasonic sensors were excited using the pulser-receiver units and the signal was monitored in the data aquisition system (DAS). The first phase of studies was conducted by exciting the target (subassembly head) using electro-dynamic exciter with known frequencies. The ultrasonic sensor S1 was excited using the pulser receiver and signal from the sensor S1 was recorded. Using the developed software vibration signal was extracted and compared with the reference LVDT installed on the target. The experiments were repeated with frequencies in the range of 2 to 10 Hz and with random signal. Figure 3 shows a typical test result plot representing the time signal as well as its frequency spectra.

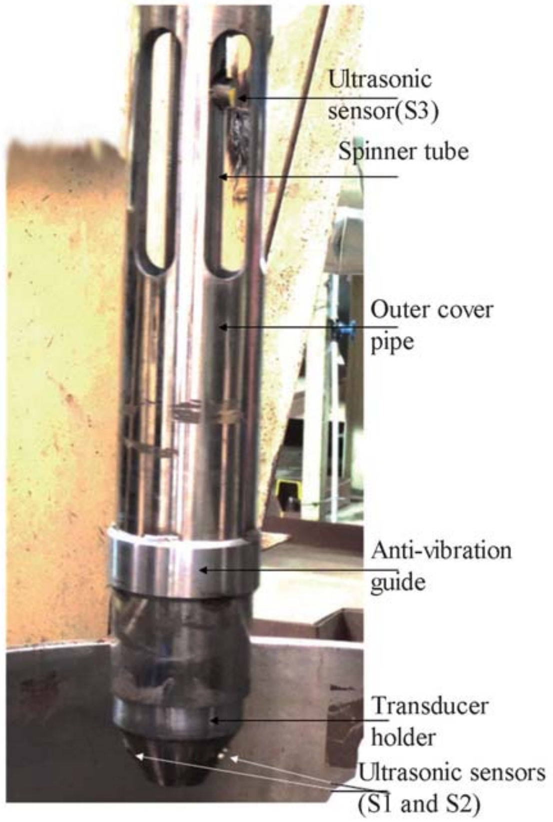

Fig. 1 *Bottom end of sonar device*

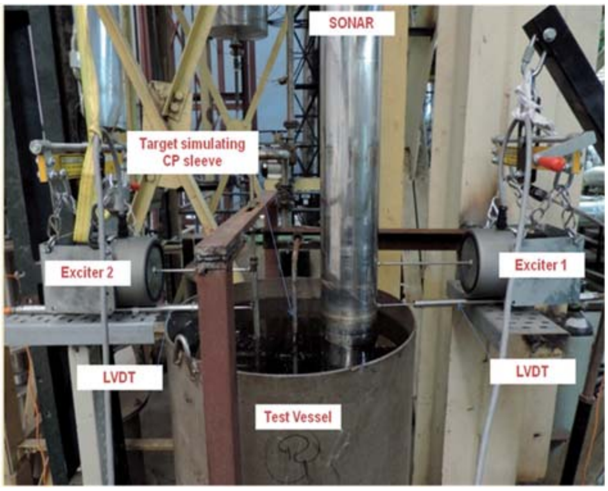

Fig. 2 *Water test setup*

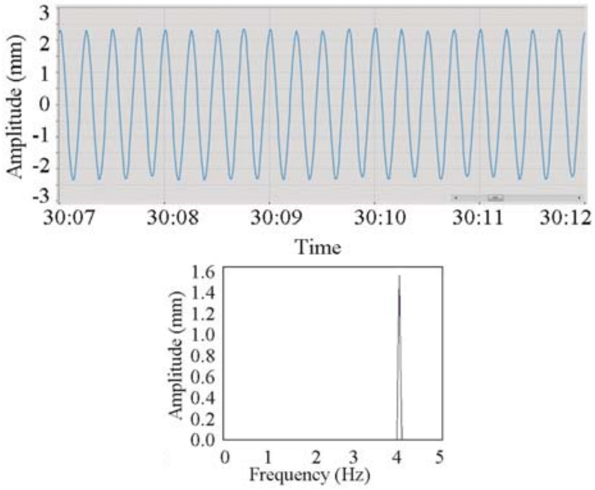

Fig. 3 *Typical test result plot when subassembly excited with 4 Hz*

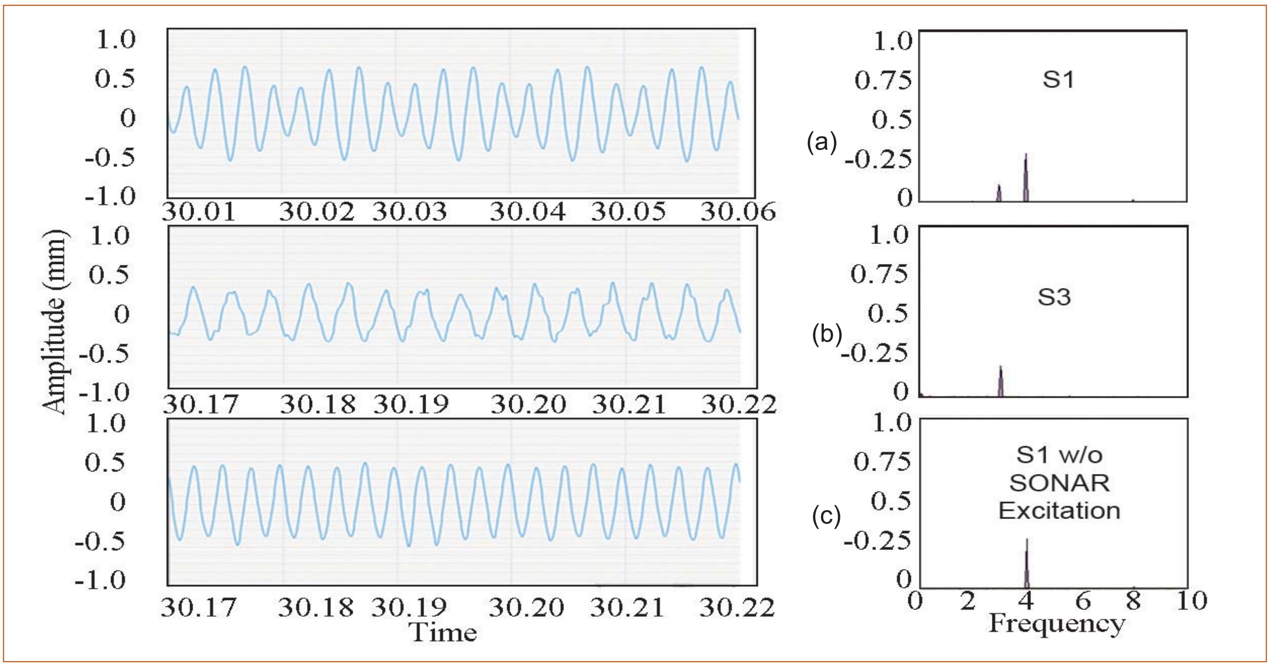

Fig. 4 *Test result plot (subassembly excited at 4 Hz and sonar device at 3 Hz)*

In the second phase of experiments, target was made stationary and sonar device was excited using electro-dynamic exciter. These experiments were also conducted for various excitation frequencies from 2 to 5 Hz and the signal from side viewing sensor S3, movement of sonar device was measured and compared with reference LVDT installed on the sonar device. This study was conducted to assess the performance of sensor S3, which in the case of reactor, is focused on the shroud tube of the central canal which is the stationary reference target for vibration measurement. During vibration measurements inside the primary pool of a FBR, there can be random movement of the sonar device in the turbulent coolant flow. Hence, this study was conducted towards developing the vibration compensation technique.

In the third phase of measurements, both the target subassembly head and the sonar device were excited using electro-dynamic exciters and simultaneous measurements were carried out using sensor S1 and S3. Sensor S1 measured the vibration of the target whereas sensor S3 measured the vibration of the sonar device. Studies were carried out with various excitation frequency combinations. Figure 4 shows typical time plots and frequency spectra, when target subassembly is excited at 4 Hz and sonar device at 3 Hz. Since, sonar moving at 3 Hz is measuring the vibration of the target, which is at 4 Hz, both the frequency components can be seen in the frequency spectra and in the time signal from S1 (Figure 4a) whereas S3, which is focused to the fixed reference measures the sonar vibration, which is 3 Hz (Figure 4b). When the excitation of sonar is stopped, S1 signal represents purely the target vibration which is at 4 Hz (Figure 4c).

In all the measurement campaigns, sonar device was able to reliably measure the vibration of the target as well as the sonar device. After measuring both the amplitudes of vibration, vibration compensation was carried out applying the correction factor. Eventhough sensors S1 and S3 are installed in the same vertical plane, sensor S1 measures the amplitude of vibration of target with respect to the sonar device at an angle of 30^0 with the horizontal, whereas S3, which is at 0^0 to the horizontal, measures the amplitude of vibration of sonar device. Sensor S3 is located at an elevation of 688 mm above sensor S1. So, in order to exactly measure the vibration of the target, sonar device vibration needs to be corrected. The correction factor, C_f is calculated as 0.921. Hence, the corrected vibration amplitude, x will be

$$x = \text{Amplitude of S1} - (C_f \times \text{Amplitude of S3})$$

Amplitudes measured during the performance testing of sonar device was tabulated after applying the correction factor and was found to be matching well with the reference LVDT reading.Using sonar device, measurements will be carried out on selected 5 fuel subassemblies in different zones of the core. Sonar device is installed in the central canal of control plug. By suitable combinations of rotation of SRP and LRP, sonar device can be positioned on top of each of the subassemblies and it can access any region within a diameter of 2670 mm in PFBR core.

II.4 Simulation of Ultrasonic Detection of Protrusion of Fuel Subassemblies in PFBR

Before starting any fuel handling operation during shutdown in PFBR, it is requried to ensure that no subassembly is protruded beyond the allowable limit and the gap between the top of subassemblies and the core cover plate is free from any obstruction. Due to the opaque nature of sodium, only an ultrasonic wave propagation based technique can be used for detection of protrusion of subassemblies. Towards this, an ultrasonic scanner has been developed and the test procedure has been developed for under sodium ultrasonic scanning (USUS) by performing various under water experiments in a 5 m diameter water tank. The methodology is based on the drop in the reflection amplitude from the peripheral subassemblies (PSAs) in case of a subassemly protrusion. The PSAs are the shielding subassemblies in the last row with rings of 130 mm diameter and 100 mm height placed on them. In the experiment, the core was divided into five sectors based on symmetry. In each sector, protrusions of different subassemblies were simulated and ultrasonic signals were acquired at 0.6 MHz using a side viewing under sodium ultrasonic transducer. Due to the space restrictions in scanning complete peripheral subassemblies and difficulty in interpreting multiple echoes resulting from PSAs, CIVA simulation and development of a 1/10th scale model of the PFBR core were undertaken to simulate various subassembly protrusion scenarios in PFBR. CIVA software is a platform to simulate actual NDT testing.

In order to validate the CIVA software for its efficacy in simulating the USUS phenomenon, various simulation studies, equivalent to the under water studies performed in the 5 metre tank, were first undertaken. A water sample of thickness 500 mm and diameter of 5500 mm was considered. Figures 1a and 1b show typical experimental and CIVA simulated B-scan images corresponding to a subassembly protrusion at 3 metre distance from the transducer. The study for different sectors confirmed that CIVA simulation can be effectively used to study the USUS phenomenon. To gain deep insight into the observed phenomenon and establish a mock-up facility for performing simultaneous scan of the complete core with various protrusion scenarios, a 1/10th scale model of PFBR core was envisaged and fabricated. Figure 1c shows the photograph of the 1/10th model. The diameters of the core and the subassemblies were taken to be 590 mm and 12.7 mm, respectively. The height of a PSA was considered to be 50 mm. The height of the core subassemblies was considered to be 40 mm (normal level). The protrusions considered above the normal level were 2.5, 5, 7.5 and 10 mm. A detailed CIVA simulation was performed to arrive at the transducer properties to have similar divergence as observed in the actual PFBR core. As the immersion transducer of 1/10th diameter (2.5 mm) was not commercially available, a spherically focused immersion transducer of 9.5 mm diameter with focal length of 45 mm was found suitable as its 6 dB divergence (4.5°) at 500 mm matches well with that of the 1 MHz side viewing under sodium ultrasonic transducer at 5 metre (5.2°) in PFBR. Figures 1d and 1e show typical experimental and CIVA simulation B-scan images obtained from protrusions at different locations. The protrusions are very clearly seen in both the images. The 1/10th model and CIVA simulation are of immense use in understanding complex signals and simulating various protrusion scenario, which is difficult to achieve in experiments involving actual sized samples.

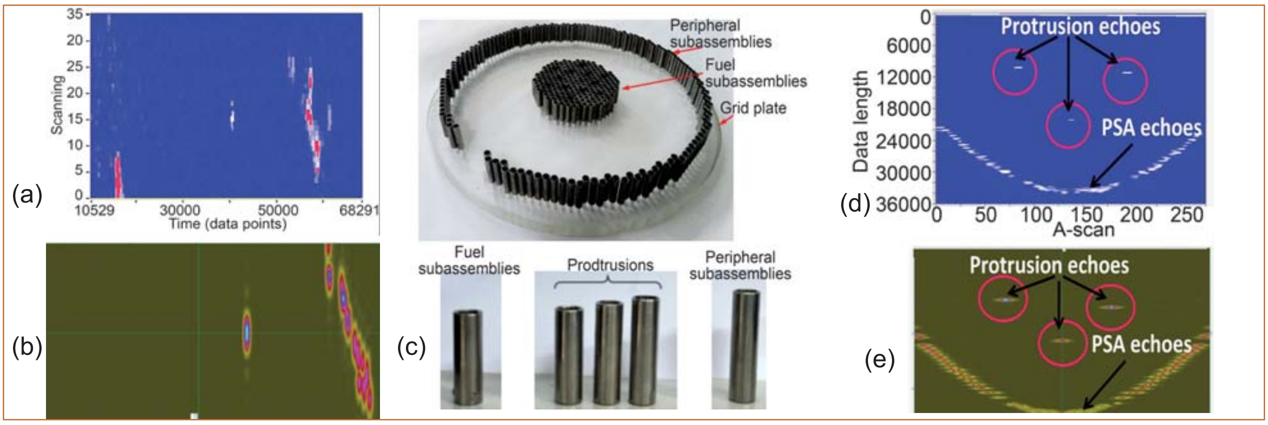

Fig. 1 (a) Experimental and (b)CIVA simulated B-scan images corresponding to a subassembly protrusion at 3 metre distance from the transducer, (c) 1/10th model of the PFBR core, (d) experimental B-scan image of 1/10th scale core with three protrusions at different locations and (e) B-scan image from CIVA simulation with three protrusions at different locations

II.5 Optimization of Primary Sodium Heating Rate to Reduce Power Raising Duration based on Control Plug Life

The heating rate of primary sodium is of concern during start-up of the reactor. In PFBR, after the shutdown of the reactor, the temperature of both hot and cold pool sodium will be at 453 K. During raising of the power, gradually the temperature of primary sodium will be increased at a specified rate. Traditionally, a slow heating rate of 20K/h is considered. This requires about 20 hours for raising of the power. Higher rate of sodium heating may cause creep and fatigue damage to the reactor components which are immersed in hot pool sodium like control plug (CP) bottom, intermediate heat exchanger (IHX) and inner vessel. In this study, the damage, possible in the control plug bottom as a function of heating rate at the critical region has been determined and the dependence of CP life on the heating rate is estimated. The heating rates considered in this investigation are 20, 40 and 60 K/hr. The evolution of sodium temperature at the top of the fuel subassembly for various heating rates is shown in Figure1.

Geometric details

The control plug bottom portion (which is immersed in hot pool sodium) consists of core cover plate (CCP), upper stay plate (USP), lower stay plate (LSP) and outer shell. The USP shell junction is the most critical location because there is argon cover gas over the sodium free level and when the sodium temperature is increased, the argon gas temperature also rises. Moreover, the rise in sodium level results in abrupt changes in the material properties of the CP at this location. Thus, the analysis has been focused on the CP at USP and the outer shell junction.

Loading conditions for upper stay plate

The level of hot pool sodium (at 453 K) at the start of power raising is ~ 26700 mm. After reaching full power (820 K), the hot pool sodium level reaches 27400 mm. The maximum sodium temperature at the inner surface of the CP is 853 K. Thus the sodium level increases by 700 mm while gaining 400 K temperature rise. The temperature of sodium within the CP is 7 K over the outside temperature.

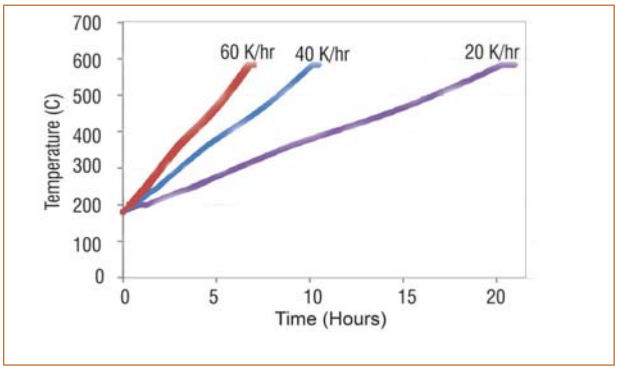

Fig. 1 *Evolution of sodium temperature at the top of the fuel subassembly*

The argon temperature is calculated using the formula given below and is updated at each iteration.

$$T_{Ar} = (((393.0 + T_{Na}) / 2.0) + T_{Na}) / 2.0$$

Where T_{Na} is sodium temperature (K) and T_{Ar} is argon gas temperature (K).

The time taken to heat the primary sodium and the rise in sodium level at all the three heating rates considered are given in Table 1.

Analysis and results

Axi-symmetric model of the USP and the outer shell with 2430 four noded isoparametric elements has been employed for the finite element analysis. Transient analysis of the CP with the above mentioned loading and boundary conditions has been carried out. The evolution of temperature at the CP and the critical locations (A - inner surface, B - outer surface, C - maximum stress) that are identified are shown in Figure 2.

The maximum stresses determined from the analysis

Table 1: Input parameters used in the analysis

Heating rate (K/hr)	Heating time (hours)	Rise in sodium level in hour (mm)
20	20.0	35
40	10.0	70
60	6.6	105

Table 2: Maximum stresses in MPa

Heating rate (K/hr)	Location A	Location B	Location C
20	41.3	51.4	91.1
40	51.7	68.4	160.0
60	55.6	76.0	225.0

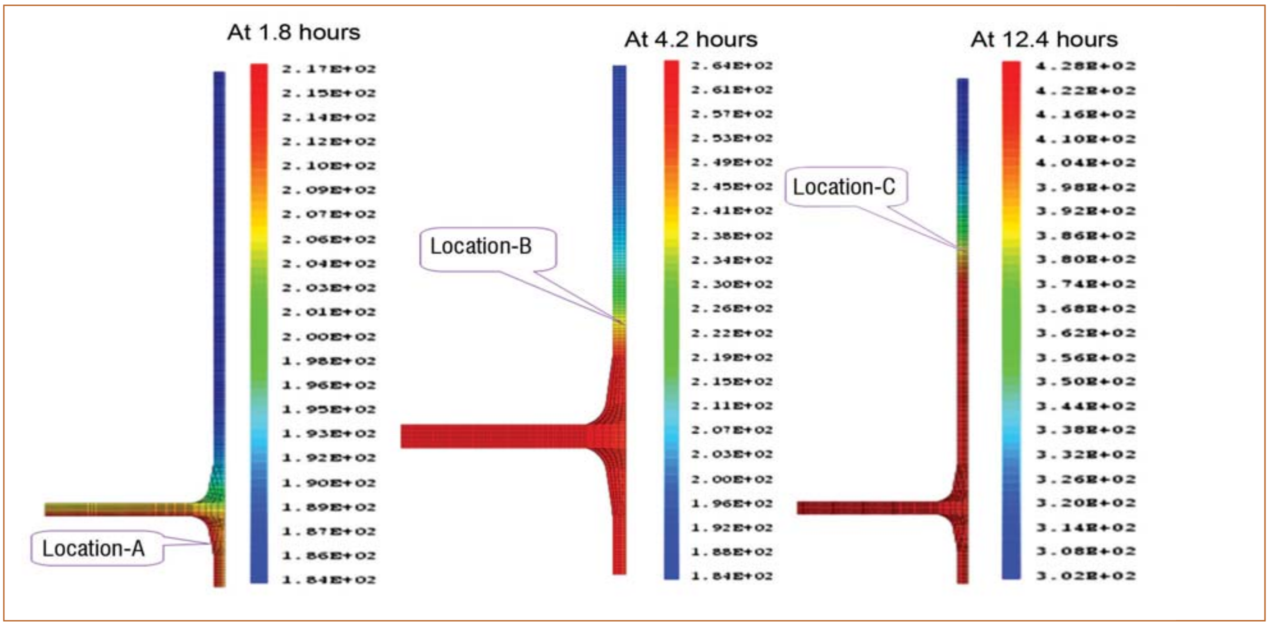

Fig. 2 *Evolution of temperature at the upper stay plate junction in control plug during reactor start-up (at 20K/hr)*

at the critical locations for the three heating rates are given in Table 2.

Assessment of creep-fatigue damage

The creep and fatigue damages have been calculated with the stresses obtained during power raising as per RCC-MR RB. It is found that Location-C is the critical region. The results at the critical region for various heating rates are given in Table 3.

Assessment of creep-fatigue damage at full power

The creep and fatigue damages (per cycle) of CP at full power for 1000 load cycles, with a hold time of 200 hours per cycle are 0.8238×10^{-3} and 0.546×10^{-5} respectively and the number of permissible cycles is 1192. The number of permissible cycles has been taken from the elastic route of RCC-MR at 823 K. These values will be much higher (at least 3 times the life) if an inelastic route is followed.

These values are for the case of SCRAM with flow reduction to 20 % in primary sodium pump. This damage is added to the damage in Table 3 to get the number of cycles permissible as shown in Table 4.

The results show that the number of cycles permissible is greater than 1000 load cycles for all the cases. The decrease in the number of cycles due to the sodium heating rate during power raising is 7 cycles at 20 K/hr, 47 cycles at 40 K/hr and 71 cycles at 60 K/hr.

Recommendations

Detailed analysis has been carried out to investigate the possible damage caused in the control plug due to the heating rate of primary sodium during power raising. The fatigue damage per cycle caused due to power raising at the maximum stress location for heating rates of 20, 40 and 60 K/hr are 1.54×10^{-17}, 1.19×10^{-10} and 9×10^{-7} respectively and the corresponding creep damage per cycle are 5.35×10^{-6}, 3.4×10^{-5} and 5.1×10^{-5}. When the values at full power for 1000 cycles are considered, the number of allowable cycles for heating rates of 20, 40 and 60 K/hr are 1185, 1145 and 1121 cycles respectively. Thus, a sodium heating rate of 60 K/hr is acceptable during power raising in view of control plug life. This reduces the power raising duration from 20 hours to 6.6 hours. However, the other components which are immersed in hot pool sodium i.e., inner vessel and intermediate heat exchanger, are being analyzed for the final recommendation of the sodium heating rate during power raising.

Table 3: Creep fatigue damage at start-up

Heating rate (K/hr)	Fatigue damage	Creep damage
20	1.545×10^{-17}	5.35×10^{-6}
40	1.190×10^{-10}	3.40×10^{-5}
60	9.000×10^{-7}	5.10×10^{-5}

Table 4: Creep fatigue damage at full power

Heating rate (K/hr)	Total fatigue damage ($\times 10^{-6}$)	Total creep damage ($\times 10^{-6}$)	Number of permissible cycles
20	5.46	8.29	1185
40	5.46	8.58	1145
60	6.36	8.71	1121

II.6 Shield Design for Fresh Fuel Transport Cask

Fresh fuel transport cask is a cylindrical vessel measuring a height of roughly 5 metre and a diameter of 87.5 cm with 1 cm thick structural steel all around and a central axle as shown in Figure 1. Six fresh fuel subassemblies can be transported using this cask. The fuel subassemblies are accommodated in a hexagonal pattern on a pitch circle of diameter 60 cm. In the axial direction 6 cm thick carbon steel plates are provided above upper axial blanket and below lower axial blanket. Shielding and criticality analysis for this cask has been carried out by modeling the geometric details of the cask using the 3D transport code MCNP. Plan and sectional view of the transport cask simulated using MCNP are shown in Figures 2 and 3 respectively.

Fresh fuel subassembly contains both neutron and gamma ray sources. Neutrons are emitted due to spontaneous fission and (α, n) reaction. Gamma rays are emitted due to fission product activities of the reprocessed PHWR uranium oxide fuel. The neutron and gamma source strengths of the fuel SA are 4.32×10^6 n/s/SA and 1.095×10^9 γ/s/SA respectively. Gamma energy is assumed as 1 MeV. For neutrons, fresh fuel inherent neutron source spectrum has been used.

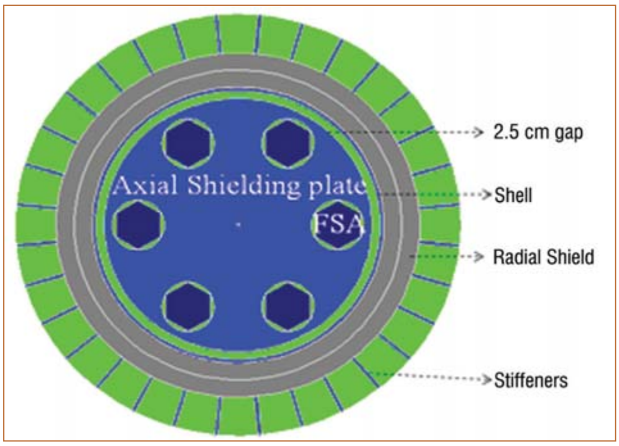

Fig. 2 *Plan View of the fresh fuel transport cask with stiffeners*

As per the design criteria, the dose rate on contact at the outer surface of the transport cask should be less than 2 mSv/h and at 1 metre distance away from the outer surface of the transport cask, dose rate should be less than 100 μSv/h.

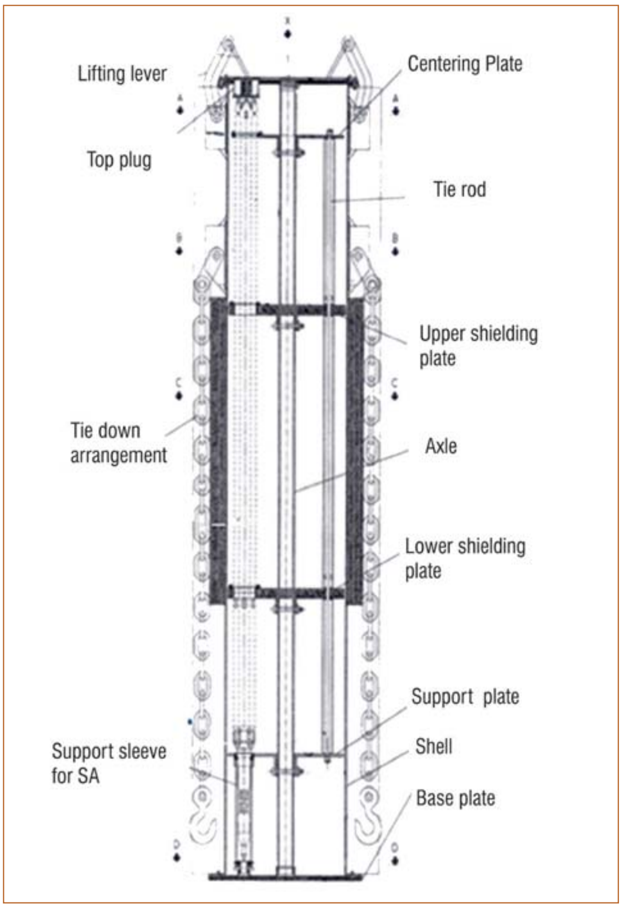

Fig. 1 *Schematic of fresh fuel transport cask*

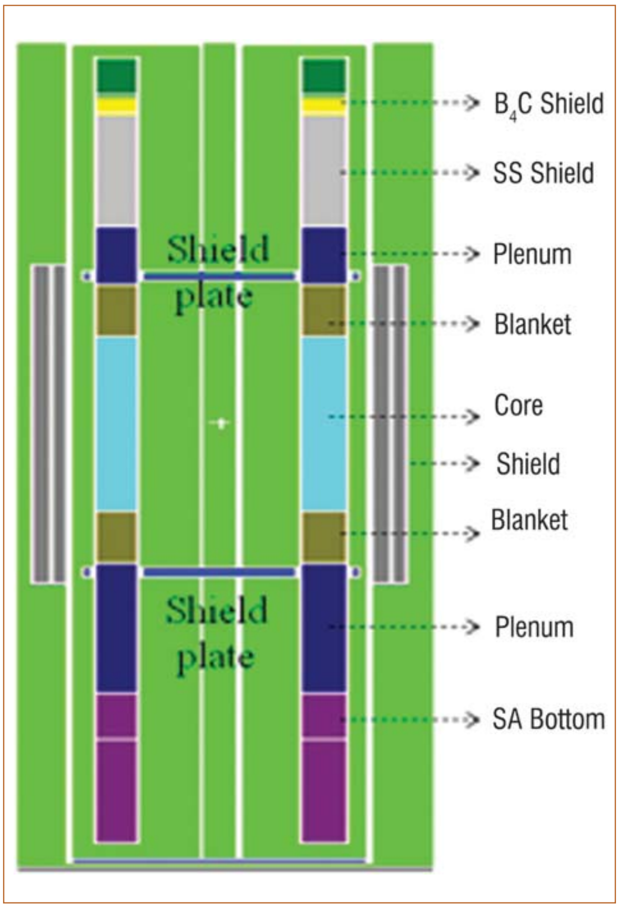

Fig. 3 *Sectional view of the fresh fuel transport cask*

Table 1: Estimated dose rates outside the cask with 11 cm carbon steel shielding

	Dose rate on contact (μSv/h)					
	Neutron		Gamma		Total	
	C	M	C	M	C	M
Single FSA	793.2	792-838	845.2	924-1080	1638.4	1754-1894
Cask with 6 FSAs	537.2	592	2.4	9.1	539.6	601.1
	Dose rate at 1 metre distance (μSv/h)					
	Neutron		Gamma		Total	
	C	M	C	M	C	M
Single FSA	41	31- 45	39.4	33-42	80.4	65-81
Cask with 6 FSAs	98.4	70	0.6	3	99	73
* C -Calculated dose rate M - Measured dose rate						

With 11 cm thick carbon steel radial shield, dose rates on contact and at 1m distance are estimated. Estimated dose rates are given in Table 1. Estimated dose rates due to single FSA as well as FSAs loaded cask are compared with measured dose rates reported by FBTR station health physicist. It is seen that the estimated dose rates are in good agreement with the measured dose rates. Among the neutron and gamma sources, neutron sources only dictate the shield design. Dose rate less than 100 μSv/h at 1 metre distance away from transport cask is the limiting criterion in deciding the shield.

With 11 cm thick carbon steel radial shield, dose rate at 1metre distance is just meeting the criteria without any safety factor. As polyethylene is a good neutron shielding material, introducing polyethylene between the cask shell and FSAs has been analyzed. To meet the design limit with safety factor, a combination of 11 cm thick carbon steel and 3 cm polyethylene shield is required. With this shield configuration, estimated dose rates on contact and 1m distance from the stiffener surface are given in Table 2.

Table 2: Estimated dose rates outside the cask
(1 cm shell +11 cm carbon steel + 3 cm Polyethylene)

Detector Location	Dose rate (μSv/h)		
	Neutron	Gamma	Total
On contact	298.5	2	300.5
At 1 m distance	52.9	0.5	53.4

Criticality analysis has been carried out in water flooded condition. Estimated effective multiplication factor for the cask in water flooded condition is 0.69 (with 10% uncertainty included). These calculations are done conservatively with fresh core-2 fuel SAs. When FSAs come closer, the maximum k-eff estimated is 0.86 for the pitch distance of 16 cm. As per PFBR safety criteria, conservatively calculated k-eff under worst conditions shall not exceed 0.95. Since the estimated maximum k-eff is less than the design limit, there is no concern with respect to criticality due to the movement of the fuel assemblies towards the centre.

II.7 Response Time Evaluation of PFBR Core Temperature Monitoring Probe

In PFBR, core temperature monitoring probes are positioned above each of 210 core subassemblies to monitor temperature of sodium. Each probe consists of 12 metre long two (duplex) MgO insulated K Type thermocouples inserted into a SS thermowell. The thermowell is an integral part of control plug. The probe is designed for continuous and reliable operation without maintenance for minimum of 40 years. It is immune to vibrations, mechanical and thermal shocks encountered during transportation, installation and operation. The schematic of the probe is shown in Figure 1.

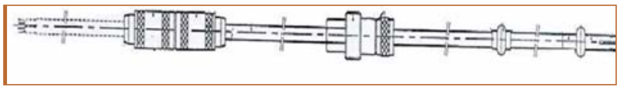

Fig. 1 Schematic of core temperature monitoring probe

Thermal response time is an essential parameter for temperature measurements or controls quick temperature changes. The presence of thermowell makes the thermal response time much longer and it is necessary to measure the response time of probe (combination of thermocouple and thermowell). Thermal response time of the thermocouple is the time required by the thermocouple to attain 63.2% of the total voltage change. It is a function of rate of heat flow into or out of the thermocouple assembly. In case of core temperature monitoring, the thermal response time for each thermocouple shall be within 6±2 seconds and maximum allowable deviation between both thermocouples in the probe shall be less than 5 °C.

The core temperature monitoring probe was tested in a constant temperature sodium bath for thermal response measurements. The experimental setup consists of a cylindrical SS container with hole at top flange for inserting thermocouple assembly (along with thermowell). Argon inlet was provided at the top of the flange to maintain inert atmosphere over sodium in the container. The top flange was provided with a SS stopper for positioning the thermowell. The stopper helped in retaining constant depth/position for the thermocouple at every insertion. The sodium container was provided with 500 W quartz insulated cord heater to heat the sodium upto 450 °C. Silicon Controlled Rectifier (SCR) based Proportional Integral Derivative (PID) controller was used for controlling sodium temperature. Two K-type MgO insulated SS sheathed thermocouples were used for sodium temperature measurement and control. Photograph of the experimental setup is shown in Figure 2.

About 250 gram of sodium in the form of brick was loaded into the SS container and heated to desired temperatures using surface heaters. Argon gas was purged continuously to maintain inert atmosphere above sodium. The duplex thermocouple was connected to two channels (channel 1 and channel 2) in data acquisition system (DAS) and continuous temperature recording with sampling time of 150 milliseconds was carried out. Experiments were carried out at sodium temperatures of 350 and 450 °C. At each sodium temperature, the thermocouple along with thermowell was inserted rapidly into the sodium bath and the rise in temperature was recorded using DAS. The consistency in response time of thermocouples was studied by repeating the experiment four times at each temperature. The effect of gap between thermocouple tip and thermowell on thermal response time was studied by maintaining constant gap (0, 1, 2 and 3 mm) between thermocouple tip and thermowell in the probe.

Table 1: Response time of thermocouple

S. No.	Temp (°C)	Gap between Tc and Th. well (mm)	Response time (s)	
			Channel 1	Channel 2
1	350	0	6.0±0.4	5.7±0.5
2	350	1	5.4±0.4	7.1±0.2
3	350	2	5.1±0.6	6.9±0.2
4	350	3	4.8±0.8	7.1±0.6
5	450	0	5.4±0.4	5.4±0.4
6	450	1	5.3±0.5	7.3±0.4
7	450	2	6.5±0.4	6.8±0.4
8	450	3	6.6±0.2	6.6±0.7

The measured response times at various gaps maintained between thermocouple tip and thermowell are given in Table 1. Typical thermal response curves for duplex thermocouples at 350 and 450 °C are given in Figures 3a and 3b respectively.

Thermal response time of both thermocouples in the core temperature monitoring probe was found to be comparable and there was not much variation in thermal response time of probe measured at temperatures of 350 and 450 °C. It was observed that the thermal response time of the probe increases with increase in gap between thermocouple tip and thermowell. It was also observed that thermal response time of the probe is a function of gap between thermocouple tip and thermowell and the speed at which the probe is dipped into hot sodium. Since dipping was carried out manually, there is randomness in measured response time. However, all the values are observed to be within the specified limit.

Thermal response time of core temperature measuring probe was evaluated by rapid insertion into sodium bath at constant temperature. The response time of both the individual thermocouples of the duplex thermocouple was found to be within the specified allowable limit (6±2 seconds). The deviation between both thermocouples in the probe was found to be less than 1 °C.

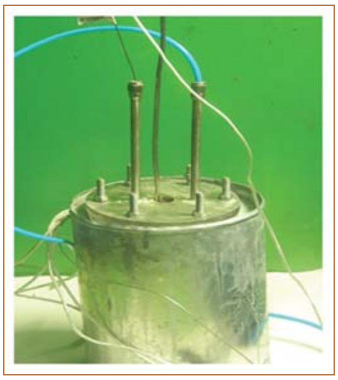

***Fig. 2** Experimental setup of sodium bath*

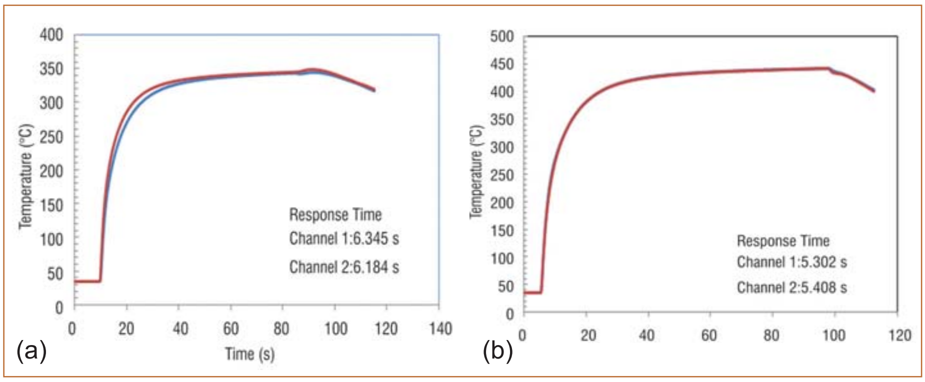

***Fig. 3** Response of thermocouple at (a) 350 °C and (b) 450 °C*

II.8 Experiments on Sodium Leak in LEENA Facility with Modified Wire Type Leak Detector Layout

When a sodium leak occurs, the leak rate, the total quantity of sodium leaked and leak detector layout governs the detection time. Early detection of leak is needed for minimizing the quantity of sodium leaked to outside and consequent damages. Wire type leak detectors (WLD) working on conductivity principle are used for detecting sodium leak in the secondary sodium circuits of PFBR. It is required to assess the performance of wire type leak detectors associated with its layout and confirm that they are meeting the requirements. It was found from the upper boundary curve based on LEak Experiments in NAtrium (LEENA) and FUTUNA (CEA facility) experimental results with present PFBR leak detector layout (wire type leak detectors positioned at 90^0 on either side) that a leak rate detection of 200 g/h and above can be achieved within 6.7 hours. To improve the detection capability of the leak detector layout, modified layout was arrived for large secondary circuit pipelines of FBR. Sodium leak experiments with modified leak detector layout were conducted in LEENA facility with different sodium leak rates.

Experimental setup and details of the experiment

Sodium leak experiments with wire type leak detectors positioned at 90° on either side by taking top as 0° were conducted earlier on horizontal test section of dia 790 mm. This test section (TS) is modified with two additional wire type leak detectors at 45° on either side by taking top as 0°. Leak simulator is provided at the top 0° position in this test section. Maximum distance between the leak point and wire type leak detector is 310 mm in test section. Test vessel (TV) was filled with sodium up to middle level and the sodium temperature was raised to 550°C. Test section and its associated lines were heated to 550°C. Sodium leak experiments were carried out by opening leak simulator and test section inlet valve. Reduction in test vessel sodium level was noted and total quantity of leaked sodium, leak rate and detection time were calculated. Sodium leak experiments were repeated with different sodium leak rates.

Table 1: Experiment results

Trial number	Total quantity leaked out (g)	Leak rate (g/h)	Detection time (min)
1	64	191	20
2	209	202	62
3	244	276	53
4	186	506	22
5	513	879	35

Experiment results

In the leak test facility 5 experiments were completed and the results are given in Table 1. Figure 1 shows the test section after sodium leak experiment. The experiments have shown that many factors are involved in the detection of sodium leak. It depends on the insulation material packing condition, distance between the leak point and detector, pipe geometry, temperature etc. To get the trend of detection time with leak rate, experimental results are plotted. Conservatively an upper boundary curve of the experimental points is drawn. The equation of the upper boundary curve is

$$y = 137.48\ x^{-0.1467}$$

Comparison of leak rate (x) versus detection time (y) upper boundary curves based on sodium leak experiments conducted with PFBR layout (WLDs positioned at 90°) and sodium leak experiments with modified leak detector layout (WLDs positioned at 45°) are given in Figure 2. It was also observed that there was considerable reduction in detection time with modified WLD lay out. This is due to the reduction in distance between leak point and leak detector (reduced from 621 to 310 mm). From the experiments it was found that a leak rate of 200 g/h can be detected in one hour.

Fig. 1 *Test section 1 after sodium leak experiment*

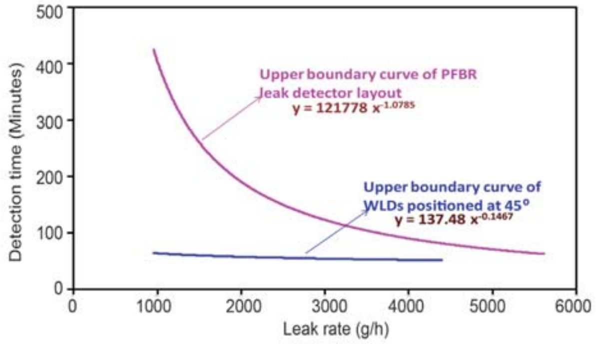

Fig. 2 *Comparison of upper boundary curves of WLD layout at 90° and WLDs at 45°*

II.9 Assessment of Structural Integrity of the Cut and Rewelded PFBR Fuel Pin by High Temperature and High Pressure Experiment

In case of Fast Breeder Reactor (FBR) core, Fuel Subassembly (FSA) is the source of heat from nuclear fission. These long standing vertical FSAs are resting on the sleeves of the grid plate. The schematic of a typical FSA is shown in Figure 1a. The coolant enters the FSA at the bottom and gets heated up while going upward and leave the FSA at the top. Each FSA houses as 217 fuel pins arranged in a triangular pitch (Figure 1b). The clad encapsulates the fuel, forms the primary barrier to prevent the release of radioactive materials. Thus, the integrity of the clad is to be ensured under all operating conditions. Longer life of the clad tube will provide longer periods of uninterrupted reactor operation. Hence utmost care has been considered while manufacturing of the clad tube. The typical fuel pin end plug weld is shown in Figure 1c. The thin clad tube is welded with the relatively thick end plug as shown in Figure 1c. The clad tube has an outer diameter of 6.6 mm and thickness of 0.45 mm. Welds are the weakest elements in the pressure boundary of the fuel clad tube. Nuclear codes specify stringent inspection requirements to ensure highly reliable primary radioactive barrier to prevent the release of radioactivity. Structural reliability of the clad tube is governed by the robustness of weld at the fuel pin end plug. Structural fabrication codes do permit repairs, but they are silent on the number and type of repairs that can be allowed in the structures.

Heat input due to the welding process apparently causes re-crystallization in the heat affected zone (HAZ) and creates large-sized grains in the fusion zone. This type of heterogeneous microstructure of the weldment will create complex material behaviour at high temperatures. This results in further reduction of strength in the vicinity of the repair due to changes in the microstructure and mechanical properties. During the fabrication of fuel pin, it may be required to cut open and re-weld top end plug due to weld defect. The cut open and re-welded fuel pin may result in shortening of the clad length by few hundred microns. The HAZ of around few hundred microns may now get in the new weld zone. Sound joints without defects could be obtained after repeated cut and weld repairs. The range of HAZs of the weld repair joints will become wider than that of the original joint.

Four fuel pin samples, with and without manufacturing deviation have been subjected for simultaneous testing, so that degradation in life due to manufacturing deviation can be assessed experimentally. Accordingly an accelerated creep test has been carried out for the cut and re-welded fuel clad tube towards ensuring the required life for the reactor operating condition. The material used for the construction of test specimen was 20% cold worked alloy D9 (15Cr-15Ni-Mo-Ti-Si). This is same as the prototype fuel pin for the FBR application. The minimum yield strength (σy) of this material is 388 MPa at 913 K temperature and minimum ultimate tensile strength (UTS_{min}) is 478 MPa at 913 K.

Larson-Miller Parameter (LMP) is followed to arrive at the test temperature. The assumed correlations for arriving at the test conditions are given below:

Out of pile creep rupture life is

$$\text{Log}\,(t_r) = [(5.712 - \text{Log}\,(\sigma))/(2.3479 \times 10^{-4}\,T)] - 13.5$$

and the In pile creep rupture life is given by

$$\text{Log}\,(t_r) = [(5.4042 - \log(\sigma))/(2.244 \times 10^{-4}\,T)] - 13.5$$

where tr is the rupture time in hours, σ is the applied stress in MPa and T is the temperature in degree K.

The test facility consists of a pressure chamber filled with argon gas and it is pressurized upto 100 bar pressure. Four fuel pins having 6.6 mm outer diameter and

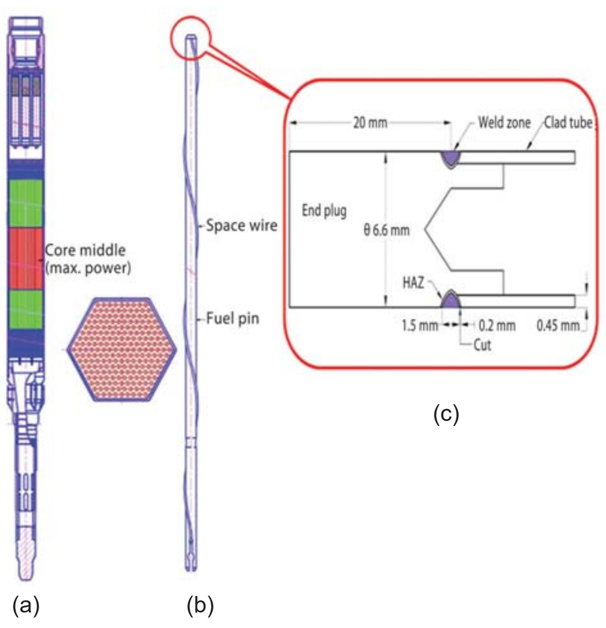

Fig. 1 *The schematic of the (a) PFBR FSA, (b) fuel pin and (c) end plug with manufacturing deviation*

0.45 mm wall thickness are welded to the common pressure chamber. The pins are enclosed in a furnace and heated up to 973 K, using the nichrome heating element. The experimental arrangement is shown in Figure 2. Two thermocouples (K-type) kept on the weld junction are used to monitor the temperature of the specimen during the experiment. The fuel pin end plug portion is kept inside a furnace, which is provided with sufficient insulation. Pressure is periodically monitored using the analog pressure gauge (Bourdon pressure gauge). The sudden drop of the steady state pressure in the chamber will be indicative of the tube failure. The hotspot temperature at the end plug location of the fuel pin under normal reactor operation is 913 K.

The cumulative damage fraction (CDF) apportioned for the reactor normal operating condition is 0.25. For the 57 bar pressure and 953 K temperature at the top of the active core region, the CDF is about 0.25 which is maximum at any location in the pin. The corresponding CDF at the end plug region for the same pressure and at a temperature of 913 K is 0.067. For this estimation, in-pile correlation is used even in the weld region. The actual dose at the end plug region is negligible when compared to the active core region. Accordingly, if out-pile correlation is considered for the damage estimation at the end plug region, the CDF is only 0.02. The reduction is due to higher time taken to rupture for similar conditions in out-pile correlation. However, for qualification of the end plug weld, irradiated correlation is only used conservatively and hence damage envisaged is 0.067.

The test is conducted at a temperature of 973 K and a pressure of 100 bar. The time required to rupture at the end plug weld location for the design qualification for the same CDF of 0.067 is 200 hours. With further weld strength reduction factor of 0.5, the minimum time required for out-pile experiments at a temperature of 973 K and a pressure of 100 bars is 400 hours.

Fig. 2 *Fuel pin test arrangement*

Under the accelerated experiments at a temperature of 973 K and a pressure of 100 bar, all the four fuel pins completed 3600 hours without failure. This is more than the required duration of 400 hours. Thus, the experimental results demonstrated that, the manufacturing deviation has not affected the required structural reliability of fuel pin for the present design life consideration. This result helps in deciding the use of the first time cut and re-welded fuel for the reactor application. The test is in progress till the failure of all the fuel pins, so that the degradation in life due to manufacturing deviation can be ascertained experimentally.

II.10 Microstructural and Microchemical Changes in 316LN SS and Modified 9Cr-1Mo Steels on Exposure to Liquid Sodium in a BIM Loop for 30,000 Hours

In PFBR, 316LN stainless steel (SS) and modified 9Cr-1Mo steel are the materials of construction for intermediate heat exchanger and steam generator respectively. These materials are in contact with flowing sodium at high temperature, which leads to the mass transfer of substitutional and interstitial alloying elements from high temperature to low temperature regions due to dissolution. This results in reduction in wall thickness of components either due to complete loss of alloying elements or preferential leaching of elements forming the modified surface layer. Formation of a carburized or decarburized layer, depending on carbon transport is a consequence of sodium corrosion, causing degradation in the mechanical properties of structural components. Both sodium corrosion process and thermal aging phenomenon affect the properties

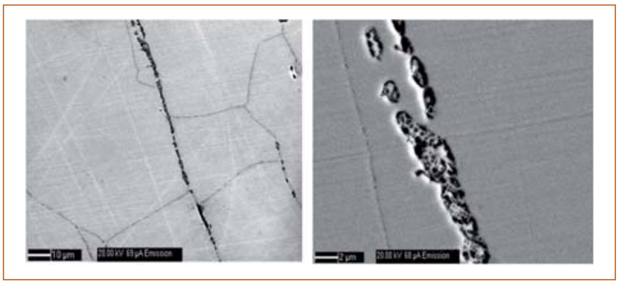

Fig. 1 *Sigma phase detected in 316LN SS after 30000 h at 798K*

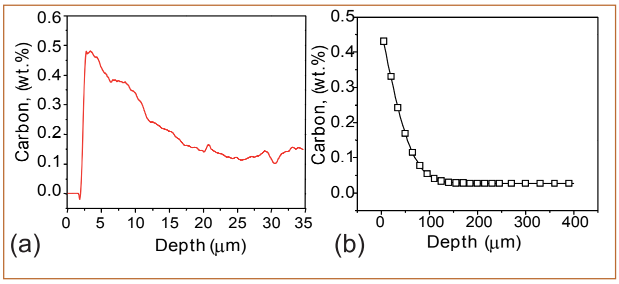

Fig. 2 *Carbon depth profile obtained for 316LN SS (a) experimentally by SIMS analysis and (b) extrapolated for 60 years*

of structural materials in service. Hence, specimens of 316LN SS and modified 9Cr-1Mo steel were exposed to flowing sodium for 30000 hours at 798 K in a Bi-metallic sodium loop, which simulated the secondary loop of PFBR and the changes in microstructural, microchemical and mechanical properties were assessed.

Dissolution of nickel and chromium from the surface of sodium exposed 316LN SS was observed, while sodium exposed modified 9Cr-1Mo steel neither showed dissolution nor deposition of any element. The average nickel and chromium content was ≈ 4 wt.% each at a distance of 2 μm from the surface, thereby confirming ferrite layer formation. Concentration of nickel and chromium reached the base composition at around 20 and 30 μm respectively. In 316LN SS, sigma phase was detected by scanning electron microscopy. The sigma phase was composed of 23.6 wt.% Cr, 8.3 wt.% Ni and 10.7 wt.% Mo. Sigma phase precipitated at the grain boundaries as long stringers (Figure 1), was further confirmed by XRD analysis. In sodium exposed condition 316LN SS showed the presence of Cr_7C_3, $Cr_{23}C_6$ and sigma phase. Modified 9Cr-1Mo steel showed the presence of Cr_7C_3, $Cr_{23}C_6$ and Laves phase. 316LN SS was found to be carburized after 30,000 hours of exposure to sodium (Figure 2a). Based on the carbon concentration profile obtained from secondary ion mass spectrometry (SIMS) measurements, effective carbon diffusion coefficient (D_C^{eff}) was calculated to be 6.8 x 10^{-19} m^2/s. Carburized depth for 316LN SS for 60 years of reactor operation was calculated to be about 200 μm, which is not significant (Figure 2b). Type 316LN SS also showed an increase in surface hardness and the hardness profile extended up to about 70-80 μm, indicating surface carburization. Modified 9Cr-1Mo steel showed a very marginal increase in the hardness at the surface which indicated neither carburization nor decarburization. Tensile properties of sodium exposed 316LN SS indicated a slight increase in yield strength and ultimate tensile strength and a large reduction in ductility compared to thermally aged specimens (Figure 3a). Modified 9Cr-1Mo steel did not show significant changes in strength and ductility on sodium exposure (Figure 3b). The drastic reduction in ductility (~60%) in 316LN SS specimen after sodium exposure was attributed to the formation of sigma phase and surface carburization. Significant decrease in impact energy was noticed in modified 9Cr-1Mo steel on exposure to high temperature sodium which was attributed to the formation of Laves phase on long term thermal aging. Surface carburization did not influence the impact energy in 316LN SS on sodium exposure.

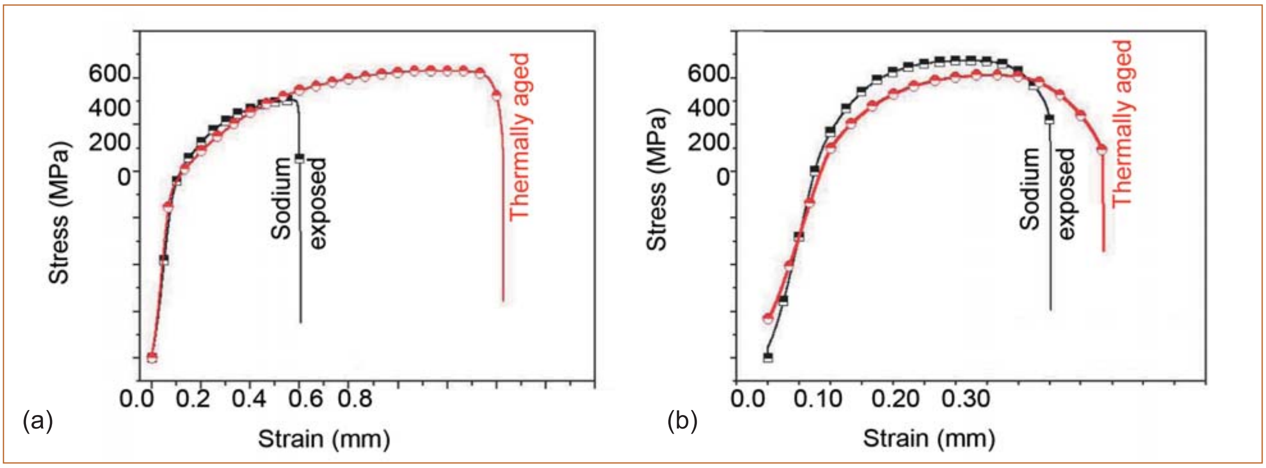

Fig. 3 *Tensile curves for (a) 316LN SS and (b) modified 9Cr-1Mo steel after exposure for 30,000 hours at 798 K*

II.11 Design & Development of cPCI Bus based 30 Channel Digital Input Card for Safety Related I&C Systems

The current Safety Related I&C system architecture for Prototype Fast Breeder Reactor consists of dual VME bus based Real Time Computer (RTC) systems with Switch Over Logic System. Since both the VME systems are exactly identical, the dual redundant system is prone to common cause failure (CCF). Probability of the same can be reduced by adopting diversity in RTC systems. Hence a Compact PCI (cPCI) bus based RTC system is being developed to replace one of the RTC in dual redundant systems. Design & development of cPCI bus based 30 channel Digital Input card is described here.

Board specifications

- Number of channels: 32 Opto-isolated
- PCI controller and glue-logic integrated in to spartan-6 LX9 FPGA
- Force-0 and Force-1 diagnostic logic provided
- 32 bit diagnostic register to check data path healthiness
- Clock fail detector
- Field connections brought through J5 connector of the cPCI backplane
- Board failure indication: LED provided on fascia panel
- Field interrogation voltage: 24V
- Board size: 233.4 mm X 160.00 mm X 1.6 mm
- Backplane connectors: J1 – 110 pin socket and pin type Connector
- Rear IO module for connecting field inputs
- Power requirements (max): 5V/1A
- PCI signaling environment: 3.3 V
- Hot-swap capability provided

The DI card was fabricated as shown in Figure 1.

Development of device driver

Device driver for the board was written as a Linux kernel module. An Application Programming Interface (API) library was created which provides the following operations:-

- Read/Write Diagnostic Register
- Read Data Register
- Read Board Failure Status Register
- Write Control Register
- Read/Write Force-0 Diagnostic Register
- Read/Write Force-1 Diagnostic Register

Testing of the board

A test application was written using functions provided by the API library. DI card was tested successfully in cPCI reference platform by running the test application in the CPU card as shown in Figure 2.

Hot swap capability was tested by plugging the board into a live system. Board was detected and configured successfully. Board removal from the live system also was detected successfully by the CPU card and resources were de-allocated.

A compact PCI bus based Digital Input card was designed & developed. Device driver and API library was developed for the board. The board was tested successfully using test applications. The live insertion and live removal capability of the board was also verified. A rear IO module also was developed to interface field inputs to the board.

Fig. 1 *Fabricated digital input card*

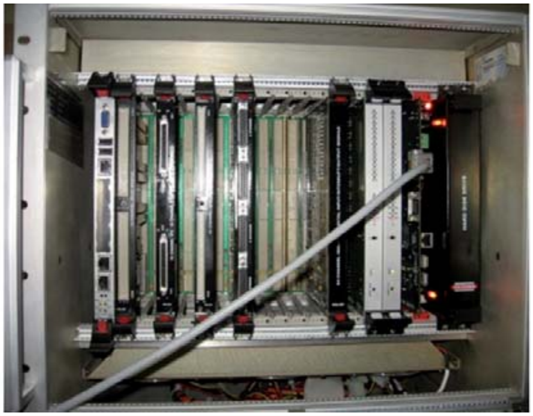

Fig. 2 *Digital input card test setup*

II.12 Estimation of Common Cause Failure Fraction for Triple Redundant Instrumentation Channels of Shutdown Systems of PFBR

Common cause failures (CCF) defeat the redundancy in a system. CCF are generally accounted for in probabilistic safety analysis by apportioning a certain fraction (say,β) of the total failures of individual channels to common causes. Often, the numerical value β, is based on engineering judgment. To bring in a more systematic approach and consistency in such assumptions in I&C systems, IEC 61508-6 (2000) suggests a score based methodology. Though this method also involves engineering judgement in many places, using this methodology is likely to give more accurate estimation of the effect of CCF. The β factor for triple redundant instrumentation channels used for processing SCRAM parameters in shutdown system is analyzed using the said method.

The methodology defined in Annex-D of IEC 61508-6 takes cognizance of the following factors:

- The probability of CCF is a dominant factor in determining the overall probability of failure of a multi-channel system and without taking it into account, a realistic estimate of the safety integrity of the overall system is unlikely to be obtained.
- Although common cause failures result from a single cause, they do not always manifest themselves simultaneously in all redundant channels.
- In case of modern I&C systems with diagnostic features, it is possible to incorporate defenses against CCF by utilizing the time available between the first failure and subsequent failures, although initiated by a common cause; provided the failures are asynchronous.

The method assigns scores for various design provisions and maintenance measures which have the potential to minimize common cause failures. The score for each measure/provision has two parts namely X and Y. If a particular provision or measure against CCF is provided, then designated score is assigned. Else there is no score for the provision. The score against X is used in providing weightage for diagnostics in the system whereas the Y component is not affected by diagnostics. Thus the ratio X:Y represents the extent to which the measure's contribution against common cause failures can be improved by diagnostic testing.

Table 1 : Calculation of β_U or β_D (reproduced from IEC 61508)

Total score (S or S_D)	β_U or β_D	
	Logic sub-system	Sensors and final control elements
120 or above	0.5%	1%
70 to 120	1%	2%
45 to 70	2%	5%
Less than 45	5%	10%

Scores are separately assigned for Logic Subsystem and Sensors/Final control elements. Based on the total score ($S=\Sigma X+\Sigma Y$), Beta factor for undetectable failures (β_U) is assigned. Table 1 lists β against the sum S.

To calculate detectable failures, a factor Z is introduced. The Z factor takes into account the level of diagnostics coverage and the test interval between two diagnostic tests (Table 2a and 2b shown for assigning Z factor). The total score S_D is calculated as $S_D=\Sigma X(Z+1)+\Sigma Y$. Beta factor for detectable failures (β_D) is assigned based on S_D based on Table 1.

Using the score based method, a Beta factor of 1% is estimated for logic sub-system and 2% is for sensors and final control elements. The estimates can be used in the Probabilistic Safety Analysis of the plant.

Table 2a : Z factor for logic system (reproduced from IEC 61508)

Diagnostic coverage	Diagnostic test interval		
	<1 minute	Between 1 and 5 minute	Sensors and final control elements
>99%	2.0	1.0	0
>90%	1.5	0.5	0
>60%	1.0	0	0
Less than 45	5%	10%	10%

Table 2b: Z factor for sensors final control elements (reproduced from IEC 61508)

Diagnostic coverage	Diagnostic test interval			
	< 2 hours	Between		> 1 week
		2 hours and 2 days	2 days and 1 week	
>99%	2.0	1.5	1.0	0
>90%	1.5	1.0	0.5	0
>60%	1.0	0.5	0	0

II.13 Development of Qualified Signal Conditioning Modules

Signal Conditioning Modules (SCM) are analog modules used to isolate, amplify and filter the signal from the sensor for further processing by data acquisition systems, which form the front-end of any I&C system. Various types of sensors like Thermocouple (T/C), Resistance Temperature Detector (RTD), strain gauge, load cell and draw wire potentiometer are used in I&C systems of a reactor. These SCMs should feature high accuracy, low drift and high stability and have to be qualified against stringent environmental and EMI/EMC conditions. The SCM currently used in the core temperature monitoring system of PFBR is an imported one, which features high accuracy, low drift and high stability. The modules are not amenable for customization as per our needs and are also expensive. Hence, it was envisaged to develop qualified indigenous SCMs, which are also customizable. Initially DIN rail mountable thermocouple input and RTD input SCM (Figures 1a and 1b) were designed and developed.

The module contains three major functional blocks, namely - amplifier, isolation and filter. The precision amplification function is achieved using a zero drift operational amplifier. The salient features of the opamp are ultra-low-offset voltage (4.5 µV) and offset voltage temperature drift (0.08 µV/ ºC). The zero drift amplifier topology was chosen to minimize its offset error contribution at an ambient temperature of 25ºC and its drift with ambient temperature variation. Galvanic isolation is provided using transformer coupling in-built in the integrated isolation amplifier to suppress the transmission of common mode signal. The three port isolation (Input-Output, Input-Power and Output-Power) is achieved using a precision 3-port isolation amplifier. The output of the isolation amplifier is followed by a low pass filter. Low pass filtering is required to reject the 50 Hz normal mode noise, attenuate the ripple from the isolation amplifier output, attenuate the injected switching noise from the power supply and to reduce the in-circuit broadband noise. The designed low pass filter is of order 5 with Bessel approximation magnitude and phase response. Bessel filters exhibit a linear phase characteristic within the passband, thus it provides an undistorted pulse response with minimum overshoot and improved response time.

Special input circuit provides protection against accidental connection of power line voltage up to 230 VAC and against transient events. Protection circuit is also present on the module output and power supply input terminals to guard against transient events and power reversal. In the thermocouple input module, transistor Base-Emitter junction diode based generic temperature sensor is used for cold junction compensation. The RTD input module accepts 2 and 3-wire RTDs, whose excitation is provided from the module using a precision OPAMP and MOSFET based current source. Lead wire resistance compensation is achieved in hardware by matching the two current paths and processing the difference signal which cancels the effects of equal lead resistance.

Table 1: Comparison of module specifications

Specification	Imported module	Indigenous module
Module accuracy Inclusive of CJC	+/- 0.05 % of span (typ.)	+/- 0.075 % of span (max)
Module non-linearity	+/- 0.01 % of span	+/- 0.02 % of span
240 VAC input protection	Yes, continuous	Yes, continuous
Isolation	Three port	Three port
CMR @ 50 Hz	160 dB	160 dB
NMR @ 50 Hz	80 dB	80 dB
Offset drift (µV / ºC)	160 (typ.)	70 (max.)
Gain drift (µV / ºC)	350 (typ.)	435 (max.)
Output noise (µV, rms)	180	210
Long term drift (1000 hrs)	Data not provided	less than +/-0.01%

The fabricated and assembled modules exhibited satisfactory functional performance. The modules were subjected to dry heat test to evaluate its temperature drift performance. The long term drift performance of the module also was characterized through a 1000 hours continuous test in power on condition. The SCMs also were subjected to EMI tests as per IEC standards to evaluate its electro-magnetic compatibility. The T/C input SCM was deployed in FBTR where it was connected to the spare thermocouple of the flywheel of pump drive system. The evaluated accuracy of performance and stability complied with the datasheet specification. The same module, modified to accept voltage input also is used in the prototype Steam Generator Hydrogen Leak Detection System deployed in FBTR. The functional performance of the T/C input SCM was benchmarked with the existing imported module. The module exhibited comparable performance as shown in Table 1.

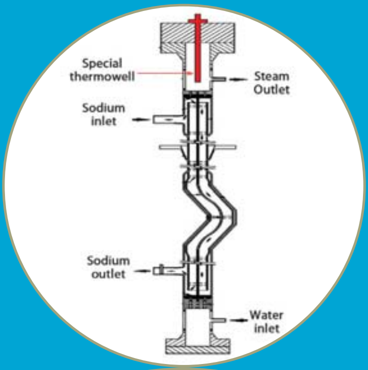

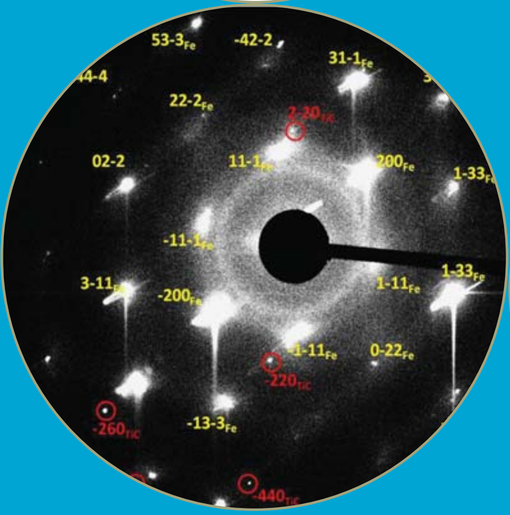

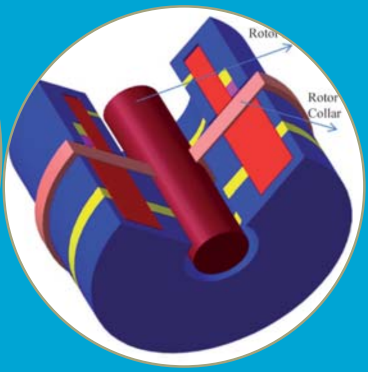

CHAPTER III

Research & Development for FBRs

III.1 Shutdown Systems for Future Breeder Reactor

New safety criteria are being evolved for Sodium cooled Fast Reactors after taking into account the currently evolving safety criteria worldwide. This article briefs about the significant new criteria that are to be met by shutdown systems of future breeder reactor and the philosophy being adopted to meet the new criteria.

For new reactor designs, several scenarios that are considered beyond design basis for previous generation needs to be addressed under design extension condition (DEC).

Design extension condition

The evolving AERB safety criteria states the following about design extension conditions

“An analysis shall be undertaken using a combination of deterministic and probabilistic approaches, engineering judgements and operating experience to determine those event/event sequences that could lead to conditions beyond the design basis events (DBE) for the purpose of further improving the safety of the NPP by enhancing the plant’s capabilities to withstand, without unacceptable radiological consequences, accidents that are more severe than DBAs or that involve additional failures. These include BDBAs without significant core degradation and those with significant core degradation. From these BDBAs, events/event sequences can be selected to identify and to implement those reasonably practicable provisions for their prevention and mitigation. These event/event sequences may be called design extension conditions. These design extension conditions shall be used to identify the additional accident scenarios to be addressed in the design and to plan practicable provisions for the prevention of such accidents or mitigation of their consequences if they do occur.”

The enveloping design extension condition for shutdown system

The GEN IV, AERB and WENRA have explicitly indicated anticipated transient without scram (ATWS) events as examples of events to be included in the DEC. The draft tech doc recently circulated by IAEA has explicitly listed “Anticipated Operational Occurrence or Design Basis Accident (DBA) combined with failure of the reactor protection system and the actuation of safety systems” as one of the preliminary reference DECs.

Based on the literature survey on failure experiences of shutdown systems and study of various evolving safety criteria it is decided that complete failure of first two shutdown systems along with station black out is the enveloping DEC to be included in the future SFR designs.

Proposal for future FBR shutdown systems

The core degradation due to ATWS has to be practically eliminated as the fast reactor core is not in its most reactive configuration during normal operation.

Deterministic demonstration of dispersal of fuel to avoid further core compaction after initiation of large scale core damage is highly challenging. Hence, the following are the important decisions related to shutdown systems for next generation SFRs, to facilitate practical elimination of core degradation due to ATWS.

- Strengthen the first two shutdown systems by addition of passive/active features
- Introduce an additional shutdown system, which is completely diverse, independent, passive & confined within core subassembly. This shall come into action on failure of first two systems.

Design augmentations of first two active shutdown

The first shutdown system (SDS-1) comprises of nine control and safety rods (CSR) and three hydraulically suspended absorber rods (HSARs). CSRs are used for both power control as well as shutdown whereas HSARs are used exclusively for shutdown. The Scram signals of first shutdown system trigger both CSR and HSAR. In addition HSARs get triggered by passive means due to flow reduction through core and ensure shutdown of the reactor. A stroke limiting device is provided in CSRDM to prevent inadvertent withdrawal of Control & Safety Rods beyond a preset level and thereby eliminate the possibility of continuous rod withdrawal and limit the consequences of inadvertent control rod withdrawal event well within limits even when coupled with the failure of other safety actions.

The second shutdown system (SDS-2) has three diverse safety rods (DSRs). DSR have the function of reactor shutdown only. The temperature sensitive magnetic switch based on Curie point is introduced in series with the power supply circuit of electromagnet of diverse shutdown rod drive mechanism as an additional passive safety feature.

Thermo siphon based passive shutdown system

Apart from this, another shutdown system, which is fully passive and gets activated due to temperature rise of coolant inside the core is also envisaged. This system gets activated by siphon action, which gets established due to temperature rise of working fluid of the system. This system neither involves any mechanical moving item nor requires any active actuation. With the provision of these systems a target failure probability < 10^{-7} for shutdown per reactor year can be achieved.

III.2 Integral Testing of Stroke Limiting Device with Control and Safety Rod Drive Mechanism

Stroke limiting device (SLD) is an add-on device to control and safety rod drive mechanism (CSRDM) to provide additional safety against the event of uncontrolled withdrawal of control rod. SLD limits the consequences of inadvertent withdrawal of control and safety rod (CSR) to category II limits by physically limiting the withdrawal stroke length of CSR to 20 mm.

SLD consists of machine elements like gears and shafts, sensors and a mechanical stopper (Figure 1). SLD when operational stops the upward movement of mobile assembly along with CSR for every 20 mm rise, Further raising is facilitated by resetting the SLD. Continuous lowering of CSR is always ensured by free-wheeling arrangement in SLD. The power from the main drive shaft is fed to driving pinion. The driving pinion is coupled to the gear of SLD. The SLD gear top surface is profiled with a ramp. The start/end of ramp has a vertical face which acts as a stopper. A teflon roller fixed on a swing arm slides over the ramp on the gear. The swing arm is fixed on a plunger with pin joint. The inclined position of the swing arm is maintained by a helical coil spring. When the SLD gear rotates, the ramp on the gear raises/lowers the plunger based on direction of rotation. The plunger is housed inside a guide way. A DC pull type solenoid connected to the plunger facilitates resetting operation by pulling the plunger up. The plunger is always pushed downward by gravity and a helical coil spring. Two micro-switches are fixed on a support which in turn is fixed on the plunger. These micro-switches are actuated by a cam fixed on the swing arm. The inclined position of the swing arm is sensed by micro-switch-1 and the over travel of swing arm is sensed by micro-switch-2. The signals to scram the reactor and start of lowering of mobile assembly are initiated by micro-switch-2.

Fig. 1 *Schematic and photograph of stroke limiting device*

Fig. 2 *Assembly of SLD with CSRDM*

Prior to integrated testing, a prototype SLD was manufactured and was tested separately for 49000 cycles in raising and 1550 cycles in lowering without any interruption.

Later, prototype SLD was assembled with prototype CSRDM upper part in Engg. Hall-3. Figure 2 shows the photograph of SLD assembled with CSRDM upper part. A new PLC based control panel was made for SLD testing. Necessary changes in the control logic of CSRDM were made.

Testing involved raising / lowering the ‘EM plus mobile assembly’ with motor. All the aspects of control logic were verified. Scramming of CSRDM in case of SLD actuation was also verified. Free downward travel of mobile assembly was also verified. Subsequently, 30 cycles of raising and lowering operations were carried out.

Overall performance of the mechanism is smooth during testing and the maximum torque for translation did not vary much. Thus, the integrated performance of CSRDM with SLD was demonstrated.

III.3 Commissioning of Large Scale Test Facility for Future FBRs

An experimental facility for carrying out thermal hydraulic studies in water related to future FBR’s has been set up in Engineering Hall IV. This is a 5/8th scale 90° sector model of primary circuit of future FBRs. This facility has been built to carry out various pool hydraulic studies with prime focus on gas entrainment phenomena in hot pool. Performance of various gas entrainment mitigation devices are planned to be tested in this model. This model consists of a vessel simulating the main vessel, core assembly, intermediate heat exchanger (IHX), control plug and decay heat exchanger (DHX). A water loop with maximum flow capacity of 4000 m^3/h has been erected to cater to the required flow rate to the model.

All the components of this model are fabricated separately and assembled at the site. Vessel assembly is fabricated in three parts and transported to Engineering Hall IV for assembly. The vessel assembly consists of major components like main vessel, inner vessel, bottom dished end and the core assembly. Fabrication of Inner vessel profile with two directional surface curvatures was challenging. The geometry of inner vessel is achieved by joining six numbers of petals. Bottom dished end curvature was achieved by pressing technique and joining of the petals. Various gas entrainment mitigation devices were also fabricated and these devices will be used during experimental studies. The top part, middle part and bottom part of the vessel assembly with base plate were assembled in Hall IV site and anchored with the support structure with bolts. Alignment between the top part and dished end part of vessel was another challenging task at the site due to heavy weight of the vessel and due to minor distortions caused during the manufacturing process. This has been corrected by proper sealing method and assembly procedure. Fabrication of control plug and IHX was also another challenging task, owing to their complicated geometry. Top structure of the 5/8th scale model has been designed and fabricated to support IHX. IHX support structure arrangement is designed to facilitate replaceable IHX tube bundle. Control plug of the 5/8th scale model has been erected with the model and supported from the top flange of the vessel. The 5/8th scale model is shown in Figure 1.

Fig. 1 *5/8th scale test facility*

Fig. 2 *Hydraulic loop*

A dedicated water loop has been designed, erected and commissioned to fulfill the process requirement of this experimental facility (Figure 2). Two large capacity pumps were erected and aligned with the 1 MW motor. Submersible pumps were installed in the reservoir to draw water from it for the loop. Plate type heat exchanger and cooling tower to maintain water temperature in the loop have been installed and commissioned. Manually and pneumatically operated butterfly valves are used in the loop for flow control. Averaging pitot tube type flow meters are used for flow monitoring. All the sensors and process indication can be monitored from control room. The 5/8th scale facility is in the commissioning stage and experimental studies will commence with the mapping of flow field in the hot pool.

III.4 Gas Entrainment Detection Experiment using Eddy Current Flow Meter

In sodium cooled fast breeder reactors, entrainment of argon gas is possible in normal as well as transient conditions. It is therefore important to develop a technique to detect it and quantify the amount of entrained gas during reactor operation. Performance evaluation of two different types of sensors viz. acoustic sensor developed at CEA, France and eddy current flow meter (ECFM) sensor developed at IGCAR was completed at Steam Generator Test Facility (SGTF) sodium facility for this purpose. This testing program was based on the implementation agreement signed between IGCAR, India and CEA, France to study and characterize the gas content in sodium. A suitable test section was selected in the sodium facility at SGTF and sensors were installed in series in sodium flow path.

The ECFM sensor has one primary and two secondary coils wound symmetrically on either side of the primary coil. The voltage induced in moving annular sodium at ECFM ring induces voltage in both secondary coils, which are subtractive to transformer voltage in upstream coil and additive to transformer voltage in downstream coil. As a result of this the voltages induced in the two secondary coils differ from each other and this difference is proportional to the sodium velocity. This output signal changes significantly when argon bubble passes through it. This change in output signal is correlated with the void fraction to evaluate the entrainment and extent of entrainment.

Fig. 1 *Test sections with sensors*

Sodium flow through the test section is measured by Permanent Magnet Flow Meter and sodium temperatures using thermocouples. The sensors in the test section are shown in Figure 1.

The presence of argon in sodium was simulated by injection of known quantity of argon in the flowing sodium. Two mass flow controllers were used to adjust the argon flow rate from 0.050 to 15 litres per minute for each sodium flow. The experiment was caarried out with ECFM at two sodium temperatures of 300 and 350 °C. ECFM primary and two secondary signals were acquired at a sampling rate of 10kHz/s. Void signal was obtained by performing demodulation (envelope extraction) on the ECFM secondary signals. RMS of the void signal was plotted against the void fraction.

During initial experiments conducted with ECFM, it was observed that ECFM could detect the presence of argon gas in sodium above a void fraction of 0.5% and detection was possible at all sodium flows ranging from 12 to 30 m^3/h.

The experiments conducted in parallel with acoustic sensor has also shown that detection was possible at 12 m^3/h (Figure 2) for void fractions above 3%. However there were no appreciable change in the ECFM signals at higher sodium flow rates from 18 to 30 m^3/h. It is also seen that sensitivity was very low at 12 m^3/h compared to initial experiments.

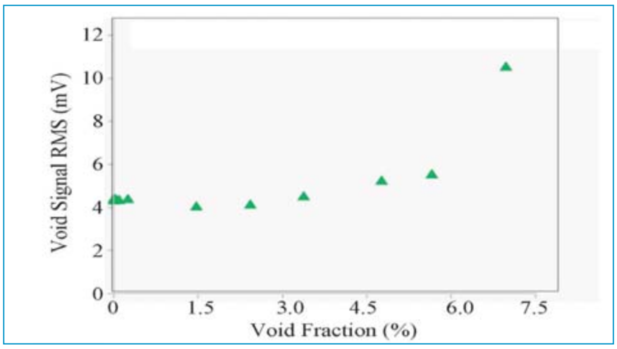

Fig. 2 *Void fraction versus void signal*

The reasons for the same may be attributed to the change in the injection hole diameter from 1 mm during initial experiments to 0.5 mm during these studies in parallel with acoustic sensor. The higher diameter holes will lead to large size bubbles which will be able to get detected easily through the ECFM. The excitation frequency of the ECFM for the present studies was 300 Hz which was higher compared to initial experiments, where the excitation frequency was only 100 Hz. This also contributed to the reduction in sensitivity.

It can be concluded from both the experiments that the successful detection of gas entrainment is possible with ECFM for higher void fraction. But the applicability of the sensor at lower void fraction can be finalised (which is the requirement for FBRs) after some more studies.

III.5 Testing of Integrated Cold Trap in Test Vessel-3 of Large Component Test Rig Sodium Loop

Demonstration of full scale model of integrated cold trap (ICT) was carried out in test vessel - 3 of large component test rig (LCTR). During testing, sodium pool was maintained around 500˚C and sodium was circulated through ICT at a flow rate of 2 m^3/h. With nitrogen inlet at 44˚C temperature, 1.2 bar (a) pressure and a flow rate of 850 m^3/h, the cold point temperature of 110 ˚C was achieved. The nitrogen outlet temperature was measured around 218˚C. 16 tonnes of sodium circulated in test vessel - 3 was purified using integrated cold trap.

During the first campaign of operation, direct current conduction pump (DCCP) failed and was not able to circulate sodium through ICT. For further testing of ICT, failed DCCP was replaced with a submersible annular linear induction pump (ALIP) of similar capacity and dimensions.

To replace the pump, ICT along with DCCP was

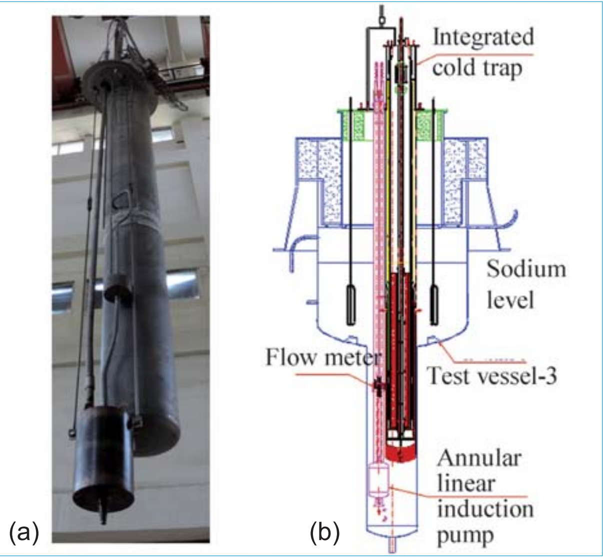

(a) (b)

Fig. 1 *(a) Erection of integrated cold trap along with annular inear induction pump and (b) schematic of ICT in test vessel-3* removed from test vessel-3 and placed in test vessel-5 for cleaning of sodium wetted surface in ICT. Sodium cleaning of ICT was carried out by wet carbon dioxide process. On completion of cleaning, ICT was taken out of test vessel-5 and DCCP was dismantled from the assembly. Support structure was suitably modified to suit the requirement of submersible annular linear induction pump. The inner assembly of the ICT (wire mesh arrangement) was removed and wire mesh was replaced with fresh mesh.

The full scale model of integrated cold trap along with annular linear induction pump has been erected in test vessel-3. Figure 1a shows the photograph of erection of ICT with annular linear induction pump in test vessel-3. Figure 1b shows the schematic view of ICT in test vessel-3.

The dry commissioning of nitrogen cooling circuit has been carried out separately. Sodium at 200 °C was filled in the test vessel-3 of LCTR. The sodium at a flow rate of 2 m^3/h was circulated through the integrated cold trap by using annular linear induction pump. The sodium pool temperature was gradually raised to 500°C. The cold point of the cold trap was maintained at 150°C during the operation. ICT is geared up for conducting experiments in all respects. The performance of ICT is in line with the design expectation. The problem faced due to failure of DCCP during first campaign of ICT was successfully resolved and further performance testing is resumed.

III.6 Thermal Hydraulic Optimization to Minimize Primary Sodium Pump Shaft Length for Future FBRs

Sodium flow in the primary circuit of future FBRs is maintained by three centrifugal pumps operating in parallel. These pumps (PSP) are mounted over the dome shaped roof slab. They have very long shaft due to the motor being located outside the reactor vessel and the impeller being submerged in sodium contained inside the reactor vessel. Due to the increase in height of main vessel in future FBRs compared to that of PFBR, length of the pump shaft is increased. The other main consideration in fixing the length of shaft is attaining comfortable temperature conditions for its spherical seat assembly. Spherical seat is provided in the pump for accommodating tilting of pump due to differential temperature among various parts of pump assembly, roof slab and pump receptible. Long shaft length is not desirable due to issues connected with vibration and balancing. Schematic of the upper part of the primary sodium pump assembly supported over dome shaped roof slab is shown in Figure 1. Excessively long shaft length may demand multiple hydrostatic bearings in the pump assembly. Multiple hydrostatic bearing makes the hydraulic configuration of pump very complex due to the bearing fluid being liquid sodium pumped by the pump itself. Optimization of shaft length requires temperature distribution of pump assembly to be established.

Thermal analysis of pump assembly has been carried out through a conjugate numerical model considering conduction, natural convection and thermal radiation modes of heat transfer. Three dimensional 180° sector model of pump assembly has been considered for the analysis. Schematic of the geometric model used for the analysis is shown in Figure 2. The domain considered for the analysis starts from free level of sodium in PSP stand pipe to top of the pump shaft. All the solid parts are considered to be of stainless steel and the effective thermal conductivity of steel ball filled region (provided for radiation shielding) in the pump assembly is estimated based on porous medium formulation. For computational simplicity, parametric studies for optimization of shaft length has been carried out by employing axi-symmetric model and a modified configuration for pump assembly has been worked out respecting various temperature constraints. Subsequently, three dimensional analysis of pump assembly has been carried out to consider the impact of multi-dimensional effects on the temperature distribution of assembly. Important multi-dimensional effects addressed are the temperature non-uniformity in the circumferential direction due to the non-axisymmetric nature of thermal boundary condition and cellular convection in narrow annular gaps. Convective effects due to shaft rotation and cellular convection in narrow annular gaps between various structural members in the pump assembly are also considered in this analysis.

Based on the temperature distribution predicted for the reference design configuration, it was found that there is scope for reducing the length of shaft due to lower values of temperatures of spherical seat. Therefore, a modified configuration-1 with 300 mm length of bottom hollow portion reduced has been considered. In this option the spherical seat assembly would be lowered by 300 mm towards the sodium free surface. With this modification also, comfortable margin was observed

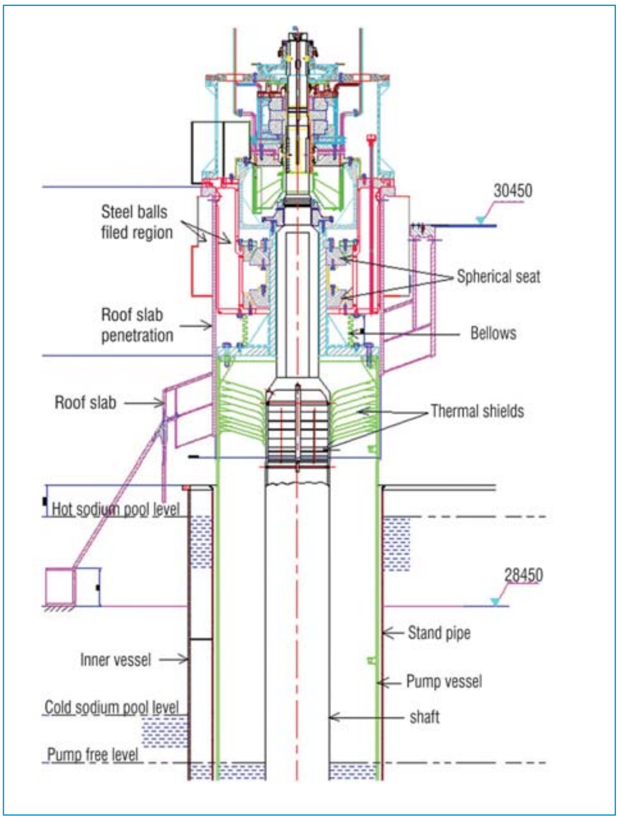

Fig. 1 Schematic of primary sodium pump assembly

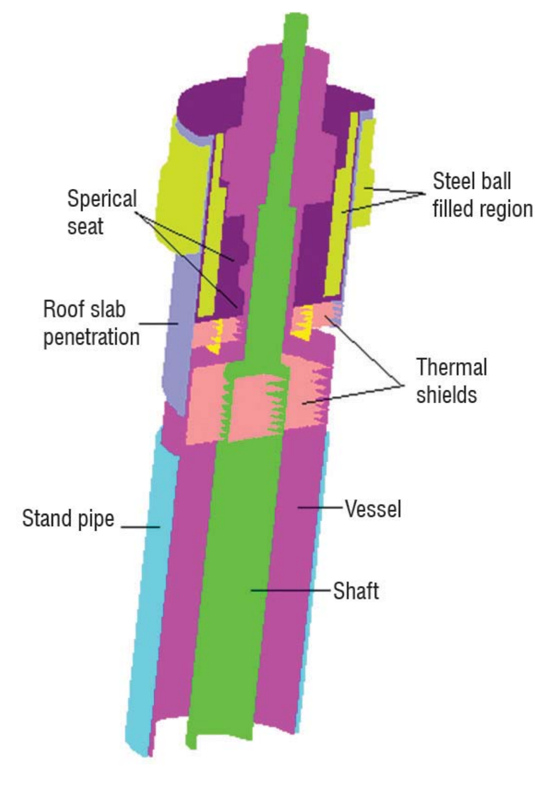

Fig. 2 Three dimensional model of pump assembly

on the temperature of spherical seat assembly in comparison to the temperature limits. Therefore, further reduction in the length of second hollow portion by 200 mm (configuration-2) was considered. This modification resulted in lowering of bellows towards the thermal shield location in the assembly. Therefore, thermal shields are considered to be provided both on inside as well as outside regions of bellows. Predicted temperature distribution of this case was also found to be acceptable and hence 500 mm reduction in shaft length was found to be possible.

Subsequently, in order to assess the influence of multidimensional effects, three dimensional analysis was carried out. Temperature distribution of the spherical seat assembly predicted by the 3D analysis was found to be lower than that predicted by the axisymmetric model. It was observed that the temperature distribution in the pump assembly is not uniform around the circumference. There was a circumferential temperature variation of 16 and 7 °C on lower and upper spherical seats respectively. Modifications in the pump assembly for reducing the circumferential temperature variation were considered. The first option considered was to provide thermal insulation over the roof slab penetration shell in the region between top plate of roof slab and steel ball filled region. (configuration-3). Reduction in the circumferential temperature variation due to this modification was not found to be insignificant. Therefore, further, modification was considered to make the thermal shields semicircular covering only 180 ° sector (Configuration-4). Number of thermal shields made semicircular is also varied as a parameter. When two thermal shields provided in bellows region were made semicircular, maximum temperature of spherical seat increased to 256 °C (Figure 3) and circumferential temperature variation in lower and upper spherical seats reduced to 9 and 6 °C respectively. The maximum temperature of upper spherical seat is 199 °C. These temperatures are within permissible limits. Therefore, configuration-4 is recommended for design.

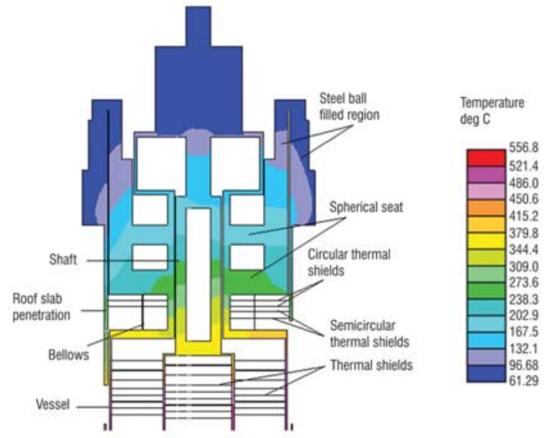

Fig. 3 Predicted temperature distribution in the primary sodium pump assembly for the recommended configuration-4

III.7 Shape Optimization of Thrust Active Magnetic Bearing for Oil Free Centrifugal Sodium Pump

In the sodium cooled fast reactors, vertical centrifugal pumps are used to pump sodium. The construction of vertical pump is such that its impeller is dipped in sodium and the pump rotor assembly is supported in sodium by hydrostatic bearings from bottom and by Kingsbury type thrust bearing and radial sleeve bearing above the cover gas space.

Hydrostatic bearing above the impeller is used to maintain concentric position of shaft. Argon is used as the cover gas and seals & bearings are lubricated by oil circuits. This arrangement has a potential of oil dripping into sodium, which is a safety issue. In view of the above, a program to develop an oil less magnetic bearing in combination with ferro-fluid seal. Magnetic bearing consists of two electromagnets on both sides of a collar attached to the pump shaft and levitates the rotor parts without touching the static parts. The electromagnet (EM) is fed with controlled current from a PID control to maintain constant air gap between collar and opposing face of electromagnet. Magnetic bearings becomes unstable when the collar comes very near to either of the electromagnets due to cumulative increase of magnetic flux. A magnetic structure design is used where lower saturating magnetic material (mu-metal) is sandwiched in normally used electromagnetic steel. In a subsequent study, upper electromagnet was biased by permanent magnet with an aim to reduce the EM current. Though mu-metal mitigates the cumulative flux addition effect by saturating itself magnetically, it reduces the EM forces available on rotor. Both position and current stiffness values deteriorates with addition of mu-metal. So, a goal seeking optimization methodology is employed with an objective of realizing trouble free large gap magnetic bearing by optimizing the geometry of magnetic structure employing all the above said materials. Adaptive response surface method (ARSM) followed by evolutionary algorithm (EA) was used for optimization. The magnetic bearing is modeled in finite element methods in magnetics (FEMM) and was interfaced through Matlab. An optimizer, Optiy was used in combination with FEMM and Matlab for the works of optimization. The proposed design geometry was parameterized, optimized and arrived at a better configuration.

This was achieved in the following steps:

a) A goal seeking optimization methodology is employed with a combination CRGO electrical steel and mu-metal. Adaptive response surface method (ARSM) followed by evolutionary algorithm (EA) was used for optimization. In the first stage, majority of parameters were taken as variables for optimization and those variables not influencing the objective functions towards the end of optimization iterations were frozen and sub-optimized model was constructed with lesser variables for further optimization.

b) In the second and final stage, a permanent magnet biased magnetic actuator with mu-metal and CRGO steel actuator was used with more demanding objective function. Figure 1 shows the 2D model of right half PM biased multi-material actuator for optimization, optimized with multi-objective optimization by evolutionary algorithm (MOEA). The nearest to optimized configurations (Pareto front) were realized. Figure 2 shows the best option chosen from Pareto table corresponding to a design having flatter position stiffness and higher current stiffness. Figure 3 compares position stiffness values between optimized and un-optimized thrust actuator.

In conclusion, it is found that the position stiffness is more flatter across the working gap of 1.5 mm compared to magnetic structure without mu metal and permanent magnet.

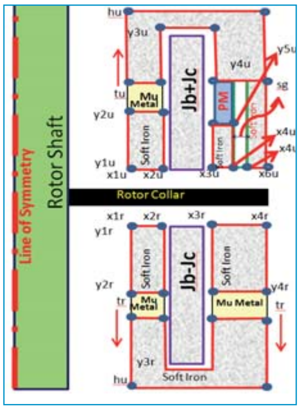

Fig. 1 *Pictorial description of variables to be optimized*

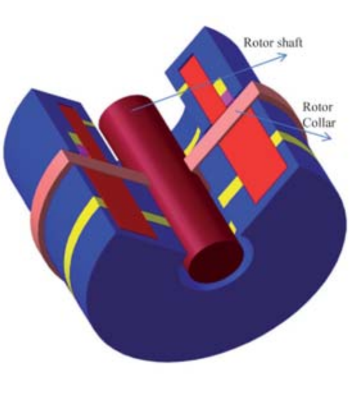

Fig. 2 *Most optimized AMB actuator after MOEA*

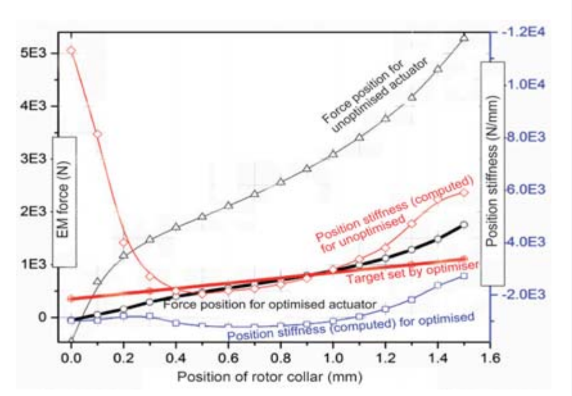

Fig. 3 *Comparison of optimized and un-optimized actuator*

III.8 Molten Fuel Coolant Interaction Studies in Simulant System

The event of a core melt down, resulting in relocation of the active core, is analyzed to understand safe termination and effective removal of decay heat. Corium interacts with coolant in the process and fragments into debris, during molten fuel coolant interaction (MFCI). Debris bed configuration on the core catcher plate assumes importance in assessing the post accident heat removal capability. The key factors affecting the coolability of the debris bed are bed porosity, morphology of the fragmented particles, degree of spreading/ heaping of the debris on the core catcher and fraction of lump formed. Towards understanding the debris bed for post accident heat removal studies, series of experiments are conducted with molten woods metal (an alloy of Bi 50%, Pb 25 %, Sn 12.5% & Cd 12.5% with melting point of 346 K) in water simulant system (Figure 1).

Woods metal-water system has hydrodynamic similarity with UO_2-sodium system of a typical LMFBR. Experiments are carried out at different melt temperatures after fixing the interaction length at 800 mm. The setup consists of furnace cum melt release system placed on top of interaction vessel with catcher tray at bottom, as shown in Figure 1.

The catcher tray is marked into different radial zones. The distribution of the mass per unit area in each zone is plotted after the experiment at different melt temperature (Figure 2). The maximum concentration of mass is observed at the centre most region (Zone 4). The mass per unit area decreases monotonically as we move towards the outer region from center. Further experiments are planned with varying spread area at higher melt temperatures.The surface morphology of the debris particles was also analysed to get insight into the mechanism of break up. Magnified images of typical debris are shown in Figure 3.

Fig. 1 *Experimental setup of water simulant system*

Study of similar MFCI event associated with water cooled reactors are also taken up at sodium fuel interaction facility (SOFI), using high temperature corium simulants. Series of experiments are being conducted under this program in collaboration with BARC. The simulant eutectic / non-eutectic material is loaded in tungsten crucible, which is used as susceptor to facilitate induction heating of ceramics. The molten simulant is poured into one of the test sections (15 x 15 x 30 cm) as shown in Figure 1.

Typical observations from first series of experiments are briefed. The water temperature at the location directly in the path of falling of melt was found to be raised and gradually dropped down to 5 °C above the initial temperature.

The surface morphology of the two simulants used in first series, were found to be starkly different. Detailed debris analysis is in progress. Images of typical debris from high temperature ceramic simulant are shown in Figure 4.

Further experimental validation and parametric studies are required to gain further understanding of phenomena, which are proposed for future.

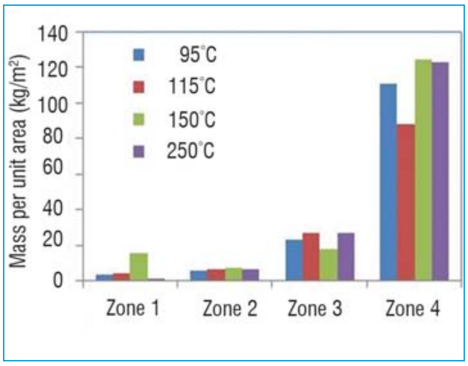

Fig. 2 *Radial mass distribution at various melt temperatures*

Fig. 3 *Typical debris of Woods metal*

Fig. 4 *Typical debris from high temperature ceramic simulant*

III.9 Installation of RISHI Mockup Loop for Irradiation of Materials in Sodium at High Temperature

An experimental loop "RISHI: Research facility for Irradiation studies in Sodium at High temperatures has been designed and erected to study the influence of neutron irradiation on fast reactor material specimens in sodium environment. The setup is designed as a test mockup for a prototype proposed to be used in the international material test reactor JHR, (Jules Horowitz Reactor) for generating material irradiation data.

The primary objective is to maintain the specimen at a particular temperature under neutron influence and in sodium environment irrespective of the reactor operating temperature. Moreover, the opening available for inserting the loop in FBTR and JHR are 100 and 90 mm respectively. Hence, the entire loop with all necessary components is designed to be within 80 mm diameter. Accordingly, an innovative design of U-tube sodium loop which works without a sodium pump but still manages the heat transfer effectively by periodic oscillations of the sodium in 'U' tube limbs is developed.

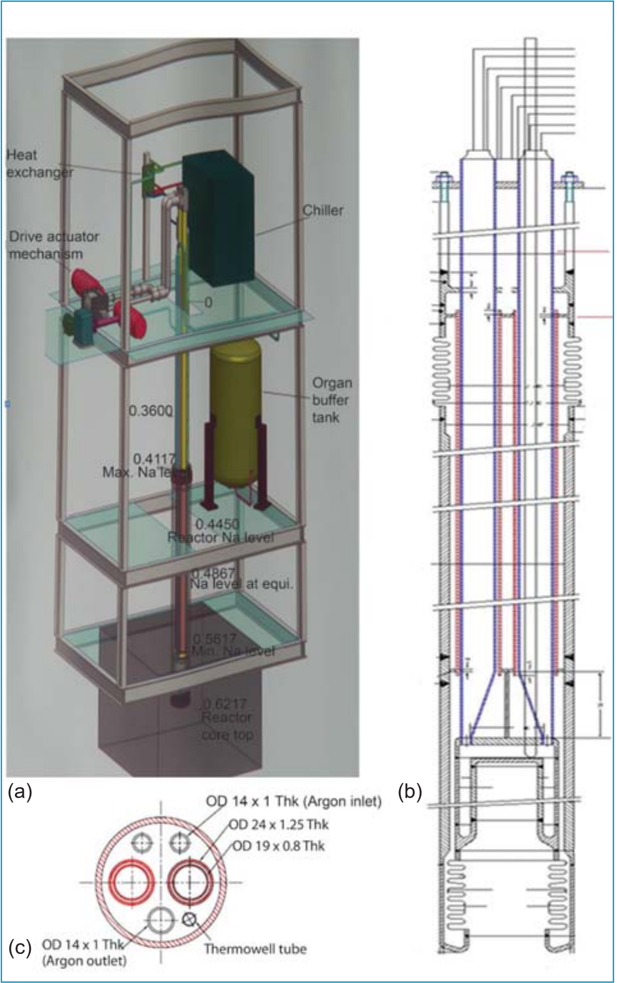

Fig. 1 (a) Semantic of the experimental facility, (b) cut view of U-tube module and (c) top view of U-tube module

Experimental setup

The setup consists of an integrated U-tube module, a sodium filling system and a cooling system as shown in Figure 1a. The U-tube module is madeup of SS 316 LN and comprises a specimen chamber, pipe limbs, cooling tubes, annular heat transfer area and cover gas lines, all enveloped in an outer stainless steel clad as shown in Figures 1b & c. The inter-space is filled with an inert gas. The outer clad pipe is provided with surface heaters, 'K' type thermocouple and insulation. The specimen chamber is provided with an external heater module which can simulate upto 2 kW heat load.

Sodium filling system

The sodium filling system consisits of a sodium tank of 2 kg capacity provided with heaters, leak detectors and insulation. The tank is also provided with argon purge and vent lines with vapor traps on either line to prevent sodium aerosol entry into argon line. The tank is isolated from U tube loop by a bellow seal valve provided at the bottom of the tank as shown in Figure 2. This system is used for transfering the sodium to the U-tube module during the initial phase.

Inert gas cooling system

The cooling system consists of an argon buffer tank, booster pump, a plate heat exchanger and an air cooled oil chiller, which sends cool therminol (heat transfer fluid) to the heat exchanger to cool argon. Thermiol is chosen instead of water so as to avoid sodium water interaction during unanticipated tube leak, if any.

Fig. 2 Sodium filling system

Cool argon from heat exchanger enters the ‘U’ tube assembly through top plenum to bottom where it enters into annular space surrounding the ‘U’ tube for heat transfer with sodium, to maintain desired specimen temperature. Argon exits at top plenum through outlet pipe, and is re-circulated.

Actuator mechanism

An actuator mechansim external to the U-tube module is deployed to create oscillations of sodium column in the two pipe limbs. The free surface above the sodium in both the limbs is filled with argon at a pressure of about 0.1 bar. The cover gas space above the sodium is connected to the bellows of the actuator mechanism, shown in Figure 3. The actuator mechanism consists of an electrical motor, gearbox, coupling, crank-slider mechanism, bellows and variable frequency device (VFD) control. A reduction gear box (25:1) is used to reduce the motor rpm at first stage. Two cranks opposing each other by 180 degree are provided on the common driven shaft of the gear box. Each of these cranks has got its own connecting rod and slider links. Crank with slider mechanism converts the rotary motion of the shaft into translator motion. Other end of both the sliders is connected to one bellow each, which in turn is connected to each leg of the ‘U’ tube loop. The motion of the slider makes the bellows expand and compress thereby displacing the gas and causing oscillation in sodium level in either limb alternatively.

This is done periodically at a certain frequency by means of an actuator mechanism. The raise and fall of sodium level will displace the sodium in the specimen chamber which will carry the heat energy from specimen and is exchanged with the heating or cooling medium. Total sodium inventory in the loop is limited by 0.9 liter.

Fig. 3 *Actuator mechanism with bellows*

Numerical studies and validation

Numerical investigation was done to find dynamic response of the loop at different actuator speeds to assess fluctuation level theoretically towards finalizing the level probe positions in the actual loop. Few experiments were also conducted in an acrylic loop with water as simulant fluid for validation. Accordingly, the level raise/ fall of liquid column in either limb is established in relation to slider motion and motor rpm as shown in Figure 4.

Experiments in RISHI facility

Experiments carried out at heat loads of 400, 500 & 650 W to the specimen chamber have demonstrated the attainment of constant specimen temperatures of 311, 325 & 367 °C respectively with ± 2 °C variation. Argon flow rate was maintained at 40 lpm in all the cases. Important events recorded during a typical experiment are shown in Figure 5.

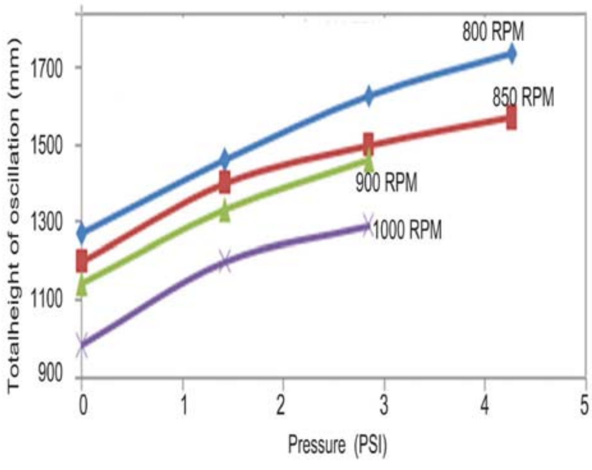

Fig. 4 *Numerical prediction of sodium level oscillations*

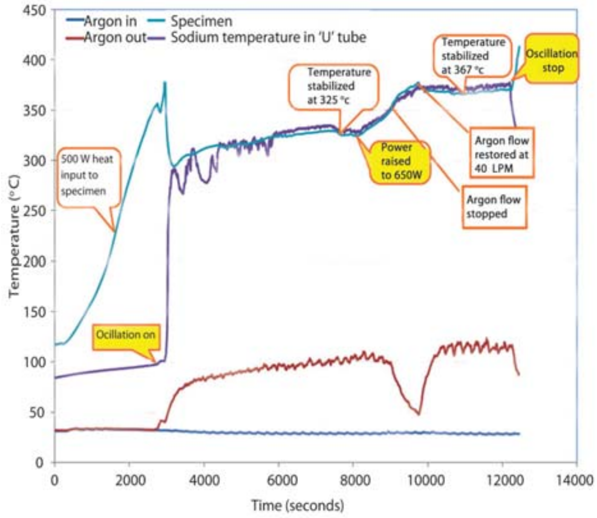

Fig. 5 *Important events during a typical experiment*

III.10 Augmentation of Decay Heat Removal Capacity on Demand through Decay Heat Exchanger

Decay Heat Removal (DHR) systems are designed with very high reliability (failure probability $< 10^{-7}$/ y), sufficient diversity and redundancy. In design, single failure criteria (SFC) is applied for all safety related systems. Multiple falures in a system is considered under design extension conditions (DEC) (GEN-IV Criteria). A postulated condition under DEC – 1 (No Activity release) is 'continuous rise in sodium pool temperatures due to mismatch between decay heat generated in the core and heat dissipated to the air (ultimate heat sink)'. Possible situations for such a mismatch are unavailability of 3 out of 4 SGDHR circuits, reduced DHR capacity through SGDHR system etc. During such an event, in order to limit the temperature of sodium in the pool to Category- 4 limits, it is necessary to augment SGDHR circuit capacity on demand. Consideration is given to augment DHR capacity of SGDHR circuit by adding additional heat transfer area in DHX central region, which removes heat from cold pool sodium on demand when the bulk sodium temperature is >550 °C in addition to the normal capacity of SGDHR circuit transferring heat from hot pool. Additional DHR capacity required to be added to SGDHR system on demand to respect Category–4 temperature limits and additional heat transfer area to be added to DHX for achieving the same is estimated and presented in this article.

Schematic of the DHX under consideration is shown in Figure1. During normal operation of SGDHR system, the tube bundle in the outer rows participates in heat transfer with primary sodium. Tube bundle inside stand pipe of DHX terminates above the cold pool level. Though there is small sodium flow in the tube bundle inside the stand pipe, DHR through these tubes is minimum. During the postulated condition of mismatch between decay heat generated and removal through SGDHR system, temperature of sodium and reactor assembly structures rise, sodium pool level rises due to volumetric expansion. When sodium temperature is 550°C, primary sodium inlet to inner tube bundle becomes covered and its contribution to DHR function is added in addition to the existing capacity (10 MWth) through outer tube bundle. Sodium pool level during DHR at various temperatures for CBR is estimated and given in Figure 2. Inner vessel spillover takes place at 648°C and hence a stand pipe on IV extending up to elevation 27.56 metre is chosen corresponding to pool temperature of 600°C for inner tube bundle.

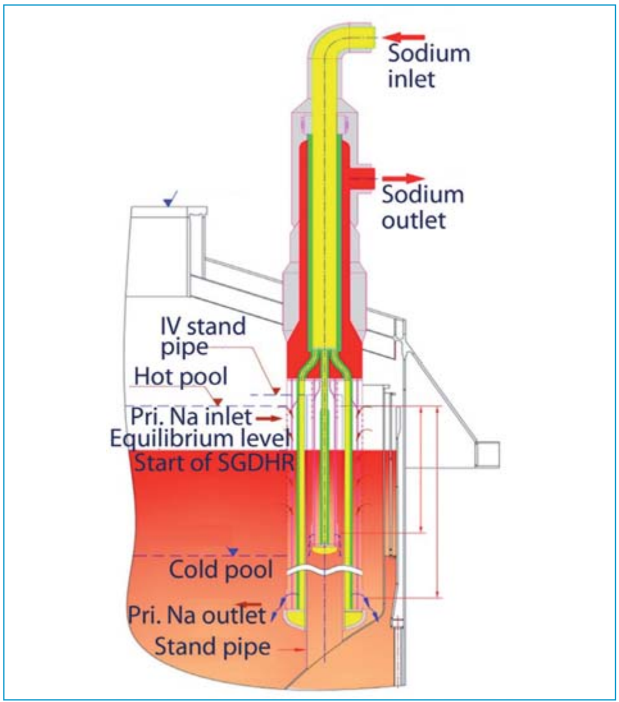

Fig. 1 *DHX connecting hot and cold pools*

Estimation of DHR capacity required restricting sodium pool temperature to Category- 4 limits on demand

Decay heat generation rate and rate of dissipation to atmosphere for PFBR is thoroughly analysed. The same methodology is adopted for CBR with initial core power of 1500 MWth.

During SGDHR, all the sodium and structures are at similar temperatures but for the small amount of

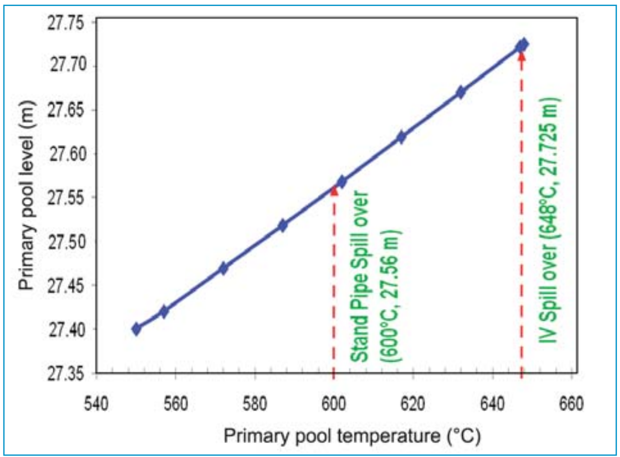

Fig. 2 *Hot pool levels when pumps are not working*

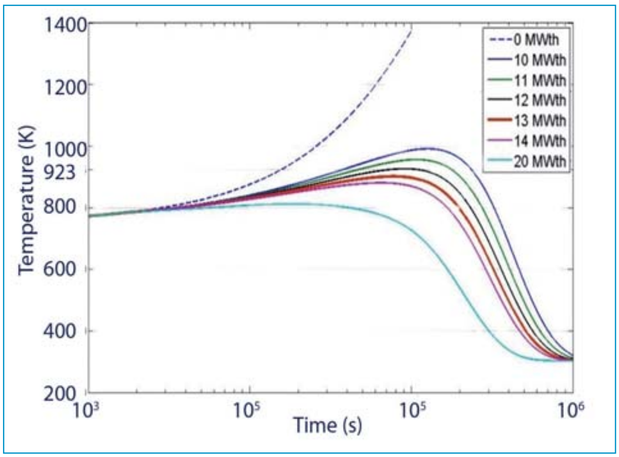

Fig. 3 *Primary sodium temperature as function of DHR capacity*

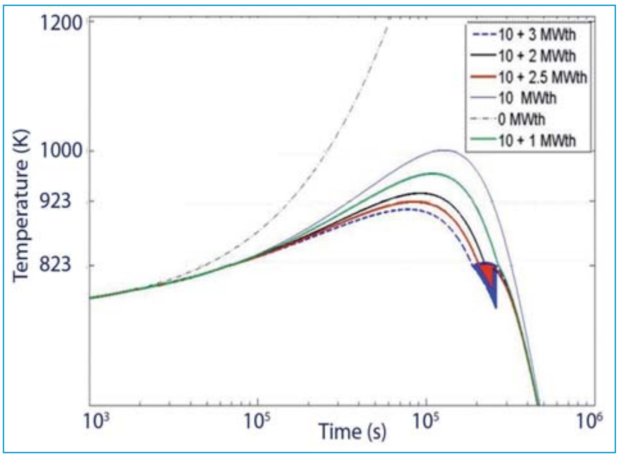

Fig. 4 *Primary sodium temperature as function of capacity addition to SGDHR circuit*

sodium participating in the DHR function (negligible in comparison). Weight of primary sodium in pool is taken as 1300 t; weight of steel in RA in Pool is taken as 1150 t.

The governing equation for heat transfer during SGDHR can be shown as

$$(M_sC_s + M_{Na}C_{Na})\frac{dT}{dt} = Q_{gen} - Q_{disp} \qquad (1)$$

Estimated evolution of pool temperature as a function of DHR capacity through SGDHR system is shown in Figure 3. It can be observed, that minimum capacity of DHR required to keep the temperatures below 923 K (650°C), i.e. Category-4 limits is 13 MWth. Thus it is conclusive that when at least two SGDHR circuits are available, Category-4 limits can be met with the normal design of SGDHR system for future breeder reactor.

Estimation of additional DHR capacity requirement for postulated event

Effect of DHR capacity addition to SGDHRS on Hot pool temperature evolution is shown in Figure 4. It can be observed, that minimum additional capacity of DHR required to keep the temperatures below 923 K (650 °C), i.e. Category 4 limit is 2.5 MWth at 550°C. Hence, the inner tube bundle is designed to have an additional heat removal capacity of 2.5 MWth.

It is also observed in the figure that there is a temperature fluctuation as the temperature is decreasing below 550°C after initial peaking, showing the effect of additional DHR capacity, which is typical of such natural circulation systems.

Estimation of effect of increase in DHX heat transfer area on overall SGDHR capacity

SGDHR circuit is a natural convection system whose heat removal capacity is a function of hot pool and ambient air temperatures. Run around loop simulation of a typical SGDHR circuit with addition of natural circulation for fluid flow is done to study the effect of change in initial conditions.

It is observed that for every 10 % rise in heat transfer area of DHX, there is ~ 1.1 % (Figure 5) increase in SGDHR Capacity, showing that the heat transfer through SGDHRS is strongly governed by sodium – air heat exchanger capacity. Accordingly, the additional area required in the inner rows is ~ 230% of the original DHX.

Feasibility of incorporation in future breeder reactor design

It is very attractive to have an option with DHRS to increase its capacity passively when, the situation demands. The current option under study is to enhance the SGDHRS capacity by increasing heat transfer area of DHX when the temperature of the primary sodium increases above 550°C.

The additional area required in the inner rows is ~ 230 % of the original DHX. Such a large area addition to the DHX, which is inoperative during normal reactor operation is not an economic option and also has a huge penalty on the space requirement over roof slab, significantly increasing the overall size of the reactor. It is observed from studies that the effect of increasing heat transfer area of DHX is not an effective means to improve SGDHRS capacity. Further, constraint on dimensional interface within reactor assembly does not permit such a large area addition.

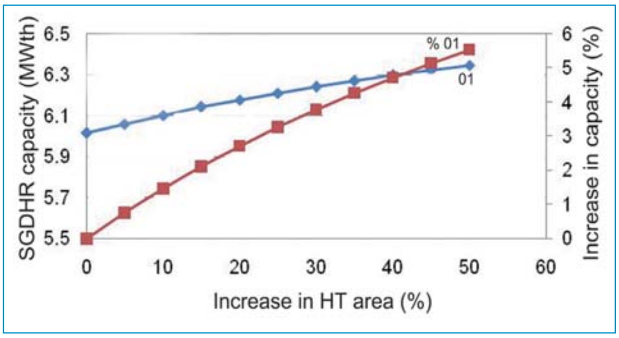

Fig. 5 *Effect of increasing DHX heat transfer area on SGDHR circuit capacity*

III.11 Steady State Modelling and Validation of Once Through Steam Generator

One dimensional steady state code is developed for counter current shell and tube once through steam generator (OTSG), where all the heat transfer processes i.e. preheating, evaporation and superheating of steam take place along the length of the tube. The code can be applied to simulate similar steam generators of any length with any number of tubes. For modelling water side, continuity, momentum and energy equations are solved for single phase water, two phase steam and superheated vapour while only energy equation is solved for sodium. The equations are solved simultaneously using numerical method and are discretized using the finite difference method. The discretized algebraic linear equations are solved iteratively to get the temperature and pressure profiles in the tube and shell side. The water side modelling is done using Steiner and Taborek asymptotic model. Subbotin correlation is used for sodium side heat transfer coefficient.

Validation of code

The results of the developed mathematical model are compared with the DESOPT code which was used earlier for PFBR steam generator. Table 1 gives comparison of the output from developed code with DESOPT code for different power levels. It can be seen from the results that the length of economiser is between 5 to 7 metre, evaporator is 6 to 7 metre and super heater is 10 to 11 metre. Both the codes predict almost same critical quality and steam outlet temperature.

Further, the 19 tube steam generator (Figure 1) tested in Steam Generator Test Facility (SGTF) has been simulated using the present code and the predicted results are compared with the experimental data.

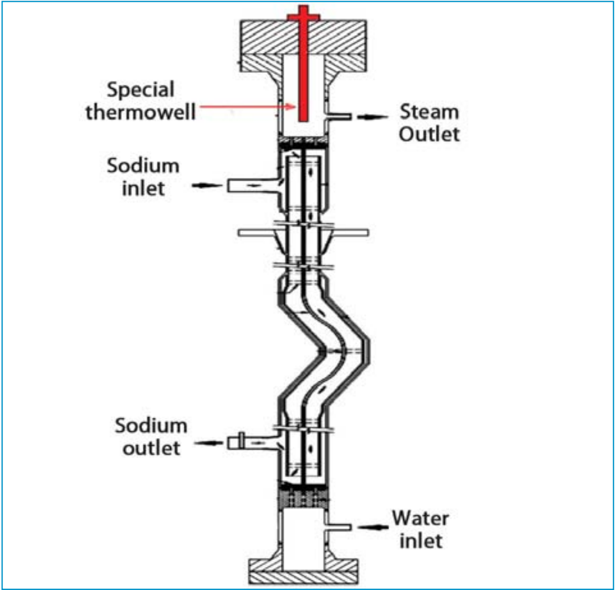

Fig. 1 *19 tube steam generator tested at steam generator test facility*

Experiments were conducted in SGTF with sodium flow rate of 25.2 kg/s, water inlet temperature of 233 °C and feed water pressure of 18.01 MPa. Based on the experimental conditions, the following scenarios have been simulated:

- Case-1: Water flow rate 2.452 kg/s and sodium inlet temperature 516.5°C
- Case-2: Water flow rate 2.645 kg/s and sodium inlet temperature 525.1°C
- Case-3 Water flow rate 2.426 kg/s and sodium inlet temperature 518.5°C.

The results from the code match well with the experimentally observed data obtained from in-house SGTF (Table 2). The power removed as predicted by the code for the abobe three cases is 5.62,

Table 1: Comparison of code results with the output from DESOPT code for PFBR steam generator

Code	DESOPT			Developed code based on Steiner-Taborek model		
Power levels	100%	80%	60%	100%	80%	60%
Sodium inlet temperature (°C)	512.00	511.60	504.60	512.00	511.6	504.60
Sodium outlet temperature (°C)	342.30	327.20	317.30	341.38	327.6	318.00
Water inlet temperature (°C)	235.00	223.50	207.90	235.00	223.5	207.90
Steam outlet temperature (°C)	493.00	493	493.00	496.00	497.7	497.00
Length of economiser (m)	5.98	6.67	6.75	5.80	6.23	5.90
Length of evaporator (m)	7.05	6.95	6.36	6.136	6.022	5.49
Length of super heater (m)	9.66	9.06	9.57	10.75	10.48	11.29
Critical quality	0.32	0.35	0.39	0.34	0.366	0.40

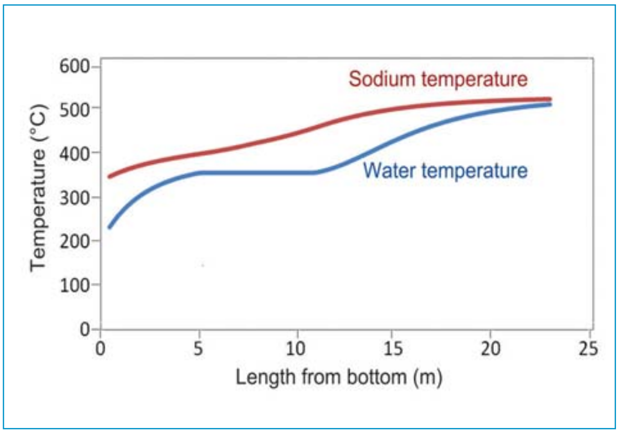

Fig. 2 *Temperature profiles for 50 control volumes*

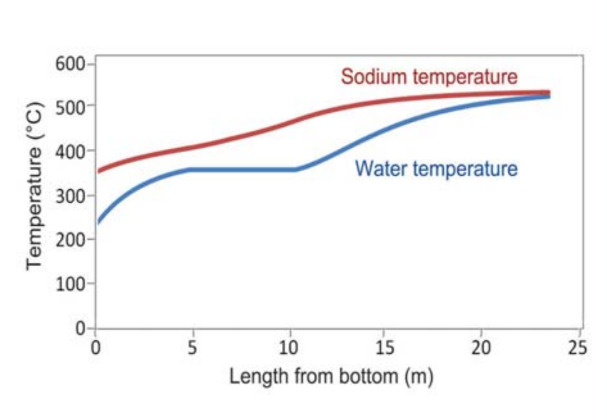

Fig. 3 *Temperature profiles for 1000 control volumes*

6.07 and 5.60 MWt respectively. Thus, the difference in power actually removed and as predicted by the code is very less. Figures 2 and 3 depict the typical tube side and shell side temperature profiles along the length in steam generator by dividing the tube into 50 and 1000 control volumes respectively, for the full power operation. The temperature of water in the economiser increases rapidly in the beginning with the length of tube because in this region the condition is more departed from the saturation temperature and specific heat of water increases with temperature at constant pressure. Once the saturation temperature is reached, the temperature of water remains constant till single phase vapour is produced. In the super heater region, the rate of temperature increase with length is high in the beginning and decreases with length of the tube. This is due to the decrease in the heat transfer rate due to the decrease in the temperature difference between sodium and steam. The same trend is followed irrespective of the number of control volumes in which the tube length is divided.

In addition, detailed grid sensitivity studies were carried out while numerically simulating PFBR steam generator condition to establish consistency in the solution. Figure 4 shows the variation of outlet steam temperature for different number of control volumes. It can be seen that as the length of tube is divided into icreasing number of control volumes, the outlet temperature of steam becomes less sensitive and is almost independent validating consistency of the solution.

The code is being developed further to include transient calculations to simulate various transients during integrated system modelling.

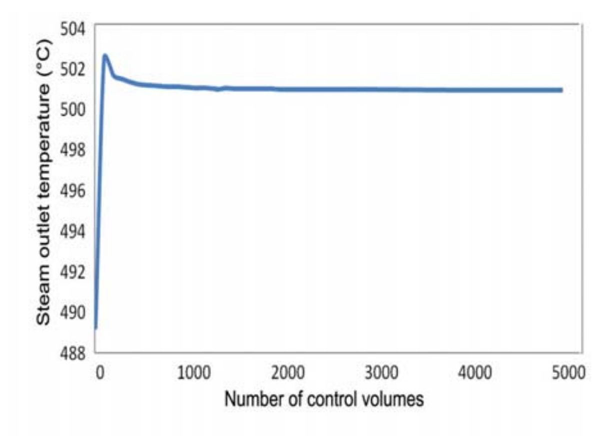

Fig. 4 *Variation of steam outlet temperature with number of control volumes*

Table 2: Comparison of code results with experimental data from steam generator test facility

Parameters	Case 1		Case 2		Case 3	
	Result from present code	Experimental value	Result from present code	Experimental value	Result from present code	Experimental value
Steam pressure (MPa)	16.77	17.10	16.77	17.10	17.46	17.10
Steam outlet temperature (°C)	502.09	493.00	503.384	493.00	502.00	493.00
SG outlet sodium temperature (°C)	341.77	341.70	336.28	337.50	345.00	345.40
Power(MWt)	5.62	5.64	6.07	6.05	5.60	5.58

III.12 Electrical System Design and Station Blackout Management in Fast Breeder Reactors

The Electrical Power System in Fast Breeder Reactors consists of main power output system, offsite power system, onsite non-safety related (Class IV) and onsite safety related & safety (Class III, Class II UPS and Class I DC) power systems. The coincidental loss of offsite grid, turbo-generator and standby emergency diesel generators (Class IV and Class III power supplies) is called “Station Blackout”(SBO). It does not include the loss of available AC power to buses fed by station batteries or the loss of power from “Alternate AC sources". Depending on the offsite and on-site power supply configurations, site characteristics and reliability of diesel generators the acceptable “SBO Duration” is arrived at for a Nuclear Power Plant in line with USNRC Regulatory Guide 1.155- Station Blackout.

Normal and emergency power supply systems in PFBR

PFBR generator output (500 MWe) is connected to the Southern Regional grid through generator transformer. This connection provides off-site power to the plant. Two independent Class IV power supply circuits are available. The emergency AC power supply system has two independent divisions arranged in two sections. Each section is provided with one standby emergency diesel generator (EDG) as onsite AC power source. In order to improve the plant robustness in emergency power supply to meet events like Fukushima accident, two SBO DGs are provided at 415 V emergency bus levels. The SBO DGs are air cooled and do not require water cooling.

Proposed normal and emergency power supply systems in future FBRs

The proposed 2x600 MWe plant has 400 kV as the transmission voltage to handle the increased power export. In FBRs, there is a third Alternate AC circuit from 230kV system to the plant and is capable of improving Class IV power supply availability to Class III system. The emergency power supply arrangement with DGs and SBO DGs is similar to PFBR. Additionally in line with the evolving practices and to meet the post Fukushima scenario, gas turbine generator is proposed as an Alternate AC power source (AAC) as back up at Class III 6.6 kV auxiliary emergency level and will be connected in the case of loss of normal power supply and all standby EDG sources (SBO).

Deterministic estimation of SBO duration

The SBO duration depends on the following factors.

a) the redundancy of the onsite emergency AC (EAC) power sources, b) the reliability of the onsite EAC power sources, c) the expected frequency of loss of offsite power and d) the probable time needed to restore offsite power. These factors are identified according to the plant configuration and plant specific data. In PFBR, to meet the redundancy, 4 EDG sets are used in addition to battery sources to support decay heat removal systems. The applicable emergency AC power configuration group for PFBR is categorized as ‘B’. The PFBR DG reliability is estimated as 0.978 based on detailed analysis. Based on site data and offsite power supply configuration, offsite group is categorized as P1. These factors are given in Table 1. The SBO duration is estimated as 4 hours for PFBR. Without giving credit to improved electrical systems in future FBRs, the same 4 hours duration is adopted.

Plant robustness to meet normal and extended SBO

SBO management is given due importance during design and implementation of FBR systems in India. To meet the instrumentation load requirements, the batteries are sized to meet full load for 1 hour, SBO loads for 4h and critical long term monitoring loads for 14 hours conservatively. In addition, each primary sodium pump pony motor and auxiliaries are provided with dedicated battery banks sized for 4 hours SBO duration. From the thermal hydraulic analysis of PFBR safety systems, it is found that the decay heat removal can be continued for more than 10 days without any risk of sodium freezing. Spent fuel storage cooling can be maintained upto 25 days. Reactor vault temperature and top shield temperature do not exceed the limits. Conservative electrical system design to meet Instrumentation and Control and pony motor loads along with robust capabilities of plant systems ensure effective handling of short term and long term SBO.

Table 1: Acceptable SBO duration capability (hours)

Offsite power design characteristics	Emergency AC power supply configuration group						
	A		B		C		D
	Unit “Average” EDG reliability						
Group	0.975	0.950	0.975	0.950	0.975	0.950	0.975
P1	2	2	4	4	4	4	4
P2	4	4	4	4	4	8	8
P3	4	8	4	8	8	16	8

III.13 Assessment of the Effects of Welding Techniques on the Creep Properties of 316LN Stainless Steel Weld Joints

Type 316 LN stainless steel is the major structural material used in the construction of fast breeder reactors. Various welding techniques are used for fabricating the components. Assessment of the effect of various welding techniques on the creep behavior of 316 LN stainless steel is discussed. Activated Tungsten Inert Gas (A-TIG) welding has been proposed to be used for welding of 316 LN stainless steel pipes having wall thickness in the range of 5-6 mm in FBRs. A-TIG welding process has been found to enhance the depth of penetration significantly during autogenous welding and also found to enhance the creep rupture life in stainless steels. The effect of TIG and A-TIG welding processes on the impression creep resistance of type 316 LN stainless steel base metal, fusion zone and heat affected zone (HAZ) of the weld joints is compared. The dimensions of the 316 LN stainless steel plates used to prepare the weld joints were 280 x 200 x 6 mm. A-TIG weld joint was fabricated using in-house developed flux in a single pass. Multi-pass weld joint with V-groove was prepared using manual TIG welding process with AISI 316L filler wire of 1.6 mm diameter.

Figure 1 shows the cross sectional views of both A-TIG and TIG weld joints. Full penetration had been achieved by the A-TIG welding process in a single pass. On the other hand, it required multiple passes using conventional TIG welding to complete the weld joint. The measured ferrite number values were 3.4 FN and 9.2 FN in the A-TIG and conventional multi-pass TIG weld metals respectively.

Table 1 gives the impression creep rate of different samples. It was found that creep rate is almost the same for base material and A-TIG weld metal. Conventional TIG weld metal exhibited higher creep rate than the base material and A-TIG weld metal. The HAZs of both TIG and A-TIG weld joints were found to have the lower creep rate when compared with the base metal and weld metals. A-TIG weld joint HAZ was found to have lower creep rate compared to conventional TIG weld joint HAZ. The grain size of the HAZ in the A-TIG weld joint was 1.2 to 1.4 times higher than that of the TIG weld joint (Figure 2).

Table 1: Impression creep rate of different samples

Sample	Impression creep rate (x 10^{-5} mm min^{-1})
Base metal	2.140
TIG weld fusion zone	3.718
ATIG weld fusion zone	2.013
TIG weld HAZ	1.464
ATIG weld HAZ	0.483

Typical creep curves for base metal, TIG and A-TIG weld metals are shown in Figure 3.

Higher deformation rate in the TIG weld metal than in A-TIG weld metal was due to the presence of finer dendritic structure in the TIG weld. The ferrite having more open BCC structure could increase the creep rate of weld metal in the TIG weld than in A-TIG weld. δ-ferrite transforms to brittle sigma and austenite at the grain boundaries and triple points on exposure to high temperature for longer duration. In addition to the loss of ductility, sigma phase formation may have a negative effect on the high temperature resistance of stainless steels, due to the removal of Cr and Mo from solid solution.

Hence, lower creep rate in A-TIG weld metal and HAZ was due to lower δ-ferrite content and coarser grains respectively. Therefore, A-TIG weld joint is expected to have better creep rupture life compared to that of the TIG weld joint in 316 LN stainless steel.

Shielded metal arc welding (SMAW) is an indispensable welding technique for fabricating large components of FBRs which are made from 316 LN stainless steel. Though exhaustive studies have been made on the mechanical properties of the 316LN stainless steel weld metal and base metal, there is limited study dealing with the mechanical properties of the composite weld joint.

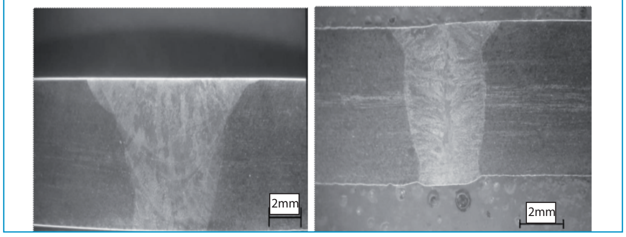

***Fig. 1** Cross sectional view of weld joints (i) TIG (II) A-TIG*

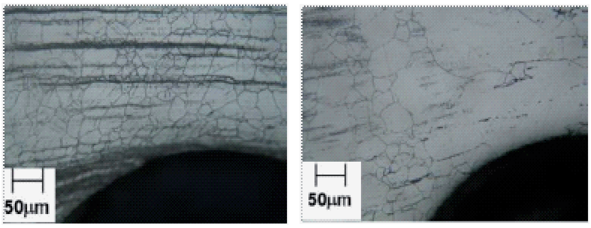

***Fig. 2** Micrograph of HAZ of (i) TIG sample (ii) A-TIG sample*

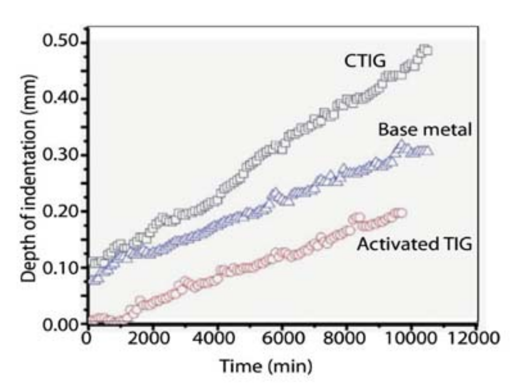

Fig. 3 *Creep behavior of base metal, TIG and A-TIG weld metal*

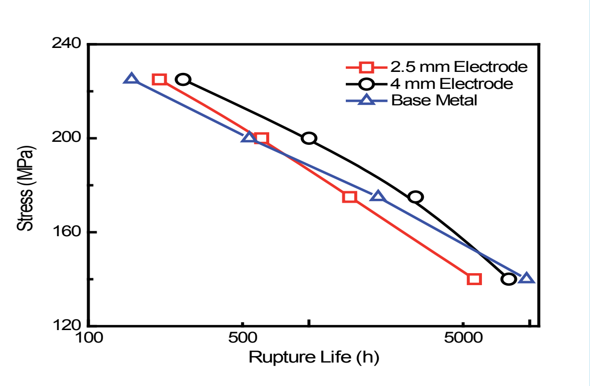

Fig. 4 *Rupture life comparison of weld joints with the base metal*

The changes in the morphology of δ ferrite in multi-pass weld joints influences the creep properties and this would invariably depend on the number of weld passes. In order to amplify the effect of weld passes and study its influence on the creep properties, two weld joints of 22 mm thickness were fabricated with two electrode diameters viz., 2.5 and 4 mm. Conventionally the lower size electrode is used for fabricating the root passes or for welding thinner sections whereas, the bigger electrode sizes are used for laying filler passes of thicker sections. The number of passes in the case of 2.5 mm electrode was 78, whereas 38 passes was needed to complete the joint with 4 mm electrode diameter. Creep deformation and rupture behaviour were evaluated on the cross-weld samples.

Microstructural investigations on the as welded samples revealed that the changes in the δ-ferrite morphology were similar in the fusion zone of both the weld joints. The ‘heat affected’ weld metal region transformed into regions containing isolated packets of δ- ferrite with a globular morphology when compared to a regular vermicular morphology. Micro hardness studies indicated that the weld joint made with 2.5 mm electrode diameter possessed higher hardness in the HAZ and the fusion zone. The creep tests carried out at 923 K (650 ° C) in the stress range of 140-225 MPa showed that the rupture life of the joints made with 4 mm electrode size was better than those made with 2.5 mm electrode size (Figure 4). When compared to the base metal the joints possessed higher rupture life at the applied stress of 225 MPa due to the presence of the as cast hard weld metal. However, with decrease in applied stress, the rupture life of both the joints was inferior to that of the base metal. The transition in the rupture life plot of the joints is due to the microstructural instability created by the transformed brittle sigma phase from δ-ferrite. This transition occurred comparatively earlier for the weld joints made with 2.5 mm electrode diameter. Microstructural investigations on the creep tested samples revealed that the region which contained vermicular δ-ferrite was more susceptible to creep cavitation in both the weld joints. The vermicular morphology with interconnected network facilitated faster molecular diffusion which enhanced the kinetics of sigma phase formation. The regions containing globular δ-ferrite were also subjected to a thermo-mechanical treatment which made propagation of creep cracks more difficult in this region. For the joints fabricated with 4 mm electrode diameter, these susceptible regions were farther apart (Figure 5), when compared to the weld joint fabricated with 2.5 mm electrode in which case these regions were comparatively closely spaced (Figure 6). Hence the rupture strength of the joints fabricated with the bigger electrode diameter was better.

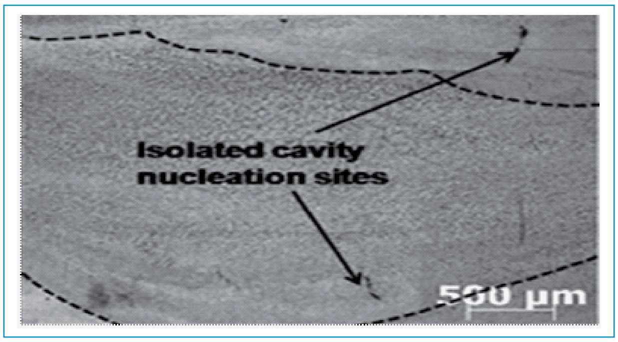

Fig. 5 *Micrograph showing isolated cavities in weld joint fabricated with 4 mm electrode*

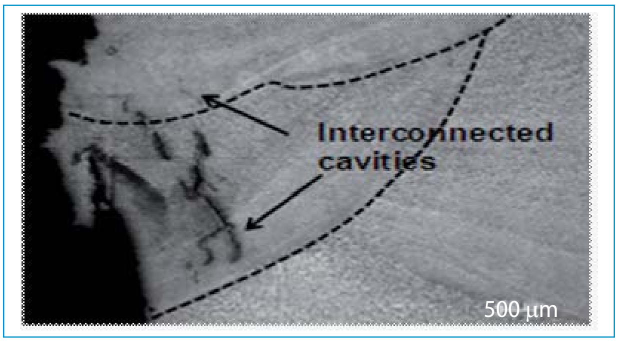

Fig. 6 *Micrograph showing interconnected cavities in weld joint fabricated with 2.5 mm electrode*

III.14 Evaluation of Multiaxial Effects on the Mechanical Properties of 316LN Stainless Steel

Components operating at high temperatures experience multiaxial state of stress as a result of discontinuities in the form of change in geometry, microstructural inhomogeneity (weld joints) and mode of loading during service. Notched specimens are widely used to study the effect of multiaxial state of stress on deformation and fracture behaviour of materials. The advantage of the notched specimens is that the different states of stress can be simulated by changing the radius at the root of the notch.

The present investigation has been carried out to assess the adequacy of the Neuber's rule and finite element analysis in predicting the local strain under cyclic loading. Circumferential notches were introduced to study the effect of notch on low cycle fatigue (LCF) behaviour. The fatigue life has been estimated considering two different approaches viz., Neuber's rule and FE analysis. The LCF tests were carried out in the total axial strain controlled mode at a constant strain rate of $3\times10^{-3}\ s^{-1}$ and strain amplitudes in the range ± 0.3 and ± 1.0 %. LCF tests were also carried out on circumferentially notched specimens having notch root radii (R) of 5 and 2.5 mm. The fatigue lives of notched specimens were found to be lower than that of smooth specimens. The extent of decrease in fatigue life was more for 2.5 mm notch, Figure 1. Fatigue damage is associated with the crack initiation at the surface of the specimen followed by stage I and stage II crack propagation and final failure. Under low cycle fatigue conditions, the crack nucleation stage generally occupies around 10-20 % of the total fatigue life of the material. However, for notched specimen, the duration of the nucleation stage would be extremely small. The higher stress concentration in notched specimens would result in higher crack growth rates than that of smooth specimens as depicted in the striation spacing in both the specimens as seen in Figure 2.

Finite element analysis

Finite element analysis was carried out to estimate the strain at the notch root and predict the fatigue life of the notched specimens. The element size was reduced at and close to the notch root and elastic analysis was used to ensure that the mesh was sufficiently refined near the notch root to predict the theoretical stress concentration factor at the notch root. The Ramberg-Osgood relationship, which relates the cyclic elasto-plastic response, has been considered to define the material's deformation characteristics. The plastic strain accumulation was found to be more at the notch root as compared to the centre of notch throat plane for both the notches. Since the low cycle fatigue failure is associated with the accumulation of plastic strain with cycling, the higher plastic strain accumulation at the notch root in the notched specimens would result in lower fatigue life as compared to the smooth specimens. Moreover, higher plastic strain accumulation for the relatively sharper notch would further decrease the fatigue life as observed experimentally.

Neuber's rule

The Neuber's rule has been extensively used for the estimation of local stress and strain in the notch throat plane for monotonic and cyclic loading. The total strain calculated by Neuber's rule was incorporated in the Coffin-Manson relationship to predict the fatigue life of notched specimens.

Fatigue life prediction

Local strain estimated from FE analysis and Neuber's rule was used to predict the fatigue life. Fatigue life predicted based on this approach has been shown in

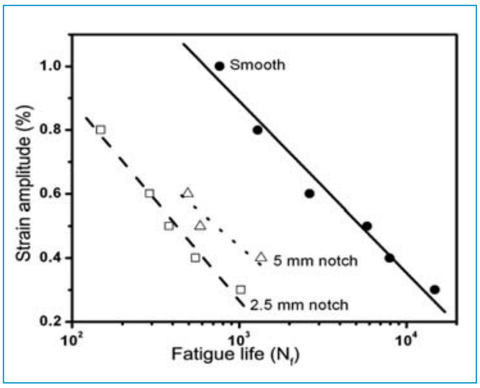

Fig. 1 *Fatigue life variation in presence of notch (316 LN SS)*

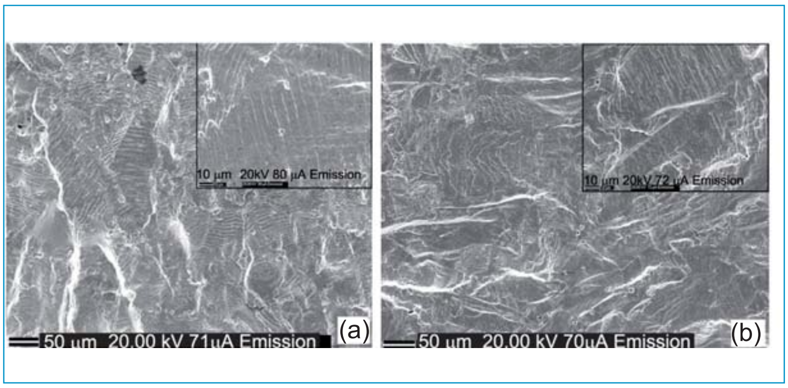

Fig. 2 *SEM fractograph of fatigue tested specimens at 0.3 % strain amplitude for (a) smooth and (b) notched specimen (2.5 mm)*

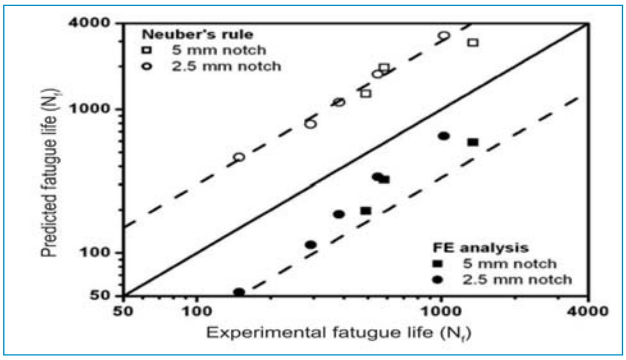

Fig. 3 *Fatigue life prediction of notched specimens based on local strain approach considering FE analysis and Neuber's rule*

Fig. 4 *Axial torsion testing system at metal forming and tribology programme*

Figure 3. The finite element analysis approach was found to underestimate the fatigue life in presence of a notch, whereas Neuber's rule overestimated the fatigue life. The prediction of fatigue life based on both the approaches was found to be within a factor of 3.

Metal forming

Bulk metal forming is another area where the large amount of metal deformation/strain, is invariably multiaxial. Tension or compression testing have limitations in evaluation of workability in terms of maximum possible strain limit as well as homogeneous deformation. Combined axial-torsion testing can be used for evaluation of flow stress and true workability up to very high levels of strains under multiaxial state of stress.

As no such testing machine existed in India, a state-of-the-art high temperature combined axial and torsion testing system (ATTS) was designed and developed in Metal Forming & Tribology Programme (MFTP) for assessing workability of various materials under multi-axial state of stress/strain up to 1573 K . The machine has torque capacity of 1000 N-m up to maximum rotational speed of 850 RPM and axial load capacity of ±100 kN up to maximum linear speed of 1.5 m/s. The angle of rotation is measured by an angular encoder with resolution of 0.036 degree. Conventional LVDT is used for measurement of axial stroke and a multi-axial load cell is used for measurement of torque and axial load simultaneously. The digitally controlled ATTS can carry out controlled thermo-mechanical tests under concurrent torsion and axial (tension/compression), sequential torsion and axial, pure torsion, compression and tension in twist, torque, axial load and stroke control modes. At room temperature tests in flowing water can also be carried out using ATTS. The ATTS is fitted with a 6 kW induction heating system with capability of programmed heating/cooling up to 100 K/sec. A controlled and programmable water jet is also integrated which can be either operated manually or linked to the test control sequence for specimen quenching as well as isothermal room temperature tests. The ATTS can handle specimens from 6 to 23 mm diameter through hydraulic grips, which can exert different clamping loads up to 120 kN. The machine is of modular design with independent actuators for torsion and axial loading of the specimen. The axial load is imparted using a double acting servo hydraulic actuator through the lower grip. A hydraulic motor mounted on the movable top crosshead imparts torsional load on the specimen through servo hydraulic valves up to 850 revolutions. The capability of imparting torsional load up to failure of the specimen and in-situ automatic quenching of the specimen are the unique features of the ATTS, which makes this machine one of its kind. The ATTS at MFTP is shown Figure 4.

Seamless tube extrusion is one of the most important manufacturing processes for manufacturing various nuclear reactor core components. Extensive concurrent torsion - compression tests on SS 316LN were carried out using the ATTS up to very high strains to simulate the compressive triaxial state of stress in seamless tube extrusion. Electron back scattered diffraction (EBSD)-orientation imaging microscopy (OIM) was employed to detail the microstructure in finer length scale and study texture formation. The resulting microstructure from combined loading as well as pure torsion is shown in Figure 5. Combined torsion-compression loading enhances the overall ductility in the material and also results in finer grain microstructure as compared to that from pure torsion. Combined axial-torsion tests in conjunction with FEA of the bulk metal forming processes would be extremely useful in optimization of the various process variables to manufacture defect free products.

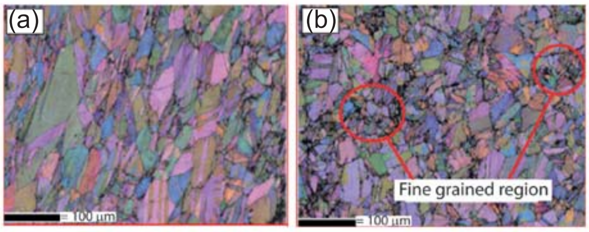

Fig. 5 *OIM measurements illustrating grain refinement in (a) only torsion and (b) combined torsion and compression*

III.15 Development of Pressurized Capsules from T91 Cladding Tubes, and Fabrication of Mock-Up Instrumented Capsule for Detection of In-Pile Stress Rupture in T91 Pressurized Capsules

The ferritic steel T91 is considered for use as fuel clad material in fast breeder reactors due to its excellent void swelling resistance and compatibility with metallic fuel. Pressurized capsules have been developed from T91 clad tube to conduct bi-axially stressed creep tests. Subsequently, T91 pressurized capsule with attachment of a thermocouple to the central gas region has been designed and developed for in-reactor tests. K-type thermocouple of Φ 1 mm and 10 metre long was welded using laser to the gas region of the pressurized capsule which will enable us to get a detailed history of the temperature seen by the pressurized capsule throughout the experiment and to detect the rupture. The full scale mock up of the instrumented capsule assembly has been designed and fabricated for the out-of-pile experiment successfully.

Development of T91 pressurized capsules

Pre-pressurized capsules from the T91 cladding tube of metallic fuel pins have been successfully developed. These pressurized capsules can be used to determine the in-pile creep behaviour of T91 material. Components have been machined and welding parameters for the T91 pressurized capsules have been standardized. The dimensions of end plug with sealing arrangement have been optimized to withstand the maximum gasket squeezing torque required to seal the gas filled inside the pressurized capsule at high pressure. P91 plates were cut into 10x10 mm slices and end plugs were machined from these slices. In the process of determining the depth of penetration of T91 welds for weld qualification, it has been found that etching with ammonium persulfate solution gives better clarity in optical viewing as compared to etchants like Vilella's Reagent and Fry's solution. For carrying out the heat treatment of T91 welded samples, a compact heating furnace was fabricated and installed inside the argon filled glove box, and heat treatment as per standard procedure was carried out. Micro hardness values of weld metal reduced from 449-503 to 234-265 VHN after heat treatment in concurrence with ASTM standard that specifies that the required hardness values after heat treatment as 190-265 VHN. Argon up to a pressure of 6.3 MPa at room temperature has been filled and sealed in the pressurized capsule. The integrity of the T91 pressurized capsule was checked by encapsulating the capsule in quartz tube under vacuum and testing it in electrical furnace at 500 °C for 100 hours. The weight of the capsule remained unchanged after testing indicating the leak tightness of the pressurized capsule. Figure 1 shows a T91 pressurized capsule encapsulated in the quartz tube.

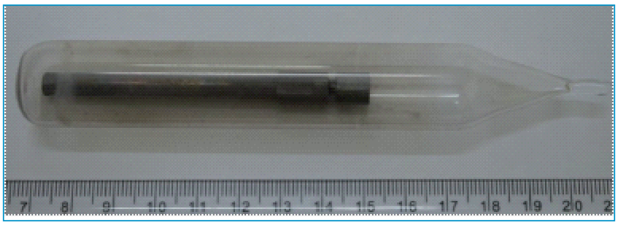

Fig. 1 *T91 pressurized capsule encapsulated in a quartz tube*

Development of T91 pressurized capsules with attachment of thermocouples

T91 pressurized capsule with attachment of central thermocouple was designed and developed to know the temperature of pressurized capsule during irradiation and to indicate the rupture of pressurized capsule. During rupture, there is a shift in the thermocouple profile which can be used to identify the rupture event. The thermocouple sheath material is SS 316 and the wall thickness is 0.18 mm. The end plug design of T91 pressurized capsule was modified to avoid a dissimilar joint at the thermocouple weld location. The thermocouple was welded to a SS316 end plug. An Inconel sleeve of 0.8 mm wall thickness was welded to T91 tube to avoid the ferritic-austenitic joint between SS316 end plug and T91 tube. Welding causes formation of fresh martensite due to rapid cooling. Therefore, all the weld joints involving T91 tube were vacuum sealed in a quartz tube and heat treated in an electric furnace at 1033 K for 30 minutes. This allows the fresh martensite formed during welding process to convert into tempered martensite and also relieves some of the residual stresses generated during welding. To verify the integrity, the pressurized capsule with attachment of thermocouple was sealed in a quartz tube to avoid oxidation and tested in furnace at 803 K for 120 hours. No leak was observed indicating the good quality of the weld joints. The pressurized capsule was provided with an outer protection tube into which the gas will expand

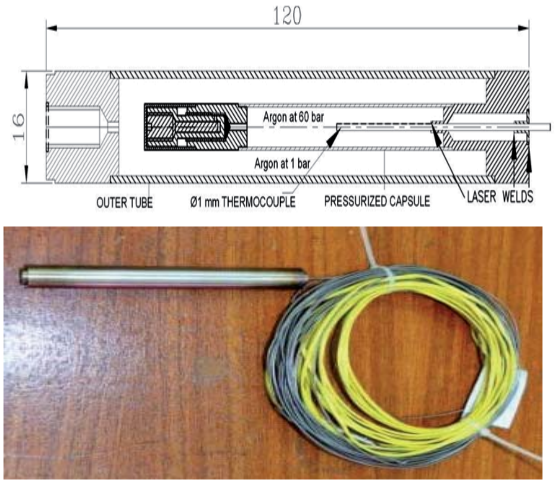

Fig. 2 *Pressurized capsule attached with thermocouple*

during rupture causing a change in the temperature profile. Figure 2 shows a pressurized capsule attached with thermocouple.

Fabrication of mock-up instrumented capsule for detection of in-pile stress rupture in T91 pressurized capsules

The full scale mock up of the instrumented capsule assembly has been designed for the out-of-pile experiment. The dimensions of the capsule are OD 20 mm and length 8.2 metre. The irradiation capsule is divided into two portions. Bottom portion consists of T91 pressurized capsules attached with thermocouples. The total length of the bottom portion is 700 mm and this portion will be in the core of FBTR during irradiation. Five T91 pressurized capsules have been fabricated with attachment of 10 metre long thermocouples for their assembly in the irradiation capsule.

The laser welding of the 10 metre long thermocouples to the T91 pressurized capsule was a challenging task due to the thin sheath and long length of the thermocouple. A collet was used at the welding end and the length of the wire was held by a supporting fixture. The pressurized capsules have been stacked in the bottom portion of the irradiation capsule one upon the other separated by intermediate tubes that allows the thermocouples to be routed out. All the five thermocouples have further been routed through a common intermediate plug that separates the bottom and top portions of the irradiation capsule, and which consisted of five high precision laser welded joints. An outer tube was welded over the bottom portion of the capsule and filled with helium. Figure 3 shows the schematic of the bottom portion of the irradiation capsule.

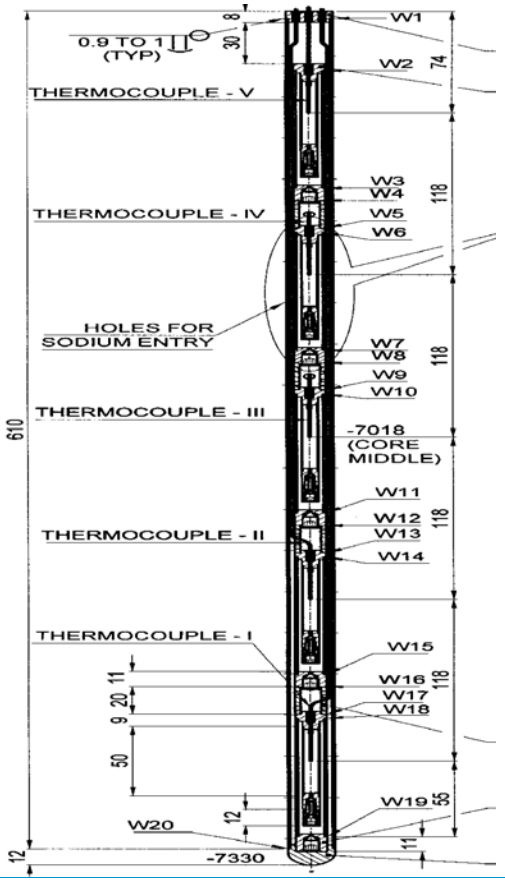

Fig. 3 *Schematic of the bottom portion of irradiation capsule*

The top portion of the instrumented capsule is of length 7.5 metre. This portion consists of a 300 mm long ferro-boron filled shielding portion to attenuate the streaming neutrons from the reactor core. The top portion is in parts for easy assembly and dismantling. All the components have been machined and sub-systems have been fabricated. The assembly of pressurized capsules with thermocouples in the bottom portion of the irradiation capsule and final integration and welding work has also been successfully completed. Figure 4 shows the fabricated mock-up instrumented capsule for detection of in-pile stress rupture in T91 pressurized capsules. This capsule is presently being used for out-of-pile tests using an electrical furnace in the laboratory.

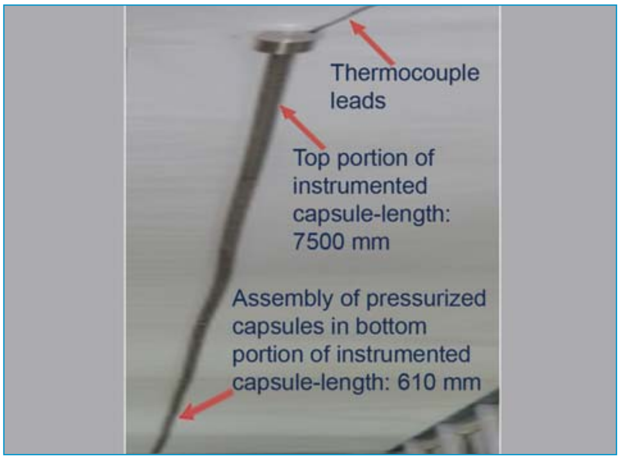

Fig. 4 *Mock-up instrumented capsule*

III.16 Ion Irradiation Studies on the Void Swelling Behavior of a Titanium Modified D9 Alloy: Role of Irradiation Induced TiC Precipitates

Emphasis on increasing the residence time of fuel in a fast reactor has led to evolution in alloys which are to be employed as cladding and wrapper materials. Damaging effects of transmutation product helium and energetic neutrons are mitigated by microstructural designs like high angle grain boundaries, twin boundaries, phase boundaries and free surfaces which can effectively absorb radiation-induced defects. In advanced steels like D9 alloys these microstructural components are fine precipitates viz., TiC and Ni_3Si which occur in high number densities and facilitate annihilation of defects and disperse helium to sub-critical sized cavities therby impeding their growth.

Critical sized cavities are neutral sinks in that there is no preferential bias for a particular type of point defect. Such cavities can grow when the net flux of vacancies overweigh those of interstitials, a condition which is facilitated by the dislocation bias for interstitials. This phenomena which is referred to as void swelling is characterized by a bell shaped temperature dependence and is also one of the major causes of dimensional instability of core structural materials. Void swelling behavior in ion irradiated D9 alloys and their response to irradition induced precipitates is presented here. D9 alloys in 18% CW condition have been implanted with 100 appm helium atoms and subsequently implanted with 2.5 MeV Ni ions up to peak damage of 100 dpa. The nickel implantations have been carried out through a range of temperatures between 450 °C and 650 °C. The evolution of cavities and TiC precipitates at various temperatures has been followed by TEM. The evidence of the formation of voids and TiC precipitates during irradiation of samples at 550 °C and 600 °C is illustrated in Figures 1a to 1c. The electron diffraction showing austenite and TiC spots is shown in Figure 1d.

The void swelling has been calculated by estimating the total void volume occupied by voids. The temperature dependence of void swelling at different temperatures is illustrated in Figure 1e. It was found that moving from 500 °C the average size of voids increased from 0.88 to 1.42 nm at 550°C and thereafter only a marginal growth up to 1.46 nm was observed at higher temperatures. Therefore the decrease in swelling beyond 550 °C can be ascribed to a decrease in density of voids rather than reduction in void sizes. Tracking the evolution of TiC precipitate densities (Figure 1e) one can observe a peak in production of TiC precipitates at 600 °C. There is a correspondence between the temperature dependence of void swelling and TiC precipitate formation. The regime below the peak swelling temperature is recombination dominated; therefore the increase in density of sinks (TiC precipitates) should have a lower effect on swelling. However, at temperatures beyond the peak swelling temperature where mobility of vacancies is increased, the regime is sink dominated. In this regime, an increase in density of sinks is expected to influence void swelling. The observed reduction in swelling at 600 °C (where the density of TiC precipitation is maximum) is an evidence of this effect.

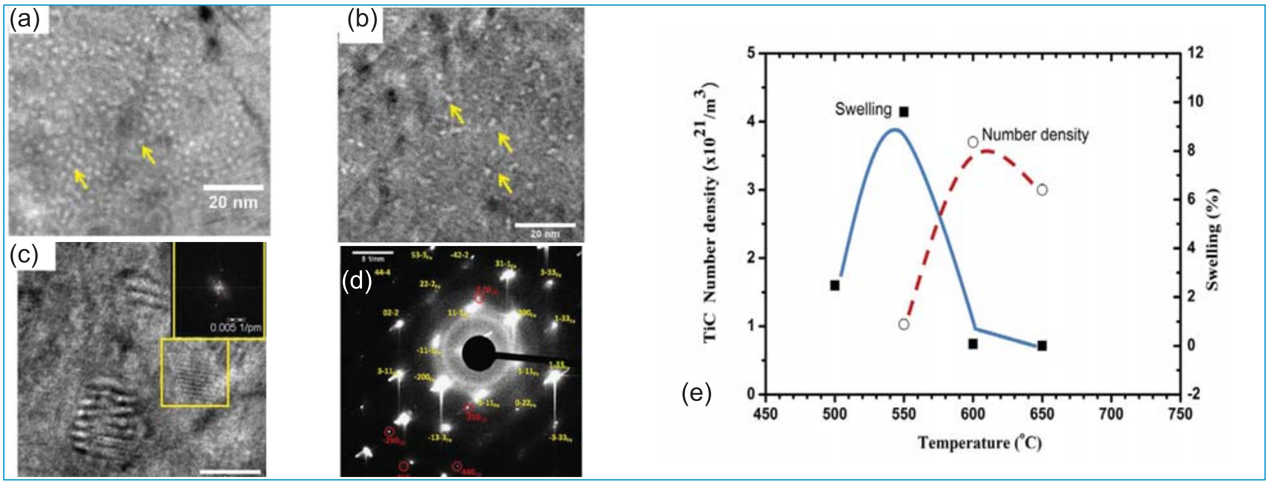

***Fig. 1** Figures illustrating voids (arrows point towards typical voids) in D9 alloys irradiated at (a) 550 °C and (b) 600 °C; As can be observed the void density is greater for irradiation performed at 550 °C. Figures showing (c) HRTEM images of TiC precipitates and (d) selective area diffraction SAD showing austenite spots (unmarked) and TiC spots (in red) and (e) void swelling and TiC precipitate density dependence on temperature*

III.17 Development of Welding Methodology for Complex Shaped Tri-Junction Forging Sectors of Roof Slab

The design of future FBRs is being powered with emphasis on enhanced safety and improved economy. The design of roof slab which is one of the important component of reactor has been re-looked and after comparing merits and demerits of box type structure in carbon steel as in PFBR with dome type structure in stainless steel, it is proposed to adopt the latter (Figure 1a) for future FBRs.

In the dome type design, main vessel along with its internals gets connected to roof slab at its outer periphery and the weight of entire reactor assembly is transferred to concrete vault through a conical shell which is also connected at the junction of main vessel and roof slab. Due to large amount of load being transferred as well as the geometrical discontinuity, the junction is heavily stressed. Maintaining geometrical continuity through the tri-junction connecting roof slab, main vessel and reactor assembly support is very important. Considering the critical location of this joint as well as higher operating temperature with significant thermal gradient, forged ring in SS 304 L is selected for this joint instead of welded joint.

As the major challenge in realizing the dome concept is indigenous availability of the forged ring, the same in a typical required cross section was successfully manufactured. Due to large diameter of tri-junction ring, the forging was developed in the form of 30° sectors (Figure 1b). Considering the complex shape of the forging, parameters like weld joint configuration to be adopted, access for carrying out welding and full volumetric examination etc. need to be finalized before taking-up the integration of the sectors. Towards this, a technology development exercise was initiated and successfully completed to develop and finalize suitable welding methodology and demonstrate fully qualified weld between the forged sectors. Following important objectives were identified for this development activity:

- Arriving at weld joint configuration to be adopted
- Finalization of sequence of welding to be adopted towards reducing weld distortion
- Demonstrating the access for carrying out welding and non-destructive examination (NDE)
- Developing a welding procedure
- Demonstrating meaningful NDE towards qualifying the joint for reactor application.

Several challenges were faced during the development exercise. One of the important challenges was in making available SS forging sectors for undertaking the welding development exercise. To overcome this, carbon steel forging sector developed by the forging industry as part of forging mock-up exercise was used. In order to overcome the difference in welding parameters between carbon steel and stainless steel, welding edges were buttered with SS electrode (309 L) to a thickness of 4 mm so that SS welding with SS 308L electrode could be adopted. Further, as only one CS sector of 30° was available, the same was cut into three pieces of 10° each so that two joints, one as qualification joint and other as demonstration joint can be welded.

Ensuring defect free root weld is critical for obtaining sound final weld. This depends on selection of suitable weld joint configuration with well defined root region which permits access for welding as well as inspection. Due to three different legs of the forging that meet at centre as well as higher thickness of material involved, visualization of weld groove which needs to be adopted itself is difficult. To overcome this, weld edge models were made (Figure 1c) and studied for root access. In order to access the centre of the tri-junction region from top, the weld edge was pushed inside by adopting a different machining radius, locally. This ensures more or less equal distance from the three welding sides to the tri-junction. Based on the clarity obtained

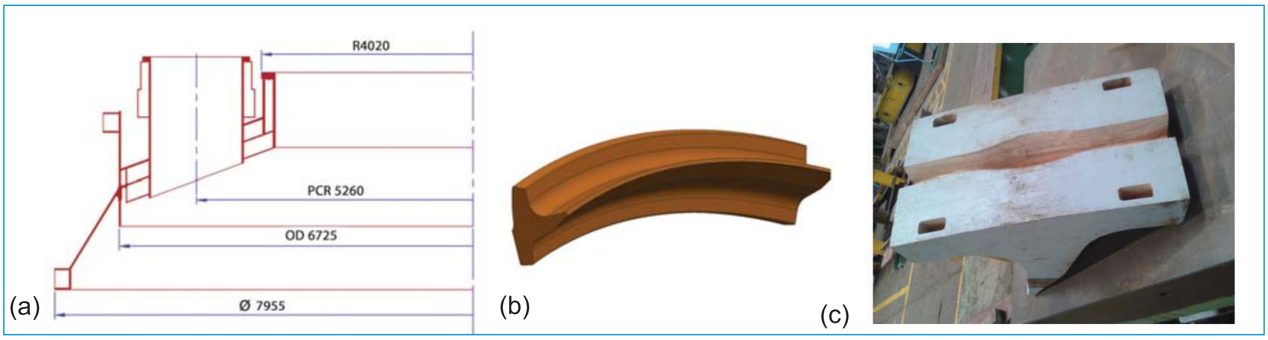

Fig. 1 (a) *Half-sectional view of dome shaped roof slab, (b) 30°C sector view of tri-junction forging and (c) wooden mock-up*

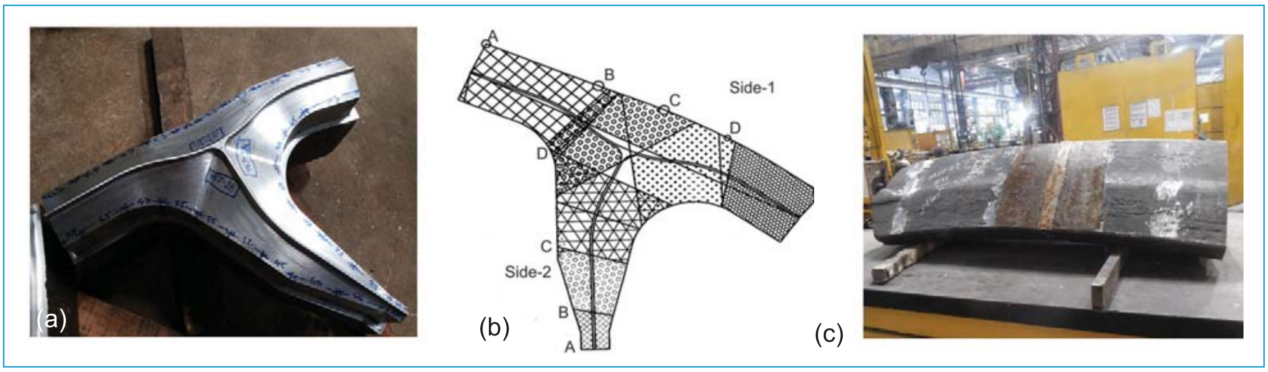

Fig. 2 (a) *Weld edge preparation, (b) RT shooting sketch showing regions covered in each stage and (c) welded forging sector*

with models, the weld joint configuration was finalized and machined over the buttered edge of forging (Figure 2a).

Distortion control in complex shaped weld joint with large weld metal deposit is really challenging. To overcome the anticipated difficulties, narrow gap welding which reduces amount of weld deposit and balanced sequential welding are adopted. In order to monitor distortion during welding so that corrective actions can be taken at intermediate stage itself, gauge marks at a gap of 150 mm between two forging pieces on weld fit-up was marked. Based on the final measurements made after the welding, weld shrinkage of 3-7 mm in a randomly distributed way was observed between the two pieces which indicates minimal weld distortion.

Non destructive examinations play very important role in the quality control of nuclear components. Access for carrying out specified non-destructive examinations covering entire weld volume is very critical in this aspect. Following non-destructive examinations were specified for the joint as per the design code requirements:

- Die Penetrant examination of weld edges
- Die penetrant examination of root pass / back pass
- Die penetrant examination after final pass
- 100% volumetric examination (radiography or ultrasonic).

Considering the complex geometry of the root as well as difficulties in carrying out repair work at later stage if defects are observed near the root region, following additional non-distructive (ND) examinations were also employed as part of development.

- Die penetrant examination after each layer
- Radiographic examination after root and hot pass
- Radiographic testing after 2/3rd of weld deposit
- Ultrasonic examination of final weld in addition to radiography examination.

Locating the radiographic testing (RT) film and source in order to provide complete coverage for the entire volume was one of the most important challenges faced in this development exercise. To overcome this, multiple exposures were carried out by placing the film and source at various locations. Prior to carrying out RT, shooting sketch (Figure 2b) was prepared identifying the location of source as well as film so as to get maximum coverage. Further, to overcome the large variation in thickness in each exposure, films of different optical density (D4 and D7) were used.

In order to demonstrate capture of any root defect by RT on the completed weld, a 3 mm dia. side drill hole was made in the root region and it was observed that RT shooting from two different locations clearly shows the presence of hole. This qualifies the suitability of RT for the joint.

Though codal requirements specifies either of RT or ultrasonic testing (UT) as volumetric examination, UT of the final weld was also carried out as a confidence enhancing measure. Prior to carrying out UT, similar to RT shooting sketch, UT scanning sketch was prepared to finalise types of probes. Combination of normal and angular probes of different angles (45, 46 and 70°C) and frequencies (4, 1.5 and 3 MHz) were used to achieve maximum volumetric coverage.

Subsequent to demonstration of access as well as defect free weld, mechanical testing (tensile, impact, bend, hardness, micro and macro) of weld specimens from first joint was carried out. Here also, considering the critical nature of root weld, the specimens were located very close to the root region and specimens for macro and micro examinations were taken from the intersection of three joints. The results of mechanical tests confirms the specification requirements and hence, the quality of weld achieved.

The comprehensive welding development (Figure 2c) exercise established the methodology to be followed for carrying out the welding of complex shaped joint and demonstrated the feasibility of undertaking meaningful non-destructive examinations towards meeting the codal requirements.

III.18 Geometrical Effect on Sodium Aerosol Characteristics in Cover Gas Region

In the normal operating condition of sodium cooled fast reactor, the temperature difference between the sodium pool and the bulk gas temperature leads to considerable evaporation of sodium from the surface of the pool and subsequent condensation results in the formation of sodium aerosol within the cover gas space either by heterogeneous nucleation or self-nucleation (homogeneous nucleation). These aerosols modify the total heat transfer to the cooled roof structure by absorption and scattering mechanisms and get deposited on the cooler surfaces like annular gaps, roof top, control plug, rotating plug and fuel handling machine resulting in deposition of aerosols, which hinders the rotational movement of rotating plug and operation of fuel handling machine. The presence of sodium aerosols also has an effect on the operation of cover gas purification system and reduces the visibility of the cover gas region during in-pile inspection. Hence, it is important to know the sodium aerosol concentration and size distribution of sodium aerosols present in the cover gas region. As the aerosols concentration is very much dependant on the temperature difference between the surface of the sodium pool and the bottom of the roof top plug and surface area of the pool, a study has been conducted by changing the pool temperatures from 250 to 550°C and in two different sodium Test Pots TP-1 (diameter is 762 mm) and TP-3 (diameter is 400 mm) and keeping the cover gas height at 810 mm in SILVERINA Loop. The results are presented below.

The aerosol sampling is performed using a custom built aerosol sampling system consisting of aerosol sampling tube, sampling bottle, line heaters, line controller and aerosol flow controlling device. Sampling bottle is filled with paraffin oil (600ml) and maintained at ambient temperature. The aerosol sample in the cover gas is made to pass through the bottle, thus solidification of aerosol particle would occur as the cover gas enters into the paraffin oil. The residence time of the cover gas is increased due to baffle arrangement, which ensures that all sodium aerosols get trapped from the cover gas before it escapes the bottle. The paraffin oil with sample is analyzed for determining the size distribution of sodium aerosols. The measurement of Na aerosols mass concentration is carried out by conductivity method using conductometer.

The mass concentration in cover gas region (Figure 1) is found to vary from 0.026 to 35.6 g/m^3 for TP-1 and 0.04 to 21.9 g/m^3 for TP-3, and the mass median diameter is found to vary from 1.5 – 10.5 µm for TP-1 and from 2.1 – 16 µm for TP-3 (Figure 2) for pool temperatures varying from 250 to 550°C.

A theoretical simulation has been carried out to predict the sodium aerosol mass concentration with respect to pool temperature for a given geometry of the vessel and cover gas temperature using an in-house developed code. A good agreement has been observed for the sodium aerosol mass concentration between theoretical prediction and experimental measurement (Figure 1). It is observed that, sodium aerosol mass concentration is more in TP-1 compared to that in TP-3 and particle size (MMD) is large in TP-3 relative to TP-1 for all temperatures of the sodium pool. Since, the volume of the cover gas space of TP-3 is smaller than that of TP-1, it promotes coagulation resulting in a larger size range MMD compared to TP-1. Since particle size is large in TP-3, the gravitational settling is more resulting in lower concentration in TP-3. These conditions are well simulated in the model.

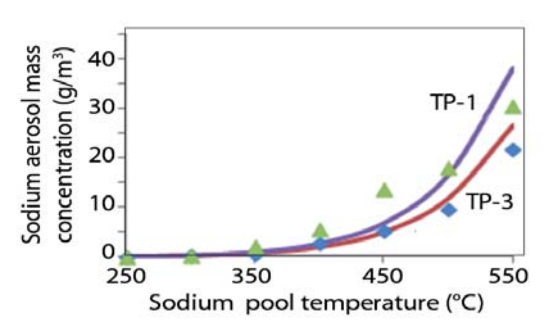

***Fig. 1** Sodium aerosol mass concentration for various sodium pool temperature for sodium test pot 1 and 3 (solid lines indicate theoretical stimulation)*

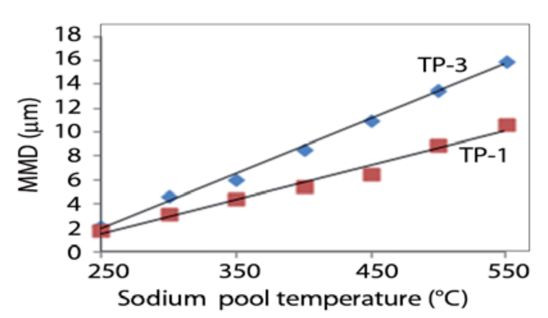

***Fig. 2** Mass median diameter of sodium aerosols for various sodium pool temperatures for test pot 1 and 3*

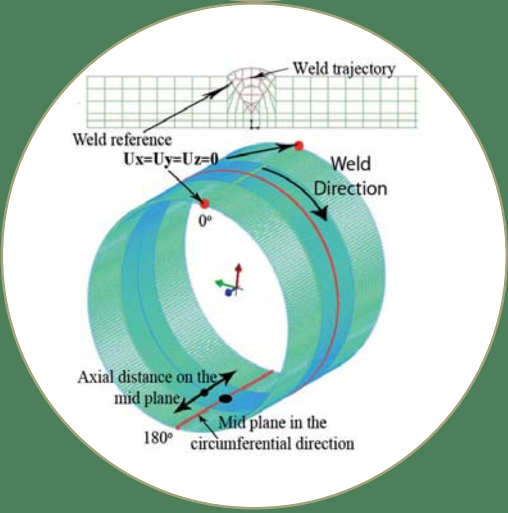

CHAPTER IV

Fuel Cycle

IV.1 Construction Status of Fast Reactor Fuel Cycle Facility (FRFCF)

Fast Reactor Fuel Cycle Facility comprising of Fuel Reprocessing, Reprocessed Uranium Oxide, Fuel Fabrication, Core Subassembly and Waste Management Plants along with necessary supporting facilities is under construction at Kalpakkam piloted by IGCAR with technical support from BARC and NFC. This facility is being built to close the fuel cycle of Prototype Fast Breeder Reactor (PFBR) and facilitate its sustained operation and it is co-located with PFBR thereby eliminating the movement of radioactive spent fuel and refabricated fresh fuel in the public domain.

Excavation work in the nuclear island area (Figure 1) is nearing completion with hard rock layers being removed by controlled blasting operations to reach the foundation depth of the various plant buildings. Geotechnical investigations and Geological mappings are underway to confirm the seismological designs of the plant building constructions and accord clearances for civil construction of the plants. At present the site for Waste Management Plant is fully geared up for the start of construction and the work order for the same is about to be placed. Constructions of a few of the infrastructure buildings such as Training Centre (Figure 2), Administration Building (Figure 3), Central Surveillance, Safety & Health Physics Buildings have crossed the second floor level and a few others such as Canteen Building, Stores & Workshop Extensions have crossed first floor level. Construction activities have commenced for some of the common services buildings such as Diesel Generator Building, Oil Storage Building and Centralised Water Chilling Plant.

On the procurement front, several bulk supplies of raw materials such as about 4250 ton of Pig Lead ingots and 3140 ton of stainless steel sheets and plates were received at site to be issued as free issue material for fabrication of shielding bricks and process vessels and tanks respectively. Fabrication of standard size glove boxes and fume hoods has commenced and a few pieces have been received at site. Orders have been placed for several long delivery high value items such as seamless stainless steel pipes, welded SS pipes, three different types of master slave manipulators and radiation shielding window glass slabs. Procurement actions are underway for process equipment for Fuel Fabrication Plant and instruments for the Characterization Laboratory.

The manpower of FRFCF after commissioning will be 1952 and in order to meet the housing requirements, about 1800 and odd dwelling units are planned to be constructed in a phased manner. In the first phase, about 600 houses are planned to be constructed in the Anupuram Township. Augmentation of infrastructure of the townships for meeting all the requirements of these additional constructions is also in progress.

Considerable progress was achieved during the year despite the major constraint of not having adequate manpower and the essential requirement of multiple clearances in view of the highest quality and safety standards of such a mega project. Further peaking of construction activity is envisaged in the coming year. FRFCF is the defining project of the second stage of the Indian Nuclear Power Programme.

Fig. 1 *Excavation in the nuclear island area for construction of plant buildings*

Fig. 2 *Training Centre of FRFCF under construction*

Fig. 3 *Administration building of FRFCF under construction*

IV.2 Performance Evaluation of Centrifuge System of DFRP

The centrifuge system is intended for efficient separation of solids suspended in a liquid medium by means of mechanical acceleration via centrifugal force. These systems are required to be operated at high speed centrifugal rotation of the order of 20000 rpm and at high throughput of the order of 400 lph. The centrifuge extractor system is very much useful in fuel reprocessing plant, in which suspended solids in highly radioactive fluids can be removed efficiently. The performance of the DFRP centrifuge system is evaluated for various rotational speeds of centrifuge bowl (20000, 18000 and 16000 rpm) for different throughput of feed liquid (90 - 470 lph). The performance is also evaluated for the half loaded condition of solid particles and varying the clarification liquid flow rate from 90 - 470 lph.

Ferric Oxide (Fe_2O_3) powder suspended in DM water (5 g/l) is used as a feed liquid. The removal efficiency of Fe_2O_3 particles from the water medium is evaluated by varying the rpm of the inner bowl for various flow rates of the feed liquid. The removal efficiency is determined by measuring the concentration of the feed liquid (suspended mass concentration of the particles per unit volume of the liquid) by laser obscuration method by using Mastersizer. The efficiency (η) of centrifuge unit is determined by the empirical equation,

$$\eta = C_i - C_o * 100/C_i$$

where C_i and C_o are inlet and outlet concentrations of liquid. The concentration of the sample liquid is estimated by using a calibration chart obtained for various concentrations.

Figure 1 shows the variation of centrifuge efficiency as a function of flow rate of feed liquid. It is observed that efficiency decreases with increase in throughput of the liquid. The total number concentration is calculated for the inlet and at the outlet for various flow rates of the feeding liquid and is shown in Figure 2. It is observed from the figure, that the particle number concentration in outlet solution decreases with decrease in flow rate of feed liquid. The efficiency of the system is noted to increase for lower flow rates of feed liquid.

Experiment is also performed with half filled bowl and with reduced particles concentration of 4 g/l and maintaining the rotation of bowl at about 20000 rpm. In the half filled bowl condition, the particle removal efficiency was reduced by 50% for larger throughputs compared to that of empty bowl conditions.

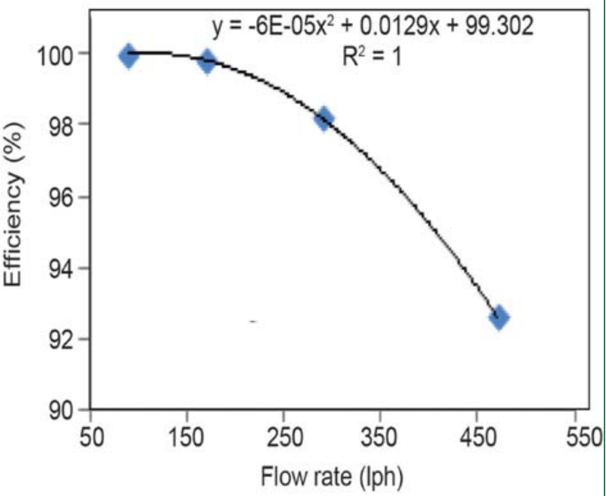

Fig. 1 *Efficiency of the centrifuge unit vs flow rate of liquid (rpm=20000)*

It is observed from the size distribution data obtained for each sample, the efficiency increases with increase in particle size and for a given particle size removal efficiency increases with decrease in feed liquid flow rates. The reduction in removal efficiency is due to the decrease in residence time of the suspended particles when the throughput is increased. Also,when the rotational speed of the bowl decreases the particles removal efficiency decreases which is due to the reduction of centrifuge force.

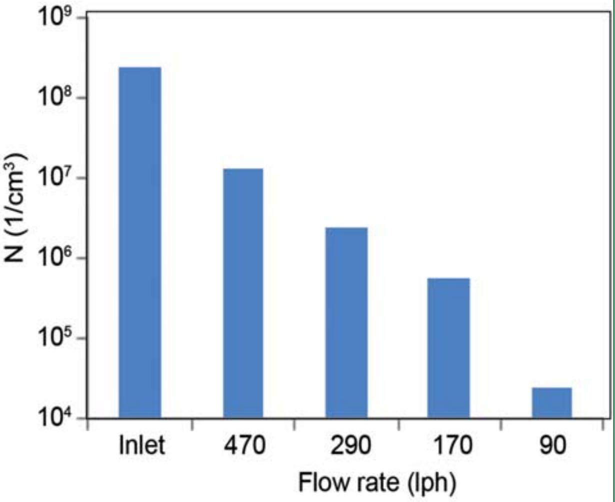

Fig. 2 *Total number concentration (N) of particles measured for various throughputs (rpm=20000)*

IV.3 Hydrodynamic and Mass Transfer Validation of Multistage Centrifugal Extractor Banks for DFRP

Reprocessing of spent fuel from FBTR (up to 155 GWD/t burnup) has been sucessfully demonstrated in the CORAL facility of Reprocessing Group. Regular processing of FBTR spent fuel and demonstration of PFBR fuel reprocessing will be carried out in demonstration fuel reprocessing plant (DFRP). Based on CORAL experience, centrifugal extractors (CEs) have been selected as contactors for solvent extraction based separation of U and Pu from fission products. These CEs are grouped in different banks for serving different parts of solvent extraction flowsheet. Two types of centrifugal banks to be employed in DFRP are 20-stage banks for extraction cycle and 22-stage banks for stripping cycle. These CEs are driven by individual electrical 3ϕ induction motor, coupled to a variable frequency drive controller. The motor drive is directly coupled to the rotor of the CE. The motor, motor seating block and rotor of the CE act as a single unified assembly for ease of installation and maintenance by remote means. For the purpose of hydrodynamic and mass transfer evaluations of the DFRP CE banks, prior to installation inside the process cell and connections to related piping, these were tested in inactive environment with 30% TBP solvent and aqueous nitric acid solutions. For hydrodynamic tests, the aqueous-organic pair used was 0.01 M nitric acid solution-30% TBP. These solutions were pre-equilibrated to rule out mass transfer during hydrodynamic runs. In the hydrodynamic runs, limiting combined throughputs of the CE banks were experimentally determined at flooding conditions. The CE is said to have flooded when other-phase carryover in the product stream equals 1%. This also limits entrainment and during operation, the other-phase carryover should be less than this limit. The actual working combined throughput is normally taken as 60% of the maximum combined throughput at flooding to ensure a stable and robust operation. By determining flooding throughputs, the DFRP CE banks were individually characterized for their operating envelop. The experimental setup shown in Figure 1 consists of the CE bank being tested, 2 VFD drive controllers for running motors, 2 MFP process pumps with Q3 heads for pumping aqueous and organic streams and one MFP process pump as interstage organic pump between the two rows of extractors at different elevation.

Fig. 1 *A view of experimental setup for testing DFRP centrifugal extractor banks*

Mass transfer evaluation of different CE banks was performed as per their operating conditions. Centrifugal extractor banks, meant for extraction were operated with fresh 30% TBP solvent and an aqueous 4 M nitric acid solution at the A/O ratios in the range 0.2-2.44. Extractor banks, meant for stripping service were operated with acid loaded 30% TBP (from extraction experiments) and a strip solution consisting of approx. 0.01 M nitric acid. The total combined throughput during mass transfer experiments ranged between 9 and 39 L/h. The corresponding combined throughputs were 5 to 7.12 L/h and 8.5 to 13.1 L/h for FBTR and PFBR fuel reprocessing flowsheet conditions respectively. Figure 2 shows a McCabe plot for mass transfer evaluation for a typical extraction run on a 1-A extraction bank.

The experimental samples of mass transfer runs were analyzed by thermometric titration for higher concentration ranges and by indicator based acid-base titration in the case of dilute concentration ranges. Scanning of the bank and its motors by an IR based thermal imaging camera during one of the extraction runs revealed that the temperature of all the motors was well within permissible limit without any hotspot, indicating a reliable operation.

In this exercise, a total of eight banks were evaluated for their hydrodynamic and mass transfer performance. In all the cases, experimental results indicated excellent performance and the tested CE banks are being installed.

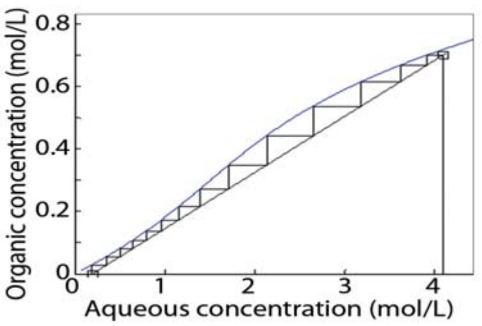

Fig. 2 *McCabe plot for mass transfer evaluation: stage performance of CE bank*

IV.4 Development of Special Connectors for Hot Cells

In the reprocessing plants, connectors are used to power induction motor, stepper motor, servo motor, in-cell camera, limit switches, lamps and RTDs that are located within the hot cell. In the hot cell highly corrosive nitric acid vapor, organic solvents and high radiation environments prevail. There is no direct human contact to the hot cell. Master slave manipulator (MSM) is used for remote operations. As the connectors which are readily available in the market do not withstand the special requirements for use in hot cell, they have to be customised as per our requirement.

The major challenges regarding the material used for connectors in the hot cell are, corrosion of the connector's electrical contacts resulting in the damage of the insulator and elastomer due to organic vapour and radiation. The connector body needs to be handled remotely using MSM and so it has to be of push–fit design. The materials used for the connector should withstand radiation dose up to 25 MRad, corrosion resistance to nitric acid (liquid & vapor phases) and organic solvent (30% TBP in dodecane), operation temperature up to 100°C, operating at 230 V AC with maximum current carrying capacity of 13 A, insulation resistance of 5000 MOhm and 500 connect-disconnect cycles of operation. For this purpose, connectors with the above said specifications were designed, fabricated and qualified for use in the hot cell.

Connector design

The design for the outer shell was specialized for MSM operation. The female connector has a flange with four holes as a permanent fixture inside the hot cell. The male portion has flat surface on all four sides of the connector to grip while handling via MSM and also a stopper to avoid slipping after gripping. The material used was 304L stainless steel. Viton (to embed on the shell to avoid axial or rotary movements) and EPDM (to prevent the ingress of acid vapor to the solder section) as O-ring, seals, Grommet cum cable guide etc., were recommended as per 7.5 of JSS-50812. The base metals were beryllium -copper alloy and brass. Beryllium-copper was used because of its superior properties like smaller size, light weight and stronger material compared to brass. The base metal was plated with nickel and gold as per MIL-G-45204. Nickel was used as an under coat for gold because it acts as a diffusion barrier that prevents any form of substrate (base metal) migration to the top coating. Type-I gold plating was imposed, as it provides good corrosion resistance. 5-8% phosphorous content in the nickel plating would impart strength and solderability of the material.

Fig. 1 *Special connectors for hot cell facility*

Fabrication process

The surface of base metal was cleaned and coated with 5 micron thick nickel by electroless nickel plating (EN) technique as per ASTM B281. EN technique was used to obtain uniform thickness over the most complicated surfaces. EN technique offers more resistant coating to corrosion than electroplating of nickel and the plating metal will not seize with other metals under pressure. An acid bath was used to remove the passivated layer on the surface of nickel. Then 2.54 micron (min.) thick gold was electroplated uniformly all over the surface. The hardness and gold purity were maintained to be better than 130 Knoop and 99.7%, respectively. X-ray fluorescence (XRF) method was used to find the thickness, composition and hardness of the coating.

Qualification criteria for connectors

Finished prototype connector, shown in Figure 1 was obtained for rigourous testing before bulk production.

Qualification approval tests such as routine and type tests were conducted based on JSS 50812, JSS 50800, JSS 50101, MIL–DTL-5015H, ASTM B-733 and ASTM B488 standards. The type test includes temperature cycling test, climatic test, damp heat test (steady state) and corrosive atmosphere test.The routine tests comprise voltage proof (5 second), engagement and disengagement force for the connector, contact and insulation resistance, life (mechanical and electrical), solderability, insert retention (in shell), contact retention (in insert), corrosion test against nitric acid vapor (gold plated contacts), plating thickness and composition of nickel and gold and intermateability.

The connectors which were designed, fabricated and tested as per the above special requirements are in use at CORAL facility of Reprocessing Group. The performance of these connectors is satisfactory.

IV.5 Design of Single Subassembly Transport Cask for DFRP

The spent fuel subassemblies of PFBR are stored and cooled within the reactor vessel for a period of 480 days. Further cooling is done at spent subassembly storage bay using de-mineralised water. The spent subassembly is transported to DFRP at a decay power of ≤ 1.5 kW for the initial demonstration of reprocessing using single subassembly transport cask (SSTC). SSTC is designed to suit the interface requirements and handling capacity of crane available at DFRP. AERB SC TR – 1 stipulates the regulations for the safe transport of radioactive material in public domain under normal and accidental conditions. Movement of cask is within the site of Kalpakkam from PFBR to DFRP during non busy hours with a restricted speed limit of maximum 10 km/h. SSTC is classified as special type of package and it is designed to meet the normal conditions for transport and need not be qualified for accidental conditions specified in the code. Choice of material for the cask is done based on structural, shielding and surface decontamination requirements.

Design requirements

Sufficient shielding is to be provided around the subassembly to limit the dose on contact / 1 metre away from the cask surface to 2 mSv/h / 100 μSv/h respectively. The cask is to be maintained subcritical under normal conditions of transport. Containment boundary of the cask is to be ensured to avoid spreading of contamination under normal conditions of transport. Cask outer surface temperature is to be maintained within 85 °C under all conditions. Design of cask retention system is to be designed with adequate tie-down suitable for road transport. All lifting devices and its attachments are to be designed as per ANSI 14.6. In addition snatch factor of 15% is also to be considered for the lifting devices.

Description of SSTC

The overall size of the cask is 1100 mm outer diameter and 5500 mm long (without impact limiters) with a inner cavity of ϕ 360mm arrived based on size of subassembly (4520 (l) x 151 mm a/c) to be handled. SSTC consists of six shielding blocks out of which shielding blocks 1 and 6 are made of SS casting as per ASTM A 351 Gr. CF3 and the remaining shielding blocks are made of cast steel as per ASTM A27 Gr. 70-40. Shielding blocks 2-5 are connected by a spigot connection and joined together by tie rods. Outer surface of the above shielding blocks are lined with SS 304L liner to facilitate its washing and decontamination and protect the carbon steel parts from corrosion. Similarly, shielding blocks 1 and 6 are also connected by spigot joint and screwed with the respective shielding blocks. The basket assembly consists of a tray called basket is supported on four pairs of rollers and moving on a pair of rails located on the basket housing at 180° apart. Cask support structure consists of fixed trunnion support and moving trunnion support with manual drive arrangement which is used to support the cask during transport and during the process of tilting the cask from horizontal to vertical and vice versa. Arrangement of SSTC is shown in Figure 1. During the transport, cask with cask support structure is rigidly tied down with the trailer. Tilting tackle is used at PFBR to handle the cask from horizontal to vertical and vice versa from the support structure with the help of moving trunnion and 100 t EOT crane as shown in Figure 2. Lifting yoke is used at DFRP to handle the

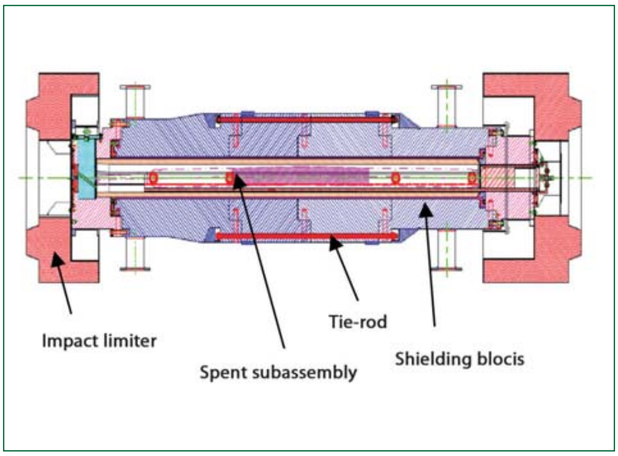

***Fig. 1** Arrangement of SSTC impact limiter*

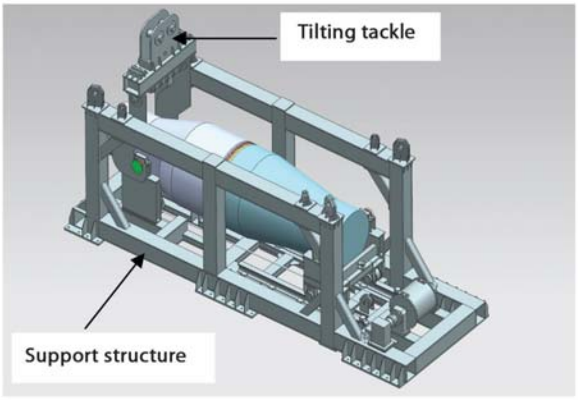

***Fig. 2** Cask handling at PFBR*

cask horizontally from the support structure as shown in Figure 3.

Design of SSTC

Adequate shielding is provided around the basket assembly to limit the radiation levels on contact and at 1m away from the surface. Possible leakage paths in the SSTC are sealed by a set of O-ring seals to ensure the containment boundary of SSTC. Provision is made to check the healthiness of O-rings provided on the cask at different locations by leak testing at periodic intervals. In addition, one gas sampling line with quick coupling arrangement is provided on shielding block-6 with valve arrangement to check the healthiness of spent subassembly before opening of the cask at the reprocessing end.

The components of cask, cask support structure and subassembly transfer mechanism are designed as per ASME Sec.III Div.1. Sub. Sec.ND Class 3. The components of cask tilting tackle, cask lifting yoke and cask trunions are designed as per ANSI 14.6 in which the components are designed for three times the load with stresses limited to yield strength. Considering snatch factor of 15% the calculated stress are within the allowable yield stress limit. Cask is tied down on to the cask support structure using rigid C-clamps. Cask support structure in turn is tied down onto the trailer using chain slings. Tie down attachments are designed to meet TS-G-1.1(ST-2) with road acceleration factors taken as 2g for longitudinal, 1g for lateral and vertical 2g up & vertical 3g down.

As per AERB SC TR – 1 code, SSTC is designed for a fall of 0.3 m onto a hard unyielding surface and the structural/containment integrity is demonstrated by calculations. Impact limiters are provided on both ends of the cask to absorb the energy of fall in order to reduce the deceleration due to fall. Polyurethane foam of density 150 kg/m^3 is used as the impact limiter material. The foam is encased with a 3 mm thick stainless steel layer on the outside. SSTC is analysed for the following cases (i) end drop, (ii) side drop and (iii) corner drop with axis of fall passing through one corner and the centre of gravity of the cask. Estimated deformation is less than the foam thickness provided in all the three directions of fall. Deformation for the side drop is shown Figure 4.

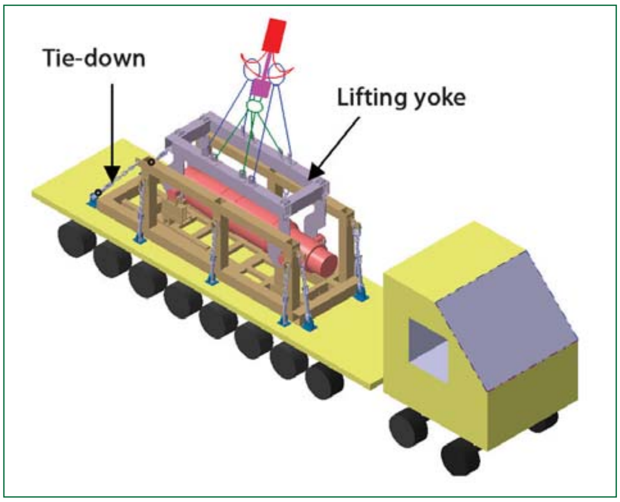

Fig. 3 *Cask handling at DFRP*

Cask body experiences maximum bending loads during the side drop. The maximum bending stresses are well within limits and hence the integrity of the cask body is ensured during side drop. The fasteners connecting shielding blocks are checked as per NUREG/CR-6007. The fasteners do not undergo any plastic deformation and hence the O-rings continue to provide sealing. The estimated temperature on the cask outer surface is 50 °C, which is much less than the design limit.

A special mechanism is designed to push the subassembly into the head end facility cell after the cask is coupled to the cell at DFRP. The pushing mechanism also has provision to retrieve the basket assembly back into the cask, if required. Subassembly transfer mechanism is shown in Figure 5. SSTC is designed to meet the interface requirements of DFRP.

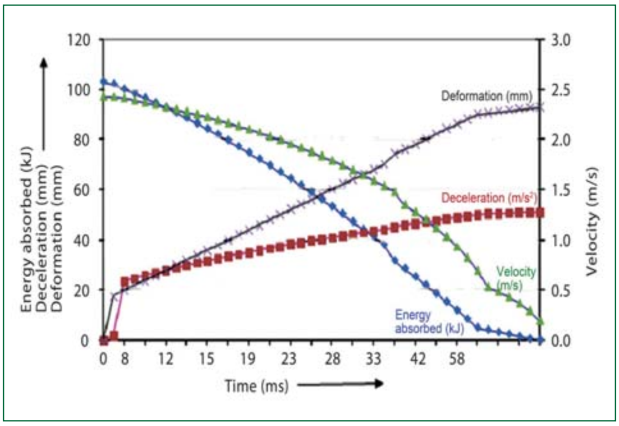

Fig. 4 *Impact limiter analysis for side drop*

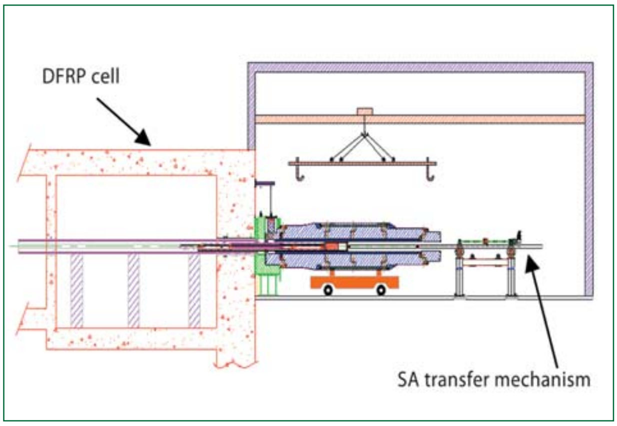

Fig. 5 *Subassembly transfer mechanism at DFRP*

IV.6 Demonstration of Distillation and Heavy Metal Melting by Nitrogen Cooled Induction Heating

Molten salt electrorefining followed by vacuum distillation and melting are the major steps involved in pyrochemical reprocessing of spent metal fuel. Molten salt electrorefining will be carried out at 500ºC. The dendritic deposits on a solid cathode will be scraped and distilled at 10 torr and 950ºC to remove the occluded salts in a high temperature vacuum retort. Subsequently, uranium dendrites will be melted and consolidated at 1200ºC and 600 torr. To demonstrate the feasibility of induction heating and melting at temperatures above 1200°C without using water, a setup was fabricated to commission and test an induction heating system for melting copper. Air was used as an alternative for water as coil coolant. A maximum of 900ºC only was attained due to low heat transfer coefficient of air. A mixture of liquid and nitrogen gas at sub-zero temperature was used and the desired temperatures were attained in the crucible. The induction heated melting system is shown in Figure 1. It consists of a 40 kW induction power supply unit, vacuum chamber, copper liner, copper coil, susceptor and crucible. Copper pellets were loaded in a graphite crucible as shown in Figure 2. A high density graphite susceptor encloses the crucible. The susceptor is insulated with graphite felt and ceramic fibre. A control thermocouple connected to the crucible was used to regulate the induction power supply. The copper coil for induction heating has a rectangular cross section. Sub-cooled nitrogen was fed through one inlet and discharged though two outlet ports. The vacuum chamber was evacuated to 10 torr by a dry vacuum pump. Temperatures of the crucible and coil were measured using alumina insulated R-type and K-type thermocouples respectively. PID controller was auto-tuned initially and then programmed for two set points (1000 and 1200ºC) with intermittent dwelling.

Fig. 1 *Induction heating system*

Tuning of the controller was done in order to optimize speed of response and stabilization of temperature. One-shot auto tuning was adopted. Induction heating experiment was first carried out using auto tuned parameters with a set point of 1000°C. Subsequently, the set point is varied by using a set point program in the controller, which is stored as a series of 'step' and 'dwell' segments. The temperature profile of the crucible with programmed configuration is shown in Figure 3. This profile was found to be ideal for vacuum distillation of salts and consolidation as there were no oscillations in temperature. At the end of 8 hours, the set point program was terminated. After cooling the system for 24 hours, the copper ingot was removed as shown in Figure 4. The PID controller was configured, tuned and programmed to achieve temperature control in the crucible during distillation and melting. Control action to an accuracy of ±1ºC could be achieved.

Fig. 2 *Copper pellets before melting*

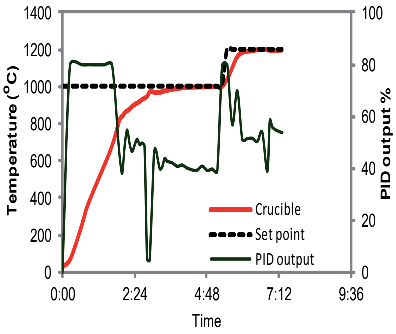

Fig. 3 *Transient temperature and power profile*

Fig. 4 *Copper ingot after melting*

IV.7 Effect of Vertical Baffle Height on the Dynamics of Sloshing in High Level Liquid Waste Storage Tank of Fuel Reprocessing Plant

In Demonstration Fast Reactor Fuel Reprocessing Plant (DFRP), the high level radioactive liquid waste (HLLW) will be stored in horizontal cylindrical tank. The liquid stored in the tank is prone to external excitations such as earthquakes. Hence, designing safe structures against such eventualities is vital to our survival. There is a possibility of wall buckling and damage to the base for liquid storage tanks during earthquake. Numerous container damages have been reported in the sloshing literature. Therefore, an attempt was made to study the dynamics of sloshing in a simple rectangular tank using numerical models. The effect of introducing baffles was investigated to control the sloshing amplitudes under resonant harmonic excitation.

The flow was assumed to be unsteady, viscous and incompressible. The governing equations for the fluid velocity in the i^{th} direction (i = 1, 2 and 3 for *x*, *y* and *z* respectively) and the pressure p are as follows

$$\frac{\partial u_i}{\partial x_i} = 0$$

$$\frac{\partial u_i}{\partial t} + u_j \frac{\partial u_i}{\partial x_j} = -\frac{1}{\rho}\frac{\partial p}{\partial x_i} + \frac{1}{\rho}\frac{\partial}{\partial x_j}(\mu S_{ij}) + f_i$$

where S_{ij} denotes the viscous stress written as $\partial u_i/\partial x_j + \partial u_j/\partial x_i$, ρ is the fluid density, μ is the dynamic viscosity, and f_i denotes a body force such as the seismic, gravity force, etc. Volume of Fluid (VOF) method was adopted for tracking the free surface. According to VOF, if the volume fraction of one fluid in the cell is denoted as α then the transport equation becomes

$$\frac{\partial \alpha}{\partial t} + \nabla.(u_i \alpha) = 0$$

where, α represents the volumetric fraction between air and water, which is equal to 0 for air, 1 for water and in between 0 and 1 at the interface between the two fluids. The numerical approach used to solve the governing equations for continuity and momentum conservation with appropriate boundary conditions is a CFD tool box, called OpenFOAM which is a finite volume method based algorithm.

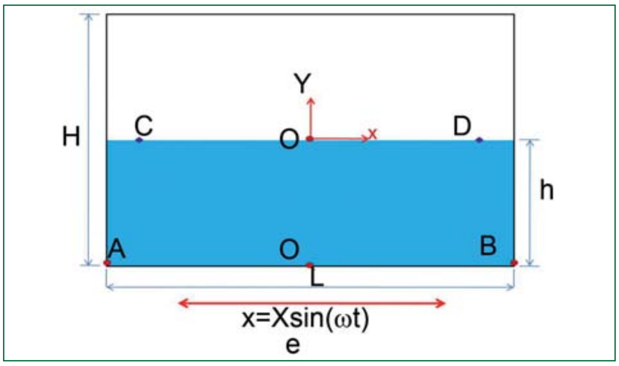

Fig. 1 *Typical domain of interest for a 2-D rectangular tank*

Effect of baffle height

In the present study, the characteristics of slosh reaction forces and exerted pressures on tank wall for three different vertical baffle heights in response to the harmonic excitation were investigated. The effect of height of slosh suppression device in a partially filled rectangular tank was studied for three different cases i.e, a tank with a vertical baffle height, h (= 0.14 metre), 2h/3 and h/3. The dimensions of the tank (shown in Figure 1) considered for analysis were length: 0.57 metre and height: 0.31 metre, filled with water to a depth of 0.15 metre. Figures 2a to 2d show the snapshots of free surface with no baffle and baffle at time, t = 6.8 seconds against resonant wave motion. In the case of baffle height h/3, the flow patterns exhibited the phenomenon in which a portion of the liquid travels up on one side of the tank near the wall, and down the opposite side similar to the case of fundamental mode, as if the liquid surface was undisturbed or quiescent, whereas, the free surface interface for the case with baffle height equal to h, was random.

The time evolution of free surface height of sloshing fluid for all the cases mentioned above and measured

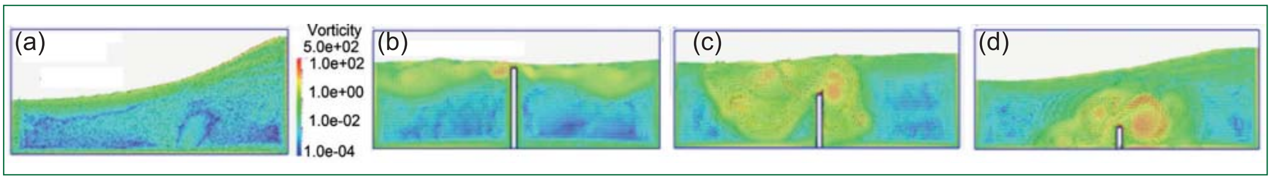

Fig. 2 *Vorticity contours of sloshing wave front in a HLLW tank with and without baffles: (a) no baffle (b) baffle height (h) (c) baffle height (2h/3) and (d) baffle height (h/3)*

at x = 0.02 m (point ‘C’) from the left wall is shown in Figure 3. Comparison of Figure 3 for the free surface wave elevation with different baffle heights revealed that the displacement was minimum for the baffle height, h. Therefore, this case provides a very effective damping mechanism of high viscous dissipation and ends up with reduction in sloshing wave height to the order of ten in magnitude compared to the case with baffle height, h/3. Certainly the magnitude of free surface height was altered by the inclusion of vertical baffle of height h/3; however, a reduction in free surface of approximately 90 % was observed with the inclusion of the baffle height of h.

The power spectra of the sloshing displacement fluctuations for the tank with and without baffles, analyzed through fast Fourier data, showed the power spectra of the sloshing displacement amplitudes for the tank without any baffle and with baffle for heights h/3, 2h/3 and h were in response to the input harmonic motion. A relatively small peak compared to the tank without baffle could be seen at resonance even for the tank with baffle of height h/3.

Literature data on sloshing with submerged bodies corroborate the observation that the baffle height just below the free surface is more effective in suppressing sloshing pressures. The dependence of pressure on time is shown in Figure 4.

Although the pressure histories for the tank with baffle appears to be reduced in all three cases, the pressure history for the tank with baffle height h/3 illustrated the impact behavior. Though the amplitude of pressure attained the steady state in the initial transient phase (about 4 seconds) itself, the behavior was found to be irregular at the middle of the tank due to the fact that the contribution of the second mode response was also predominant. Spectral analysis revealed that the fundamental frequency component of ω_n was represented by a dominant peak, with the successive peak at twice the frequency of the fundamental frequency representing the second mode and 2.5 for the third mode.

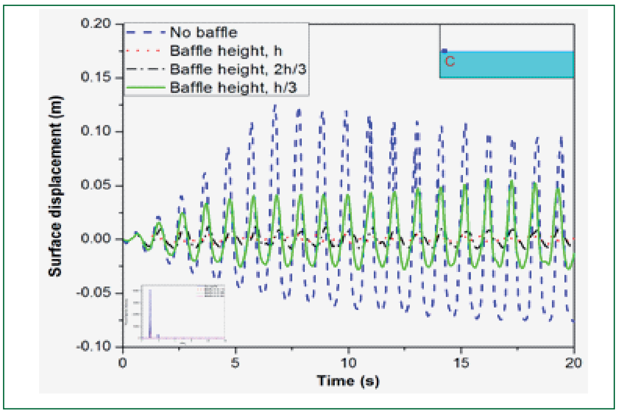

Fig. 3 *Temporal variation of free surface displacement for different baffle heights under resonant harmonic excitation*

The hydrodynamic force pattern (shown in Figure 5), estimated under resonant sloshing case was behaving in a similar manner as the pressure pattern for different baffle heights. As illustrated in Figure 5, the total force amplitude time histories measured on the left side wall for the baffled tank was also reduced in all the cases, but sloshing component was found to be very effective for tank with long baffle. The maximum force was on the bottom wall, as expected at the vertical mode.

Based on this study, it is confirmed that the baffle height has a direct effect on both the sloshing displacements and hydrodynamic pressure results. In fact, when the baffle height increases, the liquid sloshing becomes more suppressed due to the augmentation of the blockage effect of the baffle, which results in additional viscosity and energy dissipation. Therefore, it is recommended to introduce the baffle with height just below the free surface of liquid.

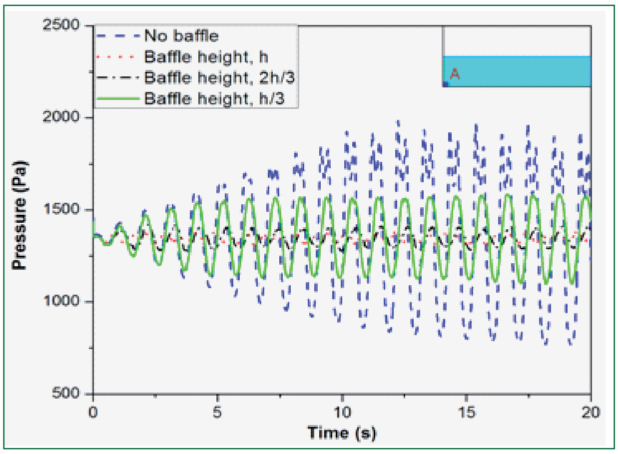

Fig. 4 *Temporal variation of pressure on bottom wall for different baffle heights under resonant harmonic excitation*

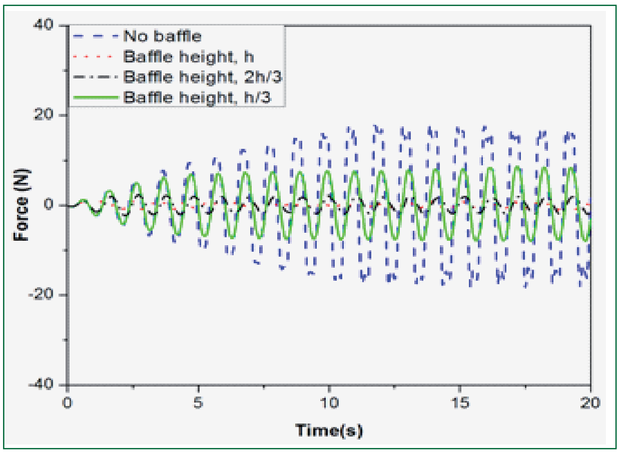

Fig. 5 *Temporal variation of hydrodynamic force on left wall for different baffle heights under resonant harmonic excitation*

IV.8 Comparison of Weld Induced Residual Stress Distributions between L-Seam and C-Seam Butt Weld Joints

In the spent fuel reprocessing plants, some of the important process vessels and equipment such as annular tanks, cylindrical tanks, vent pots, high level waste storage tanks etc., need to be fabricated either by longitudinal seam (L-Seam) or circumferential (C-Seam) weld joining process. Components whose diameters are equivalent to the available standard pipe sizes are fabricated by C-Seam weld joining. On the other hand, components which do not have diameters equivalent to standard pipe sizes are fabricated by L-Seam weld joining of rolled plates. In general, tanks and vessels which are subjected to high pressure are preferably fabricated by C-Seam weld joint, considering the effect of high hoop stress compared to longitudinal stress. Most of the reprocessing plant equipment are not subjected to high pressure and high temperature. Hence, these equipment can be fabricated either by L-Seam or C-Seam weld joining process. Also, it is of great interest to use L-Seam welds when fabricating large diameter components in order to reduce production cost. The cost reduction can be as high as 30%.

Weld characteristics, weld pool (fusion zone (FZ) and HAZ) shapes and sizes and weld induced residual stresses for L-Seam and C-Seam weld joints were investigated in this study. The results facilitated to improve the fatigue life, reduction in stress corrosion cracking and fracture. In this investigation, similar groove geometry, boundary conditions, weld sequencing (progressive welding), wall thickness and relatively constant heat input were used to compare weld characteristics between L-Seam and C-Seam butt weld joints of cylindrical components using numerical simulation and experimental validation.

For the welding experiments of both L-Seam and C-Seam 200 NB-SCH 5, 55 A current and 10 V voltage and weld speed of 1 mm/s were considered to obtain proper bead shape which was further validated in heat source calibration and fitting analysis. These process parameters with an arc efficiency (η=0.7) gave the heat input per unit length of weld as 385 J/mm, which is equal to the heat input that was used in FE simulation for 200 NB-SCH 5 case.

To accurately measure the residual stresses, full 3-D FE models were developed for both L-Seam and C-Seam welds of cylindrical components and are shown in Figure 1. In the process of FE meshing, three types of elements used were one-dimensional linear elements, 2-D and 3-D quadrilateral elements. One-dimensional linear elements were used to represent the weld trajectory and reference lines. 2-D quadrilateral elements were used to mesh the surfaces which are subjected to heat loss during welding process. 3-D quadrilateral elements were used to mesh the weld bead and the parent metal. During L-Seam and C-Seam weld experiments, parent material is not clamped. To match the experimental boundary conditions, minimum clamping was applied as the artificial boundary condition in order to prevent rigid body motion in the numerical simulation. The detailed boundary conditions used in the FE model are also shown in Figure 1.

To ascertain the influence of L-Seam and C-Seam butt weld joints of cylindrical components on residual stresses, four different numerical simulation cases were studied and the significant results are described. These four cases are L-Seam-8 inch dia. (200 NB-SCH 5 (L-8)), C-Seam-8 inch dia. (200 NB-SCH 5 (C-8)),

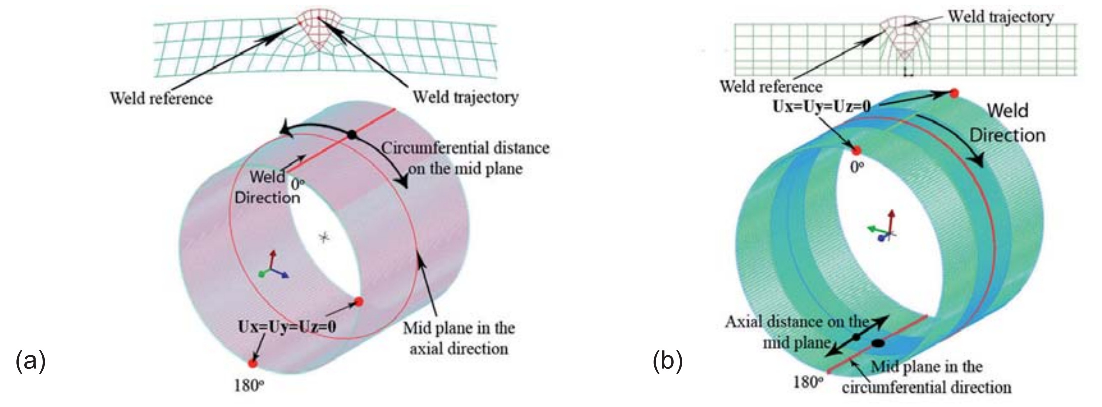

Fig. 1 FE 2-D and 3-D mesh with boundary conditions (a) L-Seam and (b) C-Seam

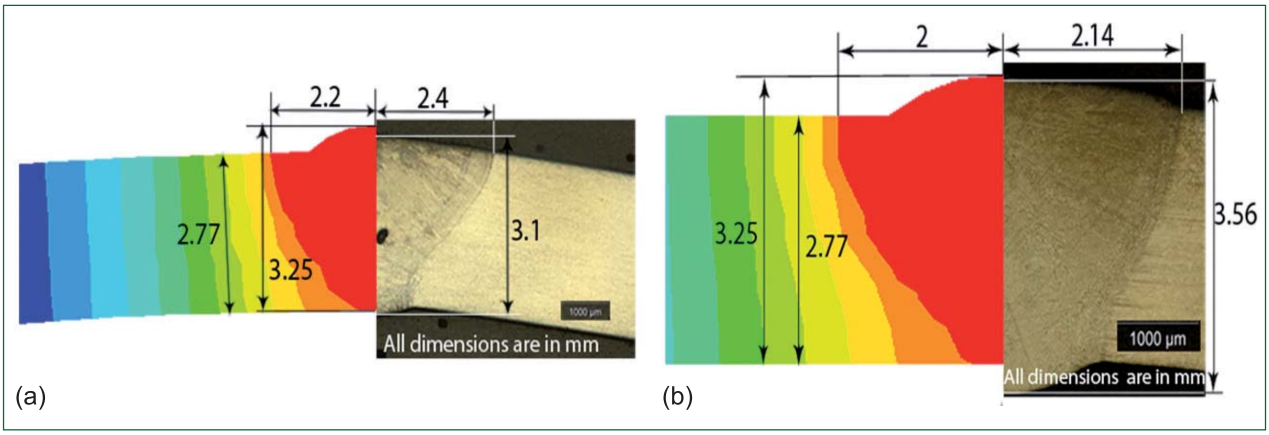

Fig. 2 *Validation of experimental macrograph and the FE weld molten pool sizes for (a) L-Seam and (b) C-Seam*

L-Seam-6 inch dia. (150 NB-SCH 5 (L-6)) and C-Seam-6 inch diameter (150 NB-SCH 5 (C-6)). The weld speed considered was 1 mm/s and the simulation was run for a time period of 10,000 seconds.

Figures 2a and 2b show an overview of the comparison between macrograph and the FE simulation weld pool dimensions. Experimental macrograph cross section and the predicted FE simulation weld molten pool for L-8 and C-8 cases are compared in Figures 2a and 2b respectively. It could be observed that the results are in good agreement with each other. The results obtained after iterative adjustment of heat sources were then saved to a function database for further use in the mechanical analysis.

Figures 3a and b present the hoop and axial stress distribution respectively on the inner surface, at 180° cross-section for C-Seam welds and at 100 mm cross-section for L-Seam welds as shown in Figure 1.

Influence of L-Seam and C-Seam weld joints on stress distribution

Figure 3a indicates that the hoop stress values increase for L-Seam weld joint irrespective of the locations along the distance from weld centre (WC) line. The increase in hoop stresses at the WC was found to be very significant with the increase in tensile stresses up to 225 MPa on the inner surface. Similar increasing trend in compressive stresses was also noticed away from the WC line for the L-Seam weld joint. Further, Figure 3b showed that for the C-Seam weld joint, axial stresses increase on the inner surface and this increase was found to be less significant when compared to hoop stress increase for the L-Seam weld joint. On the inner surface at the weld location, the magnitude of increase in tensile residual stresses was approximately 60 MPa. The peak hoop stresses were observed for L-Seam weld joint on the inner surface. Similarly, peak axial stresses were observed for C-Seam weld joint. It is a well known fact that when a vessel is subjected to internal pressure, the induced hoop stress is twice in magnitude when compared to axial stress. Based on the above observations, it can be concluded that the L-Seam weld joints are not advisable for use while fabricating cylindrical components such as annular tanks, vent pots, waste transfer containers and pressure vessels in order to improve the service life of cylindrical components.

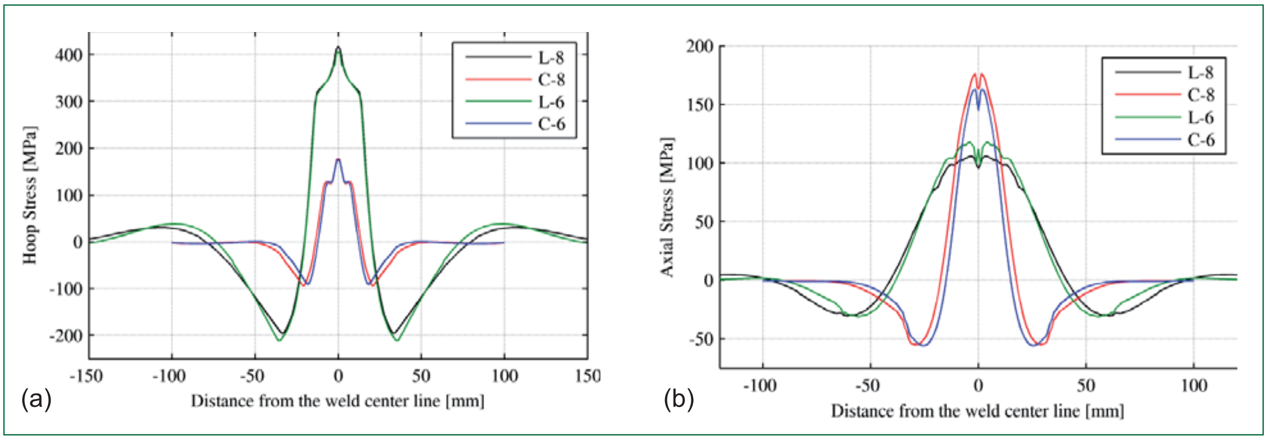

Fig. 3 *Residual stress distribution (a) hoop stress and (b) axial stress*

IV.9 Extraction and Stripping of Cesium and Strontium from Simulated Highly Active Waste by CCD/PEG-400/FS-13 Solvent

In the aqueous reprocessing route, the fuel discharged from FBR is dissolved in nitric acid and the resulting aqueous solution of nitrates of uranium, plutonium and most of the fission products is treated by solvent extraction method with 30% TBP to selectively extract U and Pu. The highly active aqueous waste (HAW) solution left out after extraction contains the fission products and is encapsulated in glass (known as vitrification) and the vitrified product has to be stored for several thousand years to allow for the decay of activity. Heat emitters like Cs-137 and Sr-90 generate a large decay heat which may be detrimental to the integrity of vitrified waste. If these heat emitting nuclides are isolated from HAW prior to vitrification through chemical processing, cooling requirement for vitrified product is drastically reduced, resulting in significant reduction of operating costs for managing these wastes.

Different methods like precipitation, ion-exchange and solvent extraction have been reported in the literature for the separation of Cs and Sr. As Cs and Sr are not extracted appreciably by TBP, speciality solvents are required for their extraction and effective separation from the other actinides and lanthanides present in the HAW. Extraction of Cs from wastes was reported using crown-ether derivatives as well as chlorinated cobalt di-carbollide (CCD). As CCD is a highly polar compound, it requires a polar diluent like nitrobenzene. Nitrobenzene was later replaced with a safer and inert diluent phenyltrifluoromethyl sulphone (known as FS-13). To co-extract Sr during Cs extraction, polyethylene glycol with molecular mass as 400 (PEG-400) is also added to the solvent. Combined process is known as CCD-PEG process for Cs/Sr recovery.

To demonstrate the viability of Cs/Sr recovery by CCD-PEG process from HAW, experimental runs were taken in an in-house developed novel micro-mixer-settler with simulated HAW (SHAW). Composition of SHAW used in this study was based on the fission product inventory of FBTR Mark-I fuel with 150 GWd/t burnup with one year cooling.

Cesium salt of CCD was dissolved in FS-13 and the clear solution was equilibrated with perchloric acid to convert Cs-CCD to HCCD. The HCCD (organic phase) was decanted and analysed for the acidity which was an indirect measure of CCD concentration in the organic solvent. This HCCD bearing organic solvent was used in the solvent extraction run in the micro mixer-settler. The micro-mixer-settler comprised of a coiled micro-bore stainless steel tubing coupled with a miniature settler (volume ~1.2 mL) as shown in Figures 1a and 1b. The interface in the settler was controlled by a movable miniature jack-leg device. In these experiments, the organic solution is heavy phase and aqueous solution is light phase, which is contrary to the conventional PUREX process. The product streams were clear without any haze or entrainment.

After extraction run, the organic product was stripped with dilute guanidine carbonate solution. The aqueous streams were analysed with a continuum source atomic absorption spectrometer. In a single-stage extraction operation, about 73% Cs and 96% Sr were extracted by CCD-PEG solvent. During the back-extraction (stripping) operation in a single-stage, about 96% Cs and more than 99% Sr in the loaded solvent were stripped by guanidine carbonate-DTPA strip solutions.

The results for the recovery of Cs and Sr indicated highly efficient extraction and stripping operations in a single-stage micro mixer-settler, validating the conceptual design of the experiment and used flowsheet conditions. Based on these encouraging results, a counter current demonstration in a multi-stage miniature centrifugal extractor bank with SHAW and CCD-PEG solvent is being planned.

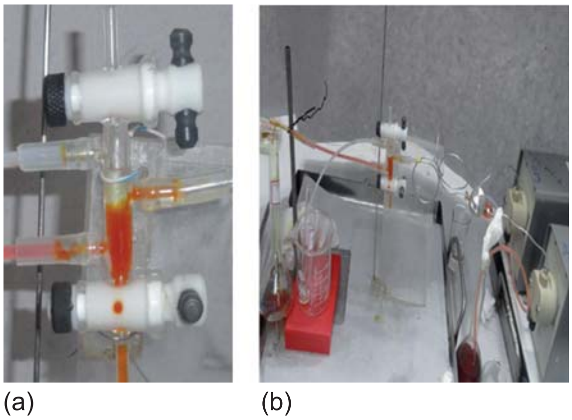
(a) (b)

Fig. 1 *A view of (a) miniature settler (1.2 mL) and (b) micro mixer-settler during CCD-PEG run*

IV.10 Kinetics of Extraction of Nitric Acid into Binary Mixture of Tri-n-butyl Phosphate and Normal Paraffin Hydrocarbon

Kinetics of solvent extraction is of paramount importance to all industrial applications and is largely determined by the interfacial chemistry. The commercial extraction equipment in operation such as mixer-settler, pulsed column and annular centrifugal extractor are designed based on the number of equilibrium stages required to effect a given separation. Design based on equilibrium isotherms automatically neglects kinetic effects. Hence, for the rational design and operation of extraction equipment, one should know the mass transfer characteristics, intrinsic kinetics and the extent of axial mixing. The chemical reaction kinetics determines the size and types of extractors to be used. The objective of the present work was to identify the reaction location and extraction regime as well as to estimate the overall rate of extraction, intrinsic rate constant and mass transfer coefficient.

Among the variety of contacting techniques, Lewis type stirred cell of constant interfacial area is a convenient apparatus for studying the rate of mass transfer and measuring the individual phase mass transfer coefficients because it allows both constant area between two phases and a variance of the rate of stirring in a sufficiently broad range. The constant interfacial area stirred cell (Lewis cell) used for kinetic studies (Figure 1) was a glass vessel with a jacket for maintaining constant temperature. The stirred cell was provided with two four-flat blade impeller of 50 mm diameter and 13 mm blade length . Vertical baffles were used to avoid vortex formation. The experiments were performed by mixing both aqueous phase (nitric acid) and organic phase (TBP diluted with NPH) using double impeller placed half dipped in each phase. Experiments were conducted by varying different parameters like aqueous phase concentration of HNO_3 (1-4 M), organic phase concentration (0.3652-1.466 $kmol.m^{-3}$), impeller speed (110 to 150 rpm), the ratio of aqueous to organic phase (0.6-1.2) and temperature (15-45ºC).

Fig. 1 *Lewis cell*

Complexation of nitric acid by TBP can be described on the basis of the reaction equilibria:

$$H^+ + NO_3^- + TBP \Leftrightarrow TBP \cdot HNO_3 \qquad (1)$$

Identification of the reaction location

The relationship between the extraction rate and the interfacial area is an important criterion to decide whether the chemical reactions that control the rate of extraction occur in the bulk phase or at the interface (Figure 2). The low aqueous phase solubility (10^{-3} M) and surface activity of TBP supported the possibility of the occurrence of reaction between nitric acid and TBP at the interface. From the experimental results shown in Figure 3, initial rate of nitric acid extraction was found to be directly dependent on the specific interfacial area, which is the characteristic of an interfacial reaction.

Identification of the reaction regime

For establishing the intrinsic kinetics of the extraction

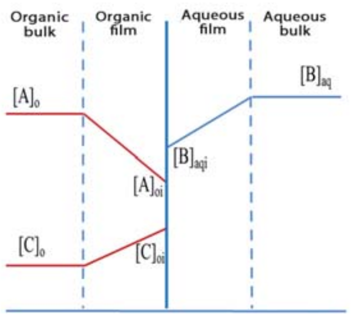

Fig. 2 *Concentration profile describing interfacial reaction occurring at diffusion/mixed controlled regime*

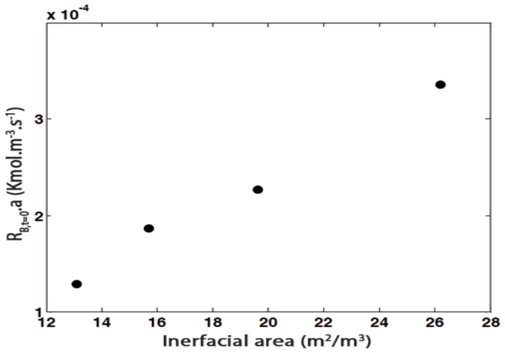

Fig. 3 *Effect of interfacial area on initial extraction rate of nitric acid*

Equations	
$\frac{d[B]_o}{dt} = \frac{S}{V} k_{oa} \left\{ \frac{K_d [A]_o \left([B]_{aq,t=0} - [B]_o\right)}{[A]_{oe}} - [B]_o \right\}$	(2)
$-\frac{d[B]_{aq}}{dt} = \frac{S}{V_a} R_B = \frac{S}{V_a} \left\{ \frac{[B]_{aq}\left(K_{eq}[A]_o + \frac{V_a}{V_o}\right) - \frac{V_a}{V_o}[B]_{aq,t=0}}{\left(\frac{K_{eq}[A]_o}{k_{Laq}} + \frac{1}{k_{Lo}}\right)} \right\}$	(3)
$-\frac{d[B]_{aq}}{dt} = \frac{S}{V_a} R_B = \frac{S}{V_a} \frac{\left\{[B]_{aq}\left(K_e[A]_o + \frac{V_a}{V_o}\right) - \frac{V_a}{V_o}[B]_{aq,t=0}\right\}}{\left\{\frac{1}{k_b} + \left(\frac{K_e[A]_o}{k_{Laq}} + \frac{1}{k_{Lo}}\right)\right\}}$	(4)
$\frac{k_L}{\nu} = 0.00025 \left(\frac{\omega}{\nu}\right)^{1.16} Sc^{-1.08}$	(5)

of nitric acid, the theory of mass transfer with chemical reaction has been used. There are primarily two regimes of extraction – the kinetic regime and the diffusion regime. In a kinetic regime system, the kinetics of solvent extraction can be described in terms of chemical reactions occurring in the bulk phases or at the interface. The extraction rate expression for the kinetic regime is given by Equation 2.

In diffusion controlled extraction process, kinetic parameters are unimportant and the extraction rate directly depends on interfacial area and turbulence.The extraction rate expression for the diffusion controlled regime is given by Equation 3.

When both chemical reactions and film diffusion processes occur at rates that are comparable, the solvent extraction kinetics is said to take place in a mixed diffusion-kinetic regime. This is the most complicated case, since the rate of extraction must be described in terms of both diffusional processes and chemical reactions and a complete mathematical description can be obtained only by simultaneously solving the differential equations of diffusion and those of chemical kinetics.

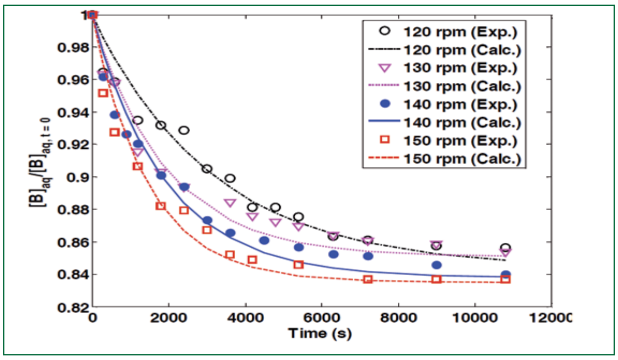

Fig. 4 *Experimental and calculated concentration profiles of nitric acid*

The extraction rate expression for the mixed diffusion-kinetic regime is given by Equation 4. The experimental data on nitric acid concentration versus time were fitted into model equations of the three regimes using a nonlinear regression technique to obtain mass transfer coefficient and rate constant. Figure (4) shows the comparison between experimental and calculated values of aqueous phase nitric acid concentration. The impeller speed dependency on the rate was checked to estimate the contribution of diffusion mass transfer to the overall rate of extraction (Figure 5). A further criterion that enables a distinction between a diffusion-controlled and a kinetic regime is the experimental determination of the activation energy from the temperature effect of the extraction process. From the slope of Figure 6, the activation energy for the intrinsic rate constant value was calculated to be 26.04 kJ/mol which assured the fact that the overall extraction rate is controlled by both the intrinsic kinetics and mass transfer of the species involved. Based on the results of the present study, a correlation was also developed for the estimation of individual mass transfer coefficients (Equation 5).

The extraction of nitric acid by TBP was found to be an interfacial reaction and overall extraction rate was controlled by both the intrinsic kinetics and the mass transfer of the species involved, for which a comprehensive model has been developed.

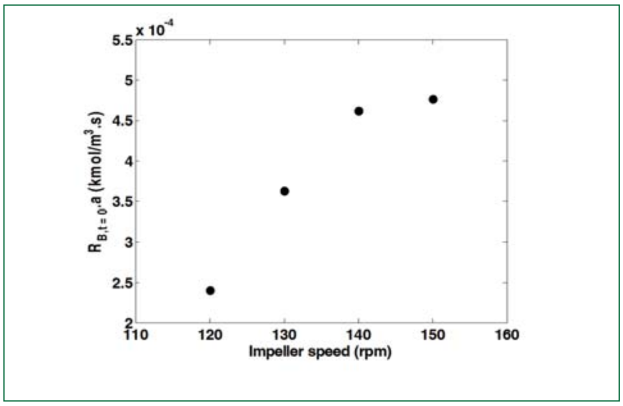

Fig. 5 *Effect of impeller speed on initial extraction rate of nitric acid*

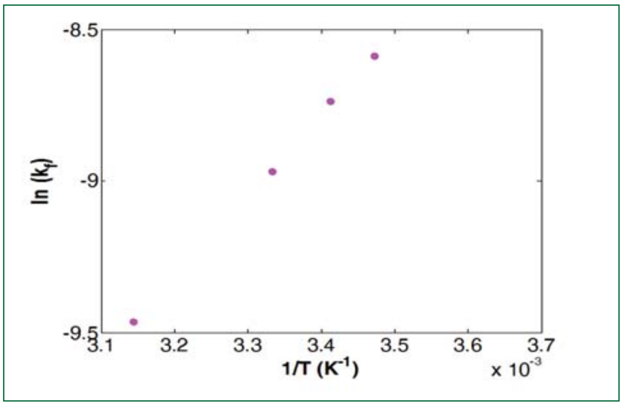

Fig. 6 *Arrhenius plot for the calculation of activation energy*

IV.11 Vapor Liquid Equilibrium of Nitric Acid – Water System at Different Pressures: Data Analysis

For the recovery and reuse of uranium and plutonium, the spent nuclear fuel is reprocessed. Though PUREX process employed in most of the existing reprocessing plants is an efficient technique, it generates large amounts of strong and dilute nitric acid waste solutions. Recovery and reuse of nitric acid from these waste solutions is beneficial as it reduces the waste volume as well as the nitric acid inventory requirement. Since distillation process, commonly employed in HNO_3 concentration plants does not result in additional waste generation, this process appears to be the most practical solution for the recovery of nitric acid from waste solutions.

For the purpose of designing a nitric acid recovery unit based on distillation, the vapor liquid equilibrium (VLE) data of nitric acid-water system at different pressures reported in literature were analyzed using different thermodynamic models. Though many activity coefficient models are reported in literature for correlating experimental VLE data, due to proven applicability of Wilson and NRTL equations for representing VLE of various systems, they were considered here. The experimental VLE data were correlated to these two models by minimizing the following objective function:

$$\mathrm{OF} = \sum_1^{\mathrm{N_{EXP}}}\left[\gamma_{1,\mathrm{EXP}} - \gamma_{1,\mathrm{CAL}}\right]^2 + \sum_1^{\mathrm{N_{EXP}}}\left[\gamma_{2,\mathrm{EXP}} - \gamma_{2,\mathrm{CAL}}\right]^2$$

For calculating the vapor pressures of pure nitric acid and water, Antoine's equation was used.

$$\log_{10}\left(\mathrm{P^0_{HNO_3}/Torr}\right) = 7.5119 - \frac{1406}{221.0-(\mathrm{T/^0C})}$$

$$\log_{10}\left(\mathrm{P^0_{H_2O}/Torr}\right) = 8.0713 - \frac{1731}{233.4-(\mathrm{T/^0C})}$$

The model parameters were regressed from the experimental data. For the non randomness factor (α_{ij}), though a range of 0.2 to 0.47 depending on the chemical nature of constituents is generally recommended, here it was allowed to vary outside this range during the regression. Using the regressed parameters, the bubble point temperature and vapor phase compositions were estimated and their comparison with the experimental data is shown in Figures 1 and 2. Applicability testing of these models for representing VLE of nitric acid-water system was carried out by analyzing the mean deviation in predicting the bubble points.

Table 1: RMSD values corresponding to each model

Pressure (Torr)	50	100	200	400	760
[a] RMSD (WILSON)	0.0260	0.0132	0.0162	0.0050	0.0107
[a] RMSD (NRTL)	0.0300	0.0118	0.0200	0.0054	0.0117

[a], $\mathrm{RMSD} = \left(\frac{1}{\mathrm{N_{exp}}}\sum_1^{\mathrm{N_{exp}}}\left(\frac{\mathrm{T_{exp}-T_{cal}}}{\mathrm{T_{exp}}}\right)^2\right)^{0.5}$

where N_{exp} represents number of data points

Applicability testing of Wilson and NRTL models was carried out based on root mean square deviation (RMSD) and it was found that Wilson equation had lower deviation in comparison to NRTL equation for all pressures, except 100 torr (Table 1). As the difference between the RMSD values was marginal, both the models seem to be equally good for representing the VLE of nitric acid-water system. Though Wilson and NRTL models are generally used only for correlating VLE of non electrolyte systems, the above results show both are applicable for electrolyte solutions as well. Based on these observations and also due to simplicity of Wilson equation, it has the potential to be used as VLE generator in nitric acid distillation simulation programs to significantly reduce the computation time without affecting the accuracy.

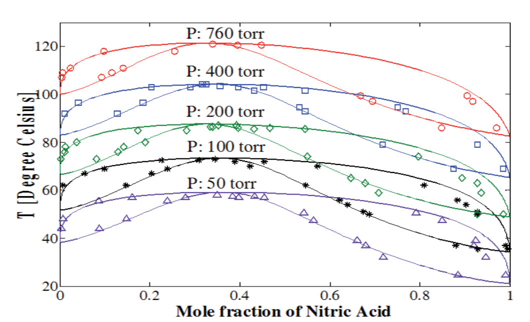

Fig. 1 VLE represented by Wilson equation

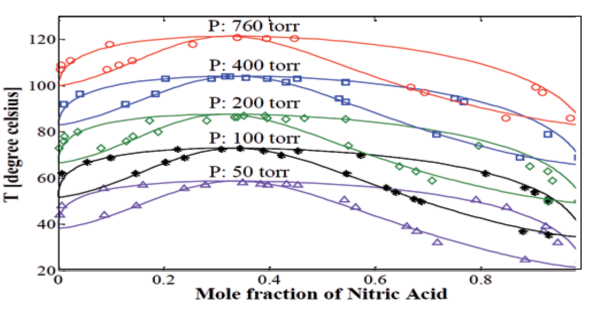

Fig. 2 VLE data represented by NRTL equation

IV.12 Characterization of Degraded Products formed during Gamma Radiolysis of PUREX Solvent

A 30% (v/v) solution of tri-*n*-butyl phosphate (TBP) in n-dodecane (DD) is adopted as the solvent for the selective extraction of U and Pu from the spent nuclear fuel solution consisting of highly radioactive fission products and activation products in about 3–4 M nitric acid. During extraction, the solvent comes in contact with acid and intense radiation. Owing to high dose of radiation, the solvent (extractant + diluent) undergoes chemical, thermal and radiolytic degradation resulting in a number of degradation products with varying physiochemical properties that disrupts the process efficiency. The major degradation products of the extractant (TBP) are alkyl phosphoric acids and are removed by alkali wash before recycling. On the contrary, the diluent degradation products get accumulated during solvent recycling. Though vast literature data are available on the identification and quantification of the degradation products of TBP either in single phase or biphasic system, data on the characterization of diluent degraded products are scanty and hypothetical. Hence, efforts were made to characterize the degradation products of TBP-DD using advanced analytical techniques such as FT-IR, GC-MS and MALDI.

A 1.1 M solution of TBP in n-DD after equilibration with 4 M nitric acid was exposed to gamma irradiation in ambient air up to 100 MRad absorbed dose. The degraded solvent was washed with 1:1 (v/v) alkali to remove the acidic degradation products of TBP. The washed solvent was fractionally distilled at 2 mbar pressure and four different fractions were collected. The FT-IR spectra of the irradiated solvent after distillation (residual) and the collected fractions (1-3) are compared in Figure 1.

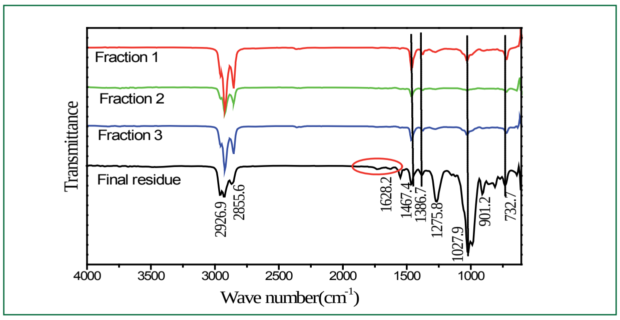

Fig. 1 *IR spectra of collected fractions*

The irradiated solution (before wash) had characteristic bands of TBP and dodecane along with peaks corresponding to nitro alkane (1553 cm^{-1}) and alkyl nitrate (1737 cm^{-1}). The distilled fractions had absorption peaks around 2926, 2856, 1467, 1386 and 730 cm^{-1}, corresponding to the hydrocarbon, dodecane. A less intense peak around 1027 cm^{-1} in the distilled samples was due to TBP, indicating that some portion of TBP also got distilled along with the diluent. The residual solution (fraction 4) was rich in TBP based compound (broad intense peak around 1028 cm^{-1}), along with the diluent degradation products.

To identify the species responsible for metal retention, the physiochemical properties (density, viscosity and phase disengagement time (PDT)) and Zr retention behavior of the various fractions collected were measured and the values (listed in Table 1) were compared with those of the diluent. The density of the first fraction collected was 0.751 g/cc and that of the residual solution was 0.929 g/cc. The respective viscosity values were 1.408 and 3.575 mPa.s. Zirconium retention values for the first three distilled fractions varied from 3 to 8 ppm (Zr stock: 2300 ppm) and for the final residue it was 1740 ppm. This indicates that the most harmful degraded products were present in the residue. Hence, the residue was characterized by GC-MS and MALDI techniques.

The FT-IR spectra of the final residue revealed all the characteristic frequencies of TBP and DD with additional features due to OH group and a peak at 1628 cm^{-1} (probably due to nitrate group). GC-MS spectrum revealed the presence of n-dodecane, 4-dodecanol and TBP. MALDI analysis indicated that the species could be phosphoric acid, TBP dimer and hydrocarbon derivatives. In distilled fractions, signatures of dodecanol and oxalic acid were found in addition to dodecane and TBP (GC-MS) whereas MALDI analysis indicated the formation of fragmented ions of TBP and DD.

This study revealed that alkali wash of the degraded solvent is not an ideal option for recycling, as most of the identified degraded products are hydrophobic. However, 65% of the degraded solvent could be recovered by distillation for recycling.

Table 1: Physiochemical properties of vacuum distilled fractions

Sample	Density (g/cc)	Viscosity (mPa.s)	PDT (s)	Zr ret. (ppm)
Fraction 1	0.751	1.408	68	4
Fraction 2	0.754	1.425	69	3
Fraction 3	0.756	1.450	ND	8
Residual	0.929	3.575	600	1740

IV.13 Advanced Alkylacetamides for Minor Actinide Partitioning

Partitioning of the trivalent actinides (Am(III) and Cm(III)) from high level liquid waste (HLLW) and their transmutation into short-lived or innocuous products is an attractive and viable option for the safe management of HLLW. The current approach for separation of trivalents from HLLW is a liquid-liquid extraction procedure that employs a hydrophobic organic phase containing an extractant dissolved in a diluent, n-dodecane (n-DD). Even though the process flow-sheets based on the reagents such as octyl(phenyl)-N,N-diisobutyl-carbamoylmethyl phosphine oxide (OΦCMPO), N,N'-DiMethyl-N, N'-DiOctyl-2-HexylEthoxyMalonAmide (DMDOHEMA), octyl derivatives of diglycolamides (DGAs) have been developed and demonstrated, it is important to note that all these reagents are suffering from some major drawbacks such as third phase formation and extraction of unwanted metal ions

However, the problem of third phase formation was usually maneuvered by adding phase modifiers to the organic phase, in significant concentrations, even though the organic phase without any modifier was preferred. The phase modifiers are usually another extractant such as N,N-dihexyl octanamide (DHOA), tri-n-butyl phosphate (TBP) or long chain alcohol etc. Addition of such phase modifiers to organic phase usually increases the extraction of unwanted metal ion present in HLLW and decreases the selectivity of trivalent actinide. The chemical and radiolytic degradation of modifier also complicates the recovery of extracted actinides and burdens the management of spent organic waste. Therefore, it is desirable to develop extractants that operate without the need of any phase modifier for trivalent actinide separation from HLLW.

Alkyl derivatives of diglycolamides (R-DGA) are regarded as promising candidates for the separation of trivalent metal ions from HLLW. The structure of R-DGA is shown in Figure 1. Due to the presence these two amidic sites, the polarity of the diglycolamide are significantly high, and perhaps this factor is responsible for the poor compatibility of the metal-solvate in a non-polar n-dodecane. One way of minimizing the polarity of the extractant is to increase the hydrophobicity of the diglycolamide by attaching long chain alkyl groups such as dodecyl (C12) or decyl groups (C10) to the amidic nitrogen atom of diglycolamide. Previously, we have shown that the third phase formation and extraction of unwanted metal ions can be minimized to a significant extent by simply increasing the chain length of alkyl group. In this context, several unsymmetrical diglycolamdies (UDGAs, see Figure 1) have been developed and evaluated for the extraction of trivalent metal ions from nitric acid medium.

On the other hand, the third phase formation can also be avoided by redesigning the structure of extractant with a single amidic functionality and retaining the etheric oxygen at the required position in the structure. Through our studies we realized that the etheric oxygen should be at the 2-position from the amidic functionality for extraordinary extraction. The structure of extractant with such modification is shown in Figure 1, and they are the alkyl derivatives of N, N-dialkyl-2-hydroxyacetamide (DAHyA). The R attached to etheric oxygen can be hydrogen or alkyl group, and R' attached to amidic nitrogen can be another alkyl group. In this context, the alkyl derivatives of N,N,-dialkyl-2-hydroxyacetamide (DAHyA), namely, N,N,-dihexyl-2-hydroxyacetamide (DHHyA), N,

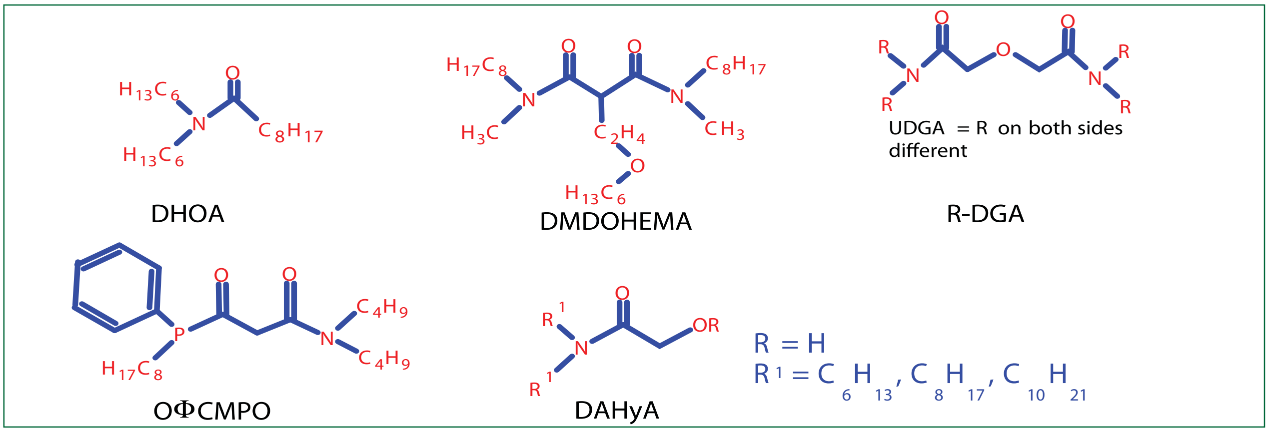

Fig. 1 *Structures of extractants used in minor actinide partitioning*

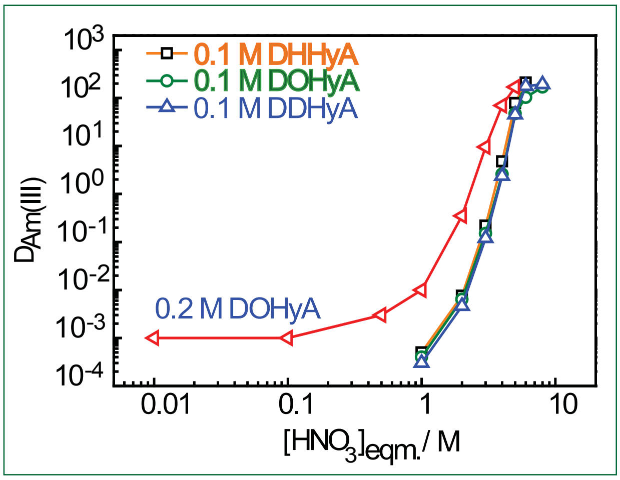

Fig. 2 *Variation in the distribution ratio of Am(III) in DAHyA/n-DD as a function of nitric acid concentration at 298 K*

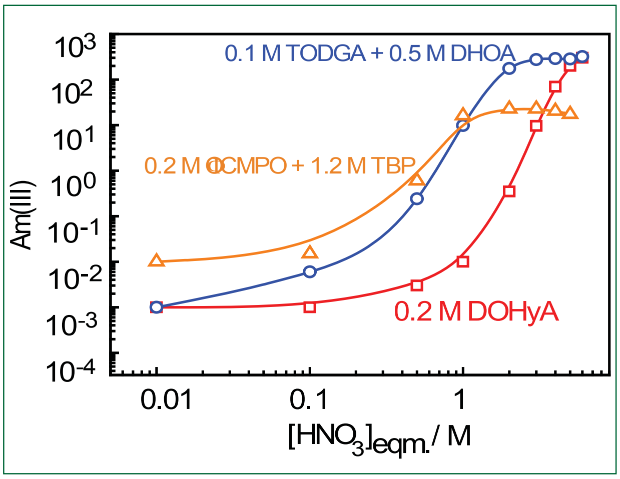

Fig. 3 *Variation in the distribution ratio of various extractants as a function of nitric acid concentration at 298 K*

N,-dioctyl-2-hydroxyacetamide (DOHyA), N,N,-didecyl-2-hydroxyacetamide (DDHyA), were synthesized and characterized by FT-IR, and NMR spectroscopy.

Figure 2 shows the variation in the distribution ratio of Am(III) as a function of nitric acid concentration in 0.1 M DAHyA/n-dodecane. A distribution ratio of 10^{-4} (negligible extraction) is obtained for the extraction of Am(III) in 0.1 M DAHyA/n-dodecane at nitric acid concentrations ranging from 0.01 to 1 M. The distribution ratio of Am(III) decreases in the order DHHyA > DOHyA > DDHyA. Figure 2 also shows the results on the extraction of Am(III) from nitric acid medium in 0.2 M DOHyA/n-DD. A distribution ratio of $\sim 10^{-3}$ was obtained in a nitric acid concentration ranging from 0.01 M to 0.1 M. At 1 M nitric acid a distribution value of 0.01 was achieved. However, at 3-4 M nitric acid concentration the distribution ratio of Am(III) varies from 10 to 70, which seems to be adequate for efficient extraction of trivalent metal ions from HLLW in few contacts. Above 4 M nitric acid a distribution value more than 200 was achieved. About five molecules of the DOHyA were coordinated to Nd(III) when Nd(III) was loaded from 3-4 M nitric acid medium and it was in good agreement with the slope analysis of the Am(III) extraction in DAHyA/n-dodecane. Studies on loading of Nd(III) in to DAHyA/n-dodecane indicate that the third phase was not observed in octyl and decyl derivatives even at the initial concentration of Nd(III) exceeded the value of ~500 mM in 4 M nitric acid, which was far above the concentration of trivalent metal ions (5 mM to 50 mM) present in HLLW. Therefore, the solvents DOHyA and DDHyA did not require any phase modifier.

To bring out the merits of using DAHyA for trivalent actinide separation, it is necessary to compare the extraction behavior of Am(III) achieved in 0.2 M DOHyA/n-DD with other promising regents such as carbamoylmethylphosphine oxide (OΦCMPO) and diglycolamide. Usually a TRUEX formulation composed of a solution of 0.2 M OΦCMPO + 1.2 M tri-n-butyl phosphate (TBP) in n-dodecane and a diglycolamide solution composed of 0.1 M N,N,N'N'-tetraoctyldiglycolamide (TODGA) + 0.5 M dihexyloctanamide (DHOA) in n-dodecane were proposed for trivalent actinide partitioning.

Figure 3 compares the distribution ratio of Am(II) obtained in 0.2 M DOHyA/n-DD with 0.2 M OΦCMPO + 1.2 M TBP/n-DD and 0.1 M TODGA + 0.5 M DHOA/n-DD. In the first place, the advantage of using the solvent, 0.2 M DOHyA/n-DD, is that it does not require any phase modifier. Therefore, the complications due to the presence of phase modifiers during trivalent actinide partitioning and spent solvent management does not arise in DAHyA system. At 3-4 M nitric acid concentration prevailing in HLLW, the DAm(III) increases in the order OΦCMPO < DOHyA < TODGA. However, the DAm(III) of 10 to 70 achieved in 0.2 M DOHyA/n-DD at 3-4 M nitric acid seems to be adequate and indeed desirable for quantitative extraction of Am(III) from HLLW in few contacts. After extraction, the recovery of Am(III) is usually carried out by using dilute nitric acid (~0.01 M). However, the use of such low concentration of nitric acid in a mixer-settler during back extraction resulted in hydrolysis of the metal ions (crud formation) present in the extracted phase. In contrast to this, the distribution ratio of Am(III) achieved in 0.1 M DAHyA/n-DD at 1 M nitric acid was only $< 10^{-3}$ and therefore the study showed that it was quite possible to recover the extracted metal ions even at 1 M nitric acid in DOHyA system. In view of these, the DAHyA derivatives are promising candidate for the separation of trivalent actinides from HLLW.

IV.14 Development of Novel Solid Phase Adsorbents for Trivalent Actinide Separation from HLLW

The long term radiation hazard of spent nuclear waste is mainly associated with the alpha emitting radionuclides such as ^{241}Am and ^{243}Cm. These metal ions are generally known as minor actinides (MA). Partitioning of these MA from HLLW and transmutation in to short-lived or innocuous products is an attractive and viable option for the safe management of HLLW. The current strategy of partitioning involves the separation of trivalent actinides from HLLW together with lanthanides in the first step, followed by mutual separation of lanthanides from actinides or vice-versa in the second step. The mutual separation is necessary prior to transmutation, since lanthanides act as neutron poisons that reduce the efficacy of transmutation of actinides.

Methods based on liquid-liquid extraction have been extensively investigated for both group separation of trivalent metal ions (actinides and lanthanides together) and their mutual separation. In contrast to this, the separation studies using solid phase extraction are not available in literature. However, solid phase extraction is very promising due to its simplicity, robustness, regenerating ability, engineered into plant scale levels from bench scale data and technologically demonstrated. In view of this, we have developed a couple of anchored resins namely (a) 2-oxy-N,N-dioctyl acetamide anchored chloromethylated resin (R-DOA) for the group separation of lanthanides and actinides from 3-4 M nitric acid and (b) glycolamic acid anchored polyamine resin (PA-DGAH) for the mutual separation of lanthanides and actinides. For the studies we have used Eu(III) as representative for lanthanides and Am(III) for actinides.

Synthesis of R-DOA resin

Synthesis of R-DOA involved a three step process. Initially, N,N-dioctyl-2-hydroxy acetamide was prepared by the two-step procedure. A solution of N,N-dioctylamine and triethylamine was reacted with chloroacetylchloride in THF at 5°C, under argon atmosphere. The product obtained was then refluxed with potassium hydroxide solution for 2 hours to obtain N,N-di-octyl-2-hydroxyacetamide. Finally the hydroxyacetamide was reacted with chloromethylated resin at 80°C to obtain the hydroxyacetamide anchored resin (R-DOA), shown in Figure 1. The product was dried overnight.

Characterization of R-DOA resin

Based on the determination of N content (0.9 %) in R-DOA, the degree of functionalization was determined to be 0.68 mmol/g. The reaction yield was ~70%, as the chloromethylated resin contained about 1 mmol/g $-CH_2$-Cl functional groups. The resin was characterized by FT-IR spectroscopy. The transmittance bands occurred at 3100 - 3000 cm^{-1} and 3000 - 2800 cm^{-1} were due to aromatic and aliphatic C-H stretching frequencies. A couple of transmittance bands observed in R-DOA, at 1649 cm^{-1} were due to amidic C=O stretching, and a sharp band at 1383 cm^{-1} was due to terminal methyl rocking vibrations of N,N-dioctyl moiety. These observations confirmed with functionalized 2-oxy-N, N-dioctylacetamide moiety on the resin.

Extraction of Eu(III) and Am(III)

The distribution coefficient (is the ratio of radioactivity of the radionuclide in the resin phase to aqeuous phase at equilibrium) of Am(III) and Eu(III) in R-DOA as a function of nitric acid concentration is shown in Figure 2a. The K_d values for both metal ions increases with increase in the concentration of nitric acid, reaching a maximum value at 3 - 4 M in nitric acid followed by decrease in K_d values. The distribution coefficients obtained for Eu(III) are higher than the values obtained for Am(III) at all acidities.

Back extraction of Am(III) and Eu(III) from the loaded resin phase is one of the important requirements for the

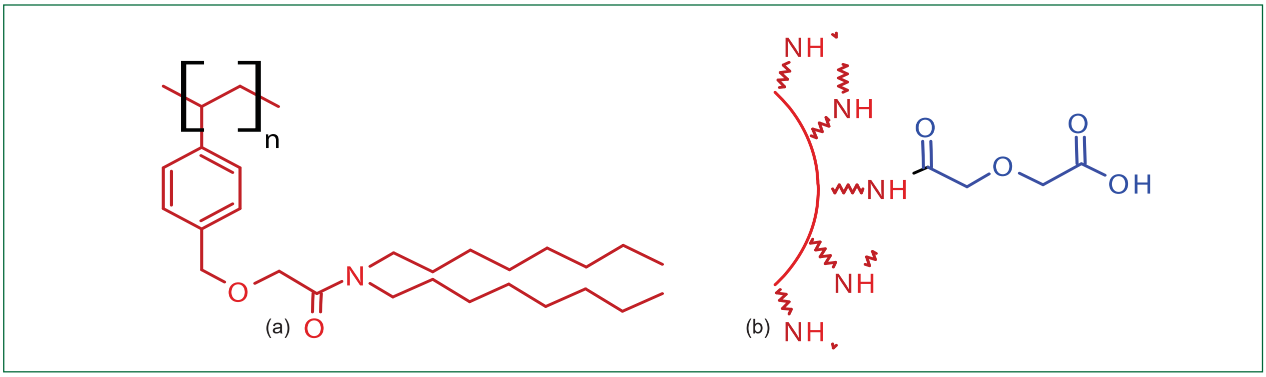

Fig. 1 Scheme for the synthesis of (a) R-DOA resin and (b) polyamine-DGAH resin

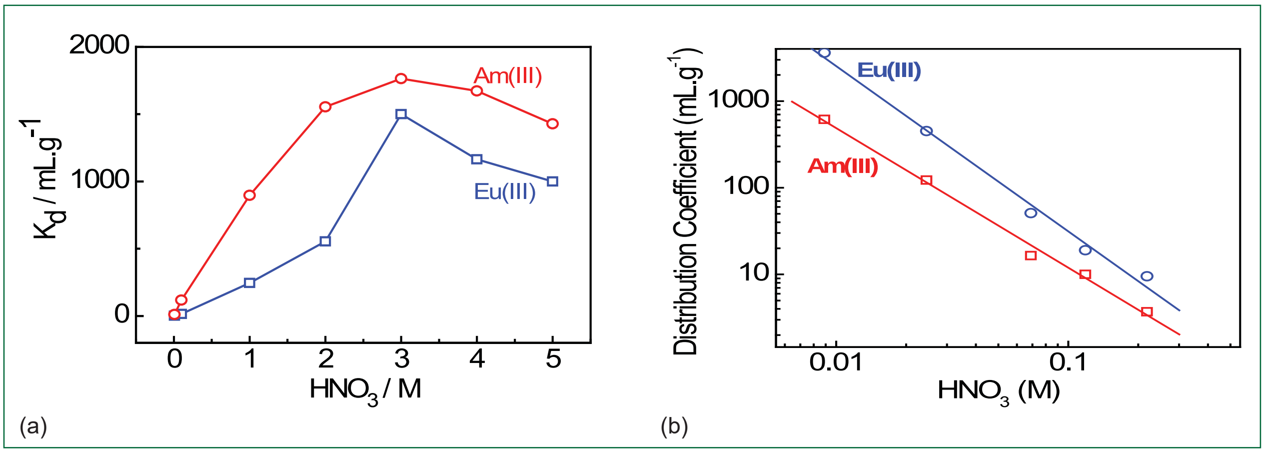

Fig. 2 Extraction of Eu(III) and Am(III) by (a) R-DOA resin and (b) PA-DGAH resin

recovery of metal ions from the loaded phase. The back extraction of Am(III) and Eu(III) from the loaded resin phase was carried out in batch mode, to understand the stripping behavior of Am(III) and Eu(III). The studies showed that the cumulative stripping of Am(III) and Eu(III) increased with increase in the number of contacts of stripping solution, in both cases, about 3 contacts are need for quantitative strippig of trilvent metal ions from the loaded resin phase using 0.01 M nitric acid. Therefore the study indicated the possibility of group separation of lanthanides and actinides using R-DOA from HLLW.

Mutual separation of Eu(III) and Am(III) by polyamine anchored diglycolamic acid resin

Diglycolamic acid anchored resin (PA-DGAH) is another PVP-DVB based copolymer needed for the mutual separation of Am(III) and Eu(III). It was syntheised by the condensation reaction between diglycolic anhydride and polyamide matrix (Tulsion A-10X-MP). The resin was characterized by FT-IR and NMR spectroscopy. The IR pattern obtained in PA-DGAH confirmed anchoring of diglycolamic acid on polyamine resin beads. The amount of diglycolamic acid present in a gram of resin was determined to be 2.5 mmol/g, which was in reasonable agreement with the amount of amine moieties (3 mmol/g), present in polyamine beads.

Extraction of Am(III) and Eu(III) in PA-DGAH

The adsorbent PA-DGAH, is a cation exchanger. The variation in the distribution coefficient of Am(III) and Eu(III) as a function of nitric acid concentration is shown in Figure 2b. It can been seen that the distribution coefficient of both metal ions decreases with increase in the concentration of nitric acid, indicating the involvement of cation exchange mechanism operating for the extraction of these metal ions in PA-DGAH. The mechanism of extraction of trivalent metal ion was determined from the slope analysis of the extraction data and it is represented as

$$\mathrm{M^{3+}_{eq} + NO^{-}_{3aq} + 2\,PA - DGAH_{sorb}} \\ \Leftrightarrow \mathrm{((PA - DGA)_2M(NO)_3)_{sorb} + 2\,H^{+}_{aq}}$$

Mutual separation of Eu(III) and Am(III)

The mutual separation of Eu(III) from Am(III) is necessary prior to transmutation, since lanthanides act as neutron poisons that reduce the efficacy of transmutation of actinides. Diethylenetriamine pentaacetic acid (DTPA) is an aqueous soluble N-donor ligand which preferentially complexes with Am(III) and retains Am(III) in aqueous phase as compared to Eu(III). Therefore DTPA has been used as aqueous complexing agent for increasing the separation factor of Eu(III) over Am(III). In the absence of DTPA the separation factor (quotient of Kd of Eu(III) and Kd of Am(III)) achieved for the extraction of these metal ions was very small (~4 to 5). The distribution coefficient of both the metal ions decreased with increase in the concentration of DTPA. However, the distribution coefficient of Am(III) decreased to a larger extent. Therefore, the separation factor increased from ~4 in the absence of DTPA to the value of 45 at the DTPA concentration of 0.05 M. Further increase in DTPA concentration did not change the separation factor to any significant extent. Therefore, it was desirable to use 0.03 to 0.05 M DTPA for the efficient separation of Eu(III) from Am(III) from dilute nitric acid medium.

Thus the study indicated that R-DOA resin is a promising resin for group separation of lanthanides and actinides from HLLW. After recovering the trivalents, lanthanide –actinide separation can be performed efficiently using PA-DGAH with high separation factors.

IV.15 Sensor-less Speed Measurement of Centrifugal Extractor Banks and Indication in Human Machine Interface

For Fast Reactor Fuel Reprocessing, centrifugal extractors are used as the contactors for solvent extraction. In CORAL, each centrifugal extractor's unit consists of a bank of sixteen stages (Figure 1). Each stage is driven by an individual 3-phase squirrel cage induction motor. The process requirement is that the speed of each motor should be maintained between 3300 and 3700 RPM, irrespective of the load. Measurement of the centrifugal extractor's motor speed with a sensor inside the hot cell has difficulties like unreliable measurement, disturbance of the sensor due to movement of materials and damage due to radiation environment. Also the variable frequency drive used to drive the motor does not give actual speed of the running motor. In view of the above, speed measurement of centrifugal extractor's induction motors in CORAL without any sensor using mathematical methods is needed.

A test bench was setup in the lab to carry out the testing and simulation of centrifugal extractor's induction motor speed from no load to full load condition with variable frequency drive. During the study, all parameters of the motor such as current, voltage, power factor etc. as well as parameters like load, actual speed using load cell and proximity switch were recorded. The above data were logged using Modbus communication from variable frequency drive into PC and calculations were carried out using mathematical equations.

Curve fitting using current as the input and speed as the output was done to establish the relationship between the two variables (Figure 2). A large set of data were obtained from the test rig before curve fitting exercise was carried out. After plotting for the curve the same set of data were tried with different degrees of polynomial equation to obtain the best fit. A software was used to generate the best fit and to determine the optimal coefficients of the polynomial equation. After trials, it was observed that the 5th degree polynomial equation gave the best result.

Fig. 1 Centrifugal extractor bank

$$\text{Motor speed (Y)} = P5 * X^5 + P4 * X^4 + P3 * X^3 + P2 * X^2 + P1 * X^1 + P0,$$

where P is the polynomial co-efficients and X is the current.

The equation derived was found to be applicable within the speed range of 2300-3700 RPM and the maximum error observed within this range was +5% at the minimum of the range as shown in Table 1.

Indication for the speed was provided in Human Machine Interface (HMI) in the Control Room of CORAL. The HMI communicates with the individual variable frequency drives by Modbus protocol. The HMI is a rugged system which provides for programming the display screens, operator inputs through touch screen, real-time computation of speeds and the control actions through ladder language.

The technique for the estimation of the speed of centrifugal extractor's motors without speed sensor has been implemented in CORAL and the speed is indicated in real-time in HMI in the control room of CORAL.

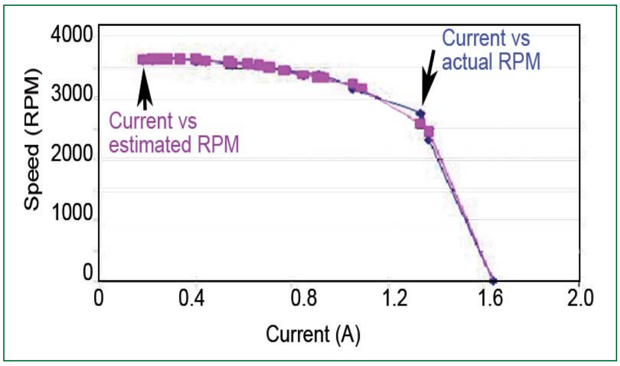

Fig. 2 Comparison of actual and estimated motor speeds

Table 1: Comparison of actual and estimated speeds

Sl. No.	Current (A)	Actual RPM	Estimated RPM	Error in %
1	0.22	3645	3654	0.24
2	0.55	3570	3596	0.72
3	0.85	3389	3405	0.47
4	1.05	3150	3226	2.36
5	1.37	2340	2458	4.81
6	1.64	0	0	0.00

IV.16 Status of Pyrochemical Processing R&D Facility

A pyrochemical method, based on molten salt electrorefining, commonly known as Pyroprocessing, is proposed for reprocessing of spent fuel from future metallic fuel FBRs. As part of the pyroprocessing technology development activities, an engineering scale facility called Pyro Processing R&D Facility is under construction. In this facility demonstration of two major process steps, viz. electrorefining and cathode processing, will be carried out for a batch size of 10 kg of uranium alloy. Un-irradiated pins containing slug of natural uranium will be processed in this facility.

The building housing the facility is of pre-engineered construction type. It is of 40 metre length, 21 metre width and 19.5 metre height. Construction of the building (Figure 1) and erection of 5 tonne EOT crane in the building has been completed. Main electrical panels and power distribution system has been commissioned. Erection of phase-1 of internal steel structure, on which major systems will be supported is completed.

A containment box of 500 m^3 volume provides the inert atmosphere required for the processes. Containment box fabrication works have been carried out at Central Workshop, IGCAR and erection at site (Figure 2) is in advanced stage. Pressure control in the containment box is achieved by two Argon Pressure Control Systems. Fabrication of feed and bleed tanks of APCS is nearing completion and other major components have been procured.

To maintain oxygen and moisture concentration below 50 vpm(each) and temperature of argon below 40°C inside containment box, argon recirculation and purification system (ARPS) is required. Detailed design of ARPS has been carried out and procurement action is in progress.

Electrorefining natural uranium pellets will be carried out in high temperature electro-refiner (HTER) and it will be housed inside containment box. Fabrication of HTER is under progress and expected to be delivered in the coming months.

Other system which will be housed inside containment box is automated vacuum distillation and melting system (AVDMS). Processing of the dendriitic deposits at cathode in HTER is carried out in this system. The AVDMS will be used to separate and consolidate Uranium from salt/Cadmium present in the product obtained from the electrorefining step. Design of the system was carried out in house and procurement action is in progress. Salt Handling and Purification System (SH&PS) is another system of PPRDF housed outside the containment box. Eutectic mixture of LiCl and KCl will be used as electrolyte in the electorefining process. SH&PS is to reduce the moisture content present in the commercially available LiCl and KCl. This system consists of a salt drying unit, chlorination unit, salt storing vessels and chlorine scrubbing unit. Salt storing vessels and chlorine scrubbing unit have been procured. Fabrication of chlorination unit is nearing completion.

Fig. 1 *Facility building*

Technical Specifications have been prepared for service utilities for the facility which include argon supply and distribution system, chilled water system, nitrogen generation system and compressed air system. Only Low level Liquid Wastes (LLW) will be generated in this facility. Two 5 m^3 (each) tanks are provided outside the building for temporarily storing this waste before transporting it to CWMF. Fabrication of these tanks is also nearing completion.

Fig. 2 *Containment box erection in progress*

IV.17 3D Modelling and Animation of Power Manipulator and Containment Box of Pyroprocessing R&D Facility

Pyro-processing Research & Development facility is being setup for demonstrating important process steps of pyro-processing technology. For housing process equipment related to electro-refining and cathode processing stages of pyro-processing technology, a large inert atmosphere Containment Box is being fabricated at Central Workshop. All operations inside the containment box will be either automated or carried out remotely using a Power Manipulator. The aim is to create a virtual 3D model of the containment box housing the power manipulator for the purpose of checking for interference with various process equipments before physical erection and studying the feasibility of remote operation and maintenance prior to execution (Figure 1). This visualization will also be used for operator training. It consists of modeling in 3D in 1:1 scale, assembly, programing interactive animation, motion constraints and interactive visualization.

The containment box is of 500 m^3 capacity (19 (L) x 3.5 (W) x 6 m (H)). It is being erected on a steel support structure. The containment box consists of stainless steel panels with viewing windows, lighting ports, material transfer ports, manipulator housing ports etc. The upper part of the containment box consists of a chamber that houses the power manipulator and a 5 ton EOT crane. The Power Manipulator is mounted on the gantry bridge with long travel and cross travel rails. It is designed to handle up to 25 kg payload. The power manipulator is having seven degrees of freedom viz. telescopic Z - axis, azimuth (rotation about vertical axis), shoulder rotation, elbow rotation, wrist rotation, rotation with gripper and gripping action. Various parts of the Power Manipulator are the long travel and the short travel carriages, telescopic motion tubes, shoulder unit for azimuth rotation and shoulder rotation, the elbow unit, the wrist unit and the gripper.

The 3D models of steel support structure, containment box and power manipulator have been created in 1:1 scale dimensions and assembled. Suitable materials were applied to the part models. Gripper motion was animated in animation software.

Fig. 1 *3D model of power manipulator inside containment box*

The models and animation were ported to a visualization platform. To capture the movement, rendering elements such as cameras, lights, 3D and 2D text frames were introduced. All the degrees of freedom of the power manipulator have been implemented by scripting in the behavioral engine. Motion constraints have been applied to all the movements in accordance to the design specifications. To give a high degree of familiarity to the operator, a virtual control panel similar in appearance to the actual control panel has been created. The controls on the virtual panel have been mapped to various degrees of freedom. All the designated functions of the power manipulator can be controlled using the virtual panel. 3D models of process equipment, such as Tilting station, Scrapping Station, EAD Station and Electro-Refining Station have been imported and placed inside the containment box at their respective locations.

The various challenges met and overcome during development are

1) Implementation of interactive control and motion constraints on long travel, cross travel, telescopic Z - axis, azimuth (rotation about vertical axis), shoulder rotation, elbow rotation and wrist rotation.
2) Implementation of virtual control panel by scripting.
3) Integration of gripper finger animation prepared in an external platform into the visualization and controlling the same inside the behavioral engine

Finally the 3D models and animations were exported to Advanced Visualization Centre for 3D visualization.

IV.18 Development of Simulation Model for Spent Metal Fuel Electrorefining

Construction of a Pyro Process R&D facility in FRTG for demonstrating the process steps of pyrochemical reprocessing using 10 kg per batch alloy of natural uranium is in progress. One of the important process steps i.e. electrorefining of alloy of natural uranium will be carried out in High Temperature Electro Refiner (HTER). The experience from this facility will be utilized in design of pyroreprocessing plant for Metal fuel reactor. As part of this, an Ambient Temperature Electrorefiner (ATER) (Figure 1) was erected and commissioned with an objective of validating the mechanism design, hydrodynamic studies and simulating electrorefining process using Cu/Cu^{2+} system.

The development of simulation code for electrorefining of spent metal fuel will help in understanding the electrorefining process and determination of important process parameters, such as electrode surface area, deposition rate, current required, applied cell voltage, and change in concentration of major and minor actinides in salt and cadmium phase with time. It also helps in reducing the number of uranium electrorefining experiments in HTER. Simulation of molten salt electrorefining process is a multiphysics problem, such as electrochemical reaction at the electrode surface, mass transfer of metal ions in electrolyte, potential distribution in the electrolyte and overall material balance of metal ions in coupled manner. Copper electrorefining experiments in ATER and in laboratory scale gives the initial base for simulation and development of electrorefining model and finally helps in validation of the code.

Modelling of the copper electrorefining process to simulate ATER and lab scale electrorefining experiment was done using elctrodeposition module of COMSOL multiphysics software. The model helps in determining the amount of copper deposit in cathode, the current density distribution on the electrode surface, and cell voltage. The average current density estimated from the simulation matches with current density determined from the experiment within 5%. Also the current density distribution on the cathode surface predicted using the model shows that the current density is maximum at bottom edge, where deposits were maximum as found in the experiment.

Fig. 1 *ATER facility*

During uranium electrorefining, it is essential to obtain dendritic deposit on solid cathode so that subsequent mechanical separation of uranium is easier and efficient. Deposit morphology is dependent on the current density and is found to occur at 1800-2000 A/m^2 for both uranium and copper. Also the copper electrorefining studies in ATER and lab scale for improving the throughput gives reasonable indication of the suitable electrode configurations for uranium electrorefining.

Initial ATER copper electrorefining experiments were carried out to know the effect of different operating parameters like stirrer RPM, anode rotation, etc on current density. Later studies to determine current efficiency and cell constant were carried out. The parameters for dendritic deposit were finalized based on labscale studies and modeling was demonstrated in ATER.

To know the effect of stirrer speed on current density with same applied cell potential, copper electrorefining experiments for different stirrer speeds were carried out in ATER. Further experiments were also carried out to know the effect of anode rotation on current density. From these experiments it was observed that the anode rotation has no effect in increase of current density but the rise in stirrer speed gives rise to increase in current density. Electro deposition study of Copper in solid cathode to determine the current efficiency was also carried out in ATER. The cell voltage was kept such that no parallel reaction takes place at the electrode surface. The current efficiency of the electrorefining operation was 98%, which concludes that there is no short circuiting of electrode or polarization of electrorefiner vessel. The total current passed is almost equivalent to the amount of copper deposited on the cathode.

The electrolytes resistance depends on electrolyte conductivity and electrode configuration i.e cell constant. Since the geometry and distance between the electrodes in ATER will be approximately same as that of HTER, experiments were carried out to determine directly the cell constant for HTER.

Experiments in laboratory scale were also carried out to study the deposit morphology of copper for various current densities (800-4000A/m^2). Scale up parameter such as specific cathode area and space time yield in laboratory scale was kept similar to ATER. It was observed that at lower current density the deposit is very hard and difficult to scrape out whereas at higher current density the deposit is very loose and falls off very easily. The optimal current density for getting scrapable deposits was observed in the range of 1800 to 2200 A/m^2. In order to validate these observations, electrorefining experiments were carried in ATER at same optimum current density (2000 A/m^2). The deposit morphology was dendritic as shown in Figure 2. It was observed that the deposit was non uniform along the length of the cathode. The deposition rates were higher at the bottom of the solid cathode because of high localized current densities.

After successful simulation and validation of copper electrorefining process for ATER using COMSOL multiphysics software the simulation was extended to actual spent fuel electrorefining. These simulation model includes all three types of overpotential i.e., activation, concentration and resistance. The model has been used to compute the evolution and distribution of each element in the system in the various phases as a function of time and operating conditions. The validation of simulation model is done using reported data available in the literature. The results show a good agreement within the available experimental data in literature within 10%. Figures 3 and 4 present the validation of the model with experimental data reported. The variation of concentration of U and Pu in the molten salt with time is shown in Figure 3. The concentration of uranium and plutonium was almost same in the molten salt in the initial stages and as the deposition of U on the cathode proceeded, the U concentration became lower in the later stages. At this point, Pu also gets deposited. Fig. 4 shows the amounts of U and Pu deposited on the solid cathode with the progress of electrorefining.

Fig. 2 *Dendritic morphology of copper deposit*

A kinetic model for the electrorefining process has been developed using the various modules of the COMSOL Multiphysics software to simulate electrorefining process for spent metal fuel. The electrorefining experiment using copper in ATER and lab scale subsequently helped in the validation of the model. Also the valuable inputs obtained during ATER experiments were useful for improving the design of HTER.

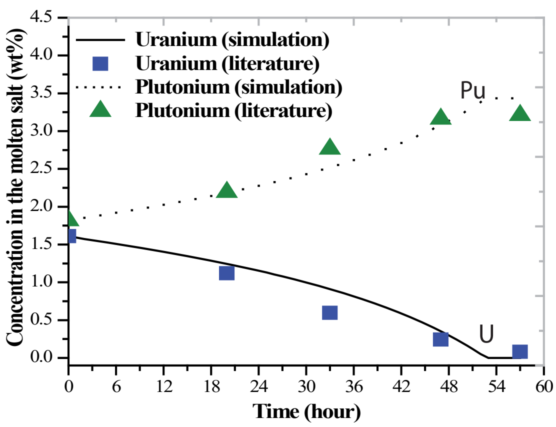

Fig. 3 *Concentration of uranium and plutonium in the molten salt model validation with reported experimental data*

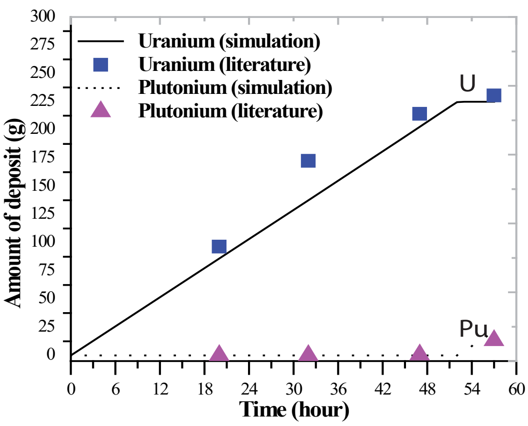

Fig. 4 *Deposition histories of uranium and plutonium on the solid cathode model validation with reported experimental data*

IV.19 Pyrochemical Reprocessing Studies on Uranium and Plutonium at Liquid Cadmium Electrode

Pyrochemical reprocessing methods are high temperature electrochemical methods ideally suited for spent U-Pu-Zr fuels for the separation of actinides from fission products. It employs LiCl-KCl as electrolyte operated at 773 K. The separation scheme is based on the thermodynamic stabilities of chlorides of actinides and fission products in LiCl-KCl. In order to investigate the electrochemical studies on plutonium, electrorefining of U-Pu-Zr was carried out in a lab scale facility comprising of a train of inert atmosphere glove boxes kept at pressures of 20 mm of water column negative with respect to the ambient. The studies were carried out at liquid cadmium cathode. The anode basket consisted of SS-430 basket containing cut pieces of U-19Pu-6Zr (wt.%) alloy rods. The reference electrode and working electrode were respectively, Ag/AgCl and liquid cadmium. The electrochemical cell assembly consisting of these electrodes is shown in Figure 1a.

Five electrorefining runs were carried out for studying the co-deposition of uranium and plutonium at liquid cadmium electrode. The cyclic voltammogram of LiCl-KCl containing $PuCl_3$ is shown in Figure 1b.

Electrorefining was carried out both employing constant potential and constant current techniques. The exchange current density for anodic dissolution of U-Pu-Zr and cathodic co-deposition of uranium and plutonium at liquid cadmium electrode was found to be 0.6 and 15 mA/cm^2, respectively. The U-Pu-Zr alloy rod after the completion of a typical run is shown in Figure 1c.

The cadmium cathode used for co-deposition of uranium and plutonium was subsequently re-melted after the completion of electrorefining runs and consolidated in ingot and rod forms, shown in Figure 1d.

The Cd ingot and rods were subsequently analysed for uranium and plutonium by gamma ray spectroscopy. Further experiments are in progress in recovering uranium and plutonium from Cd matrix.

The electrorefining cell usually has a cadmium pool at the bottom for collecting zirconium and fission product elements falling from the anode basket during electrorefining. Loose uranium dendrites also might fall into the cadmium pool from the cathode rod. Studies were carried out to recover uranium from cadmium pool by making it as anode.

240 grams of LiCl-KCl eutectic salt having 6.5 wt.% of UCl_3 was used as electrolyte. 236 g of cadmium-uranium alloy containing 1.23 wt.% of uranium and a uranium rod (9 grams) immersed in it was taken as anode whereas SS-430 rod was taken as cathode. Electrorefining was carried out at 773 K at constant current mode in the current range of 100-500 mA. The total amount of the deposit with occluded salt on the cathode was 17 grams. Current efficiency of the run was calculated to be 74%. A typical uranium deposit is shown in Figure 1e.

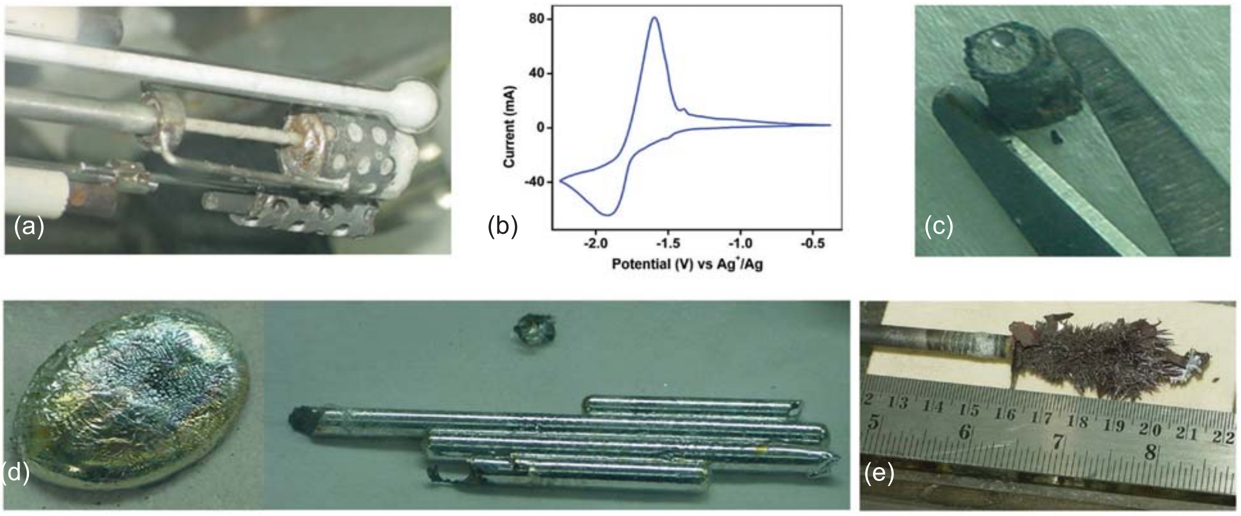

Fig. 1 (a) Electrochemical cell assembly for plutonium experiments, (b) cyclic voltammogram of LiCl-KCl eutectic containing $PuCl_3$, (c) typical cross-section of U-Pu-Zr alloy rod after an electrorefining run, (d) Cd ingot and rods containing uranium and plutonium and (e) typical uranium dendrites obtained from electrorefining run employing liquid cadmium pool as anode

IV.20 Dissolution of Zirconium Containing Metallic Alloy Fuels and Development of Analytical Method for Spectrophotometric Determination of Zirconium

In the fuel cycle of metallic alloys, estimation of zirconium in the presence of other elements is essential for controlling the processes at various stages, the reputed methods of analysis for the estimation of zirconium either by spectrophotometry or by gravimetry have some limitations.

In the present work, dissolution of Zr containing metallic alloy fuels such as U-Zr and U-Pu-Zr with varying amounts of Zr (2-10 wt%) was carried out in

(i) nitric acid media under reflux conditions,

(ii) HNO_3-HF medium and

(iii) using electro oxidative technique with cerium as the oxidizing agent.

Dissolution of U-Pu-Zr alloy in HNO_3-HF medium indicates that complete dissolution of U, Pu and Zr was possible. Dissolution of U-Zr metallic alloys in HNO_3 medium indicated that more than 98 wt% of U was dissolved in all the cases and about ~30 wt% of Zr only was dissolved under these experimental conditions. Results also indicate that even in 8M HNO_3 complete dissolution of U was possible and the percentage dissolution of Zr was found to be similar as in the case of 12M HNO_3. A black residue was settled at the bottom of container. Dissolution of metallic alloys by EODT (Electro Oxidative Dissolution Technique) indicated there was no enhancement in the dissolution of Zr compared to dissolution with traditional nitric acid reflux method. In order to compare the reflux and EODT methods, dissolution studies were carried out under identical conditions such as temperature, sample weight, and dissolution period and results indicated that dissolution kinetics were similar in both these methods i.e. EODT and reflux (Figure 1).

A systematic study was carried out for the determination of zirconium in the presence of uranium (U:Zr=1000:1). The absorbance of zirconium complex remains unaltered with uranium concentration indicating that uranium doesn't interfere in the analysis of zirconium. An attempt was made to estimate zirconium in the presence of plutonium as well. The absorbance of zirconium complex was found to increase with Pu(IV) concentration, indicating interference of Pu(IV) in the estimation of Zr. Hence suitable masking/reducing agents were identified for the reduction of Pu(IV) to Pu(III). These studies indicated that ascorbic acid is a suitable reducing agent for the determination of Zr in the presence of Pu(IV) (Figure 2). The combined effect of Pu(IV) and U(VI) in the estimation of Zr was studied and the results indicated that the absorbance of Zr-complex remains constant over a wide range of Pu and U concentration. This method has been employed for the estimation of Zr in various samples generated during the dissolution of Zr containing metallic alloy fuels.

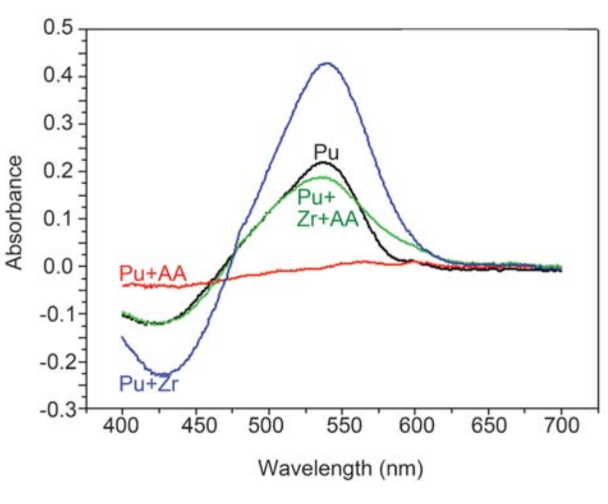

Fig. 1 *Absorption spectra of Zr and Pu with xylenol orange with and without ascorbic acid*

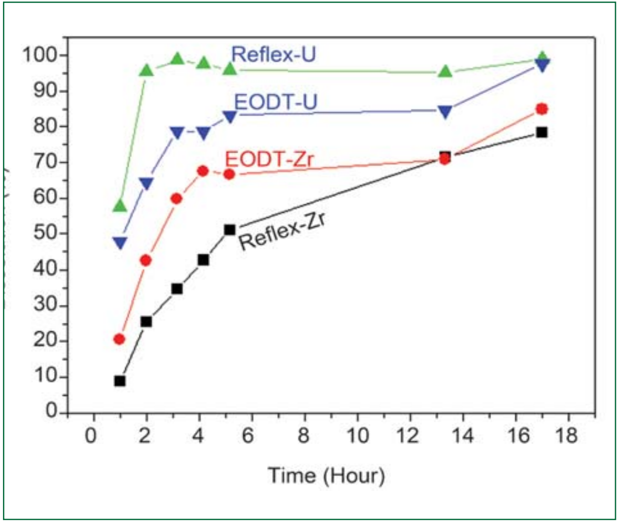

Fig. 2 *Comparison of dissolution kinetics of U and Zr in U-Zr metallic alloys*

IV.21 Platinum Nanoparticle Coated Titanium Electrodes for Reprocessing Applications

Electrochemical processes are some of the vital steps involved in the aqueous reprocessing of spent fuel discharged from fast breeder reactors. The ability of the electrode to withstand high current density and provide high current efficiency in concentrated nitric acid medium is extremely important to carry out the electro-oxidative dissolution process for the dissolution of plutonium-rich oxide fuels remotely, for longer durations in radioactive environment. The electrocatalytic activity of high performance electrodes arises as a result of excellent surface reactivity, good electronic and ionic conductivity and facile mass transport of molecules. Pt is considered as a very good electrocatalyst as it can catalyze substances at highly anodic potentials without being decomposed and it also posesses excellent thermal stability. However, cost effective Pt coated anodes are preferred over pure Pt for plant applications. Recent developments in nano- technology and surface engineering accentuate the effect of size and structure of noble metal based nano particles in improving the electrochemical activity. The increased active surface area, efficient mass transfer for reactant molecules and improved electron mobility make Pt, or noble metal based nanostructures superior to their bulk or solid counter parts. Hence, Pt nanoparticle coated Ti based electrodes were developed for reprocessing applications via a seed mediated hydrothermal reduction method. The advantage of using this two-step synthesis method over other conventional synthesis methods is in obtaining a uniform and completely covered nanoparticle coated surface with strong adhesion.

Fabrication of Pt nanoparticle coated Ti electrode

Pt seeds were first electrodeposited on pre-treated Ti surface after optimizing deposition parameters. These Pt seeded Ti samples were then hydrothermally reduced in a teflon lined stainless steel autoclave using a Pt based solution and chemical reducing agent for 10 h at 100°C. The as-synthesized electrodes were characterized using Field Emission Scanning Electron Microscopy, XRD technique, XPS and AFM. Further, the performance of the synthesized electrode was also evaluated by employing it for the oxidation of cerous ion, which is used as a mediated electrochemical catalyst.

Surface characterization

The Pt nanoparticle coated Ti surface was morphologically characterized using FESEM and AFM. It was observed that the entire surface was completely covered with nano Pt particles after hydrothermal reduction with pre seeded Pt. Figures 1a and 1b correspond to the FESEM images after hydrothermal reduction, without and with electrodeposition. The XRD (Figure 1c) and XPS analyses confirmed the presence of fcc Pt in metallic state. Good adhesion strength (5B) was observed between the coating and substrate in cross hatch test.

Cyclic voltammetric study in H_2SO_4 medium showed that the charge required for hydrogen monolayer adsorption on Pt nanoparticle coated Ti was 108 times higher than that of polycrystalline Pt surface.

Performance of the nano Pt coated Ti, polycrystalline Pt coated Ti and Pt electroplated Ti electrodes were investigated by employing them as anodes in the oxidation of Ce^{3+} ions under an applied current in 11.5 N nitric acid. Pt nanoparticle coated titanium accomplished 100% conversion of Ce^{3+} to Ce^{4+} within 2.5 hours, whereas both polycrystalline Pt coated Ti and commercially available Pt electroplated titanium anodes could oxidise Ce^{3+} completely after 4.5 hours (Figure 1d). The durability of nano Pt coated Ti electrode was further tested in the oxidation of cerous ions in concentrated nitric acid medium continuously for 1000 hours. It was observed that even after 1000 hours, Pt coating was intact with minor degradation, confirming its excellent activity, stability and durability in nitric acid medium.

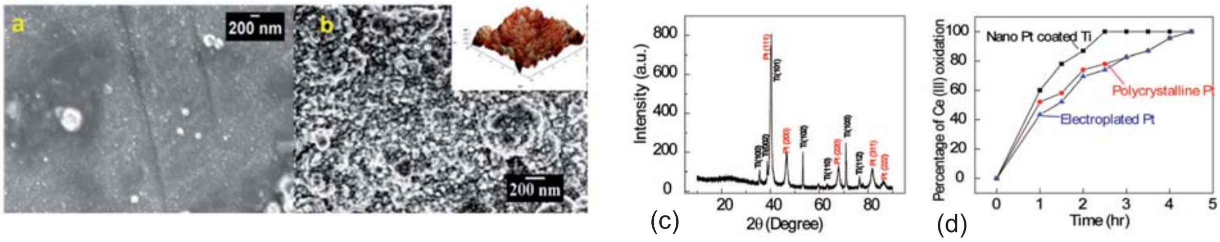

Fig. 1 *(a) and (b) hydrothermally coated Pt on Ti with and without electrodeposition, (c) XRD of Pt coated Ti anode and (d) rate of oxidation of Ce (III)*

IV.22 Direct Electrochemical Conversion of Solid Uranium Dioxide to Uranium Metal

Electrochemical conversion of metal oxides to metal by high temperature molten salt electrolysis is a new method of producing metals directly from their solid oxides. In this method the oxide in its solid form is made the cathode against an appropriate anode, generally graphite or platinum, in molten chloride electrolyte containing small amounts of its oxide. Under the influence of applied potential, the oxygen present in the oxide electrode gets ionized as O^{2-} ions and migrate to the anode and discharge there as carbon oxides (on graphite anode) or oxygen gas (on platinum anode). The schematic of the process for reduction of UO_2 with platinum anode in LiCl- Li_2O melt is given in Figure 1.

The new process has some merits over the conventional chemical reduction of metal oxides. The intermediate step of conversion of the oxide to halide and handling of reactive metals are not required in the new process. Unlike in conventional electrolysis, the oxide is not dissolved in the electrolyte, but remains as a solid block during the oxide to metal conversion. These aspects make the process a simple one. The method of preparation and physico-chemical characteristics of the oxide electrode are critical to the success of the process.

In the context of metal fuel fast reactors, a programme was initiated at Chemistry group to study the electro-reduction of solid UO_2 to U metal. The process (Figure 1) was conducted in the constant current mode of electrolysis at 650 °C. The lithium metal produced by electrolysis of Li_2O present in the LiCl melt chemically reduces the UO_2 electrode to U metal. The cell and cell reactions are as follows;

Apart from the above reactions, a small extent of reduction will also occur by the oxygen ionization mechanism, viz. $UO_2(s) + 4e = U + 2O^{2-}$.

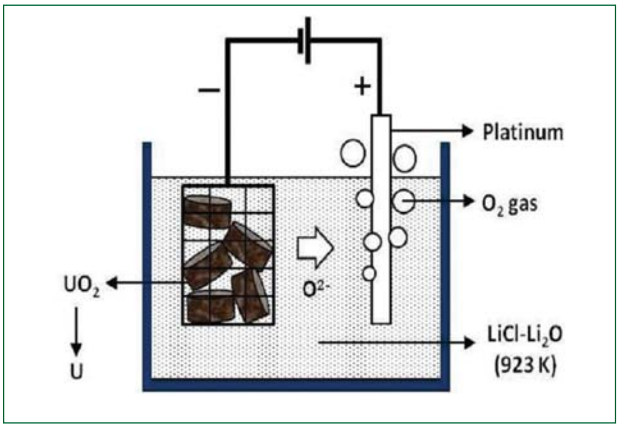

Fig. 1 *Schematic showing electro-reduction of UO_2*

Cell: Pt/LiCl-1wt.% Li_2O/UO_2

Cathode: $2Li^+$ (in melt) + 2e $\rightarrow$ 2Li

$2Li + UO_2 \rightarrow U + Li_2O$ (in melt)

Anode: O^{2-} (in melt) $\rightarrow$ O_2 (g) + 2e-

Net reaction: $UO_2(s) \rightarrow U(s) + O_2(g)$

Cylindrical pellets of UO_2 (6mm dia. x 10 mm long, porosity ~40%) were prepared in-house by powder compaction followed by sintering in (Ar+8% H_2) atmosphere at 1600 °C. The pellets weighing ~ 100g, contained in SS wire mesh baskets (Figure 2a), were electrolysed against platinum coil anode (Figure 2b) in LiCl-1wt.% Li_2O melt at 650 °C. The salt adhering to the processed pellets was distilled off under vacuum at 850 °C and representative samples were analysed for uranium metal present by measurement of H_2 gas produced in a reaction of the samples with HBr. The extent of conversion of UO_2 to U was thus estimated as >98%. The processed pellets were subjected to induction melting to consolidate the U metal formed (Figures 2c and 2d).


(a) (b) (c) (d)

Fig. 2 *(a) UO_2 pellet feed (100g) (b) platinum coil anode (c) processed pellets and (d) consolidated uranium metal*

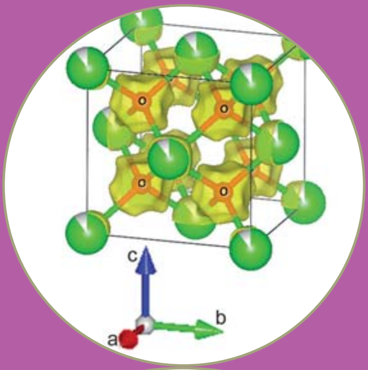

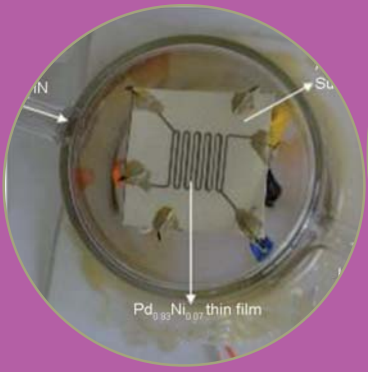

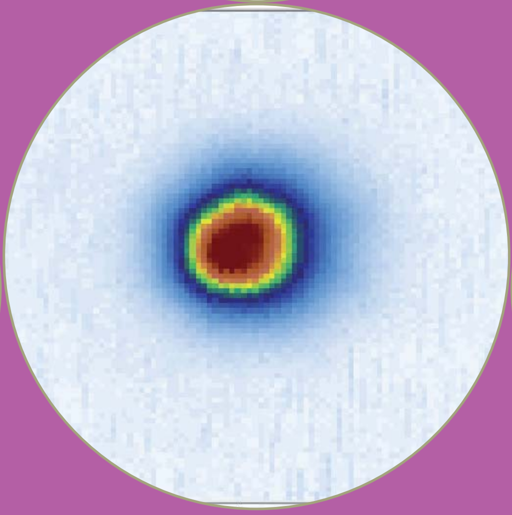

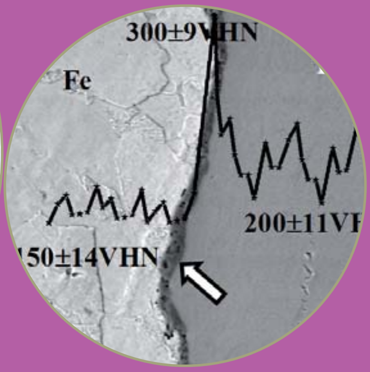

CHAPTER V

Basic Research

V.1 Production and Characterization of Enriched Para-Hydrogen for Matrix Isolation Infrared Studies

Normal hydrogen (n-H_2) contains 3:1 ratio of ortho and para forms. The production of enriched para-hydrogen (p-H_2 > 99%) is useful for several experimental techniques such as nuclear magnetic resonance, matrix isolation spectroscopy and superfluidity studies. As the ground state of p-H_2 molecule is spherically symmetric, when used in the matrix isolation experiments, the guest – host interaction is minimized. The p-H_2 solid has hexagonal closed packed structure and large amplitude of zero-point lattice vibration and hence the environment around the guest molecule is homogeneous. These properties usually result in sharp spectrum in p-H_2. Pure p-H_2 gas can be produced by passing the n-H_2 gas in a controlled manner through a catalyst kept under low temperature.

Design and fabrication of ortho/para converter

A closed cycle helium cryostat is modified to produce p-H_2. An ortho/para(o/p) converter consisting of a copper bobbin made from OFHC copper block with grooves was fabricated. A ¼" copper tube filled with hydrated Iron (III) oxide as a catalyst was wrapped over the grooves and silver soldered to give good contact. After activating the catalyst the bobbin was fixed to the cold head of the cryostat as shown in Figure 1.

Production of p-H_2

In order to produce pure p-H_2 the temperature of the bobbin was brought to 13.5 K using the closed cycle helium cryostat. After reaching the temperature, normal H_2 gas from a mixing chamber with a backing pressure of ~600 torr was slowly allowed to pass through the o/p converter using a gas dosing valve. The normal hydrogen undergoes a phase change to liquid. During this phase transition there is no increase in the downstream pressure. Once the phase change is complete, the pressure in the downstream slowly increases, indicating the production of p-H_2 gas. In order to increase the gas flow at the downstream, the upstream pressure is increased to ~1200 torr while constantly monitoring the temperature of the cryostat to remain at 13.5 K. The parameters such as backing pressure of the hydrogen gas, needle valve setting were optimized to get the pure p-H_2 gas.

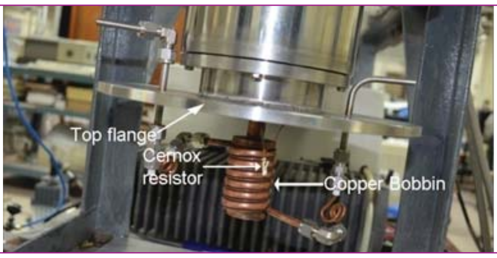

Fig. 1 *Bobbin attached to cold head of the cryostat*

Determination of %o-H_2 impurity in p-H_2

The p-H_2 gas collected from the downstream is analyzed by Raman spectra and low temperature infrared spectra. Figure 2 compares the Raman spectra of n-H_2 and p-H_2 gas produced from the o/p converter at 13.5 K and 30 K. The features observed at 4158.7, 4129.0 and 587.7 cm^{-1} are due to $Q_1(1)$, $Q_1(3)$ and $S_0(1)$ transitions of o-H_2, respectively. At 13.5 K these features were absent where as at 30 K a weak peak at 587.7 cm^{-1} was observed indicating a small percentage of o-H_2 present in p-H_2. Figure 3 shows the IR absorption spectra of solid n-H_2 and p-H_2. The IR spectra of solid p-H_2 revealed a strong $S_1(0)$ absorption line at 4485.9 cm^{-1}, a very strong double transition $Q_1(0)$ + $S_0(0)$ and $Q_1(1)$ + $S_0(0)$ line at 4510.3 and 4503.1cm^{-1} and a weak $Q_1(0)$ + $S_0(1)$ line at 4739.6 cm^{-1} were observed. Broad feature at 4152.8 cm^{-1} corresponds to the $Q_1(0)$ of o-H_2. The integrated area of the double transition line is used to obtain the thickness of the pH_2 solid. The % o-H_2 impurity in p-H_2 solid is obtained from the thickness of the matrix and the area of the $Q_1(0)$ transition at 4152.8 cm^{-1}. The %o-H_2 at 13.5, 20 and 25 K was calculated to be 0.7, 2.3 and 3.6 respectively, clearly showing that the purity of p-H_2 depends on the temperature of the bobbin.

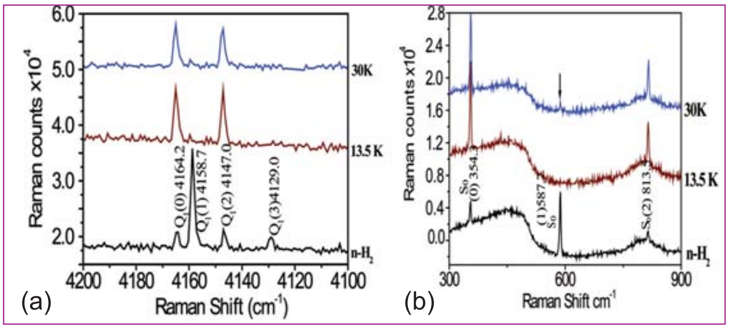

Fig. 2 *Raman spectra of normal and para-H_2 at 13.5 K and 30 K at (a) 4100 - 4200 cm^{-1} and (b) 300 - 900 cm^{-1}*

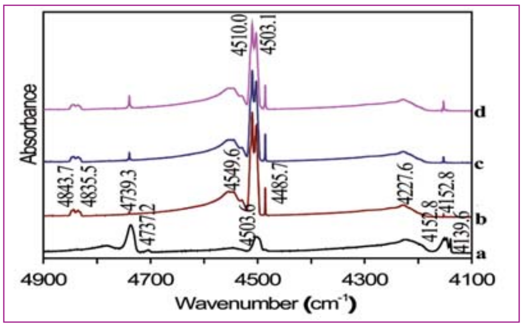

Fig. 3 *Infrared absorption spectra spanning the region 4900-4100 cm^{-1} (a) n-H_2 ; p-H_2 at different temperatures (b) 13.5 K (c) 20 K and (d) 25 K*

V.2 Effect of Ion Irradiation in Iron Phosphate Glass

The aqueous high level waste (HLW) originating from fast reactors is largely different from that of thermal reactors. Iron phosphate glass (IPG) is considered as a suitable glass matrix for the immobilization of fast reactor waste containing higher concentration of Cs, rare earth, Mo and Cr. Basically, glass matrix provides the large open volume and the leach resistance required to incorporate wide range of ions and molecular clusters within its network.

The central issue in nuclear waste disposal is the modification of the glass matrix by the α-particles and the recoiling heavy nuclei resulting from actinide decay. These effects can be simulated by ion irradiation experiments. In the present work, the structural stability of IPG under ion irradiation is reported.

IPG samples containing 40 mol% Fe_2O_3 and 60 mol% P_2O_5 (IPG) were irradiated with 4 MeV O^+ ions at room temperature using 1.7 MV Tandetron Accelerator. Ion irradiation was carried out upto different ion fluences ranging from 5×10^{13} ions/cm^2 to 5×10^{16} ions/cm^2. The samples were studied using HRTEM .

The presence of hollow rings in the electron diffraction pattern (Figure 1a) and the HRTEM image (Figure 1b) of the as prepared sample confirm its amorphous nature. The spotty rings in the electron diffraction pattern (Figure 1c) of the irradiated specimen confirm the presence of nanocrystalline phases. The HRTEM image (Figure 1d) of the irradiated sample clearly shows the presence of lattice fringes in the amorphous background. The rings in Figure 1c and the *d* values in Figure 1d are indexed to the phases $Fe_4(P_2O_7)_3$, $Fe(PO_3)_3$ and P_2O_5. It may be noted that IPG is reported to undergo an eutectic phase transition and crystallize into $Fe_4(P_2O_7)_3$ and $Fe(PO_3)_3$. In summary, it is observed that ion irradiation on IPG has led to the nucleation of different nanocrystalline phases. It is also observed that crystallisation takes place even at low ion fluence and the size of the nanocrystals increases with the ion fluence.

Crystallization of an amorphous solid is a complex process. In general, the amorphous to crystalline phase transformation is activated by thermal energy. But, in the present work, stress induced crystallization mechanism is invoked to explain the ion induced crystallization phenomena. IPG glass phase is stable compared to metallic glass phase (critical cooling rate of IPG is very small), and hence it would require large amount of energy to crystallize which is not available in the present case. So, thermally induced crystallization is ruled out.

SRIM calculations show that in the case of 4 MeV O^+ ions in IPG, the nuclear energy loss (~5.5 eV/nm) is negligible compared to the electronic energy loss (~1.67 keV/nm). So the energy is deposited predominantly by means of excitation and ionization of the electronic system. Further, the rapid energy transfer abnormally excites the material along the ion path whereas the surrounding is relatively at lower temperature. The pressure wave formed in the wake of the projectile ion can generate an outgoing transient stress and strain. When the stress within an amorphous material increases beyond a critical value, shear bands are formed. Shear bands contain homogenously distributed excess free volume. The excess free volume is the analogue of vacancies in crystalline materials and the excess free volume controls the diffusion rate in amorphous materials. This enhances atomic mobility and leads to increased short-range order and subsequent nucleation at longer time scales. The effect of the single ion induced local stress σ_{stress} is estimated using visco-elastic model (700 MPa), and it is found to be larger than the yield strength of glasses (typically 70 MPa). Hence, the surrounding matrix undergoes a substantial deformation resulting in shear band formation. Nanocrystals could have been nucleated in the vicinity of shear bands that are induced during thermal spike process.

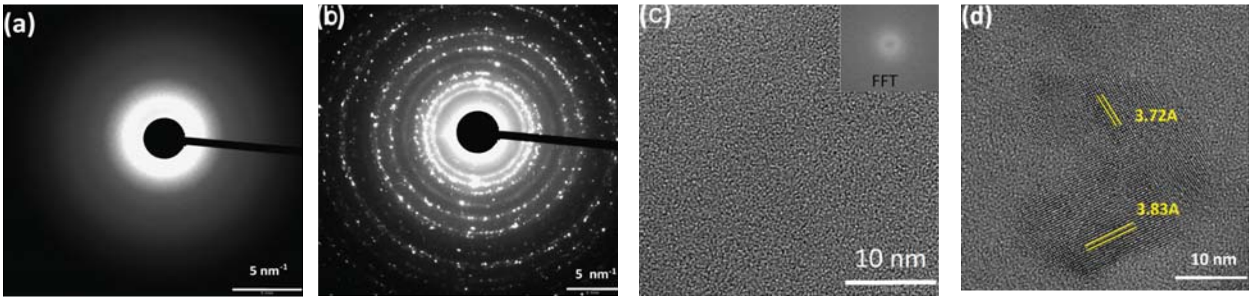

Fig. 1 *(a) & (b) electron diffraction patterns and (c) & (d) the HRTEM images of as prepared and irradiated IPG samples respectively*

V.3 Structure of Iron Phosphate Glass: Molecular Dynamics Simulation

Higher waste loading, better chemical durability and better corrosion resistance are certain promising features of iron phosphate glasses for waste handling. The better chemical durability is attributed to the presence of more hydration resistant Fe-O-P bonds compared to P-O-P bonds available generally in phosphate glasses. Available information on the structural modelling of iron phosphate glasses is limited. This is because, amorphous structures are more difficult to handle computationally than crystalline lattices since many different atomic configurations are possible. In addition, the structure of iron phosphate glasses not only depends on the composition, quenching temperature of the melt and quenching technique, but also on the concentration of Fe^{2+} and Fe^{3+} ions in the glass. Among the various composition of iron phosphate glass, the one with 40 mol % Fe_2O_3-60 mol % P_2O_5 labelled as IPG is found to be more chemically durable. However, this composition has been reported by various researchers to have different $Fe^{2+}/\Sigma Fe$ ratio. Thus it is essentail to model the structure of iron phosphate glasses specific to composition and $Fe^{2+}/\Sigma Fe$ ratio.

Molecular dynamics simulation code LBOMD was used to model the structure of glass. The two body interactions, i.e. Fe-O, P-O and O-O were modelled using a Buckingham rigid ion potential together with a Coulomb term to model the long-range interactions between ionic charges. In addition to the two-body terms, three body Stillinger – Weber potential was used to model the O-P-O and P-O-P interactions. Each of the glass structure was prepared by distributing the required number of atoms of each species randomly within a cubic box. Systems were quenched from 6000 to 10 K at a rate of 5 x 10^{12} Ks^{-1} using temperature–rescaling algorithm with constant volume molecular dynamics. The temperature of system was measured at each time step and if the temperature exceeds the desired value by 7 %, then, the velocities of all the atoms are rescaled, such that, the temperature is at the desired value. Finally the structures were minimised to 0 K using the conjugate gradient method. Molecular dynamics computation was carried out on these iron phosphate glasses contained in a cubic box with a small (~ 150) number of atoms with a varying Fe/P atomic ratio. The total number of atoms varied depending on the Fe/P atomic ratio. The potential energy of iron phosphate glasses was analysed as function of density to obtain the structure with the lowest potential energy, and hence the optimal density for each glass. Structure of glasses were then computed with large number of atoms (1100-1500) at the optimal density. The details of the composition of the sytems of iron phosphate glasses studied and the number of atoms quenched are given in Table 1. In order to compare the structures, the potential energy per atom was determined and found that system energy increases with both increasing Fe/P atomic ratio and Fe^{2+} concentration. Thus the more chemically durable iron phosphate glass with composition of 40 mol % Fe_2O_3-60 mol % P_2O_5 (IPG) need to possess minimum concentration of Fe^{2+} ions for better stability. Typical structure of IPG containing 4 % Fe^{2+} concentration is shown in Figures 1 and 2.

Table 1: Composition of various iron phosphate glasses

Sample code	Composition (at %)				Number of atoms
	Fe^{2+}	Fe^{3+}	P^{5+}	O^{2-}	
FePO-1	4.76	9.52	19.05	66.67	1260
FePO-2	-	7.69	23.08	69.23	1300
FePO-3	-	12.9	19.36	67.74	1550
IPG4	0.51	12.24	19.54	67.71	1372
IPG17	2.27	11.0	19.42	67.31	1190

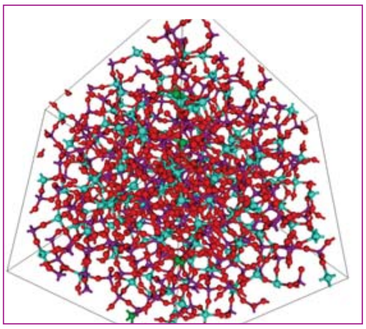

Fig. 1 *Structure of IPG4 containing 4 % Fe^{2+} concentration*

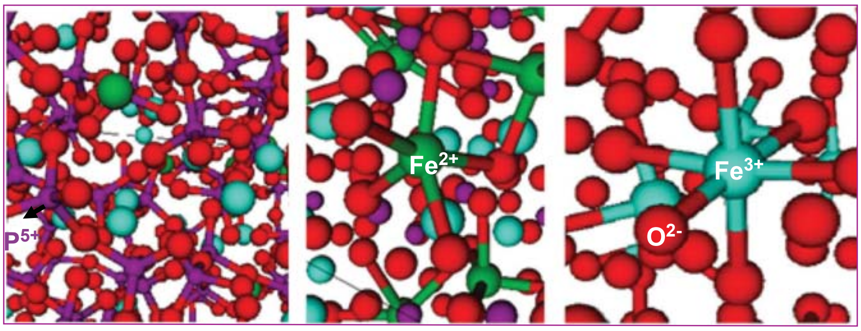

Fig. 2 *Snap shot view showing various ions in IPG4; (certain bonds are not connected for better viewing purpose)*

V.4 Atomic Scale Study of the Effect of Cesium Doping in Iron Phosphate Glasses

In this study the glass of composition $60P_2O_3$-$40Fe_2O_3$ is investigated for local structural changes and stability with Cs loading in the iron phosphate glass.

This work is aimed at understanding the local structure and valence of Fe ions in iron phosphate glass of composition $60P_2O_3$-$40Fe_2O_3$(mol%) loaded with different concentrations of Cs using ^{57}Fe based Mossbauer spectroscopy. The spectrometer is operated in transmission geometry and in constant acceleration mode. Measurements were done at room temperature and the spectra were analysed to obtain hyperfine parameters such as isomer shift (δ), quadrupole splitting (Δ) and the relative area (Ai) quantifying the fraction of Fe atoms associated with the parameters.

Mossbauer spectrum obtained with sample could be deconvoluted in to three doublets as shown in Figure 1 and the corresponding hyperfine parameters are shown in the Table 1. Based on the values of isomer shifts the two doublets (i=1,2) are attributed to Fe^{3+} valence and the third doublet to Fe^{2+} valence. Predominant fraction of Fe atoms are associated with Fe^{3+} experiencing quadrupole splitting of the order of 0.4 mm/sec. These sites are understood to be associated with tetrahedral sites. Another Fe^{3+} site associated with high quadrupole splitting close to 1 mm/sec is understood to be due to Fe^{3+} occupying octahedral sites which are distorted. The third doublet with high values of isomer shift and quadrupole splitting is understood to be due to Fe atoms with valence +2 and occupying octahedral sites. Fe^{3+} ions act as a network former in tertahedral or distorted octahedral coordination while the Fe^{2+} ions act as a network modifier in octahedral coordination. The results show that for beyond 15% of Cs loading there is an increase in Fe^{3+} at the cost of Fe^{2+}.

Concomitantly, exceeding 15% of Cs loading the relative fraction of Fe with valence 3+ and occupying octahedral sites is observed to decrease indicating an onset of changes in local structure resulting in the changes in network formers and modifiers. Mossbauer results are consistent with the evident signatures of disproportion of pyrophosphate linkages beyond 18 mol% Cs loading as deduced using Raman spectroscopy.

Table I: Results of Mossbauer parameters

% Cs	i	δ_i mm/s	Δ_i mm/s	A_i	Identification
0	1	0.32	0.92	0.6	Fe^{3+} - octahedral
	2	0.33	0.44	0.32	Fe^{3+} - tetrahedral
	3	1.02	2.2	0.08	Fe^{2+} - octahedral
6	1	0.32	0.94	0.58	Fe^{3+} - octahedral
	2	0.33	0.48	0.32	Fe^{3+} - tetrahedral
	3	1.02	2.2	0.1	Fe^{2+} - octahedral
18	1	0.32	1.05	0.47	Fe^{3+} - octahedral
	2	0.33	0.55	0.44	Fe^{3+} - tetrahedral
	3	1.02	2.2	0.09	Fe^{2+} - octahedral
35	1	0.33	0.98	0.44	Fe^{3+} - octahedral
	2	0.33	0.57	0.56	Fe^{3+} - tetrahedral

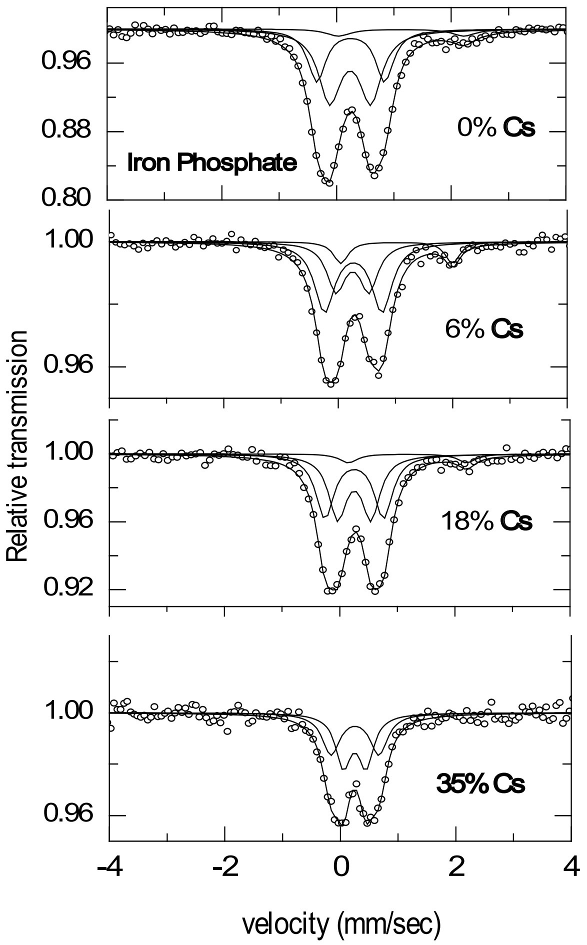

Fig. 1 *Mossbauer spectra obtained in iron phosphate glass loaded with different percentage of Cs*

V.5 Bulk Synthesis of Nanocrystalline Urania using Citrate Gel-Combustion

UO_2 and $(U,Pu)O_2$ mixed oxide are used as the driver fuel for fission nuclear reactors worldwide. Recent investigations on the fuels of both Light Water Reactors (LWR) fuels as well as Fast Breeder Reactors (FBR) have revealed that in these fuels after prolonged irradiation a unique microstructure called the high burn-up structure (HBS) is observed (grain size 100–300 nm). These studies had further revealed that in the LWR fuel the HBS is limited to the rim of the fuel while in the FBR fuel it could be found over an extended region. This phase possesses are favorable in-pile properties such as higher retention of major fission gases, higher stress relaxation through higher plasticity and less severe radiation damage compared to the conventional microcrystalline nuclear fuel. However, investigations on the synthesis of nanocrystalline actinide oxides are rather limited. Hence experiments pertaining to bulk synthesis of quantities of nanocrystalline (nc) UO_2 have gained prominence.

In view of the above an experimental procedure was devised to produce (about 60 g per batch of) free flowing urania powders with crystallite size ranging from 30 to 250 nm by using citrate gel-combustion method. The optimum composition of the combustion mixture defined by the fuel (citric acid) to oxidant (nitrate) mole ratio (R) was identified to be 0.25.

The bulk density, specific surface area, distribution of sizes among pores and particles of the urania powders showed a strong dependence on the value of R. The total pore volume of these powders was inversely correlated with their corresponding bulk density.

The specific surface area (SSA) of urania powders derived through citrate gel combustion method was comparable with those pertaining to the powders derived through ammonium diuranate (ADU), dry ADU and ammonium uranyl carbonate (AUC) processes.

The X-ray diffraction analysis of these powders revealed that they were nanocrystalline. The dimensionless lattice strain obtained from the Hall-Williamson treatment of the X-ray diffraction data revealed many interesting aspects. The lattice strain in all these powders was positively correlated with their X-ray crystallite size (XCS), indicating that larger the crystallite the more was the strain.

A detailed analysis of the XCS revealed that when the powders coarsen and become microcrystalline (XCS > 100 nm) the strain approaches a constant value.

It appears that the gel-combustion derived UO_2 powders are pseudomorphic (Figure 1). Microstructural investigation of selected samples revealed the presence of nanocrystals with macropores (Figures 1 and 2b) with interconnected porosity (Figures 1 and 2a). High magnification image of these powders revealed broccoli like" exfoliated morphology with embedded features comprising faceted cubic crystals and faceted cuboidal pores. The selected area electron diffraction (SAED) pattern pertaining to these powders confirmed that the "calcined" (Figure 2d) and "hydrogen reduced" samples comprised orthorhombic α-U_3O_8 (Figures 2c and 2d) and fluorite UO_2 respectively.

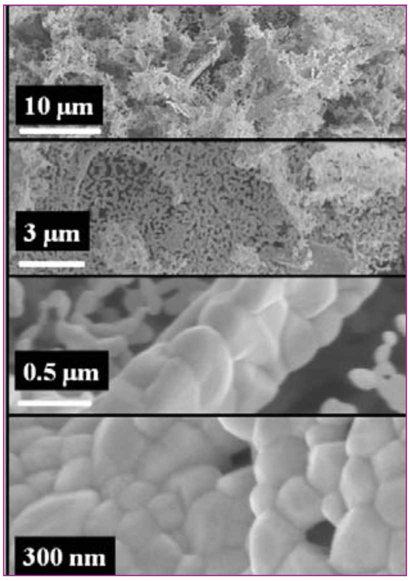

Fig. 1 SEM images of "calcined" urania powers with an R value of 0.25

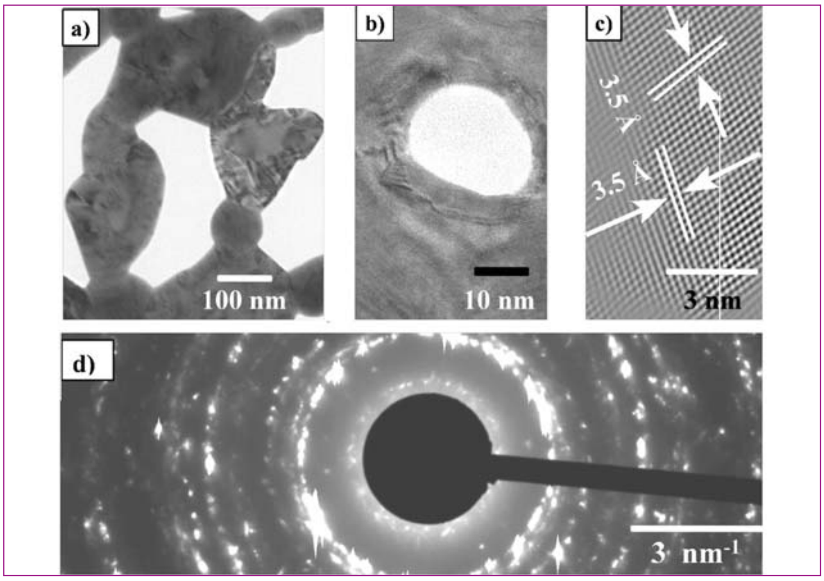

Fig. 2 TEM images of "calcined" urania powders: (a) bright field image revealing nano grains; (b) a typical nano pore; (c) HRTEM image and (d) SAED image

V.6 Novel Soft-chemical Approach for the Synthesis of Palladium Alloys and their Application in Hydrogen Sensing

Nano particles of the alloys of palladium with nickel ($Pd_{0.97}Ni_{0.03}$ & $Pd_{0.93}Ni_{0.07}$) was prepared by a novel low temperature chemical reduction (LTCR) technique using sodium borohydride as the reducing agent in acetone at 300 K. Such synthesized metal and alloys were made as thin films using pulsed laser deposition. The photograph of the assembled thin film sensor in glass chamber is shown in Figure 1. The resistance of the thin film was measured between 2000 and 20000 ppm of hydrogen in argon at 300 K using four probe technique.

XRD patterns of the powders of Pd, $Pd_{0.97}Ni_{0.03}$ and $Pd_{0.93}Ni_{0.07}$ exhibited the characteristic reflections of palladium only, indicating that nickel enters in the lattice positions of palladium. Similar observations were made with the thin film samples also.

Figures 2a shows the typical change in resistance of $Pd_{0.93}Ni_{0.07}$ thin film on its exposure to argon containing hydrogen in the concentration range of 2000 - 20000 ppm at 300 K. Figure 2b shows the plot of sensitivity

$$\left(\frac{\Delta R}{R}(\%)\right)$$

as a function of square root of partial pressure of hydrogen (atm$^{1/2}$) for Pd, $Pd_{0.97}Ni_{0.03}$ and $Pd_{0.93}Ni_{0.07}$ thin films at 300 K. A linear relationship between sensitivity and square root of hydrogen partial pressure is exhibited by all the films between 2000 and 20000 ppm of hydrogen. From the figure, it is evident that the sensitivity towards hydrogen increases with increase in the nickel content in the alloy, when compared with pure palladium thin film. The studies show promise for development of hydrogen sensor for monitoring its levels in the range of thousands of ppm in argon stream.

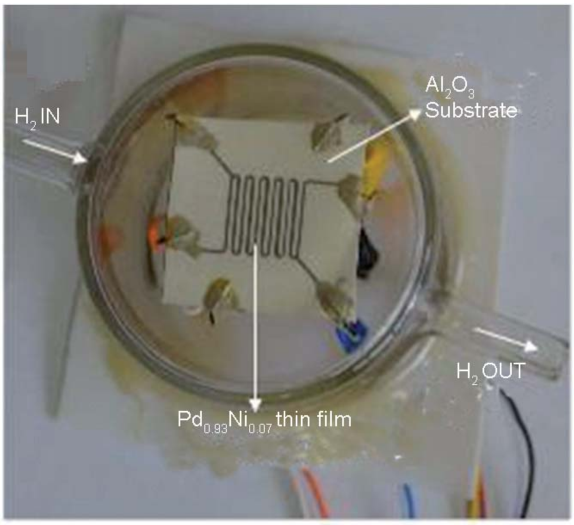

Fig. 1 *Photograph of Pd thin film installed in a glass chamber (top view)*

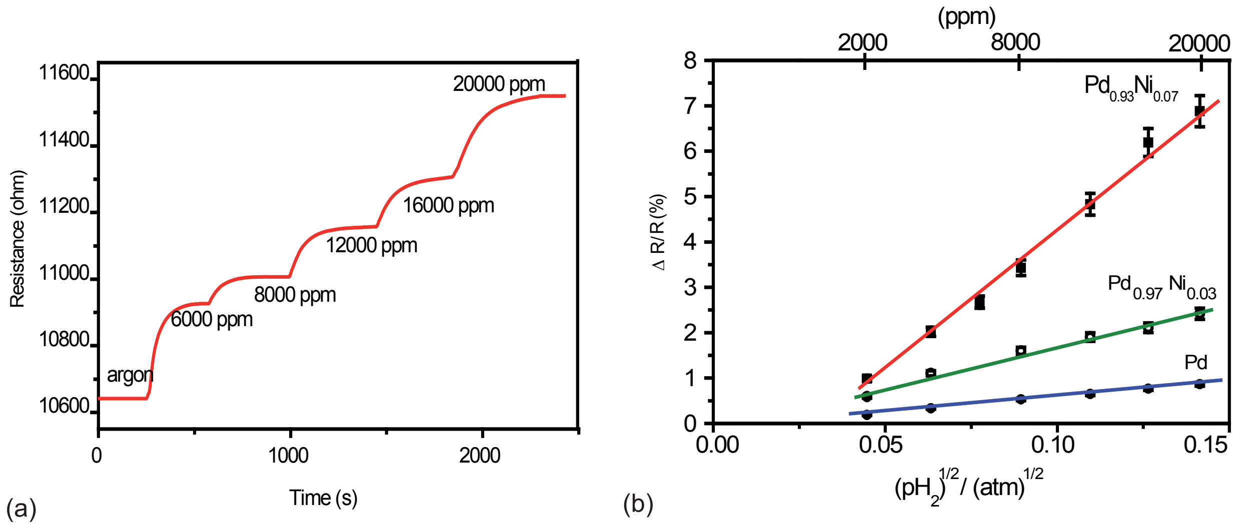

Fig. 2 *(a) Typical change in resistance of $Pd_{0.93}Ni_{0.07}$ thin film towards different concentrations of hydrogen in argon at 300 K and (b) sensitivity vs (P_{H_2}/atm.)$^{1/2}$ plot for thin films at 300 K*

V.7 Array of Sensors and Methodology for Distinguishing Analytes

It is known that semiconducting metal oxides (SMOs) are sensitive to gas ambience. Analyte molecules either react with chemisorbed oxygen or chemisorbs on the surface of the SMO in preference to that of oxygen and alter the charge carrier concentration. This chemical phenomenon is utilized in the development of miniaturized, rugged and low power operating thick or thin film gas sensors.

Most of the SMOs are not selective towards a single analyte. They show some degree of cross sensitivity towards different analytes. By considering the differential kinetics of adsorption, reaction and desorption, in principle one can distinguish the analytes both qualitatively and quantitatively. But, relying on a single sensor output in sensing multiple analytes leads to ambiguity in analysis. This can be overcome by considering an array of sensors having differential selectivity towards multiple analytes. The signals from the sensor array for different analytes have to be processed using statistical tools such as pattern recognition (PR). Different components of pattern recognition system are shown in Figure 1.

Among the listed components feature extraction and classification involves the processing of n-dimensional data from 'n' different sensors. Several supervised and unsupervised learning tools such as Maximum-likelihood estimation (MLE), Principal component analysis (PCA), Factor analysis (FA), and Artificial neural networks (ANN) etc. are applied for this data mining. An unsupervised learning methodology namely, principal component analysis is being explored. The m by n data matrix containing responses for 'm' features such as different compositions of gases from 'n' different sensors (variables) is processed using PCA. This n-dimensional response feature will be projected on 2-dimensional principal component space by maintaining maximum changes in variance among the data.

Table 1: Thick film sensors tested towards different analytes

Sensor label	S1	S2	S3	S4	S5	S6	S7	S8	S9	S10	S10
Composition	$FeNbO_4$			$Cr_{0.5}Fe_{0.5}NbO_4$			$CrNbO_4$				
Operating temprature/ (K)	598	623	648	598	623	648	573	598	623	648	673

Thick film sensors of $Cr_{1-x}Fe_xNbO_4$ with x = 0.0, 0.5 and 1.0 were fabricated by screen printing. These thick films were operated at different temperatures tested with 200 ppm each of six different analytes viz., methanol, acetone, acetonitrile, cyclohexane, petroleum gas and hydrogen individually. The sensors and their operating temperatures are presented in Table 1. All the analytes respond in a similar way and it is highly impossible to distinguish analytes using individual sensor sensitivity. By considering the variation in desorption kinetics, principal component analysis was performed on maximum slope change feature derived from all the 11 sensors towards the response for 12 samples (2 of each analyte).

The PCA resulted in the distribution of analytes and sensors in 'scores' and 'loadings' plot respectively (Figures 2 and 3). Scores plot clearly shows the qualitative discrimination of individual analytes irrespective of their cross sensitivity. Loadings plot shows the individual grouping of all $CrNbO_4$ and $Cr_{0.5}Fe_{0.5}NbO_4$ sensors. Among three $FeNbO_4$ sensors, S2 and S3 are grouped together. This shows the redundancy in the behavior of different sensors operated at different temperatures. From this study, it can be suggested that with four sensors array consisting of two $FeNbO_4$ sensors (S1 and one between S2 & S3), one $Cr_{0.5}Fe_{0.5}NbO_4$ (among S4 to S6) one $CrNbO_4$ (among S6 to S11) will have the capability of discriminating these analytes with similar distribution in PC–space.

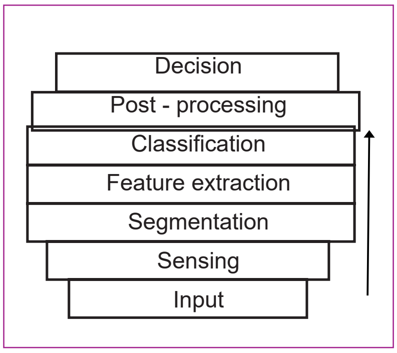

Fig. 1 Components of pattern recognition system

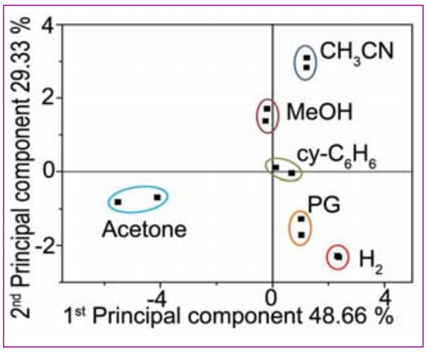

Fig. 2 Distribution of analytes in PC-space(scores plot)

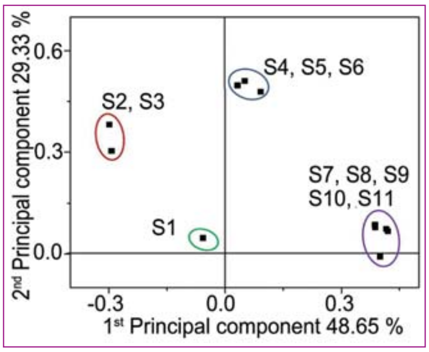

Fig. 3 Distribution of sensors in PC-space (loadings plot)

V.8 Calorimetric Measurements on U-19Pu-6Zr Alloy

Heat capacity of the fuel materials is essential for determining the thermodynamic properties of fuel materials which are required for understanding the various chemical interactions that are likely to occur during the irradiation of the fuel as well as for modeling the behavior of the fuel and to predict the performance of the fuel under accidental conditions. No experimental data are available in the literature for U-19Pu-6Zr (wt.%) alloy. Hence in the present study, enthalpy increment measurements were carried out on U-19Pu-6Zr alloy in the temperature range 653-1300 K by inverse drop method by using a high temperature differential calorimeter. The fuel samples are prone to oxidation and hydrolysis in the presence of oxygen and moisture and are also highly pyrophoric. Hence for carrying out the calorimetric measurements on these radioactive samples, the calorimeter has been attached to a leak tight glove box with high purity argon atmosphere maintained at a negative pressure of 25 mm water gauge with respect to the ambient and having an oxygen and moisture content of <10 vpm (volume per millions) each.

The samples were dropped from ambient temperature into the calorimeter maintained at the experimental temperature and the resultant heat flows were measured. Measurement on each U-19Pu-6Zr alloy sample at a given experimental temperature was sandwiched between the measurements on two α-alumina reference samples. The enthalpy increment measurements by calorimetry were standardized by carrying out measurements on ThO_2. The overall error in these measurements was thus ascertained to be ±2.5%. The temperature of the sample was measured within an accuracy of ±0.5 K. The measured enthalpy increments were fitted to a polynomial in temperature, by using the least squares method. The calculated equations for enthalpy increment (J/mol) and specific heat (J/mol/K), and the temperature ranges (K) of validity, are given in Table 1.

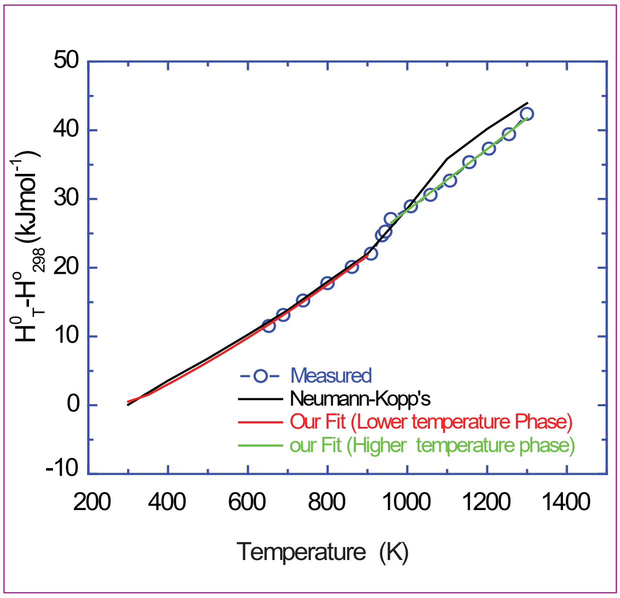

***Fig. 1** Enthalpy increments of U19wt%Pu6wt%Zr alloy*

From the fit equation, the values of other thermodynamic functions, namely, entropy and Gibbs energy functions in the temperature range 298-1300 K were computed.

The measured enthalpy increments value of U-19Pu-6Zr as well as those computed using Neumann-Kopp's value from the recommended enthalpy data of uranium, plutonium and zirconium are shown in Figure 1. The present study provides the first experimental enthalpy increment data and the heat capacity data in the temperature range of 653-1300 K for U-19Pu-6Zr.

Table 1: The calculated equations
for enthalpy increment, specific heat, and the temperature ranges (K) of validity

	Enthalpy increment, H^0_T-H^0_{298} (Jmol^{-1}) =A(T/K) +B(T/K)^2+ C(T/K)+D				Specific heat, C_p (J/mol/K) =A + B(T/K) - C(T/K)^2			Temperature ranges (K)
	A	B*10^3	C*10^{-5}	D	A	B*10^3	C*10^{-5}	
1	11.580	20.203	- 4.154	-3855	11.580	40.407	4.154	298 - 910
2	42.304	2.077	13.550	-17342	42.304	4.155	-13.550	960 - 1300

V.9 CALPHAD Modelling of U-Zr Binary System

A study of phase stability of metallic fuels is important for studying fuel restructuring during irradiation, which could be performed by coupling thermodynamic databases with kinetic simulation. A thermodynamic database consists of consistent set of Gibbs energy functions, which are obtained by thermodynamic optimization of all the stable phases. One of the motivation is to have a thermodynamic database for U-Pu-Zr-Fe system, in which U-Zr is one of the sub-systems. The thermodynamic optimization of U-Zr binary system was performed by coupling new experimental data, ab initio methods and CALPHAD methodology.

There are five phases in U-Zr system: liquid, alpha-U (orthorhombic), beta-U (tetragonal), alpha-Zr (hexagonal), gamma-(U,Zr)(bcc) and delta (UZr_2). The first four phases were modelled as random substitutional solution. The delta phase was modelled using a two-sublattice model using Wagner-Schottky constraint, wherein Zr and U are present as defects in the first and second sublattice, respectively.

The U-Zr system is characterized by four three phase equilibria: monotectoid at 966 K involving beta-U and bcc, eutectoid at 935 K involving ortho-U, beta-U and bcc, peritectoid at 890 K involving alpha-U, bcc and delta, and eutectoid at 879 K involving alpha-Zr, delta and bcc.

New experimental data on U-Zr included the recent solidus–liquidus measurements, inverse-drop calorimetry of U-Zr alloys and ab initio calculations, which were carried out in Chemistry Group. The thermodynamic optimization of U-Zr was carried out using Thermo-Calc databank system.

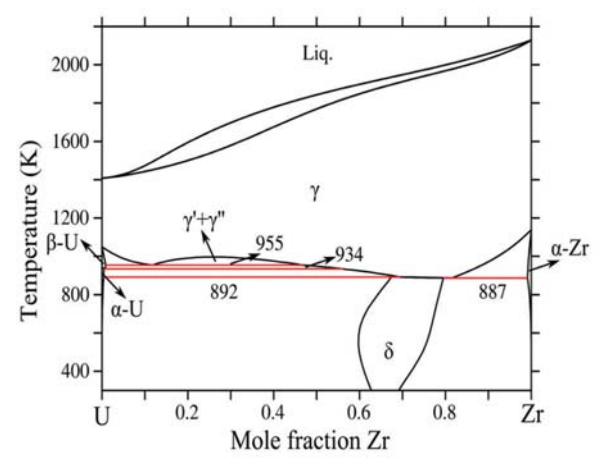

Fig. 1 *Calculated U-Zr phase diagram*

The calculated phase diagram is shown in Figure 1. The calculated phase diagram is in good agreement with the reported phase diagram in the literature. The calculated invariant reactions also are within ±10 K. A comparison of the solidus - liquidus phase boundary with the literature data is shown in Figure 2.

A comparison of the energy of mixing of the bcc phase with the ab initio data obtained in the present work and literature data is shown in Figure 3.

The present Gibbs energy functions will be used for developing a thermodynamic database for U-Pu-Zr alloys. Currently, a renewed assessment of U-Pu system has been taken up in our laboratory.

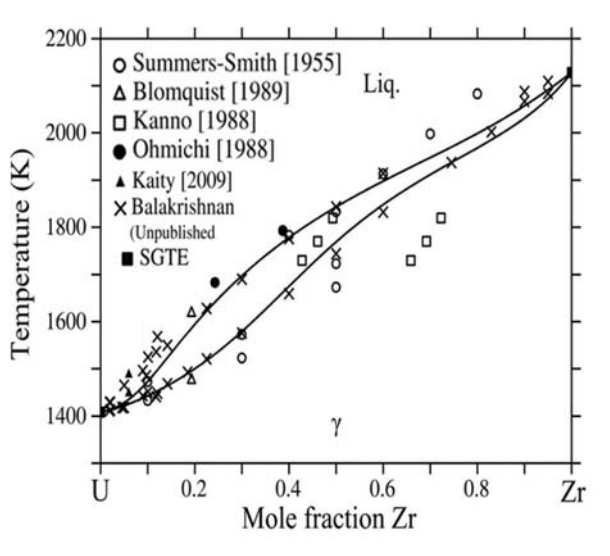

Fig. 2 *Comparison of solidus and liquidus phase boundary*

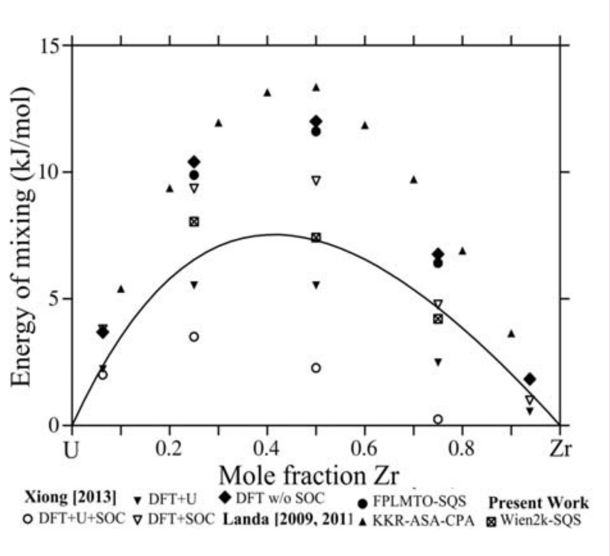

Fig. 3 *comparison of the energy of mixing of the bcc phase with the ab initio data*

V.10 Instrumentation for Tin Oxide based Hydrogen Sensor using Microcontroller

Tin oxide based hydrogen sensor

In this sensor heater and sensor films are integrated on a miniature alumina substrate and necessary electrical leads are taken out.

Due to physical constraint, temperature sensor could not be embedded on the heater surface. Hence, heater temperature control is achieved by a feedback control circuit for temperature maintenance. The sensor output (voltage signal) varies with H_2 concentration.

Instrumentation

The electronics developed to measure sensor signal and to control the heater temperature is discussed. The temperature control for the sensor heater is effectively implemented in a novel way. A suitable linear signal conditioning circuit for measuring the sensor conductivity is also included. Long term performance of the sensor and temperature control is achieved.

Sensor signal measurement circuit

The tin oxide based hydrogen sensor's conductivity is dictated by the hydrogen gas concentration. The sensor resistance varies from 2 to 100 kΩ corresponding to 2 to 80 ppm of hydrogen concentration.

Figure 1 shows block diagram of sensor signal measurement circuit and display unit. A voltage to frequency converter digitizes the output voltage and the digital signal is transmitted by a RS422 line driver to the signal processing unit. The frequency signal is received by a RS422 differential line receiver. The frequency signal is converted into voltage by a frequency to voltage converter.

The typical response characteristics of a sensor system towards different concentrations of hydrogen (2 to 80 ppm) were studied and one such is shown in Figure 2.

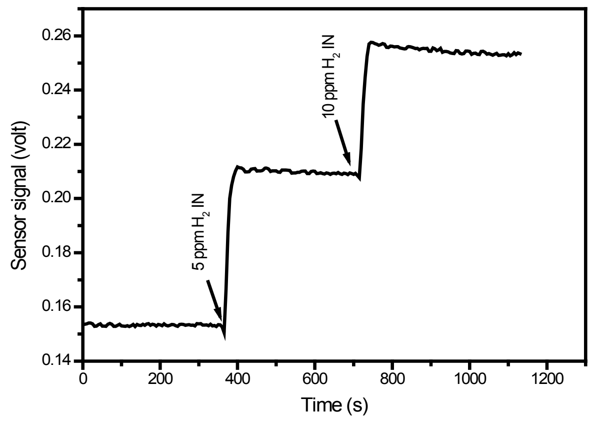

***Fig. 2** Sensor response signal for hydrogen measurement*

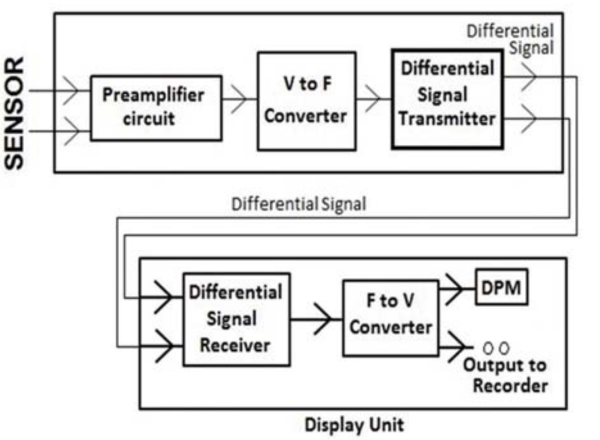

***Fig. 1** Sensor signal instrumentation – block diagram*

Heater temperature control circuit

Temperature of the heater is maintained by a microcontroller based feedback control circuit as shown in Figure 3a. This is achieved by maintaining heater resistance constant by controlling the voltage across the heater and current through it.

The heater control circuit is standardized for different heater resistance values and can be used to maintain a constant temperature. Figure 3b shows that heater temperature is maintained at 350°C with a stability of of ±0.25 °C.

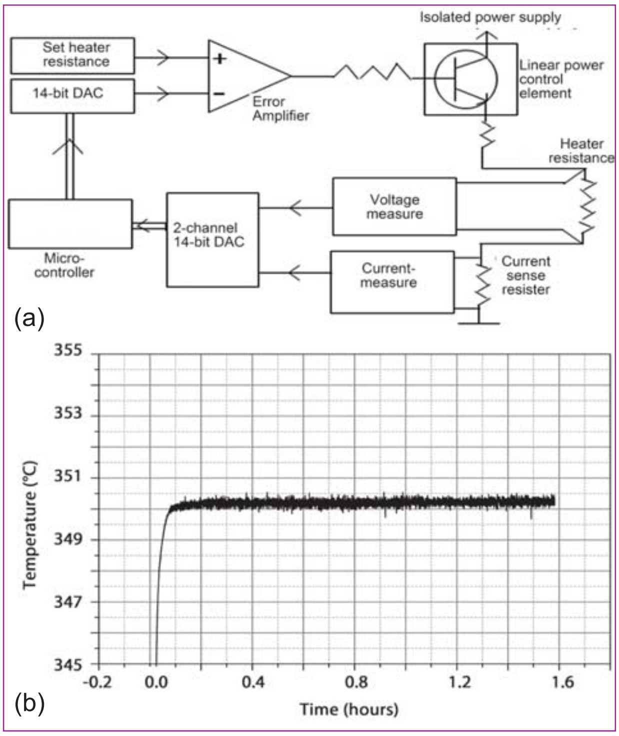

***Fig. 3** (a) Heater control circuit block diagram and (b) heater temperature stability*

V.11 Thermodynamic Properties Over ($Ni_2Te_3O_8$ + $NiTe_2O_5$) in the Ni–Te–O System: Transpiration Thermogravimetric and Knudsen Effusion Mass Spectrometric Studies

Tellurium is one of the volatile and reactive fission products generated during nuclear fission. It can attack stainless steel (SS), the most commonly used cladding material in fast-breeder nuclear reactors and hence play an important role in fuel–clad chemical interactions. In continuation of our program to generate thermodynamic data on tellurium and its compounds with oxygen or clad components (Fe, Cr, Mo, Mn and Ni) or both, vaporisation studies over ($Ni_2Te_3O_8$+$NiTe_2O_5$) in the Ni-Te-O system were carried out by Knudsen effusion mass spectrometry (KEMS) and transpiration thermogravimetry (TTG) in the temperature ranges of 950–1060 K and 850–950 K respectively. From vapour pressures, enthalpies of solid–gas and gas-phase equilibria and subsequently enthalpy and Gibbs free energies of formation of $NiTe_2O_5(s)$ were derived. A thermochemical calculation was performed to assess the possibility of formation of the ternary $NiTe_2O_5(s)$ phase on the stainless steel clad of mixed-oxide fuelled fast breeder nuclear reactors. A commercial TG/SDTA instrument was used for transpiration thermogravimetric measurements. The transpiration experiments involved measurement of mass of the substance continuously as a function of (1) carrier gas (argon) flow rate at a constant temperature and (2) temperature at a constant carrier gas flow rate. Figure 1 shows the results of some selected flow dependence experiments at 950, 975 and 1000 K. The top half displays the variation of rate of mass loss (dm/dt) with volumetric flow rate (dV/dt), and the bottom half displays the variation of apparent vapour pressure (P_{app}) with dV/dt. In KEMS, the ions observed in the mass spectra of the equilibrium vapour were Te^+, Te_2^+, TeO^+, TeO_2^+ and O_2^+. The corresponding neutral species were ascertained to be $Te_2(g)$, $TeO(g)$, $TeO_2(g)$ and $O_2(g)$. Because of the high background at the mass where the O_2^+ ion was detected, the ion intensities of O_2^+ were measured occasionally, were considered unreliable and were not used in any data evaluation. The ion intensities of $^{130}Te^+$, $^{256}Te_2^+$, $^{146}TeO^+$, $^{162}TeO_2^+$ were measured as a function of temperature in the range of 850–950 K The pressure calibration experiments needed to convert ion intensities to partial pressures were performed using $TeO_2(s)$. The partial pressure–temperature relations were obtained by least-squares fitting of all of the data points from individual runs. From the partial pressures, the enthalpy changes

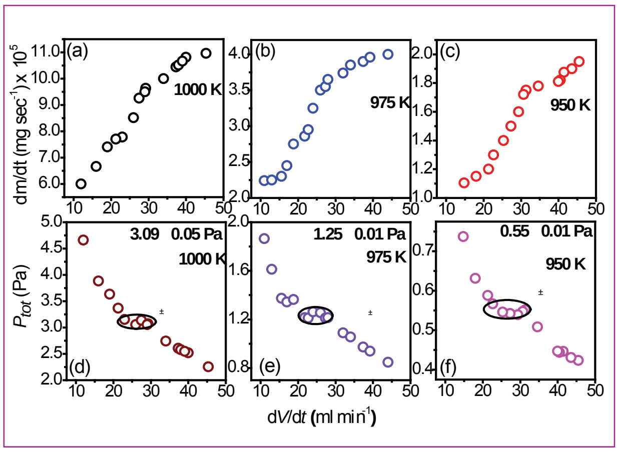

Fig. 1 Variation of (a,b,c) rate of mass loss dm/dt) and (d,e,f) apparent pressure (P_{tot}) with volumetric flow rates (dV/dt) in the transpiration experiments

for the reactions

$$2NiTe_2O_5(s) + 2TeO(g) = Ni_2Te_3O_8(s) + 0.5Te_2(g) + 2TeO_2(g); \quad (1)$$

$$2NiTe_2O_5(s) = Ni_2Te_3O_8(s) + TeO_2(g) \quad (2)$$

were evaluated using the second and third law methods. Subsequently, entropy and Gibbs free energy changes were also evaluated at 298.15 K. From the $p(TeO)$, $p(Te_2)$ and $p(TeO_2)$ obtained at each experimental temperature, the following gas phase reaction was also evaluated by the second and third law methods:

$$TeO_2(g) + 0.5Te_2(g) = 2TeO(g)$$

There is a good agreement in the equilibrium constant and in the enthalpy values obtained for the same gas phase reaction deduced previously by us over (NiO-$Ni_2Te_3O_8$), Mn-Te-O and TeO_2 systems. The enthalpy and Gibbs free energies of formation of $NiTe_2O_5(s)$ at T = 298.15 K were deduced from the corresponding enthalpy and Gibbs free energy changes for Equations 1 and 2 by combining them with the known pertinent thermodynamic data for $NiO(s)$, $TeO_2(g)$, $TeO(g)$ and $Te_2(g)$.

A thermochemical assessment was made to examine the conditions under which the ternary $Ni_2Te_3O_8$ phase could be formed on SS clad of mixed-oxide fuelled (MO_2; M = U+Pu) fast breeder nuclear reactors. Three Pu-fractions (0.20, 0.25, 0.30) and four O/M ratios (1.9998, 2.0000, 2.0002, 2.0004) were considered. The calculations indicate that this ternary phase, might not be formed on SS clad.

V.12 Effect of Laser Parameters on the Measurement of U/Nd Ratio using Pulsed Laser Deposition followed by Isotopic Dilution Mass Spectrometry

Performance of nuclear fuel in a reactor is monitored by fuel burn-up analysis. Among the various available techniques for burn-up measurement, chemical methods involving dissolution of the irradiated fuel sample, followed by laboratory analysis is prescribed by ASTM. This method is based on measurement of fission product monitor and the residual heavy atoms (actinides) in the sample of the irradiated fuel. The analytical process involves separation of rare earths fission products from the spent fuel followed by separation of the burn-up monitor (usually ^{148}Nd) and both these steps are carried out by anion exchange method. The separated burn-up monitor and the remaining actinides are then quantified by an Isotopic Dilution Mass Spectrometery (IDMS) technique using the Thermal Ionization Mass Spectrometer (TIMS). The overall procedure that yields the best accuracy for determination of burn-up, however, is labor intensive and time consuming and therefore carries the risk of exposure of the analyst to radioactivity and will add significant load in the processing of both the high and low level liquid wastes in nuclear waste processing facilities.

At high burn-ups, the composition of the nuclear fuel pellets changes in a non-homogeneous manner within its radius. The spatial profile of burn-up and hence the information on the re-distribution of fissile and fission product atoms across the pellet are needed, which cannot be obtained from the chemical dissolution method.

Laser ablation inductively coupled plasma mass spectrometry (LA-ICP-MS) would be the best suited technique for such burn-up profile measurement in the irradiated fuel pellets. However, in the case of unavailability of such a facility, a procedure involving pulsed laser deposition (PLD) of heavy element (U and Pu) and fission products (Nd, La etc.) from a spent fuel matrix followed by isotopic dilution mass spectrometry using TIMS, can be adopted to measure the heavy element to burn-up monitor (of interest) ratio in the irradiated fuel, from which burn-up can be determined. This present study reports the development of such an analytical technique. In this work, Nd-YAG laser pulses of 1064, 532, 266 nm wavelengths with 8 ns and 100 ps pulse widths as well as KrF excimer laser pulses (248 nm) of 30 ns pulse width were employed to deposit thin films of the simulated spent nuclear fuel pellets. The deposited thin films were dissolved in nitric acid and analyzed for residual heavy element (U) to burn-up monitor (Nd) ratio using isotopic dilution mass spectrometry (employing the TIMS technique) to determine the burn-up in these simulated fuel pellets. The effect of laser parameters like wavelength and pulse width on the stoichiometry of the deposited sample and on the accuracy of the measurement is summarized in Figure 1. While the use of ns-laser pulses of 1064 nm wavelength resulted in high elemental fractionation with enhanced Nd concentration compared to the target composition, the 266 nm ps-laser pulses produce films with least elemental fractionation in the film and hence best suited for this analytical application (minimum error 1.7% and maximum error 6.8%) with the actual value).

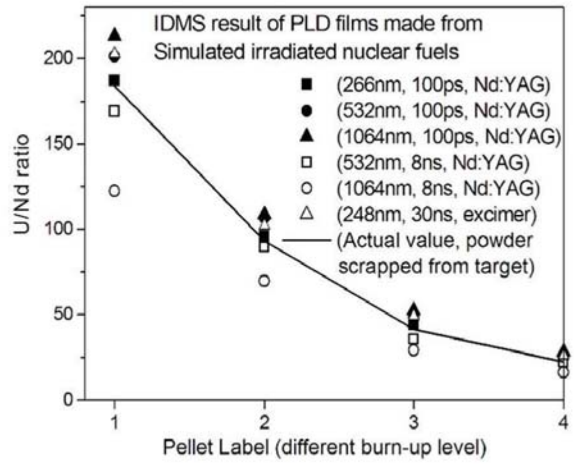

Fig. 1 Measured U/Nd ratio in the PLD thin films at different laser parameters

The method described here is attractive because only a moderate vacuum is required for PLD, it is amenable for remote sample handling, generates far less radioactive liquid waste (during dissolution) and provides the spatial profile across the fuel pellet.

V.13 Solubility of Tributyl Phosphate in Supercritical Carbon Dioxide

Recently, much attention has been paid to Supercritical Fluid Extraction (SFE) of metal ions from diverse matrices and the technique is considered as an environmental friendly and as alternative to conventional solvent extraction. SFE is an attractive technique for nuclear applications, because of its inherent potential to minimize the amount of secondary liquid waste generation. SFE of metal ions using neat CO_2 can be achieved by complexing with suitable ligands and resultant metal complex could become quite soluble in supercritical carbon dioxide (SC-CO_2). The primary criterion for the use of a ligand in SFE is that it should have reasonable solubility in SC-CO_2. Therefore, solubility of ligand and metal complex plays a crucial role in designing and optimization of a particular SFE process. Organophosphorous compounds have been widely employed in solvent extraction of metal ions, particularly in the nuclear field, for the extraction of actinides because of their high extractability of metal ions from acidic media and radiochemical stability. TBP is selective towards tetra and hexavalent metal ions and led to its use as extractant for nuclear fuel reprocessing. Solubility of TBP in supercritical carbon dioxide plays a critical role in designing a SFE process and its feasibility as extractant in SC-CO_2 medium.

A continuous flow apparatus method was developed and used for measuring the solubility of TBP in SC-CO_2. The experimental set-up consisted of a high pressure CO_2 pump, high pressure equilibrium cells, thermostat and a back pressure regulator. An appropriate amount of TBP was loaded into the equilibrium cells and filled with SC-CO_2, placed in a thermostat to maintain a constant temperature. The system pressure was regulated and controlled by a back pressure regulator. After equilibration, SC-CO_2 was allowed continuously to flow through the system at a constant flow rate using a CO_2 pump. By ensuring the adequate contact between SC-CO_2 and solute, the outgoing CO_2 stream was found to be saturated with solute. The stream was then collected in a collection vessel over a definite time period and amount of solute collected was determined gravimetrically. On the basis of total flow of SC-CO_2 and total amount of TBP collected, the solubility of TBP was measured.

The solubility of TBP was measured at temperatures of 313, 323 and 333 K in the pressure range of 100-250 bar. The solubility of TBP was found to be very high in the investigated region and shown in Table 1. The maximum solubility of TBP was found to be 1.5 mol/Lit. The solubility increases with the pressure at all isotherms investigated but showed relatively weak pressure dependence. Raising the pressure at isothermal conditions increases the density of the SC-CO_2, which enhances the specific interactions between CO_2 and solute molecules, thereby increasing the solubility. Retrograde behavior of solubility was observed and is marked by decreasing the solubility of TBP with increasing the temperature at isobaric conditions. A plot of ln(S) with ln(ρ) is linear isotherm, follows the Chrastil's equation. The solubility of the TBP in SC-CO_2 is mainly due to (i). Lewis acid – Lewis base interactions; (ii). Weak C-H--O hydrogen bonding between CO_2 and TBP. The high solubilities in the investigated pressure and temperature range may be due to the complete miscibility of the TBP with SC-CO_2. Since TBP has high solubility in SC-CO_2, homogeneous mixture of TBP-CO_2 can be prepared for the SFE of metal ions. It is obvious from the results that the solubility of TBP can be fine tuned by altering the density of SC-CO_2.

Table 1: The solubility of TBP measured at various temperatures in the pressure range of 100-250 bar

Temperature (K)	Pressure (bar)	Solubility of TBP (mol/Lit)
313	103	1.2
	123	1.3
	150	1.4
	200	1.5
	250	1.5
323	103	0.8
	123	1.1
	150	1.3
	200	1.4
	250	1.5
333	103	0.4
	123	0.8
	141	1.0
	160	1.1
	180	1.2
	200	1.3
	250	1.4

V.14 Time-Temperature-Sensitization Diagrams and Critical Cooling Rates of Nitrogen Alloyed 316L SS with Various Degrees of Prior Deformation

Nitrogen alloyed 316L SS is developed for use as structural material for future sodium cooled fast reactors. The carbon content is kept low so that sensitization at the heat affected zone can be minimized to avoid intergranular corrosion (IGC) and intergranular stress corrosion cracking (IGSCC) of weldments. To increase the life of future reactors from 40 to 60 years, high nitrogen alloyed 316L SS is being considered. Cold working of stainless steels and their thermal exposure in the sensitization temperature range are often unavoidable in service. The aim of this investigation is to understand the influence of cold work on isothermal sensitization behavior and critical cooling rates (CCR) of two varieties of 316L SS, PI-1 and PI-2 (Table 1). CCR data are helpful during solution annealing and stress relieving heat treatments.

Time-temperature-sensitization (TTS) diagrams were established as per ASTM A262 Practice A&E. For Practice E test, 80 x 10 x 6 mm specimens were kept in a glass cradle, embedded with copper turnings and boiled in 10% $CuSO_4$ + 16% H_2SO_4 solution for 15 hours. After exposure, the specimens were bent through 180^o using a mandrel over a diameter not less than the thickness of the specimen. Cracked specimens were categorized as sensitized which are susceptible to IGC. In Practice A test, electrolytic etching was carried out in 10% ammonium per sulphate solution, at a current density of 1 A/cm^2 for 1.5 min. The etched specimens were examined under an optical microscope at a magnification of 200X.

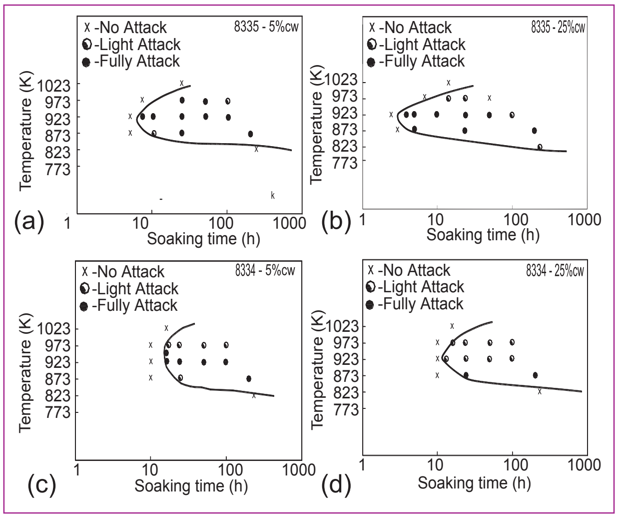

Fig. 1 TTS diagrams established for nitrogen alloyed 316L SS (PI-2): (a) 5%CW; (b) 25%CW and (PI-1): (c) 5%CW; (d) 25%CW

Table 1: Chemical Composition of the two nitrogen alloyed 316L SS. Elements are expressed in wt.%

	C	N	Mn	Cr	Mo	Ni	Fe
PI-1	0.025	0.14	1.74	17.6	2.53	12.15	bal
PI-2	0.033	0.11	1.78	17.62	2.51	12.27	bal

Initial straining (5-15%) sensitizes the grain boundaries either by activating grain boundary ledges or creating new ledges, leading to increased chromium diffusivity and enhanced carbide nucleation, which are manifested in the faster kinetics (lower t_s), (t_s is the minimum time to sensitization), as shown in Table 2. At higher cold work levels, low t_s in PI-2 is due to increased dislocation density and high C content, whereas in PI-1 recovery was observed at high cold work levels at 923 K. Carbon and nitrogen are the important elements which affect sensitization kinetics. CCR calculated from TTS diagrams (Figure 1) will be high when the kinetics of sensitization is fast. Hence, high CCR was observed in PI-2 (having high carbon and low nitrogen content), whereas in PI-1 due to low carbon and high nitrogen, kinetics of sensitization will be sluggish with low CCR as shown in Table 2. At higher cold work levels extensive intragranular precipitation had occurred in P1-2 as observed in the optical micrographs, shown in Figure 2. This will shorten the diffusion paths, and favours faster desensitization kinetics.

Table 2: Variation of time required for sensitisation (t_s), CCR (Critical cooling rates) w.r.t cold work in the nitrogen alloyed 316L SS [PI-1 &PI-2]

% CW	t_s (PI-1) (hours)	t_s (PI-2 (hours)	CCR K/h (PI-1)	CCR K/h (PI-2)
0	16	7.5	9	9
5	15	6	10	19
10	12.1	5.8	11	20
15	9	4.5	14	21
20	10	4.6	13	22
25	11.5	3	11	34

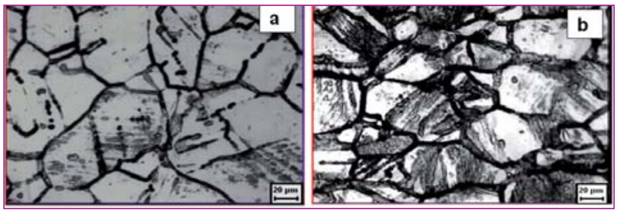

Fig. 2 Optical micrographs obtained in Practice-A test for PI-2 heat treated at 923K/24h: (a)10% CW and (b) 25%CW

V.15 Thermal Stability and Thermophysical Property Characterization of SS 304H Cu and Alloy 740 for Advanced USC Application

The selection, property characterization and indigenisation of large scale development of materials for India's first advanced ultra supercritical (A-USC) thermal power plant is indeed a challenging task. There are a spectrum of high temperature and corrosion resistant materials that are required to be developed to meet stringent design specifications, together with details of process flow sheets and testing procedures. In this connection, the current report highlights briefly the research findings on high temperature phase stability and thermophyiscal properties of two indigenously developed A-USC materials namely, 304HCu (Fe-9.3Ni-17.7Cr-2.95Cu-0.91Mn-0.58Nb-0.24Si-0.1C-0.12N) and Alloy 740 (Ni-24.7Cr-20.82Co-0.56Mo-0.26Fe-1.16Al-1.98Nb-0.03Si -0.02Mn-0.019C-1.7Ti). The basic microstructural characterization of both materials has been carried out using XRD, optical and electron microscopy (SEM & TEM). In case of SS 304HCu, the presence of $(Fe,Cr)_{23}C_6$, Nb(C,N) and nano sized Cu precipitates are observed in the 923 K/150 hours aged microstructure (Figure 1). It may be added that the presence of fine MX and Cu-particles contribute to high temperature creep strength.

The high temperature thermal stability of this material has been investigated using differential scanning calorimetry (DSC). The DSC results together with Thermocalc based equilibrium simulations are used to obtain estimates of the dissolution temperatures for Cu (1167 K), $M_{23}C_6$(1320 K) and MX(1440 K) phases. The solidus and liquidus temperatures are found to be 1607 and 1723 K respectively.

In this case, Alloy 740 in the presence of fine scale distribution of γ'-Ni_3(Al,Ti), η-Ni_3(Ti,Nb), MX, and $M_{23}C_6$ phases in Ni-rich fcc matrix provides for high temperature strength. The slow scan DSC yielded very useful information about the dissolution temperatures of various precipitates: $M_{23}C_6$ (1032 K) γ'(1105 K), η(1317 K) and Nb(C,N)(1452 K). The solidus and liquidus temperatures for Alloy 740 are estimated to be 1579 and 1649 K respectively. Figure 2 presents a typical DSC thermogram obtained on Alloy 740, wherein appropriate transformation temperatures are also marked.

Thermophysical properties

With regard to thermophysical property measurements, the enthalpy increment (H_T-H_{298}), specific heat (C_p) and thermal diffusivity (*a*) were measured using drop calorimetry and laser flash transient thermal diffusivity techniques respectively. The bulk thermal expansion was determined using dilatometry. From the knowledge of room temperature density (ρ), temperature depenedent values of bulk thermal expansion (α_l), specific heat (C_p) and thermal diffusivity (*a*), the thermal conductivity (k) was estimated using the relation, $k = \rho a C_p$. These data were obtained over a temperature range of 300 - 1273 K. A typical set of values at room temperature for various thermophysical properties are given in Table 1.

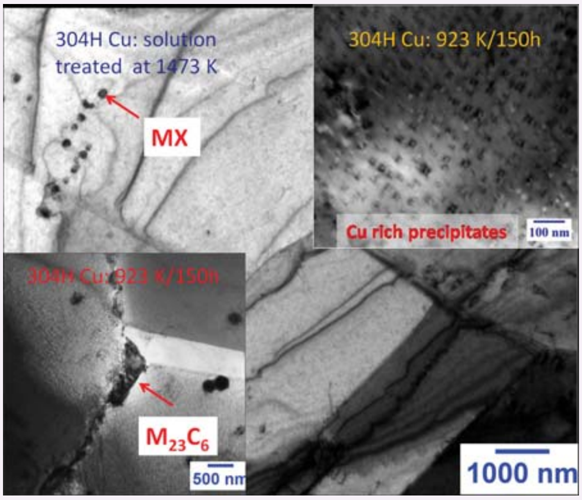

Fig. 1 *Microstructure of solution treated and aged SS 304HCu steel*

Table 1: A typical set of values at room temperature for various thermophysical properties

	Cp (*J Kg*$^{-1}$ *K*$^{-1}$)	αl (10^{-5} K^{-1})	*a* $10^{-6} m^2 s^{-1}$	k W m^{-1} K^{-1}
304HCu	506	1.57	3.42	13.63
Alloy 740	298	1.13	2.94	9.41

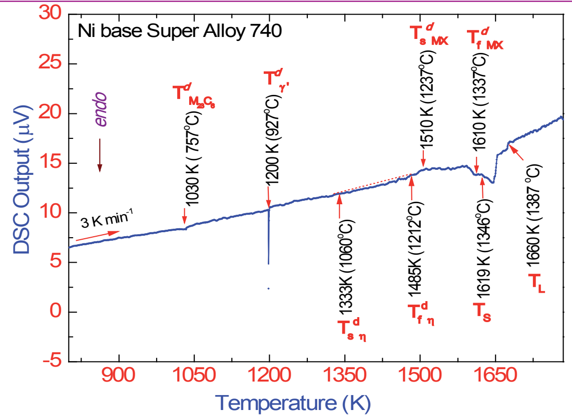

Fig. 2 *DSC on-heating thermogram for Alloy 740*

V.16 Interdiffusion in Fe-Ti Weld Joints under Equilibrium and Non-equilibrium Conditions

Equilibrium and non-equilibrium diffusion driven growth characteristics of the reaction zones in a binary Fe-Ti system has been studied in the temperature range of 773-1073 K for various durations. Interdiffusion under equilibrium conditions was studied in a diffusion annealed defect free friction joint while the non-equilibrium diffusion was studied in explosive clad joints where large number density of lattice defects and metastable microstructures influence the kinetics of interdiffusion.

Diffusion under equilibrium conditions

The Back scattered electron image showing the interface microstructure of Fe-Ti friction joints diffusion annealed at 1073 K for 100 hours duration is shown in Figure 1 with superimposed hardness profile.

Microstructural analysis showed formation of a ~8 μm wide continuous zone at the interface with dark contrast (arrow marked). This zone possessed a high hardness of ~300 VHN while well formed equiaxed ferrite grains are evident on Fe-side with a hardness of ~150 VHN. Microchemical analysis using Electron Probe Micro Analyzer (EPMA) showed a step formation at the interface suggesting the formation of secondary phases at the interface. Width of this interfacial zone was measured as ~12 μm. A correlation of microchemical data with binary Fe-Ti equilibrium phase diagram implied that composition of the interfacial zone corresponds to FeTi intermetallic phase. Further, electron microscopy investigations confirmed the presence of FeTi intermetallic phase at the Fe/Ti joint interface.

Diffusion under non-equilibrium conditions

Change in the interface microstructure of Fe/Ti explosive clads, diffusion annealed at 1073 K for 100 h is shown in Figure 2 with the corresponding hardness profile superimposed. A dark band with a thickness of ~5 μm was observed at the interface followed by ~100 μm wide Widmanstätten region on Ti side. The formation of Widmanstätten Ti is commensurate with the stabilization of high temperature βTi phase due to interdiffusion of Fe and its transformation during cooling.

The width of the diffusional zone was obtained as ~105 μm from image analysis, but measured as ~120 μm from EPMA profiles due to the difficulty in locating the interface between Widmanstätten and α Ti as the interface is diffusive in nature. Diffusion of Fe in Ti is found to be more as compared to that of Ti in Fe which is evident from the microstructure in Figure 2. The average composition at the transition point was measured as 44.7Fe-53.1Ti-2.2C (in wt%) which corresponds to the stoichiometric composition of intermetallic FeTi phase. Beyond the cross over point, constant concentration (2.5Fe-96.2Ti-1.2C) up to a distance of ~113 μm is observed on the Ti side. These composition values are superimposed on the binary (Fe-Ti) and ternary (Fe-Ti-C) equilibrium phase diagrams to identify the phases that would form with thermal exposure. According to the Fe-Ti phase diagram, presence of over Fe 0.08% stabilizes the high temperature β phase of Ti at ambient temperature. Therefore the presence of ~2 wt% of Fe in Ti side is expected to stabilize the β phase, which on cooling transformed to Widmanstätten α-β Ti phase (Figure 2). Beyond ~113μm (from the interface), the concentration of β stabilizing element (Fe) decreases and the composition reaches the base metal composition of Ti.

From the above results, it can be concluded that the interdiffusion in Fe-Ti system under equilibrium conditions resulted in a reaction zone of width limited to 12 μm while non-equilibrium diffusion resulted in a 120 μm wide diffusion zone. This difference can be attributed to faster diffusion of elements assisted by the high volume fraction of lattice defects in the explosive clad joints.

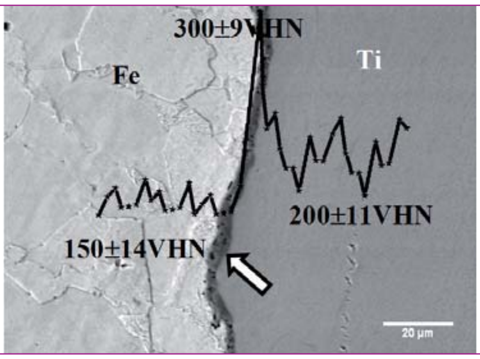

Fig. 1 *BSE image showing the interface microstructure of Fe/Ti friction joint heat treated at 1073 K for 100 h with superimposed hardness profile*

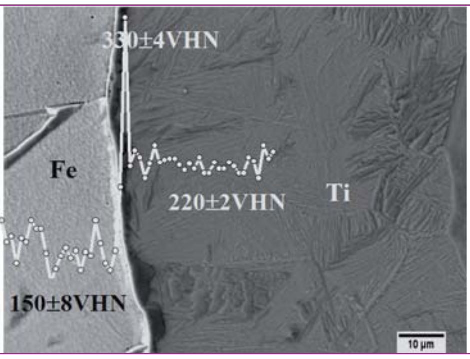

Fig. 2 *BSE image showing the interface microstructure of Fe/Ti explosive joint heat treated at 1073 K for 100 h with superimposed hardness profile*

V.17 Development of Zirconia Dispersoid based ODS Steel

The major concern in achieving high burn up in sodium cooled fast breeeder reactors (FBRs) comes from the limitations of the in core structural materials, which fail in the hostile reactor environment. Oxide Dispersion Strengthened (ODS) ferritic steels are known for their superior high temperature mechanical properties and are candidate materials for in core applications of FBRs. Ultra-fine dispersoid size and narrow size distribution range are the key to attaining the requisite high mechanical strength here. Yttria-Titania complexes are conventionally used as dispersoids for their better high temperature properties and are well studied. Yttria, bearing a cI80 structure, is known to amorphize during mechanical milling, but reappears by nucleation and growth during annealing, growing up to micron sizes. Titania addition to the matrix can refine the size by forming Yttria-Titania complexes, but the size distribution is still quite broad. In this scenario, ZrO_2 is an excellent choice as an alternative oxide, owing to its similar high temperature stability, low fast neutron absorption cross section and possibly an important characteristic of lower number of atoms in the unit cell with mP12 structure.

In the current study, a Fe-15 wt. % ZrO_2 system was ball milled for different time durations viz; 0, 10, 30, 60 and 100 hours. Objectives of this research include the study of evolution of ZrO_2 dispersoids and Fe crystallites with milling duration and optimization of the milling duration based on the achievement of desired microstructure and microchemical uniformity. Morphology studies by SEM indicated 30 hours of milling duration as optimized but chemical homogeneity was obtained only after 100 hours of milling. Figure 1a is a SE micrograph of a 100 hours milled powder particle. The corresponding X-ray mapping of the powder particle is given in Figure 1b. In the micrograph, the red and cyan indicates the Fe K-α and Zr L-α respectively. The image clearly indicates the complete homogenization of the ZrO_2 dispersoids in the Fe matrix. Crystallite size refinement investigation by XRD and TEM indicated retention of crystallinity after 100 hrs of milling with ZrO_2 crystallites measuring about 5-10 nm. The retention of crystallinity allowed us to image the ZrO_2 crystallites via dark field imaging in TEM. Figure 2 represents the same, wherein the bright spots measuring 5-10 nm are ZrO_2 crystallites. The ZrO_2 phase was found not to amorphise unlike the other popular oxide dispersoid, yttria. This was understood in terms of smaller number of atoms per unit cell for the former and considered a desired property. Amorphisation can lead to an undesired nucleation and rapid growth of the dispersoids during high temperature consolidation process. This establishes the rationale behind choice of ZrO_2 as an alternate dispersoid material for ODS alloys. Further, matrix strain analysis by modified W-H method indicated an increase in the dislocation density inside the Fe matrix. Nano hardness of the powder was found to be increasing with increase in milling duration which was attributed to the collective consequence of (i) Hall – Petch strengthening (ii) Dispersion strengthening and (iii) Strain hardening.

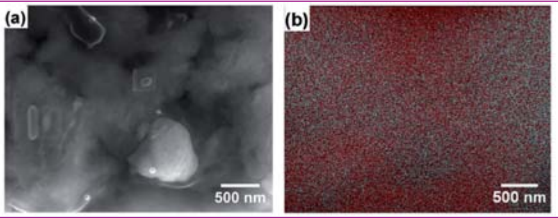

Fig. 1 *(a) SEM micrograph of a 100 hours milled powder particle and (b) X-ray map from ROI shown in Figure 1a*

Keeping in sight of these promising results, further activities are taken up to study the thermal evolution of this nanocrystalline powder. The XRD results of 100 hours milled and 900°C annealed for 2 hours is shown Figure 3. Results indicated that ZrO_2 crystallites are stable against coarsening. Crystallite size of ~54 nm is observed from XRD analysis. Results are promising considering the coaresening issues of Y_2O_3.

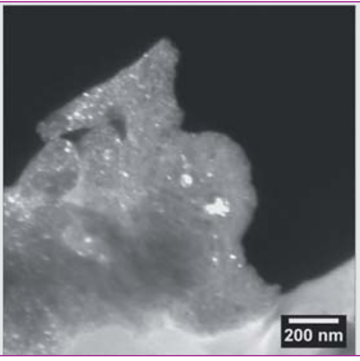

Fig. 2 *ZrO_2 Dark field TEM micrograph showing bright ZrO_2 crystallites*

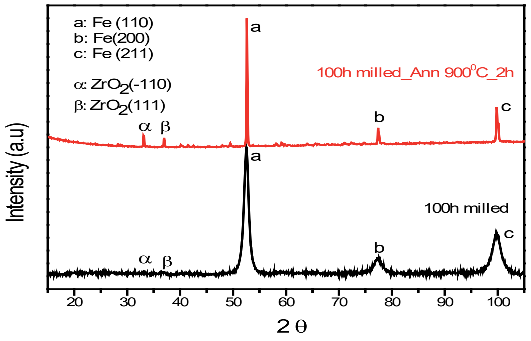

Fig. 3 *XRD plots of as milled and powder annealed at 900°C for 2 hours*

V.18 A Semi-empirical Approach to Correlate DBTTs Obtained from Different Size of Charpy Specimens

Charpy V-notch impact test is a method to determine the ductile to brittle transition temperature (DBTT) of ferritic steels, commonly using standard Charpy specimens (10x10x55 mm) as per ASTM E 23. However, for studying the neutron irradiation effect on DBTT for different nuclear applications, sub-size specimens are considered to save irradiation space. However, the reduced dimensions leads to loss of constraints, and non conservative DBTT values. Thus a correlation in this direction is of immense technological importance, especially for the candidate wrapper material of Fast Breeder Reactors (FBRs), e.g. 9Cr-1Mo steels.

Material and experiments

A normalized and tempered 20-mm-thick plate of 9Cr-1Mo steel with chemical composition (wt%) as C: 0.10, Cr: 8.44, Mo: 0.94, Ni: 0.17, Cu: 0.10, Si: 0.48, S: 0.002, P: 0.007, Al: 0.011, and balance Fe was used for this study. DBTTs were determined (as percentage of the USE, shown in Figure 1) using specimen with sizes of 10x10x55 mm, 5x10x55, 3x10x55, 5x5x55 and 3x3x55 mm.

Semi-empirical correlation for DBTT

Assuming that most of the fracture energy is consumed in crack initiation in the notch-root region, notch root volumes from smaller sized specimens (V_{NS}) have been normalized by the notch root volume of the full size specimen (V_{NF}). The notch root volume in this study means the exact volume below the V-notch region, as schematically represented in Figure 2.

Similarly, the DBTTs obtained at each %USE from smaller sizes ($DBTT_S$) were normalized with DBTT obtained from full size specimen ($DBTT_F$). $DBTT_S/DBTT_F$ (as Y) has been plotted with respect to V_{NS}/V_{NF} (as X) in Figure 3. The variation can be expressed as a power law equation of the form $Y = Z^*X^m$. The values of Z and *m* at different percentages of USE have been obtained from the allometric fit-equations. *Z* remains merely constant (~1) at different %USE. However, the exponent *m,* exponentially varies from 0.05 to 0.25 with respect to %USE. From the above results, the proposed correlation is :

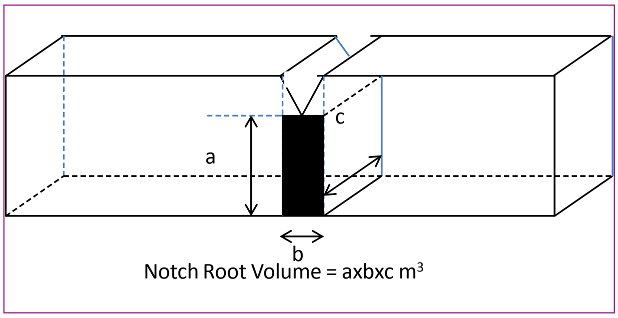

Fig. 2 The schematic representation of the notch root volume

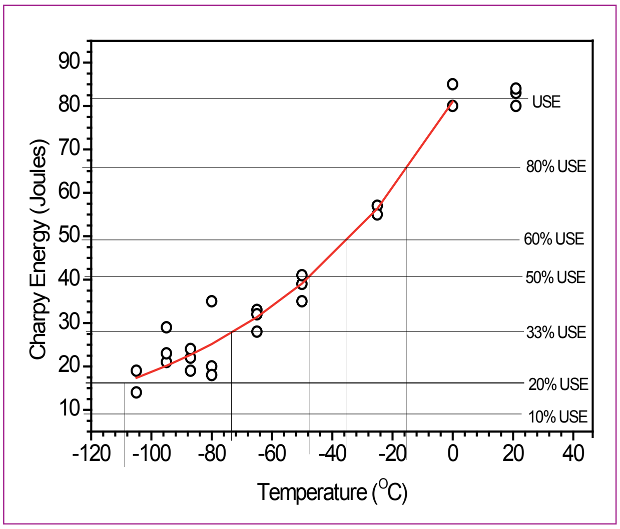

Fig. 1 *Charpy energy vs temperature(size: 5x10x55 mm)*

$$DBTT_S/DBTT_F = (V_{NS}/V_{NF})^m$$

where *m* varies exponentially from 0.05 to 0.25 with respect to %USE (20% to 80% of USE). Significance of $DBTT_S$, $DBTT_F$, V_{NS} and V_{NF} have been defined earlier.

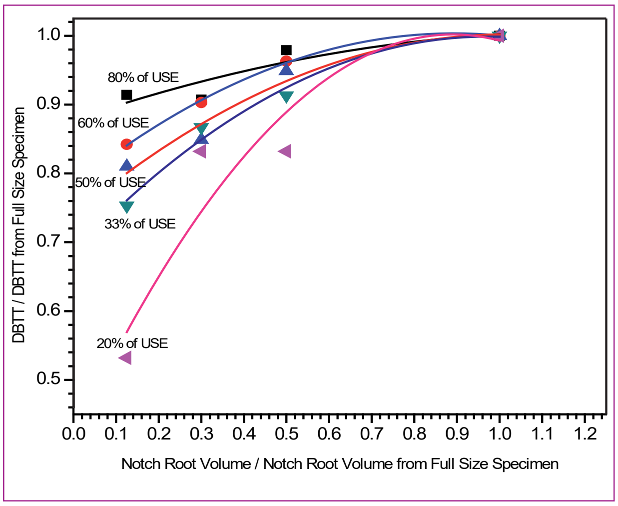

Fig. 3 *Variation of $DBTT_S/DBTT_F$ (as Y) with respect to V_{NS}/V_{NF} (as X)*

V.19 Assessment of Welding Induced Residual Stresses in Austenitic and Ferritic Steels using XRD Technique

X-ray diffraction (XRD) based residual stress (RS) measurement is widely used technique for determination of residual stresses in components. In XRD technique, the distance between the crystallographic planes ('d' spacing) is measured at various ψ angles, where ψ is the angle between the normal of the sample and the bisector of the incident and diffracted beam. The 'd' spacing at various ψ tilts are accurately determined. From the slope of $\sin^2\psi$ vs. 'd' spacing plot, the residual stress is estimated by assuming a plane stress model.

Welding induced residual stress is a major cause of failure in components. The factors influencing the residual stress profiles in a weld joint are heat input, type of welding, pre-heating, thickness, electrode, weld groove design and properties of base metals. The stresses that are introduced during welding are influenced by the non-uniform heat distribution taking place during the welding and the final distortion that is achieved after the constraints (if any) are removed. Additionally, phase transformation in ferritic steels, initially as austenite (fcc) later transforming to ferrite (bcc) causes volume expansion. The present study compares the residual stresses that develop in 4 mm thick SS 304L and 3 mm thick P91 TIG weld joints using XRD technique to study the influence of phase transformation that occurs in P91 steel during cooling of the weld pool.

Two modified 9Cr-1Mo steel plates of dimensions 125×300× 3 mm were used to prepare a weld pad of dimension 300x240x3 mm using a heat input of ~600 J/mm. Similarly, AISI type 304L stainless steel plates (thickness 4 mm) of width 75 mm and length 150 mm were welded together autogenously by using a heat input of 480 J/mm (lower) 640 J/mm (medium) and 800 J/mm (higher). Stress measurements on SS 304L and P91 were carried out using Cr K_β (λ-2.0840 Å) and Cr K_α (λ-2.2896 Å) radiation respectively.

The variation of longitudinal residual stress with distance from the weld centre is shown in Figure 1 for both the weld pads. The weld profile in SS 304L shows typical inverted V profile with peak stresses of 325 MPa being found in the weld centre (WC). This is caused by the differential shrinkage between the weld pool and the parent material which is close to the weld pool. In P91 weld pad, the residual stress profile shows typical M profile indicative of reduction in residual stress at the weld centre due to the phase transformation that occurs during cooling of the weld pool. At the weld centre of the P91 weld, tensile residual stress of ~270 MPa was observed. At 10 mm from the weld centre, peak tensile residual stress of 560 MPa was observed. A comparison of the residual stress profiles between the two weld pads shows that the stress affected zone extends up to 12 mm in both the weld pads which is attributed to the similar heat inputs adopted for these two weld joints.

The effect of heat input on weld centre residual stress in SS 304L weld pads is shown in Figure 2 along with that of the P91 weld pad. It is clear from Figure 2 that lower heat inputs show higher levels of residual stress due to the faster cooling causing higher levels of residual stress. It is noted that the SS 304L weld pad welded with a lower heat input showed similar inverted V profile. However, the stress gradients close to the weld was larger. Similarly, in the higher heat input weld pad, the stress affected zone extended up to 40 mm from weld centre. The study showed that phase transformation reduces the peak stresses at the weld centre in ferritic steel leading to M type profiles. The studies on austenitic SS 304 L showed that heat input also plays a significant role in development of residual stress in welds.

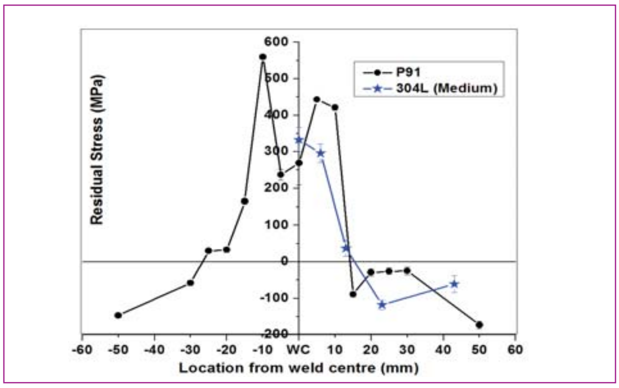

Fig. 1 *Residual stress profile across ferritic and austenitic weld pads*

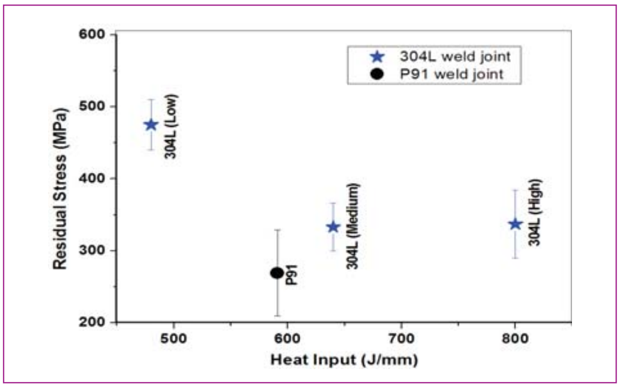

Fig. 2 *Effect of heat input and phase transformation on RS at the weld centre*

V.20 Imaging of Defects in Coarse Grained Austenitic Stainless Steel using Ultrasonic Wavelet based Approach

Ultrasonic inspection of coarse grained material has been a challenge due to presence of high amplitue back-scattered echoes. The intensity of the back-scattered echoes increases with increase in the frequency of inspection. Distortion of the phase in target echoes will take place and signals can be merged in the scatter noise completely or partially depending on the grain size to wavelength ratio. The above mentioned limitations make it difficult to detect the target echoes by conventional time and frequency domain analysis techniques due to poor signal to noise ratio. Hence, a time-frequency based wavelet approach is being developed for detection and imaging of defects in high scattering medium by ultrasonic technique.

Calibration specimen of 50 mm thickness and 200 μm grain size was specially made using AISI Type 316 austenitic stainless steel. Artificial flat bottom holes (FBH) of 3 and 6 mm diameter were machined to different depths ranging from 5 to 45 mm in the specimen (Figure 1). Ultrasonic immersion technique using 10 MHz transducer was used to acquire C-scan data by automatic scanning.

Short time Fourier transform (STFT) based approach was used for detection of defects and evaluation of frequency content at different depths in coarse grained austenitic stainless steel specimens (Figures 2a to 2c). The change in the peak frequency content of the incident ultrasonic wave with travel distance is evaluated experimentally by ultrasonic signals obtained from artificial defects located at different depths. The systematic decrease in peak frequency is also validated by an empirical model based on scattering theory and is shown by the continuous line in Figure 2d. The peak frequency of ultrasonic wave decreases with travel path and showed a systematic decrease. The frequency content of defect signals lies in the range of 2-3.5 MHz as shown in Figure 2d.

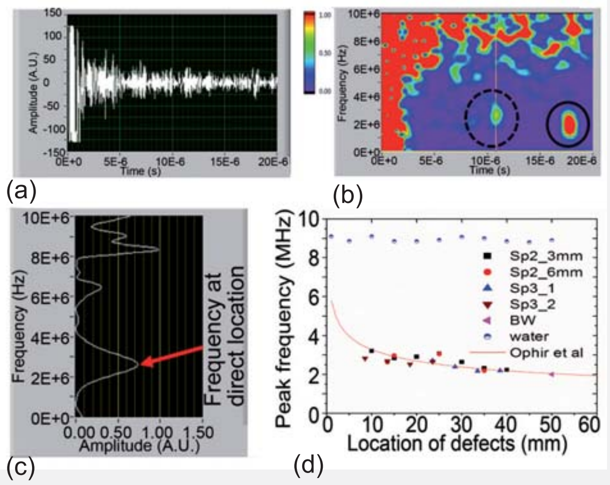

Fig. 2 (a-c) Ultrasonic signal from defect at 30 mm depth, its STFT spectrogram and frequency content at defect location (d) the peak frequency values obtained from artificial defects at different depths using STFT and comparison with empirical model

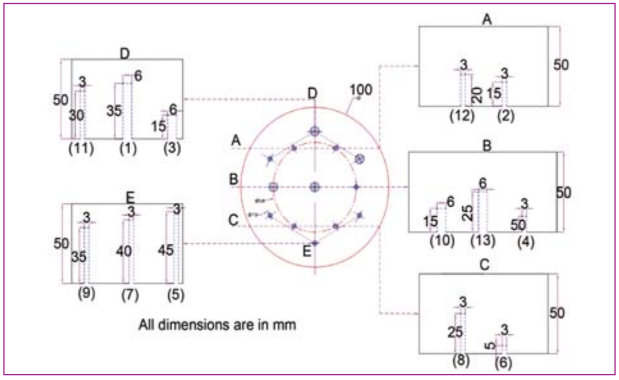

Fig. 1 Schematic of specimen with flat bottom holes made at different depths

The continuous wavelet transform based approach is adopted for imaging of defects. Computer programs were made in LabVIEW. Morlet based analysis was performed to the ultrasonic signals. Since the frequency content from the defects lies in a particular range, single wavelet scale was sufficient to image all the defects in the specimen. Figures 3a and 3b show C-scan images obtained by conventional and wavelet analysis of ultrasonic signals. It can be clearly visualised that all the defects present in the specimen could be imaged by wavelet based approach, however only one defect can be detected by conventional time domain analysis.

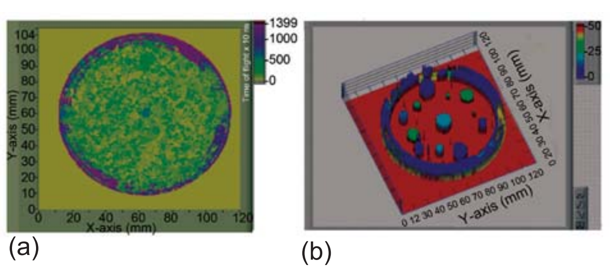

Fig. 3 (a) Conventional (time domain) and (b) wavelet processed C-scan images of defects. Ultrasonic signals were acquired from specimen shown in Figure 1

V.21 Structural and Charge Density Analysis of Mg-doped Nano Zirconia Prepared by Wet-chemical Route

Zirconia (ZrO_2) is an important ceramic material due to its excellent thermal, mechanical, dielectric, chemical and biocompatibility properties. It is widely used in many technological applications such as catalyst, fuel cells, thermal barrier coatings and gas sensors. It has three different polymorphs of crystal structures. Generally it has monoclinic crystal structure at room temperature and reversibly transforms to tetragonal (~1443 K), cubic phase at high (2643 K) temperatures and melts at 2989 K. The stabilization of zirconia in cubic structure by introduction of lower valence oxides is of great technological importance. The production and migration of oxygen vacancies and interestials are of primary interest particularly for nuclear applications because of their role in microstructure evolution under irradiation. Stabilized cubic zirconia phase also possess high ionic conductivity at high temperatures. In the present study, the effect of Mg doping on the structural aspects of zirconia is investigated by X-ray diffraction Rietveld analysis methods.

10 mol% Mg doped zirconia was synthesized by wet chemical process using zirconium oxynitrate and magnesium nitrate and calcined at various temperatures of 673 , 873 and 1073 K. X-ray diffraction measurements were carried out with Cu Kα_1 (1.54056Å) radiation. The structural analysis was carried out by full profile fitting Rietveld method followed by electron density calculation using Maximum Entropy Method (MEM). The final MEM cycles weighted reliability factors Rf = 1.19% and Rwp = 1.33% indicates that the model is well fitted. The typical Rietveld plot of 673 K calcined powder shows cubic phase of Mg doped zirconia (Figure1a). The lattice parameter of the face centered cubic (FCC) phase was found to be a = 5.1090(6) Å. which is slightly higer than that of pure cubic zirconia (4.947(2) Å) at non ambient pressure. The bond length between Zr and O was found to be 2.2123(15) Å in Mg-doped zirconia. The crystallite size of Mg-doped zirconia calcined at 673 K shows ~13 nm with RMS strain of 0.004. The three dimensional (3D) electron density distribution of Mg-stabilized cubic phase is shown in Figure 1b. It is clearly seen that the oxygen atoms tetrahedrally coordinated with Zr is highly anisotropic in nature. The anisotropic nature of oxygen may be explained by means of high thermal vibrations (Uiso = 0.008(2) Å^2) due to oxygen vacancy generation. Such localisation of oxygen electron density may stablise the crystal structure in cubic phase with other parameters like crystallite size and strain.

The powder calcined at 873 K shows 25.8%(wt%) monoclinic and 74.2% tetragonal zirconia. The lattice parameter of doped monoclinic phase was a = 5.140(1), b= 5.188(1), c = 5.3037(9) with beta = 99.05(1)º which was found to be slightly different from pure monoclinic phase of zirconia. The reduction of lattice parameter in Mg-doped zirconia was attributed to lower atomic radius of Mg (150 pm) than that of Zr (155 pm). Lattice parameter of tetragonal phase was observed as a= 3.5905(1) and c= 5.1566(2)Å. The lattice parameter change observed for doped zirconia for tetragonal phase is also attributed to the effect of doping. The crystallite size of monoclinic and tetragonal phases was found to be ~28 and ~31 nm respectively. The corresponding RMS strain observed was 0.003 and 0.002 respectively.

For the powder calcined at 1073 K, Rietveld analysis results show 90.3% of monoclinic with 9.7% tetragonal mixture. The crystallite size of monoclinic and tetragonal phases was found to be ~119 and ~46 nm respectively with RMS strain of 0.0008 and 0.002. Lattice parameter a, b and c of monoclinic phase at 1073 K calcined powder was 5.13771(9), 5.19767(9), 5.30647(9) respectively with beta = 99.208(1). Lattice parameter showed a slight decrease in “a” and slight increase in b,c directions due to Mg doping into ZrO_2 lattice. Lattice parameter of tetragonal phase was a = 3.5902(3) and c = 5.147(1) Å and in comparison with 873K calcined powder, it was observed that there was not much change in lattice parameter, indicating saturation of Mg solubility in tetragonal phase at this temperature. In conclusion, Mg-doped Zirconia phase calcined at 673 K shows cubic phase, powder calcined at 873 K shows monoclinic (25%) and tetragonal (75%) phases. At higher calcination temperature (1073 K) a mixture of 90% monoclinic and 10% of tetragonal phase was formed.

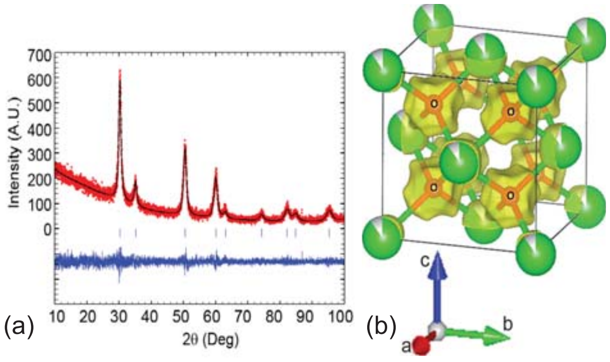

Fig. 1 *(a) Typical Rietveld plot of Mg-doped zirconia powder calcined at 673 K and (b) 3D electron density distribution (0.5e/Å^3 iso-surface) shows O_2 site has anisotropic nature due to oxygen vacancy creation by Mg doping*

V.22 Vanadium Substitution in Cubic $TiCr_2$ Laves Phase: Atomic Scale Chemistry by High Resolution Imaging

High resolution images are formed as a result of interference between the direct electron and diffracted beams. The final recorded images do not contain the phase information that carries structural information from the specimen as well as the effect of the imaging system. The contrast in such images are very sensitive to the thickness of the specimen, defocus and the aberration function introduced by the microscope and also on the local potential of the individual atomic species present in the system. This makes high resolution electron microscopy an extremely sensitive probe for elucidating atomic structure in thin samples. In addition, quantitative analysis of the inter-planar spacings and variation in the contrast may help in understanding local chemistry. However, since the contrast in high resolution images depends on several factors, direct interpretation of the images is not possible. Instead, experimental images obtained over a wide range of experimental conditions need to be compared to image simulations using atomic structure models. Nevertheless, this technique offers an attractive alternative for determination of chemistry with very high spatial resolution, as illustrated in the following example from cubic $TiCr_2$ Laves phase where 'V' is doped upto 0.15 atom% in the Laves phase matrix. The alloy has been prepared by vacuum arc melting of highly pure V, Ti and Cr of appropriate atom%. The alloy button has been remelted several times for homogenization.

As evident from the diffraction based experiments, V does not occupy independent lattice sites and hence the challenge lies in determining the site specific substitution of the V atoms. The detailed phase-structural information has been obtained with the aid of structural modeling and image simulation. Figure 1 shows the phase contrast micrograph along [011] direction of V- doped $TiCr_2$ phase with cF24 structure. Comparison between experimental micrograph and the atomic modeling along the particular zone axis suggests that only the Cr atomic columns of specific locations are imaged. For confirmation, thickness-defocus map has been generated for cubic $TiCr_2$ structure along [011] zone axis. Superposition of the atomic structure model on the simulated image confirms that only Cr atomic columns from particular lattice sites are imaged at the Scherzer defocus condition for relatively lower thickness (~18 nm) of the specimen. Superposition of the atomic structure model and the simulated image shows that Ti atomic doublets are imaged for the higher specimen thickness (~ 55 nm) at Scherzer defocus. To understand the unique nature of the atomic contrast the exit plane wave function for both Cr and Ti columns has been generated as a function of thickness along [011] zone axis. Exit plane wave function shows the presence of both Cr and Ti atomic columns along the entire thickness. The convolution of the exit plane wave with the complex aberration function of the microscope results in the disappearance of the specific atomic columns at specific thickness in the final image. In order to locate the V atomic columns, electron intensity profile has been generated along both Cr and Ti atomic site columns and has been compared with that from the simulated image of pure $TiCr_2$ cubic laves phase for the same zone axis (Figure 2). Electron intensity profile study indicates that V substitutes Ti rather than Cr from its regular lattice sites. This is further substantiated by the first principles calculations that the V substitution in the Ti sublattice is energetically favoured.

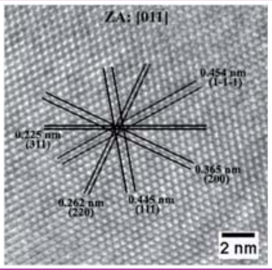

Fig. 1 *Zero loss phase contrast micrograph showing the atomic planes from the Laves phase specimen*

Thus, V site substitution has been characterised in ternary Laves phase alloy using detailed analysis and simulations of phase contrast microscopy images.

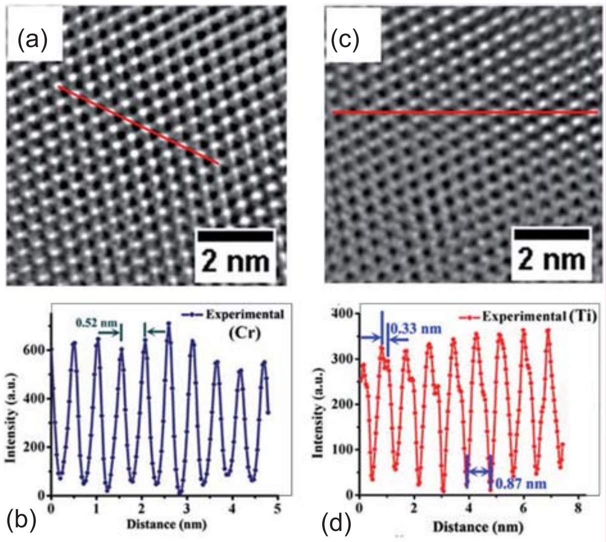

Fig. 2 *Experimental phase contrast image and the corresponding intensity profile where only the Cr atoms provide the bright contrast (a & b) and Ti columns provide the bright contrast (c&d)*

V.23 Investigation of Plasma Plume of Some Oxides by Langmuir Probe during Pulsed Laser Deposition

The plasma characteristics have a direct bearing on the kinetics and quality of thin films (Figure1). The laser produced plasma is highly transient in nature and its parameters vary in both space and time. The studies of spatio-temporal evolution of plasma plays an important role during thin film synthesis as it provides information about various processes occurring during the formation and expansion of plasma. A Langmuir probe is used as a diagnostic tool to get insight into the laser produced plasma.

Tungsten and cerium oxide plasma plume was created as a result of interaction with KrF excimer laser (λ~248 nm) with WO_3 and CeO_2 targets. Effect of oxygen pressure on the ion density and average energy of ionized species such as tungsten and oxygen ions in case of tungsten oxide and cerium and oxygen ions in case of cerium oxide has been investigated using Langmuir probe coupled with PLD system. Oxide powder of 99.99% purity was fine ground and compacted to a pellet of 20 mm diameter and 3 mm thickness by applying a pressure of 10 MPa. These pellets were sintered at about 1400 K for 4 hours and the sintered densities were calculated and found to be ~ 90%. These pellets were characterized by an X-ray diffractometer attached with a curved position sensitive detector using Cu $K\alpha_1$ (0.15406 nm) radiation. The pellets were then cleaned with acetone and mounted onto the target holder located inside a vacuum chamber using silver paste. The chamber was evacuated to 10^{-5} mbar using a combination of pumping systems. The spatio-temporal evolution of laser ablated plasma plume of tungsten oxide was investigated at an oxygen partial pressure of 10^{-2} mbar. The optimum target-substrate distance for the synthesis of good quality thin films was found to be 45-75 mm. It was found that the average energy and average electron temperature of ionized species (tungsten and oxygen) is 5.28 and 3.19 eV respectively at an oxygen partial pressure of 10^{-2} mbar. The relationship between the target-substrate distance (D) and oxygen partial pressure (P) followed the empirical relationship PD^3 with residual fit of 96.3 %. Plasma behavior of ceria was also investigated in the pressure range 10^{-2} to 10^{-5} mbar of oxygen partial pressure. It was found that the ion density of cerium and oxygen decreased with increase in the oxygen partial pressure which was found to have a maximum value of $2.25\times10^{17}\,m^{-3}$ at 10^{-5} mbar and a minimum of $7.05 \times 10^{15}\,m^{-3}$ at 10^{-2} mbar. The average energy of the ionized ceria is found to be 9.91 eV at 10^{-2} mbar and 6.06 eV at 10^{-5} mbar. The increase in the average energy with oxygen partial pressure is attributed to the gain of energy from recombination. The high value of average energy of ionized species increases the ad atom mobility for synthesis of good quality of thin films. The spatial variations were measured at different locations between the target and the substrate holder at an oxygen partial pressure of 10^{-2} mbar. The average ion density is higher only close to the target, while the electron density is maximum at a distance of 30 mm. This is attributed to the increased mobility of the electrons compared to those of ions of cerium and oxygen at this oxygen pressure.

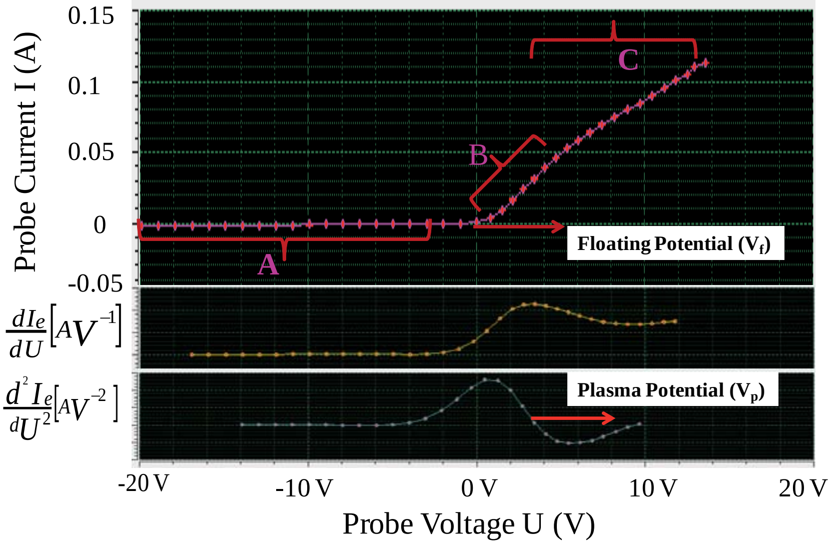

Fig. 1 *Typical probe current versus probe voltage curve and 1st and 2nd derivatives (A) ion saturation region (B) electron retardation region and (C) electron saturation region*

V.24 Atom-Column Contrast of Athermal and Isothermal ω Phase in a Ti-15wt%Mo Alloy

The ω forming bcc transition metal alloys get attention in the field of materials science not only due to their structural anomalies but also due to their detrimental effects in overall mechanical properties. The ω is a typical displacive transformation product phase formed by the collapse of alternate [222] planes in cubic bcc with orientation relationship of <111>β ∥ <0001>ω. As there are four equivalent [222] planes in cubic bcc, four ω variants are possible with mutual orientation angle of 70.5˚. The intermediate state of bcc and the nanometer-sized ω phase in four variants creates challenges in imaging and understanding of the atomic column contrast of ω.

Phase contrast images of atomic column in Ti–15wt% Mo quenched alloy with ω phase precipitates of 2-5 nm sizes show randomly distributed 'fuzzy' contrast along with bcc β matrix contrast. The ω reflections become sharp in the power spectrum (Figure 1a) from such fuzzy regions indicating that there is an overlap of β and multiple variants of nanometre-sized ω. The multiple scattering of electrons from β and variants of ω is responsible for this indistinct contrast in phase contrast images. The best solution to image ω phase at atomic resolution would be to thin the sample down to the precipitate size of 2-5 nm, which is not feasible with present sample preparation techniques. A better approach is the use of post-imaging Fourier filtering techniques such that reflections from a single phase alone are separated out. Such filtered FFTs for the various sets of reflections from the matrix and product phase variants could then be subjected to inverse FFT to obtain atomic column contrast from the individual phases. By understanding the lattice correspondence of β with different variants of ω in different crystallographic directions, the identification of reflections from each phase is possible. For example in the direction of [110]β the omega variants are in the direction $[2\bar{1}\bar{1}0]$ and other two are in $\langle 10\bar{1}4\rangle$. Hence, by filtering the diffraction pattern corresponding to one of the ω variants in $[2\bar{1}\bar{1}0]$ direction (Figure 1b) and inverse Fourier filtering gives the atomic column contrast of ω alone which is in the area where only a fuzzy contrast was seen originally. Figure 1c shows the atomic column contrast of ω embedded in β matrix. The atoms in the undisplaced [222] planes show higher intensity than partially collapsed ones.

After isothermal aging, the ω precipitates are coarsened in size to 50-80 nm. The phase contrast image yields atomic column contrast of ω phase clearly, since the particle size is nearly equal to the sample thickness. For further improved contrast, the Fourier filtering can be applied to reduce the effects of diffuse scattering, as is shown in Figure 1d. This typical contrast shows completely collapsed [222] planes and the unit cell of ω is marked in the figure. Thus phase contrast image establishes evidence of the completeness of collapse of [222] planes in isothermal ω.

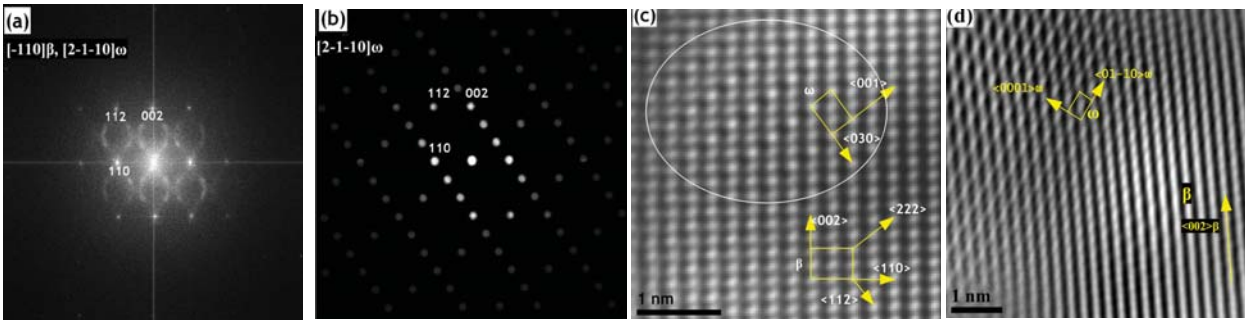

Fig. 1 *(a) Power spectrum of phase contrast image: reflections from matrix β and variants of ω are present. The β reflections 112, 002 and 110 are marked, (b) filtered reflections from single variant of ω is shown where some of the β spots overlap; (c) the Fourier filtered image of athermal ω with unit cells of β and ω marked. The atomic column contrast corresponding to athermal ω is seen in region marked by ellipse, and (d) the atomic column contrast of isothermal ω in the boundary region with β annotated with unit cell of ω*

V.25 Ab-initio Study of Lattice Stability and Thermal Properties of δ-UZr_2

U-Zr based alloys are the prospective metallic fuels for future fast reactors as they have higher breeding ratio, higher thermal conductivity and harder neutron spectrum. Fuels in the reactor undergo several transformations like phase changes, void formation and restructuring. It is necessary to understand the various phases present as well as their properties at different environments for designing the fuel. δ-UZr_2 is found to be the only stable intermetallic phase in U-Zr phase diagram. First principles calculations (FPC) are useful in the study of different properties of these systems. Although many FPCs of U exist in literature, calculations for U-Zr system are rare. Hence a detailed first principles study of lattice stability and thermal properties of UZr_2 was carried out. The calculaions were performed using the density functional theory (DFT) based Vienna ab-initio Simulation package (VASP). δ-UZr_2 exhibit the AlB_2 type structure with Al type sites (0, 0, 0) occupied by Zr and B type sites (1/3, 1/3, 1/2) and (2/3, 2/3, 1/2) by U and Zr randomly. The disordered structure can be represented by a special quasi random structure (SQS) which minimize the correlations at type B sites. We have used a 24 atom SQS for our study. We find from our calculations that the disordered structure is energetically more stable (favourable).

In order to further examine the stability, elastic constants and phonon dispersions are computed using the density functional perturbation theory (DFPT). Elastic constants are found to meet the Born stability criteria for both the ideal structure and SQS. Figure 1 shows the phonon dispersion for SQS and the ideal AlB_2 structure. Negative frequency (unstable) phonon modes are found in the phonon spectrum of the ideal structure whereas SQS showed no negative phonon frequencies. This provides additional evidence that SQS structure is stable while ideal structure is unstable. We further confirm that, even though the ideal structure satisfies the Born stability criteria, it is dynamically unstable. Thus the SQS is both elastically and dynamically stable and the disorder of B type site plays a crucial role in the lattice stability of δ-UZr_2.

We have further calculated the thermal expansion coefficient, bulk modulus and specific heat as a function of temperature within the quasi harmonic approximation (QHA). Phonon spectrum is computed at various volumes and the corresponding free energy is obtained at different temperatures. Minimising the Helmoltz free energy at different temperatures as a function of volume, the equilibrium volume at different temperatures is obtained. The equilibrium volume at different temperatures is used to calculate the thermal expansion coefficient. Calculated thermal expansion coefficient lies in between that of alpha-U and alpha-Zr and match closely with the experimental data as shown in Figure 2. The underprediction of the thermal expansion coefficient of our caculations can be attributed to ignoring anharmonic contributions to the crystal free energy. Fitting the Birch-Murnagan equation of state to free energy vs volume at different temperatures, we obtained the bulk modulus as a function of temperature and the value at 0 K is found to be 99.5 GPa. In summary, we have used the FPC to study the thermodynamic properties of δ-UZr_2.

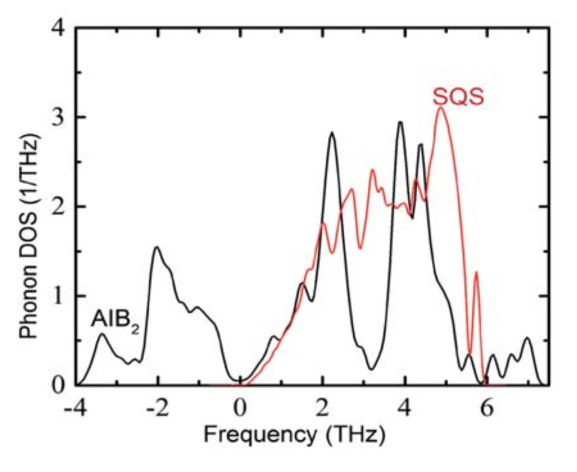

Fig. 1 *Phonon density of states of ideal AlB_2 structure and SQS*

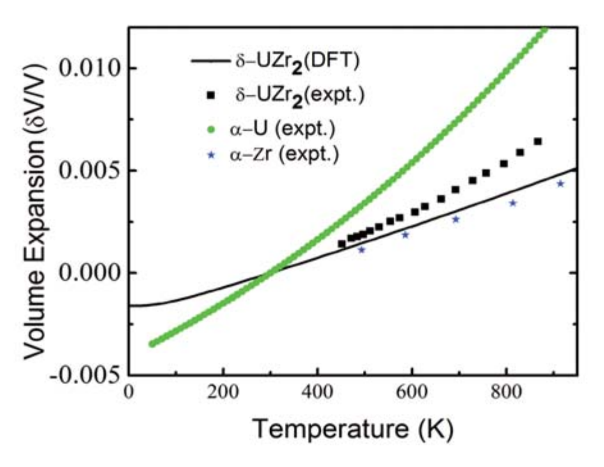

Fig. 2 *Comparison of the calculated thermal expansion coefficient with experimental data*

V.26 Orientation Dependent Deformation Behaviour of BCC Iron Nanowires

In this work, we use molecular dynamics simulations to understand the orientation dependence of deformation behaviour in body-centered cubic (BCC) Fe nanowires under tensile and compressive loading conditions. BCC nanowires with initial orientations <100>, <110>, <111>, <112> and <102> were considered in the present study. Molecular dynamics simulations were performed in large-scale atomic/molecular massively parallel simulator (LAMMPS) package employing embedded atom method (EAM) potential for BCC Fe given by Mendelev and co-workers. Atom-Eye package is used for visualization of atomic snapshots. The nanowire had a width of 8.5 nm with 2:1 aspect ratio and contained about 110000 atoms. The stable structure thus obtained is thermally equilibrated to a temperature of 10 K in canonical ensemble. The molecular dynamics simulation results showed that the single crystal deformation mechanisms vary with crystal orientation. Under tensile loading, the nanowires with initial orientations of <100>, <112> and <102> deformed predominantly by twinning mechanism on <111>/{112} system, whereas <110> and <111> oriented nanowires deformed by dislocation slip mechanism (Figure 1). A good agreement between the operative deformation mechanisms with respect to BCC nanowire orientation and those reported for the bulk single crystal counterparts based on experimental results was observed. The occurrence of twinning in <1 0 0>, <1 1 2> and <1 0 2> oriented nanowires and its absence in <1 1 0> and <1 1 1> orientations is similar to their bulk single crystal counterparts. Further, the nanowires with <100> and <110> orientations displayed opposite tension-compression asymmetry in deformation mechanisms. Under compressive loading, the nanowire with <100> orientation deformed by dislocation slip, while twinning was observed in <110> orientation (Figure 1). The deformation by twinning in BCC Fe nanowires has led to reorientation within the twinned region. The orientation dependent deformation behaviour in BCC Fe nanowires has been explained by the twinning-antitwinning asymmetry of 1/6<111> partial dislocations on {112} planes. By defining χ to be the angle between {110} plane and maximum resolved shear stress plane (MRSSP), a boundary seperating the orientations showing twinning and anti-twinning can be drawn in a standard stereographic triangle under tension and compression (Figure 1). A simple twin nucleation and growth model related to the nucleation of 1/6<111> partial dislocation along with the intrinsic stacking fault on {112} and its propagation along that plane has been derived and proposed successfully based on the present observations.

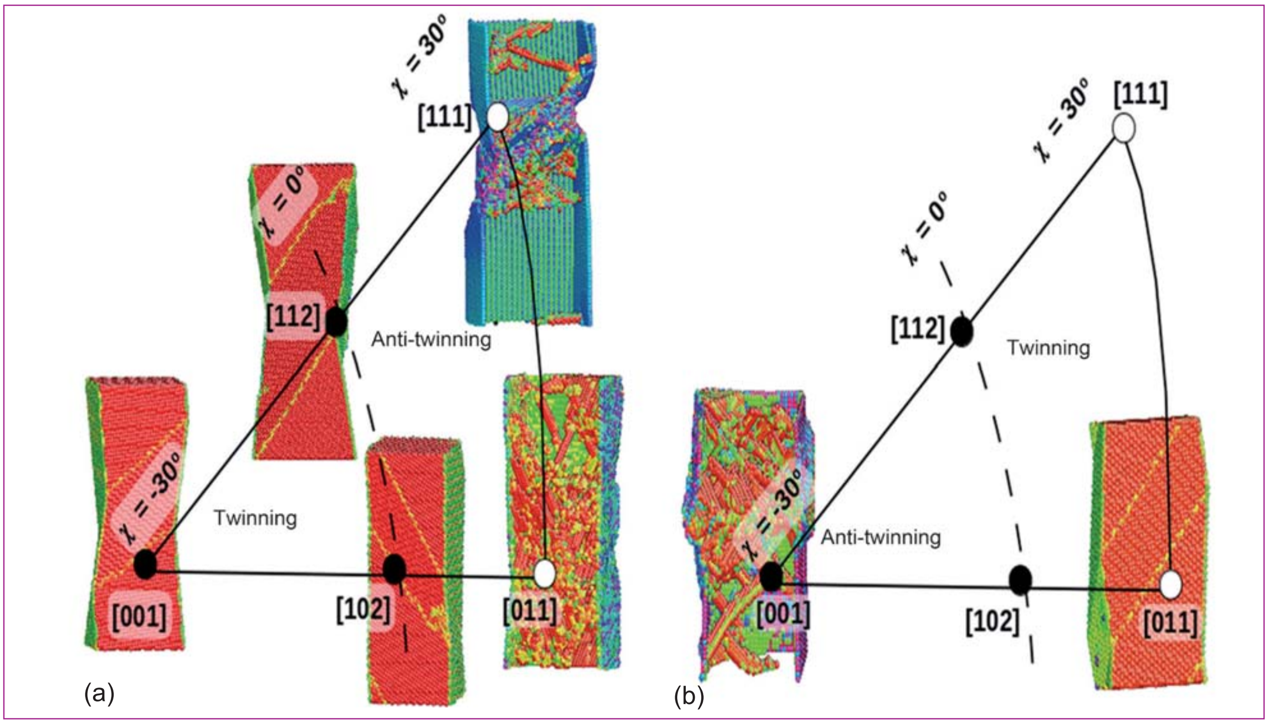

***Fig. 1** Orientation dependent deformation behaviour of BCC Fe nanowires under (a) tensile and (b) compressive loading*

V.27 Effect of Hydrophilic Silica Nanoparticles on the Magnetorheological Properties of Ferrofluids: A Study using Opto-magnetorheometer

Ferrofluids, which are suspensions of ferro- or ferrimagnetic nano particles of sizes ranging from 5 to 15 nm in suitable carrier fluids, are unique materials that exhibit simultaneous liquid and magnetic properties in the presence of an external magnetic field. They undergo transition from a purely liquid state to a viscoelastic solid state under a magnetic field. The magnetorheology of errofluids are influenced by several factors such as volume fraction, magnetization of the particle, magnetic field, shear force, surfactants, and additives, etc. Some additives give rise to interesting rheological properties useful for practical applications.

For many technological applications of ferrofluids, the magnetorheological properties require being precisely controlled. The effect of hydrophilic silica on the magnetorheology of an oil-based ferrofluid containing Fe_3O_4 nanoparticles of size~10 nm is studied. It is observed that the presence of silica nanoparticles lowers the yield stresses, viscoelastic moduli, and shear thinning behavior of the ferrofluid because of the weakening of dipolar interactions, which was evident from the observed lower yield stresses exponent (<2). The ferrofluid containing silica exhibits a dominant elastic behavior, a reduced hysteresis during the forward and reverse magnetic field sweeps, and a longer linear viscoelastic regime under nonlinear deformation. The Mason number plots at low shear rates and magnetic fields show deviations from the master curve in the presence of silica. The magnetic field induced microstructures, visualized using opto-magnetorheometer, showed columnar aggregate structures along the field directions, which are reoriented along the shear flow direction at high shear rates. The image analysis shows that the average thickness of the columnar aggregates in pure ferrofluid is much larger than that of the mixed system, which suggests that the intervening silica matrix hampers the zippering transition of columns at higher magnetic field and shear rates. Our results suggest that optimization of rheological properties of ferrofluids is possible by carefully adding suitable silica nanoparticles, which may find practical applications such as dynamic seals, heat transfer, sensors, and opto-fluidic devices, etc.

Figure 1 shows the magnetic field sweep for (a) FF and (b) FF-silica at shear rates of 0.01, 0.1, 1, 10, and 100 s^{-1}. Based on the opto-rheological data, the schematic of the microstructure of hydrophilic silica nanoparticles in (a) polar and (b) nonpolar solvent, of magnetic nanoparticles (c) in the absence and (d) in the presence of magnetic field, and of magnetic nanoparticles within a silica network (e) in the absence and (f) in the presence of magnetic field are shown in Figure 2.

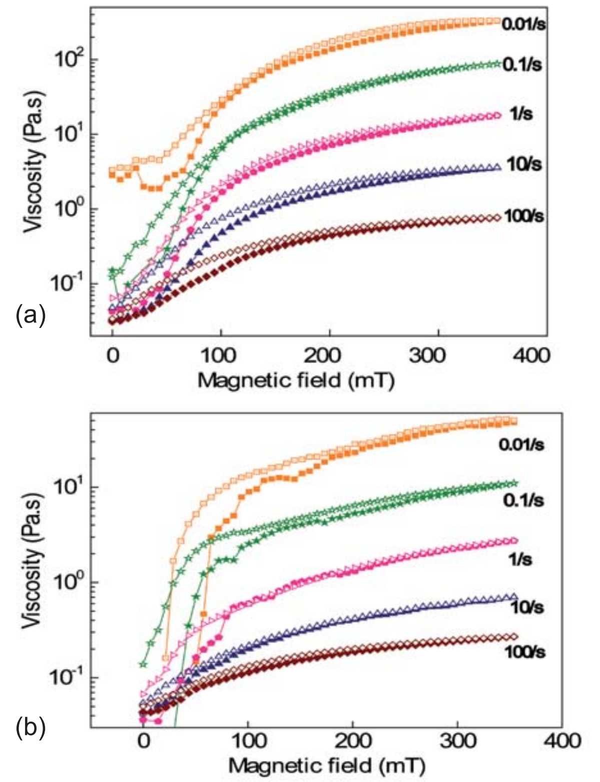

Fig. 1 *Magneticfield sweep for (a) FF and (b) FF-silica at shear rates of 0.01, 0.1, 1, 10, and 100 s^{-1}*

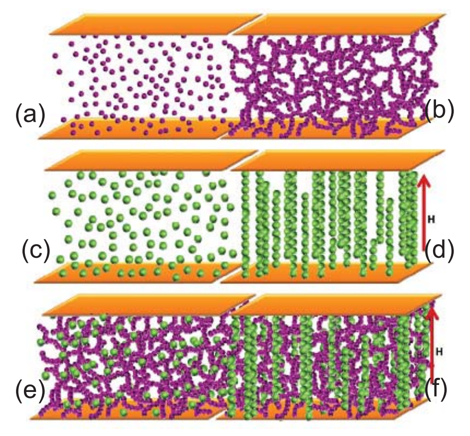

Fig. 2 *Schematic of the microstructure of hydrophilic silica nanoparticles in (a) polar and (b) nonpolar solvent, of magnetic nanoparticles (c) in the absence and (d) in the presence of magnetic field, and of magnetic nanoparticles within a silica network (e) in the absence and (f) in the presence of magnetic field*

V.28 Thickness Controlled Proximity Effects in C-Type Antiferromagnet/Superconductor Heterostructure

The discovery of colossal magnetoresistance (CMR) materials and its compatibility with high-T_c superconductors (HTS) to form good heterostructures has further intensified the research in the area of proximity effect. In general, superconductivity is incompatible with ferromagnetism due to the exchange field induced breaking up of cooper pairs. However, the strength of exchange interaction could be modulated in thin film forms, which could be suitably exploited in tailoring of critical parameters of superconductors for technological applications. It is known that $Nd_{0.35}Sr_{0.65}MnO_3$ (NSMO) exhibits C-type antiferromagnetism below Néel temperature (T_N ~270 K) with spins being aligned ferromagnetically along the c-direction but antiferromagnetically coupled within the a-b plane. Interestingly, it transforms to a canted ferromagnetic phase at around 50 K via the action of the mobile electron hopping. The thickness of NSMO is used to tune the superconducting parameters of YBCO, such as transition temperature T_c, in-plane coherence length ξ_{ab}, and upper critical field H_{c2}. Unexpectedly, a colossal magnetoresistance was observed at superconducting state in YBCO/NSMO when NSMO reached 200 nm, which involves a competition between the exchange energy and condensation energy of cooper pairs. A brief account of the important findings of the present work performed on YBCO/NSMO heterostructures with the thickness (t) of top NSMO layer with t = 40, 80, 160 and 200 nm (denoted as YN04, YN08, YN16 and YN20) deposited over YBCO layer of fixed thickness (70 nm) is given here.

The temperature dependent resistivity ρ(T) under various fields H from zero to 5 Tesla is plotted in Figures 1a to 1c for YN08, YN16 and YN20 respectively. T_c, T_{CAF} and T_r express the temperature of superconducting transition, spin canting and superconductivity re-entrance respectively as marked with arrows. The normal state resistivity of heterostructure samples at 250 K is around 2.5 mΩ-cm for all heterostructure films, implying the carrier concentration does not change much with varying t. The finite resistivity at canting state increases with increasing thickness, indicating the enhancement of vortex dissipation with increasing exchange field. The T_c of all the samples decreases linearly with increasing H. The suppression rate (dT_c/dH) changes from -1.2 to -2.7 K/Tesla with t increasing from 40 to 200 nm. The analysis of these measurements enable us to deduce upper critical field $H_{c2}(0)$ along c-direction and in plane coherence length ξ_{ab} of YBCO by using WHH theory. The values of $H_{c2,c}(0)$ = 78 Tesla and ξ_{ab} = 20.5 Å are obtained for pure YBCO film. $H_{c2}(0)$ decreases, while ξ_{ab} increases with increasing NSMO thickness t. The T_c and T_r decrease rapidly with increasing t. The severe suppression of T_c suggests that the effect of exchange field of NSMO on superconductivity is significant even NSMO is antiferromagnetic.

It is noticed that the behavior of field dependent resistivity below the canting transition (T_{CAF}) changes when t increases from 160 to 200 nm as shown in Figures 1b and 1c. Magneto-resistivity (MR) below T_{CAF} increases with increasing field for the samples with $t \leq 160$ nm, which could be attributed to the field enhanced vortex dissipation; while resistivity decreases dramatically about 50 % for t = 200 nm (YN20) (see inset of Figure 1a). Considering the YBCO/NSMO heterostructure is a system where the superconducting temperature T_c (~90 K) is higher than the temperature of canting state (~40K), the minimum energy of system may correspond to a superconducting state with a modulated magnetic structure. The exchange energy increases with increasing the thickness (t) of NSMO. When t is increased up to 200 nm, the exchange field of the canted state prohibits superconducting pairing, leading to a negative CMR. The new observation of switching from the superconducting to the CMR state in YBCO/NSMO may open up a new route to control oxide superconducting devices.

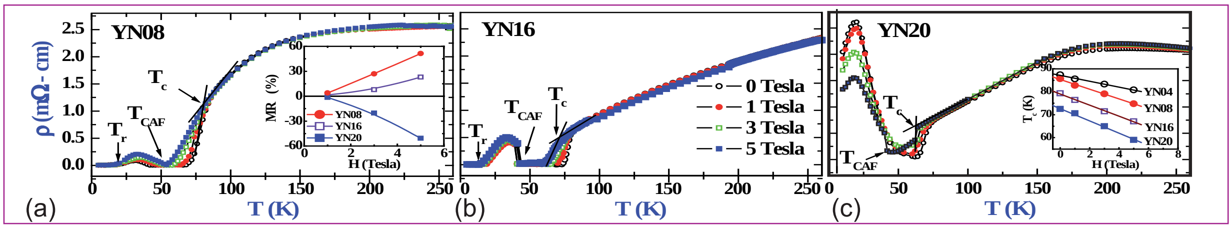

Fig. 1 *(a) - (c) Temperature dependent resistivity ρ(T) at various fields H and the inset in Figure 1a plots MR vs H for YN08, YN16 and YN20 respectively. Arrows indicate the positions of Tr, TCAF, and Tc. The inset of Figure 1c exhibits Tc versus H for all the four samples*

V.29 Thermal Expansion and Structural Stability of Dy_6UO_{12} at Elevated Pressures

RE-U-O (RE=Rare earth) are likely compounds that form during UO_2 irradiation in nuclear reactor as a result of the fuel-fission product interaction. Dy_6UO_{12} is a potential neutron absorber which can be useful in controlling nuclear reactivity. Dy_6UO_{12} has rhombohedral unit cell with 3 formula unit i.e. 57 atoms. The earlier high temperature studies shows positive thermal expansion coefficient for all RE_6UO_{12} (RE: La, Gd, Nd, Sm, Tb and Dy). The lattice thermal expansion coefficients increase with increasing temperature and expansion is more along the *a*-axis compared to the *c*-axis which is attributed to lesser density of atoms along the *a*-axis. Also, the heat capacity measurements are reported and is seen that heat capacity values increase with increasing temperature.

In-situ high pressure and high pressure-high temperature (HP-HT) study have been carried out on Dy_6UO_{12} to study the structural stability of dysprosium uranate as a function of pressure and temperature. Structural stability studies of these oxides, at extreme conditions, are of importance as these are formed in the nuclear reactor. These sort of studies have not been reported in the literature so far for any of the RE-U-O systems.

Dysprosium uranate (Dy_6UO_{12}) is prepared by citrate gel combustion method. The prepared sample is characterized using synchrotron source and found to be in single phase. High Pressure X-ray diffraction experiment on the polycrystalline sample of Dy_6UO_{12} is carried out using a Mao-Bell type diamond anvil cell (DAC) at INDUS-2 synchrotron beam line, RRCAT, Indore. High pressure and high pressure-high temperature laboratory based X-ray diffraction studies have been carried out using micro focus X-ray generator. The measured FWHM of the focused beam is 130µm and the flux is ~$15.5*10^6$ photon/s at 50 kV and 1 mA. The high flux at such low operating power is due to the focusing geometry of the multi-layer optics. Membrane diamond anvil cell used for generating simultaneously high pressure and temperature. Membrane diamond anvil cell is designed to achieve 25 GPa and 1273 K simultaneously.

High pressure x-ray diffraction (HPXRD) on Dy_6UO_{12} is carried out up to 28 GPa. The structure is found to be stable up to the highest pressure studied. Analysis of high pressure x-ray diffraction data shows that lattice parameters decreases in a linear fashion with pressure. However, c axis contracts more compared to a axis in contrast to what has been reported in high temperature X-ray difraction studies. This can be understood from the polyhedral representation of crystal structure of Dy_6UO_{12} (two UO_6 polyhedra separated by two DyO_6 polyhedra along the c axis). DyO_6 polyhedra share edges whereas UO_6 and DyO_6 polyhedra are linked at the corner. Corner sharing is considered to be more stable compared to the edge sharing by Pauling's rule for ionic structures leading to the observed trends in the lattice parameter variation as a function of pressure. Bulk modulus and its derivative is estimated from the pressure volume relationship and is found to be 144 GPa and 7.0 respectively. Above 21 GPa broadening of almost all the peaks is observed indicating onset of disorder in the system above this pressure.

High pressure and high pressure-high temperature X-ray diffraction study on Dy_6UO_{12} is carried out up to 11.3 GPa and 673 K (Figure 1). The X-ray diffraction patterns obtained up to the highest pressure and temperature studied, clearly indicates the crystal structure to be stable at these extreme conditions. Volume expansion of ~ 0.33% was observed in the temperature interval of 293 to 473 K at ambient pressure. Thermal expansion coefficient is found to be $14.5x10^{-6}$ K^{-1} at ambient pressure. However, at 1 and 2.6 GPa the thermal expansion coefficient increases to $21.4x10^{-6}$ and $32x10^{-6}$ K^{-1} respectively in the temperature interval of ~ 293-673 K.

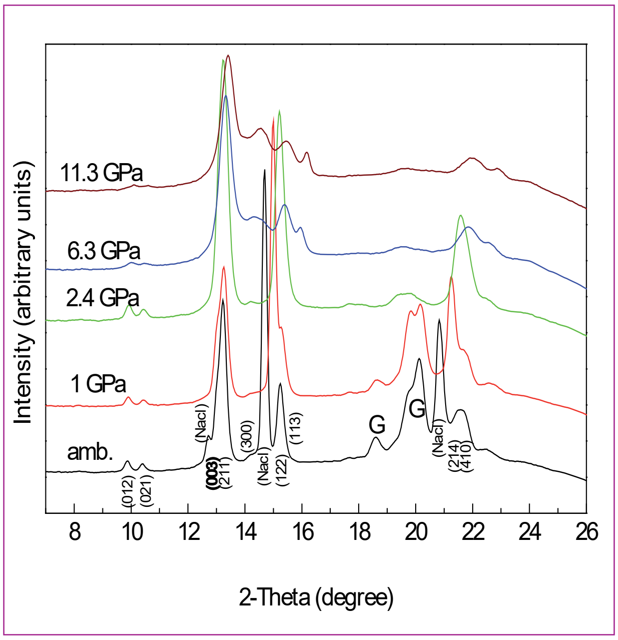

Fig. 1 *The diffraction patterns at highest temperature (~673 K) and different pressures*

V.30 Polarization and Strain Coupling in Disordered Ferroelectrics

Lead-based disordered ferroelectrics, also called relaxors, are special class of ferroelectric materials that show unusual and complex physical behavior. Relaxors are characterized by the strong dielectric dispersion over a wide frequency range around and below T_m, the temperature of dielectric maximum with no macroscopic structural phase transition. The unusual dielectric response of these materials is generally understood to be the manifestation of anomalies of relaxation processes over a broad temperature and frequency ranges.

The origin of the complex dielectric behavior is attributed to the nucleation and growth of the so called polar nanoregions (PNRs), which are nanometer-scale regions having local, randomly oriented ferroelectric polarizations. PNRs begin to appear at very high temperature known as Burns temperature T_B well above the temperature of dielectric maximum T_m.

In Pb based relaxor systems, the anomalous behavior of acoustic phonon modes have been studied extensively through Brillouin light scattering studies. In these systems, acoustic phonon begins to exhibit anomalous behavior around T_B. The observed anomalous behavior is found to be strongly correlated with the temperature evolution of dynamics of PNRs. Three important temperatures are associated with the temperature evolution of PNRs: T_B, T^* (local condensation temperature) and T_f (freezing temperature). T^* has been suggested as the onset temperature of the development of strong correlations between the local polarization and strain in PNRs. Existence of this temperature, T^* so far was revealed by the Raman scattering and acoustic emission studies.

In the present study, the condensation temperature T^* was obtained from the simple mean field analysis of the anomalous behavior of the elastic constant of the prototype relaxor $Pb(Mg_{1/3}Nb_{2/3})O_3$ (PMN).

Single crystal of PMN was grown by flux method. Brillouin light scattering measurement was carried out on (100) plane of the crystal in back-scattering geometry using a high contrast 3+3 pass Sandercock tandem Fabry-Perot interferometer. A diode pumped solid-state laser (Innolight Diabolo 500) of wavelength 532 nm was used as an excitation source. Measurements were carried out in the FSR range of 75 GHz in the temperature range of 800 – 100 K using Linkam (FTIR 600) stage with temperature stabilization of ± 0.1 K.

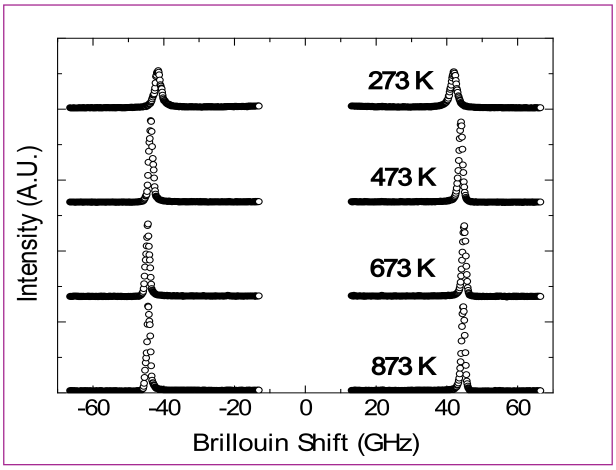

***Fig. 1** Brillouin spectra of PMN at some selected temperatures*

The typical Brillouin spectra of PMN at some elected temperature is shown in Figure 1. The spectra display the Brillouin doublet of longitudinal acoustic phonon mode. The temperature dependence of the corresponding elastic constant C_{11} and the attenuation α is given in Figure 2. C_{11} exhibits a broad minimum followed by a broad maximum in α in the region of T_m = 280 K. In order to investigate the coupling between the polarization and strain, a mean field model is used. In this model, the temperature dependence of the elastic constant C_{11} is given by

$$C_{11} = A_1 - A_2 T - A_3 (T - T_o)^{-p}$$

The first two terms of the equation correspond to the normal anharmonic behavior and the third term

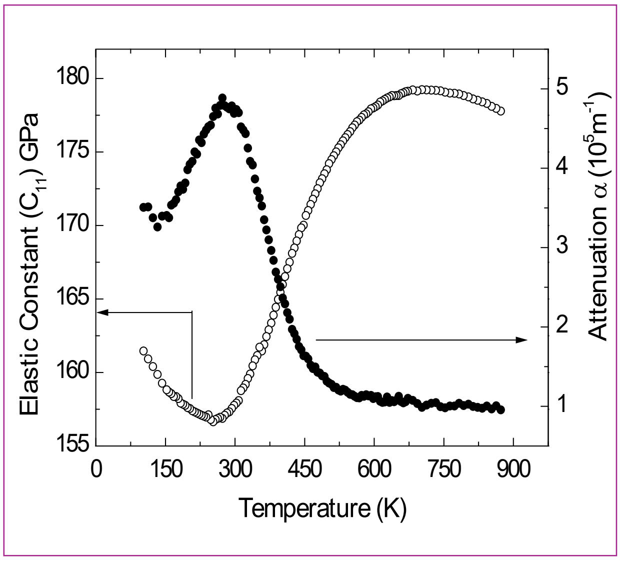

***Fig. 2** Temperature dependence of the elastic constant C11 and attenuation α of PMN*

describes the critical softening due to the critical fluctuations of the polarization of PNRs.

The critical exponent *p* is predicted to be 0.5 for three-dimensional (3D) fluctuations, 1 for 2D fluctuations and 1.5 for 1D fluctuations. As PNRs begin to appear well above T_m, the temperature dependence of C_{11} was fitted with the above equation for the temperature higher than T_m. Since the structure of both PMN is cubic, there can be no anisotropy in the fluctuation of the order parameter. Therefore, during fitting the critical exponent *p* was fixed at 0.5 and all the other parameters were allowed to vary. T_o obtained from the fitting was 483 K.

The result of the fitting for PMN is shown in Figure 3. The mean field model is in good agreement with the experimental C_{11} above the temperature around T_o+40K. Below this temperature, the elastic constant C_{11} shows a marked deviation from the mean field model and exhibit reduced softening. The attenuation also begin to rise precisely at the temperature where C_{11} deviates from the mean field model. The temperature at which C_{11} begins to show reduced softening can in fact be clearly identified with the characteristic intermediate temperature T^*. The characteristic temperature T^* obtained for PMN in this study is 523K. The T^* obtained in the present study falls well within the range 500 ± 30K predicted for all Pb based relaxors.

The reduced softening of C_{11} followed by the increasing attenuation below T^* clearly indicates the appearance of the additional strain in the crystal. In the case of Pb based relaxors, this excess strain ΔS arises from the electrostrictive coupling between the polarization and strain and is expressed as ,

$$\Delta S = (Q_{11} + 2Q_{12})\langle P^2\rangle$$

where Q_{11} and Q_{12} are the electrostriction coefficients. The mean field model does not consider the contribution from the electrostriction *Q* to the elastic constant C_{11}.

The phonon frequency and damping of the longitudinal acoustic phonon inclusive of electrostriction *Q* can be estimated using Kubo's formalism. The result of Kubo's formalism is that the polarization fluctuations δP contain two components with very distinct dynamics,

$$\delta P = \delta P_d + \delta P_s$$

δP_d is the usual quasi-dynamic part corresponding to third term of the equation, while δP_s are much slower fluctuations (quasi-static), with long range correlations present at the temperature below the quasi-dynamic region. The quasi-static part δP_s corresponds to the existence of Edwards-Anderson order parameter,

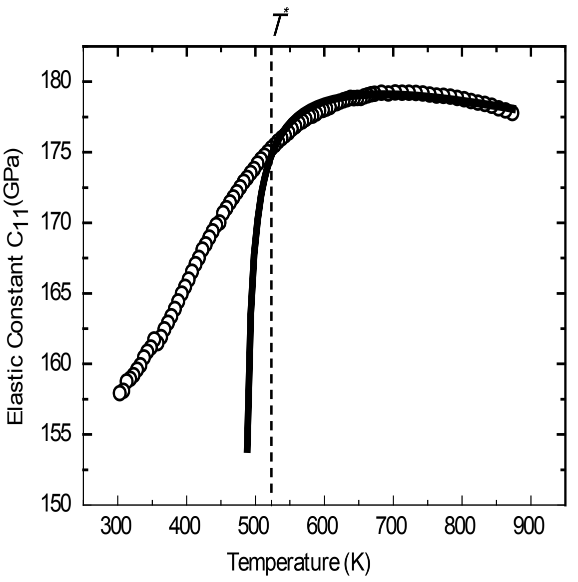

Fig. 3 *Fit of the experimental C11 (open circles) with mean field model (solid line) of PMN*

$$q^{EA} = V^{-1}\int \langle(\delta P_s)^2\, dV$$

where *V* is the volume over which long range correlations exist. The elastic constant changes ΔC involving the quasi-static order parameter q^{EA} can be written as

$$\Delta C_s = -4(R_{11} + R_{12})^2 q^{EA}\chi\kappa''$$

where χ is the low frequency dielectric susceptibility and κ'' is the imaginary part of the low frequency dielectric susceptibility.

The direct determination of q^{EA} by ^{93}Nb NMR for PMN in general shows a strong increase with decrease in temperature below T^*. The deviation of the elastic constant C_{11} from the mean field behavior below T^* is therefore evidently connected with the appearance of the additional contribution ΔC_s due to the development of quasi-static polarization within PNR. It is therefore the strong coupling between the polarization and the strain below T^* that results in the appearance of additional strain and hence the reduced softening of the elastic constant C_{11} and the increased attenuation. In conjunction the reported Raman scattering, acoustic emission and NMR studies, present Brillouin scattering results also confirms the condensation of dynamic clusters into quasi-static PNRs: it is the formation of these quasi-static PNRs that results in the observed reduced softening of the elastic constant C_{11} and in the increased attenuation below T^*.

V.31

Low Temperature Raman Studies on Yttrium Substituted $GdMnO_3$: Observation of Spin-phonon Coupling

Materials exhibiting more than one ferroic property, (magnetic, electric and strain) are called multiferroic materials. Among these, materials possessing simultaneous electric and magnetic order with a strong coupling between them are of special interest as they promise exciting application, especially control of magnetic property on application of external electric field.

These materials are broadly classified as type I and type II multiferroics based on their electric and magnetic coupling strength. Type I multiferroic systems have different origin for their electric and magnetic ordering and the coupling between them is weak. These systems also have a large difference in their electric and magnetic ordering temperatures. $BiFeO_3$ and $BiMnO_3$ belongs to this category. On the other hand type II systems have strong coupling between their ferroic orders. Interestingly, ferroelectric ordering in this system is not by structural symmetry changes as seen in conventional ferroelectric system but by magnetic transition leading to spontaneous polarization. $TbMnO_3$ is the best studied type II multiferroic system. Because of the coupling between the ferroic properties, polarization direction can be changed by changing the direction of the applied magnetic field.

$RMnO_3$ with orthorhombic Perovskite structure have the attribute that their crystal structure and hence their magnetic structure can be changed by varying the rare earth ionic radius. This tunability gives the advantage of inducing multiferroic property even in those which are otherwise non multiferroic $RMnO_3$ systems. For $RMnO_3$ systems to show multiferroic property they should have long wavelength modulated magnetic structure incommensurate with that of crystal lattice. This happens only over a narrow window range of rare earth ionic radius (Tb-Dy). For few others this can be brought in by substituting at the R site with suitable ionic radii of the rare earth element. Towards this we have substituted Yttrium (Y) at Gadolinium (Gd) site in $GdMnO_3$ to induce multiferroic property in its ground state.

The multiferroic property in these systems is attributed to the spin-lattice coupling where the ferroelectricity arises due to lattice distortion as explained by inverse D-M interaction. These magnetic and crystallographic changes are expected to have strong correlation with the underlying lattice phonons. The shift in phonon modes across the magnetic transition has been attributed to spin-phonon coupling. Presence of spin-phonon coupling is one of the necessary but not sufficient conditions for a material to be multiferroic.

Raman spectroscopy has been used to study the phonon modes from room temperature down till 10 K in $Gd_{1-x}Y_xMnO_3$ (x=0-0.4) to ascertain the presence of spin-phonon coupling and hence its multiferroic nature.

Anharmonicity of the lattice force constant is prime factor responsible for shift in phonon frequency with temperature in insulating magnetic systems. Any deviation from this variation is attributed to presence of spin-phonon coupling. Among all the modes the $B_{2g}(1)$ mode belonging to the in-plane stretching of the oxygen in the MnO_6 octahedra is observed to show maximum deviation.

This is shown in Figure 1 by fitting the anharmonic contribution as a function of temperature to phonon shift. The variation of FWHM of the Raman peaks gives an idea of life time of the relaxation. This has also been studied as function of temperature and has been shown to have additional relaxation in the form of spin-phonon coupling. These studies confirm the presence of spin phonon coupling and hence the multiferroic nature of Y substituted $GdMnO_3$.

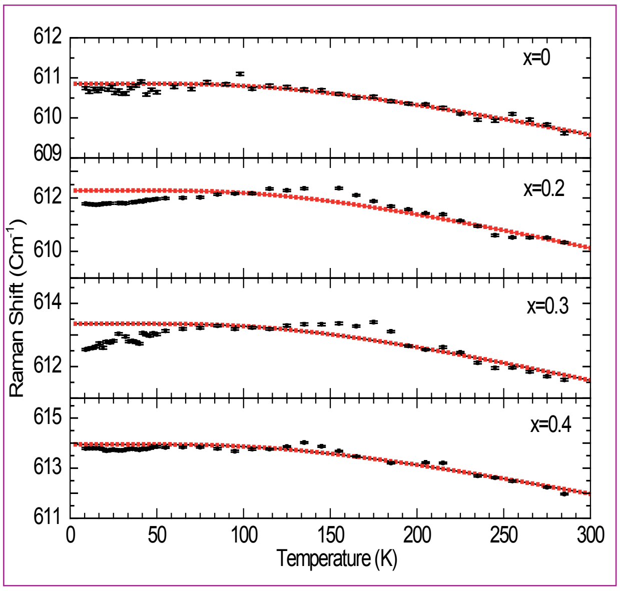

Fig. 1 *Variation of $B_{2g}(1)$ mode with temperature. Red curve shows fitting of anharmonic behaviour*

V.32 Molecular Dynamics Simulation of Displacement Cascades in Fe-Y-Ti-O System

Molecular dynamic (MD) is the best tool to study displacement cascade characteristics at atomistic length scales and nanosecond time scales. MD needs accurate interatomic potentials that model the interactions between different atomic species and thus control the observed dynamics. Good interatomic potentials for Y_2TiO_5 crystal has been developed and the displacement cascades in Fe-Y_2TiO_5 bilayers using the developed potential was studied.

A composite potential of the form

$$V_{ij}(r) = A_{ij}e^{(-r_{ij}/\rho_{ij})} - C_{ij}r_{ij}^{-6} + kq_iq_j/r_{ij}$$

was used to model the pair wise interactions between X_i and X_j ionic species ($X\__i, X\__j \in$ Y,Ti,O). Here, r_{ij} is the distance between the two nuclei and A_{ij} ρ_{ij}, C_{ij} are the Buckingham potential parameters to be obtained from fitting. The 1st term models the Pauli repulsion between electrons, 2nd term models the attractive dipole-dipole interactions and the 3rd term is the Coulomb interaction between X_i and X_j with charges q_i and q_j. The parameters of this function are obtained by fitting to a database of atomistic configurations, total energies and crystal properties containing both experimental and first principle calculations data.

The elastic constants, shear modulus, bulk modulus, Poisson's ratio, 16 structural distortions in lattice parameters and angles, and vacancy, interstitial and Frenkel defect formation energies (12 configurations) were used for the fitting. The parameters A_{ij}, ρ_{ij} and C_{ij} are obtained for all the ionic combinations. The potential is then tested for its reproducibility by again calculating the Frenkel defect formation energies from MD and tested by calculating the phonon dispersion and density of states using lattice dynamics. The calculated phonon dispersion (Figure 1) shows all the phonon modes to be positive.

The interatomic potential obtained was used along with Fe EAM potential for Fe-Fe and Morse potentials for Fe-X_i interactions to study displacement cascades in Fe-Y_2TiO_5 bilayer comprising of 313,984 atoms. The crystal temperature is 300 K. After equilibration, a Fe, Y, Ti, or O PKA of energy 8 keV, at a distance of 12 or 23 Å from the interface, is started towards the interface from the Fe or Y_2TiO_5 layer for 6 different simulations for every PKA. Total simulation time is 100 picoseconds. The maximum in total number of displaced atoms is reached at ~0.28 picoseconds for all PKAs, after which the defects start recombining. The mean square displacement (MSD) of the displaced atoms rises steeply during the cascade and then, after ~6 picoseconds, saturates at a constant value (Figure 2), which shows that under the ballistic phase of the cascade, atoms move vigorously, while by the end of the cascade, they start settling in equilibrium positions. It can be seen that Ti atoms undergo the highest ballistic movement, while the Y and O atoms move by approximately the same amount in the ballistic regime. In self-ion irradiation experiments on model Fe-Y-Ti-O ODS alloys, it is seen that Ti diffuses most while Y virtually remains stationary during irradiation. The results point out that Ti goes out from Y-Ti-O matrix quite early during irradiation. This study represents the dynamics only in the ballistic motion regime. The simulations to large time scales using accelerated molecular dynamics methods to get details of long time atomic species diffusion.

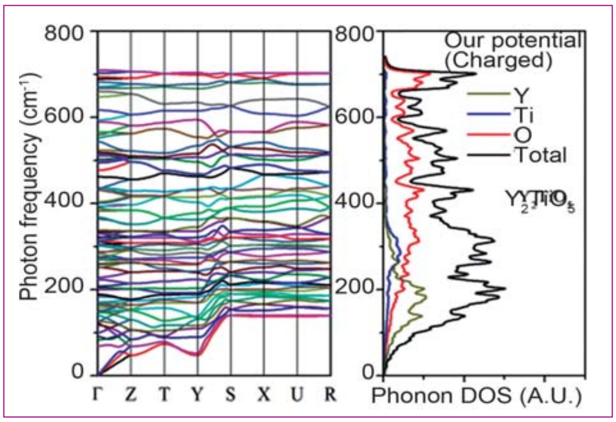

Fig. 1 *Phonon dispersion in the whole Brillouin zone and the total and atom decomposed density of states for Y_2TiO_5 crystal obtained from lattice dynamical calculations using the developed potential*

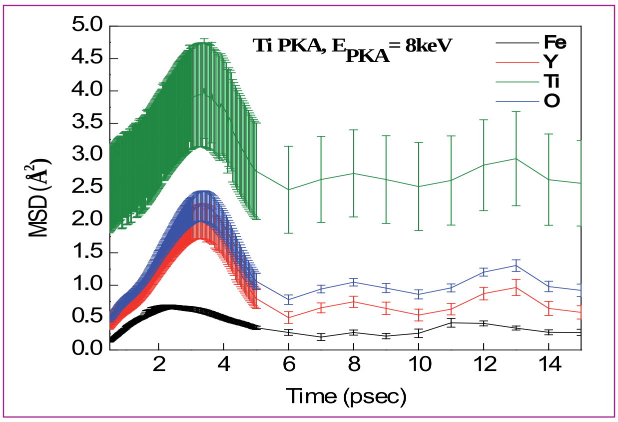

Fig. 2 *Mean square displacement of displaced atoms in the ballistic motion regime during the displacement cascades in the Fe-Y_2TiO_5 bilayer*

V.33 Defect Evolution in High Entropy Alloys

The novel approach to alloy design has paved way to an entirely new class of alloys called the high entropy alloys (HEAs) containing elements in near equiatomic proportions. The phrase "high entropy" derives its name from the high entropy of mixing due to the presence of multiple elements in the alloy thus stabilizing the system to form a simple disordered FCC, BCC or HCP solid solution rather than intermetallics. HEAs exhibit high mechanical strength, high temperature resistance, good corrosion and oxidation resistance and therefore are potential candidates for high temperature structural applications in nuclear reactors. It is of interest to know the phase stability as well as the defect microstructure in these alloys under both high irradiation doses and temperature. Positron annihilation spectroscopy is an unique defect characterization technique. In particular, with positron beam, depth resolved defect studies pertaining to vacancies and voids can be carried out from near surface up to a depth of a few hundreds of nm. The present work reports for the first time, the evolution of the defect microstructure with thermal annealing in Ni ion implanted (1.5 MeV, 5x10^{16} ions/cm^2 ~96 dpa) *FeCrCoNi* alloy using the variable low energy positron beam. SRIM calculation shows the damage distribution in the range 0-800 nm with a peaking around 400 nm. Glancing angle X-ray diffraction measurements reveal that *FeCrCoNi* (FCC phase) remains stable under both implantation and high temperature annealing (1173 K). Figure 1 shows the Doppler S-parameter as a function of positron beam energy (E_p) at different annealing temperatures. For defect free *FeCrCoNi*, the S-parameter saturates at 0.49 (S_b) beyond 16 keV. For the as implanted condition, the S-parameter saturates beyond 3 keV at 0.542 (S_d) corresponding to positron annihilation in implantation induced vacancy defects. A normalized S-parameter (S_d/S_b=0.542/0.49) of 1.10 correlates well with that of positrons annihilating from monovacancies in nickel indicating that the defects are monovacancies. With increasing temperature, the saturation S-parameter slowly decreases from 0.542 to 0.49 and the S versus E_p matches with that of defect free *FeCrCoNi* beyond 1073 K. The average S-parameter in the peak damage depth is shown as a function of temperature in Figure 2. Two distinct recovery stages (Figure 2) are observed, 300-723 K range corresponding to defect recovery process and 773-973 K range attributed to the formation of stacking fault tetrahedrons (SFTs).

For higher annealing temperatures, SFTs collapse and vacancies are annealed out completely. Evidence towards formation of SFTs was obtained from the stacking fault probability (α) deduced from the relative positions of (111) and (200) planes with annealing temperature. Formation of monovacancies in as implanted condition and aggregation of these defects with thermal treatment to form stable SFTs is consistent with Molecular Dynamics simulations in binary alloys reported earlier. Our work shows that *FeCrCoNi* is structurally stable under high irradiation (~100 dpa) and under high annealing temperatures and also that only SFT's are formed and no microvoids are formed in as implanted condition as well as under thermal annealing. This makes HEA's as potential structural candidates in nuclear reactors having higher swelling resistance.

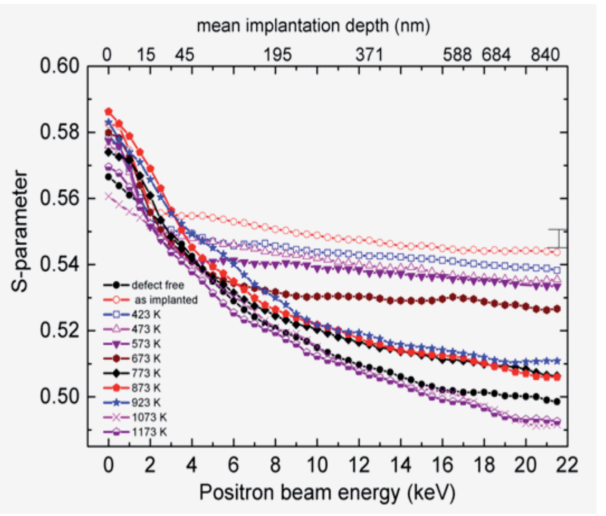

Fig. 1 *S versus E_p curves for 1.5 MeV Ni ion implanted FeCrCoNi*

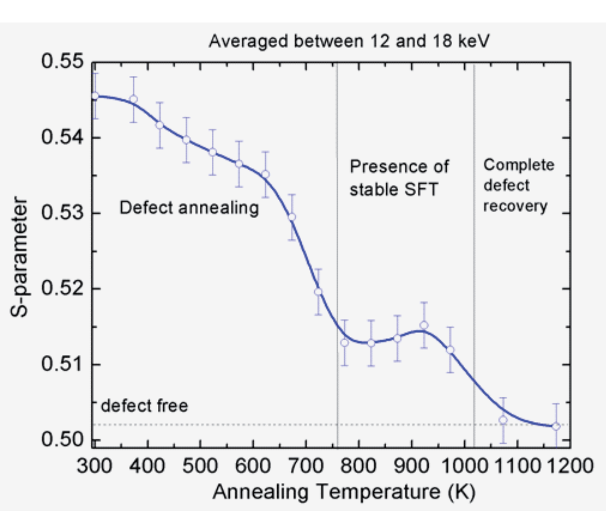

Fig. 2 *Average S-parameter versus temperature*

V.34 Quantum Information Investigations using Entangled States

The emergence of quantum cryptography, quantum teleportation and quantum computation presage a paradigm shift in the field of information science: "Information is physical!" and quantum superposition and entanglement are fundamental physical resources. With these resources one can carry out certain tasks in ways that are superior to classical methods or even unimaginable without quantum resources. For example, several commercial solutions for quantum cryptography or secret encoding of information have been developed. The teleportation of information without the physical transfer of the carrier of information has been demonstrated over couple of hundred kilometres. Several technological routes are being pursued throughout the world to develop quantum computers. While both material objects and electromagnetic radiation are harnessed for these tasks, light itself is an extraordinarily robust carrier of information both classically and quantum mechanically. Indeed, much of modern communication relies on fibre optic networks that transfer massive amounts of data which are optically encoded. Classically, light is described by Maxwell's equations. At very low intensities, the particulate or more accurately the photonic character of light becomes manifest. One then finds that classical electromagnetic theory is quite inadequate. If we consider the polarization of light for example, every photon could have a linear polarization that is both horizontal and vertical with respect to a certain direction. This situation is called quantum superposition. Using nonlinear crystals, one could generate pairs of photons (Figure 1) that exhibit non-local correlations such that, both photons are say, either horizontally (H) or vertically (V) polarized. Prior to measurement, the pair of photons exists in a quantum superposition of both possibilities and so each outcome is equally probable. Nature seems to preclude the assignment of a definite polarization, before the measurement, to the photons. It also prohibits a description for each of the individual photons separately. Upon a measurement however, we could get HH or VV as the outcome.

So, when the polarization is measured one of the photons in the pair, H or V can be obtained. The other photon would automatically end up being definitely H or V respectively, depending on the state of the first photon. The extraordinary aspect is that this second photon could be arbitrarily far away from the first one at the time of measurement and yet, its state is non-locally and instantaneously altered by the measurement outcome on the first photon. A theory incorporating the assumption that the photons have definite polarizations prior to measurement and that instantaneous non-local influence are prohibited is called an objective local realistic theory. Extensive experiments show that atomic systems as well as light can be prepared in states which violate expectations of objective local realistic theories. Such states are called entangled states. In the polarization example given earlier, the polarization of the two photons behave this way and they are said to be in an entangled state. The first phase of a new facility for the generation and study of entangled photons set-up as shown in Figure 2.

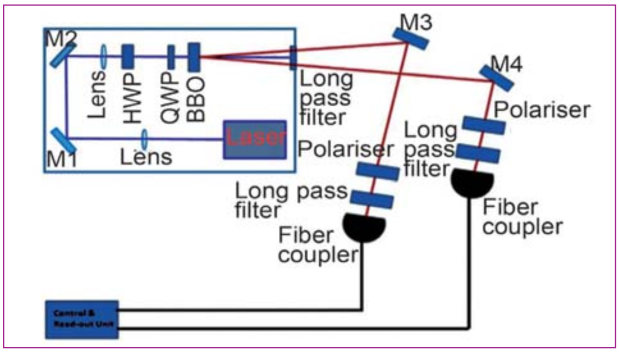

Fig. 1 *Lab facility with a SPDC source generated with a 405 nm diode laser*

To confirm that they are so, statistical tests generically called Bell's inequalities were carried out to show that the results cannot be explained by any local realistic theories. Quantum Theory however is in exquisite agreement with experimental data. An FPGA based four channel coincidence counting unit (a critical component) has been developed in-house by as a part of this program.

The world over, basic research in the field of quantum states of light is actively pursued with promising applications in field of metrology, computation information processing and imaging. These are however early days and the technological challenges are formidable. With more advanced facilities we are building, we hope to be part of these developments.

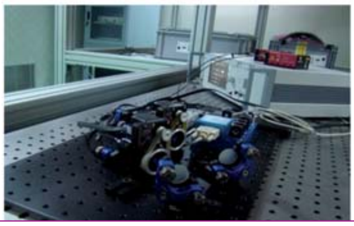

Fig. 2 *First level Lab facility with a SPDC source generated with a 405 nm diode laser*

V.35 Synchrotron XAS Study of Spray Pyrolysis Grown N: TiO_2 Thin Films

X-ray Absorption Fine Structure(XAFS) spectroscopy is used to study, the local structure around a selected element in a material,at atomic and molecular scale. It can be used for all kinds of materials including crystalline, semi-crystalline, amorphous and liquids. It is an intrinsically quantum mechanical phenomenon that is based on the X-ray photoelectric effect, in which an X-ray photon incident on an atom within a sample is absorbed and liberates an electron from an inner atomic orbital (e.g. 1s). The “photoelectron” wave scatters from the atoms around the X-ray absorbing atom, creating interferences between the outgoing and scattered parts of the photoelectron wave function. These quantum interference effects cause an energy-dependent variation in the X-ray absorption probability, which is proportional to the X-ray absorption coefficient $\mu(E)$, a measurable quantity. When properly decoded these modulations provide information about the structure, atomic number, structural disorder, and thermal motions of neighboring atoms. X-ray absorption co-efficient $\mu(E)$ describes how strongly X-rays are absorbed as a function of X-ray energy E. Generally $\mu(E)$ smoothly decreases as the energy increases(approximately as $1/E^3$), i.e. the X-rays become more penetrating. At specific energies, when the X-ray photon has sufficient energy to liberate electrons from the low energy bound states in the atoms, $\mu(E)$ increases giving rise to pre-edge peaks corresponding to electronic transitions and an absorption edge corresponding to a particular orbit; mostly the core shells like K-shell or L-shell.

In a typical XAFS measurement $\mu(E)$ *vs* E is measured between 100eV below(Pre-edge region) to 200 eV(known as post edge region; contains white line and extended fine structure) above the absorption edge.(Figure 2). $\mu(E)$ in case of thin films is measured by measuring the fluorescent x-ray, i.e the X-Ray generated due to the refilling of the core-hole. In such a case $\mu(E)$ is directly proportional to I_f / I_0. I_f was measured by a solid state detector and I_0 was measured by an ionization chamber, thus generating $\mu(E)$. The experimental arrangement for a fluorescence measurement is given in the Figure 1. In the present case, TiO_2 and N-doped TiO_2 thin films were synthesized by open atmosphere spray pyrolysis technique at three temperatures; viz. 400, 450, and 500 °C. The XAS measurements of the above synthesized thin films were carried out in fluorescence mode at the scanning XAS beamline of the Indus-2 Synchrotron Source (2.5 GeV, 125 mA). The XAS spectra are given in Figure 2.

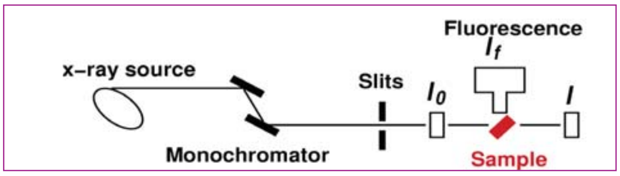

Fig. 1 *Experimental arrangement for a typical fluorescence measurement*

In X-ray absorption spectroscopy, the variation in electron transition probabilities give rise to absorption spectra. The dipole selection rule for XAS is $\Delta l = \pm 1$; $\Delta l = +1$ being the favored transition. The white line observed above the edge in the present study is characteristic of anatase phase and can be attributed to the promotion of a photoelectron to the vacant np orbital of Ti or the antibonding orbitals of Ti−O system. When a system lacks a center of inversion symmetry the pre-edge features consists of weak dipole forbidden 1s−3d transitions. Anatase has distorted TiO_6 octahedrons. Hence, three pre-edge peaks (A_1, A_2, and A_3 at 4957, 4961, and 4963 eV, respectively) are seen in the spectra (Figure 2). The pre-edge peaks A_2 and A_3 are attributed to the $1s{-}2t_{2g}$ and $1s{-}3e_g$ transitions in the octahedral field, respectively.

For a detailed analysis of the spectrum, the data in $\mu(E)$ is converted to another absorption function $\chi(E)$ using the equation;

$$\chi(E) = \frac{\mu(E) - \mu_0(E)}{\Delta\mu_0(E_0)}$$

where E_0 is the absorption edge energy, $\mu(E)$ is the experimentally measured fluorescence, $\Delta\mu_0(E_0)$ is the edge step, and $\mu_0(E)$ is a smooth background curve that is fit to the data to remove extraneous contributions from absorption due to lower-energy edges by the atoms of interest, absorption from other elements, absorption from the ion chamber (used to

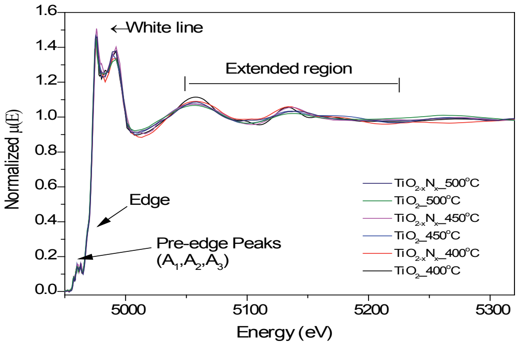

Fig. 2 *XAS spectrum of TiO_2 and N: TiO*

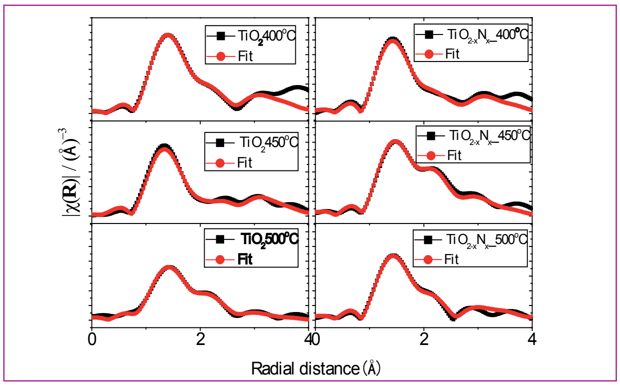

Fig. 3 *Extended region fitting using ARTEMIS in R-space*

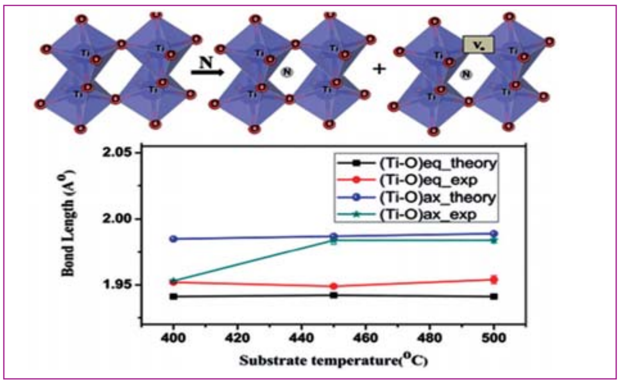

Fig. 4 *Schematic of position of N and oxygen vacancy (V_o) and the comparison of Ti-O experimental and theoretical bond length*

measure I_0) and air path between the chambers. The pre-processing of data before getting any physical parameters from the spectra is done using a software package ATHENA, which facilitates the background correction above edge using a cubic spline function, normalizing the edge step to unity to account for the effects of sample concentration, thickness, detector solid angle, filter thickness, slit position, etc.

Data analysis in the extended region EXAFS is either done in k-space or in Fourier transformed R-space. Hence, the absorption coefficient χ(E) is converted to k-space (χ(k)) using the following relationship:

$$k = \sqrt{\frac{2m(E - E_0)}{\hbar^2}}$$

Where, m is the mass of the electron and $\chi(k)$ is weighted by k^3 to amplify oscillations at high k. The k^3 $\chi(k)$ functions are Fourier transformed to R-space using ARTEMIS software package. $\chi(R)$ versus R (radial distances) plots are then used to derive the coordination number and radial distances of the atoms in various coordination spheres (TiO_6 octahedrons in this case) (Figure 3). The above curves were then fitted using four paths (Two paths belonging to Ti-O and two belonging to Ti-Ti) in case of pristine TiO_2. A total of five paths were used for to fit the N: TiO_2; four from the pristine TiO_2 along with an additional Ti-N path. Each path had parameters corresponding to bond length, co-ordination number and Debye Waller factor. The bond lengths and co-ordination number of Ti with respect to axial and equatorial oxygen atoms were subsequently derived for both pristine and N: TiO_2 and is given in Table 1 and 2. From Table 1 it can be observed that, the coordination number of Ti in the first coordination sphere for the pristine TiO_2 samples synthesized at 400, 450, and 500 °C is 4.8, 6.2, and 4.4, respectively. The films obtained at 450 °C were found to be stoichiometric compared to those obtained at 400 and 500 °C. The stoichiometry of sample synthesized at 450 °C is due the reaction pathway, which is described here. When the aerosols approach the substrate, first the solvent evaporates, and then the precursor undergoes vaporization, followed by reactive decomposition of vapors at the substrate to give TiO_2 films of well-defined grains. A look at the coordination number of Ti−O atoms in the first coordination sphere for doped samples (4.6, 4.9, and 4.3 for 400, 450, and 500 °C respectively) in Table 2 reveals that, when nitrogen is introduced to the interstitial position at a bond distance of ~2.33 Å, the number of oxygen atoms in the first coordination sphere decreases (in comparison to pristine samples), pointing to the creation of oxygen vacancies. The position of these oxygen vacancies were delineated by comparing the Ti-O bond distances of N: TiO_2 thin films with that of theoretically calculated oxygen defected TiO_2 sample (from the literature) (Figure 4). It was observed from the above comparison that oxygen vacancies occupy both axial and equatorial positions in TiO_6 octahedra of N: TiO_2.

Table1: Ti-O bond distances and co-ordination number (C.N) of TiO_2

Synthesis temperature	Path	Bond length(Å)	C.N
400°C	Ti-O	1.913(1)	4.00(1)
	Ti-O	*1.915(5)*	*0.866(2)*
450°C	Ti-O	1.910(1)	4.80(1)
	Ti-O	2.184(2)	1.468(04)
500°C	Ti-O	1.960(1)	3.204(3)
	Ti-O	1.824(1)	1.298(6)

Table 2: Ti-O bond distances and co-ordination number (C.N) of N:TiO_2

Synthesis temperature	Path	Bond length(Å)	C.N
$TiO_{2-x}N_x$ 400°C	Ti-O	1.952(1)	3.072(7)
	Ti-O	1.953(1)	1.536(7)
	Ti-N	2.326(2)	1.344(7)
$TiO_{2-x}N_x$ 450°C	Ti-O	1.949(1)	3.292(3)
	Ti-O	1.984(3)	1.646(3)
	Ti-N	2.334(1)	1.056(3)
$TiO_{2-x}N_x$ 500°C	Ti-O	1.954(3)	2.920(03)
	Ti-O	1.984(2)	1.460(04)
	Ti-N	2.371(02	1.614(03)

V.36 Functionalized Nanographite based Lubricants

Graphite, graphene and other lamellar solids such as crystalline molybdenum-disulphide (MoS_2) and tungsten disulphide (WS_2) are known to be good solid lubricants and, thus, are widely used in several practical applications. When the liquid lubricant is chemically grafted with lamellar materials via functionalization it allows shear and high strength boundary film formation across sliding interfaces leading to low friction coefficients. However, dispersion of nano-materials in the lube media is challenging due to the difference in cohesive forces. But high specific surface area of lamellar materials provides energy for chemical functionalization and dispersion in polar lube medium. Here, direct dispersion and functionalization of graphite nanosheets (Gr-NS) in poly(ethylene-glycol) (PEG200) applying γ-irradiation dose is proposed. Oxygen functional group of Gr-NS is grafted by the hydrogen bonding with hydroxyl group of intercalated PEG molecules. Prior to γ-ray treatment, graphite powder (weight 30 mg) was dispersed in 3 ml PEG200 by ultrasonication at a working frequency 30 kHz for 3 hours. The resultant dispersion of nano-graphite (weight 30 mg) in 3 ml PEG200 was then irradiated in a γ-ray chamber which housed a ^{60}Co γ-ray source for a dose of 275.4 KGy under atmospheric sealed condition. After completion of reaction, brown colour of graphite oxide becomes black, indicating reduction of oxygen functional groups. The sample was processed after centrifugation, washed in water and dried in a vacuum oven at 60°C for obtaining powder form of PEG200 functionalized Gr-NS.

FTIR analysis was conducted to characterize the changes in functional group that occurred during the γ-radiolysis of Gr-NS dispersed in PEG200. The pure PEG200 spectrum shows characteristic bands of specific functional groups (Figure1a). The doublet at 2938 and 2872 cm^{-1} belongs to symmetric and anti-symmetric C-H stretching modes, O-H at 3407 cm^{-1} and C-O-C at 1062 cm^{-1}. These three characteristic bands appeared in Gr-NS dispersed - PEG200 samples subjected to γ–radiolysis at a dose of 275.4 kGy. The spectra indicates existence of hydrogen bonding between PEG200 and Gr-NS (Figure1b). FTIR signals are very weak in zero dosed samples, indicating absence of effective anchoring of Gr-NS with PEG200 (Figure 1c).

Similar magnitude of friction coefficient ~0.15 in pure PEG200 and Gr-NS at zero dose was observed (Figure 2). This indicates that without γ-irradiation, Gr-NS does not have friction reducing capability due to absence of chemical grafting with PEG200. However, this value reduces to ~0.09 in γ-ray exposed sample. Such an improvement in tribological properties is explained by (a) effective shearing of graphite interlayer due to anchoring of PEG200 with Gr-NS and (b) formation of chemisorbed Gr-NS tribo-film in wear track. The deposited Gr-NS prevents the direct contact between the tribo-pairs and exhibited remarkable improvement in wear property.

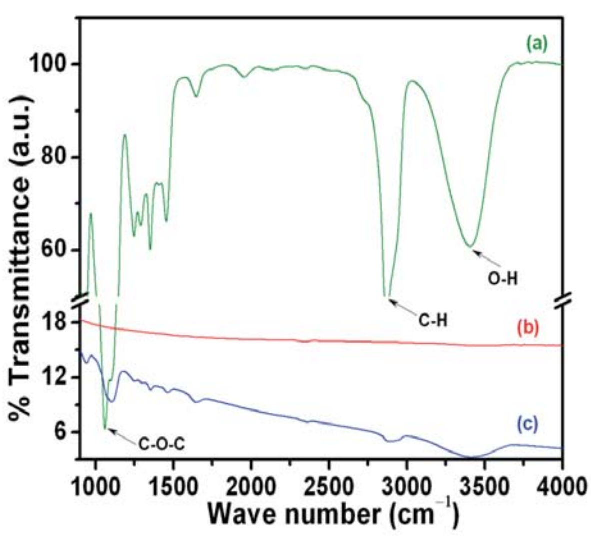

Fig. 1 FTIR of (a) pure PEG200, γ– radiolysis of Gr-NS at (b) 0 dose and (c) 275.4 kGy

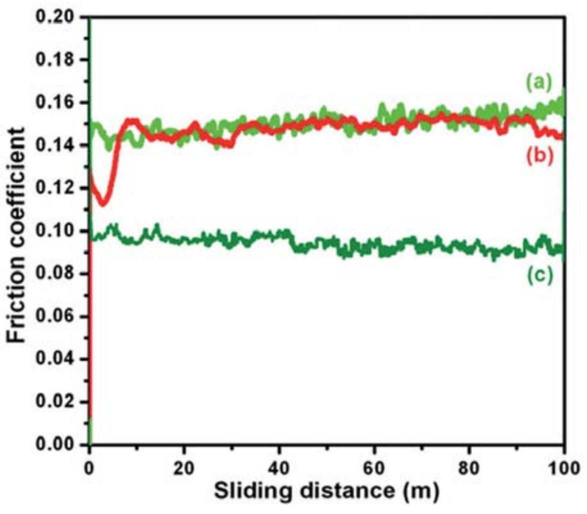

Fig. 2 Friction coefficient (a) pure PEG200 (b) γ– radiolysis sample (b) 0 dose and (c) 275.4 kGy. Tribo-test condition: PEG-Gr-NS concentration 0.03 mg mL^{-1}, load 1 N, sliding speed 3 cm/s

5.37 Focused Ion Beam Applications in Nanofabrication and Characterization

Focused ion beam (FIB) microscope has been widely used for basic material characterization and technological applications for the past several years. It has the potential of imaging and milling (also referred as etching/machining). Its operation is analogous to a scanning electron microscope (SEM), but a gallium (Ga) beam rasters the sample surface and the secondary electrons/ions produced are used for imaging. As the energy of the ion beam is ample to sputter etch the target material (sample), it is also used for material removal. FIB system described in this article is combined with a high-resolution field emission scanning electron microscope (FE-SEM) and a gas injection system (GIS). This combination has the capabilities of ion beam activated deposition and enhanced etching, electron beam induced deposition and imaging with both ion and electron beams. An additional advantage of this so-called dual-beam system is that the ion beam assisted routines can be monitored (imaged or recorded) by electron beam. Deposition and material removal is typically performed at length scales of a few nanometers to hundreds of micrometers. Therefore this system plays a vital role in nanofabrication.

Figure 1 shows a schematic of the FIB-SEM system with a GIS facility. The electron column is placed vertical and the ion column is fixed at an angle of 54 degrees from the vertical column. Hence, this system is also referred as a 'cross-beam' system. Coincidence point of both the beams is at 5 mm down to the electron column pole-piece and it is the typical working distance of the system. GIS is a five channel system which offers precursors of platinum, tungsten (W) metals and silicon dioxide insulator for deposition; water and xenon difluoride for assisted etching. Acceleration voltage of electron and Ga ion beam could be (continuously) varied up to 30 kV. Lateral resolution is about 1 and 2.5 nm for the electron and ion microscope, respectively. The probe current can be varied from a few pA to few tens of nA for both the beams. The system has a standard in-chamber Everhart-Thornley detector and an in-lens detector. Secondary electrons generated by the interaction of the electron/ion beam at the sample surface are collected by these detectors for obtaining high spatial resolution images.

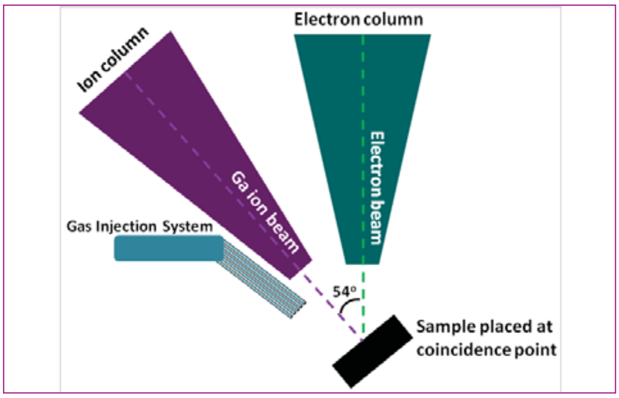

Fig. 1 *FIB-SEM dual-beam system with five-channel GIS facility. Sample is tiled to 54 degrees and placed at 5 mm working distance*

An in-built basic lithography option of the system enables milling and deposition of simple geometric patterns. Creation of complex patterns, however, needs a dedicated lithography module which might control both the beams. Nanomanipulation could be done using *nanomanipulators* which are analogous to robotic arms that operate inside the FIB-SEM chamber and controlled from outside. The nanomanipulators extend the system utility to several applications including TEM lamella preparation, electrical and mechanical testing of nano-features and nano-manipulation desired for advanced nanofabrication. Using the facilities presently available with the system, the following categories of works are being carried out and a few examples for each category are provided in this article.

Etch rate of the sample could be controlled with the probe current (of Ga ion beam). Therefore, it is possible to perform a rough milling to a fine polishing, on almost any solid matter, with high and low probe currents,

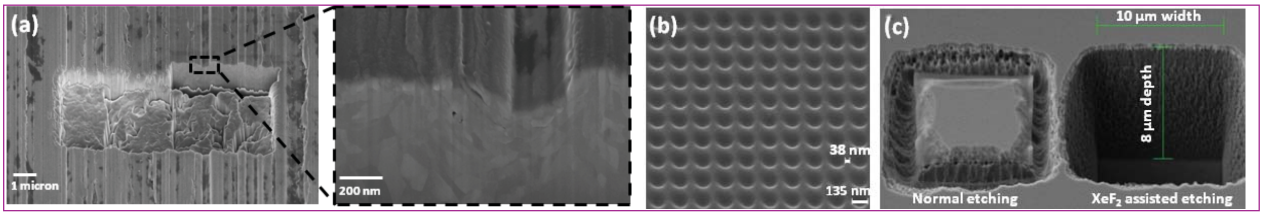

Fig. 2 *(a) FE-SEM image of a FIB-milled wear track across the rolling direction. Magnified view shows the subsurface details; (b) array of etch-pits created by FIB on Si surface and (c) for an equal etching time, XeF_2 assisted etching on Si shows an enhancement in etch-rate and homogeneity in material removal compared to normal etching*

respectively. The example in Figure 2a shows the application of ion milling in exposing the subsurface of a wear track, where the deformation, nanocracks and pores are exposed by ion milling and subsequently imaged by FE-SEM in secondary electron mode. In this work, a rectangular trench (10 x 3 μm^2) was made across the wear track for about one micron depth by rough-milling and one of the side-walls (which is perpendicular to the rolling direction) was fine-polished to expose the microstructure details. Ion beam etching can also be used for nanofabrication as shown in Figure 2b, where a lithographic array pattern (with a pit size of ~135 nm and gap of ~40 nm) was etched out on a silicon surface. This type of patterns, at various length scales, finds variety of applications from material science to biomedical science. FIB etching sometimes suffers from redeposition and anisotropy in material removal (due to the dependence of sputtering yield on crystallographic direction). The same could be solved, to a larger extent, with gas assisted enhanced etching. GIS reserves two nozzles for the injection of XeF_2 and H_2O, which are normally used for etching silicon and carbon based materials, respectively. Figure 2c shows a significant enhancement in the etching of silicon with XeF_2. It is evident that both the etch rate and homogeneity in etching are greatly improved.

Along with GIS, either Ga ion or electron beam could be used to deposit Pt, W and SiO_2 from nano- to micron-scales. Deposition occurs, at areas where the beam rasters, by decomposing the gaseous precursor material injected by GIS over the sample surface (Figure 3). As shown in Figure 3 precursor molecules supplied through GIS are physisorbed on the surface and decompose under the (Ga ion or electron) beam to leave a well-defined deposit on the surface, while volatile fragments are pumped-out. Diffusion of any Ga and carbon species into the deposit are indicated with orange and violet discs, respectively. Deposition rate depends on the geometry of GIS nozzle and sample, probe current and etching rate. This facility finds several applications including, fabrication of electron beam lithography masks, nanodevices fabrication and repair, patterns and templates formation. Figure 4 shows a few applications using ion and electron beam induced depositions.

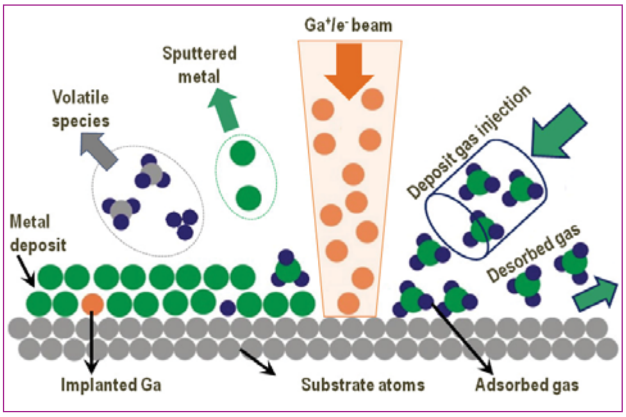

Fig. 3 *Schematic of a gas assisted deposition procedure*

Therefore FIB-SEM with GIS is a vital and versatile tool in nanofabrication and this article is aimed to provide the basic information and application of the system in fundamental materials science and technological applications.

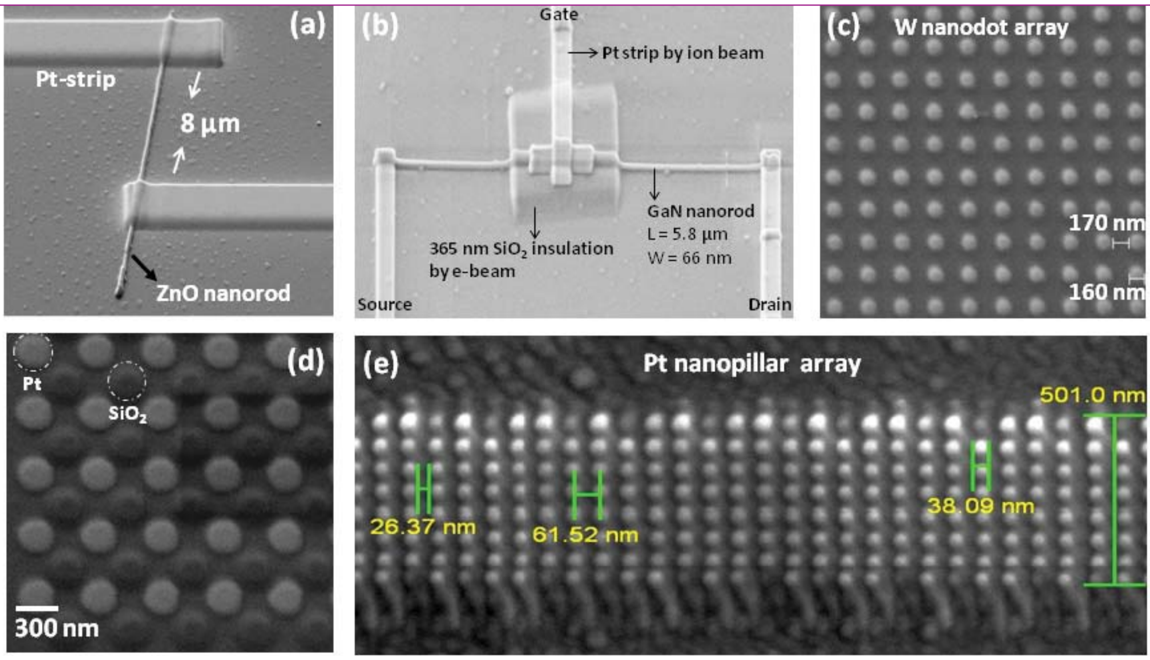

Fig. 4 *(a) ZnO nanorod two terminal device with FIB-deposited Pt strips; (b) GaN FET structure with Pt strips by ion beam and SiO_2 by electron beam, (c) W nanodot array deposition by FIB; (d) Pt/SiO_2 interpenetrated nanodot array by FIB and (e) Pt nanopillar array by electron beam induced deposition*

V.38 Localized Charge Transfer Process in Methane Sensing by GaN Nanowires

Intrinsic or extrinsic defects in materials strongly influence the physicochemical processes at the surfaces of semiconductor nanostructures involved in electrochemical and sensing devices. Intentional lattice oxygen defects were created on the surfaces of GaN nanowires for the elucidation of charge transfer process in methane (CH_4) sensing to understand the surface controlled sensing mechanism. Possible presence of $2(O_N)$ and V_{Ga}–$3O_N$ defect complexes were confirmed by both experimental and simulation results of electron energy loss spectroscopy studies on oxygen rich GaN nanowires. A comprehensive resistive response for sensor devices of ensemble nanowires along with a localized charge transfer process in single GaN nanowires were studied *in situ* by scanning Kelvin probe microscopy. A localized charge transfer process, involving the V_{Ga}–$3O_N$ defect complex on nanowire surface was ascribed in controlling the global gas sensing behavior of ensembled GaN nanowires rich with oxygen content.

Nonpolar GaN nanowires having different oxygen concentrations were synthesized using chemical vapor deposition technique in a vapor-liquid-solid growth mechanism. Four nanowire samples (Figure 1a) were grown under different oxygen impurity concentrations of ~10^5 ppm (R1), 10^3 ppm (R2), 10^2 ppm (R3) and < 2 ppm (R4), for the present study.

In this report, responses of the devices were obtained at different concentrations and temperatures in the N_2 (99.999%) background at 10^{-2} mbar base pressure of the sensor chamber. In the dynamic gas sensing, the gas was flown at a fixed flow rate over the sensor device while maintaining a fixed pressure in the sensing chamber under constant pumping using a dry pump. Nanonics Multiprobe (MultiView 4000) system was used for the *in situ* localized gas exposure studies at elevated temperature of 100 °C on single nanowires under vacuum. A two-lock-in amplifier setup was used for the simultaneous topography and surface potential imaging. Tuning fork based (f_z ~34.4 kHz and Q-factor

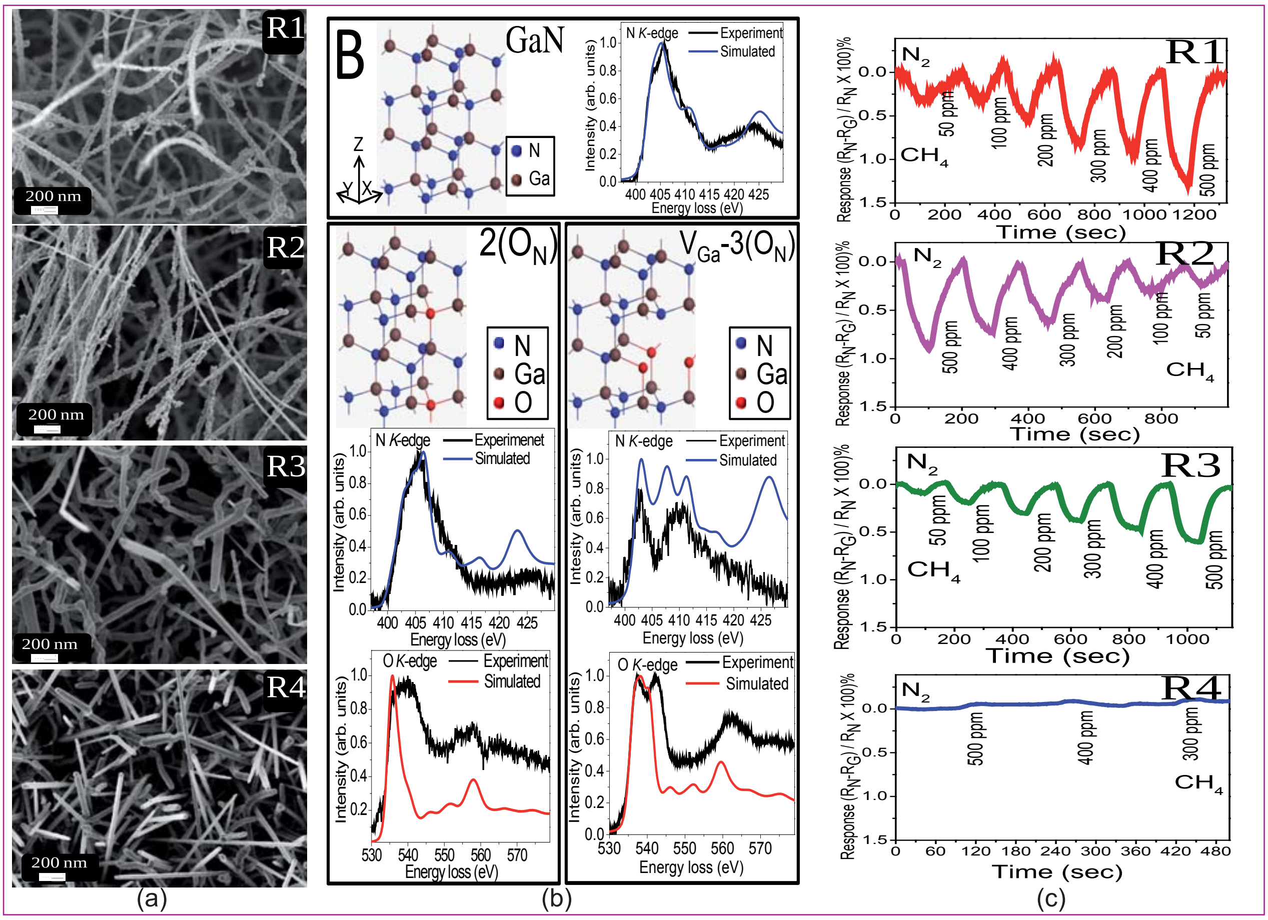

(a) (b) (c)

Fig. 1 (a) Morphology (b) experimental and simulated lectron energy loss spectroscopy spectra of GaN nanowires for O defect concentrations and (c) resistive gas sensing for GaN nanowires

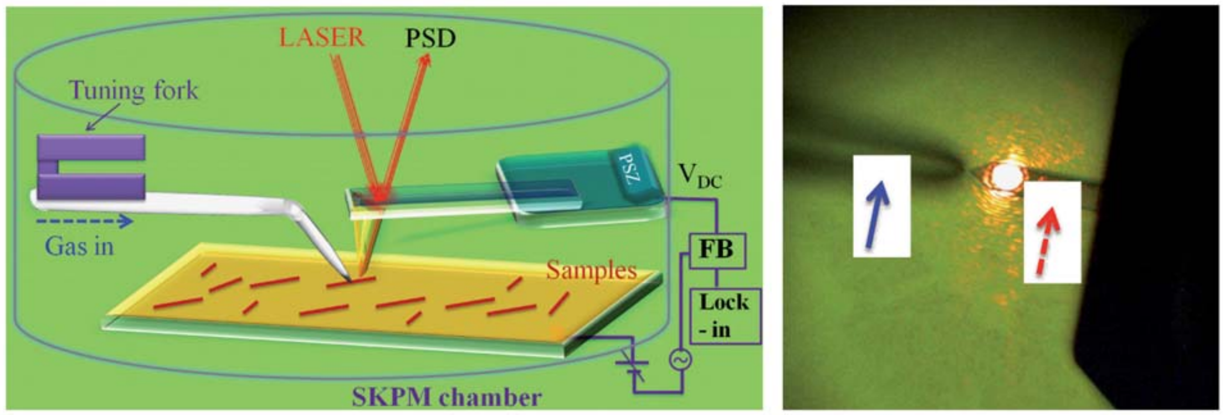

***Fig. 2** Schematic scanning Kelvin probe microscopy measurement setup*

~1080) nano-pipette (aperture size ~200 nm) gas delivery system was used for localized pico-liters (10^{-12} liters) of gas delivery on a single nanowire.

The experimental and the simulation of electron energy loss spectroscopy studies on oxygen impurities in GaN NWs established the possible presence of $2(O_N)$ and V_{Ga}–$3O_N$ defect complexes (Figure 1b). The resistive gas sensor devices made of GaN nanowires with different oxygen impurity concentrations showed the response with the reduction in resistance with the exposure to CH_4 (Figure 1c). The scanning Kelvin probe microscopy measurements showed (Figures 2 and 3) a reduction in the surface potential value with an increase in the diameter. A reduction in the surface potential value is also recorded as the oxygen concentration increases in nanowires. The observed variations in surface potential (Figure 4), depletion width, and surface charge density (not shown in figures) during the scanning Kelvin probe microscopy measurements on nanowires exposed to CH_4 established the occurrence of gas adsorption and charge transfer processes in these nanowires. A localized charge transfer process, involving V_{Ga}–$3O_N$ defect complex in nanowires is ascribed in controlling the global gas sensing behavior of the oxygen rich ensembled GaN nanowires. By tuning the surface lattice oxygen defects on nanowires, control of the sensing behavior of GaN nanowires could demonstrated. The present study provides an insight for controlling the defects in III-nitride based nanostructures for advanced gas sensor applications.

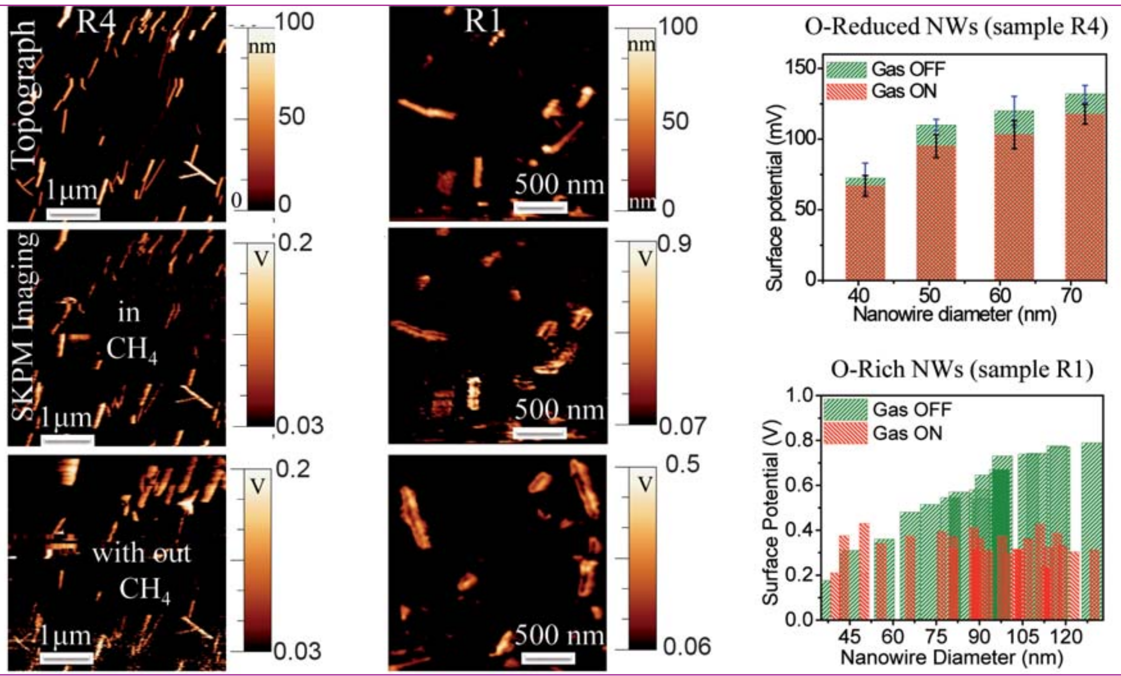

***Fig. 3** Typical topographs and scanning Kelvin probe microscopy maps of samples before and after exposure to CH_4. Nanowire diameter dependent SP values extracted from the scanning Kelvin probe microscopy maps*

V.39 Raman Spectroscopy Study at Sub-diffraction Limit

GaN nanowires (NWs) with Mg dopants (GaN:Mg) and AlGaN were grown by the atmospheric chemical vapor deposition (APCVD) technique in the catalyst assisted vapor-liquid-solid (VLS) process. Spectroscopic imaging and analysis of nanostructures are performed in the sub-diffraction limit. Adopting the plasmonics, the localized effect of impurities in single GaN nanowires of diameter ~40 nm in the sub-diffraction limit of ~ 300 nm (λ/2N.A.), using an excitation wavelength (λ) of 514.5 nm and 100x objective with a numerical aperture (N.A.) value of 0.85, is reported using the study of lattice vibrational modes in the evanescent field of Au nanoparticle assisted tip enhanced Raman spectroscopy (TERS). The TERS measurements on dispersed GaN NWs on Cu(100) substrate were carried out using the scanning probe microscopy setup coupled with a laser Raman spectrometer in the backscattering configuration. The probe is atomic force microscopic (AFM) bent glass tip attached with Au particle (diameter < 100 nm) and it is operated under non-optical normal force feedback. The Raman signals are collected by exciting the samples with 514.5 nm laser and are dispersed with a 1800 gr.mm^{-1} grating and a thermoelectric cooled charged couple device (CCD) detector.

In the TERS study, along with the symmetry allowed Raman vibrational modes, surface optical mode of A_1 symmetry is also observed for both the undoped and the Mg doped GaN samples (Figure 1). Study of the local vibration mode shows the presence of Mg as dopant in the single GaN nanowires. We demonstrate polarized resonance Raman spectroscopic (RRS) studies (Figure 2) with strong electron-phonon coupling to understand the crystalline orientation of a single AlGaN nanowire of diameter ~100 nm in the [0001] direction with A_1(LO) mode being absent in the cross polarization, as per selection rule. As a matter of fact, optical confinement effect due to the dielectric contrast of NW with respect to that of surrounding media assisted with electron-phonon coupling of RRS are useful for the spectroscopic analysis in the sub-diffraction limit of 325 nm (λ/2 N.A.) using an excitation wavelength of 325 nm and near ultraviolet 40x far field objective with a numerical aperture value of 0.50.

Thus, TERS study showed presence of surface optical modes originating from the surface defects for both the undoped and Mg doped GaN samples. Observation of local vibrational mode pertaining to GaN:Mg sample confirms the presence of Mg as dopant in the single GaN nanowires. Thus the TERS can be used for the localized effects by impurities in a single nanowire for developing the nanowire based electronic and optoelectronic devices. Polarized resonance Raman spectroscopy studies with strong electron-phonon coupling is used to understand the crystalline orientation of a single AlGaN nanowire. The crystallographic orientations predicted by the polarized Raman spectroscopy shows a good agreement with the structural analysis (not shown in figure). The optical confinement effect due to the dielectric contrast of NW with respect to that of surrounding media along with strong electron-phonon coupling of resonance Raman spectroscopy is useful for the spectroscopic analysis in the sub-diffraction limit of ~100 nm using a wavelength of 325 nm.

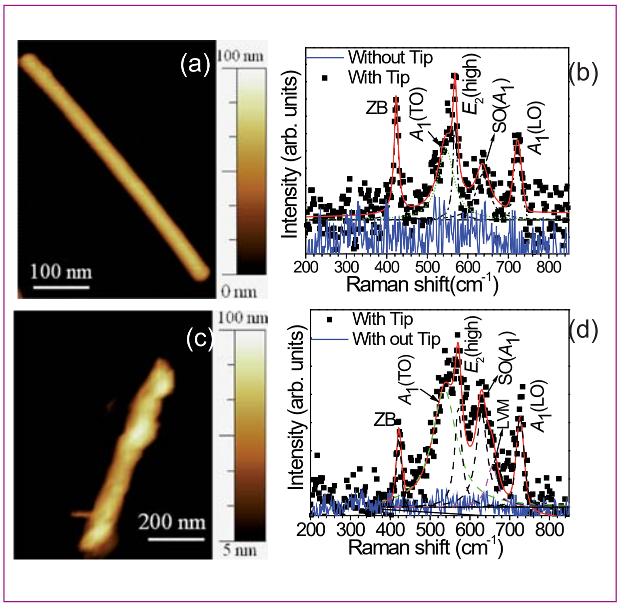

Fig. 1 (*a) AFM image and (b) TERS spectra of undoped; (c) AFM image and (d) TERS spectra of GaN:Mg single NW without and with TERS tip*

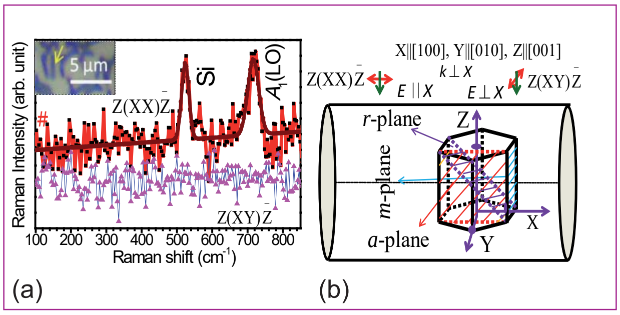

Fig. 2 (*a) Polarized resonance Raman spectra for single AlGaN NW for different polarization configurations and (b) the schematic diagram with possible stacking arrangement of unit cells in the cylindrically shaped nanowire*

V.40 Effect of Surface Stress on the Resonance Frequency of Uncoated Microcantilevers

Micro fabricated cantilever structures have been demonstrated to be extremely versatile sensors. Measurement of adsorbed mass on these structures result in decrease in resonance frequency, which offers one of the most sensitive mass sensing techniques approaching single molecule detection. Although, one would expect the frequency shift to be inversely proportional to the square root of the added mass, there are several other mechanisms like non-uniform mass loading, flexural rigidity of the adsorbate, surface stress, surface elasticity, etc which will influence the stiffness of the cantilever, making the mass measurement qualitative. In the present work, the influence of surface stress on the stiffness of three uncoated microcantilevers (MCs) with reducing dimensions is studied.

Commercially available tipless microcantilevers were used in the present work (Table 1). Resonance frequency of microcantilevers were measured using laser photo diode arrangement of an AFM head. For adsorption of water molecules, experiments were performed by placing the AFM head along with the cantilever, inside an airtight chamber purged with nitrogen gas which reduces the relative humidity (RH). For increasing the RH, N_2 was bubbled through deionised water (Figure 1).

The unloaded resonance frequency, ‘f_1’, of an oscillating microcantilever and is given by

$$f_1 = \frac{1}{2\pi}\sqrt{\frac{k}{m^*}}$$

where ‘k’ is the spring constant and ‘m*’ is the effective mass of the microcantilever. When adsorbates are deposited uniformly on the cantilever surface, the resonance frequency will shift to ‘f_2’ and is given by,

Table 1: Physical dimensions and resonance frequency of three microcantilevers studied in the present work

Name	Length (L) (µm)	Width (W) (µm)	Thickness (T) (µm)	Resonance frequency (f1) (kHz)
MC1	450	40	2.5	12.10104
MC2	225	30	3	66.85423
MC3	125	35	4.5	332.19681

$$f_2 = f_1\sqrt{\frac{k+\Delta k}{k}}\sqrt{\frac{m^*}{m^*+\Delta m}}$$

where, ‘Δm’ and ‘Δk’ are the changes in mass and spring constant respectively due to adsorption. It is evident from equation that if $\Delta k = 0$, added Δm will always result in negative frequency shift ($f_2 < f_1$).

Figure 2 shows the typical relative resonance frequency shift of three microcantilevers as a function of increasing RH i.e., during physisorption of water. It is clear that for the cantilever MC1, the frequency decreases with added mass, as would be expected, whereas for MC2 and MC3, the frequency hardens initially with the added mass. At higher mass loading, in the case of MC2, the frequency decreases. These trends clearly indicate that the observed frequency change is a combination of both the mass loading and stiffness change during the adsorption of water.

In order to discriminate the contribution of each of these two effects, the frequency shift due to added mass on MC surface is numerically computed. The expected frequency shift, due to added mass alone, for each

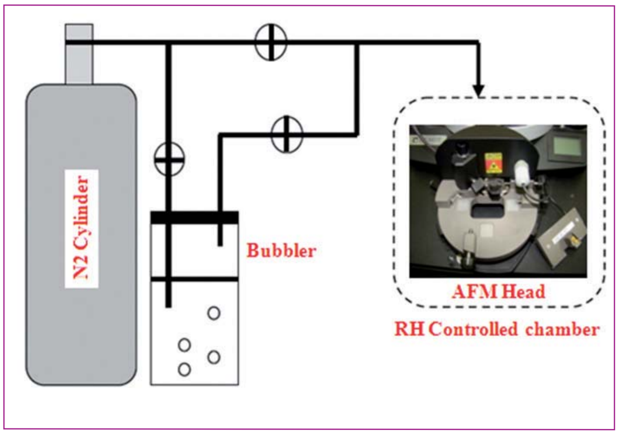

Fig. 1 Block diagram of the experimental setup used in the present work for adsorption / desorption of water molecues on microcantilever surface

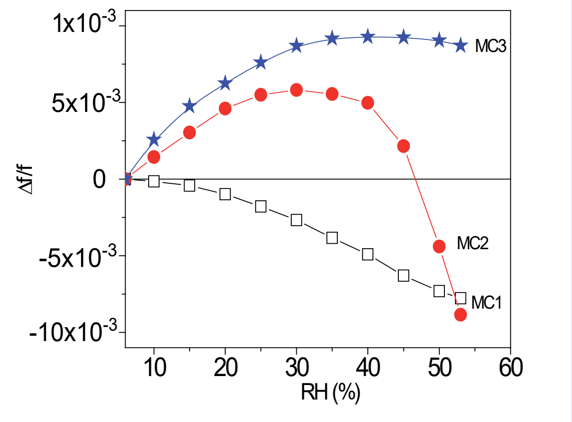

Fig. 2 Relative shift in resonance frequency with increasing RH in MC1, MC2 and MC3

MC is calculated by substituting Δk = 0 in equation. The difference between the observed frequency shift and that calculated, is converted into to the variation in Δk for all the microcantilevers. Figure 3 shows the computed relative change in spring constant (Δk/k) for three microcantilevers with added mass per unit area (surface density). From this figure it is clear that Δk/k is maximum in MC3 and as expected is negligible for MC1. The observed Δk/k arises due to the surface stress generated during adsorption.

To estimate the surface stress, microcantilever bending measurements were carried out, using the same set up. From the deflection data (Δz), differential surface stress (Δσ) is estimated using the modified Stoney's equation given by,

$$\Delta\sigma = \frac{ET^2}{4(1-\upsilon)L^2}\Delta z$$

where, 'E' is Young's modulus, 'υ' is Poisson's ratio and 'L' and 'T' are length and thickness of the MC, respectively. Δσ generated during adsorption with surface density in all the MCs is shown in Figure 4a.

In Figure 4b we plot Δk/k, as obtained from Figure 3 with Δσ, as obtained above. A linear correlation between the change in spring constant and the measured change in surface stress due to adsorbed water is clearly seen for the smaller cantilevers MC2 and MC3, in which a positive frequency shift is observed with added mass. These experimental observations are attributed to the in-plane stress generated during adsorption at fixed end of MC i.e. clamping effect. Clamping exerts reaction forces to cancel out the curvature induced by the bending moment during adsorption. It must be emphasized that MCs are rigidly clamped to a chip substrate and does not participate in the vibration during dynamic measurements. This results in non uniform curvature at fixed end there by increasing the stiffness of MC which will be dominant when MC dimensions reduce. Further, Δk/k estimated was found to follow a linear relationship with Δσ scaled to the cube of width to height ratio of MCs. This clearly indicates that the stiffness is proportional to both surface stress generated during adsorption and dimensions of MC.

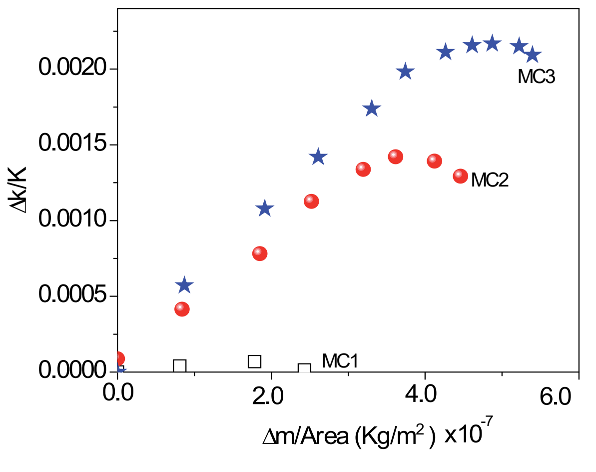

Fig. 3 *Variation of stiffness change with respect to mass per unit area of threemicrocantilevers*

In conclusion, the influence of surface stress on microcantilever stiffness during adsorption of water molecules was studied. Spring constant change (from resonance frequency shift) and differential surface stress generated (from static bending data) during adsorption in three microcantilevers with reducing dimensions were estimated. It is concluded that the surface stress generated during adsorption influences the stiffness of microcantilever and this effect increases with reducing the dimensions of the cantilever. It is pointed out that reducing the dimensions of the microcantilever can greatly influence the adsorption induced stiffness changes.

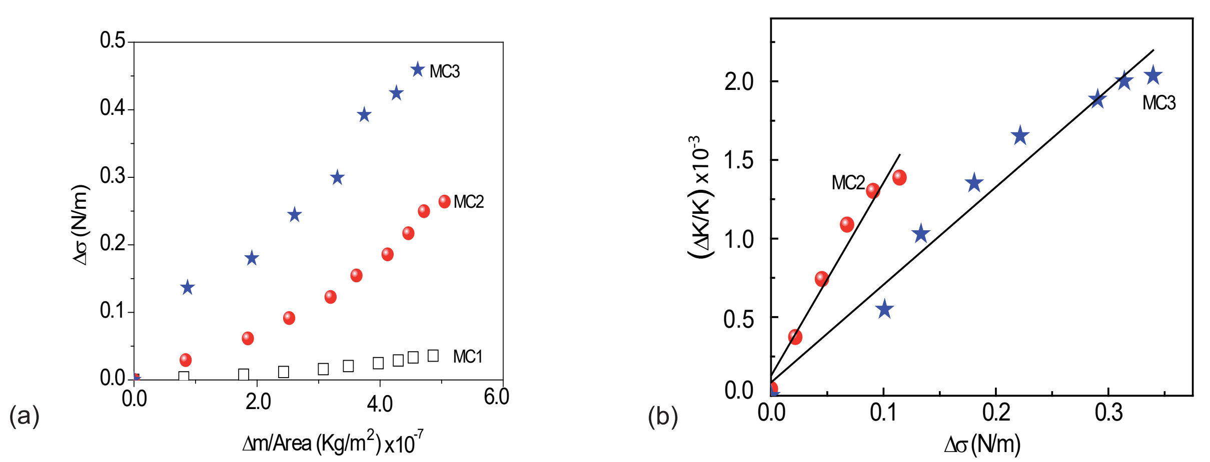

Fig. 4 *(a) Surface stress generated during adsorption in all the microcantilevers with respect to mass per unit area and (b) linear fit of (Δk/k) with (Δσ)*

V.41 Probing of Competitive Displacement Adsorption at Oil-in-Water Interface

Understanding the nature and reversibility of competitive displacement adsorption of smaller molecules at interfaces covered with macromolecules is important from practical applications point of view. Such competitive displacement adsorption provides an unique possibility to reuse adsorbents. The competitive interactions between different adsorbing species determine the stability and product lifetime. Several studies have been carried out on the interaction of protein with other molecules at the air−*water and oil−water interface.* The recent neutron reflectivity studies show that a synergistic interaction between certain nonionic surfactants and proteins can lead to spontaneous self-assembly at the air−water interface to form layered surface structures. Such protein−anionic surfactant interactions can also effectively be used to tune electrostatic interactions. Irrespective of intense research on protein adsorption behavior at interfaces, the understanding is still vague because of the complex interaction between the protein molecules and surfaces through van der Waals, electrostatic, hydrophobic, and hydrogen bonding interactions. Measurement of interaction forces in the presence of adsorbing species at a solid interface is attempted using atomic force microscopy and surface force apparatus.

Better insight into the complex interactions between proteins and oil−water (O/W) interface in the presence of diblock polymers is obtained using in-situ colloidal force measurement. The competitive displacement adsorption efficiency of casein at an oil−water interface stabilized with either negatively charged surfactant or neutral polymer is probed by employing intermolecular force, zeta and hydrodynamic diameter measurements. The equilibrium force distance measurement is employed for the first time to probe the competitive and displacement adsorption of casein at an oil−water (O/W) emulsion interface that was initially adsorbed with either a diblock polymer or an anionic surfactant. A significant change in the force−distance profile was observed under the competitive displacement adsorption of casein, which is further confirmed from the hydrodynamic diameter and zeta potential measurements. A decrease in the onset of repulsion and decay length are observed on competitive adsorption of smaller size casein molecules at O/W interface. With addition of casein in PVA-vac diblock polymer stabilized emulsion, the onset of repulsion decreases from 88 to 48 nm whereas the magnitude of force increases from 1 to 19 nN. The force decay length is reduced from 10.5 to 4.5 nm upon addition of casein. Our results suggest the complete replacement of adsorbed diblock polymers by casein molecules. The hydrodynamic diameter and zeta potential measurements corroborate the casein mediated polymer displacement and the competitive adsorption of casein at the O/W interface. In the case of anionic surfactant covered O/W interfaces, casein molecules weakly associate at the interface without displacing the smaller size surfactant molecules where no significant changes in the onset repulsion and force profiles are observed. These results suggest that the casein molecules are effective displacers for replacement of adsorbed macromolecules from formulations. Based on our results, the conformation of polymer and casein at the O/W interface of casein are schematically shown in Figures 1b and 1c.

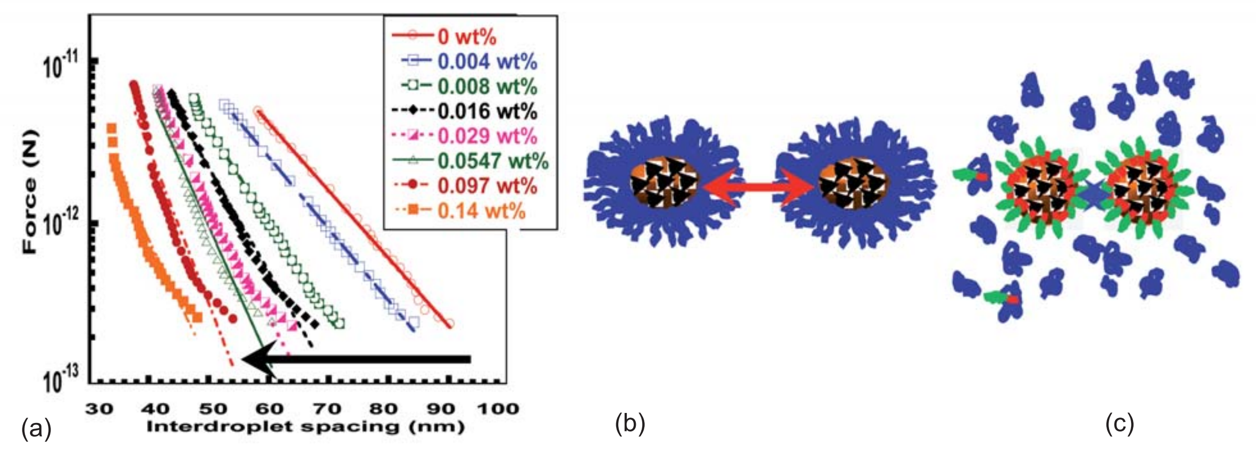

Fig. 1 *(a) Force−distance profiles at different casein concentrations for PVA-vac (115 K) stabilized emulsion. Solid lines correspond to the theoretical fit, (b & c) schematic representation of droplets without and with casein, respectively*

V.42 Enhancing Mechanical Properties of Concrete using Nano Additives

The utilization of fly ash in concrete as a raw material for cement production, and as a partial replacement of cement in concrete is well established. Though the performance benefits that fly ash provides to mechanical and durability properties of concrete have been well documented, sometimes these mixes suffer from early-age performance issues like delayed setting time, low early-age strength, and more stringent curing conditions. Recent developments have been reported on incorporation of different nanoparticles in concrete, to achieve improved physical and mechanical properties. Nanoparticles act either as heterogeneous nuclei for cement pastes further accelerating cement hydration because of their high reactivity,or as nano-filler, densifying the microstructure, thereby, leading to reduced porosity. The combination fly ash and nano materials also tightly bind the hydration products and compensates for the increased early strength development.

Photocatalytic effect of TiO_2 and filler effect of $CaCO_3$ is utilized in the construction industry, however, there has been limited progress on the effect of addition of nano TiO_2 (NT) and $CaCO_3$ (NC) individually and in combination (NTC) of both in fly ash concrete in terms of early and long-term strength and durability properties. The effectiveness of these nanoparticles on strength development and durability properties of fly ash concrete and to evaluate the optimum replacement level was studied.

Six series of concrete mixes of grade M35(Mix of characteristic compressive strength 35N/mm^2) were prepared by replacing cement with NT, NC and NTC particles, with six different contents ranging from 0.5 to 3% by weight of cement, with an increment of 0.5%. The concrete containing NT, NC and NTC particles were labelled under mix series T1 to T6 (T-series), C1 to C6 (C-series), and TC1 to TC6 (TC-series) respectively. NT particles with average size 50-60 nm and NC particles with average size of 50-70 nm was used. The specific gravity of NT and NC particles were 3.76 and 2.69 respectively.

NT and NC particles had a specific gravity of 3.76 and 2.69 respectively. Fly ash was used as a 40% partial cement replacement material and crushed sand with a maximum size of 4.75 mm was used as a 30% partial replacement material for fine aggregate. The coarse aggregate used in the mix was black Granite with maximum size 20 and 12.5 mm. Chemical admixture used to achieve workability was of high range water reducer type, having sulphonated naphthalene formaldehyde as base. F0 concrete mix was control mix without any nanoparticles. The total powder content (cement + flyash + nanoparticles) for all mixes was 375 kg/m^3. Water to powder ratio was 0.44, fly ash content was 150 kg/m^3, river sand 549 kg/m^3, crushed sand 235 kg/ m^3, coarse aggregate 1130 kg/m^3 and chemical admixture was 4.5 kg/m^3.

Slumps of fresh concrete were determined immediately to evaluate the workability. Concrete cubes of 150 mm size to carry out compression test and cylinders of length 200 mm and diameter 100 mm to find the split tensile strength and chloride permeability were cast and stored in a chamber maintaining 90 % relative humidity and a temperature of 27°±2°C for 24 hours and thereafter demoulded. Further, the specimens were submerged in a laboratory curing tank filled with fresh water at a temperature of 28±1°C. To determine the consistency, cement pastes with different percentages of nanoparticles were made. Crushed specimens were utilized further for determining the pH value of concrete. The rapid chloride penetrability test was conducted as per ASTM 1202-97 by slicing the cylindrical specimen into 50 mm thick and 100 mm diameter size. Small pieces from fractured surface of 2% substitution

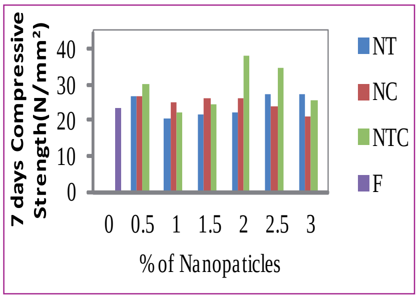

Fig. 1 Early strength of concrete

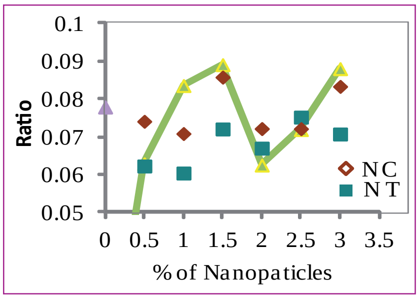

Fig. 2 Ratio of split tensile strength to compressive strength

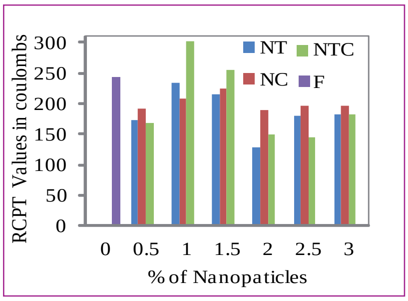

Fig. 3 RCPT value variation

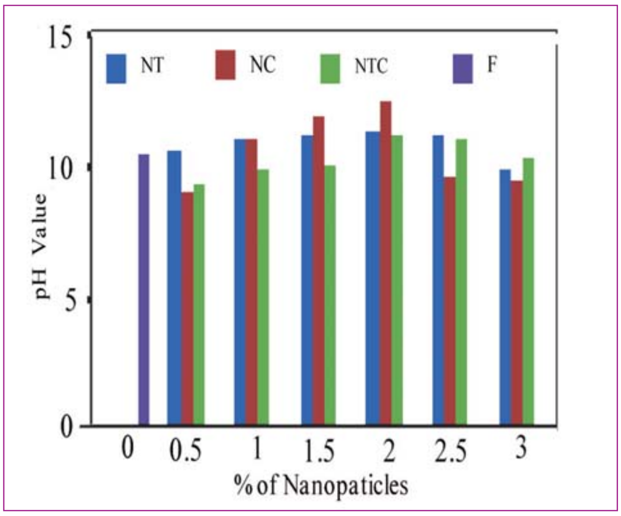

Fig. 4 *pH value variation*

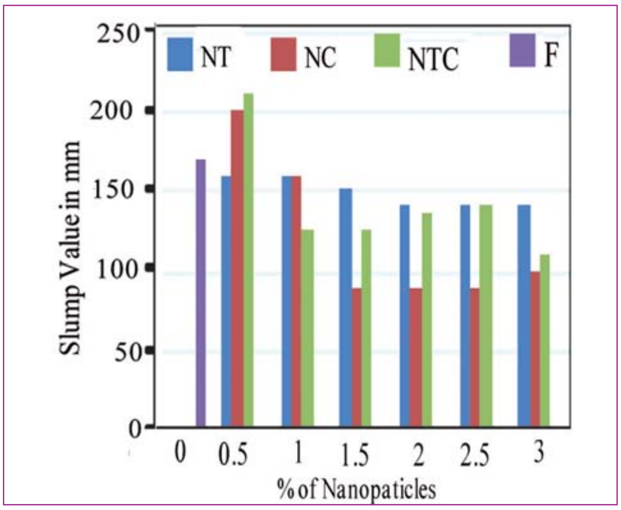

Fig. 5 *Slump value variation*

concrete were used for microanalysis examination using a scanning electron microscope (SEM).

The results show that the addition of nanoparticles greatly enhanced the early and higher age strength of fly ash concrete (Figures 1 and 2). The TC series concrete showed a maximum strength at 2% substitution. The 2% substitution of T and C series concrete yielded slightly lower strength when compared to the maximum strength attained but the rapid chloride penetration test (RCPT) values were very low at this percentage indicating a good impermeable concrete.

The RCPT values (Figure 3) were in the range of 100 – 500 coulombs for all the mixes, which indicated that the chloride ion penetrability is very low. But, the lowest value among all the mixes was observed at 2% substitution and also the maximum pH value (Figure 4) of concrete was seen at 2 % substitution of nanoparticles.

The results show that all the mixes blended with nanoparticles showed a decline in slump value (Figure 5) as the percentage of nanoparticles increased in the mix which was most evident in C series mix. As the percentage of NC particles increased, there was a decrease in the fluidity and increase in water demand of the mix which was confirmed from the consistency values (Figure 6). Though there was a decline in slump value, the concrete was workable.

As the strength, pH and RCPT results were encouraging for the specimens with 2% substitution; these fractured specimens were subjected to microanalysis using SEM. While comparing images of T4, C4 and TC4 with F0, it appears that a homogenous dense microstructure is attained in the given order of mixes (Figure 7). This justifies the mechanical as well as penetrability properties for the above mixes. Dense appearance of hydrated products in C4 justifies the high pH.

Comparing all the results it was found that 2% is the optimum level of nanoparticle substitution which could yield a durable and strong concrete.

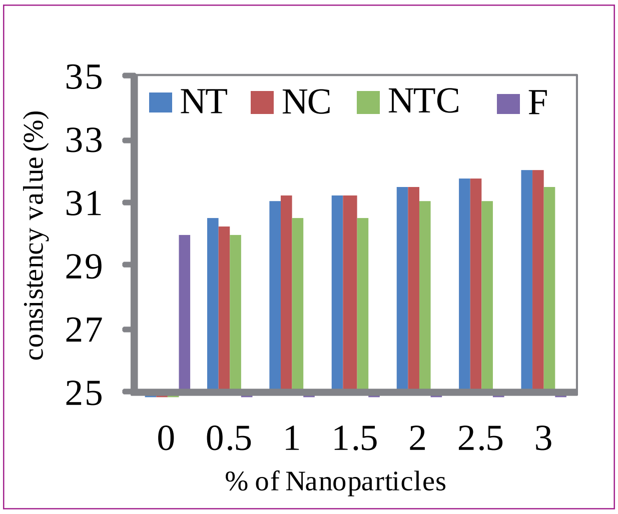

Fig. 6 *Consistency values variation*

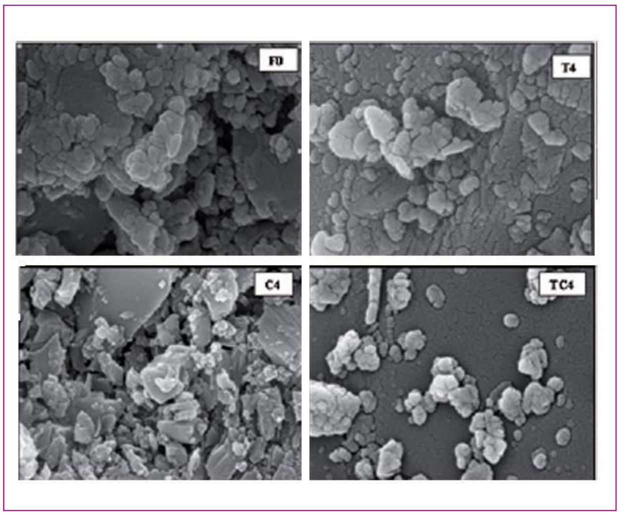

Fig. 7 *SEM images*

V.43 Comparison Study of Environmental Dose due to Ar-41 Plume Recorded in Argon Fluence Monitor and Autonomous Gamma Dose Logger

Environmental radiation monitoring programme has been carried out on 24X7 basis for more than a decade using instruments like gamma tracer, Online-EGDL (environmental gamma dose loggers) and autonomous gamma dose loggers (AGDL). The instruments have been deployed in field locations within the fenced complex of Kalpakkam site covering 9 wind direction sectors each of 22.5° on the land side of emergency planning zone (EPZ) of Madras Atomic Power Station (MAPS). The data obtained from these instruments are periodically compiled and monthly reports are documented. The dose rate observed is further analyzed by correlating with the meteorological parameters of Kalpakkam site, in particular with wind direction, which is used to corroborate the contribution of sky shine dose due to Ar-41 plume released from MAPS stack. The real time data is used for back calculating the source term in emergency response system. The dose rate excess over environmental background recorded in the monitors and correlated with wind direction and wind velocity, is used as an input for the software module. In order to ascertain the excess dose contribution by Ar-41 plume, a study has been conducted by deploying argon fluence monitor (AFM) and AGDL at WSCD for a period of four months September-December, 2014 and dose rates are recorded. The analysis of dose rate is presented in this report.

A stand alone energy fluence monitor tuned to ^{41}Ar gamma energy (1.29 MeV), called AFM, is developed in RSD, IGCAR to detect sky shine dose rate due to very low concentration of Argon plume in the atmosphere. The instrument is based on CsI(Tl) detector and uses indigenous conditioning electronics for pulse processing and controlling and data management through application software.

A portable autonomous gamma dose logger (AGDL) is indigenously designed and developed for environmental radiation monitoring and recording. The system is a G.M. tube based instrument and uses a microcontroller based circuit, for data acquisition and storage and it is sensitive to all energies unlike AFM. The registered data can be easily retrieved at any time for analysis and documentation as they are recorded in a removable compact flash card.

Photograph of AFM and AGDL deployed near WSCD is shown in Figure 1. The wind direction pattern during the period of study was obtained from the meteorological station located at Edaiyur. On a typical day of observation 29 Sep 2014 the direction of the wind was found to be Southwest in the morning time which changed to Southeast by sea breeze development in the afternoon. The general background at the location was found to be approx. 15 μR/h. During the sea breeze time an increase in environmental dose above normal background was observed (Figure 2). It is evident from the figure that, both monitors responded in a similar fashion. Area under the individual well-defined peaks after subtracting the background provides the total sky shine dose due to the Ar-41 plume, for both the systems are calculated and found to be nearly equal. A correlation of 0.992 is obtained between the individual measurements by the two systems confirming a good linear fit. The slope of the linear fit is 1.07 which shows that the dose rates recorded by both the systems agree with each other.

***Fig. 1** Autonomous gamma dose loggers and argon fluence monitor in the field*

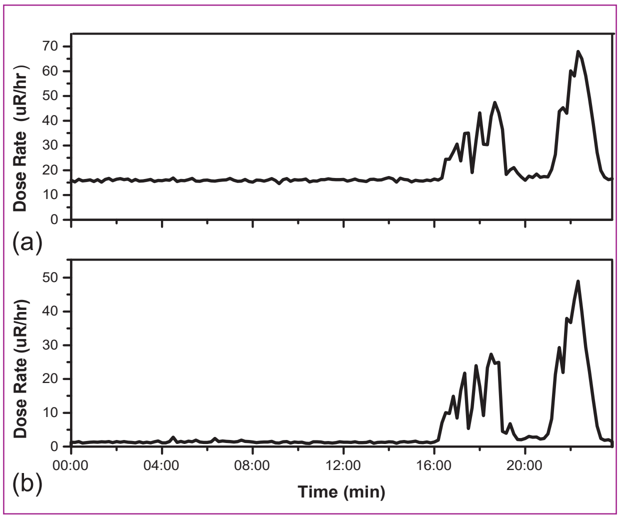

***Fig. 2** Dose rate plot for (a) autonomous gamma dose loggers and (b) argon fluence monitor in the field*

V.44 Validation of Source Term Module ASTER in ONERS-DSS using the Routine Release of Ar-41

In the event of a nuclear accident where large quantities of radioactive material are released to the environment estimates of atmospheric release rates (source term) of radioactive material is highly important for predicting the consequences and mitigating radiological impact to the public residing in the nearby areas by implementing suitable counter measures. A source term model called ASTER (Assesment of Source Term during Emergency Response) is developed and implemented in the Online Nuclear Emergency Response decision support system (ONERS) for Kalpakkam site. This model is designed based on the hypothesis that the measured dose at a ground receptor (C_i) due to a released substance is a function of the source emission rate (Q in Bq/s) and the dispersion factor (D_i) between the source and that receptor, as given below:

$$Q = \frac{1}{n}\sum_{i=1}^{n}\left(C_i D_i^{-1}\right)$$

A random walk dispersion model SPEEDI is used in ASTER to compute the dispersion factor D_i i.e., dose per unit release rate at a given receptor location (i) for a given emission source like MAPS reactor using the actual meteorological observations at the site. This computed dose for unit release is then inverted with measured doses at receptors to obtain Q. SPEEDI is configured to compute plume dispersion in a short distance range of 4.0 kilometres around MAPS reactor using real-time observations from the meteorological tower situated at Kalpakkam site. A set of 24 environmental radiation monitors comprising ethernet based Environmental Gamma Dose Loggers (EGDL) and wireless Autonomous Gamma Dose Loggers (AGDL) are installed in two rings of radii 0.5 and 1.5 kilometres distance from MAPS to cover various wind direction sectors (Figure 1).

A point-kernel cloud integration scheme is incorporated in ASTER, in which the simulated particle positions and location coordinates of detectors are used to compute the gamma dose rates at various detector points. To reduce the uncertainty in estimation, the program scans the detectors which fall in a sector of ±15º of the actual plume direction and computes source term at these receptors alone. A simple statistical 'Pivot' method is implemented which first sorts the computed source-term values in asceding order and then calculates pivots (X). The final estimate of source term is taken as the normalized sum of the lower (X_l) and upper (X_u) pivots with the pivot depth (X_u-X_l).

The source-term module is validated using the continuous release data on ^{41}Ar from MAPS reactor for over 90 days during 2014-2015. First the computed dose rates for actual release rates of ^{41}Ar are compared with detector data for various plume directions. It has been found that the computed dose rates agree with observations within a factor of 2 and a correlation of R = 0.59. The scatter plot of normalized values of computed source term and actual values (Figure 2) indicates the source-term is slightly underpredicted with a correlation, bias and RME of 0.58, 0.152 units and 0.192 units respectively. About 90% of predicted source term values agree with the actual releases within a factor of 4 which is a good estimate within the limits of uncertainties of measurements and modelled plume distribution .

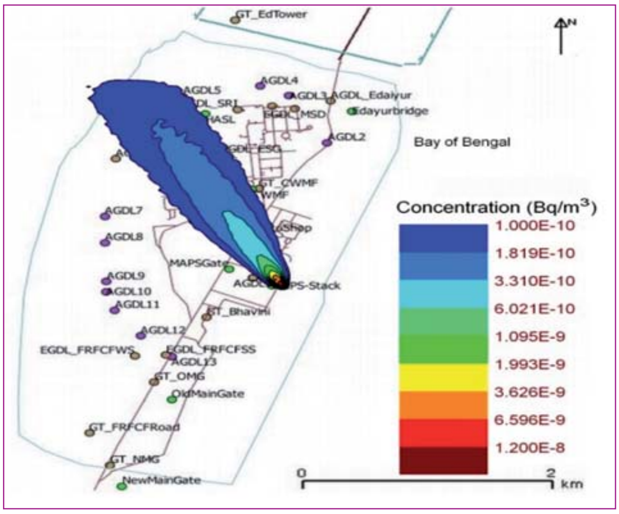

Fig. 1 *Distribution of environmental gamma monitors*

The difference between the computed and actual source term arises because of i) application of daily release rates for comparison ii) distribution of environmental monitors iii) effects of buildings and tree canopies where some of the monitors are located. Presently the temporal variation in the release data is not available. To reduce the uncertainty in the source-term estimation it is proposed to increase the number of detectors and populate them evenly in all the wind direction sectors at the site.

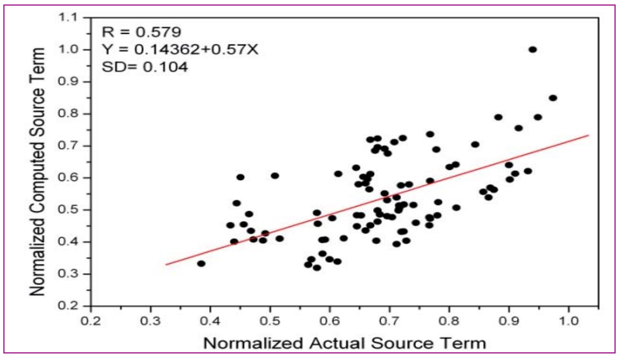

Fig. 2 *Comparison of normalized values of computed and actual daily source term*

V.45 Wave Height Prediction near Kalpakkam Coast using a Numerical Model SWAN

Coastal environment in the southeast coast is frequently prone to cyclones, storm-surges and extreme waves particularly in the post-monsoon season. Extreme waves from tropical storms create hazard both at the coast and at sea. Several factors such as coastline geometry, basin topography and seasonal wind pattern affect the height and fetch of waves. Monitoring and prediction of ocean waves along the coast is important for environmental safety at DAE sites.

A numerical ocean wave model called Simulating WAves Near Shore (SWAN) has been implemented for Kalpakkam site for the prediction of extreme waves during stormy events to provide advance warning. SWAN is a phase averaged Eulerian model in which the wave evolution is formulated on a grid. The waves are described with the 2D wave action density spectrum. The evolution of wave spectrum is described by the spectral action balance equation (1):

$$\frac{\partial N}{\partial t} + \nabla_x \cdot \left[\left(\vec{c}_g + \vec{U}\right)\right] N + \frac{\partial c_\sigma N}{\partial \sigma} + \frac{\partial c_\theta N}{\partial \theta} = \frac{S}{\sigma} \qquad - (1)$$

Here, N is the action density (= E/σ), E is distributing wave energy over frequencies σ in propagation direction θ, U is the ambient current. The first term represents rate of change of action density, 2nd term propagation of action in geographical space with group velocity c_g, 3rd and 4th terms shifting of relative frequency due to variation in depths and currents and the 5th term depth and current induced refraction. The right hand side which contains 'S' is source or sink that represents all physical processes which generate, dissipate, or redistribute wave energy and non-linear wave-wave interactions. The significant wave height (SWH) can be obtained from the wave action in the governing equation.

A crucial parameter in wave height prediction is the ocean-surface winds. The winds are obtained by off-line coupling of SWAN to the operational weather prediction model WRF. The nested wave model is configured with a high resolution domain covering southeast coast incorporating the bathymetry data at arc 30 seconds from General Bathymetry Chart over Oceans (GEBCO) database. The SWAN model is tested by performing simulations for a number of fair weather and stormy events in different seasons. The time series of simulated significant wave heights (SWH) are compared with the Wave Rider Buoy (WRB) observations situated near Pondicherry and Tuticorin and the spatial distribution of SWH are compared with operational global wave watch 3 (WW3) model products.

Comparison of predicted SWH along with WRB observations at Pondicherry (Figure 1) for the cyclone Nisha shows that the model slightly underestimates the wave heights but shows the observed trends of gradual increase in SWH with intensification of the storms. Results of predictions for eight fair-weather and eight stormy events in all four seasons indicated the SWAN simulated SWH is about 15% less than the observed wave heights. Comparison of spatial wave heights from SWAN with global Wave Watch model products shows that SWAN produces a more realistic wave pattern along the coast (Figure 2) which could be due to high resolution and realistic winds from WRF. It is seen that the SWH gradually increased from 2 metre at initial stages of the storm to 7 metre when the cyclone reached its peak intensity while approaching the coast. Unlike WW3 in which the SWH is symmetrically distributed around the storm centre, the predicted maximum SWH in SWAN is aligned in the north-northwest directed storm track along the coast indicating a more realistic wave height simulation. This validation exercise demonstrates the potential utility of SWAN in predicting the extreme waves near Kalpakkam coast.

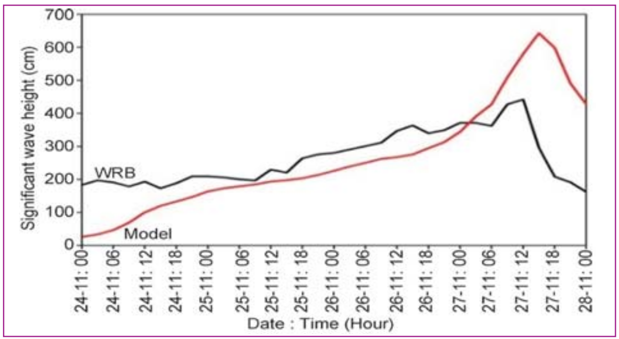

Fig. 1 *Time series of simulated significant wave heights along with wave rider buoy data for cyclone Nisha on November 24,2008*

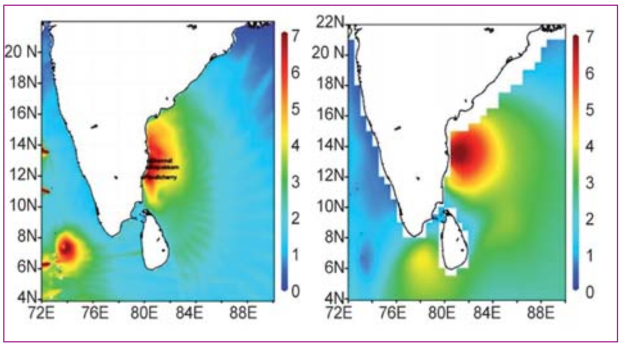

Fig. 2 *Significant wave height along eastcoast during the landfall of cyclone Nilam on 1800 IST October 31, 2012*

V.46 Simulation of Airborne Effluent Dispersion in a Tree Canopy using Open FOAM CFD

Nuclear plants are often surrounded by tree canopies as a part of landscaping and green belt development. Tree canopies generate turbulence in the atmospheric flow and consequently influence the transport and dispersion of air borne pollutants within the canopies and their immediate vicinities. The degree of turbulence generated depends on the height and type of the trees and the density of the canopy. Individual trees create wakes where turbulence is mechanically produced and dissipated by partial flow through the gaps between the trees. To study the mechanical effects of tree canopy on the dispersion and consequent ground level concentration pattern from a ground level release of radioactivity, a CFD code called OpenFOAM is used. The main task of this study is modelling the flow and dispersion through plant canopies in OpenFOAM by incorporating the canopy drag effect. This can be achieved in two ways. One is simplifying the problem by porous body formulation and the second is by considering the leaf area index to barometric canopy drag. The second approach is implemented in the CFD code. The momentum equation is incorporated with a source/sink term; while the turbulence kinetic energy and dissipation equations are modified with different source/sink terms respectively. The semi-empirical terms were checked for dimensional consistency after introducing necessary constants of proportionality. The Edaiyur site on the northern part of IGCAR is chosen to represent the tree canopy. This site is often selected for tracer gas and aerosol dispersion experiments. The north east sector of the site is covered with a canopy of trees. In OpenFOAM, a domain of plain land is described with the tree canopy in an arc form (Figure 1).

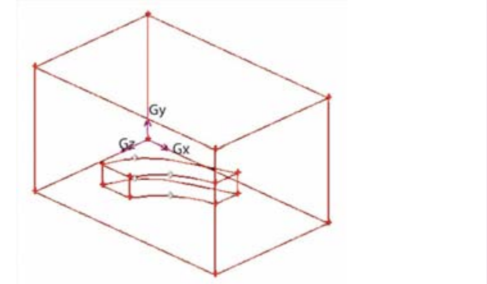

Fig. 1 *Model domain of tree canopy in an arc on a plain land*

The canopy is introduced in the domain in such way that the leaf area index varies with height and the canopy is represented at three layers with leaf area indices of 1.2, 4 and 2.5 respectively with height. Each layer is of 5 metre high amounting to a tree height of 15 metre. A uniform wind profile is assumed (5 m/s) at the inflow which gets modified due to the canopy. The wind profiles without canopy and in the presence of canopy are shown in Figure 2. The vertical wind profile shows that at the stem area, the wind speed is rather same as that of the inlet (there may be acceleration at the stem due to obstruction of the stem, which leads to acceleration around the stem by mass conservation). Above this area there is a reduction in wind speed caused by the canopy drag.

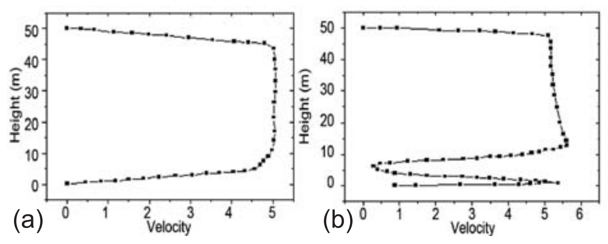

Fig. 2 *Vertical profile of wind velocity (a) without canopy and (b) in the presence of canopy*

Dispersion of a radioactive gaseous plume is simulated assuming a ground level release at the lower left corner of the domain. The spatial distribution of concentration at the ground level is compared between canopy and non canopy cases in Figure 3. When there is no canopy, the contours show a classical Gaussian plume dispersion pattern. In the case of canopy, the dispersion is enhanced due to the in-homogeneity in the flow and also due to stronger turbulence. By the canopy effect, the areas which are otherwise not expected to receive the concentration are seen under the influence of the plume. The plume residence time also increased due to the canopy. However the concentration decreased along the plume centre line. Results suggest that in the presence of canopy more area will be contaminated by the plume and over a longer time compared to no-canopy case. The study is important when ground level release of radioactive gases and particulates occurs in a multi-facility site like Kalpakkam where tree canopies are well developed.

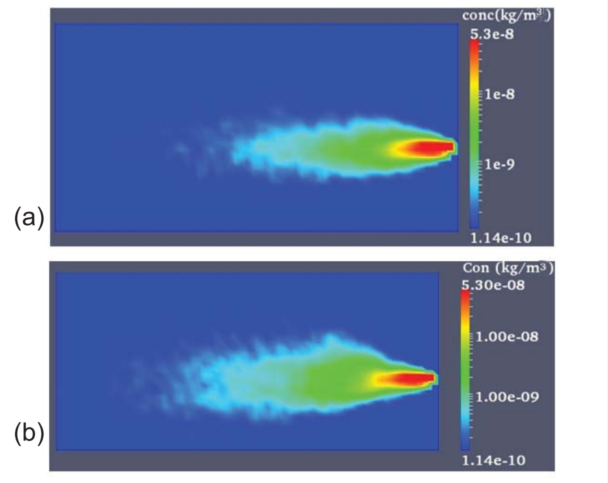

Fig. 3 *Ground level concentration in the case of (a) no canopy and (b) for the case of canopy*

V.47 Distributional Characteristics of Nutrients in Aquatic Surface microlayer and Subsurface Water

The surface microlayer (SML, uppermost 1-1000 µm layer), the interface between the atmosphere and water is a highly productive and metabolically active interface. SML is a highly efficient and selective micro-reactor, effectively concentrating and transforming materials brought to the interface from the atmosphere and bulk water column. These processes are very intriguing and important for pollution studies. The complex interplay between biological, chemical and physical processes regulates the nutrient dynamics between SML and subsurface water column. The distinctive physical and chemical characteristics of SML can explain the diversity and abundance of species in the SML as well as underneath SML. Designing sampling device and sampling strategy for the SML is always a major challenge. In view of this, it was planned to study the nutrient dynamics in the SML and subsurface water of various aquatic bodies including sea at Kalpakkam.

The SML sampling involved a glass plate of 60 × 60 cm active surface. The plate was immersed vertically through the water column all the way down to the holder (i.e.) 60 cm deep. The plate was then hauled up from the water at a speed of about 5-6 cm s^{-1} and the water was drawn off to a wide mouth bottle from both the side of the plate using a neoprene wiper. To obtain about 100 ml of SML, 20-25 samplings were required. SML of Kalpakkam coastal waters revealed significantly high content of nitrogenous nutrients in the microlayer sample than that of the sub-surface water. Content of nitrate and total nitrogen (TN) were about 10-12 times higher in the surface microlayer (nitrate- 80.1; total nitrogen- 643.25 µmol l^{-1}) as compared to sub-surface samples (nitrate-7.42; total nitrogen- 49.18 µmol l^{-1}). Ammonia contents were also significantly high in the surface microlayer samples (Figure 1). However, phosphate and silicate content of SML and that of subsurface were almost similar. Nutrient distribution in local water bodies viz. open reservoirs (both old and new reservoir), KKM Lake and Sadras backwater were also investigated. Marginally high nitrate content was observed in the SML of the old reservoir (OR), however, nitrate content in the new reservoir (NR) SML was about 14 times higher than the normal water sample (normal sample - 1.49 µmol l^{-1}; microlayer sample- 20.52 µmol l^{-1}). Ammonia also showed a similar increase in microlayer samples in both the reservoirs, however, difference between SML and normal sample was higher (about 3 times) in the old reservoir. Phosphate contents did not show any significant variation between SML and the subsurface samples in both the reservoirs. Total nitrogen and total phosphorus followed the same trends as that of nitrate and phosphate respectively. Silicate content was found to be relatively higher in the microlayer samples at all the three locations. Unlike the reservoirs, KKM lake samples showed relatively low nutrient concentrations, except silicate, in the microlayer samples as compared to bulk water.

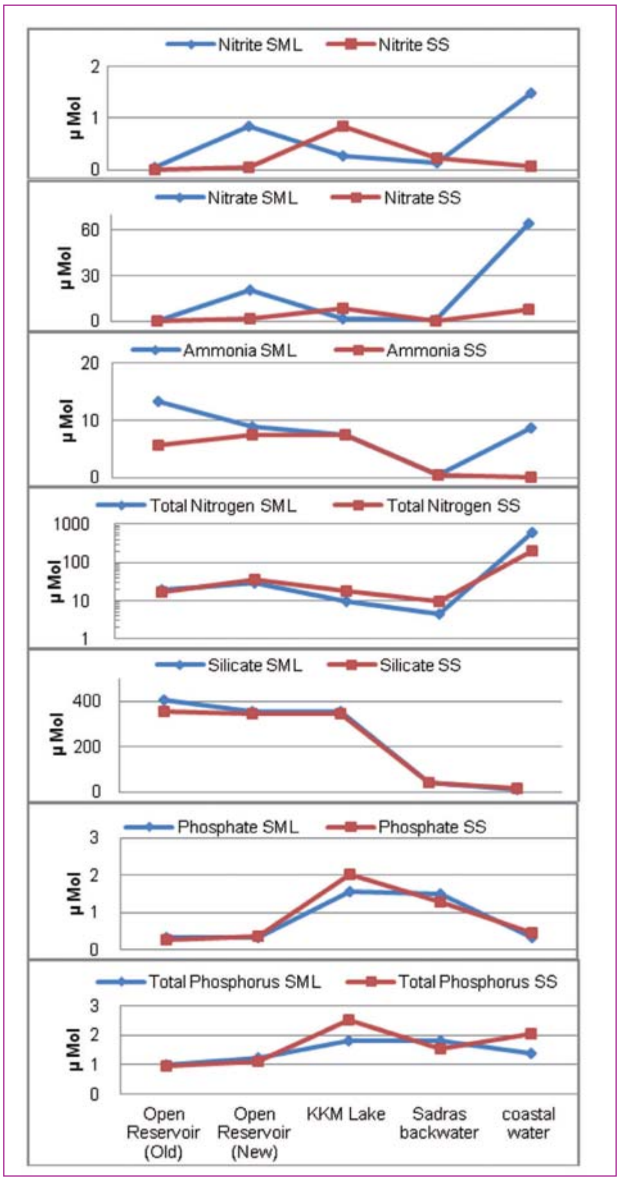

Fig. 1 *Variations in total nitrogen, silicate, phosphate and total phosphorus content in surface microlayer and sub-surface samples of different water bodies in and around Kalpakkam*

V.48 Characterization of Ultrasonic Transducers by Beam Profiling Method

Ultrasonic trasnducers, known as search units, are the main devices in ultrasonic non-destructive testing. Reliability of the test result, heavily depends on the characteristics of the transducers used. The ASTM standard, A1065, provides the guidelines for evaluating characteristics of ultrasonic search units. The procedures given in this standard are applicable to manufacturing acceptance and inspection of new search units or to periodic performance evaluation of search units throughout their service life.

In non-destructive testing, different types of ultrasonic transducers are being employed. Over a period of time, properties of the piezoelectric crystal implanted in the transducer may deteriorate which affects the performance of the transducers and reliability of the test results. Hence, a periodic characterization of the transducers for the time, frequency and profile characterizations as per accepted standards become mandatory in many industries. Hence, with the help of a fully automatic transdcuer characterization system, all the commercial as well as in-house made transducers are being subjected to characterization. The parameters centre frequency, peak frequency, lower frequency, higher frequency, frequency band width, wave form duration, sensitivity, near field, aperture size, beam spread (focus), focal length, focal spot size, depth of field, ultrasound response (echo amplitude), sound field pattern etc. are evaluated.

These parameter are valuable in selecting a search unit for specific applications and analyzing the received data. In the transducer characterization system, it is possible to make the axial as well as cross sectional images of the ultrasound field pattern so that the directionality and spread of the ultrasonic wave generated along with all other parameters mentioned above can be evaluated over a period of time during its life span. Axial sound field pattern of a commercial 5MHz unfocused longitudinal transducer is shown in Figure 1a. It is seen that, the field intensity distubution is uniform about the axis and it is confirmed from the uniform cross sectional intensity distribution shown in Figure 1b. These types of search units are best suitable for non-destructive testing. Figure 1c shows a non uniform distribution of the sound field pattern from a transducer which can not be employed in NDT. Corresponding cross sectional intensity distribution is shown in Figure 1d. The sound field patterns that propagate from ultrasonic search units vary with frequency, size, shape, and design.

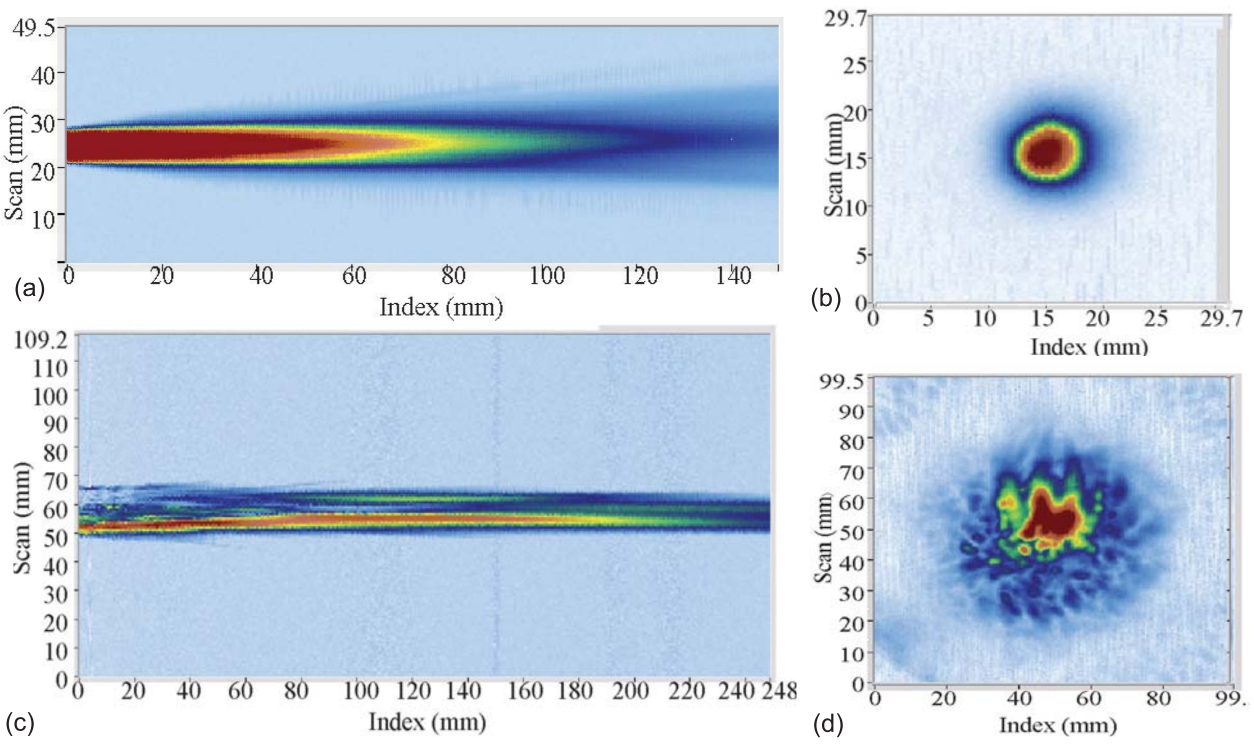

Fig. 1 *(a) Uniform axial sound field intensity distribution of a transducer which can be employed for non-destructive testing, (b) uniform cross-sectional intensity distribution, (c) non-uniform axial sound field intensity distribution of a transducer which cannot be employed for non-destructive testing and (d) uniform cross sectional intensity distribution*

V.49 Development of Planar First Order Gradiometer Coupled to HTS SQUID Sensor

The Superconducting Quantum Interference Device (SQUID) using high temperature superconductors (HTS) is a promising sensor for the detection of extremely small changes in magnetic fields in the range of femto to pico. The development of gradiometer based HTS SQUID devices is essential for practical applications in noisy environments in laboratory and at field sites wherein shielded rooms are not practical. Compared to low temperature superconductors (LTS) SQUID sensors based on Niobium (which require liquid helium temperatures for their operation), the use of HTS SQUID sensors has advantages with respect to the less stringent requirements on thermal isolation of the sensor, simpler cooling system and the possibility of minimizing the distance between the sensor at low temperatures to the actual specimen under investigation at room temperature. Here, the design and development of HTS SQUID and first order gradiometer coupled to HTS SQUID sensor using highly reliable advanced micro-fabrication techniques such as deposition of superconducting thin films by pulsed laser deposition (PLD), UV photolithography and RF ion beam etching is reported.

The fabrication of HTS SQUID sensors on bicrystal $SrTiO_3$ (STO) substrates with 24° misorientation angle involves deposition of high quality YBCO thin films by pulsed laser deposition technique with superconducting transition temperature (T_c) above 90K and high J_c of $\sim 10^6$ A/cm^2. Ten micron wide microbridges crossing the bicrystal boundary were used as Josephson weak links and were placed outside the slit washer. The SQUID had an inner sensing area of 25 × 25 µm and an outer superconducting washer of 250 × 250 µm. A first order planar gradiometer with two planar loops in opposition with the Josephson weak links in the form of microbridges located at the Centre was designed. Figure 1 shows HTS SQUID fabricated on a bicrystal STO substrate.

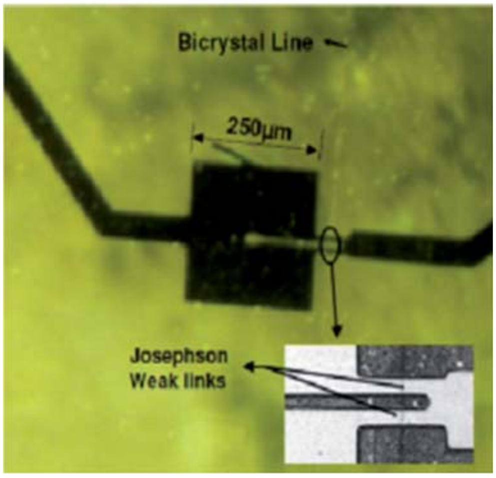

Fig. 1 *HTS SQUID fabricated on bicrystal substrate*

The two pick-up loops in opposition constituting the planar gradiometer, located on either side of the SQUID had a line-width of 1 mm and an inner diameter of about 4 mm (Figure 2).

All the necessary photomasks were designed and fabricated in-house. Using photolithography and three step etching process, the device geometries were patterned. This procedure yielded sharp definition of HTS planar gradiometers on 10 x 10mm $SrTiO_3$ bicrystal substrates. The SQUID sensor coupled to a planar first order gradiometer was mounted at the end of a dip-stick and the measured I-V characteristic showed Resistively Shunted Junction (RSJ) like behaviour. Magnetic flux (Φ) was coupled into the sensing area of the SQUID using an external wire-wound coil. The V-Φ characteristic showed that voltage across the device was a periodic function of applied flux with the periodicity of a flux quantum Φ_o.

Modulation depth was measured at various applied bias currents and the maximum modulation depth of 11.2 µV has been measured at an applied bias current of 105 µA (Figure 3).

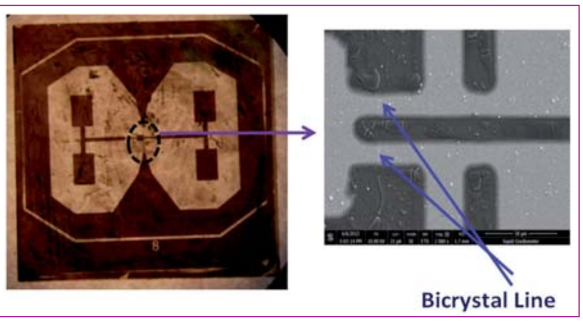

Fig. 2 *Optical micrograph of gradiometric loop & SEM image of bicrystal line*

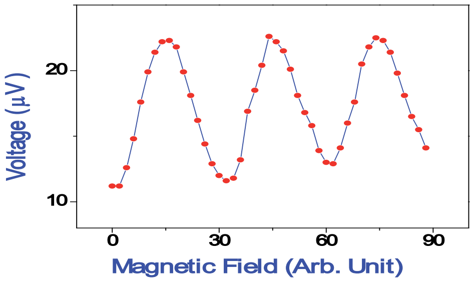

Fig. 3 *V-Φ characteristics of first order gradiometer coupled to a HTS SQUID device*

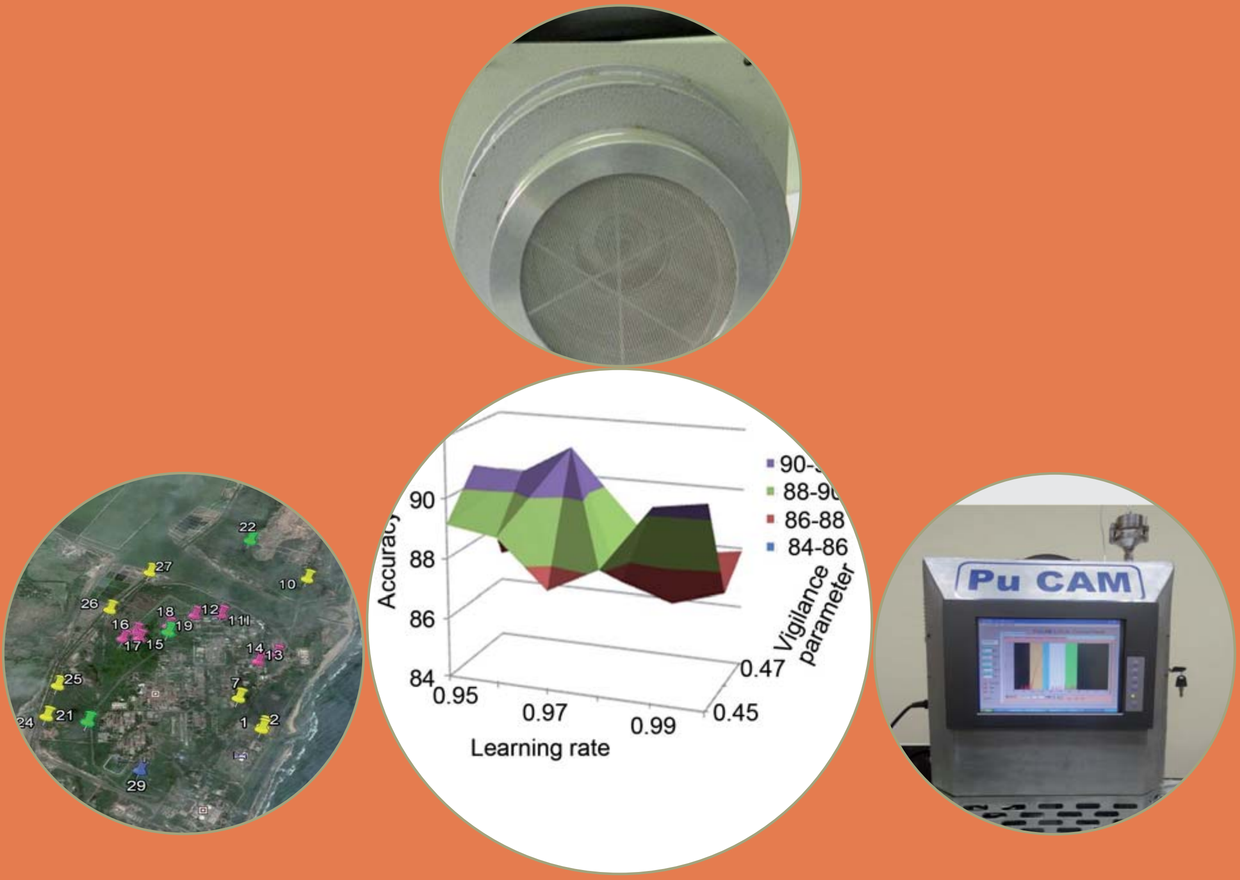

CHAPTER VI

Infrastructure Facilities

VI.1 Deployment of Wireless Sensor Networks at IGCAR

Wireless Sensor Network (WSN) consists of spatially distributed autonomous sensors to monitor physical parameters and to cooperatively pass their data through the network to a main location. As the need for WSN in future nuclear facilities is felt, the development and deployment of WSN in and around nuclear facilities has been initiated. Two of them are briefed here.

WSN at FBTR Complex

Wireless Sensor Network has been deployed at FBTR with twenty seven nodes for measuring temperature, vibration, pressure signals etc. from various locations of FBTR and interim fuel subassembly storage building (IFSB) (Figure 1). The typical areas covered are: secondary sodium loop, sodium flooding, Ward Leonard system, blower cabin in the filter room and reactor containment building (RCB). Measurement systems connected to WSN are:

- Temperature measurement: Twelve numbers of K type Thermocouples catered to secondary sodium loop, inside RCB and flooding area are connected to WSN. Since the temperature signal conditioner has the ability to accept multiple inputs, geographically closer temperature signals are grouped to a single WSN node
- Vibration measurement: Vibrations of blowers placed in the maintenance building & IFSB and Ward Leonard systems are monitored continuously by connecting eight numbers of vibration sensors interfaced with WSN nodes
- Air flow measurement: Air flow at IFSB vault and highbay are also being monitored using WSN. These nodes are interfaced to sensor nodes using 4-20 mA signal conditioner boards
- Ambient temperature and humidity measurement: To analyze the annual trend for temperature and humidity across FBTR complex, these sensors are installed and connected to WSN.

For WSN, the industrial grade nodes with IP54 metallic enclosures were used. Router nodes were placed optimally to provide fault tolerance. Sensor data collected by the base station are displayed and analysed by the Wireless Network Management Station (WNMS) at control room. Wireless network is operating successfully for more than two years.

WSN for radiation monitoring

Radiation monitoring is an integral part of any nuclear power plant. For monitoring the radioactive material movements in Kalpakkam Nuclear Complex, Area Gamma Monitors (AGM) with local alarm facilities have been placed at various entry/exit points. In order to provide a centralized view and to have the record of events for future analysis, WSN has been deployed. WSN nodes were proficiently designed to protect from rain without compromising on RF transmitting and receiving power, thus making it apt for outdoor deployment. Efficient powering options are provided in the nodes which can be powered through solar panel or from the lamp poles with the battery backup for 48 hours.

Before deploying these nodes, site survey has been carried out using different in-house developed networking tools (like Wi-Spy, ZigBee Sniffer) for planning and designing of the wireless network. Router nodes are deployed with redundancy after careful examination of link quality between the nodes. AGMs present in the following locations are connected using wireless sensor nodes: Main Gate (9 AGMs), IGCAR gate (2), Central Stores (6), Kunnathur Gate (2) and one AGM each in non-radiological labs/buildings such as HBB, MSL, MDL, QAD, HASL, CDO and CWD.

Dedicated WNMS has been developed to display the radiation dose and topology of the network. It also indicates the health status of individual nodes like presence of RF link, power supply and AGM. Presently, the WSN for radiation monitoring is functioning successfully with 70 nodes. It collects data from 28 AGMs using 41 router nodes to transmit the dose information with reliability to the base station kept at health physics room of FBTR where it is manned 24x7.

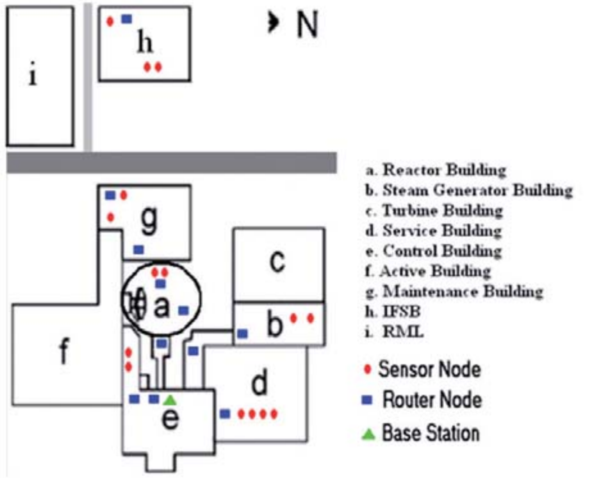

Fig. 1 *Node locations in FBTR wireless sensor network*

VI.2 Design, Construction and Commissioning of 2 MIGD SWRO Plant at Kalpakkam

To augment the growing need of water requirements of DAE units at Kalpakkam, a sea water reverse osmosis desalination plant (SWRO) of 380 m^3/h (2 MIGD) capacity of potable water is designed, constructed and commissioned. Desalination of seawater using reverse osmosis process is the most efficient desalination process widely used all over the world owing to its low specific energy consumption per meter cube of water produced and low capital cost. Necesssary regalatory clearences from the various agencies were obtained.

The 2 MIGD plant is designed with the state of art technology to meet the variable operation requirements of 25 , 50, 75 and 100% of the plant capacity with low specific energy consumption (3.18 Kwh/m^3). The plant is environment friendly and designed to confirm the requirements of ISO 14001. The Figure 1 shows the photograph of reverse osmasis system.

The sea water intake for the plant is 1200 m^3/hr which is met from the existing intake system of NDDP / PFBR. The in-feed sea water for the plant is stored in the underground tank of 1200 m^3 capacity located in the NDDP premises (Figure 2).

An automated electro chlorinator of 2.1 kg/hr capacity chlorinates the in-feed sea water and controls the biological growth. The feed water is pumped by four pumps of 280 m^3/h capacity each and sent to pre-treatment section consisting of pressure sand filters and ultra filtration system (UF) to remove the suspended particles. The pre-treated water with Stilt Density Index (SDI) <3 is passed through the two stage reverse osmosis (RO) membrane skids to remove the dissolved salts (Figure 3).

The total dissolved salts (TDS) at the first stage and second stage RO outlet is < 250 and < 50ppm respectively. The 380 m^3/h permeate water is further treated through the lime stone columns and the TDS in the final product water is achieved <250 ppm. The product water quality is confirming to the ISO 10500 standards.

The brine from the 2 MIGD SWRO plant is discharged to the existing PFBR condenser outfall canal of 1.2 kilometer long leading to sea through a dispersion system. The brine is thoroughly mixed and diluted with the PFBR condenser out fall water before it enters the sea.

The plant is designed to operate with fully automated PLC based SCADA systems with provision for manual intervention. The equipment, machineries and piping related to the process & services are robust in design and the construction material is used for manufacture of the different systems in the plant is popular and widely used in desalination plants around the world. Broadly, Glass reinforced plastic (GRP) material is used in the low pressure system and duplex stainless steel (DSS) with PREN>40 is used in the high pressure systems. The equipments and piping were manufactured and tested as per ASME SEC VIII, Div 1 and ANSI B 31.1.

To minimize the specific energy consumption per meter cube of water and to operate the plant at reduced costs, different innovative features are incorporated. Advanced systems like Pressure Exchangers are used as Energy recovery device to recover the hydraulic energy from the high pressure reject stream and transfer the energy to low pressure feed. Variable Frequency Drives (VFD) are used in the High pressure and low pressure pump drives to reduce the energy consumption.

The plant is designed, constructed and commissioned by M/s Tecton Engineering and Construction (I) Pvt Ltd, Chennai on Design, Build and Operation and Maintain (DBOM) mode. The plant has operated successfully, producing potable water to the design specification. The plant will be operated and maintained by the firm.

***Fig. 1** Reverse osmosis plant*

***Fig. 2** Reverse osmosis feed water system*

***Fig. 3** Reverse osmosis membrane skids to remove the dissolved salts*

VI.3 Sodium Technology Complex

It is necessary to augment the sodium facilities to carry out functional testing of the reactor components of future FBRs in simulated reactor operating conditions. Improved designs of the shutdown mechanism and the concept of the third shutdown mechanism for future FBRs have to be demonstrated with tests in air and sodium. Mapping of core of future FBRs using prototype under sodium ultra sonic scanner (USUSS) are also to be carried out. A Sodium Technology Complex (STC) is thus conceived to accommodate these testing requirements for future FBRs, qualification of design modification of shutdown mechanism and for conducting experimental studies in the area of sodium technology and sodium instrumentation. STC is designed to have a facility for sodium cleaning and disposal also. This building is being constructed on the west side of the UGC complex in the northern site of IGCAR, Kalpakkam.

STC is a reinforced cement concrete frame cum shear wall structure with a total floor area of 5700 m^2. The STC building consists of a large high bay of size 40 length x 21 width x 43 metre height, a dump pit for positioning two Sodium Storage Tanks (SST) with dimensions of 13 x 7.75 x 6.9 m depth and material storage area of size 12 m length x 8 m width x 15 m height located on the eastern side of the building adjoining the high bay. Steel structure supported on reinforced cement concrete columns is planned for the sodium facility within the high bay space.

STC is designed to withstand the environmental loads such as wind, flood and earthquake. Design basis flood level (DBFL) for STC takes into account a combination of tide, storm surge, rainfall as well as tsunamis. Finished floor level (FFL) for STC is 13.2 metre. All the civil structures, mild steel structures, sodium components and piping are designed to withstand a design basis earth quake as per IS 1893.

Key design basis process parameters of the sodium facility are maximum sodium temperature of 600°C, argon cover gas pressure of 0.02 MPa in test vessels, maximum sodium pressure of 0.9 MPa and sodium velocity of 6 ms^{-1} with a design life of 40 years.

The documents pertaining to STC were reviewed by various safety committees and clearances for construction of STC building and manufacture of the components for the sodium facility was obtained.

STC will house a large non-radioactive experimental sodium facility with three test vessels of capacity 8, 18 and 66 m^3, sodium purification system, sodium heating and cooling system, Electromagnetic pump of 50 m^3/h capacity for circulating sodium, dedicated sodium cleaning, and disposal facilities. Sodium test vessel-1 of one metre and sodium test vessel-2 of one and half metre diameter are for testing of shut down mechanisms and any other slender components of future FBRs. Sodium test vessel-3 of six metre diameter is used for testing of USUSS. Total sodium requirement for the sodium facility in STC for carrying out various experiments is around 100 tonnes. Two vertical storage tanks of SS316LN material each of capacity of 50 tonnes are planned for storing this sodium. Process design, loop layout, process flow sheet, mechanical design of components/ steel structure, electrical, instrumentation and control systems for STC have been completed and reviewed by an expert committee.

The excavation for the foundation of the substation and high bay building of STC have been completed to a depth of 9.5 metres and the construction work on the substation, foundation of the building is under progress.

The concreting of the raft, main pillars, walls of the pit for sodium storage tank up to -3 metre of floor level and roofing of sub-station building have been completed. Figure 1 show the photographs of STC construction site.


(a) (b) (c)

***Fig. 1** Photographs of STC construction site*

VI.4 Design and Development of Indigenous High Volume Air Sampler

Towards indigenization of radiation monitoring instruments, developmental activities have been taken up and as part of this, an indigenous portable high volume air sampler was developed in collaboration with industry (Figure 1).

Portable high volume air samplers are being used in nuclear facilities for the collection of air samples at workplaces, to estimate the air activity levels. These air samplers need to have a very large flow rate of upto 1000 lpm to ensure a representative air sample of the area being monitored. Only a few manufacturers in the world offer portable high volume air samplers and these manufacturers are in the US and Japan. Of these, the US make air samplers (trade name: Staplex) are used world over in view of their large flow rate, as compared to the other sampler and their ruggedness. No standard Indian equivalent is available in the market.

In house studies were made which included the evaluation of the performance of the presently available air sampler, compatibility of the instrument with the monitoring environment etc., and internal discussions were held with the users of the air samplers, regarding addition of features meeting user requirement like flow rate adjuster etc. The constructional drawing submitted by the fabricator was vetted and approved by a quality assurance engineer. Field trials were conducted and necessary feedback and suggestions were given. The requirements were taken into consideration for design and after confirmation prototype was made. The final product was tested by using standard procedures for estimating the true flow rate of the sampler. For this, a standard kit comprising of a calibration orifice, a series of resistance plates for regulating different flow rates and a water manometer calibrated in an National Accreditation Board for Testing and Calibration Laboratories (NABL) accredited laboratory, was used. The flow rate indicated in the rotameter and the true flow rate estimated experimentally were matching within ± 5% margin. Subsequently, the sampler was tested extensively at facility environments available viz,. FBTR, Chemistry Group and CORAL and its performance was compared with the imported sampler. In all the three locations, the performance of the indigenously developed portable high volume air sampler was found to be satisfactory and comparable to the imported sampler. It was further observed that the natural activity rejection, which is essential for the precise estimation of air activity, of the new sampler with centripeter head was also satisfactory. and comparable to the imported sampler. The results suggest that the indigenous sampler can be used for collection of particulates in filter papers to estimate the gross beta and gamma particulate air activity. Thus, the portable high volume air sampler, which is indispensible for any nuclear facility has been successfully indigenized. Some of the results obtained are given in Table 1.

Table1: Results obtained from imported and indigenous air samplers

	Gross α	Gross β	α/ β ratio
Imported	12.25	14.8	1.21
Indigenous	12.66	14.89	1.18
Imported (centripeter)	0.34	4.38	12.93
Indigenous (centripeter)	0.35	4.56	13.14

***Fig. 1** Photo of indigenously developed air sampler*

VI.5 Development of Superconducting based Level Sensor for Liquid Helium Level Measurements

To measure the level of the liquid helium in the experimental cryostat or Dewar, imported superconducting level sensors are presently being used but are relatively expensive. In view of this, experimental work related to design and development of the superconducting level sensor based on niobium-titanium (NbTi) superconducting wire was undertaken. If a long length of straight NbTi wire is partially immersed in liquid helium, part of the wire having a temperature below 9 K will have zero resistance and hence the measured resistance of the wire arises from the part of the wire having a temperature above 9 K. If suitable current is passed through the wire resulting in Joule losses in the resistive part of the wire, poorer heat transfer in the vapour phase above the liquid helium level ensures that the part of the wire above the liquid helium level is in the normal state while an efficient heat transfer in the liquid phase ensures that the part of the wire below the liquid helium level is in the superconducting state. Measured resistance of the wire (high when the liquid level is low) is a linear function of the liquid helium level under these circumstances.

A single filament insulated NbTi wire embedded in a copper matrix with an overall diameter of 50 μm has been taken for the fabrication of the level sensor. The diameter of the bare NbTi wire is about 25 microns after the outer copper is completely etched. The reason for choosing such a thin superconducting wire is that the resistance of the wire in the normal state is very high so that the liquid helium level can be measured with greater accuracy and the wire itself can act as a heater to heat the part of the wire just above the liquid helium level with a view to ensure that the part of the wire in the gaseous helium region above the liquid helium level is in the normal state while the part of the wire below the liquid helium level is in the superconducting state. In the present study, we have chosen the active length of the liquid helium level sensor to be 300 mm. The one sided PCB sheet has been cut with a length of 450 mm and a width of 6 mm. The thin film of copper on the PCB has been retained in a selected region while the remaining copper thin film on the PCB has been removed by etching or milling. The superconducting wire with the PCB strip has been inserted into a thin walled stainless steel tube for mechanical protection in such a way that the bare superconducting wire has no physical contact with the stainless steel tube.

The level sensor has been initially characterized to find out the optimum excitation current. The V-I characteristic of the sensor has been measured with the superconducting level sensor immersed in liquid helium for different depths at an interval of every 50 mm (Figure 1). Then the resistance of the wire has been recorded for different levels of liquid helium in the dewar by keeping the excitation current of 40 mA constant. The resistance of the wire is found to decrease linearly as the liquid helium level increases. The experiment has been repeated for different excitation currents ranging from 35 to 70 mA. In all cases the resistance of the sensor over the active length was found to be identical for a given liquid helium level as shown in Figure 2. The sensitivity of the home built liquid helium level sensor has been estimated to be about ± 1 mm.

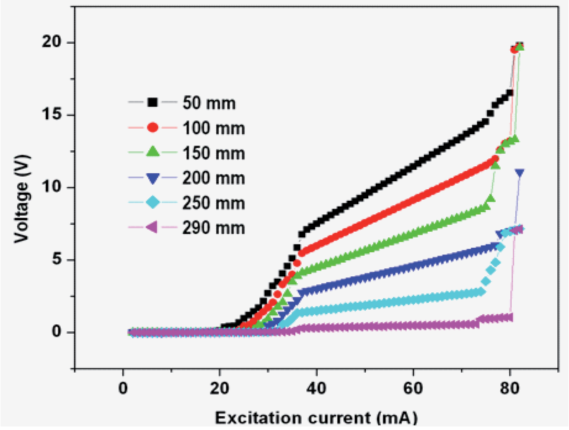

Fig. 1 *V-I characteristics of the superconducting level sensor for different liquid levels*

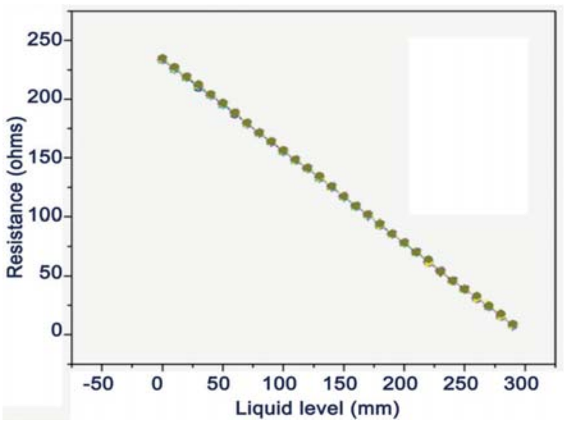

Fig. 2 *The total resistance of the superconducting wire at different liquid levels*

VI.6 Development of Indigenous Plutonium in Air Monitor

Liquid Metal Cooled Fast Breeder Reactors use large amounts of plutonium in powder form during reprocessing of the spent fuel and re-fabrication of the plutonium obtained into fresh fuel. The potential inhalation hazard from plutonium airborne contamination is a major risk in such facilities. In many plants, especially those with extensive use of glove boxes, plutonium release may take place over extremely small time intervals, with long periods when no release is seen. Conventionally, continuous air monitors using ZnS(Ag) detectors are used where one gets gross alpha radionuclide concentration in air and the detection limits obtained are much higher compared to that of the limits required. Further, confirmation of any release depends upon offline counting of the continuous air monitor filter papers after giving sufficient time for decay of natural radioactivity. Thus it is essential to have dedicated plutonium in air monitors (plutonium continuous air monitors) in which spectrometric information is obtained and plutonium concentration in the environment is derived based on region of interests (ROI) or response function making the instrument capable of detecting much lower air concentrations (very near to the limits) than the gross alpha based systems. Considering the quantities handled in reprocessing and fuel fabrication plants, plutonium continuous air monitors becomes a critical component of the air monitoring program in the working environment. Inadequate number of such equipment would lead to safety issues and could affect the progress of the programme. Presently, very few foreign vendors supply reliable plutonium in air monitors. Experience in various DAE units has shown that these monitors have problems in operating in our working environment.

In view of the above, an urgent need arises for the indigenous manufacture of plutonium continuous air monitors. This report details the development carried out jointly by IGCAR and BARC in this regard.

Principle

The air in the environment is sampled using a filter head and the dust along with any radioactive aerosol is left behind in the filter paper. The detection unit consisting of an ion implanted Silicon detector (used for alpha spectrometry) with a preamplifier positioned just above the filter paper and any alpha particle emitted in that direction would register in the detector. The detector pulses are processed and the output is sent to a USB port 1 k multichannel analyzer which sorts out the pulses by energy. The pulses due to artificial radionuclides would have energy in the range of 4.5 to 5.5 MeV. However, these pulses would be submerged by the tailing of pulses due to the naturally occurring radionuclides – daughter products from the uranium and thorium series – and hence require complex algorithms and peak stripping procedures to obtain the number of pulses due to artificial radionuclides. This has been carried out using in-house developed algorithms (based on different ROI) as well as spectrum fitting methods. The data acquisition system receives the raw data from the multichannel analyzer and executes both the algorithms. Based on the analysis, it generates alarm and displays the processed data, raw spectrum and accumulated spectrum locally and also stores the data. At the same time, all the data are transmitted to the remote personal computer through Ethernet for alarm and display. The alarm limits can be configured locally as well as through remote personal computer on authentication. All the modules were individually tested and integrated. The assembled plutonium continuous air monitors shown in Figure 1, was successfully tested and calibrated. The unit is currently deployed in the field for long term testing.

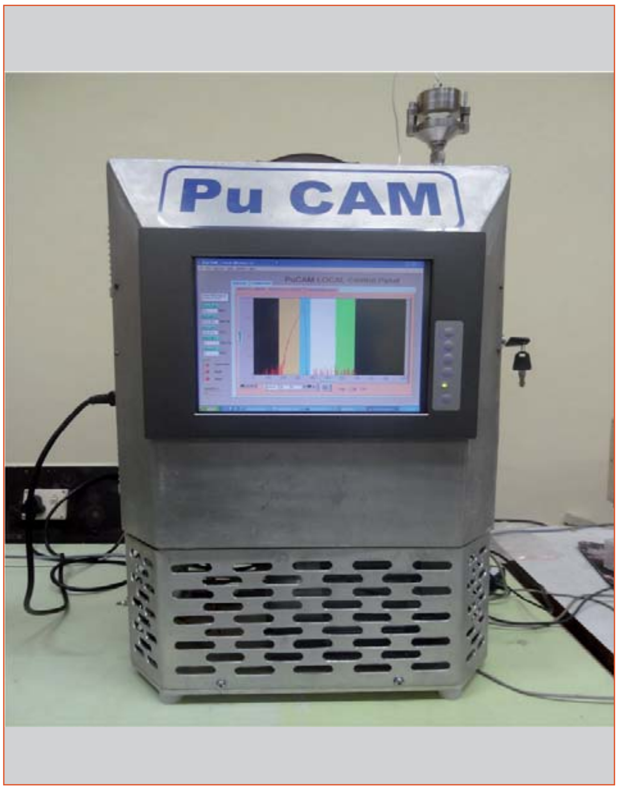

Fig. 1 *Indigenous plutonium continuous air monitors*

VI.7 Seismic Stability Assessment of Nuclear Components using 100 tonnes Shake Table

To meet the growing demand for the seismic qualification of safety related structures, systems and components of nuclear power plants, a high capacity (100 tonnes) multi axial seismic test facility has been installed and commissioned. The system consists of a large stiff square table (6 × 6 × 1.8 metre depth) connected to eight number of hydraulic actuators (4 in vertical direction and 4 in horizontal directions). These hydraulic actuators are powered by 2MWe hydraulic power pack consisting of 9 motor-pump sets which circulate around 15000 liters of oil to produce the required eneregy to excite the 100 tonnes specimen up to 1.5 g acceleration in the frequency range of 0.1 to 70 Hz. The shake table system is installed on a large isolated seismic mass structure, made of 4000 tonnes of reinforced concrete as shown in Figure 1. This six degree freedom system is controlled by a high precision PULSAR controller which can accurately reproduce the desired vibration signals on the shake table by closed loop control using feed back signals received from the accelerometers, differential pressure sensors and position sensors. The motion of the hydraulic actuators are controlled by 3 stage servo valves mounted on each actuator, The system can perform various vibration tests such as frequency sweep, continuous sine, random and tri axial earthquake simulation tests. The required earthquake input excitaion can be in the form of response spectrum, time histories or power spectral density. The dynamic responses of the specimen during the base excitation is captured by high precision sensors such as accelerometers, strain gauges and LVDTs which are connected to a 64 channel data acquisition system equipped with data processing and analysis softwares.

Seismic qualification of spent fuel trays

Spent Fuel Storage Facility (SFSF) at Tarapur has been designed, constructed & commissioned for handling and storage of 1200 tonnes of PHWR fuel bundles in a stack of 30 trays which are placed around 270 locations in the spent fuel pool. It was proposed to increase storage capacity of the pool to 1600 tones by stacking up to 40 trays. The main concern to be addressed before increasing the capacity of the spent fuel pool is the stability of the storage trays during a postulated seismic event. To assess the stability of the storage trays kept in the spent fuel pool, shake table experiments were performed on 100 tonnes capacity multi axial earthquake shaking table at IGCAR by simulating the earthquake vibrations corresponding to safe shutdown earthquake (SSE) of Tarapur.

Fig. 1 *High capacity seismic shake table*

Full scale shake table testing of two stacks of 40 spent fuel trays, containing dummy bundles submerged in water in the test tank with dimensions 2.5 x 2.0 x 6.3 metre height were carried out. The dummy bundles were made of mild steel rods of 80 mm diameter. Water level was maintained at 1.2 metre above the top trays. Initially, the specified gap of 150 mm was maintained between two stacks similar to actual Spent Fuel Storage Facility pool. The test tank was surrounded by dyke wall of dimensions 6.0 x 6.0 x 1.0 metre height to safeguard electronic system of shake table against splashes of water during testing. Total weight of tank including water, trays and bundles was approximately 57 tonnes. Three underwater uni-directional accelerometers were provided on the top tray of each stack to capture accelerations in three orthogonal directions. Two tri-axial accelerometers were

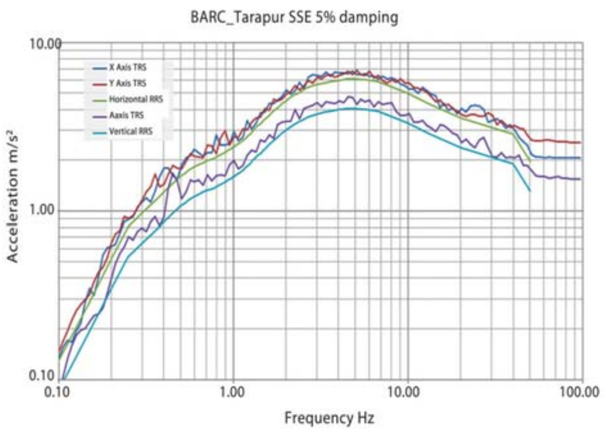

Fig. 2 *Matching of RRS and TRS*

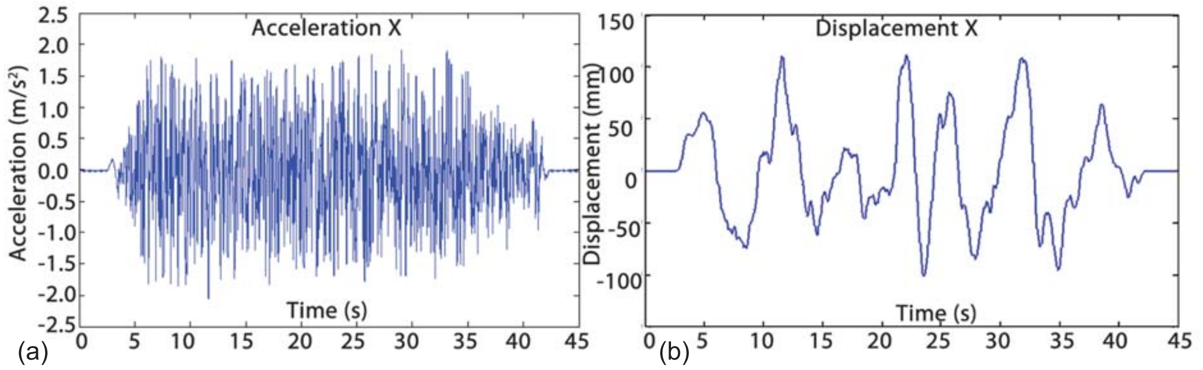

***Fig. 3** Exitation (a) acceleration and (b) displacement along X direction*

installed on outside of the test tank; one at the bottom and another on the top of the tank. Biaxial strain gauges were pasted at the bottom of the tank.

The stacks of trays were qualified for design response spectra of Tarapur site. Spectrum compatible time histories are generated such that the Test Response Spectrum (TRS) envelops the Required Response Spectrum (RRS) from 0.1 Hz in lower side and up to 100 Hz in Higher side. The matching of RRS and TRS is shown in Figure 2. The time histories of acceleration and displacement along X direction are shown in Figures 3a and 3b respectively demonstrating the capability of the system to reproduce the input signals accurately meeting both low and high frequency requirements for displacements and accelerations.

Tests were conducted in steps with acceleration levels as 25, 50, 75 and finally 100 % of the design excitation. A number of tests were carried out at 0.2g PGA i.e at 100% of RRS and responses were captured by under water accelerometers and strain gauges and video camera. The response of the tank during testing is shown in Figure 4.

The following are the important aspects and observations of the above test series. Clear distance of 150 mm maintained between two stacks got diminished on upper part during the initial tests conducted for 25% and 50% of target PGA. Subsequent tests were conducted without re-adjusting the gap between the stacks. No toppling of stacks was observed and there was no lifting or falling of dummy fuel bundles from the top trays. The movement of the tray stacks were in phase but touching of top trays was observed during the tests for 75% and 100% of target PGA, as evident from the under water accelerometer response histories, a sample of which is shown in Figure 5

From the analysis of the response behaviour of the tray stacks, it can be concluded that stack of 40 trays immersed in the water pool is stable and no lifting of fuel bundles from the top trays is obsrved. Probability for large level water splashing from the storage pool is very low. Hence, there is no safety concern in stacking 40 trays in spent fuel pool of Tarapur Spent Fuel Storage Facility.

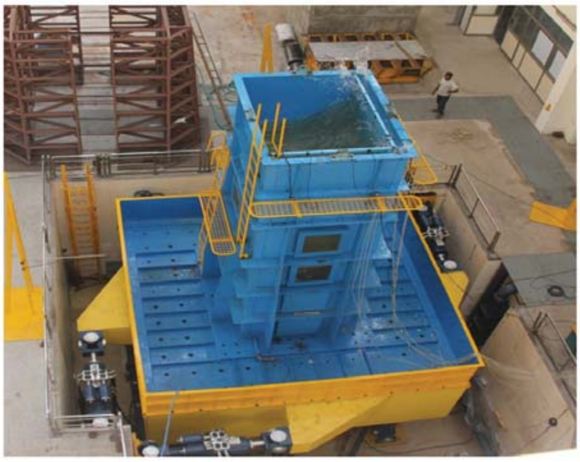

***Fig. 4** Seismic testing of spent fuel trays*

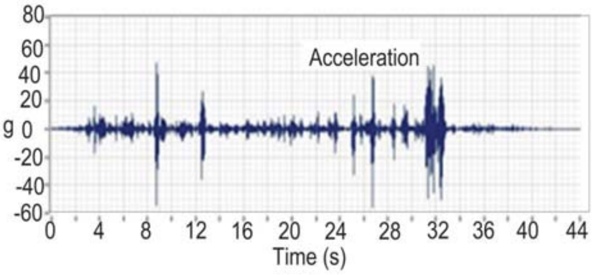

***Fig. 5** Response of underwater accelerometers kept on tray top*

VI.8 CAD-augmented Control of a Robotic Arm for Remote Work-site Operations

Augmented Reality (AR) can enhance the control and operation of robots used in nuclear facilities for carrying out complex inspection, maintenance and repair tasks. The use of Computer Aided Design (CAD) based AR brings digital (virtual) information to the real-world scenario combined with video streaming from the remote work-site. The information conveyed by the virtual objects helps the operator to perform real-world tasks. Towards this, a prototype CAD-augmented system has been developed for remote tele-operation of a 2 Degrees-of-Freedom (DOF) robotic arm.

A robotic arm has been fabricated with aluminum links and assembled with two corresponding revolute joints, actuated by high torque servo motors (1.5 Nm at 6V). These servo motors provide potentiometer feedback for closed loop control. An ATmega2560 8-bit microcontroller is used for actuation and control of the robot joints.

A digital camera captures the real-time video frame of the robotic arm at remote work-site. Marker based registration is done to identify the base point on the scene, using a chess-board pattern as identifier, with modules developed with Open Computer Vision (OpenCV). Software libraries are built with Open Graphics Library (OpenGL) for generating the virtual graphic model of the robotic arm for subsequent rendering and embedding of the model over the real-time video frame to generate the CAD-augmented control interface. The complete scheme of the interface is shown in Figure 1.

The operator manipulates the virtual robot on the CAD-augmented control interface, as required, for the remote work-site task. Direct geometric transformations update the position and orientation of the virtual robot. The operator validates the virtual robot path sequence and the joint position information is received by the microcontroller for subsequently driving the joint motors of the remote work-site robot using pulse width modulation (PWM) signals. The complete integrated set-up for CAD-augmented system for remote tele-operation of 2-DOF planar robotic arm is shown in Figure 2.

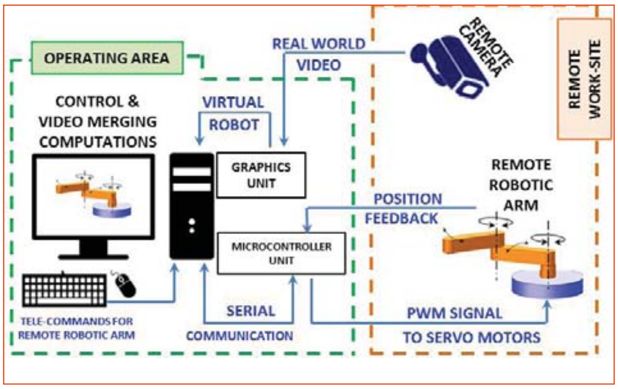

Fig. 1 *Scheme of CAD-augmented system for remote tele-operation of robotic arm*

The video frame captures the robotic arm within the view (in black; Figure 3) and also augments the scene using the virtual robot (wireframe in yellow; Figure 3). In order to perform the tele-operation of the robot arm, the operator contols the robot arm joint movements in steps of 5º.

The CAD-augmented control interface based on AR principles enriches the operator's perception and interaction with the real-world, along with improved safety. The task simulation reduces collision errors, and prevents the robot from reaching undesirable configurations. The developed module will be helpful to operators for real-time verification and error correction of the desired robot movements in cluttered remote work-sites.

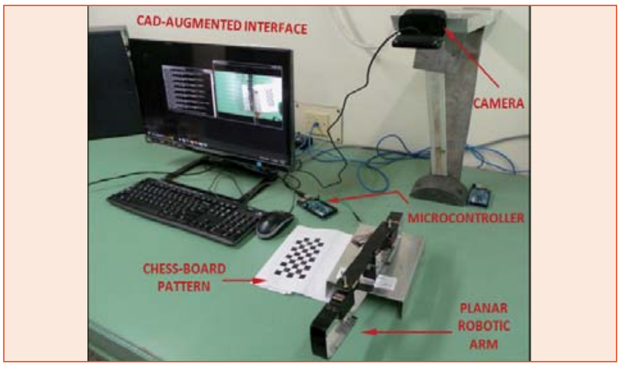

Fig. 2 *Integrated set-up for CAD-augmented system for remote tele-operation of robotic arm*

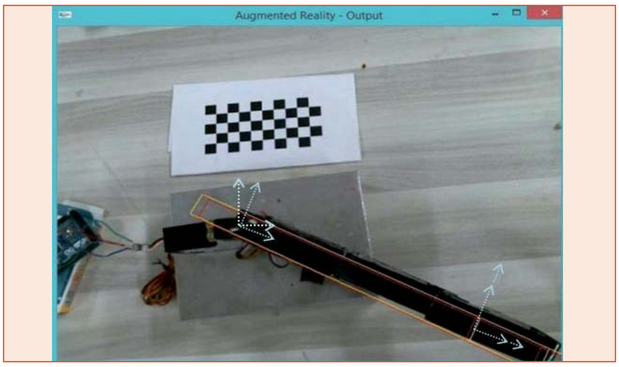

Fig. 3 *The AR output of the robot with control command, "rotate 30º for base joint", seen on the operator control console*

VI.9 Identification and Quantification of Radioactivity Levels in Water Bodies Located within Kalpakkam DAE Complex

A study was undertaken to generate and document the data regarding the radioactivity levels in water bodies located in the common areas of DAE complex at Kalpakkam. The work involved identification of water bodies, such as bore wells, open wells, lakes/ponds and reservoirs located within the common areas of the complex and subsequent sampling and analysis. There are 20 bore wells, 9 open wells, 3 reservoirs, 1 sump and 6 ponds/lakes located within the complex. The water bodies were identified and tagged using GPS. The locations of these water bodies are given in the Figure 1. Collection and analysis of water samples for gross alpha and gross beta activities were carried out in accordance with Indian standard – 'Radionuclides in environmental samples-methods of estimation for Water samples' and using calibrated equipment. Analysis for tritium concentration in the water samples was estimated using Liquid Scintillation System (LSS).

For gross alpha and gross beta activity estimation, water sample was plancheted by evaporation technique and the planchette was counted in a calibrated counting system. According to World Health Organization (WHO) guidelines screening levels for gross alpha and gross beta are 0.5 and 1.0 Bq/l respectively and guidance levels for tritium is 10,000 Bq/l. Regular consumption of water, whose gross alpha, gross beta and tritium levels are within the screening and guidance levels, would result in Individual Dose Criterion (IDC) not exceeding 0.1 mSv/y. The Minimum Detectable Activity (MDA) value for the alpha and beta counting systems, were 0.23 and 0.72 Bq/l respectively. The MDA value for the LSS was 20 Bq/l. It was observed that the gross alpha and gross beta activity levels and tritium concentration levels in all the samples were well within the screening levels and guidance levels recommended by WHO. This suggests that the radioactivity level in water samples collected from common areas of Kalpakkam DAE complex, does not cause any concern.

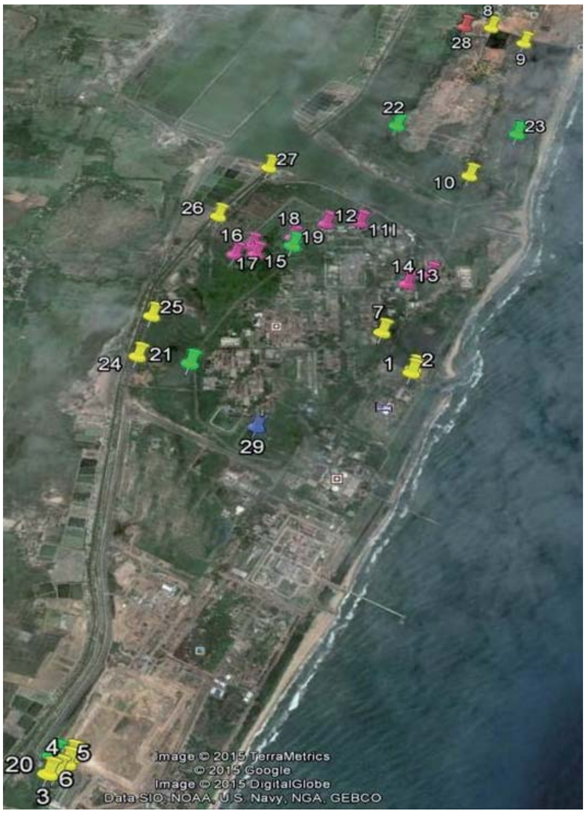

Fig. 1 Location of the water bodies

Name of the Location

1 - PRP Borewell-1
2 - PRP Borewell-2
3 - Main Gate Borewell-1
4 - Main Gate Borewell-2
5 - Main Gate Borewell-3
6 - Main Gate Borewell-4
7 - IGCAR Gate borewell
8 - KKM west borewell
9 - KKM Borewell
10 - Two borewells Edaiyur
11 - HASL Open well
12 - SRI Open well
13 - Admin Open well
14 - Nursery open well
15 - CWCP well-1
16 - CWCP well-2
17 - CWCP well-3
18 - CWCP well-4
19 - CWCP Lake
20 - Poiyakarai Lake
21 - WIP Lake
22 - Lake Edaiyur Bridge West
23 - Lake Edaiyur Bridge East
24 - Kunnathur Borewell-1
25 - Kunnathur Borewell-1
26 - Kunnathur Borewell-1
27 - Kunnathur Borewell-1
28 - Pond KKM gate
29 - Palar Reservoir

VI.10 Migration of Radioactivity within a Building of Several Interconnected Rooms

IGCAR has a number of active facilities and it handles active elements and gaseous chemicals with utmost care. In the event of an accidental release of any radioactive aerosol/ toxic gas inside a laboratory, it will be transported due to the mixing of air caused by the air circulation systems. Moreover, if the said room is a part of a building with interconnected rooms, the pollutant will migrate from one room to the other by the circulation of indoor air. This may pose a serious issue related to the safety of the operating personnel and thus a detailed analysis is required.

Theoretically, it is possible to address the problem by solving the Navier-Stokes equation for the entire building but in reality, this is an impossible task because of the constraints of computer memory. So a computational strategy is adopted to address this issue. For an isolated room, one can solve conservation equations (mass, momentum, energy) for a given distribution of internal objects to get the concentration profile of the pollutant as a function of space and time. On the other hand, if the room is part of a building with several rooms which are connected by the circulation of indoor air and the aim is to simulate the migration in the whole building, one has to resort to a Box Model approach. Here, every room of the building is represented by a box and thus the total building is considered to be a collection of boxes. The assumption is that the contaminant entering a box mixes immediately with the air already inside the room and so the concentration of the pollutant inside a box is uniform everywhere. This means that there is no spatial distribution of the concentration of the pollutant inside a room. When there is no air mixture present within the room, this assumption may not be a very accurate one but still it gives a reasonably good estimation of the concentration. One important point is that though the approach seems to be a gross one, it always provides a conservative estimate which is very important from the safety point of view. Figure 1a shows a schematic picture the Box Model for an isolated room. The equation governing the time dependent concentration profile inside a single box is given below.

$$C = \left(C_o + \frac{G - A}{Q} \right) + \left(C_i - \frac{G - A}{Q} - C_o \right) e^{-\gamma t}$$

Here, γ denotes the air exchange rate and C_i is the initial concentration. With these assumptions, a building with four identical interconnected rooms and one lobby has been modeled. The schematic picture of the building is shown in Figure 1b. The dimensions of all the rooms are 5 x 4 x 4m while the same of the lobby is 10 x 2 x 4m. In each room, air is flowing in through an AC at a rate of 0.1 m^3/sec. Now 90% of the indoor air of a room is sucked by the AC unit and 10% is leaking to the lobby. On the other hand 2% of inlet air is coming to any room from the lobby and a fraction of 98% of inflowing air is pumped by the AC from outside atmosphere. Under this condition, a gaseous pollutant leaks continuously in the Room A at a rate of 1gm/hr. A simulation of the accidental case has been carried out using the Box Model approach and the result is shown in Figure 2. It can be seen that the maximum concentration is observed in Room A. It is followed by the same in the lobby. The concentrations in all other rooms (Room B, C, D) are same. As expected, concentrations in all the rooms reach saturation values over a period of time. From the results it can be seen that though this approach is somewhat gross but still the simulation provides the baseline information about the concentration levels at different parts of a complicated building.

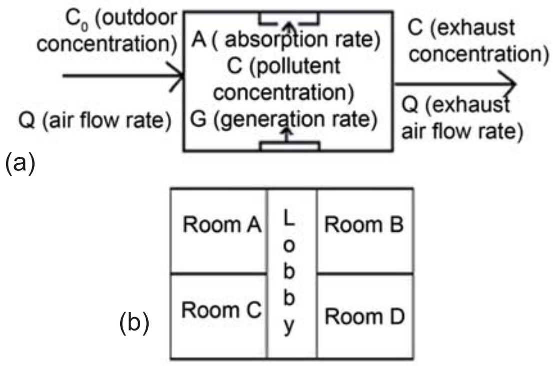

Fig. 1 (a) Box model for a single room and (b) schematic picture of the building

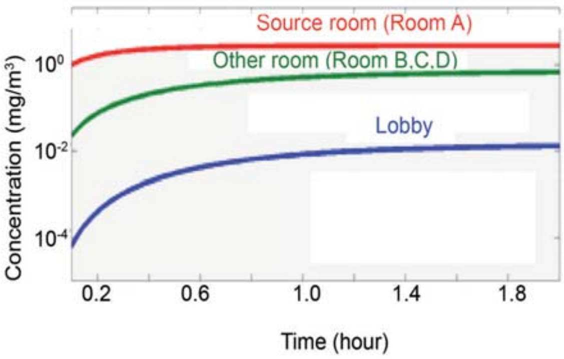

Fig. 2 Concentration as a function of time

VI.11 Storage of Water in Open Reservoir for Condenser Cooling Requirement: Effect on Chlorination and Chlorination by Product Formation

Chlorination is widely used to combat biofouling in industrial cooling water systems and drinking water treatment process to inactivate many waterborne pathogens. However, in addition to its intended function, chlorine reacts with organic compounds in the water to produce halogenated by-products including trihalomethanes (THMs), haloaceticacids (HAAs), haloacetonitriles (HANs), haloketones (HKs). Among these, THMs are the most commonly found regulated chlorination byproducts (CBPs). Flowing water when stilled in reservoirs, undergoes physical, chemical and biological changes. Evaluation of impact of these changes on chlorination is necessary to devise suitable strategies to minimize the adverse effects. The present study was focused on the total trihalomethanes formation potential (TTHMFP) of two different water types, mainly (i) How changes on the water quality parameters on storage influences the TTHMFP (ii) whether dissolved organic carbon (DOC) and UV$_{254}$ can be correlated with chlorine demand (CD) and THMs formation and (iii) finally, the role of bromide in the distribution of THMs species.

Water samples from covered, concrete lined infiltration well located inside the Palar river bed (GW) and from IGCAR open reservoir (RW) were studied. Both RW and GW had moderate DOC with an average of 1.68 and 0.82 mg/L and UVA$_{254}$ with an average of 0.057 and 0.049 respectively. The wide variation in DOC values of both the water types were not quantitatively reciprocated in their respective UVA$_{254}$ variation. High biological activities as expected in the reservoir have led to an increase in organic content in the water and thus caused higher chlorine demand than that of GW (Figure 1). However, the extent of compensations for the organic content in both the water types were different owing to the differences in their chlorine reactivity. Temporal trend of THM formation was always higher for RW than that of GW (Figure 2). The location being near coast, appreciable amount of bromide is present in these waters, ranging from 0.15 to 0.26 mg/L for GW and from 0.17 to 0.65 mg/L for reservoir water. Upon chlorination, the coexistence of HOCl and HOBr formed due to oxidation of Br^- by HOCl has resulted in THM species to be non-selectively distributed among all the four species and not favoring preferential formation of any particular species. At different chlorine dose and reaction time, speciation of THMs for both the water types are depicted in Figure 3(a) and 3(b). The instantaneous oxidation of bromide to HOBr and easier formation of Br-C bond than Cl-C bond resulted in enhanced overall TTHM yield and greatly altered the species composition of THMs. No distinct difference in the species distribution character was observed between GW and RW. Figure 4 demonstrates the comparative variation of UVA$_{254}$ with respect to TTHMFP (5 ppm, 24 hr) for both the water types. In our study we did not observe any correlation of UVA$_{254}$ with TTHMFP of both the source water (Figure 4). Thus, it appears that, some special natural organic matter (NOM) moieties, most probably non-humic, non UV absorbing and hydrophilic nature is responsible for the THM formation in these source waters. In addition, these moieties possibly comprised only a small portion of all NOM and therefore DOC also showed no correlation with THMs.

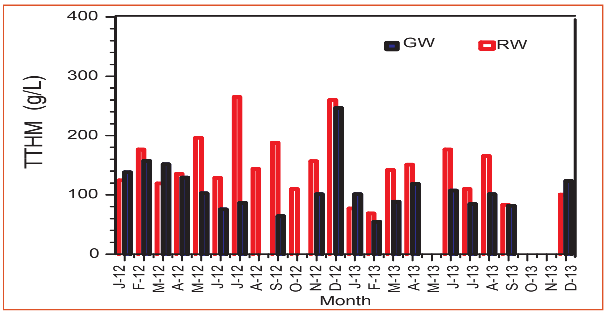

Fig. 2 *Temporal variation of TTHMFP of RW & GW (Cl$_2$: 3 mg/L, time: 24 hours)*

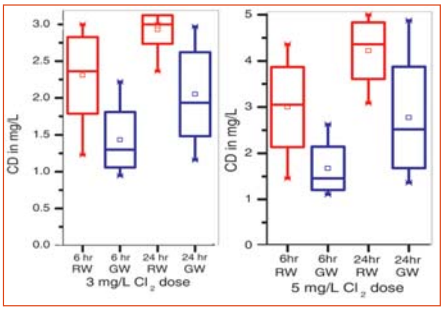

Fig. 1 *Comparison of CD for RW and GW*

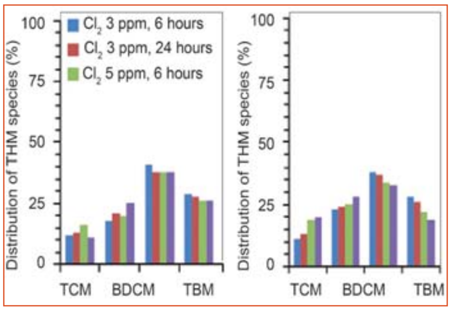

Fig. 3 *Percentage distribution of four THM species in chlorinated RW and GW*

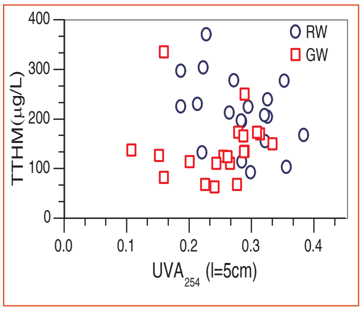

Fig. 4 *Correlation of UVA$_{254}$ with TTHM formation at 5 ppm Cl$_2$ after 24 hours*

VI.12 EURADOS International Intercomparison Exercise of TLD Personnel Dosimeters based on $CaSO_4$:Dy

Personnel monitoring services laboratory at Radiological Safety Division (RSD) caters to the monitoring of all radiation workers of IGCAR and BARCF. The lab is accredited by BARC for carrying out personnel monitoring of radiation workers using $CaSO_4$:Dy embedded Teflon discs since 2000. $CaSO_4$:Dy has an effective atomic number of 15.3 which is higher than that of tissue (7.4). This makes the dosimeter energy dependent resulting in an over estimation of about 10 times at low energies (<100 keV). The presently used Thermoluminescent dosimeter (TLD) badge for personnel monitoring consists of three discs clipped to an aluminum card. This energy dependence has been overcome by means of a metallic filter arrangement (1 mm Cu and 1 mm Al) for one of the discs in the cassette holding the TLD card.

The laboratory participated in the international inter-comparison exercise for the physical whole body dosimeters conducted by European Radiation Dosimetry Group (EURADOS). As a part of this exercise 30 numbers of TLDs were sent to EURADOS for irradiation and these dosimeters were irradiated in the range 1- 500 mGy at the Dosimetry Laboratory Seibersdorf to X-ray/gamma radiation of different energies viz 47, 57, 104, 662 and 1250 keV and at different angles (0 and ±60^0). All irradiations in the reference radiation fields were performed using phantoms to determine personal dose equivalent $H_p(10)$ and $H_p(0.07)$ for individual monitoring. After irradiation, the dosimeters were returned and normal routine procedures were followed for the evaluation of the doses. The evaluated dose values were communicated to EURADOS. On receipt of the evaluated dose values from the participants, the irradiated true doses were communicated to the participants.

The performance of our dosimetry system was analysed based on the ANSI 2009 criteria and trumpet curve method (standard followed during the regular QA check). The trumpet curve of the data of irradiated TLDs along with the ANSI values are given in Figure 1. From the ANSI criteria analysis, the tolerance level (L) is well within the acceptable limit of 0.3. From the trumpet curve it is seen that 6 of the data points lie outside the range of the acceptable limits. On analyzing the results it was observed that, for gamma ray photons above 100 keV, the variation between the estimated and true dose is within 20% and lie within the limits of trumpet curve. For TLD badges irradiated to 57 and 47 keV, as per the present dose evaluation algorithm, the readout pattern is like <40 keV and hence dose was evaluated for less than 40 keV which resulted in an underestimation of almost 40%. However, after knowing the energy values, when the dose was evaluated using the empirical relation for region above 40 keV, the variation was within 20% only which can be seen from Figure 2.

This intercomparison exercise helped us in evaluating the performance of our system and it also serves as a quality assurance index by benchmarking the dosimetry system and the dose evaluation procedures to international standards. Above all, this exercise has provided good opportunity to identify potential pitfalls in our dosimetry system at low energy regions and to perform possible corrective measures on par with international standards.

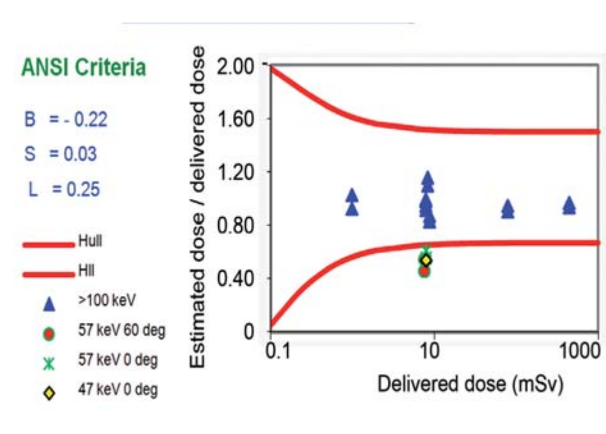

***Fig. 1** Trumpet curve analysis of the irradiated TLD cards as submitted to EURADOS*

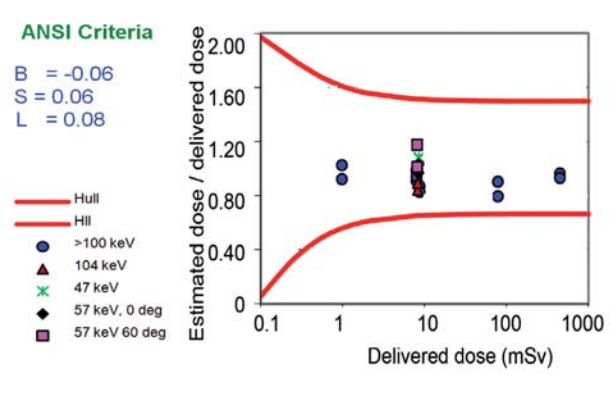

***Fig. 2** Results of EURADOS intercomparison IC2014ph after algorithm correction*

VI.13 Design and development of IT-enabled Advanced Knowledge Management System for IGCAR

A Knowledge Management (KM) system for codification of all multi-disciplinary knowledge assets accumulated over decades of nuclear research, development & operation at IGCAR is essential for improved organizational productivity, new insights and high-levels of innovation. IGCAR Knowledge Management System is designed as a federated structure consisting of a Gateway Server and number of Group Servers having distributed knowledge repositories. A web-enabled, taxonomy-based Knowledge Management system with advanced features has been designed, developed and deployed at different Groups to acquire, store, share and utilize the organizational knowledge assets in the explicit form of technical design reports, activities, facilities etc., along with the tacit knowledge multi-media modules. The knowledge management portal is a generic, customizable framework developed in-house fully using open-source platform and APIs. It is designed and implemented with the following advanced features.

- Taxonomy based categorization of documents for efficient organization/access
- Multi-format documents upload facility
- Automatic extraction of meta-data (Title, Authors, Abstract, Keywords etc)
- Enhanced access control with multi-level rights management
- Generic keyword-based and Advanced meta-data based Search facility
- Dynamic viewing of meta-data and full-text of documents
- Online analytics and graphical reports generation
- Customizable menu & contents and interactive user interface

Knowledge management portals have been developed and deployed for EIRSG, RDG and PFBR Records with a poly-hierarchical structure based taxonomy built for efficient categorization and retrieval of documents in related subject domains. The organization hierarchy and user accounts for all contributing employees have been created with assigned roles. The divisional representatives acting as coordinators are given additional privileges for management of contents and users. All uploaded documents need to be validated by Heads of Divisions/Sections before adding them to the repository.

The customized KM portal developed for Fast breeder Records Management facilitates the authenticated users to upload, organize, list, search, view and print the records available in the repository in the form of Control Notes, Design Notes, Operation Notes, Experiments Notes, Specifications, Project Reports, Commissioning Documents, Test Procedures & Reports, Manuals, Drawings etc in a secure way. Also, a KM Portal for ROMG is under development for managing the FBTR Records and associated workflow.

The screenshots of KM Portals developed for EIRSG and PFBR Records Section are shown in Figure 1.

Electronics, Instrumentation & Radiological Safety Group (EIRSG) consists of Instrumentation Control Group, Radiological Safety & Environmental Group, Computer Division and Security Electronics Section. The major activities of the group are

- Design & Development of Electronic Instrumentation & Control systems for Fast Breeder nuclear Reactor and Reprocessing facilities.
- Providing high-performance computing & data communication facilities; development of PFBR Operator Training Simulator, Wireless Sensor Networks, 3D visualisation & walkthrough, computational intelligence systems; implementing organizational Knowledge Management system & related activities.
- Design & Development of Innovative Instruments and implementation of Security Electronics systems.
- Providing radiation safety services for the radioactive facilities including occupational dose assessment and carrying out related R&D activities; catering the Quality Assurance, Inspection, NDT and Quality Audit activities; taking care of occupational health safety and industrial & fire safety, and conducting industrial safety training programme for employees of IGCAR and contractors.

The Group is Steered by **Dr. S.A.V. Satya Murty**, Director, EIRSG

Sine chemical dosimetry using pulsating sensor based instrumentation (Gyanendra Prasad)

Pulsating Conductometric Titration for Assay of Alkalinity in Water (Gyanendra Prasad)

A novel approach for high precision rapid potentiometric titrations: Application to hydrazine assay (Gyanendra Prasad)

Electronics and Computer Engineering
- Computer Science & Engineering
- Electronics Instrumentation & Control

Radiological Saftey & Environment
- Radiological Safety
- Radiation Dosimetry
- Radiation Impact Assessment
- Radiation Application and Monitoring
- Quality Assurance/Surveillance of Projects
- Environmental Research
- Environmental & Occupational Health
- Industrial Safety

Designed and Developed By Knowledge Management Section Computer Division

Drawings

- NUCLEAR STEAM SUPPLY SYSTEMS
  - MATERIALS
  - REACTOR ASSEMBLY[728]
  - PRIMARY SODIUM CIRCUIT[184]
  - SECONDARY SODIUM CIRCUIT
  - SAFETY GRADE DECAY HEAT REM
  - COMPONENT HANDLING[230]
  - RADIOACTIVE WASTE MANAGEME
  - BIOLOGICAL SHIELD COOLING
- SITE
- GENERAL PROJECT
- CIVIL STRUCTURES[4]
- CONSTRUCTIONS
- SAFETY STUDIES
- CONVENTIONAL AUXILIARY SYSTEMS
- ELECTRICAL POWER SYSTEMS
- INSTRUMENTATION AND CONTROL[34]
- STEAM WATER SYSTEMS

1 to 10 of 1450 Search Results

Restricted Docs: 0

1 PFBR plot plan

2 Arrangement of cells for primary sodium and primary argon system

3 Lead Block Wall layout & Details RCB-Area 21a

4 Lead block shielding door arrgement for pri cold temp cell

5 Secondary argon SGDHR Argon vapour trap for surge tank/expansion tank assembly & details

6 Primary argon SGDHR Argon vapour trap for primary tank storage tank assembly & details

(a)

(b)

Fig. 1 KM portal for (a) EIRSG and (b) PFBR records

VI.14 Implementation of User based Authentication for Internet Access in IGCAR Network

To enhance information security further in IGCAR network, existing IP (Internet Protocol) based authentication mechanism was augmented with user based authentication system for internet access. In this new system, the internet users have to get authenticated with user name and password from the IP address allotted to them for internet access.

To achieve this multiple proxy servers have been configured, tested, security hardened, security audited and deployed in the network. All servers are running on Linux operating system. For load balancing and for better throughput, multiple instances were configured on all proxy servers. To provide uninterrupted internet service, proxy servers have been commissioned in high availability mode. Typical setup implemented in IGCAR network is shown in Figure 1.

HTTP (Hyper Text Transfer Protocol) Digest authentication mechanism has been adopted for authenticating the users and in this mechanism authentication communicated to the proxy server from the browser are encrypted. Logging is enabled for all allowed and denied traffic with full URL (Uniform Resource Locator) for easy forensic analysis.

To maintain same user credentials across all proxy servers, an LDAP (Lightweight Directory Access Protocol) server has been configured to act as central authentication server. All proxy servers are configured to authenticate users using this LDAP server. A web site has been developed to facilitate users to change their proxy password. The web site in turn changes the password in LDAP server for that user and proxy reads the password from LDAP and authenticates the user in the subsequent internet access attempt.

In addition to preventing unauthorized access to internet, all the internet traffic passing through proxy servers is checked for virus content. A plug-in was installed and configured in all proxy servers to scan the web traffic for virus, trojans, spyware, worms etc and is being blocked if they are detected. Another plug-in has been installed and configured in all proxy servers for URL based filtering. All web site URLs being visited are checked and non-productive domains as per IGCAR's internet policy is filtered out to improve the productivity and to prevent malicious code entering in to the network.

To analyze the logs generated by proxy servers and to generate the statistical reports, an open source software has been installed, configured and tuned to suit network setup. Shell scripts were developed to fetch logs from all proxy servers and to merge them in to a single file. This merged single log file was used to generate per user based daily/weekly/monthly reports for all users. NTP (Network Time Protocol) was configured in all servers to maintain time precisely and to generate accurate usage reports.

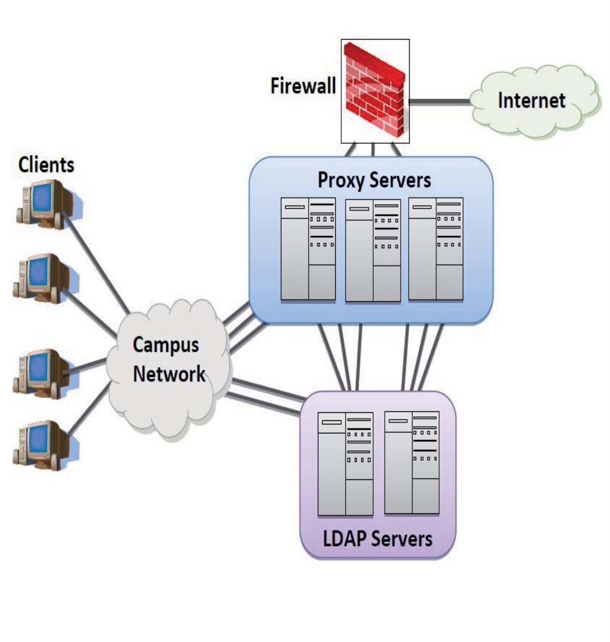

Fig. 1 *Typical setup of user based authentication for internet access*

With the above implementation, the following security enhancements have been achieved:

- Blocking of communications to Command and Control server by Botnets
- Precise identification of end user of internet access for forensic analysis
- Provides gateway level antivirus protection for all web traffic
- Deep analysis of web traffic at web-page level
- Prevention of anonymous access to internet, using tools like TOR, Ultrasurf etc

User based authentication for internet access was implemented in phased manner to have a smooth transition from the existing system. The user based authentication has been implemented for all users of IGCAR, FRFCF , BARC (F), BHAVINI and SRI successfully.

VI.15 Design, Development & Deployment of Smart Utilities Service Portal

A Service Portal has been developed and implemented in Computer Division to provide all authorized users any time self-service access to useful utilities and valuable information resources. The unified portal platform (Figure 1) gives online options to carry out and manage work processes of different activities with status monitoring and reporting features.

The modular and extensible service framework is designed for automating workflow associated with the following activities:

- Project review/work progress reports
- Tech-meet schedules & presentations
- Value engineering committee (C&N) tasks

Budget, indents & expenditure

Individual users can upload their respective indent details to the portal with current status and payment information (expected/actual) under various budget heads. It helps to keep track of the status of all the indents raised by computer division and their payment details. Division Head, Section Head and Budget coordinator can plan budget targets, monitor the progress, and generate various expenditure statements monthly, quarterly or yearly for a budget head.

Project/work progress reports

The module facilitates online creation, modification, submission and viewing of the monthly/quarterly work reports by the employees. These reports can be reviewed by the respective Section/Division Heads. The user can access all his/her reports at any point of time for consolidation or printing. It also enables authorized users to upload/view quarterly progress reports of the division.

Technical knowledge sharing meetings

As part of knowledge sharing initiative, periodic technical knowledge sharing sessions are conducted in Computer Division. The module facilitates any employee to register a presentation topic with the preferred date. It enables tech-meet coordinator to schedule the tech-meet and generate automated mails to intimate the speaker and all employees. The presentation material and audio recording can be uploaded to the portal and are made viewable by all users.

VEC activities

This utility allows the indentors to prepare and submit the forms along with the soft copy of the indents to the Value Engineering Committee (Computer & Network). The indentors can also check the status of approval of indents after the committee meeting. The VEC Committee members can view the uploaded VEC indents and record their comments. They can access the details of previous VEC meetings, indents submitted/cleared and their present status. Functionalities are provided for the VEC secretary to schedule VEC meeting, update the status of the indents and prepare the minutes of meeting.

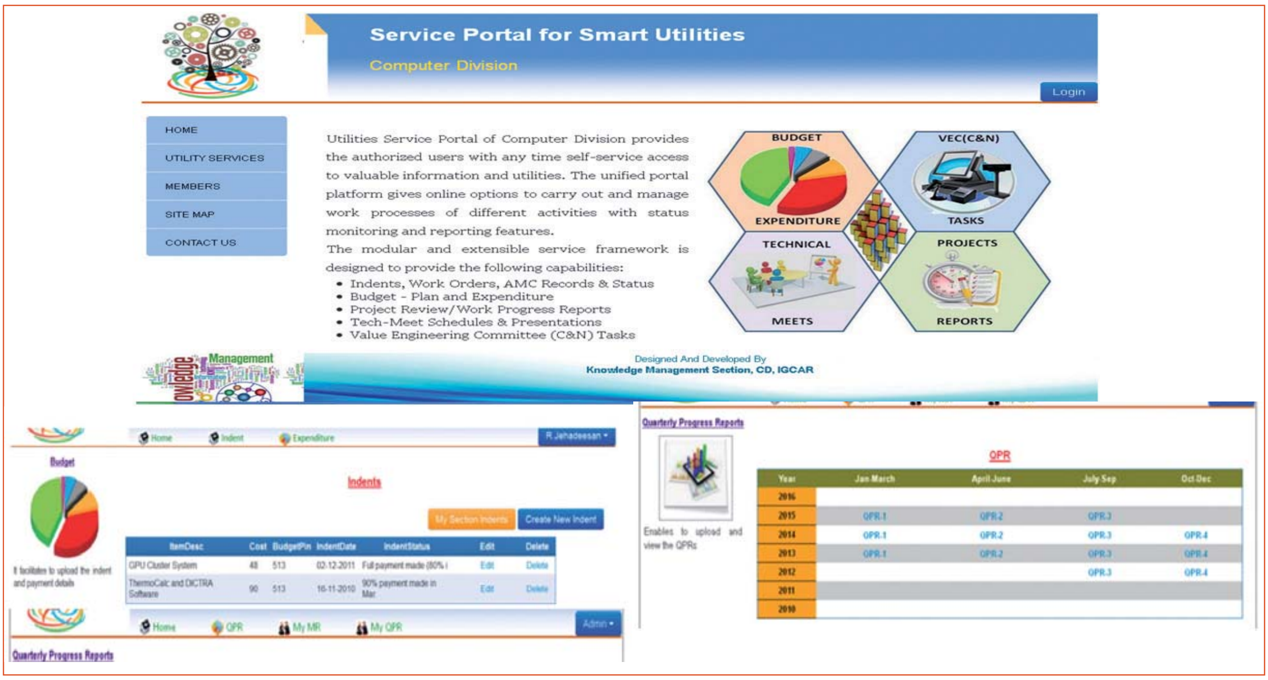

Utilities Service Portal of Computer Division provides the authorized users with any time self-service access to valuable information and utilities. The unified portal platform gives online options to carry out and manage work processes of different activities with status monitoring and reporting features.

The modular and extensible service framework is designed to provide the following capabilities:

- Indents, Work Orders, AMC Records & Status
- Budget - Plan and Expenditure
- Project Review/Work Progress Reports
- Tech-Meet Schedules & Presentations
- Value Engineering Committee (C&N) Tasks

Designed And Developed By
Knowledge Management Section, CD, IGCAR

It facilitates to upload the indent and payment details

ItemDesc	Cost	BudgetPin	IndentDate	IndentStatus	Edit	Delete
GPU Cluster System	48	513	02-12-2011	Full payment made (80% i	Edit	Delete
ThermoCalc and DICTRA Software	90	513	16-11-2010	90% payment made in Mar	Edit	Delete

Enables to upload and view the QPRs

Year	Jan March	April June	July Sep	Oct Dec
2016				
2015	QPR.1	QPR.2	QPR.3	
2014	QPR.1	QPR.2	QPR.3	QPR.4
2013	QPR.1	QPR.2	QPR.3	QPR.4
2012			QPR.3	QPR.4
2011				
2010				

Fig. 1 Web based smart utilities service portal

VI.16 Artificial Neural Network based Computational Intelligent Models for I/O Performance Prediction in HPC Cluster

High performance computing (HPC) Clusters use parallel file systems such as Lustre to meet the large Input/Output(I/O) requirements of parallel scientific applications. The file system performance plays a major role in the overall performance of the cluster. The objective of this work was to develop an artificial neural network (ANN) based computational intelligent model for learning the I/O performance behaviour of parallel cluster file-system, classifying the performance patterns and predicting the performance for a given I/O scenario. The variants of adaptive resonance theory (ART) networks viz. simplified ARTMAP using ART-2 and supervised ART-I were considered for implementation. Also a Genetic Algorithm(GA) based Backpropagation neural network model has been developed for comparative study

ANN network architectures

Supervised ART-I and Supervised ART-II have simple architectures because they have been built from a single ART module rather than a pair of them, connected by a map field. This leads to time reduction during both learning phase and testing phase. The supervised ART has the ability to learn and classify an arbitrary sequence of multi-values binary and analog input patterns. GA based ANN model is a variation of the standard backpropagation model and it uses genetic algorithm for weight adjustment instead of the gradient descent method. The conventional gradient descent method used for weight optimization has the disadvantage that it could get trapped in a local minimum.

Training

Read and Write (I/O) performance data of 134-noded HPC Cluster for different input parameters has been collected using the standard I/O benchmark to create a training data set. The features that were considered for predicting the class of the bandwidth of a read operation of the HPC File system are: Number of Processes/ Clients, Transfer Block Size, File Size, Lustre Stripe Size. These features were normalized and complement coded before presenting to the Supervised ART-I model in order to prevent category proliferation. These features were normalized and presented to the genetic algorithm based neural network model.

Results

The Supervised ART-I algorithm gave excellent accuracies with lesser number of iterations during training of the HPC performance data. The optimal accuracies achieved for different combination of vigilance parameter and learning rate are shown in Figure1. The simplified ARTMAP using ART-2 algorithm, although not achieving the accuracies of the former algorithm, also performed reasonably well in offline and is generally suited for an increased number of classes and more susceptible to unknown inputs. The GA based model took large number of generations to converge during the training process. Figure 2. shows the variation of the error rate with respect to the number of generations for the 4-8-1 network with a population size of 40. The Supervised ART-I model achieved a testing accuracy of 92% and the Genetic Algorithm based Backpropagation neural network model achieved a testing accuracy of 90%. The computational intelligent models developed help to predict the performance levels for the given workload with a set of identified I/O parameters and to optimize the file system parameters for specific workloads.

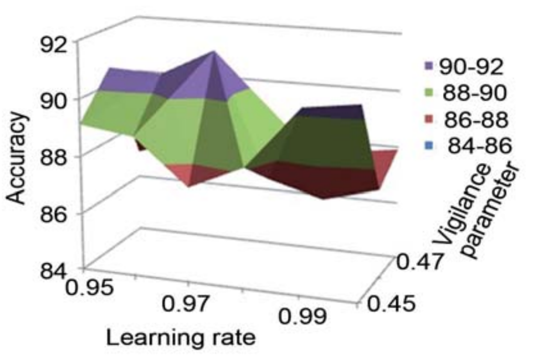

Fig. 1 *Accuracy graph for ART1 model*

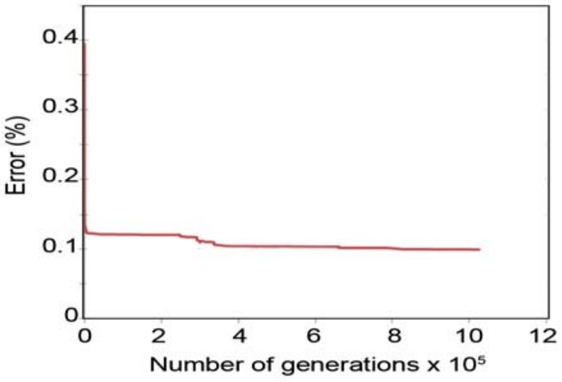

Fig. 2 *Error graph for GA based ANN model*

VI.17 Development of Solution based Approach for Auto-Parallelization of Serial Codes

Recent trends in processor micro-architecture are gradually increasing towards the larger number of processing elements on a single chip. Making intact use of the potential of the multicore processors through parallel programming is a significant challenge. Amid several approaches to address this issue, one that is very promising is automatic parallelization. It eliminates the involvement of programmer in the process of parallelization and optimization which is very attractive.

Auto parallelization tools and techniques

In a study, OpenMP based auto-parallelizers namely Cetus, Par4all, Pluto, and Parallware were considered to identify their capabilities and limitations. Totally 84 programming features including loops, loop conditions, statements, functions, operators were tested to evaluate the support provided by the tools in handling these coding constructs in parallelizable regions. In many cases of unsupported features, minimal coding changes with manual intervention could resolve the issues and make the code amenable for parallelization by the tools. Figure 1 depicts improved proficiency of the auto-parallelizers after resolving the coding pitfalls through manual intervention.

Analysis with benchmark problems

Polybench Benchmark suite (23 benchmarks) was used as a workload to carry out a detailed analysis on handling of programming features and dependencies by the tools during parallelization. The difficulties encountered by the tools while performing source-to-source transformation were identified along with the root causes. We could deduce solutions in the form of coding changes (or restructuring) for successful parallelization in many cases. Figure 2a shows on the increase in acceptance ratio of benchmarks by tools due to this effort.

Dependency analysis and loop transformation characteristics

Dependency analysis has become absolutely essential for parallelization to retain the order in which the original code flows. Parallelization issues with respect to different types of dependencies present in the code have been identified. Parallelizers are reasonably successful in parallelizing problems with independent dependencies but have difficulties with problems involving cross-iteration dependencies. Cross iterations dependency with vectors can be handled efficiently by applying loop transformation techniques like loop peeling and loop fission. The effect of loop transformation techniques like loop unrolling and loop tiling on parallelization has been studied in detail. Tiling with parallelization on many occasions leads to greater speedups. Unrolling in many cases is ineffective. Parallelization when combined with code optimization produces optimal results.

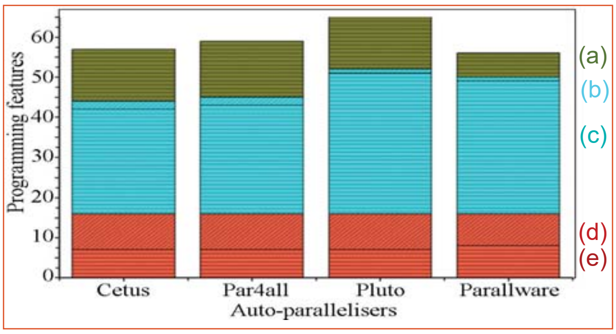

Fig. 1 *Parallelizers support for programming features. Loop body (a) additional programming features parallalised by default (b) statements and functions parallalised with manual intervention (c) statements and functions parallalised by default. Loop and loop conditions parallalised (d) with manual intervention (e) by default*

Interactive auto-parallelization approach

Analysis proves that with manual intervention with minimal coding changes improves the overall efficiency of the auto-parallelizers to greater extent. Figure 2b illustrates a solution based approach for effective parallelization by combining tools and semi-automated process of alleviating code pitfalls. A pre-compiler framework handles the source program with unsupported coding features with manual intervention and performs necessary code transformation to make the source code amenable for parallelization. The transformed code is then subjected to the chosen auto-parallelizer to generated parallel code. This approach of interactive parallelization will enhance the performance of automatic parallelization with minimal efforts.

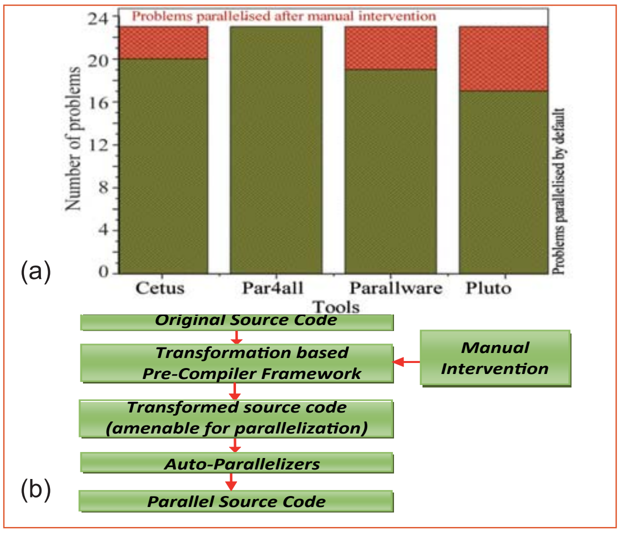

Fig. 2 *(a) Enhacing paralleization with manual intervention and (b) interactive auto-parallelization approach*

VI.18 Sustainable Design of a Large Span Industrial Space using Pre-engineering Concept

The pre-engineered industrial structure consists of steel building with enclosed rigid frames that are fabricated from plate steel. These rigid frames consist of roof beams and columns that are assembled at field and bolted together. These frames can span larger distances without intermediate supporting columns. The frames are spaced at intervals between five to ten metres and can span, column-free, up to 100 metres across a building. On top of and running perpendicular to these frames are roof secondary structural spanning members, often referred to as purlins manufactured through cold form procedures. They are spaced roughly 1.5 metres apart across the width of a building. The roofing system attaches to the purlins. The wall systems include wall secondary structural members called girts that also span from frame to frame. Girts support a wall cladding system.

The pre-engineered metal building system is advantageous because it is very economical and allows for the creation of large column-free enclosures. The best applications for the pre-engineered metal building system include industrial applications such as complex industrial facilities, warehouses and aircraft hangers. Buildings can be easily expanded in length by adding additional bays. Building can be supplied with various types of fascias, canopies, and curved eaves and are designed to receive pre cast concrete wall panels, curtain walls, block walls and other wall systems.

By adopting pre engineering concept, pyro-reprocessing R&D building with a plan dimension of 21 x 40 and 17 metre height at eaves level is being built. The facility is for the development of pyro-chemical reprocessing based on molten salt electro refining which is ideally suited for treatment of metallic fuels from FBRs.

The finished floor level of the pyro-process R&D facility is taken at RL +10.70 metres based on Design basis flood of 100 year return period. The finished floor level is around 2 metres above the existing ground level. Hence, construction of Random rubble masonry along the periphery of the building, including berm with pitching is provided for the stability substructure.

Fig. 1 (a) Embedment of steel column into concrete pedestal and (b) rigid frame using bolted connections

Rigid frame members are made up of welded I sections designed as per IS 800-2007. Materials used in reinforced concrete elements are M30 grade of concrete and Fe 500D grade of reinforcing steel (IS456-2000, IS 13920). High strength steel of minimum yield strength 350 MPa is used for fabrication of steel elements. The building is braced and the stability is provided by bracings in the three mutually perpendicular planes. (a) X bracings in vertical plane in the end bays in the longitudinal direction, (b) X bracings in vertical plane in the end bays of the gable ends and (c) X roof bracing in the end bays. The foundations have been designed as isolated footings founded at 3.5 metres from the natural ground level to achieve a safe bearing capacity of 150 kN/m^2. No tension at base of foundation is permitted under any of the load combinations considered for design.

Wind loads input such as basic wind speed was converted to deign wind pressure as per IS 875 (Part 3) are applied to the different members of the building according to the coefficients mentioned in the codes. The site is in zone III as categorized by IS 1893. Response spectrum for hard soil is considered independently in NS, EW and vertical directions with 2% damping. For vertical motion, two thirds of the acceleration response spectrum values in horizontal direction were adopted.

The pre fabricated steel columns are designed as embedded for 1.6 metres within the reinforced concrete foundation to ensure fixity (Figure 1a) as per Eurocode (EN 1994-1-1 (2004). Steel columns are designed as per IS 800-2007 and checked for local capacity, buckling due to compression and elastic lateral torsional buckling, overall member buckling resistance, axial compression, axial tension and shear capacity. Steel beams, rafters are checked for shear, web crippling, lateral torsional buckling and deflections. Bracings are designed with ISA sections in star formation with tack welding along the length to avoid buckling failure.

The structural steel column sections, beam sections, rafter sections and bracket sections were fabricated with welded connections at the fabrication yard (Ambur), and all sections were tested using 100% DPT. The other connections which were to be established at site are designed and executed as bolted connections. High strength friction grip bolts are used for all bolted connections (IS 4000). Galvalume cladded roofing with puff panels rests on purlins and girts. Purlin and girts are designed as cold formed Z-section beams as per EN 1993-1-3 (2006).For procurement of materials, fabrication, quality assurance and erection relevant ASTM, ASME, IS are followed.

In fact the building is custom-engineered to specific dimensions, structural criteria and materials in accordance with the building codes . The pre-engineered metal building system has evolved over the years into assemblages of structural elements that work together to provide a very efficient system as shown in Figure 1b. Each part of the system is designed to precisely fit together which transforms into buildings that can be built with greater speed and accuracy than is possible using conventional methods. Additionally, systems construction offers significant cost and performance advantages over conventional construction methods including lower life cycle costs for greater return on investment, unlimited design flexibility and sustainability attributes such as 100% recycling of steel and superior thermal building envelopes.

VI.19 Commissioning of 30 kWp Grid Connected Solar Plant at IGCAR

Grid connected solar system is an emerging technology to harvest solar incident radiation for production of electricity which can be fed to the grid directly. As part of the energy conservation activities and also considering the importance, the Government of India has given importance to harness solar energy. Our Centre has initiated projects in this regard. To start with, a pilot plant of 30 kWp grid connected solar plant is installed and commissioned on August 14, 2015 on the roof top of ESG annex building (Figure 1).

Features

On an average, this system produces 120 to 150 units of electricity per day. On days with good solar insolation, the production clocked 175 units. This is the largest solar system installed at Kalpakkam so far. All the operations are automatic and no manual intervention is envisaged for normal operation. It is not provided with any battery backup as the electricity generated is transferred to the gird on real time basis and no storage is necessary. This arrangement will ensure better efficiency at a lesser capital and maintenance cost. Control panels and display showing power versus time are shown in Figure 2a and 2b.

Components of the system

Solar photovoltaic modules

It comprises of 120 numbers of crystalline silicon type solar modules. Each module has an output 250 Wp. Twenty numbers of solar photovoltaic modules modules are connected in series to form one array. Totally there are 6 such arrays.

Array structure

Array structure is made of hot dipped galvanised iron and it holds the solar photovoltaic modules . This structure is designed to withstand a wind speed of 200 kmph.

Direct current distribution box

Direct current distribution box receives direct current output from the array field. There is provision for voltage and current measurement from different arrays so as to check any failure in the array field.

Grid interactive inverter

It converts direct current power produced by solar photovoltaic modules into alternating current power and adjust the voltage & frequency levels to suit the local grid conditions. The inverter works in fully automatic mode and is provided with automatic synchronization unit. In a short time after the sunrise the inverter gets activated and synchronizes the solar system with the grid. With that, the export of energy produced to the grid starts. In the evening towards sunset, the inverter disconnects from the grid and switches into sleep mode. It also has built in maximum power point tracker. Maximum power point tracker ensures that the solar photovoltaic modules operate on the maximum efficiency point of the voltage - current characteristics of the module and adjusts the voltage of the module in such a way that the power produced will be maximum. This is carried out on real time basis. It also has the facility to store the records and display the same.

AC distribution box

Alternating current distribution box receives alternating current power from Grid interactive Inverter and feeds power to the grid. It also has the facility to measure the voltage, current, power, energy, power factor and frequency.

After observing the performance of the pilot project, two numbers of similar systems each with 60 kWp is proposed to be implemented and action has been initiated towards this.

Fig. 1 *Solar photovoltaic panels at the roof top of ESG annex building*

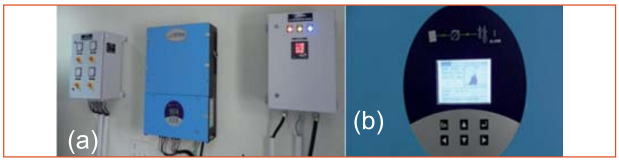

Fig. 2 *(a) Control panels and (b) display showing power versus time*

VI.20 Major Expansion of Electrical System Towards Capacity Building with Improved Reliability

As part of the augmentation and refurbishment to the electrical infrastructure, works on 33 kV Central Switching Station at IGCAR was completed with emphasis on improved reliablity and safety. The philosophy is further extended to the distribution system at 11 kV & 415 V levels. Apart from this, to meet the additional load requirements, reach of the 11 kV system also has been enhanced by commisssioning new substation. Towards this, the following major activities are successfully completed:

1. Commissioning of PDC VIII substation to meet the electrical load requirement of 2 MGD Desalination plant.
2. Commissioning of PDC IX substation as a replacement to main gate substation and also to meet the FRFCF construction needs.
3. Commissioning of 6.6 kV system at PDC V substation.

Commissioning of PDC VIII substation

PDC VIII substation was commissioned in March 2015 to meet the electrical demand of newly built 2 mgd desalination plant . The substation feeds the 6.6 kV & 415 V loads of desalination plant. The substation receives two numbers of 33 kV feeders in one out of two configuration. 33 kV is stepped down to 6.6 kV with the help of two numbers of 7 MVA 33/6.6 kV transformers. PDC VIII 6.6 kV switchboard is shown in Figure 1.

Both 33 kV and 6.6 kV Transformers are designed by keeping in mind the future electrical requirement for one more 2 MGD plant.

This Substation also provides 415 V power supply to other utility buildings such as STF Barrack & street lights etc.

Commissioning of PDC IX substation

The major consideration to construct and commission a new substation at maingate – (PDC IX substation) was to meet the addtional load requirment such as construction power requirement of FRFCF, introduction of higher capacity pumps near main gate for Anupuram water supply scheme and capacity limitation of existing main gate substation. Against the available of capacity of 500 kVA in the main gate substation, total projected requirement was 4 MVA. Considering the limited space available at old main gate substation, it was impossible to augment the capacity to meet the additional demand.

PDC IX substation is being constructed with two numbers of 2 MVA, 11 kV/ 415 V transformers connected in 1 out of two configuration (Figure 2). The substation can feed 2 MVA load in 415 V level and 2 MVA load in 11 kV level .

Commissioning of 6.6 kV system at PDC V substation

PDC V substation was constructed as a major hub to feed electrical loads of newly built facilities like Engineering Hall IV, Structural Mechanics Lab, Training School & Centre, High performance computing cluster etc. The 11 kV and 415 V systems were commissioned earlier. Presently 6.6 kV system comprising 3 MVA transformer, 6.6 kV switchboard and connected feeders are commissioned. This will meet the power requirement of 6.6 kV motors for the water test facility set up in Engineering Hall IV.

To meet the growing power demand, two numbers of new substations have been constructed and commissioned. In one of the substations, augumentation of the system was carried out in HT system with state of the art protection scheme. Additional safety features which were evolved at IGCAR to give maximum ptrotection to the operating personnel have been incorporated. The introduction of numerical relays and addition of innovative protection scheme helped to enhance the reliability of the system.

Fig. 1 *PDC VIII 6.6 kV switchboard*

Fig. 2 *PDC IX 415 V switchboard*

VI.21 Monitoring and Evaluating Skill of Welders using Data Acquired with High Speed Data Acquisition System

Arc welding is a stochastic process in which dynamic variations in the arc voltage and current occur while welding is in progress. With the help of high speed data acquisition systems like Digital Storage Oscilloscope (DSO), these variations can be monitored, recorded and subsequently analyzed for understanding the process. Voltage and current signals acquired during Shielded Metal Arc Welding (SMAW) using a DSO (Agilent Technologies, DSO7054B) of 500 MHz band width and maximum sampling rate of 4 GSa/s have been successfully analyzed for monitoring progress of learning during training of welders as well as to assess their skill levels. For acquisition of current signals Hall Sensor clamps and for voltage, signals differential probes were used. Data was acquired for a duration of 50 seconds at a sampling rate of 100,000 samples/s which were then filtered to remove the noise. Figure 1 shows part of the voltage and current signal (data for 50 ms) thus acquired. There is little variation in the welding current except when metal transfer takes place by short circuit mode which is accompanied by a large dip in the voltage signal. Unlike in the case of current, variation in the voltage is more as voltage would vary with variation in the arc gap, which in turn depends on the skill of the welder.

For the purpose of monitoring the progress of learning by the trainee welders, welding data was acquired at different stages of learning (initial, after six months and after one year). Probability Density Distribution (PDD) was generated from the voltage data thus acquired. PDD provides, for each voltage, the fraction of the entire data recorded. Figure 2 shows the voltage PDDs for a typical welder trainee at different stages of his training along with that of an experienced welder. PDD for the experienced welder is characterized by a smooth curve with two distinct peaks, one at low voltage corresponding to short circuit (refer Figure 1) and another for steady state. Voltage PDD of the trainee welder at the initial stage of training is far different from that of the experienced welder and it moved closer to the latter with the progress of training. This study was conducted on a group of four trainee welders and results of all the welders were similar indicating that this procedure can be used to monitor the progress of the learning during weld training.

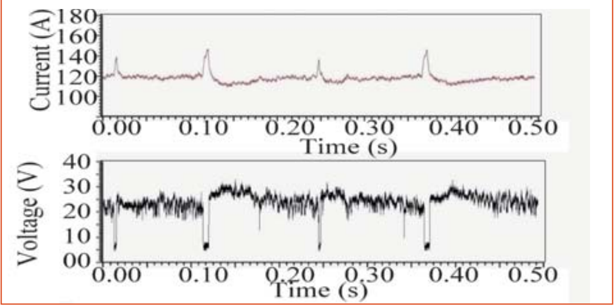

Fig. 1 *Current and voltage variation while welding is in progress*

Welders who completed their training were also ranked based on their skill using this procedure. Figure 3 shows voltage PDDs for some of the welders among the thirty welders who participated in this study and the ranking given to them based on the shape of the PDDs. This ranking matched closely with the ranking given by the training institute independently based on the dimensions and appearance of the weld bead prepared by them. Thus, it is demonstrated that high speed data acquisition during welding and subsequent analysis of this data is an ideal technique for evaluating the skill of welders. Adoption of this technique can bring down the time and cost involved in the training and is relevant in the skill development initiatives in the country.

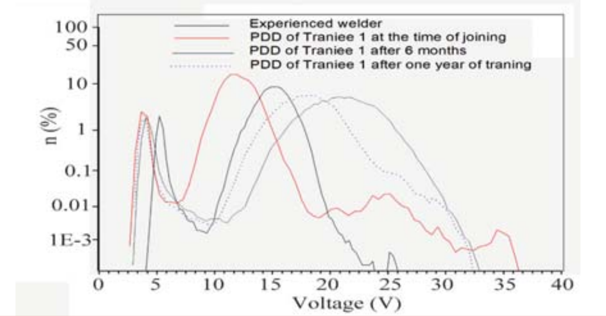

Fig. 2 *Probability density distribution (PDD) of voltage signal of the welding by a trainee at different stages of training along with that of an experienced welder*

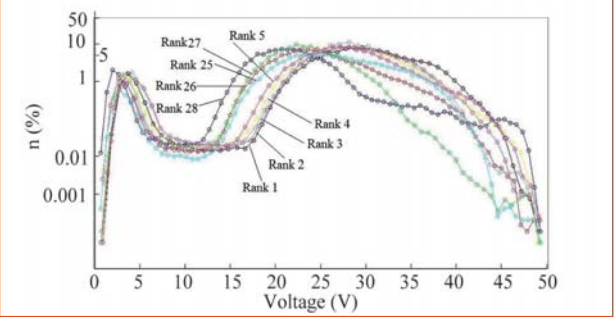

Fig. 3 *Voltage PDD for the welds prepared by different welders and the shape of the voltage signal of the welding by a trainee at different stages of training along with that of an experienced welder*

VI.22 Pilot Plant for Eco-Friendly Disposal of Waste Sodium

A pilot plant for eco friendly disposal of waste sodium is in operation at FRTG since 2013. Waste sodium is melted and allowed to react with air in a controlled manner. The resulting gas stream containing sodium aerosols is passed through two water scrubbers, one a quench tank and a venturi scrubber, viz.,to remove the aerosols by forming caustic solution so that the gas discharged into atmosphere contains minimum sodium hydroxide aerosols within the threshold limit of 2 mg/m^3. The caustic solution is neutralized before disposal.

Problems faced during burning of sodium

Initially waste sodium was melted in the reaction vessel itself by surface heaters. As sodium undergoes oxidation within the reaction vessel, due to the heat of oxidation of sodium (11 MJ/kg), the reaction vessel temperature drastically increased to 900-1000°C . As the disposal process ended, the vessel temperature was drastically reducing. Thus, very high temperature associated with high thermal transients resulted in cracks in the reaction vessel after few campaigns of operation.

Reaction vessel modification

After considering various options to limit the vessel temperature it was decided to insulate the sodium wetted inner surface of the reaction vessel with refractory material compatible with burning sodium.

On literature survey, it was found that the Alumina (Al_2O_3) based refractory materials are suitable candidates for sodium environment. In consultation with expert refractory manufacturers, it was decided to internally insulate the reaction vessel with two layers of two different grades of pure alumina based monolithic refractory viz., TABCAST 97L (97% (w/w) alumina) and TABCAST 99 (99% (w/w) alumina(Figure 1).

The thickness of each layer for burning 5 kg of waste sodium at a time, with the reaction vessel temperature limited to within 300-350°C, is arrived as 20 mm after numerical heat transfer analysis. The height of the insulation arrived at is 200 mm, which is just below the air inlet nozzle. Since, with internal insulation, it is not possible to melt sodium in the reaction vessel itself, waste sodium is melted in a separate vessel with surface heating and drained into the reaction vessel by gravity. Figure 2 depicts the flow diagram of pilot waste sodium disposal plant with the modified reaction vessel.

Operation of plant with modified reaction vessel

The disposal plant was operated with the modified reaction vessel for disposing 4.2 kg of waste sodium. It took 90 minutes for the complete disposal of waste sodium. During the disposal process, the maximum surface temperature of the reaction vessel was 332°C. So far, about 35 kg of waste sodium has been safely disposed in this plant. The total sodium aerosol concentration obtained in the exhaust stream to atmosphere is less than 2 mg/m^3.

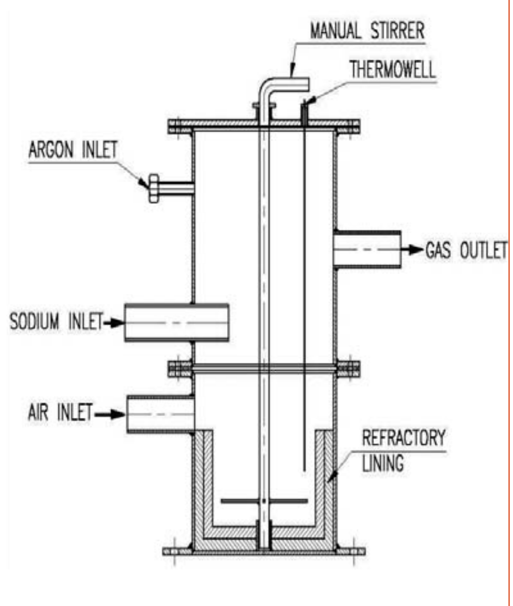

Fig. 1 *Reaction vessel modified with internal refractory insulation*

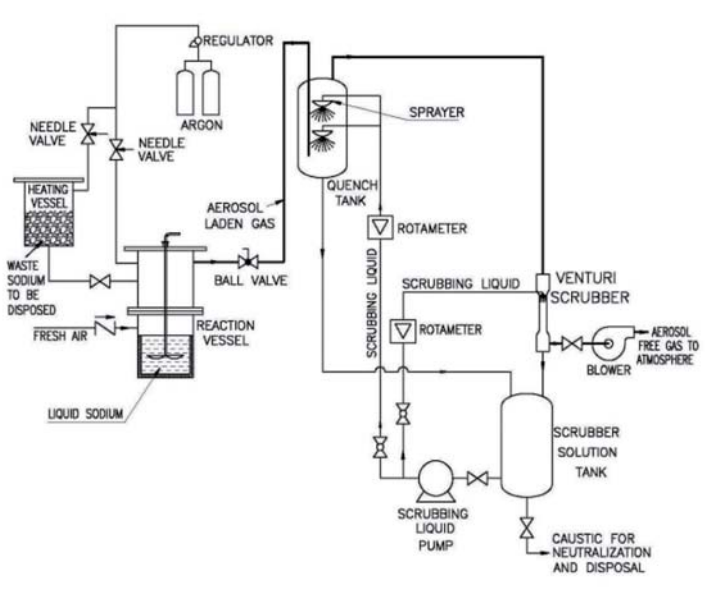

Fig. 2 *Flow diagram of pilot waste sodium disposal plant*

VI.23 Enrichment of Infrastructure and E-resources at SIRD

Scientific Information Resource Division (SIRD) continuously strives towards enhancing the digital library architecture and systems to ensure the efficient information access by scientists/engineers and students pursuing R&D. In the recent past, SIRD has undertaken several efforts to enrich it's information resources and also the supporting infrastructure in order to provide value added information services across the IGCAR campus and quick dissemination of information.

Infrastructure development activities

Adding workstations

In order to cater to a large community of students visiting the library for reference and to enable the Trainee Scientific Officers to access the information resources in the library even while consider the optimum use of the available space, Zero client systems with centralized servers were procured and commissioned (Figure 1). Servers were configured with LINUX and WINDOWS operating systems to enable the users to choose an operating system.

Fig. 1 *Zero Client Systems at Training School*

Enhancing the networking

The speed of networking was upgraded from the existing 100 Mbps to 1 Gbps. Five numbers of 24 port-1G switches along with necessary cables and input/output boxes were procured and connected effectively in order to increase the speed of information retrieval by the patrons.

Computerization of card catalogue

A card catalogue is a physical listing of the contents of a library, organized as a single card entry for each of the item available. In order to quickly identify and locate the holdings, SIRD has developed an automated version of the card catalogue, for the benefit of users. The physical appearance of these index cards are replicated in systems through programs.

Repository of technical and scientific videos

Our Centre conducts seminars, conferences, colloquium series and special lectures in a variety of topics during the entire year. The lectures and presentations made during these events are captured and stored in an organized fashion for quick access by patrons. Besides, initiative has also been taken to collect scientific and technical videos available on internet, relevant to the patrons, for hosting on library gateway site as shown in Figure 2.

Enrichment of e-resources

There is a tremendous growth of e-contents for libraries. Much of the library resources are now available in digital format and can be made accessible to the users on the desktops. SIRD continues to enrich it's information resources to match the requirements of scholars in the Centre. In this context, the following resources have been added recently.

The scientific citation indexing services Web of Science and Sci-Finder have been subscribed and are made available for users. Web of Science covers core collection with back file access since 1945 and Sci-Finder is aimed to enhance the knowledge database which provides integrated access to chemistry and related science information.

Research writing tool

A research writing support tool providing support for technical writing and enhancing a document. This tool has been added to help in manuscript preparation especially for the young scholars

Fig. 2 *SIRD video library*

VI.24 Automation of Purchase Process

Automated Workflow Management System (ATOMS), is an online, role and workflow based system. It enables the smooth and transparent flow of work across the areas of Administration, Accounts, Stores and Budget management, implemented in our Centre as a part of initiative towards e-governance and creation of a "paper-less" management. Taking into consideration the increasing volume of purchases being made by the Department to meet the targets year after year and also have a continuous update on the expenditure, automation of the purchase processes at Madras Regional Purchase Unit (MRPU). Integration of purchase process under ATOMS will bring the entire process from indent raising to making payment for purchases on the same platform, without the need for re-entering any data during the entire process.

All the purchase requests of IGCAR are processed by Madras Regional Purchase Unit located at Chennai. MRPU also caters to the purchase requirements of other Units viz., GSO, BARCF and HWP(Tuticorin). Presently all the indents received from different Units are processed using a client-server based software. The number of indents received at MRPU from different Units has increased significantly over a period of time. To cope-up with the increased workload there was an urgent need to augment the IT services at MRPU.

The purchase process involves the following major activities.

a) Indenting

b) Tendering

c) Post tender communications with indentors\ vendors

d) Awarding purchase order

e) Post PO communications with vendors

f) Handling of Earnest Money Deposits, Bank Guarantees, Letters of Credit etc.

g) Payment to the vendors

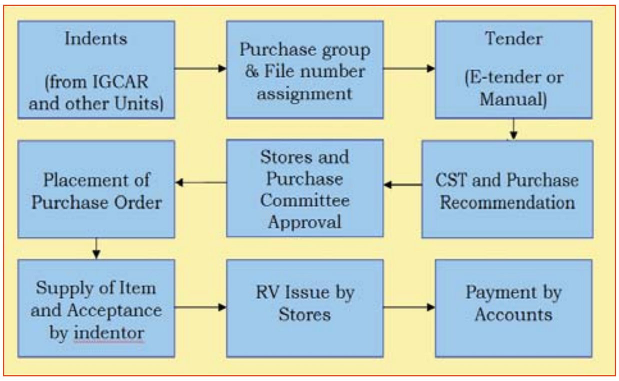

Fig. 1 *Various stages in purchase process*

All the above mentioned activities have been automated through ATOMS (Figure 1). The indents, when transmitted to MRPU, are assigned a file number and tendered through an e-tender (most often used) or manual tender (need based) mode. ATOMS provides interface for flow of data to e-tender portal. For manual tender action, it generates various tender forms and also the comparative statement after receipt of quotations from the vendors. Based on the recommendations of the indenters, the files are further processed towards placing the purchase orders.

Apart from performing the purchase functions like indenting, tendering and purchase order etc., the provision for communication with the click of a button, between the MRPU and suppliers and also between MRPU and indenters, in the form of auto-generated emails, email alerts etc. have been made available.

The indenters also have a provision to access the status of their indents almost immediately to track the developments at any given time. Automated email information on purchase file number, tender due date, file sent to site for recommendation, purchase order generation etc., periodically reach the desktop for any follow-up action required.

The purchase process also connects to the Madras Regional Accounts Unit (MRAU) for making payments to suppliers for items purchased based on the Receiving Voucher (RV), which are submitted by indentors to the local Stores. As the Stores is already linked to the ATOMS, the RVs issued by Stores reaches MRAU immediately upon processing and this precludes any delay in receipt of physical copy of RVs and also re-entry of RV data at MRAU.

Following are the salient features of the system.

a) Online web based system

b) Interface with e-tender portal

c) Linking of MRPU and Stores IGCAR

d) Generation of automated email alerts

e) Various MIS and exception reports

This system has been successfully commissioned and is operational. It is intended to ease the workload of limited staff available at MRPU, to cater to the increasing requirements of purchases made by various Units.

CHAPTER VII

Awards / Publications / News & Events/ Organisation

Awards & Honours

Dr. P. R. Vasudeva Rao, the then Director, IGCAR has been selected as the Vice President for the Council of Materials Research Society of India during the year 2015-2018

Dr. A. Ravishankar Project Director, FRFCF has been conferred with the INS Outstanding Service Award on Nuclear Fuel Cycle Technologies, including radiation safety and Environmental Protection

Dr. U. Kamachi Mudali is awarded AICTE-INAE Distinguished Visiting Professorship by INAE, New Delhi for the year 2015-16

Dr. B. P. C. Rao has been conferred with International Recognition Award, by the Indian Society for NDT

Dr. Anish Kumar has been conferred with ISNT National NDT Award for Research and Development

Dr. T. Jayakumar, MMG has been bestowed with "VA Chandramouli Award" by the Indian Society for Non-destructive Testing, Hyderabad Chapter - award received on April 02, 2015

Dr. S. Thirunavukkarasu has been conferred with ISNT National NDT Award for NDT Systems Innovation and Development

Dr. N. V. Chandra Shekar has been selected by President, MRSI to receive the MRSI Medal for the year 2015

Dr. John Philip has been elected as a member of the editorial committee for the Indian Journal of Engineering & Materials Sciences since 2015

Dr. S. Amirthapandian has received the "Young Scientist Award" for the year 2014 from the Academy of Sciences, Chennai

Kalpakkam Community Radio Station (KCRS) was awarded second place under the category of best community radio program conducted by Anna University along with UNICEF

Dr. N. R. Sanjay Kumar has received the Best Thesis award for his thesis titled "High Pressure High Temperature Synthesis and Study of Novel Transition Metal Carbides" during the 59th DAE Solid State Physics Symposium The award is instituted by Indian Physics Association

Ms. K. Kamali has received the "Dr. K. V. Rao Research Award" for the year 2014 -15, in Physics for her research work titled "Selective Soft Mode Frustration in $KMn[Ag(CN)_2]_3$ Single Crystals Studied by Raman Spectroscopy and First-Principles Calculations" from Dr. K. V. Rao Scientific Society

Dr. M. Sai Baba, has been elected as a Fellow of the Academy of Sciences, Chennai on April 10, 2015

Dr. Rani P. George has been elected as a Fellow of the Indian Institute of Metals and also received

Shri. S.K. Seshadri Memorial Mascot National Award, 2015 from Electrochemical Society of India, Bangalore in the area of corrosion and electrochemistry

HBNI Awards

On the occasion of HBNI completing 10 years of excellence, distinguished faculty and out standing students were felicitated. Awards were presented in a special ceremony organised at Mumbai to commemorate the occasion.

Distinguished Faculty Award

Dr. B.V. R. Tata; Dr. John Phillip; Dr. K. Velusamy; Dr. U. Kamachi Mudali

Outstanding Doctoral Student Award

Dr. Prasana K. Sahoo for the thesis titled "Quasi One Dimensional GaN Nanostructures: Growth Kinetics, Physical Properties, and Applications" in Physical Sciences

Dr. Shima P. Damodaran for the thesis titled "Synthesis, Characterization, Thermal and Rheological Studies in Nanofluids" in Chemical Sciences

Dr. S. Ravi for the thesis titled "Design and Development of In-Sodium Creep Testing Facility and Influence of Dynamic Sodium on Creep Properties of Structural Materials for Fast Reactors" in Engineering Sciences

Outstanding M. Tech. Student Award

Shri Aritra Sarkar for the thesis titled "Deformation Behaviour under Ratcheting of a Type 316LN Stainless Steel"

Shri V. Arjun for the thesis titled "Finite Element Model Based Optimization of Pulsed Eddy Current Probe for Sub-Surface NDE"

DAE Awards

Department of Atomic Energy has instituted annual awards for excellence in Science, Engineering and Technology in order to identify best performers in the area of Research, Technology Development and Engineering in the constituent units (other than Public Sector Undertakings and Aided Institutions). The Young Applied Scientist, Young Engineer, Young Technologist, Homi Bhabha Science and Technology Award and Scientific and Technical Excellence Award fall under this category. Group Achievement awards for recognition of major achievements by groups have also been instituted. Life-time Achievement Award is awarded to one who has made significant impact on the DAE's programmes. They are the icons for young scientists and engineers to emulate. The awards consist of a memento, citation and cash prize.

The recipients of the Awards from IGCAR for the year 2014 are:

Scientific and Technical Excellence Award : Shri A. Palanivel, RDG
Shri A. John Arul, RDG

Young Applied Scientist / Technologist Award : Shri Barid Baran Lahiri, MMG
Shri Satyabrata Mishra, RpG

Young Scientist Award : Dr. Arun Kumar Rai, MMG

Young Engineer Award : Shri A. Viswanath, MMG
Shri Sanjeev Kumar, RDG
Shri T. Raj Kumar, RDG
Shri Juby Abraham, RDG

Meritorious Technical Support Award : Shri G. Ramadoss, ESG
Shri P. Bakthavachalam, FRTG
Shri K. Arumugam, ROMG
Shri R. Rajaram, CG

Meritorious Service Award : Ms. Shanthi Rajendran, FRTG
Ms. Sasikala Manohar, MSG

Group Achievement Awards:

Development of Indian Reduced Activation Ferritic Martensitic (INRAFM) Steel for India's Test Blanket Module (TBM) in ITER

Dr. T. Jayakumar, MMG, Group Leader

Dr. Arun Kumar Bhaduri, Dr. K. Laha, Dr. Saroja Saibaba, Shri Raju Subramanian, Dr. R. Sandhya, Dr. V. S. Srinivasan, Dr. Aniruddha Moitra, Dr. A. Nagesha, Dr. Vani Shankar, Dr. R. Mythili, Shri Sunil Goyal, Shri M. Nandagopal, Shri G. V. Prasad Reddy, Shri V. David Vijayanand, Ms. J. Vanaja, Shri Arun Kumar Rai, Shri Aritra Sarkar, Shri K. Mariappan, Shri N. S. Thampi, Shri R. Balakrishnan, Ms. S. Panneer Selvi, Shri M. Govindasamy from MMG

Design and Development of Wireless Sensor Networks for Nuclear Facilities

Dr. S .A. V. Satya Murty, EIRSG, Group Leader

Ms. Jemimah Ebenezer, Shri Sukant Kothari, Ms. D. Baghyalakshmi, Ms. G. Sandhya Rani, Ms. Vinita Daiya, Shri T. S. Shri Krishnan, Ms. Deepika Vinod, Ms. R. Vijayalaxmi, Dr. R. Baskaran, Shri V. Gopalakrishnan, Dr. M. T. Jose, Shri R. Nandakumar, Shri N. Radhakrishnan, Shri V. Balu, Shri Ibrahim Khan, Shri P. Solai Raj, Shri A. Boopalan, Shri N. Sathish Kumar, Shri K. Rajesh from EIRSG, Shri S.Vannia Perumal, Shri P. Venkatesh, Dr. B. Prabhakara Reddy from CG, Shri T. Chandran, Shri M. Shanmugavel, Shri B. Babu from FRTG, Shri Kalyan Rao Kuchipudi, Shri D. Loganathan, Shri R. Shunmugavel, Shri P. Immanuel Stephen from ROMG

Experimental Verification and Qualification of Equipment towards Demonstrating Safety of Sodium Systems of PFBR

Dr. D. Ponraju, RDG, Group Leader

Shri P. Selvaraj, Shri B. K. Nashine, Shri E. Hemanth Rao, Shri S. S. Ramesh, Shri Sanjay Kumar Das, Shri G. Punitha, Shri Arjun Pradeep, Ms. G. Lydia, Ms. B. Malarvizhi, Shri M. Kumaresan, Shri S. S. Murthy, Shri Anil Kumar Sharma, Shri S. Athmalingam, Shri V. Balasubramaniyan, Shri P. Mangarjuna Rao, Shri S. Srinivasan, Shri K. E. Jebakumar, Shri Ch. S. S. S. Avinash, Shri Avinash Kumar Acharya, Ms. V. Snehalatha, Shri G. Venkat Reddy, Shri S. Muthu Saravanan, Shri J. Anandan, Shri T. Lokesh, Shri V. Sebasti John, Shri S. Satheesh Kumar, Ms. Sujithra, Shri R. Suresh Kumar, Shri M. Aravind, Shri R. Manu from RDG, Shri V. Venkatachalapathy, Shri N. Suresh, Shri M. K. Satheesh Kumar, Shri D. Balamurugan, Ms. R. Thilakavathi, Shri D. Hari, Shri G. Ramanathan, Shri P. Senthil Arumugam from ESG, Shri T. V. Maran, Shri K. Mohan Raj, Shri Chandramouli, Shri G. Kempul Raj, Shri R. Iyappan, Shri R. Parandaman, Shri S. Kannan, Shri P. Lakshmayya, Shri P. Pothi from FRTG

Design, Development and Experimental Testing of Sodium Submersible Annular Linear Induction Pump (SALIP) for FBR

Shri B. K. Nashine, FRTG, Group Leader

Shri B. Babu, Shri K. V. Sreedharan, Shri B. K. Sreedhar, Shri S. Chandramouli, Shri G. Vijayakumar, Ms. J. I. Sylvia, Shri V. Ramakrishnan, Shri S. K. Dash, Shri Prashant Sharma, Shri Vijay Sharma, Shri R. Rajendra Prasad, Shri Gautam Anand, Shri S. Kannan, Shri R. Iyyappan, Shri P. Lakshmayya, Shri P. Pothi, Shri P. Vijaya Mohan Rao, Shri G. Anandan, Shri P. Bakthavatchalam, Shri V. Krishnamoorthy, Shri Pitambar Padhan, Shri A. Ashok Kumar, Shri S. Krishnakumar, Shri Parmanand Kumar, Shri N. Venkatesan, Shri A. Thirunavukkarasu, Shri P. C. V. Murugan, Shri N. Mohan, Shri M. Karthikeyan, Shri K. Ramesh, Shri Shaik Rafee, Shri L. Mohanasundaram, Shri L. Muthu, Shri N. Sreenivas, Shri L. Eagambaram, Shri D. Muralidhar, Shri S. Ravishankar, Shri S. Alexander Xavier, Shri C. Rajappan, Shri K. Ganesh, Shri Ashish Tiwari, Shri P. R. Ashokkumar, Shri K. Arumugam, Shri Shiv Prakash Ruhela, Shri R. K. Mourya, Shri R. Ramalingam, Shri Vijay Tirkey, Shri P. Sonai, Shri M. Kathiravan, Shri K. A Bijoy, Shri A. Selvakumaran, Shri D. Laxman, Shri M. Anbuchelian, Shri N. Chakraborty, Ms. Indra G. Ramadoss from FRTG

Design, Numerical and Experimental Simulations, Development and Qualification of Principal Fuel Handling Machines of PFBR

Shri S. Raghupathy, RDG, IGCAR & Shri R.J. Patel, RD&DG, BARC - Group Leaders

Shri Jose Varghese, Shri A. Venkatesan, Shri N. Subramanian, Shri E. Balasundaram, Shri M. A. Sanjith, Ms. T. Suguna, Shri P. Shanmuganathi, Shri R. Suresh Kumar, Shri C. Ragavendran, Shri S. D. Sajish, Shri S. K. Rajesh, Shri M. Babu Rao, Shri R. Manu, Shri S. Ramesh, Shri M. Aravind, Shri G. Venkataiah, Shri V. Devaraj, Shri P. Raja, Shri V. Balasubramaniyan, Shri Sriramachandra Aithal, Shri Abhishek Mitra, Shri S. Saravanan, Ms. M. M. Shanthi, Shri P. Selvaraj, Dr. R. Gajapathy, Dr. K. Velusamy, Shri R. Arulbaskar, Shri K. Natesan, Shri S. Jalaldeen, Shri Bhuwan Chandra Sati, Shri Sanjay Kumar Pandey, Shri C. S. Surendran, Shri V. N. Sakthivel Rajan, Shri S. Arumugam, Shri Sanjeev Kumar, Shri P. Lennin, Shri L. Chandrasekaran, Shri S. Duraikannu from RDG, Shri S. Jaisankar, Shri G. Kempulraj, Shri B. S. Ramesh Babu, Shri M. Krishnamoorhy, Shri V. Praveen Kumar, Shri S. Parivallal, Shri S. A. Natarajan, Shri S. Murugan, Shri S. Satees Kumar, Shri C. Palani, Shri T. Saravanan, Shri D. Dileep, Shri U. Gunasekaran, Shri S. Ramesh, Shri G. Janarthanan, Shri V. Kodiarasan, Shri S. P. Jaisankar, Shri A. Padmanabhan, Shri S. Yuvaraj, Shri E. Venkatesan, Shri B. Ramalingam, Shri A. Gunasekaran, Shri P. Shanmugam from ESG, Shri B. K. Sreedhar, Shri G. Padmakumar, Shri S. C. S. P. Kumar Krovvidi, Shri Nilayendra Chakraborty, Shri V. V. Nagaraja Bhat, Shri R. Nirmal Kumar, Shri S. Ignatius Sundar Raj, Shri P. Madan Kumar, Shri J. Saravanan, Shri R. Krishnamurthy, Shri M. Sambanmurthy, Shri A. Kolanjiappan, Shri R. Ramalingam, Shri A. Sudarsana Rao, Shri P. Varadan, Shri Rakesh Kumar Mourya, Shri P. A. Kalaimannan, Shri N. Thulasi, Shri Anant Kumar, Shri T. V. Maran, Shri K. Mohanraj, Shri A. T. Loganathan, Shri D. Kuppusamy, Shri A. Anthuvan Clement, Shri S. Sureshkumar, Shri J. Jaikanth, Shri R. Shanmugam, Shri M. T. Janakiraman, Shri C. Adikesaven, Shri A. Ashok Kumar, Shri L. Muthu, Shri S. Bavanirajan, Shri B. K. Nashine, Shri P. R. Ashok Kumar, Shri L. Egambaram, Shri N. Sreenivas, Shri K. Arumgam, Shri A. Alexander Xavir, Shri P. Chenthil Velmurugan, Ms. M. Chandra, Shri G. Vijaya Kumar, Shri S. Chandramouli, Shri R. Rajendra Prasad, Shri D. Muralidhar, Shri S. Ravishakar, Shri J. Prabhakaran, Shri R. Parandaman, Shri N. Mohan, Shri R. Iyappan, Shri K. Ramesh, Shri Sheik Rafee, Shri M. Karthikeyan, Shri V. Kumaraswamy, Shri Gautam Anand, Shri D. K Saxena, Shri B. Veeraraghavan, Shri C. Rajappan, Shri S. Kannan, Shri R. Punniyamurthy, Shri S. Krishnakumar, Shri R. Arjunan, Shri K. Ganesh, Shri Vijay Sharma, Shri Ashish Tiwari, Shri L. Mohanasundaram, Shri Parmanand Kumar, Shri N. Venkatesan, Shri Pabbineedi Lakshmaya, Shri P. Pothi, Shri A. Thirunavukkarasu, Shri V. Ramakrishnan, Shri K. Jayagopi, Shri D. Laxman, Shri P. Sonai, Shri S. Shamugam, Shri R. Rajendran, Shri H. Rafiq Basha, Shri J. Prem, Shri M. Kathiravan, Shri V. Gunasekaran, Shri N. S. Shivakumar, Shri Gautam Kumar Pandey, Shri P. Lijukrishnan, Shri Vijay Singh Sikarwar, Shri S.Sathishkumar, Shri Nagaraju Bekkenti, Shri K.H. Anub, Shri N. Mariappan, Shri Asif Ahmad Bhat, Shri V. Nandakumar, Shri R. Nagaraj, Shri K. Thanigairaj, Shri L. S. Sivakumar, Shri S. P. Pathak, Shri P. Narayana Rao, Shri Sukanta Kumar Roy, Shri B. Babu, Ms. M. Mohana, Shri M. V. Subramanya Deepak, Shri Chandra Sekhar Singh, Shri T. Mohan, Shri J. Vincent, Dr. J. I. Sylvia, Shri P. Vijaya Mohan Rao, Shri V. S. Krishnaraj, Shri M. Anbuchelian, Ms. S. Divya, Ms. S. Nagajothi, Shri G. Anandan, Shri P. Bakthavatchalam, Shri C. Ambujakshanan Nair, Shri A. Kulanthai, Shri R. Gunasekaran, Shri V. Krishnamoorthy, Shri Pitambar Padhan, Ms. Indra G. Ramadoss from FRTG, Dr. Arun Kumar Bhaduri, Dr. Shaju K. Albert, Dr. Chittaranjan Das, Shri Hemant Kumar, Shri P. Chandrasekaran, Dr. S. Venugopal from MMG, Shri P. Rajasekar, Shri M. P. Prabhakar, Shri G. Vijayaraghavan, Ms. Alka Kumari from EIRSG, Shri N. Murugesan from CG, Shri N. Mahendran from FRFCF

The award was also shared by colleagues from BARC, BRIT and VECC

Best Paper/Poster Award

Ab-initio study of the Magnetism, Structure and Spin Dependent Electronic States of Ti substituted MO (M=Mg, Ca, Sr)
Dr. G. Jaiganesh and Dr. S. Mathi Jaya
59th DAE Solid State Physics Symposium
Best Poster Presentation Award

Development of SiC coating by pack cementation as interlayer over graphite for deposition of yttria by plasma spray process
Shri H. Thirunavuakkarasu, Shri E. Vetrivendan, Dr. Ch. Jagadeeswara Rao, Dr. C. Mallika, Shri R. Subramanian and Dr. U. Kamachi Mudali
National Symposium on Advances in Materials and Processing (NSAMP-2015), PSG College of Technology, Coimbatore, May (2015)
Best Paper Award

Bioinspired Superhydrophobic Surface by Deposition of Fluorinated Si nano Particles on Type 304L Stainless Steel
Ms. M. Ezhil Vizhi, Ms. S. C. Vanithakumari, Dr. R.P. George, Ms. S. Vasantha and Dr. U. Kamachi Mudali
International Corrosion Symposium for Research Scholars (CORSYM 2015) at IIT, Madras,
Best Paper Award

Deployment of Wireless Sensor Network for Radiation Monitoring
Ms. Jemimah Ebenezer and Dr. S. A. V. Satya Murty
International Conference on Computing and Network Communications (CoCoNet'15) at IIITM-K, Trivandrum
Best Paper Award

Theoretical Analysis on Designing Full Functional Device of WSN using Wireless Power Transfer
Ms. Vinita Daiya, Shri T. S. Shri Krishnan, Ms. G. Sandhya Rani, Ms. Jemimah Ebenezer, Dr. S. A. V. Satya Murty and Dr. B. P. C. Rao
12th IEEE India International Conference (INDICON 2015) at Jamia Millia Islamia, New Delhi
Best Paper Award

Patent

"Wash Solution Suitable for use in Continuous Reprocessing of Nuclear Fuel and a System Thereof"
authored by Dr. P. Govindan, Shri K. Dhamodharan, Shri K. S. Vijayan, Dr. R. V. Subba Rao, Shri M. Venkataraman and Dr. R. Natarajan, has been granted as patent by Japan - (Japanese Patent No. 5643745)

IGCAR Publications during the Year 2015

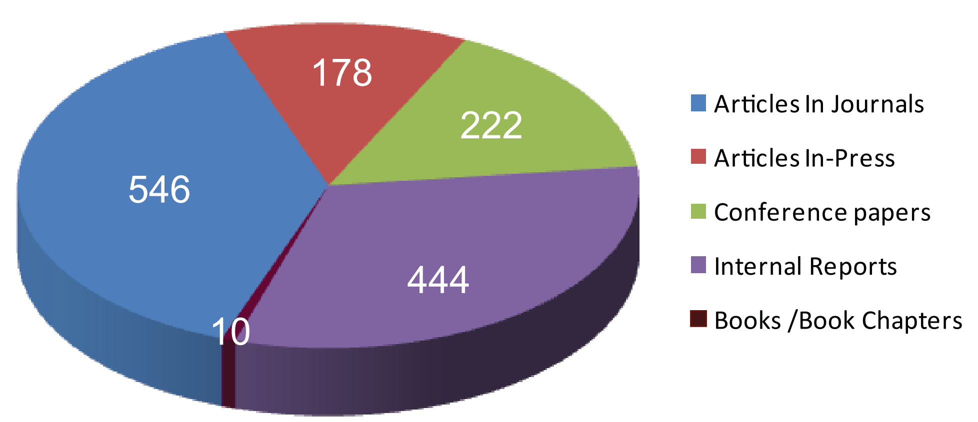

Special Lectures and Colloquia Series

IGC Colloquium

1. "Semiconductor Materials and Device Research and Development at Solid State Physics Laboratory-an Overview" by Dr. R. Muralidharan, Director, Solid State Physics Laboratory, DRDO, New Delhi, January 6, 2015
2. "Nuclear Power: The Need, Perception and the Realities", by Dr. S. K. Malhotra, Head, Public Awareness Division, DAE, Mumbai, January 23, 2015
3. "Can India have Uninterrupted Power in all its Homes: Leveraging Decentralised Solar –DC", by Prof. Ashok Jhunjhunwala, IIT Madras, February 19, 2015
4. "General Relativity: A Hundred Years Later" by Prof. Ghanashyam Date, IMSc, Chennai, May 12, 2015
5. "Pathways to Energy Sustainability for India" by Dr. Baldev Raj, Director, NIAS, Bengaluru, July 9, 2015
6. "Cardiac Health: Probing by Non-Invasive Methods" by Prof. Riccardo Fenici, Director of Clinical Physiology, Centre for Biomagnetism Catholic University, Rome, Italy and European Director, Society for Police and Criminal Psychology, July 23, 2015
7. "Expanding Nuclear Power Programme in India, the Prospects & Challenges and the Role of FBRs" by Dr. C. Ganguly, former Chief Executive, NFC, Hyderabad, August 11, 2015

Special Lectures

8. "Self-Assembled Photoresponsive Materials", Bhatnagar Memorial Lecture by Dr.Suresh Das, Director, NIIST, Trivandrum, February 9, 2015
9. "Safety Regulation of Nuclear and Radiation Facilities in India" Lecture by Shri S. S. Bajaj, Chairman, AERB, February 24, 2015, as a part of Know your DAE Lecture series organized to commemorate the Diamond Jubilee Celebration
10. "Energy Security and Sustainability: Approaches and Priorities for Growing and Aspiring India" by Dr.Baldev Raj, Director, National Institute of Advanced Studies, Know your DAE Lecture series organized to commemorate the Diamond Jubilee Celebration, March 14, 2015
11. "Big World of Small Neutrinos", IANCAS (SRC), Seaborg Memorial Lecture by Prof.M.V.N.Murthy, Institute of Mathematical Sciences, Taramani, Chennai, April 20, 2015
12. "Nuclear Power : Past, Present and Future" N. Srinivasan Memorial lecture by Dr. R. K. Sinha, Chairman, Atomic Energy Commission & Secretary, Department of Atomic Energy, 19 May, 2015
13. "Harnessing Technology for Development: A Governance Challenge in Indian Context", DAE Diamond Jubilee Colloquium by Dr. Anil Kakodkar, INAE Satish Dhawan Chair of Engineering Eminence, and Former Chairman, Atomic Energy Commission and Secretary, Department of Atomic Energy, July 03, 2015

14. “India’s Nuclear Programme: The Main Thrust and the Spin-Offs” DAE Diamond Jubilee Colloquium by Dr. R. Chidambaram, Principal Scientific Advisor, Government of India, Know your DAE Lecture series organized to commemorate the Diamond Jubilee Celebration, July 24, 2015
15. “Chemistry R&D in DAE: Technology Incubation and Transfer” Special Lecture by Dr. B.N. Jagatap, Director, Chemistry Group, BARC, July 30, 2015
16. “Nano Catalysis- Doing the Impossible” Acharya P.C. Ray Memorial Lecture by Prof. M.O. Garg, Director General, Council of Scientific & Industrial Research (CSIR), New Delhi, August 26, 2015
17. “Development of Alloys for Application in the Nuclear Energy Sector: Some New Perspectives” Dr. Placid Rodriguez Memorial Lecture by Dr. G.K. Dey, Associate Director, Materials Group, BARC, October 5, 2015

Seminars, Workshops and Meetings

1. Theme Meeting on “Advances in Back End Fuel Cycle Technologies”, January 20, 2015
2. DAE-BRNS Theme Meeting: “Chemistry in Nuclear Technology - CHEMNUT 2015”during July 30-31, 2015
3. National Workshop on “Luminescence Material Devices and Applications (LMDA-2015)” during August 19-20, 2015
4. “Indo-UK Workshop on MSSMNA-2015” during December 16-17, 2015

Nurturing Activities

1. “Orientation Programme for Young Officers”, March 04-05, 2015
2. “Women’s Day Celebration”, March 20, 2015
3. “International Women’s Day” March 23, 2015
4. “Technology Day Meet 2015”, May 11, 2015
5. “BITS Pilani Practice School” May 22 to July 16, 2015
6. “Summer Training in Physics and Chemistry (STIPAC - 2015) from May 25 to July 3, 2015
7. “One day Awareness Workshop for Women” as a part of DAE Diamond Jubilee Celebrations organized by Tamil Nadu Science Forum, July 5, 2015
8. “Tamil Nadu State Level Quiz Program” as a part of DAE Diamond Jubilee, July 24, 2015
9. Graduation Function of the OCES-2015, 9th Batch of BARC Training School at IGCAR, July 29, 2015
10. “SACSE Outreach Program for Tamil medium Schools around Kalpakkam”, August 22, 2015
11. “Quality Circle Annual Meet (QCAM-2015)”, September 9, 2015
12. Prof. Brahm Prakash Memorial Material Quiz organized by IIM Kalpakkam Chapter, September 18-20, 2015

Administrative Seminars/Meetings

1. “World Hindi Day Celebration”, January 9, 2015
2. ATI/DAE Workshop on “Art of Technical Writing”, March 26, 2015
3. ATI/DAE Training Programme – “Pension and Retirement Benefits” during July 16, 17 and August 6, 2015
4. ATI/DAE Programme on “Tamil Language Essentials” during August 25 & 26, 2015
5. “Hindi Fortnight-2015 Celebrations” during September 14-30, 2015
6. ATI/DAE’s “Capacity Enhancement” Workshop for Personnel Staff during Oct.6 - 9, 2015
7. “Vigilance Awareness Week” during October 26-30, 2015
8. ATI/DAE’s “Capacity Enhancement” Workshop for Clerical Staff during Dec.14 -17, 2015
9. ATI/DAE Training program for CISF, December 21, 2015

Conference and Meeting Highlights

Orientation Programme for Young Officers

February 16 – March 6, 2015

Dr. P.R. Vasudeva Rao, the then Director, IGCAR addressing the young officers during the valedictory function

Orientation Programme for the directly recruited young officers and officers from Training Schools other than IGCAR, who have joined our Department in the recent past, was organized during February 16 – March 6, 2015

This three week long programme, was designed to give an outline of the research and development activities of our Centre to the young officers. Each day a senior colleague from the DAE facilities delivered a lecture on the research activities of their Group and it was followed by a visit to the respective facility.

The officers were also informed about the activities of other DAE units located at Kalpakkam by senior colleagues of the respective Units. Visits were arranged to MAPS, BHAVINI and BARC-Facilities located at Kalpakkam.

Interactive sessions were also organized for bringing awareness about Administration, Accounts and Purchase procedures, Rules in Contributory Health Service Scheme and Industrial Safety Practices. Officers from BARC Training School, IGCAR joined in the recent past were also invited to participate in this interactive session.

The orientation programme concluded with a feedback session from the participants and with a address by Dr. P. R. Vasudeva Rao, the then Director, IGCAR as a part of the valedictory function.

Group photograph of participants with Dr. P.R. Vasudeva Rao, the then Director, IGCAR and colleagues of RMG during the valedictory function

11th CEA-IGCAR Annual Meeting on Liquid Metal Fast Breeder Reactor Safety

March 23-27, 2015

Dr. P.R. Vasudeva Rao, the then Director, IGCAR along with the delegates from CEA

IGCAR and CEA, France have worked together in the field of liquid metal fast breeder reactor safety. Under this bilateral cooperation, many collaborative projects have been taken up and completed. The 11th CEA-IGCAR annual meeting to review the ongoing collaborative project took place during March 23-27, 2015. The CEA team led by Dr. Christian Latge consisted of ten experts and the IGCAR team was led by Dr. P. R. Vasudeva Rao, the then Director IGCAR. During the meeting Implementing Agreements for collaboration on new projects were also signed. Following ongoing collaborative projects among others were reviewed during the meeting.

- Fluid structure interaction applied to core mechanical behavior
- Carbonation of Na aerosols
- Atmospheric dispersion modeling
- Bench mark on Oxide (Phenix pin) and Carbide (FBTR Pin) Fuels Safety Criteria evaluation
- Testing of IGCAR ECHM on a sodium facility at Cadarache
- Experimental & theoretical studies for under sodium viewing for navigation and object detection
- Characterization of gas content in sodium
- Severe accident in sodium cooled fast reactor
- Dislocation precipitate interaction at high temperature in model ODS Alloys
- Thermodynamic Modeling of the actinide carbides and oxides systems
- Sodium Fast Reactor Education and Training

Delegations from United States Nuclear Regulatory Commission

May 4-5, 2015

Delegations from United States Nuclear Regulatory Commission led by Dr. William Ostendorff with Dr. T. Jayakumar, Director, MMG and senior colleagues of the Centre

A delegation from United States Nuclear Regulatory Commission led by Dr. William Ostendorff, Commissioner, US Nuclear Regulatory Commission visited the Centre during May 4- 5, 2015. After a meeting with Dr. T. Jayakumar, the then Director, MMG and other senior colleagues, the delegation visited the Fast Breeder Test Reactor, Radio Metallurgy Laboratory, facilities in Fast Reactor Technology Group and Structural Mechanics Laboratory. The team also visited Madras Atomic Power Station and construction site of Prototype Fast Breeder Reactor.

BITS Practice School

May 22 - July 16, 2015

Students from BITS Practice School with Dr. S. Venugopal, the then Director, MMG and Dr. M. Sai Baba, Associate Director, RMG during the valedictory function

Twenty five students from BITS Pilani, Hyderabad and Goa campuses underwent Summer Practice School at our Centre during May 22-July 16, 2015. This programme is aimed at exposing the students to industrial and research environments, how the organizations work, to follow and maintain work ethics, study the core subjects and their applications in the organization, participate in the assignments given to them in the form of projects. The students were from various disciplines like Chemical Engineering, Computer Science & Engineering, Electrical & Electronics Engineering, Electronics & Instrumentation Engineering, Electronics & Communication Engineering, Mechanical Engineering and Information Systems. Dr. Parameshwaran, BITS Practice School Division was the programme coordinator. Students carried out challenging projects in various Groups of the Centre according to their discipline. During the period of their stay, they visited various facilities at IGCAR, BHAVINI and MAPS. As a part of the curriculum, quiz, project work presentations, group discussions and report writing were done. The valedictory function was held on July 16, 2015 with Dr. S. Venugopal, the then Director, Metallurgy and Materials Group delivering the valedictory address and distributing the certificates to the students.

Dr. S. Venugopal, the then Director, Metallurgy and Materials Group delivering the valedictory address and distributing the certificates to the students.

Summer Training in Physics and Chemistry (STIPAC - 2015)

26 May - 03 July, 2015

Dr. Anil Kakodkar, Former Chairman, Atomic Energy Commission and Dr. P. R. Vasudeva Rao, the then Director, IGCAR along with the students during the valedictory function

The STIPAC programme for the year 2015 (being conducted for the 17th time) coincided with the International year of Light. The theme chosen was "Lasers in Physics & Chemistry". Forty students, twenty each from 157 applicants for Physics and 130 applicants for Chemistry were selected for the STIPAC-2015 based on their academic credentials, their write up and the interest evinced to pursue scientific research. Theoretical courses were held in forenoons. The students were given hands-on experience by either doing project work or carrying out experimental work on various topics. Towards the end of the course, the students gave a presentation on the work done and answered questions from the audience.

Apart from this, quiz programs and lectures on special research topics were also held. Problem solving sessions were conducted by Dr. S. V. M. Satyanarayana, a former scientist of IGCAR and currently an Assistant Professor in Central University, Puducherry. In addition, the students were also taken on a site visit to MAPS, BHAVINI and DAE-UGC node. The STIPAC-2015 was inaugurated by Dr. C. S. Sundar, J C Bose Fellow & former Director, MSG. He gave a historical perspective of evolution of Light as a tool in the research on Condensed Matter. This was followed by a keynote address on Photonic Crystals & Band Gap Materials by Dr. B. V. R. Tata, Head, CMPD, MSG. Prof. S. Anantha Ramakrishna, IIT Kanpur, gave a talk on the need for and the research potential in Optical Meta Materials.

Dr. Anil Kakodkar, INAE Satish Dhawan Chair of Engineering Eminence, Former Chairman, Atomic Energy Commission & Secretary, Department of Atomic Energy and Dr. P. R. Vasudeva Rao, the then Director, IGCAR & GSO addressed the students during the valedictory function on 03 July, 2015.

Dr. Anil Kakodkar distributed the certificates to the students of STIPAC 2015.

Dr. Anil Kakodkar, INAE Satish Dhawan Chair of Engineering Eminence, Former Chairman, Atomic Energy Commission & Secretary, Department of Atomic Energy delivering the valedictory address and distributing the certificates to the students.

Graduation Function of the 9th Batch of Trainee Scientific Officers of BARC Training School at IGCAR

July 29, 2015

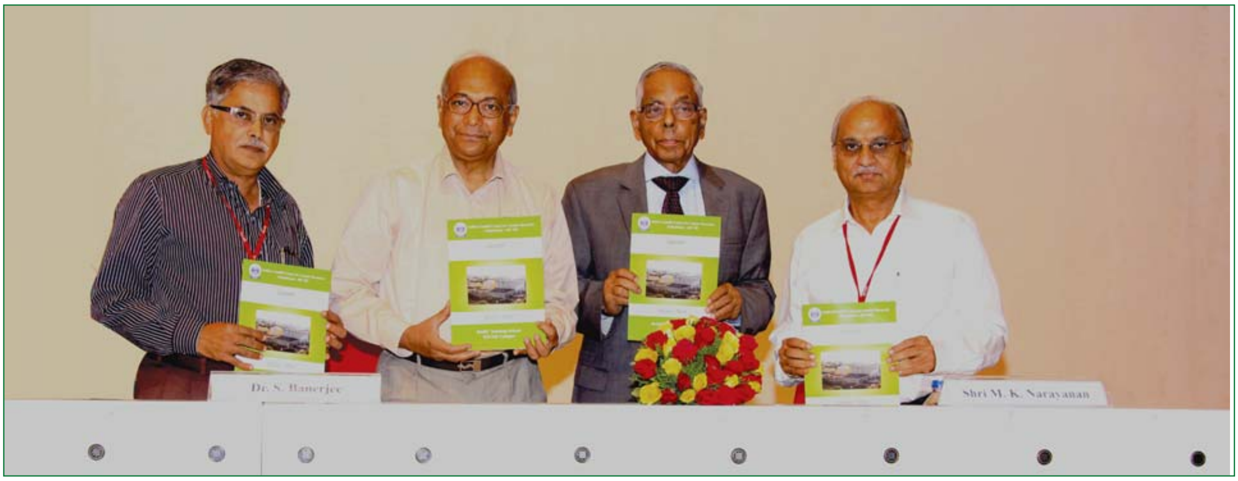

Dr. Srikumar Banerjee, Shri M. K. Narayanan, Dr. P. R. Vasudeva Rao and Dr. M. Sai Baba during the release of souvenir at the graduation function

The 9th batch of forty six Trainee Scientific Officers from the BARC Training School at IGCAR have successfully completed their training and were graduated in a special ceremony that took place on July 29, 2015. Shri M. K. Narayanan, Former National Security Advisor and Former Governor of West Bengal was the Chief Guest. Dr. Srikumar Banerjee, Homi Bhabha Chair and Former Chairman, Atomic Energy Commission presided over the function. Dr. P. R. Vasudeva Rao, the then Director, IGCAR and GSO, welcomed the gathering. Dr. Vidya Sundararajan briefed the audience about the Orientation Course in Engineering and Sciences programme. Dr. Srikumar Banerjee delivered the presidential address. Shri M. K. Narayanan released the souvenir featuring the training school programme in the previous academic year and Dr. Srikumar Banerjee received the first copy. Shri M.K. Narayanan gave away the prestigious 'Homi Bhabha Prizes' comprising of a medallion and books worth Rs.5000 to the toppers from each discipline and addressed the gathering. He also gave away the course completion certificates to all the graduates passing out. A few of the Trainee Scientific Officers passing out shared their experience, gave a feedback on the academic programme and their stay at the hostel.

Dr. M. Sai Baba, Associate Director, Resources Management Group, proposed the vote of thanks.

Graduates of BARC Training School at IGCAR with Shri M.K. Narayanan, Former National Security Advisor & Former Governor of West Bengal, Dr. Srikumar Banerjee, Homi Bhabha Chair and Former Chairman, AEC , Dr. P. R. Vasudeva Rao, the then Director, IGCAR & GSO, Dr. M. Sai Baba, AD, RMG and senior colleagues of the Centre and the Department

Quality Circle Annual Meet (QCAM) - 2015

September 08, 2015

Dr.P.R.Vasudeva Rao, the then Director, IGCAR & GSO and G.Srinivasan, Director, ROMG & RDG along with the participants during the valedictory function

Quality circle is a small group of employees doing similar or related work who meet regularly to identify, analyze, and solve work related problems usually led by a senior team member. After completing their analysis, they present their solutions to management for implementation and to improve the performance of the organization. Thus, implemented correctly, quality circles can help the organization to reduce costs, increase productivity, and improve employee morale.

In IGCAR, every year Quality Circle Annual Meet (QCAM) is conducted and the QC case studies are presented by the QC teams. QCAM–2015 was conducted on 08 September, 2015 at Convention Centre and SRI Seminar Hall, Anupuram in parallel sessions. Welcome address was delivered by Shri A. Jyothish Kumar, Director, ESG, the Presidential address by Shri G. Srinivasan, Director ROMG & RDG. Inaugural address was delivered by Dr. T. Paul Robert, Professor, Department of Industrial Engineering, Anna University, Chennai and vote of thanks by Shri G. Kempulraj, Head, Central Workshop Division.

Twenty Five Quality Circles and delegates (about 300 members) from IGCAR, schools from Kalpakkam and neighborhood presented QC case studies in a wide spectrum of topics covering Technical, Research & Development, Services and Education. Professional judges from Quality Circle Forum of India, Chennai chapter, adjudged the QC case study presentations. Under the ‘Mechanical and Manufacturing’ stream, the PLUTONIUM QC Team bagged ‘Dr. Placid Rodriguez memorial trophy’, while EXCEL QC team bagged the ‘Shri M. K. Ramamurthy memorial trophy’ for Plant Operation and Services category. EINSTEIN QC form AECS-2, SIGMA VIER MAGNA QC from KV-2 and KURUMBU QC, Government HSS,Vengampakkam have won the "Dr. Sarvepalli Radhakrishnan memorial trophies" in the School category.

During valedictory function, the events were summed up by Shri. K. G. Subramanian, Convenor, QCAM-2015. The programme was concluded with the valedictory address and the prizes were distributed to the participants by Dr. P. R. Vasudeva Rao, the then Director, IGCAR & GSO and Shri G. Srinivasan, Director, ROMG & RDG. Vote of thanks was proposed by Shri T. V. Maran, EIC, ZWS, Member Secretary, Organising committee.

Inauguration of 2MIGD Reverse Osmosis Desalination Plant

18 December, 2015

Dr. Sekhar Basu, Chairman, AEC, Secretary, DAE & Director BARC, along with Dr. S. A. V. Satya Murty, Director, IGCAR and senior colleagues of the Centre during the inauguration of the 2 MIGD Reverse Osmosis Desalination Plant

A two-stage 2 MIGD Sea Water Reverse Osmosis desalination plant has been commissioned recently with a flexible capacity in operation and maintenance to suit the varying demand of water in different seasons. This plant was inaugurated by Dr. Sekhar Basu, Chairman, Atomic Energy Commission, Secretary, Department of Atomic Energy, Government of India and Director, BARC on 18 December, 2015 in the presence of Dr. S. A. V. Satya Murty, Director, IGCAR, CMD, BHAVINI, Shri T. J. Kotteeswaran, the then Station Director, MAPS, Shri Amitava Roy, Facility Director, BARC-F, Dr. P. R. Vasudeva Rao, RRF and former Director, IGCAR and senior colleagues from IGCAR and from other Units of the Department.

The inauguration function started with a welcome address by Dr. S. A. V. Satya Murty, Director, IGCAR, followed by Shri A. Jyothish Kumar, Director, ESG, briefing the audience about the successful commissioning of the 2 MIGD sea water reverse osmosis desalination plant at IGCAR, Kalpakkam. Shri G. Kempulraj, Head, CWD, ESG delivered the vote of thanks.

2 MIGD Reverse Osmosis Desalination Plant

Piping and Filtration Chambers

Diamond Jubilee Celebrations

Diamond Jubilee Celebrations of the Department of Atomic Energy at Kalpakkam

Posters and Exhibits at Anu Vigyan 2015

Department of Atomic Energy established on 3rd August, 1954 has completed six decades of remarkable performance. Presently, we are commemorating the Diamond Jubilee of the Department. A series of lectures, exhibitions and visits to facilities at IGCAR for students from various colleges and educational institutions were organized as a part of these celebrations. Some of the initiatives undertaken during this year until conclusion in August are highlighted below:

Inauguration of DAE Diamond Jubilee Commemorative Structure and Sand Sculpture:

DAE diamond jubilee commemorative structure was designed, created and was remotely unveiled by the then Chairman, Dr. R. K. Sinha during his visit to IGCAR on May 19, 2015. Also on the same day, a sand sculpture exhibition was organized at the DAE Township, depicting the picture of Dr. Homi Bhabha along with DAE logo. This sculpture was designed by Shri Gajendran, a sand sculptor from Kelambakkam.

State-level Quiz and Painting Competitions

Dr. R. K. Sinha, the then Chairman, Atomic Energy Commission & Secretary, Department of Atomic Energy at the DAE Diamond Jubilee Commemorative Structure

Outreach & Awareness Programmes :

Participation in DAE Pavilion at the Science Congress in Mumbai University:

Our Centre has taken an active part by putting up posters and exhibits at the DAE Pavilion during the Science Congress, Mumbai University premises in the month of January 2015.

ANU VIGYAN-Exhibition at Kalpakkam

Anu Vigyan, a science exhibition at Kalpakkam Township, targeting residents and neighborhood was organized for two days during January 24-25, 2015. All the units of DAE at Kalpakkam have participated in the event by way of putting up stalls. The exhibition was aimed at popularizing various activities of the Department, while highlighting the contribution of DAE towards the well being of mankind, and also allayed the fear of radiation in the perception of the public. Impressive demonstrative models and illustrative posters attracted more than two thousand visitors including schools students and residents of the townships.

Exhibits were displayed at Anu Vigyan Exhibition conducted at Subbiah Vidyalayam Girls Higher Secondary School, Tuticorin organised by HWB, Tuticorin on July 05, 2015 and at nearby villages at Kalpakkam by Sahodari Mayam, Tamil Nadu Science Forum, Anupuram in coordination with IGCAR during

July 10-11, 2015. Posters depicting various activities of IGCAR were displayed at NESCO CARNIVAL during July 31 to August 9, 2015.

IANCAS(SRC) Radiochemistry workshop

IANCAS(SRC) Radiochemistry workshop was conducted at Meenakshi College, Chennai on January 24, 2015 (Saturday). Shri K. A. Venkatesan, Dr. T. G. Srinivasan, Dr. R. Kumar, Dr. N. Ramanathan and Shri G. V. S Ashok Kumar of IGCAR attended the workshop as resource persons. About hundred students from B.Sc. Physics and Chemistry disciplines participated in the workshop. The morning session comprised of two lectures, one on Fundamentals of Radiochemistry and the other on Applications of Radioisotopes were delivered by Dr. N Ramanathan and Dr. R Kumar. The afternoon session comprised of practical demonstrations aimed at determination of half-life of Barium-137 m isotope, and half-value thickness of lead. The workshop was well received.

State-level Quiz and Painting Competitions:

We have organized a State level Inter-Collegiate Quiz competition for the science students of undergraduate (UG) and postgraduate (PG) level separately. For each zone, a college was identified to serve as the zonal co-ordinator and the quiz competition was held in this college. The topics covered in quiz are: History of radiation and radioactivity, basic nuclear physics, nuclear chemistry, nuclear reactors and locations of nuclear installations in India and uses of ionizing radiation in the fields of medicine, industries, food irradiation etc.

Preliminary screening in each zone was done by a written test and the top twelve teams were selected at UG and PG level respectively from the list of teams registered for the quiz event. There were three students in each team. Semifinal quiz was conducted in parallel session for the two groups and top three teams from each group were selected for final round of quiz. Top three teams were selected in final round of quiz and awarded with trophy and certificates. The winners and runners of each zone a total of 18 UG teams and 18 PG teams participated in the Grand finale held at Chennai. The grand finale of this quiz competition for all the six zones was conducted at Stella Maris College, Chennai on July 23, 2015. The zonal winners were invited to Kalpakkam on July 24, 2015. Totally 36 teams participated in the event. Transportation was arranged from Kalpakkam to Stella Maris College, Chennai for the participants.

Similar to the zonal finals, Twelve teams each from UG and PG level were made into two groups and semifinal was conducted in parallel sessions. The first, second and third places was bagged by Malankara Catholic College, Kaliakkavilai from Zone 1,Ayya Nadar Janaki Ammal College, Sivakasi from Zone 4 and Loyola college, Chennai from Zone 2 respectively at the PG level and Stella Maris College, Chennai from Zone 2, Sri Vasavi College, Erode from zone 5 and Kamban College for women, Tiruvannamalai at the undergraduate level. Overall, a total of 1215 students from more than 100 colleges participated in this event. In conjunction with the quiz, an exhibition highlighting the Indian Nuclear Energy program, beneficial applications of ionizing radiations and demonstration of radiation detection and measurement equipments was also organized. The exhibition with posters and models was a grand attraction.

More than 1500 students from schools and colleges attended and benefited from this science exhibition. The major focus of the programme was to create a general awareness on nuclear science and technology, its benefits, varied applications in society and research and career prospects. The Prize Distribution ceremony was held on 24 July, 2015 at Homi Bhabha Building, IGCAR, Kalpakkam. Dr. R. Chidambaran, Principal Scientific Advisor, Prime Minister’s Office, New Delhi distributed the memento and certificates to all the winners. The finalists from all zones had the opportunity to visit the Fast Breeder Test Reactor and the various other laboratories at IGCAR. The program organized under the guidance of Dr. P. R. Vasudeva Rao, the then Director, IGCAR & GSO and coordinated by Dr. M. Sai Baba, Associate Director, RMG, Dr. B. Venkatraman, Associate Director, RSEG, Shri S. Chandrasekaran, RSD, Ms. Jalaja Madan Mohan, RMG and colleagues from EIRSG, RMG and other groups was a grand success.

Indian Nuclear Society (Kalpakkam) had prepared a monthly calendar depicting the beneficial applications of ionizing radiations, pioneering role of BARC, the activities of IGCAR and other major DAE units and the career and research prospects in DAE. The calendars were distributed to all colleges in each zone for the benefit of students and college teachers to provide the glimpses of DAE activities in societal applications of ionizing radiation in addition to nuclear energy programme.

Eminent Visitors to IGCAR

Dr. Jitendra Singh, Minister of State with Dr. R. K. Sinha Chairman, Atomic Energy Commision and Dr. P. R. Vasudeva Rao, the then Director, IGCAR & GSO during his visit to the Centre

Honourable Dr. Jitendra Singh, Minister of State for Development of North Eastern Region (Independent charge) and Minister of State for Prime Minister Office Personnel, Public Grievances & Pensions, Department of Atomic Energy and Department of Space, Government of India visited various Units of the Department at Kalpakkam on 21 August, 2015.

He was accompanied by Dr. R. K. Sinha, the then Chairman, Atomic Energy Commission, Dr. Sekhar Basu, Director, BARC and Shri K.C. Purohit, CMD, NPCIL.

Honourable Minister visited the Madras Atomic Power Station. Programme started with introductory remarks by Dr. R. K. Sinha and Dr. P. R. Vasudeva Rao, the then Director, IGCAR and GSO delivering a presentation. He visited exhibits of Fuel bundle for Thermal Reactors, Control Room and Fuel Handling facility at the Madras Atomic Power Station.

During his visit to our Centre, he has seen the Fast Breeder Test Reactor, exhibits of Fuel Sub-assemblies for Fast Breeder Test Reactor and Prototype Fast Breeder Reactor, the Reactor Containment Building and an exhibition of models and charts covering all the important activities of the Centre.

Honourable Minister, also visited Protoype Fast Breeder Reactor at BHAVINI. Before concluding the visit, addressed senior DAE Scientists and Engineers across all Units, wherein Dr. P. Chellapandi, CMD, BHAVINI, welcomed the gathering, Dr. R. K. Sinha, Chairman, Atomic Energy Commission gave the introductory note and Dr. P. R. Vasudeva Rao delivered the vote of thanks.

Dr. R. K. Sinha, the then Chairman, Atomic Energy Commission & Secretary, Department of Atomic Energy delivering the first “N. Srinivasan Memorial Lecture”

Dr. R. K. Sinha, the then Chairman, Atomic Energy Commission & Secretary, Department of Atomic Energy visited IGCAR on 19 May, 2015 to participate in a multitude of important official engagements. To mark our respect and tribute to the eminent scientist and founder director of IGCAR (then Research Reactor Centre), Late Shri N. Srinivasan, a memorial lecture was organized at IGCAR. Dr. Ratan Kumar Sinha, delivered the first “N.Srinivasan Memorial Lecture” on the topic “Nuclear Power : Past, Present and Future”.

Technology Day is being organized every year at IGCAR in order to encourage and motivate the technical fraternity to come forward and present their ideas. Dr. Sinha also distributed certificates to the recipients of Best Presentation Award of the Technology Day Meet 2015 before his lecture.

ECIL has been collaborating with IGCAR in many projects. A memorandum of understanding was signed with ECIL on furthering the progress with respect to Wireless Sensors Networks during the visit of Chairman.

During his visit to IGCAR, Dr. Sinha remotely unveiled the DAE Diamond Jubilee structure located at intersection point of major Units at Kalpakkam (IGCAR, MAPS and BHAVINI) which was evolved as a part of the commemoration of Diamond Jubilee celebration depicting the concept of 60 years of achievement of DAE.

Dr. R. K. Sinha also visited Fast Reactor Fuel Cycle Facility and BHAVINI. He also visited the sand sculpture erected at the beach sands of Kalpakkam as part of Diamond Jubilee celebration. This sculpture depicted Dr. Homi Jehangir Bhabha embedded on DAE Logo was carved by Shri Gajendran, a sand sculptor from Kelambakkam.

Dr. R. K. Sinha, the then Chairman, Atomic Energy Commission and Secretary, Department of Atomic Energy, Dr. P. R. Vasudeva Rao, the then Director, IGCAR and senior colleagues of the Centre at the sand sculpture exhibition

Prof. M.O. Garg, Director General, Council of Scientific & Industrial Research delivering Acharya P. C. Ray Memorial Lecture

Prof. M.O. Garg, Director General, Council of Scientific & Industrial Research (CSIR), New Delhi delivered Acharya P.C. Ray Memorial Lecture on "Nano Catalysis- Doing the Impossible" during his visit to our Centre on August 26, 2015.

Dr. R. Muralidharan, Director, Solid State Physics Laboratory, DRDO, New Delhi, delivering the IGC Colloquium

Dr. R. Muralidharan, Director, Solid State Physics lab, DRDO, New Delhi, delivered the IGC Colloquium on "Semiconductor Materials and Device Research and Development at Solid State Physics Laboratory an Overview", during his visit to the Centre on January 06, 2015.

Dr. S. K. Malhotra, Head, Public Awareness Division, DAE, delivering the IGC Colloquium

Dr. S. K. Malhotra, Head, Public Awareness Division, DAE, delivered the IGC Colloquium on " Nuclear Power: The Need, Perception, and the Realities ", during his visit to the Centre on January 23, 2015.

Prof. Ashok Jhunjhunwala, Indian Institute of Technology, Madras, delivering the IGC Colloquium

Prof. Ashok Jhunjhunwala, Department of Electrical Engineering, Indian Institute of Technology, Madras, delivered the IGC Colloquium on " Can India have Uninterrupted Power in all its Homes: Leveraging Decentralised Solar-DC", during his visit to the Centre on February 19, 2015.

Prof. Ghanashyam Date, Professor, IMSc, Chennai, delivering the IGC Colloquium

Prof. Ghanashyam Date, Professor, IMSc, Chennai, delivered the IGC Colloquium on " General Relativity: A Hundred Years Later", during his visit to the Centre on May 12, 2015

Dr. Baldev Raj, Director, National Institute of Advanced Studies, Bengaluru and former Director, IGCAR delivering the IGC colloquium

Dr. Baldev Raj, Director, National Institute of Advanced Studies, Bengaluru and former Director, IGCAR delivered the IGC Colloquium on “Pathways to Energy Sustainability for India” on July 09, 2015

Prof. Riccardo Fenici, MD, Director of Clinical Physiology, Centre for Biomagnetism Catholic University during the IGC colloquium

Prof. Riccardo Fenici, MD, Director of Clinical Physiology, Centre for Biomagnetism Catholic University, Rome, Italy and European Director, Society for Police and Criminal Psychology visited our Centre during 20-24 July,2015. During his visit he delivered IGC Colloquium on "Cardiac Health: Probing by Non-Invasive Methods" on July 23, 2015

Dr. C. Ganguly, INSA Senior Scientist & INAE Distinguished Visiting Professor, delivering the IGC colloquium

Dr. C. Ganguly, INSA Senior Scientist & INAE Distinguished Visiting Professor Hony. Adviser, Engineering Staff College of India (ESCI) and former Chief Executive, NFC visited the Centre on August 11, 2015 and delivered IGC Colloquium on "Expanding Nuclear Power Programme in India, the Prospects & Challenges and the Role of FBRs".

Diamond Jubilee Colloquium

Shri S.S.Bajaj, Chairman, AERB, delivering the Diamond Jubliee Colloquium

Shri S. S. Bajaj, Chairman, AERB, delivered the lecture on " Safety Regulation of Nuclear and Radiation Facilities in India", on February 24, 2015, as a part of "Colloquium" series organized to commemorate the Diamond Jubilee Celebration.

Dr. Baldev Raj, Director, National Institute for Advanced Studies, Bengaluru, delivering the Diamond Jubliee Colloquium

Dr. Baldev Raj, Director, National Institute for Advanced Studies, Bengaluru, delivered the lecture on "Energy Security and Sustainability: Approaches and Priorities for Growing and Aspiring India" , on March 14, 2015, as a part of "Colloquium" series organized to commemorate the Diamond Jubilee Celebration.

Dr. Anil Kakodkar, former Chairman, Atomic Energy Commission during the colloquium

Dr. Anil Kakodkar, INAE Satish Dhawan Chair of Engineering Eminence, and Former Chairman, Atomic Energy Commission and Secretary, Department of Atomic Energy, delivered DAE Diamond Jubilee Colloquium on “Harnessing Technology for Development: A Governance Challenge in Indian Context” on July 03, 2015. During his visit, he visited Fast Reactor Fuel Cycle Facility

Dr. R. Chidambaram, Principal Scientific Advisor, Government of India delivering the Diamond Jubilee colloquium

Dr. R. Chidambaram, Principal Scientific Advisor, Government of India visited our Centre and delivered a talk on "India’s Nuclear Programme: The Main Thrust & the Spin-Offs" on July 24, 2015 as part of DAE Diamond Jubilee Colloquium. He visited Metal Fuel Development Laboratory at Chemistry Group and 100 Tonne Shake Table Facility during his visit.

IGC COUNCIL

Chairman

Dr. S. A. V. Satya Murty
Distinguished Scientist & Director, IGCAR

Dr. S.A.V.Satya Murty is a distinguished scientist, who has made pivotal contributions in establishing efficient computer network, high end computing systems, establishing unique facilities like, PFBR Operator Training Simulator and Advanced Visualization Centre at IGCAR. His work on Wireless Sensor Networks has gained international recognition and he is coordinating one of the IAEA projects aiming at enhancing the application of wireless sensor networks in the nuclear reactor domain. He is also piloting the development of Time Domain Electro Magnetic System, which enables an efficient method for identifying uranium mineral sources in the Country. He has several research publications to his credit and is on the editorial board of five journals. He is a gold medallist from Jawaharlal Nehru Technological University and Doctorate from Homi Bhabha National Institute. He is from the 21st Batch of Training School and received Homi Bhabha medal for topping the batch. He has several awards to his credit which include Outstanding Service Award from Indian Nuclear Society and DAE Group Achievement awards.

Members

Dr. Sekhar Basu , a renowned nuclear scientist, is currently Chairman, AEC, Secretary, DAE & Director, BARC. Earlier he worked as the Project Director of Nuclear Submarine Programme and later as the Chief Executive of the Nuclear Recycle Board in the same institute. Dr. Basu is an engineer of exceptional ability who has played a lead role in multiple areas of nuclear science and engineering and is a major contributor in establishing India as a leader in nuclear field.

Dr. Basu, born on 20th September 1952, did his schooling from Ballygunge Government School, Kolkata and graduated in Mechanical Engineering from Veermata Jijabai Technological Institute (VJTI), University of Mumbai in 1974. After completion of one year of BARC Training School programme in nuclear science and engineering, he joined the Reactor Engineering Division of BARC in 1975. He started his career by designing fuel for Boiling Water Reactor, which showed excellent reactor performance. Later he took up the responsibility of the development of nuclear submarine propulsion plant and built the land based prototype at Kalpakkam from scratch. He continues to guide the Indian nuclear propulsion programme for the sea going versions. Since 2000, he was also responsible for the design, development, construction and operation of nuclear recycle plants at Tarapur and Kalpakkam, involving reprocessing and nuclear waste management. These plants are performing to international standards. He is pursuing the design of the Integrated Nuclear Recycle Plant, which will take this programme to a higher platform.

As the Chairman of Project Management Board he is responsible for the development of Indian Neutrino Observatory at Tamil Nadu and as Apex Project Co-ordinator, he is pursuing the development of 1 GeV Superconducting Accelerators for the Accelerator Driven System Programme. Dr. Basu is also guiding the establishment of nuclear fuel cycle park involving research reactors, fuel fabrication and reprocessing facilities at the Vizag campus of BARC. Work on the design of Indian Pressurised Water Reactor has also been initiated by him.

As Director, BARC, Dr. Basu has taken special initiatives for major expansion of the societal programmes of DAE in the field of nuclear agriculture, food preservation and nuclear medicine. While pursuing the basic research in the field of nuclear science and engineering, he is also working towards the expansion of enrichment and strategic programmes. He represented India in concluding ‘Arrangements and Procedures’ with the US Government for reprocessing of US hypothecated fuel and he has chaired the International Committee for the design review of three modules of International Thermonuclear Experimental Reactor (ITER).

He has several publications to his credit in national and international journals. Dr. Basu has been conferred several awards and these include: Indian Nuclear Society Award 2002, DAE Awards in 2006 and 2007. He is also a Fellow of the Indian National Academy of Engineers (INAE) and Indian Society for Non Destructive Testing (ISNT). Jadavpur University awarded him with DLit (Honoris Causa) degree in 2013. He was awarded Padma Shri by the Government of India in 2014.

Dr. G. Amarendra obtained his M.Sc (Physics) from Sardar Patel University, Gujarat in 1980, passed out from 24th batch of BARC Training School and joined MSG, IGCAR in 1981. He had obtained his Ph.D degree from University of Madras in 1991 and carried out post-doctoral work at Brandeis University, Boston during 1993-94. Currently Dr. Amarendra is the Director, Materials Science Group. He was instrumental in indigenous design and development of an unique variable low energy positron beam in 1995, which enabled non-destructive depth-profiling of defects at surfaces and interfaces of materials. His broad areas of research include defect studies in materials, nuclear spectroscopy, radiation damage studies of structure materials, thin films and nanomaterials. Dr. Amarendra is a senior professor of Homi Bhabha National Institute, Mumbai. He had guided five Ph.D students and has over 200 Journal and conference publications and two edited books. He is a recipient of INSA Young Scientist Award (1991), IPA S.N.Seshadri Memorial Award (1996), Kalpakkam Science & Technology Award (1996), DAE Homi Bhabha Science & Technology Award (2006) and MRSI Medal Award (2013).

Dr. Arun Kumar Bhaduri, obtained his Ph.D. in Metallurgical Engineering from Indian Institute of Technology, Kharagpur, joined Department of Atomic Energy in 1983. He is with Metallurgy and Materials Group at Indira Gandhi Centre for Atomic Research, Kalpakkam since 1984, where he is presently Distinguished Scientist and Director, Metallurgy and Materials Group, and also a Senior Professor, Homi Bhabha National Institute. He received Research Fellowship from Alexander von Humboldt Foundation, Germany in 1994 for a 2-year post-doctoral research at University of Stuttgart, Germany. He anchors the development of materials and their fabrication technologies for Indian programmes on sodium-cooled fast reactors, fusion reactors and advanced ultra supercritical thermal power. He specialises in the field of materials joining, and has to his credit more than 200 journal publications, 300 conference presentations and 2 international patents. He is a fellow of Indian National Academy of Engineering, Indian Institute of Metals and Fellow, Indian Institute of Welding. He is a recipient of the Metallurgist of the Year Award during National Metallurgists' Day (2003), Homi Bhabha Science & Technology Award (2002), Indian Nuclear Society Medal Award (2002), VASVIK Award (2005), eight DAE Group Achievement Awards (2006-2014, three as Group Leader), and Sir L.P. Misra Memorial Lecture Award (2010).

Shri M. Bhaskaran, Distinguished Scientist, has assumed the office of Chairman &Chief Executive Heavy Water Board, Department of Atomic Energy on August 1, 2015, by taking over the charge from Shri Rajnish Prakash on July 31, 2015. Shri Bhaskaran has joined Heavy Water Board on August 1,1980 after graduating from 23rd Batch (1980) of BARC Training School, subsequent to acquiring engineering degree (Chemical) from University of Calicut in 1979. During his 35 years association with HWB, Shri Bhaskaran has made significant contribution to the programs of Department of Atomic Energy through production and sustained supply of vital input materials for Indian Nuclear Power Programme (like heavy water, nuclear solvents, boron isotopes,etc). He played vital role in setting up, commissioning, operation of India's first ammonia based indigenous Heavy Water Plant at Thal with the innovative project management concept of collaborating with a government undertaking, Rashtriya Chemicals & Fertilizers Ltd. He was instrumental in process debugging, performance improvement and energy conservation initiatives for HWP, Thal. Shri Bhaskaran has contributed significantly for indigenous development of Ammonia-Water Exchange

Process of Heavy Water production to make the operation of Ammonia based Heavy Water Plant independent of fertilizer plant, for feed supply. He played key role in setting up Technology Demonstration Plant including detailed engineering and technology support to consultants. Shri Bhaskaran has played a prominent role in diversified activities of HWB including development of advanced technology and materials. He has provided engineering input and technology support for in-house production of nuclear solvents and development of solvent extraction technology & efficient contacting devices for nuclear fuel cycle applications. He was involved in debugging and up-gradation of solvent extraction process for Technology Demonstration Plant, operating at RCF, Mumbai. This technology is now available for industrial deployment. He has also provided engineering and technology input for in-house production of boron isotopes (Boron-10 & 11) using two different processes. ShriBhaskaran has steered the entire spectrum of activities for development of cryo- technology for reducing the radiation burden in heavy water from PHWRs. ShriBhaskaran was instrumental in promoting and patronizing non-nuclear applications of Deuterium and Heavy water. His concerted efforts led to networking with several industries, academic institutions and R&D organization to take up development work in this area. His efforts also led to indigenous production of Deuterium labeled compounds, particularly Deuterated NMR Solvents at HWP, Baroda. He played pivotal role in demonstrating thermo-stabilization of Oral Polio Vaccine using Heavy Water. He has pioneered R&D for exploring anti-cancer potential of Deuterium Depleted Water (a spin-of product in Heavy Water Plants) in collaboration with Tata Memorial Centre, Mumbai. Shri Bhaskaran is a recipient of DAE group achievement award three times for the years 2010, 2012 and 2013 for development work for indigenous production of D-labeled compounds, Boron Enrichment and Solvent Extraction technologies, respectively.

Dr.P.Chellapandi is a Distinguished Scientist and Chairman & Managing Director of BHAVINI. He was the Director, Reactor Design Group, IGCAR before taking up the Chairmanship of BHAVINI. He is one of the key persons involved in the design and development of 500 MWe PFBR since its inception which will be commissioned by this year end. He has contributed significantly for the PFBR over a wide spectrum of design, analysis and research activities involving academic and R&D institutions in the country. He is the convener of the Standing Task Force responsible for the manufacture and erection of reactor components and also member of the Project Design Safety Committee. His current responsibilities focus on the design and construction of FBR 1&2 beyond PFBR with innovative concepts for the commercial exploitation. Dr. Chellapandi is a Senior Professor of Homi Bhabha National Institute and Fellow of Indian National Academy of Engineering. He has so far guided ~80 postgraduate and ~18 doctorate students and published ~158 journal papers. He has received many awards and honors. To name a few : Homi Bhabha Science and Technology Award, VASVIK award, Indian Nuclear Society Award, National Design Award from Indian Institute of Engineers, Agni Award for Excellence in Self-reliance from DRDO and DAE Group Achievement Awards for four constitutive years. Dr.P.Chellapandi has received the Distinguished Alumnus Award of IIT Madras in the year 2010.

Ms. Chitra Ramchandran is from the Indian Administrative Services of the 1985 Batch, Andhra Pradesh Cadre. She is a Post-Graduate in Political Science. Major postings held by her so far include Municipal Commissioner of Hyderabad and Telangana; District Collector, Krishna, Ranga Reddy. She has held the portfolios of Industries, Rural Development, Infrastructure, etc. as Principal Secretary. In August, 2013, she joined the Department of Atomic Energy as Joint Secretary in charge of I&M wing which deals with units like AMD, BRIT, NFC and HWB. Currently holding charge of R&D wing which deals with units like BARC, IGCAR, RRCAT, VECC and all aided Institutions under DAE and Additional Secretary (in-charge)

Shri S. G. Ghadge is a Mechanical Engineering Graduate from Visvesvaraya National Institute of Technology, Nagpur, and Post Graduate in Nuclear Technology in BARC now known as Homi Bhabha National Institute. He has a distinguished career in the Department of Atomic Energy, Nuclear Power Corporation of India spanning 36 years, which covered multiple fields of Nuclear Reactor Process Design, Commissioning, Operational Improvements, Safety, Thermo Hydraulic Analysis with complex code development. He spearheaded the internal reviews for post Fukushima safety assessment taking into account international thinking and worked out safety enhancement measures arising out of these reviews apart from reviews by AERB. He was member of the Indian delegation to IAEA in the Convention of Nuclear Safety and contributed in generation of design and safety codes and guides for IAEA and AERB. He has several international and national publications to his credit. He is a Distinguished Scientist of the Department of Atomic Energy. Presently his responsibilities encompass design, health & safety, safety and licensing analysis, procurement for 700 MWe PHWR and building up of R&D facility at Tarapur. He is a full time Director on the Board of NPCIL from 1st July 2013.

Dr. P.D. Gupta, Distinguished Scientist is the Director, Raja Ramanna Centre for Advanced Technology, Indore. Dr. Gupta is an internationally known laser-plasma physicist who has made pioneering research contributions in this area. He passed M.Sc. Hons (Physics) from Punjab University in 1972 and joined Bhabha Atomic Research Centre. He is a recipient of four gold medals for securing first rank in various university examinations. He joined BARC in August 1973 after passing out from 16th batch (1972-73) of Training School and was awarded Homi Bhabha Medal and Prize. He received his Ph.D. from Bombay University in 1984 and did his Post-doctoral work at the Department of Electrical Engineering, University of Alberta, Canada during 1984-86. He is recipient of Young Scientist Award of Indian National Science Academy (1984) and Young Associateship of Indian Academy of Sciences (1986-91) and became Fellow of the National Academy of Sciences, India, in 2004. As Director, Dr. Gupta is steering many R&D programmes in frontline areas of accelerators and lasers at RRCAT. These include synchrotron radiation sources and their utilization, development of superconducting radio-frequency cavities for high energy accelerators, proton linac spallation neutron source, cryogenics, magnet technology, ultra-intense laser-plasma interaction, and lasers in research and industry. Dr. Gupta is a Senior Professor of Homi Bhabha National Institute (HBNI), Mumbai, and a member of the Academic Council. He has guided many young researchers for the award of Ph.D. / M.Tech / M.Sc. degrees. He has made ~500 research contributions of which ~200 are published in international journals.

Shri A. Jyothish Kumar, is an Outstanding Scientist & Director of Engineering Services Group. He is from the 29th Batch of Training School and joined IGCAR in 1986. He graduated in Electrical engineering from Kerala University. He was working in FBTR during the initial 18 years and contributed significantly towards the commissioning and operation of Fast Breeder Test Reactor. He was actively involved in the commissioning of Turbine Generator set and solved many of the technical issues. He contributed significantly in the area of energy audit and implemented various measures in the area of energy conservation. He had planned and implemented the augmentation of electrical infrastructure considering the load growth for the next 10 years. He took active role in the implementation of safety improvement in the electrical system. State of art technologies were implemented by the introduction of numerical relays. He was instrumental in the introduction of grid connected solar system and focus is for the utilization of alternate energy sources & DC power supply. He took a lead role in the construction, installation & Commissioning of 2 MIGD desalination plant.

Shri Y.S. Mayya obtained his B.Tech. in Electronics & Communication Engineering in 1979. He is a product of 1980 batch of the BARC Training School. As a Scientific Officer in BARC, he has been engaged in design and development of Automation and Control systems for Nuclear facilities, accelerators, telescopes and strategic systems of DAE, DRDO & ISRO for more than three decades. He pioneered the development and deployment of the real-time networks and distributed systems in nuclear facilities. Some of his important contributions in the area of computer controlled servo systems include Giant Metre-wave Radio telescope (GMRT) in India, Stabilized Antenna platform for the TEJAS Light Combat Aircraft's Multi-Mode Radar, Stabilization & tracking system for airborne Radars, Antenna Control Servo System for the 32-metre Deep Space Network antenna for the Chandrayaan-1 mission and Telescope Control Servo System for the 21 meter MACE telescope being erected in Ladakh India. He led the Indian team in the development of software systems for the magnet test facilities of Large Hadron Collider (LHC) project at CERN, Geneva. Shri. Mayya was the Chairman & Managing Directorof Electronics Corporation Of India Ltd, Hyderabad during 2009- 2012. While at ECIL, he was responsible for directing the operations of company in the area of strategic electronics for nuclear, defence, aerospace and security sectors and steered its steady growth. He piloted many projects of national importance such as Integrated Security Systems of CWG-2010 Delhi, COMINT and Electronic Warfare systems, C4I systems, Antenna for Chandrayaan-I and C&I systems for Nuclear facilities. Currently in BARC Mumbai, he is the Project Director of Global Centre for Nuclear Energy Partnership (GCNEP) project of DAE and Director of Electronics & Instrumentation Group of BARC. He has published around 30 papers in national and international conferences. He is the recipient of DAE Technical Excellence award.

Shri S. Paramasivam graduated as a Mechanical Engineer from Madras Institute of Technology in the year 1981 and joined BARC in the 25th batch of Training School. After successful completion of training, he was posted at Heavy Water Board Head Office, Mumbai and was associated in mechanical project activities for Heavy Water Plant (Manuguru). In the year 1986, he was transferred to HWP (Manuguru), where he was involved in erection and commissioning activities pertaining to exchange units. He was promoted as Deputy Maintenance Manager (Mechanical) in the year 1998 and as head of Mechanical Maintenance Section in the year 2003. He was posted to HWP (Tuticorin) as Maintenance Manager in the year 2005 and promoted as Officer On Special Duty in the year 2008, subsequently as General Manager of Heavy Water Plant, Tuticorin. In July, 2013, he was appointed as Regional Director, MRPU, DPS, Chennai.

Dr. K. K. Rajan is currently a Distinguished Scientist and Director of Fast Reactor Technology Group. He is from 24th batch of BARC Training School and joined IGCAR in 1981. He graduated in Electrical Engineering from NIT, Calicut. His initial contributions include purification, transportation and charging of sodium required for FBTR, calibration of FBTR sodium flow meters and other sodium experiments in support of FBTR. Over the years he has been steering a multidisciplinary programme in the area of Sodium Technology. He is primarily responsible for design, construction, commissioning, safe operation and maintenance of high temperature experimental sodium facilities and conducting sodium experiments in support of FBR. He has made substantial contributions towards testing of PFBR model steam generator in SGTF, PFBR fuel handling machines, shutdown mechanisms and Under Sodium Ultrasonic Scanner at reactor operating conditions in LCTR, experiments to study the adjascent tube wastage phenomenon in SG tube, demonstration of in-situ regeneration of secondary cold trap etc. He was also involved in the development of permanent magnet flow meters and special type of heaters required for FBR sodium systems. He has played a key role in the receipt and safe transfer of 1750 tonnes of nuclear grade liquid sodium to PFBR storage tanks. In the last few years, he was actively involved in guiding the group for the construction of sodium technology complex and pyro-processing R&D facility. He has published more than 150 papers in reputed national and international journals. He is a member of Indian Nuclear Society, Instrument Society of India and a fellow of Institution of Engineers (India).

Shri M. Raju is from Indian Administrative Service of the 2005 Batch, Jammu & Kashmir Cadre. He has done M.Sc. (Microbiology) and M.A. (History). Major postings held by him so far include District Magistrate and Collector, Kargil District (2010-2012), Vice-Chairman, Kargil Renewable Energy Development Agency, Chairman, DSSRB, Additional Secretary, Department of Rural Development, Government of Jammu & Kashmir. In October 2013, he joined Department of Atomic Energy as Internal Financial Adviser, Indira Gandhi Centre for Atomic Research.

Dr. A. Ravishankar, Mechanical Engineer from 25th batch of BARC training school, joined the Department of Atomic energy in 1981. He is presently Project Director, Fast Reactor Fuel Cycle Facility (FRFCF) and Hot Cell Systems and Projects Group (HCSPG). Under his leadership, many Hot cell systems, Head end equipments and Remote handling systems required for COmpact facility for Reprocessing of Advanced fuels in Lead shielded cells (CORAL) and Demonstration Fast Reactor fuel Reprocessing Plant (DFRP), has been successfully developed. Some of his important achievements include development of special purpose machines like multi fuel pin chopper, electrolytic dissolver, centrifugal extractor, high speed centrifuge, Laser based fuel sub-assembly dismantling system, various versions of Master slave manipulators, robotic sampling system etc. Some of these developments are import substitutes. He has made outstanding contribution to the design, construction and commissioning of CORAL for reprocessing of irradiated FBTR fuel. He played a vital role in the operation of CORAL and successfully processed many campaigns including fuel irradiated up to 155 GWD/Te burn-up, which is a first of its kind in the world. He has incorporated many novel features in the design of CORAL facility so that development of new process and R&D related activities can also be taken up in the future. He was involved in the design and development of equipment for Thorium fuel reprocessing participating in the Thorium fuel reprocessing campaigns and successfully recovered ^{233}U. Currently he is responsible for construction and commissioning of FRFCF and also DFRP. He has established a sound infrastructure for the successful closing of the fast reactor fuel cycle with his outstanding capability and skills. He has over 150 classified reports, 54 technical presentations and publications to his credit. He has been conferred INS – Gold medal by Indian Nuclear Society in 2001, NOCIL award for Excellence in Design/Development of process Plant and Equipment for the year 2005, DAE group award in the year 2006, 2011 & 2012 and DAE-Homi Bhabha Science and Technology award in 2010 and INS Outstanding Service Award in 2014. He is a Fellow of the Indian National Academy of Engineering.

Dr. N. Saibaba is a Gold medalist from Andhra University. He joined the 19th batch of Training School, Mumbai and is the recipient of Bhabha Award for topping the batch. He developed expertise in the manufacture of seamless tubes in a variety of strategic and exotic materials employing hot and cold deformation processes for meeting critical requirements of Atomic Energy, Space and Defence. He has made several pioneering contributions in the manufacture of critical core components of Power Reactors, some of which were developed for the first time in the country. He was responsible, for developing a new manufacturing route for extremely thin walled "Seamless Calandria Tubes" for the first time in the world. These tubes have been in use in the Nuclear Power Reactors for the past 11 years, offering excellent promise and specially shaped pressure tubes for Advanced Heavy Water Reactors, development of hexagonal channels for Prototype Fast Breeder Reactors and square channels for Boiling Water Reactors through pilger route, development of pressure tubes by heat treated and strengthened route and establishment of process technology for manufacture of double clad tubes with zirconium lining.

Shri Saibaba, as a team leader, developed a test loop with components made of high temperature alloy Nb-1Zr-0.1C. It is to his credit that the seamless tubes in 304H (Cu) and Inconel-617 for use in the Advanced Ultra Supercritical Boilers were developed to enhance the thermal efficiency of the Thermal Power Plants from 28 to 47%. He is presently engaged as Director on the Boards of UCIL & IREL and IGCAR Council. Presently, he is the Chairman of Indian Institute of Metals (IIM), Hyderabad Chapter and Chairman for Indian Society for Non-Destructive Testing (ISNT), Hyderabad Chapter. He is appointed as Chairman for Center of Plant Engineering Services (CoPES). He received Bharat Ratna Sir M. Visvesvaraya Award from the Institution of Engineers (India), DAE Award for Group contribution as Group Leader - 2006, 2009, 2010, 2011 & 2012,INS Award for contributions in the field of Nuclear Fuel Cycle Technologies – 2008, Annual NFC Award for Meritorious contribution – 2005, 2006 & 2007, Outstanding contribution from NFC Management – 1993 & 1998 and Gold Medal from Andhra University for securing First Rank – 1975. He is a Fellow of Andhra Pradesh Academy of Sciences, Life Member of IIM, ISNT and INS.

Shri G. Srinivasan is a mechanical engineer from the 18th batch of BARC Training School. He joined FBTR project as a designer in 1975, and participated in the design, fabrication and installation of Reactor Assembly Components. He moved over to O&M in 1983. After holding the positions of Senior Engineer (Planning) and Senior Engineer (Technical), he took over as Technical Services Superintendent and later as AD (O&M). He is Director, ROMG since September2008. In February 2015, he took additional charge as Director, Reactor Design Group.

Dr. P. K. Vijayan is a chemical engineer from the 1975 batch of the University of Calicut and obtained his PhD from the Department of Energy Systems Engineering, IIT Bombay in 1989. A Distinguished Scientist, Dr Vijayan is currently working as Director, Reactor Design and Development Group at the Bhabha Atomic Research Centre (BARC). His field of expertise is experimental and theoretical thermal hydraulics of nuclear reactors and has more than three and a half decades of experience in this field. He played a key role in the thermal hydraulic design of Advanced Heavy Water Reactor (AHWR). Dr. Vijayan is presently involved in the thermal hydraulic design validation for AHWR and Pressurised Heavy Water Reactor (PHWR-700). He is also leading the Indian High Temperature Reactor and molten salt reactor program. Dr. Vijayan and his group established several major research facilities for the Indian PHWR and the AHWR. Besides he is leading the group developing the solar thermal power plant based on the beam down concept. He participated in several International Atomic Energy Agency (IAEA) coordinated research projects and bilateral research projects like Indo-Italian, Indo-German, Indo-UK, Indo-Korea and AERB-US NRC. He also worked as a guest scientist at Gesselschaft for Reaktor Sicherheit (GRS), Garching, Munich, Germany and IAEA, Vienna, Austria. He was invited by IAEA to formulate a training course on 'Natural circulation phenomena and passive safety systems for advanced water cooled reactors and is a lecturer for this IAEA training course since 2004. He has delivered invited talks at several international conferences and served as an examiner for PhD thesis of several reputed national and foreign universities. He is professor and convener, Board of Studies, Homi Bhabha National Institute. He has guided six doctoral students of HBNI and Indian Institute of Technology, Bombay. He has more than two hundred publications to his credit. He is a recipient of the DAE Technical Excellence and Homi Bhabha Science and Technology awards. He is a life member of several professional bodies like the Indian Nuclear Society, Indian Institute of Chemical Engineers and Indian Society for Heat and Mass Transfer. He was also the vice president of the Indian Society for Heat and Mass Transfer during the period 2009-13.

Organisation and Activities of Various Groups

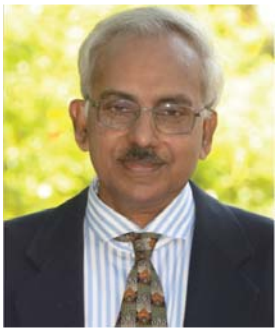

Dr. S.A.V. Satya Murty
Director, IGCAR

Chemistry Group

Dr. S.A.V. Satya Murty
Director, CG

Dr. M. Joseph,
AD, FChG & Head, FChD

Dr. R. Sridharan,
AD, MCG &Head, MCD

Shri R.R. Ramanarayanan
Head, CFD

The Chemistry Group is responsible for carrying out R&D to provide inputs with respect to all the chemistry aspects of the fast reactor and its fuel cycle. Besides the R&D activities, the Chemistry Group also provides extensive analytical support using a wide range of analytical techniques to all the programmes at Kalpakkam. The areas of R&D in Chemistry Group include sodium chemistry, chemistry of un-irradiated as well as irradiated fuel materials, development of fuel cycle, high temperature chemistry, analytical chemistry and spectroscopy. Chemistry Group also has been developing instrumentation and facilities in support of the R&D programme. Development of sensors for PFBR and sensors for environmental applications, development of radionuclide traps for PFBR, development of cleaning and decontamination techniques for fast reactor components, development of wasteform matrices for immobilisation of high level radioactive waste and pyroprocessing are some of the R&D programmes on the anvil. Recent achievements include development of new method for direct reduction UO2 to U metal, establishing a new facility for measuring the viscosity of Pu containing broths to be used for the preparation of MOX microspheres, demonstration of electrorefining of U-Pu-Zr in 20 g scale and electrorefining of uranium using liquid cadmium as anode.

Electronics, Instrumentation and Radiological Safety Group

Dr. S.A.V. Satya Murty
Director, EIRSG

Shri K. Madhusoodanan
AD, ICG & Head, RTSD

Dr. B. Venkatraman
AD, RSEG & Head, RSD

Shri B. Anandapadmanaban
Head, QAD

Shri G. Prabhakara Rao
Head, SISD

Dr. K.K. Satpathy
Head, EnSD

Dr. D. Thirugnanamurthy
Head, EID

The Electronics, Instrumentation and Radiological Safety Group is actively involved in the development of Instrumentation, Control, Health Physics, Radiation safety services, Radiological and Environmental Impact assessment studies, Quality Assurance services and industrial and fire safety related services for fast reactor and fuel cycle technologies and related projects of DAE. Towards this the I&C systems are designed with safety and availability of the reactor as the guiding requirements through redundant systems and also keeping in mind the simplicity of design and maintainability. A judicious combination of hardwired and computer based I&C systems, state-of-the-art design, manufacturing processes and testing were employed in the design of I&C systems. The systems developed include safety critical, safety related and non safety I&C systems. The prototype systems were qualified after rigorous environmental, EMI/EMC and seismic testing. The application software developed was subjected to thorough Verification & Validation procedures. The group is also developing a full scope replica type Operator Training Simulator for PFBR. An advanced visualization centre was established and various PFBR systems are modeled for visualization in 3D and walkthrough. R&D activities in the areas of innovative instrumentation using pulsating sensors, Wireless Sensor Networks for use in future reactors, computational intelligence, knowledge management etc. are in progress. State-of-the-art computational facilities with a total processing power of about 30 tera FLOPS and data communication facilities are being provided. To take care of the security challenges the security electronics systems are constantly deployed and upgraded. Currently indigenous I & C components are being developed for import substitution to minimize the cost of the future FBRs with improved safety. The group is also responsible for providing quality assurance/quality control services for all the major projects being undertaken by IGCAR through the ISO 9001-2008 certified Quality Assurance Division. The Radiological Safety Division of the Group is responsible for R&D activities in the areas of radioactivity transport and improving the radiation detection and measurements through advanced techniques. This Division provides health physics and radiation safety services for the radioactive facilities in IGCAR. An Aerosol Test Facility (ATF) was established to study the characteristics of sodium aerosols generated in fast reactor in various scenarios. Whole Body Counting, Nuclear Counting, TLD Personnel monitoring, HEPA-Filter Test facility, Bio-assay, Bio-dosimetry, Waste Inspection Tomography are some of the facilities catering to the health physics services to all the facilities at the centre. An Online Nuclear Emergency Response System (ONERS) was indigenously developed for the Kalpakkam site for decision support during nuclear emergencies by implementing the numerical weather forecast and dispersion models in operational mode and by setting up meteorological towers and environmental gamma dose monitors at the site with real-time data access. An early warning system based on state of art operational weather forecast models was also implemented for cyclone emergency preparedness and disaster management. Environmental and Industrial Safety Division provides industrial safety services to all the facilities at IGCAR. This Division also carries out R&D in the domain of aquatic and terrestrial biodiversity and sediment characterization. The Group organizes public awareness programmes on radiation safety and nuclear energy in addition to training and awareness programmes on industrial, radiation and fire safety to occupational workers.

Engineering Services Group

Shri A. Jyothish Kumar
Director, ESG

Shri B. Harikrishnan
AD, CEG & Head, CMWD

Shri C. Chandran
Head, AC&VSD

Shri G. Kempulraj
Head, CWD

Shri K.P. Kesavan Nair
Head, ESD

Shri N. Suresh
Head, CED

Shri H.R. Sridhara
Head, ASED

The Engineering Services Group (ESG) is responsible for providing quality services and activities pertaining to Civil engineering, Electrical Engineering, Voice Communication Systems, Air-conditioning and Ventilation Systems, Material Handling Equipments and Central Workshop activities. The group also coordinates the BSNL requirements of the Centre. The group has a mandate to establish additional infrastructure requirements so as to meet Design, R&D and operational objectives of IGCAR. The group has expert teams with capability to design, engineer and execute systems under their jurisdiction. Electricity, water, quality-air and other services including services from Central Workshop are being extended to other units of DAE located at Kalpakkam. The nature of work involves interaction with several State Government and Central Government Organisations. AC&VSD is responsible for providing reliable air-conditioning and ventilation services to various radioactive laboratories and R&D facilities of the Centre.

Fast Reactor Fuel Cycle Facility

Dr A. Ravishankar
Project Director

Shri Anupam Sharma
CE & AD, Constn.

Shri B. Anandapadmanaban
AD, QA

Shri B. M. Anandarao
AD, HCSPG & DFE

Shri C. Sudhakar
Head, B&PD

Shri K Rajan
Head, RPDD

Fast Reactor Fuel Cycle Facility is entrusted with the work of planning, designing, constructing and commissioning the Fast Reactor Fuel Cycle Facility to close the fuel cycle of PFBR. FRFCF is a multi unit project involving BARC, IGCAR and NFC. IGCAR is piloting the construction of FRFCF. The Group continuously interacts with the participating groups from different units of DAE. Having completed the initial part of its mandate of coordinating the activities related to design of the facility, obtaining regulatory and statutory approvals of the project, preparation of the detailed project report, processing and obtaining financial sanction and developing all the infrastructure of the project, the group is currently engaged in the later part of its mandate, namely, the construction and commissioning of FRFCF. Construction of several infrastructural buildings is in progress while the construction in the nuclear island is about to start after completing the deep excavation activity needed for laying the foundation of various plant buildings with seismological design. Successful commissioning of FRFCF is an essential step for embarking on construction of second stage nuclear power plants based on plutonium fuel that would pave the way for achieving energy security for the Nation.

The Hot Cell Systems and Projects Group (HCSPG) is responsible for the design, development and manufacturing of various hot cell systems, head end equipments and different types of remote handling systems required for radiological facilities in particular to Fast Reactor Fuel Reprocessing Plants. The group is also involved in the design, development and manufacturing of special equipments such as laser based fuel sub-assembly dismantling machine, multi fuel pin chopper, electrolytic titanium dissolver, feed clarification equipments, centrifugal extractors, robotic based sampling system, etc., for deployment in fast reactor fuel reprocessing plants.

Fast Reactor Technology Group


Shri K.K. Rajan
Director, FRTG


Shri B. Babu
Head, IDSD


Shri B.K. Nashine
Head, DDRSD


Shri G. Padmakumar
Head, SEHD & CTD


Shri V. Prakash
Head, VDD

Fast Reactor Technology Group (FRTG) has the mandate of development and testing of reactor components of FBRs. The group is responsible for the engineering development and testing in air, water and sodium of many components of PFBR. Design validation of critical components of FBRs are achieved through experiments in sodium and in water using full scale/scaled down models. FRTG has acquired expertise in the development of sensors and devices for sodium application, such as- EM flow meters, level probes, leak detectors, cold traps and electromagnetic pumps. The group is entrusted with the responsibility of engineering development towards scaling up of pyro processing techniques from laboratory to engineering scale and setting up of engineering scale facilities which is in progress. Expertise has been developed in sodium handling in the design, construction, commissioning and operation of high temperature sodium systems. The major sodium test facilities of FRTG include 5.5 MWt Steam Generator Test Facility (SGTF) for testing the model steam generators of FBRs, SADHANA loop for experimentally demonstrating natural convection based safety grade decay heat removal system of FBRs, Large Component Test Rig (LCTR) for testing critical full scale FBR components, In Sodium Test facility (INSOT) for creep and fatigue testing of advanced materials and Sodium Water Reaction Test (SOWART) facility to study self wastage and impingement wastage of SG tubes. Recent achievements of FRTG towards PFBR include qualification and testing of reactor components like Inclined Fuel Transfer Machine (IFTM), Transfer Arm(TA), under sodium ultrasonic scanner, design, fabrication and qualification of extended spark plug type leak detector, in-sodium calibration of permanent magnet flowmeters and sodium testing of RADAR level probes, in-situ regeneration of Cold trap and experiments on gas bubbles detection in sodium. , FRTG is also involved in the developmental efforts towards improving the economics and enhancing the safety of future FBRs. The fabrication of integrated cold trap for in-vessel purification, development of model sweep arm scanner, integrated testing of Stroke Limiting Device with CSRDM, development of in-sodium pressure measurement device, high temperature ultrasonic transducer and ex-vessel level probe for sodium applications are some of the activities that arepursued for future FBRs. Major activities currently being pursued in FRTG include development of SONAR device for subassembly vibration measurement, conduct of high temperature tribology and thermal striping experiments for evaluating FBR component materials and design. Fabrication and erection of sodium test facilities namely Sodium Facility for Component Testing in Engineering Hall-I and Sodium Technology Complex are in progress. In Engineering Hall-IV, fabrication and erection of 5/8 scale sector model for hydraulic studies and facility for conducting FIV tests on seven subassembly cluster are completed.

Materials Science Group

Dr. G. Amarendra
Director, MSG

Dr. B.K. Panigrahi
Head, MPD

Dr. B.V.R. Tata
Head, CMPD

Dr. A.K. Tyagi
Head, SND

The Materials Science Group (MSG) has the mandate of pursuing high quality basic research on topical problems in Materials Science relevant to fast reactors and the group comprises of three divisions. The Condensed Matter Physics Division focuses on the investigation of structure and physical properties of materials under extreme conditions such as high pressures, low temperatures, high temperatures and high magnetic fields. Active research programs related to the use of Raman Spectroscopy for studies of vibrational properties of materials, use of Dynamic Light Scattering and Confocal Microscopy for studies on soft condensed matter, use of laser heated diamond anvil cell facility for synthesis of materials under high pressures and high temperatures and investigations on physical properties of novel materials at low temperatures, high magnetic fields and high pressures are being pursued. Several SQUID based measuring systems such as high field SQUID magnetometer, SQUID VSM, SQUID based set-up for Non-Destructive Evaluation (NDE), and multichannel SQUID based systems for Magneto-cardiography (MCG) and Magneto-encephalography (MEG) have been successfully designed and assembled. The Materials Physics Division focuses on studies on Ion beam simulation of radiation damage using a 1.7 MV tandem accelerator, studies on defects using Positron Annihilation Spectroscopy and Computer simulation of material properties. Several nuclear techniques such as Time Differential Perturbed Angular Correlation (TDPAC), Auger Electron Spectroscopy, Mossbauer Spectroscopy etc. have been used for the study of condensed matter, while positron beam set-up is used for depth resolved studies of defects. The Surface and Nanoscience Division focuses on studies on thin films, multilayers and hard coatings using a variety of techniques such as Secondary Ion Mass Spectrometry, nanomechanical testing and Scanning Probe Microscopy. Research activities relating to sensors based on nanomaterials, micromachined cantilevers and MEMS are being pursued.

Metallurgy and Materials Group


Dr. A.K. Bhaduri
Director, MMG


Dr. U. Kamachi Mudali
AD, CSTG


Dr. M. Vijayalakshmi
AD, PMG


Shri Jojo Joseph
Head, PIED


Dr. Saroja Saibaba
Head, MTPD


Dr. K. Laha
Head, MMD


Shri E. Mohandas
Head, MSSCD


Dr. B. Purna Chandra Rao
Head, NDED


Dr. Shaju K. Albert
Head, MTD


Dr. S. Murugan
Head, RHIERD


Dr. C. Mallika
Head, CSTD

The Metallurgy and Materials Group (MMG) of IGCAR has been nurturing a vibrant research and development programme which is targeted to provide a comprehensive knowledge-base and active support to a variety of materials related issues of India's sodium cooled fast reactors (SFR) agenda and associated closed fuel cycle activities. In the recent past, MMG has made major strides towards the successful development of three generations of nuclear structural materials aimed at withstanding demanding operating and environmental conditions. A few notable among them include: swell-resistant austenitic and high Cr-based ferritic steels, especially the oxide dispersion strengthened (ODS) variety for SFR core components. Besides, MMG is also involved in the development of an array of novel application specific or functional materials such as ferroseals for sodium pumps, ferroboron for meeting the requirement of cheap and alternate neutron shield material, iron based soft magnetic alloy for control rod applications and corrosion resistant materials, coatings for aqueous and pyrochemical reprocessing applications. In addition, MMG has also pioneered the design, fabrication and in-pile testing of irradiation capsules. Extensive post irradiation examination facilities established have been effectively utilized for obtaining extremely valuable data on the in-pile performance of various fuels, structural and shielding materials. In an allied perspective, MMG has immensely contributed towards developing a spectrum of nuclear application specific non destructive evaluation (NDE) techniques for inspecting and qualifying large sized and intricate reactor components. The human resource expertise of MMG is one of a balanced and unique blend of experienced and energetic talents, whose specialty touches almost all branches of theoretical and experimental aspects of materials science, component manufacturing & inspection-qualification technology. Mention must be made of MMG's contribution on the development of advanced welding techniques for joining special materials with tight control over process parameters and ensuring component integrity, automated and robotic systems for remote inspection of critical nuclear engineering components as well as for post irradiation examination facilities. On the theoretical front, robust modelling protocols for predicting high temperature phase stability, thermophysical properties, deformation behavior and mechanical properties of materials under various loading conditions etc. are also being pursued by MMG. It is not an exaggeration to say that MMG houses a truly sprawling and state of the art materials characterization and testing facilities that have been put into adroit use for catering to the materials developmental issues of not only fission and fusion nuclear reactors; but also for the advanced ultra super critical (AUSC) power plant programme. Besides, availability of top quality technical expertise has made it possible to attract many a young brain to pursue their research programmes at MMG under the banner of Homi Bhabha National Institute.

Reactor Design Group

Shri G. Srinivasan
Director, RDG

Shri P. Puthiyavinayagam
AD,CDG

Shri P. Selvaraj
AD, RAG

Ms. S. Usha
AD, PPG

Shri V. Balasubramaniyan
Head, RCD

Dr. K. Devan
Head, RND

Shri A. John Arul
Head, RSDD

Shri B.K. Nashine
Head, SED

Shri S. Raghupathy
Head, CH & MD

Shri N. Theivarajan
Head, PPCD

Dr. K. Velusamy
Head, MHD

The Reactor Design Group (RDG) is responsible for analysis of FBR power plant systems, design and development of components including core, shutdown, handling mechanisms and balance of plant. The group is responsible for getting safety clearance from Atomic Energy Regulatory Board (AERB). The group comprises of Core Design Group (CDG), Reactor Analysis Group (RAG), Power Plant Group (PPG), Reactor Components Division (RCD) and Component Handling & Mechanism Division (CHMD). The group also executes R&D in the domain of structural mechanics, thermal hydraulics and safety engineering, involving national and international institutions. It provides design support to the construction and commissioning of 500 MWe Prototype Fast Breeder Reactor (PFBR), which is under construction at Kalpakkam. It also provides analytical support to other groups in the Centre including Fast Breeder Test Reactor (FBTR) as well as for other strategic and high end technologies in the country. The responsibility of the group includes developing high quality human resource for the design and analysis of SFRs in the country. It is currently engaged in conceptualizing as well as detailing the innovative reactor components for the reactor assembly of future SFRs. The group has about 145 scientists and engineers. These apart, it has a modern design office with many advanced modeling and analysis softwares, Structural Mechanics Laboratory (SML) having state-of-the-art facilities for carrying out tests on large components, high temperature structural integrity and seismic tests with large sized shake tables and safety research laboratory (SRL) for carrying out tests in the domain of severe accidents and to study the science & technology of sodium fires and fire extinguishers. This group has expertise in the domain of design of mechanisms operating in sodium, mechanical design and analysis of components as per the American (ASME) and French (RCC-MR) design codes, thermal hydraulics of liquid metal, plant dynamics etc. The group is periodically providing design supports to other national mission projects, especially in space and other energy sectors.

Reprocessing Group

Dr. S.A.V. Satya Murty
Director, RpG

Dr. U. Kamachi Mudali
AD, MPEDG

Shri V. Vijayakumar
AD, RPOG & Head, RPOD

Shri B. Krishnamurthy
Head, RpMD

Dr. C. Mallika
Head, RRDD

Shri K. Rajan
Head, FRPD

The success of Indian Fast Breeder Reactor (FBR) programme depends on closing the fuel cycle within a short period so that the inventory of fissile material outside the reactor can be as small as possible. The Reprocessing Group (RpG) of IGCAR is responsible for achieving this objective. Various activities pertaining to fast reactor fuel reprocessing technology such as the design, construction and operation of the reprocessing plants are being undertaken by this Group. Facilities are available to carry out extensive engineering scale testing of equipment and systems before installation in radioactive hot cells. Chopper, dissolver, feed clarification equipment, centrifugal extractors and different types of pulse columns are few important equipment that are being developed for deployment in fast reactor fuel reprocessing plants. Apart from equipment development, research is focused towards understanding and solving various process, chemistry and analytical problems relevant to fast reactor fuel reprocessing such as process flow sheet studies to improve the plant performance for higher recoveries and reduced waste generation, mathematical modeling of solvent extraction of the complex U-Pu system, solvent extraction kinetics of troublesome fission products, solvent management, development of alternate solvent-diluent systems, development of online monitoring of Pu for process control, liquid flow metering in high radioactive fields, development of material handling equipment inside the hot cells, etc. In one of the hot cell facilities, uranium was recovered from irradiated thorium rods using THOREX process which is used as fuel in KAMINI reactor and in FBTR (as PFBR test fuel). The hot cell facility, called CORAL (Compact facility for Reprocessing Advanced fuels in Lead cells) commissioned in 2003, is being deployed as a versatile test bed for validating the process flow sheet and scaling up of equipment designs for fast reactor fuel reprocessing, by processing the FBTR spent fuel. This experimental facility has been used for reprocessing several batches of mixed carbide fuels irradiated in FBTR with 25, 50, 100 and 155 GWd/t burn-ups. This has provided valuable experience to the design of Demonstration Fast Reactor Fuel Reprocessing Plant (DFRP) in which mixed carbide and oxides of different compositions will be reprocessed on a regular basis. DFRP is also designed to reprocess PFBR fuel sub-assemblies for demonstrating the reprocessing of irradiated PFBR oxide fuels. In addition to these activities, RpG is carrying out the design of the reprocessing plant, for reprocessing the spent fuels of PFBR on commercial basis and is also involved in the development of aqueous reprocessing method to reprocess metallic spent fuels of commercial breeder reactors, as an alternate to pyro-chemical process.

Reactor Operations and Maintenance Group

Shri G. Srinivasan
Director, ROMG

Dr. S. Anthonysamy
Project Manager, DFMF

Shri K.V. Suresh Kumar
AD, OMG

Shri S. Varatharajan
AD, TTG & Head, TSD

Shri A. Babu
Head, RMD

Shri N. Kasinathan
Head, RAD

Shri G. Shanmugam
Head, ROD

The Reactor Operation and Maintenance Group (ROMG) is responsible for safe operation of Fast Breeder Test Reactor (FBTR) and KAMINI Reactor within the limits given in technical specification documents. The group also takes part in the operational safety review of PFBR Project documents. The Training section of the group is responsible for training the O&M staff of PFBR and future FBRs besides training O&M staff of FBTR and KAMINI. Progressive modifications in FBTR to increase its availability and for gaining newer experience in operation, utilizing the reactor for irradiation of advanced fuels and materials for fast reactors and conducting safety related experiments form a major part of ROMG's activities.

Resources Management Group

Dr. M. Sai Baba
AD, RMG & Head, SIRD/ SPHRDD

Resources Management Group comprises of the Scientific Information Resource Division, Strategic Planning and Human Resource Development Division and OCES-Training Section. The mandate of the Group is towards planning and management of resources like financial (budget), human and scientific information resources in the Centre. This significant activities of the Group include: Strategic planning and human resource management, Conducting the academic programmes of BARC Training school at IGCAR, Formulating and monitoring Capital projects towards budget planning and management including providing necessary reports and proposals to DAE, Automation and integration of activities pertaining to administration, accounts, stores, budget and procurement on a single platform, Coordinating the visits of important dignitaries and delegations to the Centre, formulating and facilitating collaborations and MoU including patents, Providing technical coordination with various agencies and conducting public awareness programmes for the benefit of public and media, Providing information resources through conventional library and the library on the desktop by digital networking with special emphasis to cater to the needs of students and young scholars and publishing important documents of the Centre like IGC Newsletter, Annual Report, Benchmarks, preparation of annual reports and plan related documents. This group also coordinates the facilitation of undergraduate and post graduate projects by students from various academic institutions, internships of students pursuing M.Tech. in Nuclear Engineering, summer schools of Harischandra Research Institute and BITS, and industrial visits of students from institutions on a continuous basis

Technical Co-ordination & Quality Control Division

Shri R.V. Subba Rao
Head, TC&QCD

Technical Co-ordination & Quality Control Division is primarily responsible for quality control and manufacturing process development of several critical equipments for IGCAR manufactured in the Western Region of the Country. It provides technical co-ordination services for the Centre with BARC as well as the Headquarters of DAE. TC&QCD also participates in a number of R&D activities which are being carried out at BARC towards meeting the mandate of IGCAR, PFBR and FRFCF. Some of the major contributions of TC&QCD in the recent years are QA of 800 mm thick SA 516 welding by SAW and its qualification as per RCC-MR, sodium to air heat exchanger, Analytical system robot & Sample handling robot, stainless steel in-cell crane, dry type transformers, power cables, instrumentation cables, MI heaters and PFBR Neutron Detector Assembly. TC&QCD is continuing to participate in the R&D activities for development of high temperature fission chambers, other neutron detectors for PFBR along with various divisions of BARC and ECIL, under sodium ultrasonic scanner, PIED scanner for pressure tube, sweep arm scanner and sputter ion pump development at BARC and inspection. Presently it is also engaged in the inspection of Glove Boxes and Fume Hoods being fabricated in bulk quantity for FRFCF and High Temperature Electro Refiner and salt purification system for Metallic Fuel Reprocessing activity.

Madras Regional Purchase Unit

Shri S.Paramasivam
RD, MRPU

Material Management activities for IGCAR, GSO, BARCF & HWP(T) are taken care of by Madras Regional Purchase Unit (MRPU) which comes under Directorate of Purchase & Stores of Department of Atomic Energy. Procurement and payment to suppliers are carried out at Chennai and inventory and accounting are carried out by Central Stores at Kalpakkam. MRPU was the first DAE unit to introduce e-tendering and more than 75% of files were processed by e-tendering mode in the e-tender portal www.tenderwizard.com/DAE. During the year 2015, MRPU processed about 3481 indents with an estimated cost of 500 Crores and released about 3290 purchase orders worth 285 Crores.

Administration & Accounts

Shri M. Raju
Internal Financial Adviser

Shri A.K. Vikraman Nair
Director (P&A)

Shri K.R.Sethuraman
AO(R&SR) & Secretary, IGCSC

LIST OF IMPORTANT ABBREVIATIONS

AC&VSD	Air Conditioning and Ventilation System Division
AERB	Atomic Energy Regulatory Board
A&SED	Architecture & Structural Engineering Division
BARC	Bhabha Atomic Research Centre
BARCF	Bhabha Atomic Research Centre Facilities
BHAVINI	Bharatiya Nabhikiya Vidyut Nigam Limited
BPD	Budget & Procurement Division
CD	Computer Division
CDG	Core Design Group
CED	Civil Engineering Division
CEG	Civil Engineering Group
CERMON	Continuous Environmental Radiation Monitoring Network
CFD	Chemical Facilities Division
CG	Chemistry Group
CTD	Chemical Technology Division
CH&MD	Components Handling & Mechanism Division
CMPD	Condensed Matter Physics Division
C&MWD	Contracts & Major Works Division
CORAL	Compact facility for Reprocessing Advanced fuels in Lead cell
CSTD	Corrosion Science & Technology Division
CSTG	Corrosion Science & Technology Group
CWD	Central Workshop Division
DDRSD	Device Development and Rig Services Division
DFMFF	Demonstration Facility for Metallic Fuel Fabrication
DFRP	Demonstration Fuel Reprocessing Plant
EID	Electronics and Instrumentation Division
EIG	Electronics and Instrumentation Group
EIRSG	Electronics and Instrumentation and Radiological Safety Group
EnSD	Environmental & Safety Division
ESD	Electrical Services Division
ESG	Engineering Services Group
FBR	Fast Breeder Reactor
FBTR	Fast Breeder Test Reactor
FChD	Fuel Chemistry Division
FRFCF	Fast Reactor Fuel Cycle Facility
FRPD	Fuel Reprocessing Process Division
FRTG	Fast Reactor Technology Group
HSCPG	Hot Cell Systems and Project Group & Design and Field Engineering
GSO	General Services Organisation
IAEA	International Atomic Energy Agency
IIT	Indian Institute of Technology
ID&SD	Instrumentation Development & Services Division
IMSc	Institute of Mathematical Sciences
I&CD	Instrumentation & Control Division
MAPS	Madras Atomic Power Station
MCD	Materials Chemistry Division
MHD	Mechanics & Hydraulics Division
MMD	Mechanical Metallurgy Division
MMG	Metallurgy and Materials Group
MPD	Materials Physics Division
MPEMD	Materials, Process and Equipment Development Group
MRPU	Madras Regional Purchase Unit
MSG	Materials Science Group
MSSCD	Materials Synthesis & Structural Characterization Division
MTD	Materials Technology Division
MTPD	Microscopy & Thermo-Physical Property Division
NDED	Non-Destructive Evaluation Division
NFC	Nuclear Fuel Complex
NICB	Nuclear Island Connected Building
NPCIL	Nuclear Power Corporation of India Ltd.
PFBR	Prototype Fast Breeder Reactor
PHWR	Pressurized Heavy Water Reactor
PIED	Post Irradiation Examination Division
PMG	Physical Metallurgy Group
PPCD	Power Plant Control Division
PPG	Power Plant Group
PDCG	Process Design & Commissioning Group
QAD	Quality Assurance Division
RAD	Reactor Analysis Division
RAG	Reactor Analysis Group
RCD	Reactor Components Division
RDG	Reactor Design Group
RIRD	Remote Handling, Irradiation Experiments and Robotics Division
RMD	Reactor Maintenance Division
RMG	Resources Management Group
RND	Reactor Neutronics Division
ROD	Reactor Operation Division
ROMG	Reactor Operation and Maintenance Group
RDD	Reprocessing Plant Design Division
RpMD	Reprocessing Maintenance Division
RpG	Reprocessing Group
RPOD	Reprocessing Plant Operations Division
RpOG	Reprocessing Operation Group
RRDD	Reprocessing Research and Development Division
RSD	Radiological Safety Division
RSDD	Reactor Shielding and Data Division
RSEG	Radiological Safety & Environmental Group
RTSD	Real Time Systems Division
SED	Safety Engineering Division
SE&HD	Sodium Experiments & Hydraulics Division
SGTF	Steam Generator Test Facility
SIRD	Scientific Information and Resource Division
SND	Surface and Nanoscience Division
SOWART	Sodium Water Reaction Test facility
SP&HRDD	Strategic Planning & Human Resource Development Division
TC&QCD	Technical Coordination & Quality Control Division
TSD	Technical Services Division
TTG	Technical & Training Group
VDD	Vibration Diagnostics Division

INDIRA GANDHI CENTRE FOR ATOMIC RESEARCH

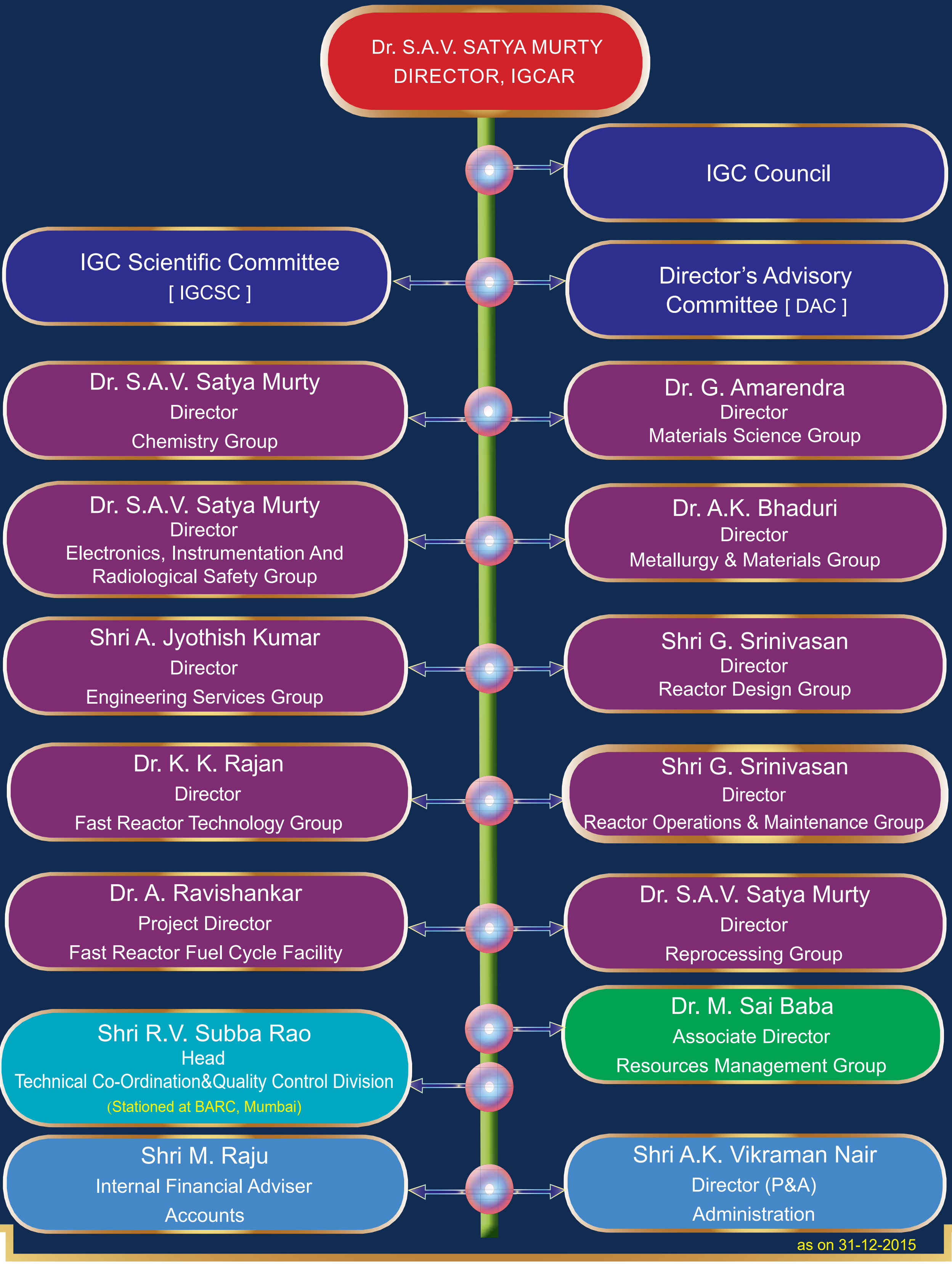

Dr. S.A.V. SATYA MURTY
DIRECTOR, IGCAR

IGC Council

IGC Scientific Committee
[IGCSC]

Director's Advisory Committee [DAC]

Dr. S.A.V. Satya Murty
Director
Chemistry Group

Dr. G. Amarendra
Director
Materials Science Group

Dr. S.A.V. Satya Murty
Director
Electronics, Instrumentation And Radiological Safety Group

Dr. A.K. Bhaduri
Director
Metallurgy & Materials Group

Shri A. Jyothish Kumar
Director
Engineering Services Group

Shri G. Srinivasan
Director
Reactor Design Group

Dr. K. K. Rajan
Director
Fast Reactor Technology Group

Shri G. Srinivasan
Director
Reactor Operations & Maintenance Group

Dr. A. Ravishankar
Project Director
Fast Reactor Fuel Cycle Facility

Dr. S.A.V. Satya Murty
Director
Reprocessing Group

Dr. M. Sai Baba
Associate Director
Resources Management Group

Shri R.V. Subba Rao
Head
Technical Co-Ordination&Quality Control Division
(Stationed at BARC, Mumbai)

Shri M. Raju
Internal Financial Adviser
Accounts

Shri A.K. Vikraman Nair
Director (P&A)
Administration

as on 31-12-2015

Groups / Divisions / Heads

Chemistry Group

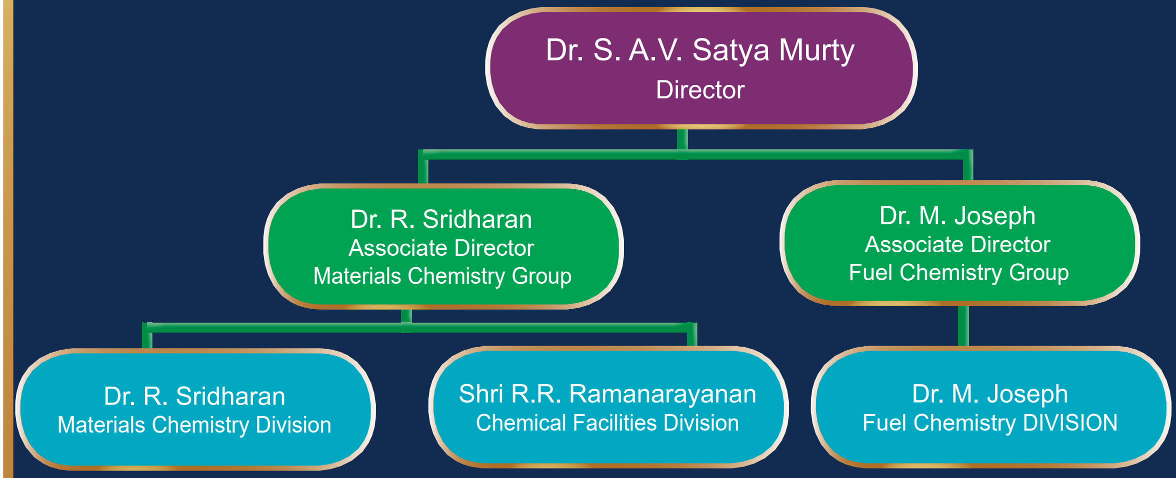

- **Dr. S. A.V. Satya Murty**
  Director
  - **Dr. R. Sridharan**
    Associate Director
    Materials Chemistry Group
    - **Dr. R. Sridharan**
      Materials Chemistry Division
    - **Shri R.R. Ramanarayanan**
      Chemical Facilities Division
  - **Dr. M. Joseph**
    Associate Director
    Fuel Chemistry Group
    - **Dr. M. Joseph**
      Fuel Chemistry DIVISION

Electronics, Instrumentation and Radiological Safety Group

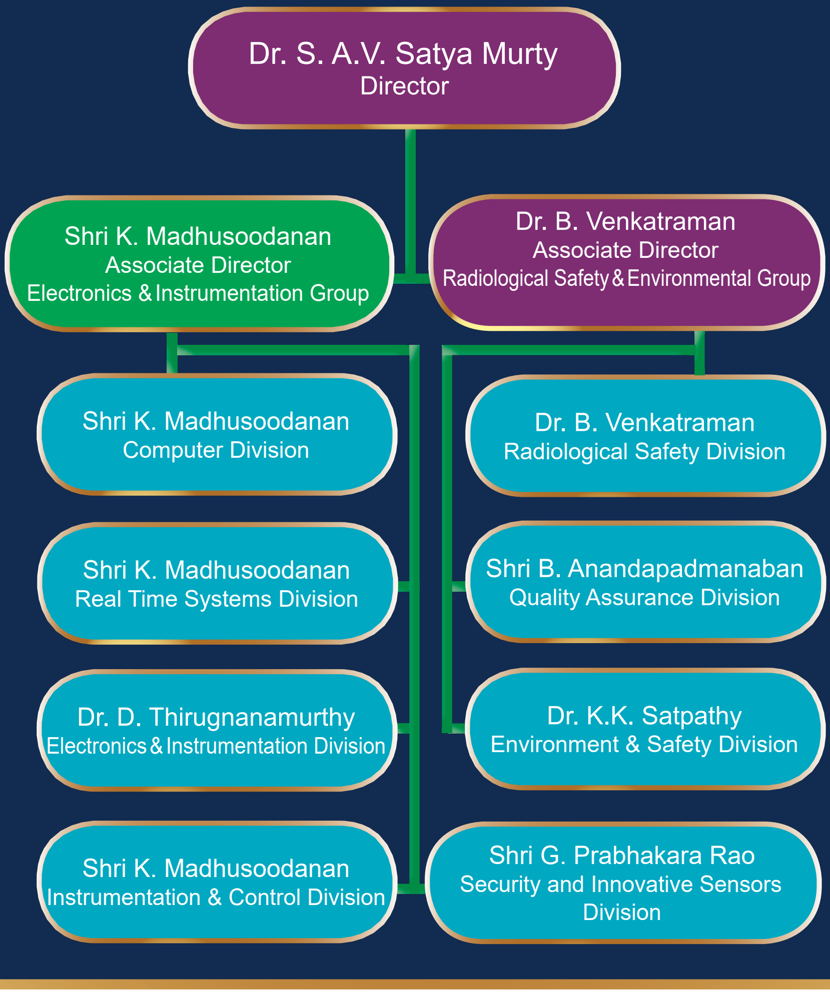

- **Dr. S. A.V. Satya Murty**
  Director
  - **Shri K. Madhusoodanan**
    Associate Director
    Electronics & Instrumentation Group
    - **Shri K. Madhusoodanan**
      Computer Division
    - **Shri K. Madhusoodanan**
      Real Time Systems Division
    - **Dr. D. Thirugnanamurthy**
      Electronics & Instrumentation Division
    - **Shri K. Madhusoodanan**
      Instrumentation & Control Division
    - **Shri G. Prabhakara Rao**
      Security and Innovative Sensors Division
  - **Dr. B. Venkatraman**
    Associate Director
    Radiological Safety & Environmental Group
    - **Dr. B. Venkatraman**
      Radiological Safety Division
    - **Shri B. Anandapadmanaban**
      Quality Assurance Division
    - **Dr. K.K. Satpathy**
      Environment & Safety Division

Groups / Divisions / Heads

Engineering Services Group

- Shri A. Jyothish Kumar
  Director
  - Shri K.P. Kesavan Nair
    Electrical Services Division
  - Shri G. Kempulraj
    Central Workshop Division
  - Shri C. Chandran
    Air-Conditioning & Ventilation System Division
  - Shri B. Harikrishnan
    Associate Director
    Civil Engineering Group
    - Shri N. Suresh
      Civil Engineering Division
    - Shri H.R. Sridhara
      Architecture & Structural Engineering Division
    - Shri B. Harikrishnan
      Contracts & Major Works Division

Fast Reactor Technology Group

- Dr. K.K. Rajan
  Director
  - Shri V. Prakash
    Vibration Diagnostics Division
  - Shri G. Padmakumar
    Chemical Technology Division
  - Shri B.K. Nashine
    Device Development & Rig Services Division
  - Shri G. Padmakumar
    Sodium Experiments & Hydraulics Division
  - Shri B. Babu
    Instrumentation Development & Services Division

Fast Reactor Fuel Cycle Facility

- Dr. A. Ravishankar
  Project Director
  - Shri B.M. Ananda Rao
    Associate Director, Hot Cell Systems and Projects Group & Design and Field Engineering
    - Shri K. Rajan
      Reprocessing Plant Design Division
  - Shri Anupam Sharma
    Associate Director
    Construction
  - Shri B. Anandapadmanaban
    Associate Director
    Quality Assurance
  - Shri C. Sudhakar
    Budget & Procurement Division

Materials Science Group

- Dr. G. Amarendra
  Director
  - Dr. B.V.R. Tata
    Condensed Matter Physics Division
  - Dr. B.K. Panigrahi
    Materials Physics Division
  - Dr. A.K. Tyagi
    Surface & Nanoscience Division

Groups / Divisions / Heads

Reactor Design Group

- Shri G. Srinivasan
  Director
  - Shri P. Puthiyavinayagam
    Associate Director
    Core Design Group
    - Dr. K. Devan
      Reactor Neutronics Division
    - Shri A. John Arul
      Reactor Shielding and Data Division
  - Ms. S. Usha
    Associate Director
    Power Plant Group
    - Shri N. Theivarajan
      Power Plant Control Division
  - Shri P. Selvaraj
    Associate Director
    Reactor Analysis Group
    - Dr. K. Velusamy
      Mechanics & Hydraulics Division
    - Shri B. K. Nashine
      Safety Engineering Division
  - Shri V. Balasubramaniyan
    Reactor Components Division
  - Shri S. Raghupathy
    Components Handling & Mechanism Division

Metallurgy & Materials Group

- Dr. A.K. Bhaduri
  Director
  - Dr. M. Vijayalakshmi
    Associate Director
    Physical Metallurgy Group
    - Shri E. Mohandas
      Materials Synthesis & Structural Characterization Division
    - Dr. Saroja Saibaba
      Microscopy & Thermo-Physical Property Division
  - Dr. U. Kamachi Mudali
    Associate Director
    Corrosion Science & Technology Group
    - Dr. C.Mallika
      Corrosion Science&Technology Division
  - Dr. B. Purna Chandra Rao
    Non-Destructive Evaluation Division
  - Shri Jojo Joseph
    Post Irradiation Examination Division
  - Dr. K. Laha
    Mechanical Metallurgy Division
  - Dr. Shaju K. Albert
    Materials Technology Division
  - Dr. S. Murugan
    Remote Handling, Irradiation Experiments and Robotics Division

Groups / Divisions / Heads

Reactor Operations & Maintenance Group

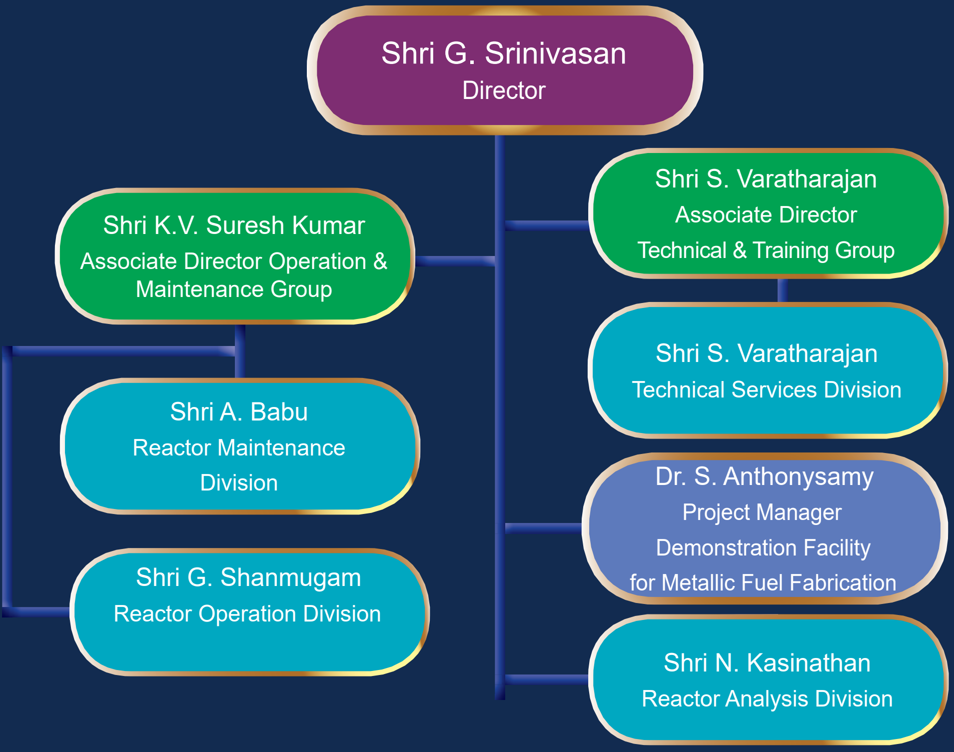

Shri G. Srinivasan
Director

Shri K.V. Suresh Kumar
Associate Director Operation & Maintenance Group

Shri A. Babu
Reactor Maintenance Division

Shri G. Shanmugam
Reactor Operation Division

Shri S. Varatharajan
Associate Director
Technical & Training Group

Shri S. Varatharajan
Technical Services Division

Dr. S. Anthonysamy
Project Manager
Demonstration Facility for Metallic Fuel Fabrication

Shri N. Kasinathan
Reactor Analysis Division

Reprocessing Group

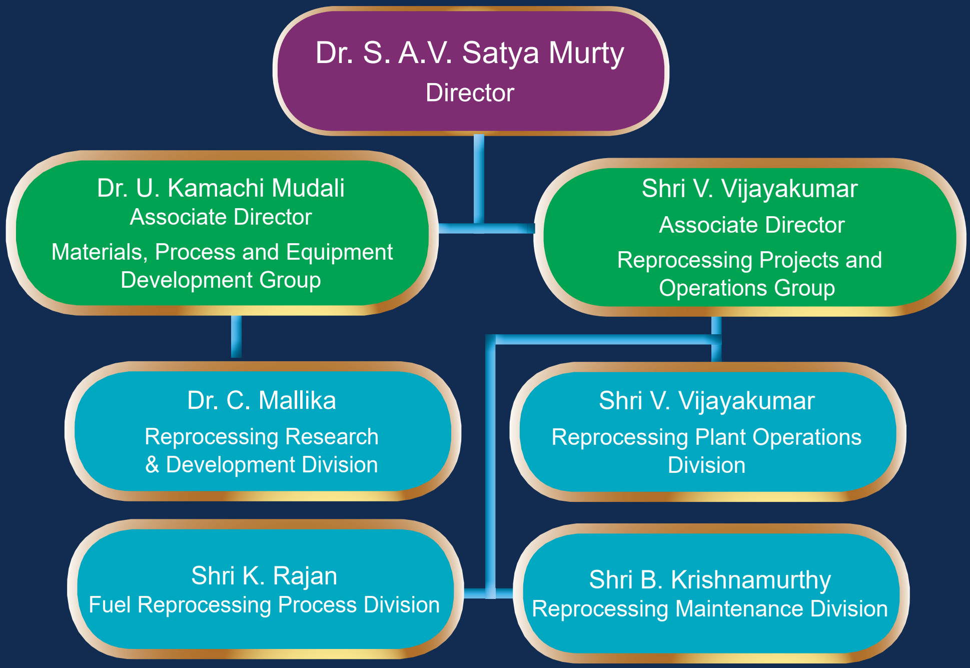

Dr. S. A.V. Satya Murty
Director

Dr. U. Kamachi Mudali
Associate Director
Materials, Process and Equipment Development Group

Dr. C. Mallika
Reprocessing Research & Development Division

Shri K. Rajan
Fuel Reprocessing Process Division

Shri V. Vijayakumar
Associate Director
Reprocessing Projects and Operations Group

Shri V. Vijayakumar
Reprocessing Plant Operations Division

Shri B. Krishnamurthy
Reprocessing Maintenance Division

Groups / Divisions / Heads

Resources Management Group

Dr. M. Sai Baba
Associate Director

Dr. M. Sai Baba
Strategic Planning & Human Resource Development Division

Dr. M. Sai Baba
Scientific Information Resource Division

Administration

Shri A.K. Vikraman Nair
Director (P&A)

Shri K.R. Sethuraman
Administrative Officer (R&SR)

Shri S.S. Boopathy
Administrative Officer (P)

Accounts

Shri M. Raju
Internal Financial Adviser

Shri T.M.G. Kutty
Deputy Controller of Accounts

Ms. S. Renganayaki
Pay & Accounts Officer







Published by Scientific Information Resource Division, IGCAR, Kalpakkam - 603 102